Modeling flood-induced processes causing Russell lupin mortality in the braided Ahuriri River, New Zealand

by

Luke A. Javernick

Thesis submitted for partial fulfillment of the requirements

for the degree of Doctor of Philosophy (PhD)

Civil and Natural Resources Engineering

University of Canterbury

2013

Table of Contents

Acknowledgments

The research presented in this thesis was possible due to the generous donations of time and expertise of many individuals as well as funding by the University of Canterbury and Department of Conservation's Project River Recovery.

My primary supervisor Brian Caruso was the reason that this research and opportunity were initially possible and his continued support, patience, and knowledge were more appreciated than words can express. While his expertise in this project was extremely valuable, his management abilities kept the project on track and sought the best, which led to the additional supervisors that were critical to this project's success. Co-supervisors included Tim Davies and James Brasington, and external-supervisor Murray Hicks. Tim Davies' input always provided a unique perspective to assess issues and regularly pushed my knowledge and critical thinking. Further his attention to detail, commitment, and impressive rate of return were always motivating and appreciated.

While James Brasington is likely the busiest person I know, his endless patience and knowledge were instrumental during the initial design and organization of all river surveying data collection. Further, his ambition to push boundaries and utilize new and exciting methods drastically improved the quality of data as well as the contributions of this research. Finally, Murray Hicks affectively filled all gaps of this research with his extensive knowledge and experience. With numerous previous studies on braided river, morphology, and vegetation, his knowledge helped shape all aspects of this research. Further, Murray's efforts in organizing my training in Delft3D were invaluable to this research.

In addition to official supervisors, the contributions of Paul Bealing, Chris Woolmore, and Richard Measures should qualify them as supervisors. Requiring RTK-GPS equipment, training, and software, Paul's patience and continuous help improved the efficiency of this project. However, Paul went above and beyond his obligations and generously offered his time for extensive field work and only moderately complained while carrying a dinghy through a 500 m stretch of heavily vegetated floodplain. Chris Woolmore's extensive knowledge of the Upper Waitaki Basin's braided rivers fauna and flora was very helpful

during the early proposal stages of this research. However, his continued support in organizing field data collection and postponing herbicide spraying within the study site were critical to the projects results and validity. With little experience in numerical modeling, I needed a crash-course in everything modeling. Thankfully, Richard Measures provided excellent initial training and graciously offered continuous support and trouble-shooting advice that were paramount to this research's success.

Throughout this research, numerous custom fabricated tools and apparatuses were required and built by the creative and talented minds of Alan Stokes, Russell McConchie, and Graham Furniss. I would like to thank Dave Conder for helping me organize, plant, and transport cultivated lupins necessary for experiments. Also, I would like to thank Peter McGuigan, David MacPherson, and Justin Harrison for their help in organizing field safety and supplies often with short notice. Lastly, but of most importance I would like to thank my wife Tiffany who's encouragement, patience, and love have helped me succeed in all aspects of my life.

Abstract

The braided rivers and floodplains in the Upper Waitaki Basin (UWB) of the South Island of New Zealand are critical habitats for endangered and threatened fauna such as the black stilt. However, this habitat has degraded due to introduced predators, hydropower operations, and invasive weeds including Russell lupins. While conservation efforts have been made to restore these habitats, flood events may provide a natural mechanism for removal of invasive vegetation and re-creation of natural floodplain habitats. However, little is understood about the hydraulic effects of floods on vegetation and potential mortality in these dynamic systems. Therefore, this thesis analyzed the flood-induced processes that cause lupin mortality in a reach of the Ahuriri River in the UWB, and simulated various sized flood events to assess how and where these processes occurred.

To determine the processes that cause lupin mortality, post-flood observations were utilized to develop the hypothesis that flood-induced drag, erosion, sediment deposition, inundation, and trauma were responsible. Field and laboratory experiments were conducted to evaluate and quantify these individual processes, and results showed that drag, erosion, sediment deposition and inundation could cause lupin mortality. Utilizing these mortality processes, mortality thresholds of velocity, water depth, inundation duration, and morphologic changes were estimated through data analysis and evaluation of various empirical relationships.

Delft3D was the numerical model used to simulate 2-dimensional flood hydraulics in the study-reach and was calibrated in three stages for hydraulics, vegetation, and morphology. Hydraulic calibration was achieved using the study-reach topography captured by Structure-from-Motion (SfM) and various hydraulic data (depth, velocity, and water extent from aerial photographs). Vegetation inclusion in Delft3D was possible utilizing a function called ‘trachytopes’, which represented vegetation roughness and flow resistance and was calibrated utilizing data from a lupin-altered flow conveyance experiment. Morphologic calibration was achieved by simulating an observed near-mean annual flood event (209 $m^3 s^{-1}$) and adjusting the model parameters until the simulated morphologic changes best represented the observed morphologic changes captured by pre- and post-flood SfM digital elevation models. Calibration results showed that hydraulics were well represented, vegetation inclusion often improved the simulated water inundation extent accuracy at high flows, but that local erosion

and sediment deposition were difficult to replicate. Simulation of morphological change was expected to be limited due to simplistic bank erosion prediction methods. Nevertheless, the model was considered adequate since simulated total bank erosion was comparable to that observed and realistic river characteristics (riffles, pools, and channel width) were produced.

Flood events ranging from the 2- to 500-year flood were simulated with the calibrated model, and lupin mortality was estimated using simulation results with the lupin mortality thresholds. Results showed that various degrees of lupin mortality occurred for the different flood events, but that the dominant mortality processes fluctuated between erosion, drag, and inundation. Sediment deposition-induced mortality was minimal, but was likely under-represented in the modeling due to poor model sediment deposition replication and possibly over-restrictive deposition mortality thresholds. The research presented in this thesis provided greater understanding of how natural flood events restore and preserve the floodplain habitats of the UWB and can be used to aid current and future braided river conservation and restoration efforts.

Keywords: Braided rivers, invasive vegetation, Black Stilt, Russell lupins, digital elevation model, Structure-from-Motion, numerical modeling, trachytope, Delft3D

Deputy Vice-Chancellor's Office
Postgraduate Office

UNIVERSITY OF CANTERBURY
Te Whare Wānanga o Waitaha
CHRISTCHURCH NEW ZEALAND

Co-Authorship Form

This form is to accompany the submission of any thesis that contains research reported in co-authored work that has been published, accepted for publication, or submitted for publication. A copy of this form should be included for each co-authored work that is included in the thesis. Completed forms should be included at the front (after the thesis abstract) of each copy of the thesis submitted for examination and library deposit.

Please indicate the chapter/section/pages of this thesis that are extracted from co-authored work and provide details of the publication or submission from the extract comes:

Chapter 5 / Section 5.2 / Pages 117 – 181. Submitted to Geomorphology for publication in September of 2013. Co-Authors are J. Brasington and B. Caruso.

Please detail the nature and extent (%) of contribution by the candidate:

The candidate was first author on all publications and contributed 80%.

Certification by Co-authors:
If there is more than one co-author then a single co-author can sign on behalf of all
The undersigned certifys that:

- The above statement correctly reflects the nature and extent of the PhD candidate's contribution to this co-authored work
- In cases where the candidate was the lead author of the co-authored work he or she wrote the text

Name:	Signature:	Date:
Brian Caruso		10/10/13

Deputy Vice-Chancellor's Office
Postgraduate Office

UNIVERSITY OF CANTERBURY
Te Whare Wānanga o Waitaha
CHRISTCHURCH NEW ZEALAND

Co-Authorship Form

This form is to accompany the submission of any thesis that contains research reported in co-authored work that has been published, accepted for publication, or submitted for publication. A copy of this form should be included for each co-authored work that is included in the thesis. Completed forms should be included at the front (after the thesis abstract) of each copy of the thesis submitted for examination and library deposit.

Please indicate the chapter/section/pages of this thesis that are extracted from co-authored work and provide details of the publication or submission from the extract comes:

Chapter 5 / Section 5.2 / Pages 117-181. American Geophysical Union, 2012 conference proceedings. Co-Authors: B. Caruso, J. Brasington, D. M. Hicks, and T. R. H. Davies.

Please detail the nature and extent (%) of contribution by the candidate:
The candidate was first author on all publications and contributed 80%

Certification by Co-authors:
If there is more than one co-author then a single co-author can sign on behalf of all
The undersigned certifys that:

- The above statement correctly reflects the nature and extent of the PhD candidate's contribution to this co-authored work
- In cases where the candidate was the lead author of the co-authored work he or she wrote the text

Name:	Signature:	Date:
Brian Caruso		10/10/13

Deputy Vice-Chancellor's Office
Postgraduate Office

UNIVERSITY OF CANTERBURY
Te Whare Wānanga o Waitaha
CHRISTCHURCH NEW ZEALAND

Co-Authorship Form

This form is to accompany the submission of any thesis that contains research reported in co-authored work that has been published, accepted for publication, or submitted for publication. A copy of this form should be included for each co-authored work that is included in the thesis. Completed forms should be included at the front (after the thesis abstract) of each copy of the thesis submitted for examination and library deposit.

Please indicate the chapter/section/pages of this thesis that are extracted from co-authored work and provide details of the publication or submission from the extract comes:

Data of Chapter 5 / section 5.2 and Chapter 6 / Sections 6.4 and 6.5. American Geophysical Union 2013 conference proceedings. Co-Authors: B. Caruso, R. Measures, D. M. Hicks, and J. Brasington.

Please detail the nature and extent (%) of contribution by the candidate:
The candidate was first author on all publications and contributed 80%.

Certification by Co-authors:
If there is more than one co-author then a single co-author can sign on behalf of all
The undersigned certifys that:

- The above statement correctly reflects the nature and extent of the PhD candidate's contribution to this co-authored work
- In cases where the candidate was the lead author of the co-authored work he or she wrote the text

Name:	Signature:	Date:
Brian Caruso		10/10/13

List of Figures

List of Tables

List of Acronyms

- 2D: Two Dimensional
- 3D: Three Dimensional
- aDcp: acoustic Doppler current profiler
- AlfaBs: Transverse bed slope gradient
- AlfaBn: longitudinal bed slope gradient
- AMS: annual maximum series
- BSRP: Black Stilt Recovery Project
- CA: camera accuracy parameter
- MA: marker accuracy parameter
- PA: projection accuracy parameter
- CAESAR: Cellular Automaton Evolutionary Slope and River model
- $C_{D:}$ Drag coefficient
- DEM: Digital elevation model
- DGPS: Differential GPS
- DMVR: Dense multi-view stereo reconstruction
- DoC: Department of Conservation
- DoD: DEM of Difference
- ECNZ: Electricity Corporation of New Zealand
- $Fit_{congruent}$: Congruent water extent fit
- Fit_{We}: Effective width
- GCD: Geomorphic Change Detection software
- GCPs: Ground Control Points
- GEV: Generalized Extreme Value
- GOF: Goodness of Fit test
- GPS: Global Positioning System
- HEC-RAS: Hydrologic Engineering Center River Analysis System
- HEP: Hydro-Electric Power
- K: Eddy diffusivity
- k_s: Nikuradse roughness length
- LiDAR: Light Detection and Ranging
- LP3: Log Pearson 3 distribution
- MAE: Mean Absolute Error
- ME: Mean Error
- minLoD: Minimum Level of Detection
- MorFac: Morphological Acceleration Factor
- MVS: Mutli-View Stereo
- NIWA: National Institute of Water and Atmospheric Research
- NMEA: National Marine Electronics Association
- Pa: Pascals
- PRR: Project River Recovery
- RGB: Red, Green, Blue color imagery bands
- RMSE: Root Mean Squared Error
- RTK: Real Time Kinematic
- SDE: Standard Deviation Error
- SDU: Standard uncertainty
- SfM: Structure-from-Motion
- SfM+ToPCAT: SfM edited point cloud using ToPCAT
- SfM-Veg: SfM vegetation noise reduction using ToPCAT
- SGC: Sand, Gravel, and Cobble sediment composition
- SV: Spatially Varying error propagation
- SV 95%: SV with a threshold of 95% confidence interval
- SV 95% BU: SV 95% with Bayesian Updating
- TLS: Terrestrial Laser Scanning
- ToPCAT: Topographic Point Cloud Analysis Toolkit
- UWB: Upper Waitaki Basin

Part I

Thesis Context

Chapter 1

Thesis Introduction and Outline

1.1 Introduction and general problem statement

Braided rivers are complex systems of highly active multi-channeled reaches that traverse wide floodplains creating islands and bars through constant channel division and merging (Hughey & Warren, 1997; Carson & Griffiths, 1987 as cited by Warburton, Davies, & Mandl, 1993). There are two types of braided rivers found throughout the world. The most common form transverse bars in fine sediment and the second type form longitudinal bars in gravelly beds (Stephenson et al., 1983). Gravel-bed braided rivers flow from steep, rapidly eroding mountains and form relatively flat outwash surfaces (Hughey & Warren, 1997). Gravel-bed braided rivers occur around the world in such places as North America, Siberia, the Himalayas, Europe, and New Zealand (Stephenson et al., 1983; Rawlings, 1993). New Zealand has 163 braided rivers in 11 of the 14 administrative regions of the country; 94% are found in the South Island, 60% are in the Canterbury region, and 7% are within the Upper Waitaki Basin (UWB) (Wilson, 2001).

The UWB has an area of approximately 9,400 km^2 and is bounded to the west by the main divide of the Southern Alps and to the east by Lake Waitaki (Figure 1.1; Caruso, 2006). The UWB has 12 braided rivers due to its tectonic activity and high precipitation. The braided rivers of the UWB (from south to north) include, the Ahuriri, Ohau, Hopkins, Dobson, Pukaki, Tekapo, Tasman, Jollie, Murchison, Cass, Godley, and Macaulay rivers (Peat & Patrick, 2001) and occupy 32,308 hectares (ha) or river bed (Wilson, 2001). Uplift has been estimated up to 5 mm $year^{-1}$ throughout the Southern Alps of the South Island and along the western and northern UWB boundaries annual precipitation can reach up to 10,000 mm, rapidly eroding these mountains and the glacial and pro-glacial deposits (Beavan, et al., 2010; Kamp, 1992; Fitzharris et al., 1982, as cited by Williams and Wiser, 2004; New Zealand

Meterological Service, 1985 as cited by Caruso, 2006). The eroded sediment is washed downstream to the plains of the UWB. These deposits have minimal soil development, such as metamorphosed gleyed soils, and consist of coarse shist and greywacke to produce what appears to be a desolate landscape (DoC, 2000d). However, a closer investigation reveals a complex and thriving ecosystem (DoC, 1996; Peat & Patrick, 2001).

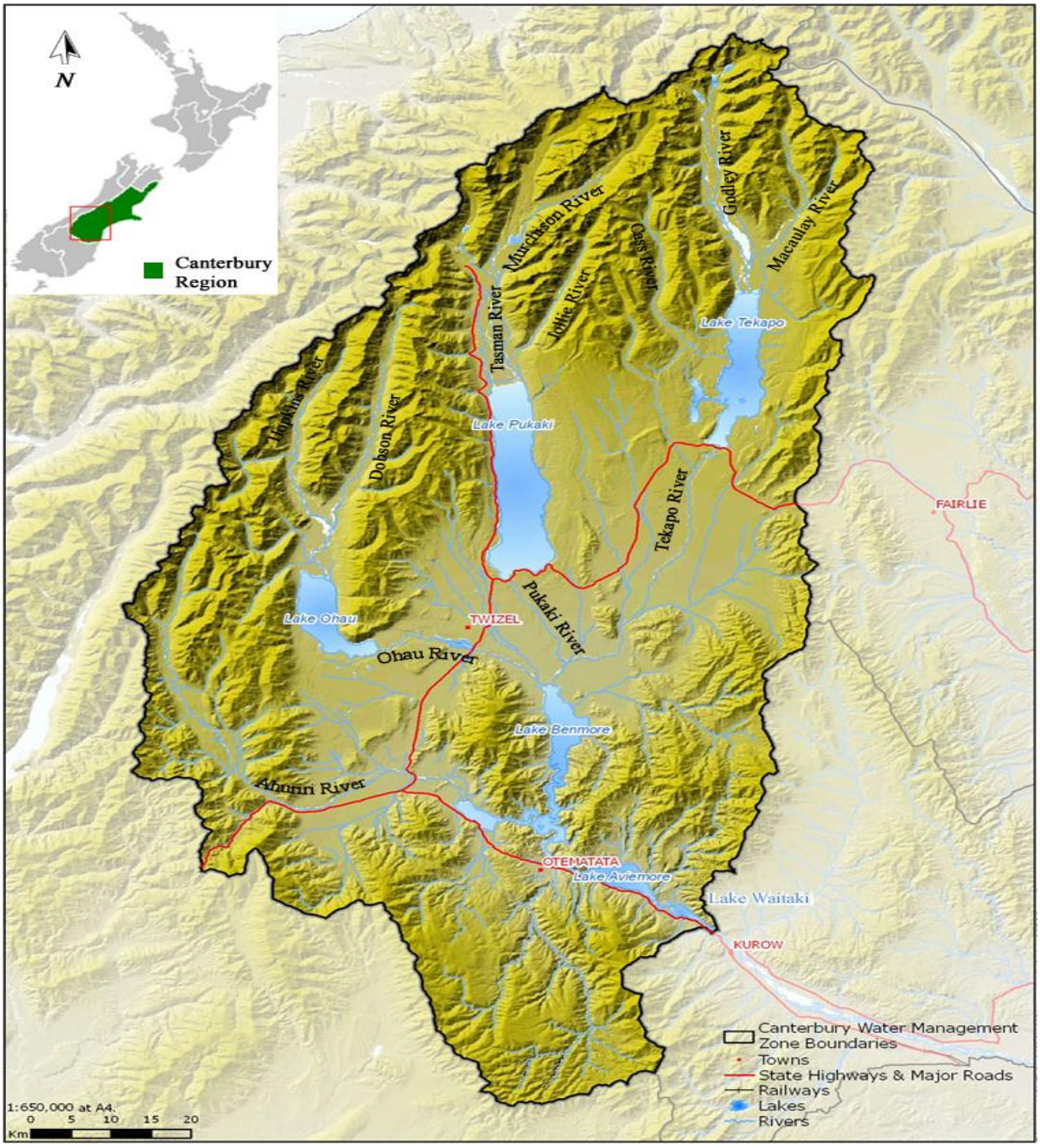

Figure 1.1: Upper Waitaki Basin (Environment Canterbury, 2013).

1.1.1 Vegetation

Compared to pre-human settlement, the vegetation in the UWB is very different today. Much of the UWB was once covered by forest that was later destroyed by fires (Wilson, 2001). Discoveries of large logs by European settlers in the UWB, charcoal remains, and soil and pollen samples indicate that totara trees (*Popocarpus totara*) and other small hardwood trees were likely the dominant species (Burnett 1927; Nordmeyer 1981; Challis 1995; as cited by Wilson, 2001). Early European settlers described the Mackenzie Basin as "an open, barren, desolate tussock land swept by all extremes of weather, just waiting to be tamed" (Rawlings, 1993, p. 14). While this area was described as 'barren,' it had diverse vegetation. Settlers recorded the UWB having tussock grasslands with Maori cabbage *(Bulbinella gibbsii var. balanifera*), blue grass (*Elymus solandri*), and barley grass (*Hordeum glaucum or H. murinum*). Burnett's documentation (as cited by Wilson, 2001) of the vegetation in the mountain valleys included Mount Cook lily (*Ranunculus lyallii*), *Matagouri (Discaria toumatou)* in the Tasman valley, and torokeo (*Corokia cotoneaster*) forest around Lake Ohau, and *Nothofagus spp*. forest in Dobson and Hopkins valleys. The riparian vegetation consisted of Discaria toumatou, blue Spaniard (*Aciphylla colensoi*), toetoe (*Carex geminata*) and tutu (*Coriaria sarmentosa*) *Coprosma spp*., manuka (*Leptospermum scoparium*) *Olearia spp*., *Hebe cupressoides*, Kowhai (*Sophora spp*.), Bog Pine (*Halocarpus bidwillii*), and ribbonwood (*Hoheria spp*.) (Burnett, 1927; Espi et al., 1984, as cited by Wilson, 2001). Islands in the rivers had patches of scrub consisting of Discaria Toumatou, Hebe cupressoides, Ribbonwoods (*Hoheria spp*.), Corokia cotoneaster, *Olearia spp*., *Coprosma spp*., Aciphlly squarrosa, and tussock (von Haast, 1879; Burnett, 1927; Elwell, 1978; & Robinson, 1983; as cited by Wilson, 2001).

Today the landscape of the UWB consists of large un-vegetated open gravel areas, the previously mentioned native vegetation species, and introduced exotic vegetation (Wilson, 2001). The Department of Conservation reported that 33% of the 395 plants recorded in the braided rivers of the UWB were exotic (Woolmore, 2003). Introduction of exotic vegetation started over a century ago when European settlers planted a range of species in the UWB for shelter, bank stabilization, and aesthetic reasons (DoC, 1996; Rawlings, 1993). While seemingly harmless at the time, these exotic species have altered the ecosystem by invading and affecting the critical habitats of endangered fauna (DoC, 2009). The species causing most

destruction are crack willow (*Salix fragilis*), broom (*Crsticis scoparius*), gorse (*Ulex europaeus*), and Russell lupin (*Lupinus polyphyllus*) (DoC, 1996; Rawlings, 1993).

Introduced for bank stabilization, willows are highly successful due to their ability to reproduce asexually and sprout from cut or damaged stems (Rawlings, 1993). These eventually separate from the parent and quickly establish roots allowing willows to spread rapidly (Rawlings, 1993). Russell lupins, introduced for aesthetics and purposely spread along roadsides (DoC, 2007), are even faster colonizers. Friend and Sanders (2000) recorded dense lupin stands to have a mean seed-fall of 754 seeds per square meter. In addition, lupin seedpods explode in the heat of summer, allowing lupins to spread a few meters each year on land, and even further if unprotected from wind or located near the river banks (DoC, 2007). While many plants cannot survive in the nutrient deficient soils of the UWB, lupins are nitrogen fixers allowing them to produce their own nitrogen and thrive (Peat & Patrick, 2001). These aggressive species have spread over much of the basin and are altering the riparian zone by accelerating bank and island accretion by trapping fine sediment. This results in higher banks and islands, and causes deeper and fast flowing river channels between the islands (DoC, 2009). Given the lupins' aggressive spread and ability to negatively alter the UWB river's habitats, this research will focus on Russell lupins.

1.1.2 Fauna

While much of the braided river habitat has been invaded by exotic vegetation, the UWB has 21,579 ha of open area habitat which is 14% of the national total (Wilson, 2001). Open areas and slow flowing channels of the braided rivers and wetlands are vital habitats for the basin's endangered bird, fish, and invertebrate species (Patterson, 2001). The fish and birds of the basins' wetlands and rivers feed on insects such as dobsonflies, mayflies, stoneflies, caddisflies, waterboatmen, giant dragonflies, red coat damselflies, and sandflies (Patterson, 2001). In addition, the land insects of the basin include the 'rediscovered' and endangered robust grasshopper (*Brachaspis robustus*), the alpine grasshopper (*Brachaspis nivalis*), and the minute grasshopper (*Sigaus minutes*) (Peat & Patrick, 2001; Patterson, 2001). Native braided river fish of the basin include six galaxiid species, bullies, and eels. The Lowland longjaw (*Galaxias cobhitinis*) is classified as critically threatened, and the Upland longjaw (*Galaxias prognathus*), Bignose galaxias (*Galaxias macronasus*), and Long Finned eel are

threatened. Additional native fish such as the Canterbury galaxias (*Galaxias vulgaris)*, Koaro (*Galaxias brevipinnis)*, and Alpine galaxias (*Galaxias paucispondylus*) are more common with no threat classifications (Peat & Patrick, 2001; C. Woolmore, personal communication, July 20, 2011). Introduced species of fish include rainbow trout, brown trout, quinnat salmon, and sockeye salmon (Patterson, 2001).

New Zealand has two types of lizard, skinks and geckos and both can be found in the UWB. Skinks and geckos occupy a wide range of landscapes from dry and rocky areas to forests. There are five skinks and two geckos: McCann's skink (*Oligosoma maccanni*), the common skink (*O. polychroma*), the long-toed skink (*O. longipes*), the Spotted skink (*O. lineoocellatum*), the Scree skink (*O. waimatense*), the Southern Alps gecko (*Hoplodactylus aff. Maculates* 'Southern Alps'), and the Jeweled gecko (*Naultinus gemmeus*) (DoC, 2009).

The rivers of the UWB provide as much as 50% of the bird habitat remaining on the South Island (Maloney, Rebergen, Nilsson, & Wells, 1997). In the last three decades, attention has been focused on the birds that utilize the UWB. Of the estimated 26 water bird species that inhabit this area at various seasons of the year, the birds of particular interest are the black stilt, (*Himantopus novaezelandiae*), the wrybill (*ngutuparore Anarhynchus frontalis*), the black-fronted tern (*tarapiroe Sterna albostriata*), the banded dotterel (*Charadrius bicinctus*), and black billed gulls (*Larus bulleri*) due to low populations and threatened classification (Peat & Patrick, 2001; Heppelthwaite, 1999; C. Woolmore, personal communication, July 20, 2011). These birds require un-vegetated gravel areas near shallow channels for nesting, feeding, and protection from predators; thus making the gravel braided rivers of the UWB an ideal habitat. These birds have developed specialized features to deal with the braided river habitat. For example, to cope with flooding and loss of nests, they can re-nest and lay a second clutch of eggs. Eggs and chicks are typically well camouflaged against the gravel. Finally, the wrybill is the only bird in the world that has a bill that is bent to the right, allowing it to find prey underneath riverbed stones (Maloney et al., 1997; Peat & Patrick, 2001; Patterson, 2001).

Even though these birds are well adapted for the braided river environment, they are under serious threat to the point that the black stilt is critically endangered and the black-fronted tern and wrybill are threatened species (Patterson, 2001). It has been estimated that 100% of

the remaining black stilts, 60% of the remaining black fronted terns, and 15% of the remaining wrybills utilize the habitat of the UWB (Brown & Sanders, 1999; Maloney et al., 1997). These species are threatened by the aggressive spread of exotic vegetation which alters their habitat and provides cover for predators (Peat & Patrick, 2001).

In addition to introducing exotic plants to New Zealand, settlers also introduced many animals for grazing, pest control, and game, and some by accident (DoC, 2000a; DoC, 2009). Examples are rabbits, sheep, red deer, possums, ferrets, stoats, cats, weasels, hedgehogs, rats, and mice (Sanders & Maloney, 2002; Patterson, 2001; DoC, 2009). While all of these have caused changes to the ecosystem in some way, none are as devastating to the UWB's birds as cats, ferrets, hedgehogs, and stoats. In a video surveillance study over a five year period in the Ohau and Tekapo Rivers between 1994 and 1999, 172 nests were monitored for predation. The results found that of the 138 nests that were targeted, the perpetrators were cats (43%), ferrets (19%), and hedgehogs (18%), totaling 80% of attacks on the birds, chicks, and eggs (Sanders & Maloney, 2002; Peat & Patrick, 2001). While this study identifies the dominant predators in the lower rivers, different predator guilds exist between the upper and lower rivers of the UWB. While the lower rivers are dominated by cats, ferrets, and hedgehogs, stoats are a key predator in the upper rivers of the UWB (C. Woolmore, personal communication July, 20 2011). These predators are highly successful, in part due to the introduced vegetation which crowds the birds' habitat, allowing predators to stalk undetected and predate the birds (DoC, 2009).

1.1.3 Hydro-electric power development

New Zealand was ranked the seventh (of 149) greenest country in the world by Yale University's in depth Environment Performance Index in 2008, and 15th (of 163) in 2010. These rankings were based on 25 'indicators,' three of which were based on greenhouse gas emissions and carbon intensity (Emerson et al., 2010). It should be no surprise that New Zealand excels in environmental stewardship when 73% of its electricity was produced by renewable energy resources in 2009. Hydro-electric power (HEP) is the largest contributor producing 55.6% of New Zealand's electricity with approximately 18.5% being produced by the eight hydro-electric power stations of the UWB (Electricity Authority, 2010).

The first public supply of hydro-electricity in New Zealand was in 1888 in the town of Reefton (Resources and Networks Branch, 2005). In 1904 the Waitaki Basin's hydro-electric potential was recognized by Mr. P. S. Hay, a Publics Works Department employee, but it would be another 34 years before the first power station was operational (Meridian Energy Limited, 2008). This was the Waitaki Dam completed in 1938. It was followed by the Tekapo Dam and Tekapo A power station in 1953, the Benmore Dam in 1965, the Aviemore Dam in 1968, the Tekapo B power station in 1977, the Ohau A Dam and power station in 1979, the Ohau B power station in 1984, and finally the Ohau C power station in 1985 (Meridian Energy Limited, 2008; Sheridan, 1995).

Throughout this time, modifications to the landscape were made for power generation. Four artificial lakes (Benmore, Aviemore, Waitaki, and Ruataniwha) were created by damming, and the three natural lakes (Tekapo, Pukaki, and Ohau) were altered by dams to increase their capacity. Lake Pukaki's level was raised twice: by 9 m in 1957 and by 37 m in 1976 (Sheridan, 1995). This second raising was critical to the overall function of the entire Waitaki power scheme because Lake Pukaki at 1951 levels was the lowest in elevation of the three natural lakes. In order to optimize the power generation, the elevation needed to progressively drop from Lake Tekapo, through Lake Pukaki, then to Lake Ohau (Palmer & Petrie, 1989). To further optimize power generation, water was also diverted from the natural rivers into a series of canals in order to minimize the water elevation drop (head loss) between power stations. In total, six canals totaling 56 km in length were constructed between the lakes and power stations as shown in Figure 1.2 (Meridian Energy Limited, 2008).

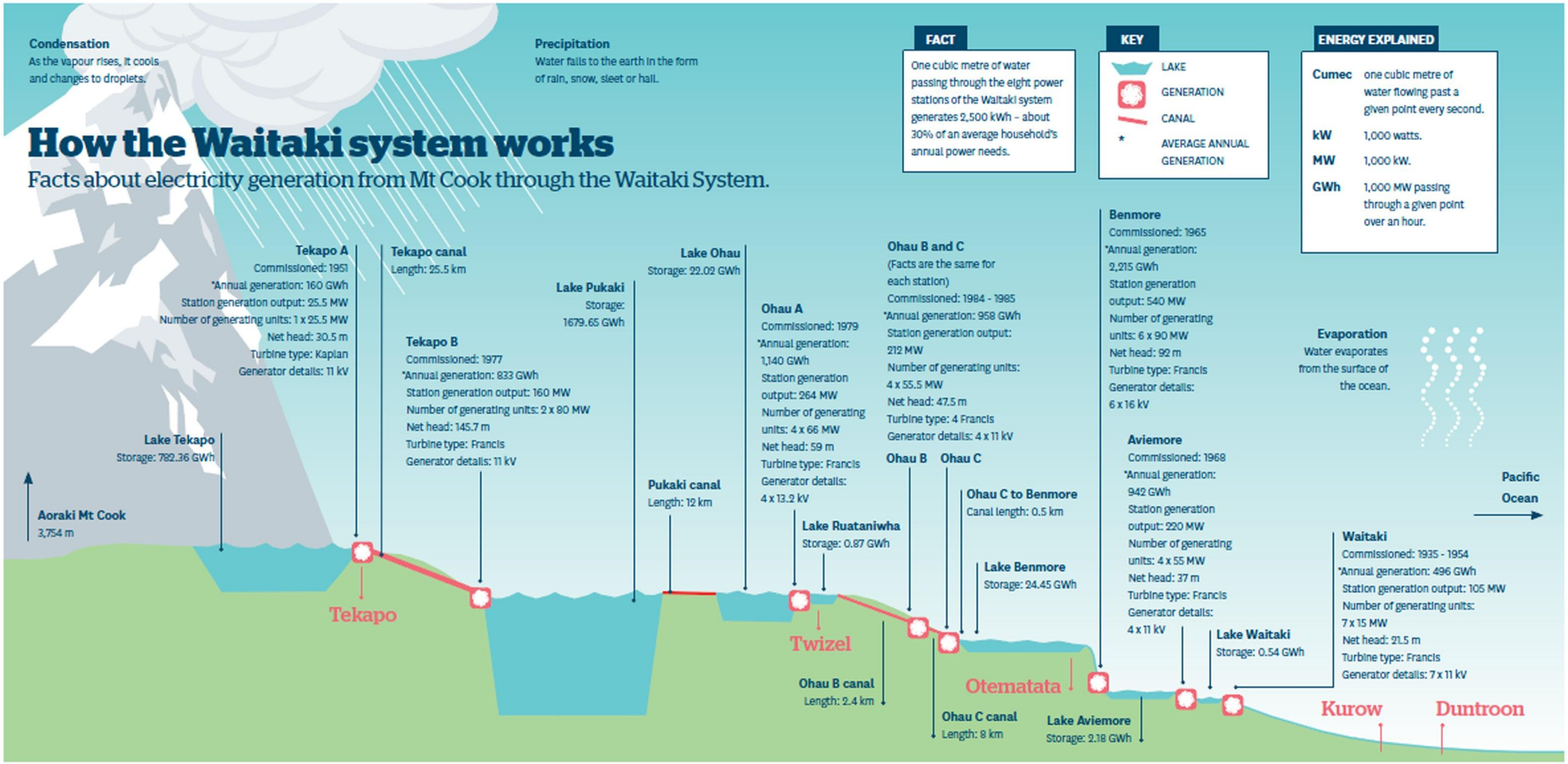

Figure 1.2: The Upper Waitaki Basin hydro-electric scheme (Meridian Energy Limited, 2008)

While HEP and its required landscape modifications have been invaluable to New Zealand's economy, they have had negative impacts on the ecosystem of the UWB. Damming in the UWB has produced an additional 22,264 ha (197% increase) of open water habitat and 288.2 km (245% increase) of shoreline. Inundation due to damming has reduced the braided river floodplain area (including wetlands) of the UWB by 12,537 ha (27.5%) and another 9,727 ha of surrounding land have been flooded (Wilson, 2001). Further, during typical, non-excess flows, 99.8% of the flow that would have occupied the Tekapo, Pukaki, and Ohau rivers now flows in the canals, resulting in 4,188 ha of dewatered braided river habitat (James, 1985, as cited by Wilson, 2001). Combining the dewatered rivers with the floodplain inundation, 16,688 ha (36.7%) of braided river habitat in the UWB has been lost. If the new lake area is included, then a grand total 26,452 ha of the UWB braided river habitat has been affected. These changes have been devastating to the previously mentioned endangered avifauna through habitat degradation (Palmer & Petrie, 1989 after communication with Dave Murray).

In addition to the canals altering flows of the higher-elevation rivers, the lower Waitaki River is affected by controlled releases from the dams. Flow produced during large snowmelt events and storms are stored in the lakes instead of producing natural floods. During the winter months when electricity demand is high, larger than natural flows are released for electricity generation (Palmer & Petrie, 1989). The reductions in naturally occurring flooding has reduced disturbance to the vegetation, which has encouraged the spread of the aggressive exotic plant species (Palmer & Petrie, 1989 after comm. with Mark Davis). These exotic plant species establish at a faster rate than the native species; resulting in fewer seed sources for the native plant species to re-colonize, and further accelerating the dominance of exotic vegetation (Meurk & Williams, 1989). This increased spread of vegetation has led to an improvement in predator habitat through increased cover and access to riverbed islands, the preferred nesting area of avifauna (Palmer & Petrie, 1989 after comm. with Dave Murray). Therefore, the reduced flows due to the HEP scheme increase the spread of invasive vegetation, which improves the habitat of introduced predators, thereby reducing the habitat and safety of the endangered bird species (Brown & Sanders, 2001). A conceptual model of these relationships is shown in Figure 1.3 (Caruso, 2006).

Of the twelve braided rivers of the UWB, the threatened and endangered bird species utilize the Ahuriri and the Cass rivers most often. These rivers are recognized as possessing the "highest wildlife value." The remaining rivers such as the Tasman and Ohau were also considered "important", and the Pukaki and Tekapo rivers possessed "lesser wildlife value" due to the heavy modification resulting from the HEP development (Caruso, 2006, p. 849). While the Ahuriri River retains a high conservation value, it is heavily affected and threatened by the spread of exotic vegetation (Maloney, 1999, as cited by Caruso, 2006).

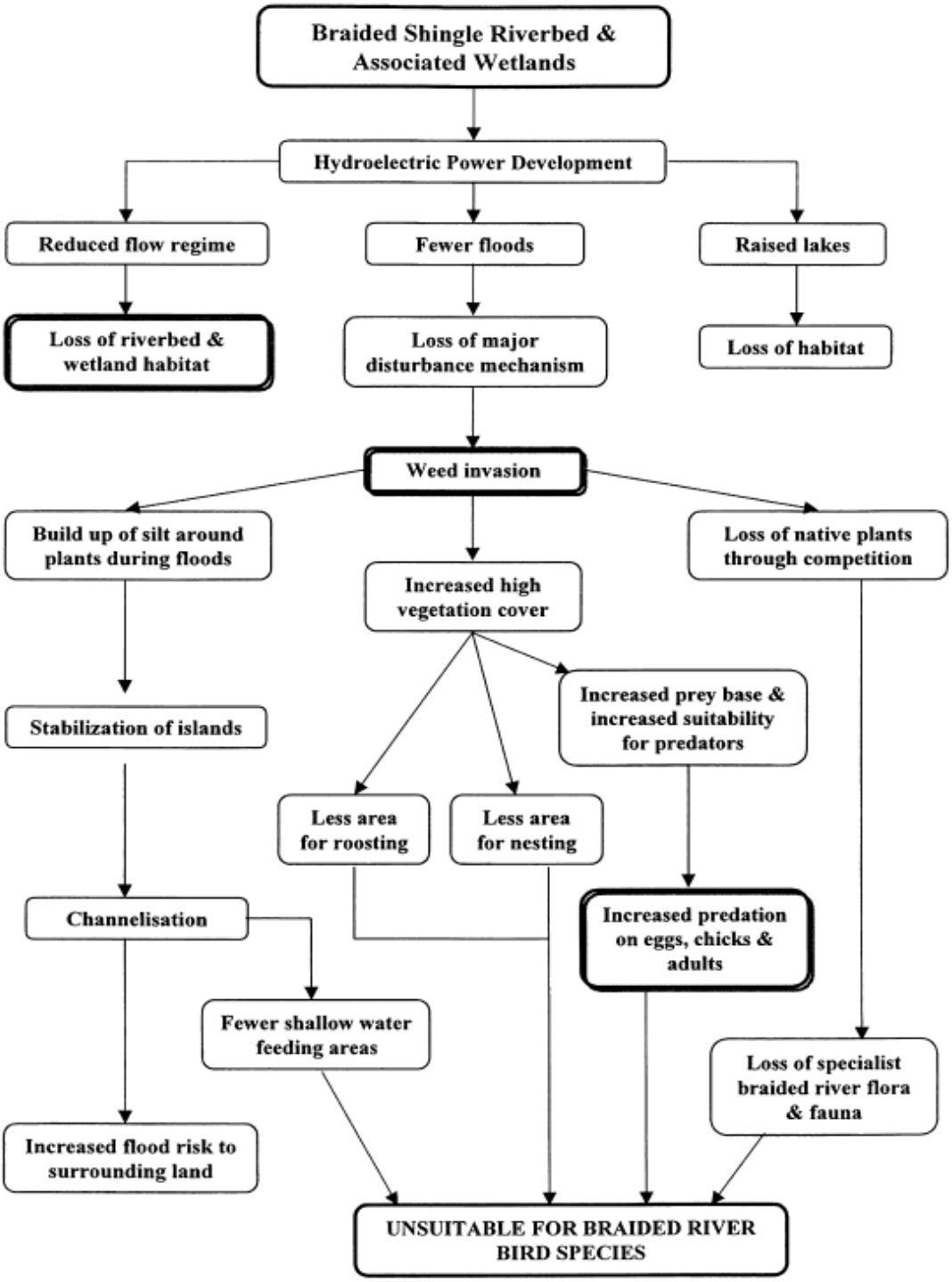

Figure 1.3: Conceptual model developed by Project River Recovery to illustrate relationships amongst HEP development, weed invasion, and endangered birds (as cited in Caruso, 2006).

1.1.4 Project River Recovery

To address these issues, the Department of Conservation's Project River Recovery (PRR) was established in 1990 and began operation in 1991. In 1988, 18 organizations formed the Waitaki Water Rights Working Party to discuss the water rights of the Electricity Corporation

of New Zealand (ECNZ, now replaced by Meridian Energy Limited), as the rights to use the water of the Waitaki Basin for power generation were due to expire in 1990. Various agreements were formed between the ECNZ and the working parties, one of which was between ECNZ and Department of Conservation (DoC) and focused on the effects caused by the HEP scheme in the UWB. This agreement, known as the *Compensatory Funding Agreement*, was the foundation of PRR and stated this objective: "to carry out jointly agreed programs of wetland habitat restoration and enhancement with the goal of providing habitat and conditions equivalent to or greater than the net loss of habitat and conditions attributable to the Waitaki hydro-electric power development." To work towards this objective, PRR has six areas of focus: 1) maintain indigenous vegetation and enhance habitat by removing problem weeds, 2) explore opportunities to enhance wetland conservation, 3) continue to build knowledge of natural heritage in braided river ecosystems, 4) test the effectiveness of large-scale predator control, 5) facilitate research by external agencies to improve our understanding of the ecology of braided river systems, 6) continue to increase public awareness of braided rivers and wetlands. Funding for PRR is also outlined in the agreement. Originally, annual funding was set at $NZ360,000, but this fluctuates with the consumer price index. Funding for the 2010/2011 year was $NZ485,000 and was distributed as follows: 41.9% on weed control, 31.7% on project management, 16.6% on research and monitoring, 9.3% on predator control, and the remaining 0.5% on advocacy (Woolmore, Anderson, Garside, 2011). Funding will continue until April of 2025, when the Compensatory Agreement expires (Woolmore & Sanders, 2005; C. Woolmore, personal communication, January 19, 2011).

PRR's objective statement and six areas of focus are ambitious when considering that the eight hydro-electric power stations have negatively impacted at least eight rivers of the UWB, including approximately 26,400 ha of river habitat (Wilson, 2001). With only two fulltime employees, and an extensive work load, PRR must manage its limited resources effectively (Woolmore, Anderson, & Kimber, 2008). This is accomplished by hiring contractors to do work such as weed spraying and predator control (C. Woolmore, personal communication, March 17, 2011). Further, PRR prioritizes certain areas deemed 'pristine', and these include the Godley, Cass, Hopkins, Dobson, Macaulay, and Upper Ahuriri rivers. PRR believes more conservation can be achieved by maintaining large pristine areas of higher conservation

value, as opposed to focusing on smaller and heavily degraded areas (Woolmore & Sanders, 2005; Peat & Patrick, 2001).

Throughout the last 20 years, PRR has been successful in various areas. Over 35,000 ha of pristine river beds have been maintained, and a weed surveillance system is in operation to help identify and prevent weed invasion in the early stages (Woolmore & Sanders, 2005). Widespread weeds that were already established have been addressed through chemical, mechanical, biological, and physical removal (Brown & Sanders, 2001). Mechanical methods are preferred to remove the deeply-rooted and well-established willow thickets, and chemical spraying of grazon (active ingredient triclopyr) is the preferred method for lupins, gorse, broom, and some willows (Heppelthwaite, 1999; C. Woolmore, personal communication, March 17, 2011). Weed removal efforts have included 350 ha in the lower Ahuriri River, 200 ha of Tekapo River, 160 ha of willow removal in the Tekapo River delta, and during the year 2000, more than 2000 hours of weed spraying was conducted on one managed wetland and nine rivers with more than a 95% kill rate (Sanders, 2003).

Through collaboration with the DoC's Black Stilt Recovery Project (BSRP), major improvements in bird survival rates and breeding have occurred. Together, PRR and the BSRP have undertaken an aggressive predator control initiative. The goal of this effort is to reduce the predation of the river birds to a level where endangered birds are in a recovery state. The year 2007 marked the fourth complete year of basin-wide trapping and monitoring in the Tasman Valley as well as the first full year that the full range of kill-traps were deployed. During 2007, a total of 1,284 traps were set and captured 1,301 predators. (Woolmore et al., 2008). In addition to trapping, electric fences are also used for predator control around the constructed Ruataniwha and Waterwheel wetlands near Twizel. These constructed wetlands provide over 100 ha of suitable habitat for the basins water birds and have increased breeding survival rate from less than 40%, to approximately 90%. Over 25 species of water birds utilize these wetlands, including black stilts, wrybills, and black-fronted terns. Constructed wetlands feature low vegetation density for un-obstructed view, and the ability to raise and lower water levels to enhance and maintain optimal foraging and weed control. Further, these wetlands have been used for releasing the BSRP's captive-reared black stilt chicks (Heppelthwaite, 1999; DoC, 2000b; Sanders, 2003).

There have been a number of limitations in PRR's success. The first is the limitations of grazon. While very effective in killing the targeted plants of lupin, gorse, broom, and willow, grazon has no residual impact on viability of seeds already in the soil seedbank. Therefore, even though a certain area may be sprayed, remaining seeds can re-populate areas of earlier eradication (Friend & Sanders, 2000). Other setbacks include public opposition to weed removal and corresponding methods. Originally, PRR obtained a resource consent to allow weed removal in the 28 km stretch of the Ahuriri River from Longslip Creek to Lake Benmore. However, farmers and anglers objected to the use of grazon and willow removal for fear that it would affect the fish habitat and bank stability. Other community members valued the visual appeal of lupin flowers in the riverbed. This opposition ultimately resulted in weed removal being restricted to the lower 8 km of the river (Peat & Patrick, 2001). Further opposition has prevented PRR from performing weed control along Longslip Creek. This is a real setback because Longslip Creek is a tributary to the Ahuriri River and is the river's main lupin seed source. Upstream of the Longslip tributary, the Ahuriri is considered to be a pristine area where PRR effectively manages lupins at zero density; whereas downstream it is heavily infested with weeds (C. Woolmore, personal communication, March 17, 2011). Therefore, PRR's success at managing lupin impacts in the river is limited. The hope is that with the willows removed from the active and central parts of the riverbed below Longslip Creek, the softer weeds (such as lupin) will be naturally removed and controlled to some extent by frequent flood events (Peat & Patrick, 2001). However, there is currently no evidence that typical floods are capable of removing lupins.

1.1.5 Problem Statement

The braided rivers of the UWB are habitats for a wide variety of fauna and flora that have adapted to live in these harsh environments of intense sun, extremes of temperature, fierce winds, and occasional floods (Peat & Patrick, 2001). These rivers provide critical habitat for endangered and threatened fauna such as the black stilt. However, this habitat is degrading due to introduced predators, exotic weed invasion, and water manipulation. These impacts have accelerated over the last seven decades due to the development of HEP (Palmer & Petrie, 1989). Over the last two decades, the HEP company Meridian Energy Limited and the DoC have committed to mitigating some of the impacts of HEP development through PRR.

During the 2010/2011 fiscal year, PRR spent $203,243 on pest plant control, and $228,056 the previous year (Woolmore, et al., 2010, 2011); however, most of PRR efforts are focused on pristine areas, leaving a significant portion of the UWB's braided rivers vegetation unregulated.

1.2 Thesis aims and objectives

The main motivations behind this research are the degrading river habitats of the UWB and the limited information available to understand how flood events affect the exotic vegetation partially responsible. Two objectives are designed to identify hydraulic requirements and processes that remove Russell lupins (the most aggressive and widespread weed) with the aim to increase the understanding of if, how, and where flood events naturally regulate lupins.

The main objectives of this research are to:

1) determine what flood-induced processes are responsible for lupin mortality typical of the UWB's river floodplains, and
2) model where these flood-induced processes are likely to occur for various sized future flood events.

These objectives are outlined below in the following sections and are more completely described in the research scope section of Chapter 3.

1.2.1 Objective 1

Determine what flood-induced processes are responsible for lupin mortality typical of the UWB's river floodplains.

Currently, there is little literature that discusses or identifies flood-induced mortality of riparian vegetation. However, initial observations have shown that flood events can be detrimental to lupins yet the specific processes that cause mortality were uncertain. This thesis will analyse flood-induced mortality of Russell lupins. Using initial observations,

specific lupin mortality processes were postulated and further examined with extensive field observations, field data collection, and laboratory experiments. Once processes were confirmed to be detrimental, mortality thresholds in terms of velocity, water depth, inundation duration, and morphological changes were estimated using field and laboratory data and statistical relationships. Knowledge of the mortality processes and thresholds can provide insight into the UWB rivers natural ability to regulate and preserve the critical habitats.

1.2.2 Objective 2

To model where flood-induced lupin mortality processes are likely to occur for various sized flood events.

While the identification of lupin mortality processes and estimated thresholds will advance the understanding flood effects on riparian vegetation, insight could be gained through simulating various sized flood events and assessing the mortality results. Using the hydrodynamic numerical model Delft3D, flood events with magnitudes equating to those of floods ranging in return period from a 2- to 500-years will be simulated and lupin mortality will be identified using the data from Objective 1. These simulations have three goals. First, to determine if and where the various lupin mortality processes occur throughout the floodplain. Second, to determine how the various processes interact and overlap as well as which mortality processes dominate the varying sized flood events. Third, using the latest available vegetation extent data, the simulations can determine how well natural flood events can remove floodplain lupins as well as preserve vegetation free areas.

1.3 Thesis organization

This thesis is organized into four parts across eight chapters and appendices. Part I introduces the problem background, outlines the problem statement, sets out the thesis aims and objectives, and provides a comprehensive literature review that investigates previous work for both information and for identifying knowledge gaps. Part II describes the research and data collection conducted during this study. This includes a hydrological assessment of the Ahuriri flood regime, various lupin observations and experiments, a digital elevation model

generated for the specific study site, and the numerical model calibration. Part III is the synthesis of this research and the final assessment of all data.

Part I

Part I consists of chapters 1, 2, and 3. Chapter 1 provides the necessary background and problem identification, a brief outline of the research objectives, and the thesis organization. Chapter 2 provides an extensive literature review for braided rivers, morphology, vegetation impacts on hydraulics and the feedback of hydraulics on vegetation, and current technology used to study braided rivers and vegetation. Chapter 3 provides the context and justification of this research. This starts with the research rationale, followed by the knowledge gained and knowledge gaps of the literature review. With the gaps identified and initial flood observations conducted, the main lupin-mortality hypothesis is presented. This is followed by an extensive discussion of the project objectives and their scope, as well as limitations of this research. Finally, the study site for this research is presented and justified.

Part II

Part II consists of chapters 4, 5, and 6, which provide the necessary data for this research. Chapter 4 consists of the hydrological assessment, which provides the time frame by which all other data are considered. However, the main focus of Chapter 4 is the research and results on the individual flood processes that cause lupin mortality. Chapter 5 presents the observed flood event and the methods and data utilized to develop digital elevation models and vegetation mapping. Chapter 6 focuses on the numerical model calibration which was essential to simulate flood events and to identify lupin mortality.

Part III

Part III consists of Chapters 7 and 8 and concludes the thesis. Chapter 7 combines all information determined from Part II. Combining all the observations, experiments, and the calibrated numerical model, various sized flood events were simulated and corresponding lupin mortality was assessed and presented for a final assessment. This is then followed by Chapter 8 which provides the thesis summary, conclusions, and recommendations.

Part IV

In addition to the three main parts of this thesis, references and appendices are included in Part IV. Appendices include additional figures, tables, and sample calculations, as well as additional background information where necessary.

Chapter 2

Literature Review

2.1 Channel form, hydraulics, and vegetation

As presented by James et al. (2001) there is an important relationship between a river's vegetation, hydraulics, and channel form. James et al. (2001) describe this as a "three-way mutual feedback" where "vegetation and channel form determine hydraulic conditions for a given discharge; hydraulic conditions and channel form define habitat for vegetation establishment and growth; vegetation and hydraulics determine channel form by controlling the movement, trapping, and storing of sediment" (Jordanova & James, 2003, p. 474). Below is a review of the literature on braided river hydrology and morphology, vegetation effects on braided rivers, vegetation effects on hydraulics, flow effects on vegetation, and new and improved technologies used in recent river studies.

2.1.1 Braided river hydrology and morphology

The braided rivers in the UWB are driven and reshaped by their volatile hydrologic regimes and sediment supplies (Gray & Harding, 2007; T. Davies, personal communication, April 29, 2011). The Ahuriri River for example, has a mean discharge of 23.3 $m^3 s^{-1}$, a mean annual flood of 223 $m^3 s^{-1}$, a 100-year flood at 686 $m^3 s^{-1}$, and a maximum recorded discharge of 570 $m^3 s^{-1}$ (NIWA flow records 1963 to 2011, Section 4.2). While prolonged low flow rates are typical in late summer, autumn, and winter seasons, violent floods can occur during the spring and early summer months. These floods are typically induced by westerly storms and can often be compounded by snowmelt (Gray & Harding, 2007). During flood events, braided rivers dissipate their energy across the floodplain. As discharge increases, braided rivers' main channels become deeper, faster, and wider; however, additional flow is routed through newly developed, or pre-existing, secondary channels throughout the floodplain (Mosley, 1982). In addition to flood forces being dissipated through these additional channels, these channels offer relatively constant flow conditions of lower velocity and depth for instream uses (such as fish). Therefore, Mosley (1982) concluded that in some ways, braided rivers may be more stable during flood events than single thread rivers.

While floods are generally recognized as shaping river channels, there is little agreement amongst geomorpholgists whether large and infrequent floods or smaller annual floods are responsible for river patterns (Hickin & Sichingabula, 1988). To address this, Hickin and Sichingabula (1988) investigated the impacts of a 30+ year flood event on the Squamish River of British Columbia. This river is unusual in that the upper reach is braided and the lower reach is meandering, offering an opportunity to investigate how different river planforms react in the same flood. Hickin and Sichingabula (1988) determined, through the use of aerial photographs taken before and after the flood event, that the braided reach underwent significant geomorphic adjustment while the meandering reach showed only slight adjustment. However, the authors acknowledged several additional influences may have attributed to the extreme impacts along the braided reach, including deeper inundation due to the confined floodplain by the relatively narrow valley walls. As illustrated by Hickin and Sichingabula (1988) and Mosley (1982), braided rivers and single thread rivers can react differently to floods. Further, Mosley (1983) illustrated that braided rivers of similar physical properties vary in relation to discharge. In an attempt to discover a relationship between braided rivers and their discharge, Mosely (1983) studied the braided Ashley, Hurunui, Rakaia, and Ahuriri Rivers in the South Island of New Zealand. Mosley (1983) concluded that between the four rivers, there was no similarity between a braided river's discharge and the number of branch channels, nor the proportion of flow within each channel (p. 64).

Due to high precipitation rates and large sediment supply, the sediment yields of New Zealand's braided rivers in the Southern Alps are estimated to be among the highest in the world (Griffiths, 1979). Braided river sediment deposits are continually re-worked throughout the floodplain by bar and island erosion, sediment deposition, and channel avulsion (Bertoldi et al., 2009). In a field study on the braided Ashley River, Warburton et al. (1993) determined that channel patterns are most drastically changed due to flood flows re-occupying older channel segments and that the dominant channel change mechanisms are avulsion and bank erosion that produces bank notching. Recent morphology studies in the Waimakariri River have shown that within a 3 km study-reach, up to 265,000 m^3 of sediment had eroded and 340,000 m^3 had deposited (Hicks, Westaway, & Lane, 2003) and that two-thirds of the Waimakariri's floodplain could be re-worked annually and is likely to be entirely re-worked within a five-year time period (Hicks, Duncan, Lane, Tal, & Westaway, 2008).

2.1.2 Vegetation effects on braided rivers

In addition to hydrologic and sediment regimes reshaping rivers, vegetation has also been linked to river channel form (e.g. Jordanova & James, 2003; Tal, Gran, Murray, Paola, & Hicks, 2004). Building on previous literature that showed a relationship between vegetation density and river type (meandering, braided, etc.), Gran and Paola (2001) conducted an experiment using a scaled physical model and alfalfa to simulate the effects of vegetation density on a gravel bed braided river planform. Results showed that as vegetation density increased, active channel numbers decreased, bank stability increased which reduced migration rates, and narrower and deeper channels developed; all of which shifted the channel pattern from braided toward meandering. Tal et al. (2004) used three different approaches to investigate the effects of vegetation on multi-threaded rivers. Combining aerial photographs of the Waitaki River, a flume experiment similar to that of Gran and Paola (2001), and a computer cellular-automata model, they concluded that the three approaches all showed that as vegetation increased, channel size and numbers decreased. Further, Tal and Paola (2007) used a physical model and alfalfa to simulate vegetation invasion on braided rivers to show that under 'natural' varied discharge, braided rivers can develop into single-thread channels.

Braided rivers are highly dynamic and vary drastically over time and space making them very difficult to model and understand (Morisawa, 1985). Therefore field work is an important component of the research and understanding of braided rivers. In a field study comparing the flow regulated Waitaki River, and the unregulated Waimakariri River, Hicks et al. (2008) assessed the influence of invasive riparian vegetation on river morphology. Using a predictor from Paola (2001, as cited by Hicks et al., 2008), they examined whether floods or vegetation would dominate a river's morphology. It was determined that the unregulated floods in the Waimakariri River were capable of re-working the morphology within a five year time frame, leaving the braided bed as bare gravel. By contrast, the floods of the regulated Waitaki River were less effective at morphologic change and the river's braiding has decreased since flow regulation began (Hicks et al., 2008, p. 580). Hicks et al. (2008) state that the current braiding of the Waitaki River is a result of the human intervention of vegetation removal which, similarly to the experiments of Tal and Paola (2007), suggests that some braided rivers will eventually develop into single-thread rivers when flood events cannot naturally regulate vegetation encroachment.

2.1.3 Vegetation effects on hydraulics

For over a century, attempts have been made to understand and quantify vegetation and its influence on hydraulics. The first attempt was made by Ganguillet and Kutter (1869) to quantify the flow resistance caused by vegetated streams (as cited by Corenblit, Tabacchi, Steiger, & Gurnell, 2007). Later, Manning (1891) published Manning's equation, which is still the most widely used formula to represent flow resistance in vegetated open channels. Further developments since Manning have highlighted various vegetation conditions (morphology, density, and rigidity) and the correlating hydraulic effects (flow resistance, shear stress, sediment transport, and erosion). Recent studies (e.g. Jarvela, 2002) have used the dimensionless Darcy-Weisbach friction factor f to determine the energy loss of flow passing through vegetation (see Appendix A.1 for Darcy-Weisbach and Manning's relationships).

Vegetation's effect on open channel flow has long been studied, and general findings suggest that vegetation increases flow resistance and reduces conveyance (e.g. Palmer, 1945; Kouwen & Unny 1973; Kouwen & Li 1980; Fathi-Maghadam & Kouwen 1997; Freeman, Rahmeyer, & Copeland, 2000; Helmiö, 2002). In these studies, analysis of rigid and flexible vegetation has been conducted using both real and artificial vegetation (Corenblit et al., 2007; Rhee, Woo, Kwon, & Ahn, 2008). In experiments, rigid and flexible vegetation are classified by their ability to remain vertical or their ability to waver in the flow (Thornton, 1997, p. 1284). Experiments using rigid structures (such as cylinders, a horsehair mattress, and wheat stocks) to simulate stiff vegetation have shown that flow resistance is a function of the water depth and velocity, and of the vegetation's density, diameter, and morphology (e.g. Petryk & Bosmajian, 1975; Wu, Shen, & Chou, 1999; Tanino & Nepf, 2008). Experiments using flexible vegetation (such as various grasses, plastic strips, and tree saplings) found that flow resistance is a function of plant deformation, relative roughness, flow depth, and density (e.g. Palmer, 1945; Kouwen & Li, 1980; Fathi-Maghadam & Kouwen, 1997; Nepf & Vivoni, 2000; Järvelä, 2002) These various investigations can be classified into two categories: flow through tall, *nonsubmerged* (also referred to as *emergent*) vegetation, or flow over short, *submerged* vegetation (Jarvela, 2002).

In an experiment using strips of vinyl plastic to simulate flexible vegetation, Nepf & Vivoni (2000) defined the hydraulic variance between submerged and emergent vegetation as functions of depth of submergence, canopy morphology, density, and flexibility. These varying flow depths create two distinct zones. The upper zone is referred to as the *vertical exchange zone* because water exchanges momentum vertically. In this zone a shear layer develops at the top of the vegetated canopy that strongly influences both the mean and turbulent velocity characteristics. The lower zone is referred to as the *longitudinal exchange zone* because momentum exchanges mainly through longitudinal advection. In this zone, the vegetative stem wakes influence the turbulence, which then influences the stem wake conditions. Both zones develop for submerged flow, but only the lower layer develops in emergent flow (Nepf & Vivoni, 2000). Jarvela (2002) illustrated the importance of varying flow depth in an experiment using sedges, and determined that the flow resistance is maximized at the transition between emergent and submerged flow.

As mentioned above, flow resistance was found to be a function of vegetation density in both rigid and flexible vegetation, as well as submerged and emergent categories. Studies have heavily focused on the effects of vegetation density (e.g. Freeman et al., 2000; Jarvela, 2002; Bennett, Pirim, & Barkdoll, 2002) and equations have been developed relating Manning's *n* in part to vegetation density (e.g. Kouwen, Unny, & Hill, 1969; Petryk & Bosmajian, 1975). Testing willow density, Jarvela (2002) found that doubling the willow density approximately doubled the value of the Darcy-Weisbach friction factor *f,* and Bennet et al. (2002) found that as density increased, flow resistance and flow depth increased. Li and Shen (1973) determined that density and orientation also influences flow resistance. Using rigid cylinders to simulate rigid vegetation, their experiment demonstrated that drag can increase or decrease on corresponding cylinders as compared to a single cylinder (Li & Shen, 1973). This is called a *sheltering effect*, and it has been shown that as the Reynolds number increases (approximately above 1000) the sheltering effect causes a decrease in drag on downstream cylinders (Poggi, 2003; Nepf, 1999 as cited by Righetti & Armanini, 2002).

Vegetation density has also been linked to variations in shear stress along a river reach, particularly in compound channels (Thornton, Abt, Morris, & Fischenich, 2000). During over-bank flooding, vegetation size difference between the main channel and floodplain has a

large influence on the flow resistance and flow depth (Freeman et al., 2000). Myers and Elsawy (1975) analyzed the lateral shear stress of main channels and floodplains separately and combined. They concluded that, when compared to their isolated conditions, the interaction between the two increased floodplain shear stress up to 260%, reduced main channel shear stress up to 22%, and the maximum shear was generally at the junction between the floodplain and main channel. Thornton et al. (2000) validated this finding and further concluded that this influence was a function of flow depth, vegetation density, and velocity variation.

Studies relating velocity profiles to vegetation have also been conducted. Using flexible strips of styrene, Kouwen et al. (1969) found a logarithmic velocity profile with flexible vegetation. More recent studies suggest that vegetation morphology influences the velocity profile shape. Carollo, Ferro, and Termini (2002) used various grasses in a submerged flow experiment and concluded that the velocity profile took on a three-zone '*S*' shape (Figure 2.1). The lower zone I, within the vegetation, was marked by very slow velocity gains with elevation increase. The middle zone II, was the transition between vegetation and the free stream zone and was marked by a rapid increase in velocity with elevation. The top zone III, was marked by progressively less velocity gain with elevation. Carollo et al. (2002) further concluded that as stem concentration decreased, the velocity within the vegetation increased, resulting in less curvature of the velocity profile. However, different observations have been made for vegetation with foliage canopies in both submerged and emergent flow conditions. Experiments with vegetation that contains leaf mass, or a basal stem region, have created local velocity maxima near the flume bed. These results are thought to be due to reduced stem drag near the bed resulting in flow deflection downward, which has been documented to cause scour and increased sediment transport (Leonard & Luther, 1995; Nepf & Vivoni, 2000; Freeman et al., 2000).

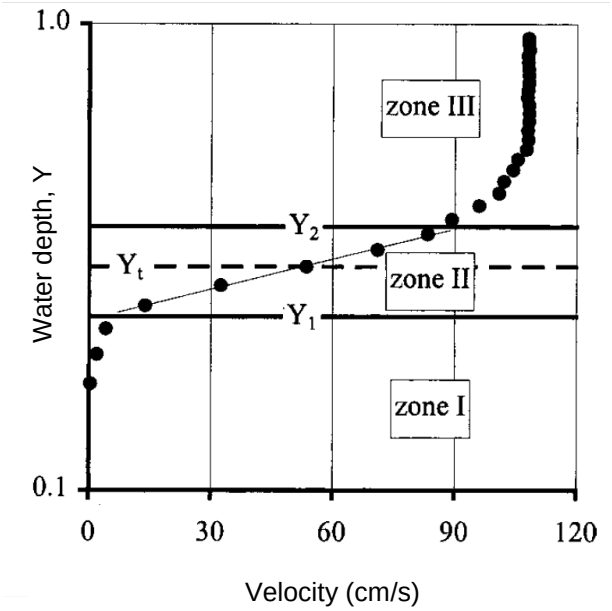

Figure 2.1: Logarithm velocity profile of submerged vegetation and corresponding zones (I, II, and III) (Carollo et al., 2002).

While foliage canopies can increase sediment transport by deflecting flow downward, research has shown that grasses reduce sediment transport (Samani & Kouwen, 2002). Prosser, Dietrich, & Stevenson, (1995) showed that progressively reducing the height of grass will reduce the critical shear stress and increase sediment transport. If completely trimmed, it can be reduced to 11-38% of that under full length conditions. In addition to vegetation type, orientation can affect sediment transport. Li and Shen (1973) demonstrated that using various orientations, the same number of cylinders, and comparing against a non-vegetated condition, a '*staggered*' orientation could significantly reduce sediment transport by as much as 62%. However, some vegetation will not only discourage sediment entrainment, but will encourage deposition (Abt, Clary, & Thornton, 1994). Using various grass lengths, research has shown that taller vegetation can also retain larger percentages of sediment based on the relationship between canopy deflection height and un-deflected height (Abt et al., 1994; Samani & Kouwen, 2002). While modeling the effects of roots on erosion remains limited (Corenblit et al., 2007), it has been shown that there is typically an exponential decrease of erosion with increasing root density (Gyssels, Poesen, Bochet, & Li, 2005). Further, larger diameter roots, typical of woody vegetation, provide better stream bank soil reinforcement when compared to smaller roots typical of herbaceous species (Wynn & Mostaghimi, 2006). However, tree roots are often exposed along river banks, which illustrates that bank erosion continues.

2.1.4 Hydraulic effects on vegetation

While there are numerous studies that have investigated vegetation effects on flow, studies investigating flow effects on vegetation are scarce (Brookes, Hooke, & Mant, 2000). Notable exceptions to this are Friedman and Auble (1999), Kollmann, Vieli, Edwards, Tockner, and Ward (1999), and Hering, Gerhard, Manderbach, and Reich (2004). Brookes et al. (2000) discuss the approach taken to modeling vegetation interactions along river channels and floodplains, and identify the effects of vegetation on flow and the feedback of flow on the vegetation. However, the authors suggest that a lack of data on the vegetation's physical properties was problematic and resulted in "crude approximations" (p. 112). When modeling erosion, it was assumed that plants would be removed if the erosion reached 40 to 70% of root depth. Further, it was assumed that the plant would be killed if completely buried by sediment deposition, and while the authors acknowledge that sediment-movement-induced plant trauma can kill the vegetation, no such analysis was added to their model (Brookes et al., 2000).

Tree death and removal, and large woody debris (LWD), have been studied in both single-thread and braided rivers (Kollmann et al., 1999; Friedman & Auble, 1999). Inspired by uprooted trees and shrubs from a large 1996 flood, Kollmann et al. (1999) investigated interactions between LWD and island formation on the braided Tagliamento River, Italy. Using a combination of aerial photographs, GIS mapping, and tree ring analysis for estimating island age, they concluded that significant loss in island area and resulting vegetation loss occurs in time intervals as short as 5 years. Further, tree-ring analysis showed that trees were rarely older than 20 years, suggesting that the same was true for islands (Kollmann et al., 1999). In Colorado, USA, Friedman and Auble (1999) investigated the death of box elders along the Gunnison River. To analyze tree mortality, they used a hydraulic model to investigate the maximum shear stress required to mobilize underlying sediment, and conducted field work to investigate the number of days trees were inundated. They concluded that mortality by both inundation and shear stress can be modeled as threshold functions. If the critical shear stress for underlying sediment is exceeded, or if box elders are inundated during the growing season for more than 85 days, mortality occurs (Friedman & Auble, 1999).

The Isar River, between Germany and Austria, is similar to the rivers in the UWB in that it is braided and its flow regime is affected by upstream hydro-electric power schemes. However, in 1999 the Isar River experienced a 100-year flood event and the various aspects of the flood's impact were documented (Hering et al., 2004). Most notable is the effect on floodplain vegetation. Previous work by Erber, Kambergs, Lampe, and Reich (1997) had documented the floodplain vegetation through transect mapping as late as 1996 and included herbaceous species mountain avens (*Dryas octopetala*), reedgrass (*Calamagrostis*), and *myricaria germanica* grouped together and referred to as 'pioneer' vegetation. After the flood, vegetation mapping using the same method as Erber et al., (1997) was conducted in 1999 and again in 2000. Analyzing the pre- and post-flood vegetation data, Hering et al. (2004) concluded that vegetation, almost entirely categorized as pioneer, was reduced by 22%, while willow thicket removal was very small.

Finally, Ross and Shuker (2010) examined the relationship between vegetation and flood events of the Ahuriri River, New Zealand. Using three sets of aerial photographs (taken in 1991, 1995, and 2000) and detailed flow records, they examined a 21 km reach of river bed and vegetation over the period between 1991 and 2000, with special emphasis on the 1994 flood event. Although unable to identify vegetation impacts caused by individual flood events due to the infrequent aerial photographs, they determined that between 1991 and 1995, the active area bed decreased from 877 ha to 862 ha (2%) and vegetation covered 42% of the riverbed area. From 1995 to 2000, the riverbed area increased from 862 ha to 923 ha (7%) and the vegetation cover reduced to only 38% (Ross & Shuker, 2010). These changes are small compared to the 22% reduction in vegetation found by Hering et al. (2004). Ross and Shuker (2010) acknowledge this in comparison to a report by Dick and McHale (2006, as cited by Ross & Shuker, 2010) that found a 56% reduction in wetland area following a flood event in the Upper Gila River. Further, Ross and Shuker (2010) used the US Army Corps of Engineers' Hydrologic Engineering Center River Analysis System (HEC-RAS) model to examine the areas of inundation, flow depths, flow velocity, and shear stress created by a low flow rate of 10 $m^3 s^{-1}$, and 2, 10, 100, and 500-year flood events. However, Ross and Shuker (2010) acknowledge some of their results were doubtful and suggest that the one-dimensional HEC-RAS model may not be realistic. This was attributed to the inability of the model to properly simulate two-dimensional velocity as well as the model's inability to properly simulate high water depths. For example, as the main channel overtops, the remaining

floodplain fills up equally based on low elevation (rather than location) resulting in misleading areas of inundation. While the intention was to compare vegetation removal to hydraulic conditions, Ross and Shuker (2010) were unable to correlate any quantitative results and conclude that a two-dimensional model would better simulate the Ahuriri River's hydraulics and that additional research is necessary to identify the vegetation removal processes and corresponding hydraulics.

2.2 Technology

2.2.1 Terrestrial laser scanning and global positioning system

During the past decade, advances in survey and sensor technology have generated new opportunities to investigate the structure and dynamics of fluvial systems (Brasington, & Vericat, 2010; Williams et al., 2011). Key geomatic technologies include the global positioning system (GPS), digital photogrammetry, light detection and ranging (LiDAR), and terrestrial laser scanning (TLS, also referred to as ground LiDAR) (Brasington & Vericat, 2010). The application of these has resulted in a profound increase in the dimensionality of topographic information with traditional cross-section models replaced by three-dimensional (3D) point clouds and digital elevation models (DEMs) (Brasington, Rumsby, & McVey, 2000).

GPS is a 3D (xyz) satellite-based positioning system that is accessed with ground-based receivers and can receive velocity, weather, and time information in addition to position. While GPS is a significant aid in positioning, its precision is limited for non-military users. To overcome this limitation, many have used a 'relative positioning' method that utilizes two GPS receivers. Using one of the receivers in a fixed location (called the base station) and the second receiver (called the rover) used to survey the surrounding area, accuracy can be improved by reducing clock errors and atmospheric distortion (Brasington et al., 2000). Many relative positioning methods are available. However, real time kinematic (RTK) GPS has proved to be a fast, convenient, and accurate method to produce high resolution DEMs (Brasington et al., 2000). According to Twigg (1998, as cited by Brasingon et al., 2000), RTK-GPS can capture topographic data with accuracies around 1 to 2 cm for plan measurements and around 3 cm vertically. Further, each survey point can be acquired within

1 to 4 seconds allowing thousands of points to be collected within a day (Brasington et al., 2000).

LiDAR and TLS are recent technologies and collect data through optical sensing. By determining a time delay difference between a light's pulse transmission and the reflected signal detection, these tools can measure an object's range, and horizontal and vertical direction (Merrett Survey Partnership, 2007). TLS creates 3D datasets called *point clouds* in minutes by scanning its radial surroundings (Figure 2.2a) (J. Brasington, personal communication, March 31, 2011). Point clouds are then rendered together with software to produce DEM's of high precision (2-4 mm in x, y, z) and high resolution point spacing (sub-centimeter) as shown below in Figure 2.2b (Williams et al., 2011; J. Brasington, personal communication, June 15, 2011).

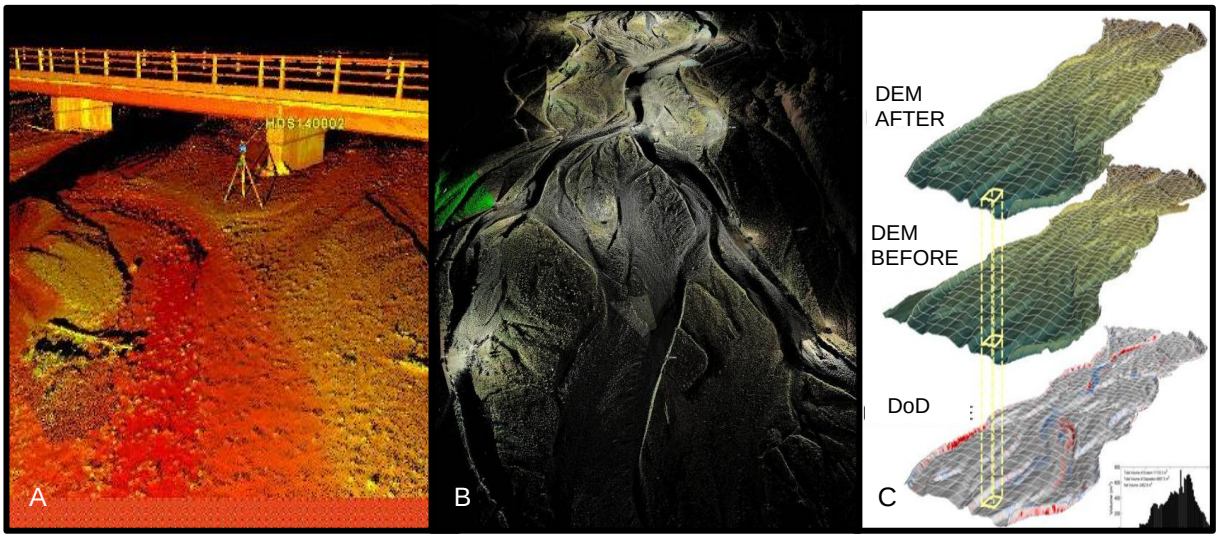

Figure 2.2: A) TLS point cloud. B) TLS point clouds rendered DEM. C) DEM of Difference (DoD) (Brasington & Vericat, 2010; Brasington, n.d.)

With the ability to capture topography in detail, river studies are now capable of quantifying subtle topographic changes by comparing DEMs of Difference (DoD) shown in Figure 2.2c (Williams et al., 2011). Brasington and Vericat (2010) examined the benefits of TLS-generated DoDs compared to RTK-GPS-generated DoDs and found TLS can produce as much as 150% more topographic detail. A current river study utilizing TLS is the ReesScan Project on the braided Rees River in New Zealand. From October 2009 through May 2010,

morphologic changes due to seven flood events have been captured with TLS and aerial photography (J. Brasington, personal communication, June 15, 2011). These data will then be utilized to create DEM's and DoD's to investigate channel change caused by flood flows in order to develop improved models (Brasington et al., 2009). In addition to TLS utilized to study morphologic adjustments, TLS has also been used to examine riparian vegetation (Antonarakis, Richards, Brasington, & Bithell, 2009). Antonarakis et al. (2009) used TLS to capture poplar tree canopy structures in the Allier River of France to determine the roughness parameters for high river flows. Earlier in the study, airborne LiDAR data was determined to be ineffective to represent the vertical relief of the vegetation; therefore, TLS was used and found to be an effective method to determine the forested area (Antonarakis et al., 2009).

2.2.2 Photogrammetry

Photogrammetry offers an efficient technique of deriving DEMs (Chandler, 1999) and has shown success in modeling fluvial environments (e.g. Pyle et al., 1997; Butler et al., 1998; Lane, 1998; Stojic et al., 1998 as cited by Westaway, Lane, & Hicks, 2003). Photogrammetry is an age-old technique used to measure 3D objects from photographs and can be traced back to Leonardo da Vinci's observations (Doyle 1964, Gruner 1977, as cited by Shaffner, Heisler, Krosley, Kottenstette, & Wright, 2009). In the simplest form, photogrammetry is the method used to reconstruct the original 3D object that was transformed into two dimensions (2D) when captured by a photograph (Geodetic Systems, 2012; Kraus, 2007). However, when the photograph transforms the 3D world into 2D, it inherently loses information (primarily depth). To recover this information, photogrammetry requires at least two overlapping photographs taken at different locations and utilizes *triangulation* to determine the location of the camera at the time of image capture. Triangulation is the mathematical process of calculating the point of interest's three-dimensional location (x, y, and z coordinates) in space through intersecting lines as shown below in Figure 2.3 (Kraus, 2007; Geodetic Systems, 2012).

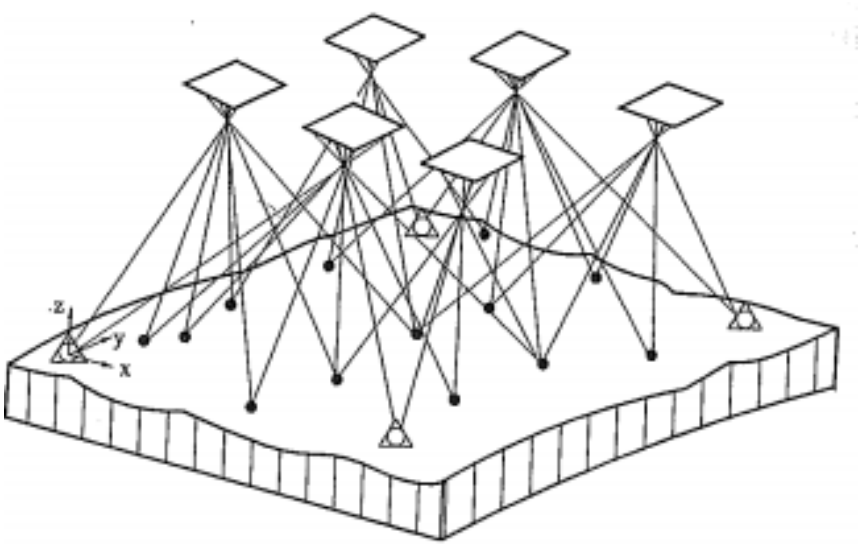

Figure 2.3: Triangulation as taken from Kraus, 2007.

Next the camera's orientation is determined by utilizing the identifiable objects in the image set. This process of determining the cameras location and orientation is often completed using a *bundle adjustment* (Geodetic Systems, 2011; Kraus, 2007; Triggs, McLaughlan, Harltey, & Fitzgibbon, 2000). Bundle adjustment refers to "the 'bundles' of light rays leaving each 3D feature and converging on each camera center, which are then 'adjusted' optimally with respect to both feature and camera positions" (Triggs et al., 2000, p. 298). The result is a 3D model with an arbitrary scale in an arbitrary coordinate system. However, this can easily be *transformed* to an absolute model by utilizing common points with known locations called *control points* (Shaffer et al., 2009; Chandler, 1999, p. 53). Control points are objects (natural or man-made) that can clearly be identified in the photographs, and are accompanied with their corresponding coordinate locations (x, y, z) (Shaffer et al., 2009; Chandler, 1999).

The accuracy of photogrammetry is dependent on many factors. These include: the resolution and quality of the camera, the size of the measured object, the number of photographs taken, and the geometric layout of the photographs relative to the object of interest as well as photograph overlap (Shaffer et al., 2009). Chandler (1999) suggests at least three ground control points in every image; however, using more control points could only improve the DEM's reliability and precision. In order to determine the overall quality of the DEM, Chandler (1999) suggests that the user performs two operations. First, the user should withhold a sample of the ground controls that are utilized to transform the DEM. By

withholding some of the control points, these can later be utilized as *check points* to compare the photogrammetric coordinates with the accepted surveyed coordinates. Second, it is advised to acquire surveyed coordinates of locations distributed throughout the study area. This is called *ground truthing* and is used to evaluate the accuracy of the DEM generation (Chandler, 1999). Using these methods, one can then calculate the variance, mean error, and standard deviation of the compared coordinates. The variance and standard deviation are measures of the precision, and the mean error is a measure of the accuracy (Chandler, 1999; Lane et al., 2000; Westaway et al., 2003). Photogrammetry has been shown to give exceptional topographic representation of exposed areas and provide accuracy comparable to conventional survey techniques (Westaway et al., 2003, p. 222-224). However, there are challenges with photogrammetry. These include areas where objects are not represented the same in different pictures (e.g. water, moving objects) as well as misrepresenting elevation. Further, photogrammetry measures and models the surface captured by the photograph (Chandler, 1999). Therefore, in vegetated areas the DEM will be representing the top of the vegetation instead of the underlying terrain. However, by estimating or measuring the vegetation's height, a correction can be applied and a quality DEM can still be obtained (Chandler, 1999).

2.2.3 Structure-from-Motion

Initially, photogrammetry was expensive and required a strong understanding to process the data. However, throughout recent decades, photogrammetry has become increasingly more affordable and user-friendly as it has transformed through the three stages of analogue, analytical, and digital methods (Kraus, 2007; Fonstad et al., 2011a; Westoby et al., 2012). Analogue photogrammetry uses conventional printed photographs and processes the data using optical mechanical instruments. Analytical photogrammetry starts with conventional photographs, but the data is processed using computers. And more recently, digital photogrammetry utilizes digital photographs and processes the data using computers (Kraus, 2007); which in turn has allowed the processes to become increasingly automated (Chandler, 1999; Lane et al., 2000; Westoby et al., 2012). Traditionally, all of these stages required the use of photogrammetric, or *metric*, cameras which are properly calibrated and equipped with special lenses whose geometry are designed around collinearity equations (see Kraus, 2007 for further details). However, new photogrammetry techniques such as *Structure-from-Motion* (SfM) can produce high resolution DEMs with standard consumer grade cameras at

low cost with little user experience (Fonstad, Dietrich, Courville, Jensen, Carbonneau, 2011b).

Currently, there are several SfM software packages freely available and for purchase. Many, like Microsoft's PhotoSynth, are internet-based allowing the user to load images via the internet and process the data remotely without user parameter input. While these provide the ultimate user-friendly application and do not require high PC computational requirements, they limit users to default parameters. Therefore, while internet-based programs are important and applicable to produce quality fluvial DEMs (e.g. Dowling, Read, & Gallant, 2009; Fonstad et al., 2011b), the main focus in this study will be on the two PC based SfM software packages: SFMToolkit and AgiSoft's PhotoScan.

In contrast with traditional photogrammetry, SfM does not require the 3D location and orientation of the cameras at image capture, nor the 3D location of the control points to be known prior to scene reconstruction (although the control points are still required in post processing to transform the model from relative to absolute coordinates) (Westoby et al., 2012). Instead, SfM starts by identifying image features of overlapping photographs. The freely available SFMToolkit performs this using the Scale Invariant Feature Transform (SIFT) object recognition system as discussed in Lowe (2004) (Westoby et al., 2012). The principle behind SIFT is to identify points of interest, or *keypoints*, within the images that are invariant to scaling, rotation, and even partially invariant to illumination differences (Lowe, 2004). This method produces numerous features that blanket the photograph, yet keypoint matches are sent through highly distinctive keypoint descriptors to ensure strong matches are produced (Lowe, 2004). The next step is the execution of the sparse bundle adjustment system called *Bundler* (Snavely et al., 2008; Westoby et al., 2012). This process takes each pair of images and matches the keypoint descriptors using the approximate nearest neighbors package by Arya et al. (1998, as cited by Snavely et al., 2006). Random Sample Consensus, or *RANSAC* (Fischler and Bolles, 1987; as cited by Westoby et al., 2012; Snavely et al., 2006) algorithms are utilized to produce the fundamental matrix used to relate the corresponding matches. Finally, Bundler organizes matching keypoints (minimum of two) across multiple images (minimum of three) into *tracks* that are later used for point cloud reconstruction (Snavely et al., 2006; Westoby et al., 2012). Throughout this process, any

inconsistent matches are removed as well as outliers to the matrix which helps to remove transient features; such as people moving across the images, or ever-changing objects like moving water (Westoby et al., 2012; Snavely et al., 2006). Next, the camera(s) parameters (rotation, translation, and focal length) and 3D location for each track are recovered and errors are minimized by using a non-linear least squares problem and solved with algorithms such as Levenberg-Marquardt (Nocedal and Writh 1999; as cited by Snavely et al., 2006). Finally, triangulation is utilized to generate the point cloud's x, y, and z-positions and generates the visual geometry (Westoby et al., 2012). At this stage in the processesing, the result is a sparse point cloud in a relative coordinate system (Snavely et al., 2006).

The next step of the SFMToolkit is to increase the density of the point cloud. This is performed utilizing the Clustering View for Multi-view Stereo (CMVS) and the Patch-based Multi-view Stereo (PMVS2) algorithms created by Yasutaka Furukawa (Furukawa & Ponce, 2007; Furukawa, Curless, Seitz, & Szeliski, 2010; Astre, 2010). Since multi-view stereo (MVS) algorithms typically have scaling issues when excessive images are used, CMVS takes the output from Bundler as input and decomposes the overlapping images into sets, or 'clusters,' of images of a more manageable size; it also removes unnecessary image redundancy in order to speed up PMVS2 and improve reconstruction accuracy. PMVS2 then takes the clustered images and camera parameters and reconstructs the 3D structure which produces a denser product than the original Bundler (Furukawa et al., 2010; Westoby et al., 2012). As mentioned above, the resulting DEM is in a relative coordinate system. Similarly to traditional photogrammetry, a transformation can be applied to manipulate the data into the desired coordinate system with the help of ground control points and their known locations. The full SFMToolkit process is shown in Figure 2.4.

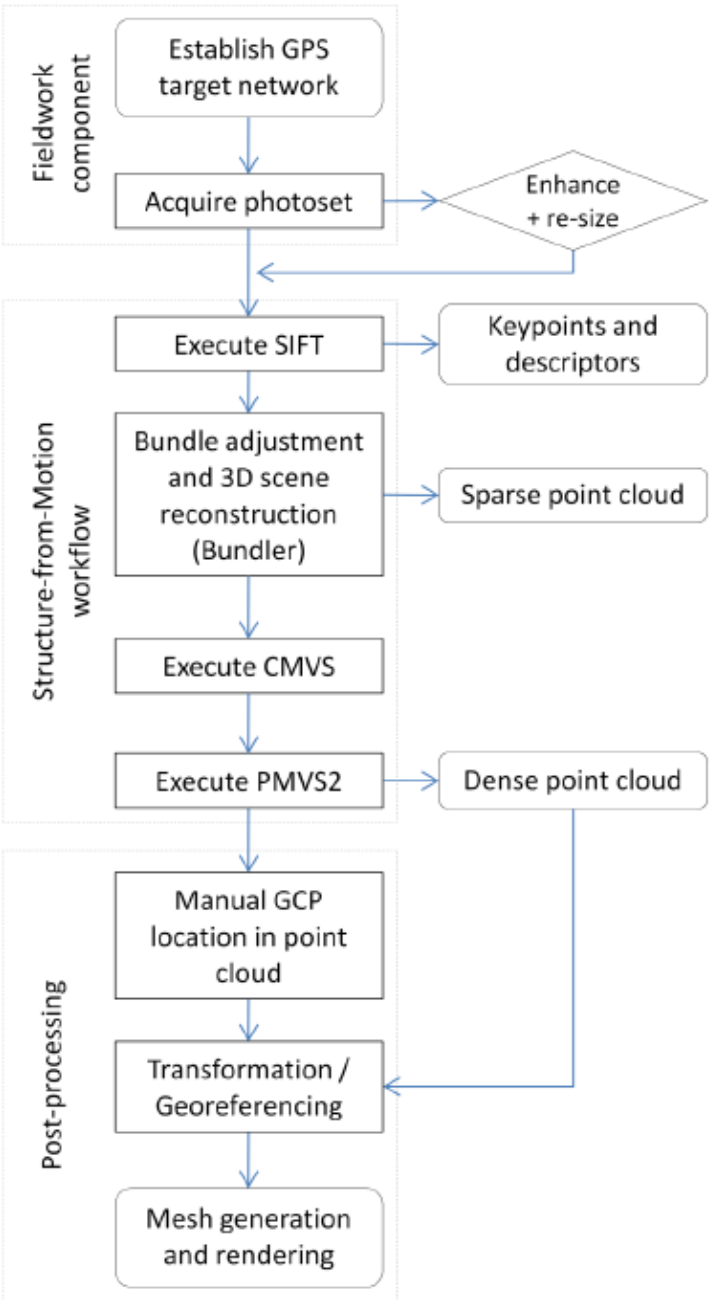

Figure 2.4: "From photograph to point-cloud: the Structure-from-Motion workflow" (as cited in Westoby et al., 2012).

AgiSoft's PhotoScan (version 0.9.0) software is available for purchase and offers a complete SfM package with the main features of aerial triangulation, polygonal model generation, setting coordinate system, and georeferenced DEM and orthophoto generation (AgiSoft, 2010). To date, there is little literature that documents PhotoScan's ability, and even less on the software's workflow. According to AgiSoft's website, PhotoScan can produce high quality photogrammetric data and high quality DEMs by users with little or no experience

(Agisoft, 2010). PhotoScan's forum describes the workflow as "similar" to SFMToolkit's; however, PhotoScan does not use Bundler, PMVS2, or CMVS processes (Semyonov, 2011). Instead, PhotoScan uses a three step process in which it implements its own algorithms that produce higher alignment quality (Semyonov, 2011).

PhotoScan SfM and dense multi-view stereo reconstruction (DMVR) generated point clouds are produced in three stages. During the first stage, SfM utilizes supplied photographs and tracking algorithms to identify, match, and monitor the movement of unique features (Verhoeven, 2011; AgiSoft, 2012a). Many SfM packages use the Scale Invariant Feature Transform (SIFT) object recognition system (Lowe, 2004) for this process; however, PhotoScan claims to achieve higher alignment quality using custom algorithms that are similar to SIFT (Semyonov, 2011). The second stage determines the camera's intrinsic (focal length, principal point, and lens distortion) and extrinsic (projection center location and the six exterior orientation parameters that define the image) orientation parameters by initially using a greedy algorithm to calculate camera positions, and later improves their positions with a bundle-adjustment algorithm (Robertson and Cipolla, 2009; Semyonov, 2011; Verhoeven et al., 2012). In contrast to traditional photogrammetry, SfM does not require the 3D location and orientation of the camera at image capture, nor the 3D location of the control points to be known prior to scene reconstruction (Westoby et al., 2012; Verhoeven et al., 2012). Following the completion of the first two stages, a sparse point cloud has been generated as well as the location and position of every supplied image (Figure 2.5a).

The third stage utilizes the previously determined intrinsic and extrinsic camera locations, a DMVR, and every pixel of the provided images to produce a dense surface reconstruction referred to as a *mesh* (Figure 2.5b) (AgiSoft, 2012a). PhotoScan offers five reconstruction methods: arbitrary–smooth, arbitrary–sharp, height-field–smooth, height-field–sharp, or point cloud (AgiSoft, 2012a). The first four methods are based on DMVR, and the fifth method offers a quick reconstruction based solely on the point cloud (AgiSoft, 2012a; Agisoft, 2012b). The resulting dense point cloud is generated in an arbitrary coordinate system; however, PhotoScan can transform the model into the absolute coordinate system provided ground control points (GCPs) or camera coordinates have been recorded. Transformation was accomplished through linear similarity using seven parameters (three translation, three rotation, and one scaling). Such transformation can only compensate a linear model

misalignment; however, non-linear deformations can occur in the final model. This is due to PhotoScan's estimated intrinsic and extrinsic camera orientation parameters using only image data; therefore, errors in the final estimate may occur. The model's accuracy depends on factors such as the amount of overlap between neighboring images and the object surface shape (AgiSoft, 2012a). To compensate for non-linear deformations, PhotoScan offers an *optimization* tool which utilizes the modeled point cloud and camera parameters to reduce the difference between the model and supplied coordinates. Agisoft recommends that optimization be performed if measurements are to be taken from the model, as optimization can increase a model's accuracy (AgiSoft, 2012a). However, PhotoScan's transformation algorithms are not fully disclosed.

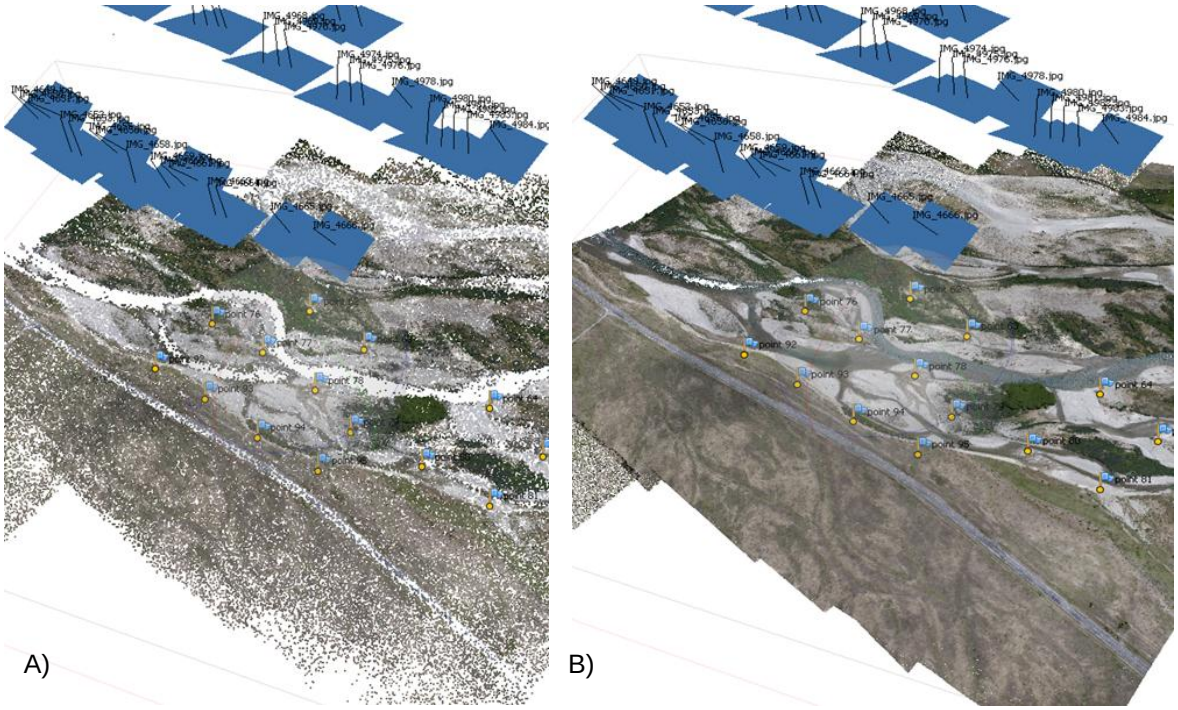

Figure 2.5: PhotoScan located camera positions and generated: A) sparse point cloud, and B) 3D mesh.

While both SFMToolkit and PhotoScan are relatively new, it is clear that these and other SfM products offer the inexperienced and low budget researcher the opportunity to create high quality DEMs (Fonstad et al., 2011a). Traditional photogrammetric DEMs were typically less accurate and precise than airborne LiDAR (Baltsavias, 1999; Niethammer et al., 2012); however, SfM has produced results with centimeter precision and point cloud resolutions that

fall between LiDAR and TLS (Fonstat et al., 2011b, 2011a; Doneus et al., 2011). Recently, three authors have compared TLS and SfM. Westoby et al. (2012) compare the accuracy of SfM using the SFMTookit (Astre, 2010) and terrestrial captured photographs taken with a consumer-grade digital camera against a Leica Geosystems ScanStation TLS. Both datasets were decomposed to a 1 m^2 resolution and resulting DEMs were compared by DEMs of difference (DoD). The results showed that "94% of models fall into the range of -1.0 to 1.0 m differences, with 86% found in the range of -0.5 m to 0.5 m" which suggests that the SfM method algorithms produce promising results when compared to TLS (Westoby et al., 2012). James and Robson (2012) compared a Microsoft Photosynth SfM model against a Riegl Z210ii TLS model of a coastal cliff (50 x 3 m) and found an overall root mean squared error of 0.07 m. While James and Robson (2012) conclude that SfM produced results with less precision than the TLS, SfM did produce similar results at considerably less cost and time spent in the field. Finally, Doneus et al. (2011) compared the SfM software PhotoScan against a Riegl LMS-Z420i laser scanner using a 16 m^2 area of an archaeological site. Using vertical images captured 5 to 6 m above the ground, PhotoScan produced a point cloud with 0.020 m point distribution, and the TLS produced 0.017 m point distribution. Comparing numerous PhotoScan generated DEMs to the TLS data, root mean squared errors between the two datasets reached as low as 0.021 m and Doneus et al. (2011) stated the PhotoScan SfM produced the same general accuracy as the TLS.

2.2.4 Bathymetric mapping

While TLS and SfM currently offer the highest detail for studying fluvial environments, both are incapable of collecting data below the water surface (Brasington, Vericat, & Rychkov, 2012; Snavely et al., 2006). This leaves a significant portion of the topography unmeasured, and these inundated areas are highly prone to geomorphic adjustments (Williams, et al., 2011). There are many methods to acquire this bathymetric data including remote sensing methods such as traditional photogrammetry, bathymetric LiDAR, and *optical* remote sensing (Westaway et al., 2003; Wedding et al., 2008 as cited by Williams et al., 2011; Carbonneau et al., 2006); as well as field data collection methods using radar, sonar, and RTK-GPS surveys (Williams, et al., 2011; Fonstad & Marcus, 2005; Brasington et al., 2003). However, traditional photogrammetry and LiDAR methods are expensive (Jordan & Fonstad, 2008) and extensive field data collection can be an overwhelming task for large river studies. Thus,

optical remote sensing is the best bathymetric method to model the river bed elevation at sub-meter resolution (Marcus & Fonstad, 2008).

In the simplest form, optical bathymetric mapping utilizes aerial photographs and field depth data to provide a calibrated depth measurement based on the water's color (Williams et al., 2011; Carbonneau et al., 2006). This method requires relatively clear and shallow water (less than 12 m (Gao, 2009)) and the water column must be completely visible (e.g. no ice, trees, clouds, shadows, overhanging materials, to block the water) (Fonstad & Marcus, 2005). Many authors (e.g. Williams et al., 2011; Williams et al., 2012a; Legleiter, Roverts, Marcus, & Fonstad, 2004; Winterbottom & Gilvear, 1997) have used Lyzenga (1981) algorithms to produce bathymetric maps.

The Lyzenga algorithm (equation 2.1) describes the relationship of light reduction with increasing depth and uses an additional variable to account for the depth in which the light's reflection is completely consumed.

$$X_i = ln(DN_i - DN_{max}) \qquad \text{(Eqn: 2.1)}$$

where X_i is the depth relationship, DN_i is the light variable, and DN_{max} is the light value at the deepest point detectable (Williams et al., 2011). To use this algorithm, the user must simultaneously (or as closely as possible) obtain aerial photographs and depth data from the field. Multispectral imagery was originally considered the optimal method for bathymetric mapping; however, standard color imagery has recently been shown to be advantageous due to its reduced cost and better resolution (sub-meter) (Carbonneau et al., 2006). Therefore, only standard color imagery is considered herein.

Prior to using this algorithm, Carbonneau et al. (2006) suggest performing pixel averaging since it is undesirable to use single pixel brightness values due to the water color fluctuations caused by bed material variation. Once the image pixels are averaged, it is possible to compare the sensitivity of the standard color imagery bands (red, green, and blue – RGB) against the field recorded depth in individual or mosaicked image sets (Williams et al., 2011).

In most cases, the red band shows the highest level of sensitivity (e.g. Williams et al., 2011; Winterbottom & Gilvear, 1997; Lejot et al., 2007); however the blue band has been utilized by Fonstad and Marcus (2005) and the green band has been shown to be sensitive to aquatic vegetation (Lejot et al., 2007). In addition to assessing individual bands, utilizing band ratios has proven effective. Williams et al. (2012a) showed that the blue-over-red band ratio performed best, and Legleiter et al. (2004) showed that the green-over-red band ratio was effective at depth measurements across varying substrate types. Once the band(s) of highest sensitivity are selected, it is possible to calibrate this data with the field depth data collected. To do this, Williams et al. (2012a) separated the field depth data into two separate classes. The first is approximately two-thirds of the depth data which was used to develop and calibrate the water depth correction model. The second class was the remaining one-third of the depth data and was used to validate the model. The final step is the completion of the DEM by combining the bathymetric data with the exposed surface data supplied (e.g. TLS or SfM). To do this will require a model of the water surface elevation in order to convert the water depth to elevations. This can be accomplished by taking the existing DEM (from TLS or SfM) and locating the water edge and interpolating across the wetted channels (Brasington et al., 2003; Williams et al., 2011).

Despite the simple concept, optical bathymetric mapping is a difficult task (Jordan & Fonstad, 2008). Using the empirical calibration discussed, depth is determined by slight variations in the water's color; however, other factors can influence the water's color. These can include: substrate composition, water turbulence, turbidity, bank vegetation shading, and sun glint (Jordan and Fonstad, 2008; Brasington et al., 2003). Since these are never uniform throughout a river, it is inevitable that these will cause difficulties and errors. Further, multiple images will be required in large study areas which can create significant illumination differences between photographs (Carbonneau et al., 2006). However, while many of these effects are unavoidable (substrate and turbulence), the impacts of some (sun glint, turbidity, and shading) can be minimized with proper pre-photograph planning.

These challenges prevent the precision of optical bathymetric mapping reaching that of echo-sounding or GPS surveying (Carbonneau et al., 2006); however, optical techniques offer an affordable and high resolution option (Williiams et al., 2011). The results of many studies use

the coefficient of determination (R^2) to compare how well the calibrated depth compares to the actual measured depth (with $R^2 = 1$ the best possible fit) and are shown below in Table 2.1. It's important to note that despite a weaker R^2 relationship, one can still provide adequate results. Williams et al. (2011) had an $R^2 = 0.52$; however, obtained a mean error of -0.01 m, standard deviation error of 0.09 m, and a RMSE of 0.10 m, which was still of the same order of magnitude as the TLS RMSE (p. 521).

Table 2.1: Optical methods used to determine water depth.

Reference	Sensor type	R2	Band Color
Winterbottom et al., 1997	Multispectrial	0.67	
	Black and white	0.55	
Brasington et al., 2003	Color imagery	0.74	red
Legleiter et al., 2004	Multispectrial	0.79	green/red
Fonstad and Marcus, 2005	Color imagery	0.76	blue
Lejot et al., 2007	Color imagery	0.81	red used on substrate
		0.9	green used on vegetation
Williams et al., 2011	Color imagery	0.54	red
Williams et al., 2012	Color imagery	0.806	blue/red - mosaicked images
		0.732	blue/red - individual images
		0.594	red - mosaicked images
		0.315	red - individual images

2.2.5 Digital elevation models of difference

DEMs of difference (DoD, shown in Figure 2.2c) are widely used to assess fluvial geomorphology and to determine sediment budgets from repeat topographic surveys, and numerous developments have occurred over recent decades from simple morphological DEM differencing (Lane et al., 1994) to more recent developments of computer software toolkits such as the Geomorphic Change Detection (GCD). GCD (version 5.0.24) is a user-friendly program that offers numerous advanced DoD assessments for non-expert users such as DEM uncertainty, probability confidence intervals, and Bayesian updating (Wheaton, 2012).

DEM and DoD uncertainty has been widely researched (e.g. Lane et al., 1994, Brasington et al., 2000, Wheaton et al., 2010) to determine if geomorphic changes can be distinguished from DEM noise. In fluvial environments, DEM noise can often be comparable to the

topography, surface roughness, and morphologic changes; thus, the uncertainty of the DEMs must be considered and applied in order to accurately assess the survey results (Wheaton et al., 2010). Wheaton et al. (2010) investigated the software they helped develop to estimate the DEM quality and influence on DEM differencing. Originally, this software was called DoD Uncertainty Analysis Software, and through recent redevelopments, it is now freely available online under the name GCD and available as a plugin for ArcGIS.

The most widely used method to account for uncertainty in DEMs is to determine a minimum level of detection based on the DEM's accuracy, and to discard changes that occur below this threshold in an effort to distinguish real and artificial changes (Wheaton et al., 2010). This minimum level of detection is calculated from Equation 2.2.

$$minLoD = \sqrt{(DEM_{new})^2 + (DEM_{old})^2} \quad \text{(Eqn: 2.2)}$$

where DEM_{new} and DEM_{old} are the individual errors of the respective DEMs. These errors can be either general errors representative for the entire DEM, or spatially varying. It is important to note that if the minLoD value is lower than the equipment precision, then the greater of the two errors should be taken (e.g. if using TLS with precision of ±5 mm, and the minLoD is calculated at 2 mm, then the user should use the ±5 mm (which the minLoD equation calculates as 7 mm)).

Determining whether one should choose uniform or spatially varying error propagation depends on the project and data available. Milan et al. (2010) compared uniform minLoD DoD and a spatially variable minLoD DoD (from DEMs based on total station surveys with precision of ±5 mm) and concluded that the spatially varying method produced greater detection over low vertical relief areas such as bar surfaces and channel beds. In addition to utilizing spatially varying errors for minLoD, GCD also offers probability confidence intervals and Bayesian updating. Once the user has specified DEMs and uncertainty errors, the confidence intervals in which the results are calculated can be specified. Bayesian updating can also be applied, which offers a sophisticated method in which neighbouring cells are considered (based on the sampling window size specified by the user; default is 5 x

5) in order to determine an adjusted probability of change significance for the cell in question (refer to Chapter 4 or Wheaton (2008) for further details).

2.2.6 River modeling

Major advances in braided river physical modeling have developed in New Zealand over the last three decades. Starting in the late 1970's, braided river scaled modeling began with the experiment by Hong and Davies (1979) at Lincoln College, New Zealand, and continued there with the work reported in Warburton (1996). Scaled models have since been used to study various topics including vegetation effects on braided rivers (e.g. Gran & Paola, 2001; Tal, Gran, Murray, Paola, & Hicks, 2004). The developments in geomatic technologies and three-dimensional morphologic analysis have been partially driven by the need for high resolution topography for physical and numerical fluvial modeling (Rumsby et al., 2008). In addition to physical models, numerical models have also been applied successfully to river engineering projects and are becoming increasingly sophisticated (Lesser, Roelvink, van Kester, & Stelling, 2004; Nicholas & McLelland, 2004, as cited by Rumsby et al., 2008). To represent 3D flow structures, these models require high resolution topography of the entire reach (Rumsby et al., 2008). In addition to roughness parameters, the topographic boundary conditions are highly influential in numerical models and technologies such as LiDAR have been shown "to significantly improve finite element discretization" (Bates et al., 2003 and Cobby et al., 2003, as cited by Runsby et al., 2008, p. 41)

Numerous fluvial models are available, but the models recently utilized on braided rivers have included the cellular model of Murray and Paola (1994, 1997, 2003) and the depth averaged models Hydro2de, Mike 21C, and Delft3d. Cellular models such as that of Murray and Paola (1994) have been applied to braided rivers and were able to simulate braid development using simple discharge rules and sediment transport based on local slope (Coulthard and Van De Wiel, n.d., Murray and Paola, 1994). However, Murray and Paola's (1994) cellular model simplified the physics involved and excluded depth, momentum, and velocity calculations in their model. These reduced-physics cellular models are often referred to as reduced complexity models. Murray and Paola (2003) further utilize their cellular model to investigate the impacts of vegetation on channel development. Using the assumptions that vegetation reduces sediment transport and increases bank stability, Murray and Paola's model

produced results that showed vegetation can reduce braided rivers to single threads; however, additional sediment supply and aggradation can cause the river to remain braided. The Cellular Automaton Evolutionary Slope and River model (CAESAR), was 'inspired' by Murray and Paola's cellular model (Coulthard and Van De Wiel, n.d., pg. 3). However, this model included the depth calculations which provided an improved sediment transport simulation (Coulthard and Van De Wiel, n.d.) and over the last decade, CEASAR has been utilized to simulate various rivers. However, cellular models and reduced complexity models are often scrutinized due to their occasional unrealistic morphology simulations and simplification of governing physics that are widely used in other models, such as depth averaged models (Nicholas, 2010).

Depth averaged models such as Hydro2de has been utilized by New Zealand's National Institute of Water and Atmospheric Research (NIWA) on the braided Waiau River to model depths and velocities, and found to have a good overall agreement between modeled and gauged data (Duncan & Bind, 2009). While Hydro2de has had success in modeling braided rivers, it is limited because it is a fixed bed model. Fixed bed models are criticized because they cannot simulate the evolving river pattern (Coulthard et al., 2006).

Mobile bed models, such as Mike 21C and Delft3D, are capable of modeling a river's sediment transport and morphodynamic feedbacks (DHI Water and Environment, 2004; Best, 2008). Mike 21C was utilized in a study on the braided Brahmaputra-Jamuna River in Bangladesh to forecast hydrodynamic and morphological conditions in a reach during bridge construction (Enggrob & Tjerry, 1999). This model simulated a short (1 year) as well as a longer (30 years) time scale. The results of the short-term simulation successfully modeled the braided river's wavelength, braiding intensity, channel width, shape and size of the main bars (Enggrob & Tjerry, 1999).

Delft3D has also been utilized recently for braided river studies. Following an extensive calibration regime, a 2D depth-averaged hydrodynamic model of a 2.5 km reach of the braided Rees River, New Zealand, was modeled and produced flow velocities, braiding, and water extent with encouraging results for both low-flow and high-flow conditions (Williams et al., 2013). Schuurman and Kleinhans (2010) utilized Delft3D to model the emergence of

river patterns from a plane bed which produced both meandering and braided rivers. These models were based on characteristics of actual river datasets (such as initial bed slope, grain size, discharge, channel width, and water level) which produced results that matched the "empirical relations describing natural river bars in both meandering and braided rivers" (Schuurman & Kleinhans, 2010). Further, Delft3D was utilized in 3D mode to study the influence of sediment-induced density and corresponding channel pattern on the Yellow River, China, which provided insight into the sediment concentrations and hydraulics that cause meandering channels at high and low concentrations and braiding channels at moderate concentrations (van Maren, 2007).

In addition to braided rivers, Delft3D has also been utilized to simulate hydraulic and vegetation interactions. Petts and Kennedy (2005) utilized Delft3D to simulate a single thread river to investigate two case studies of morphology and vegetation interactions. The first case study used Delft3D's 2D morphodynamic mode and simulated the vegetation with increased hydraulic roughness. The second case study used the 3D hydrodynamic model and simulated the vegetation as rigid cylinders. Comparing the results of the two studies, the vegetation simulated by rigid cylinders produced realistic bed shear stress, which is key starting point to successfully model sediment transport and fluvial geomorphology (Petts & Kennedy, 2005). Finally, van Holland et al. (2010) utilized Delft3D and the incorporated function called *trachytopes* (that can represent vegetation roughness upon local hydraulics in 2D depth-averaged simulations) to investigate sediment transport in a vegetated polder and results showed that water levels and inundated patterns had "good representation*"* (p. 1780).

2.3 Summary

Although progress has been made in modeling braided river hydraulics, there is not enough information available to quantify or model vegetation mortality due to flooding events on braided rivers such as those of the UWB. While much research has focused on the effects of vegetation on hydraulics, little is understood about the feedback of the hydraulic effects on vegetation. Further, braided rivers are a relatively recent subject of research (Warburton, 1996) and because they vary drastically in both time and space, they are very difficult to model and understand (Morisawa, 1985).

Chapter 3

Thesis Scope and Limitations

3.1 Thesis rationale

The braided rivers of the UWB are critical habitats for endangered and threatened fauna such as the black stilt. However, this habitat is degrading due to introduced predators, exotic weed invasion, and water manipulation. While PRR and the HEP operators have put forth great effort and funding to restore these habitats through weed control, predator control, and artificial habitats, flood events may provide a natural method to recreate habitat lost to vegetation (Caruso, 2006). During the past decade, the advances in survey and sensor technology and three-dimensional morphologic analysis have been partially driven by the need for high resolution topography for physical and numerical fluvial modeling (Rumsby et al., 2008) and have in return created new opportunities to investigate and model the structure and dynamics of fluvial systems through the development and differencing of high quality digital terrain models (Brasington et al., 2012; Hicks et al., 2011; Wheaton et al., 2010).

With new technologies like SfM offering an affordable method to produce sub-meter resolution terrain models with decimeter accuracy (Doneus et al., 2011; James and Robson, 2012), and numerical models capable of simulating hydraulics, vegetation, and morphology of large scale braided river reaches (Williams et al., 2013; Deltares, 2010), new opportunities exist to identify and model the flood-induced processes that cause vegetation mortality; thus, benefiting habitat preservation and restoration knowledge and possibly methods.

3.2 What we know and knowledge gaps

Numerous studies have investigated open-channel hydraulics for various channel forms, and the hydraulic effects of various vegetation types, which through centuries of questions and research have provided powerful equations and tools such as Manning's equation, Navier-Stokes equations, and recent tools such as hydrodynamic models that can aid in answering new questions. While much research has focused on the effects of vegetation on hydraulics, little is understood about the feedback of the hydraulic effects on vegetation.

This knowledge gap is highlighted by the UWB's degrading habitat, and the lack of knowledge describing the potential of flood events to naturally regulate the encroaching vegetation. While information is limited in this field, important research has been conducted. As illustrated by Hicks et al. (2003), some New Zealand braided rivers are highly morphodynamic, where the majority of the river's floodplain can be reworked annually; suggesting that vegetation could be well regulated. However, studies such as Gran and Paola (2001) and Tal and Paola (2007) illustrate that vegetation encroachment on braided rivers can reduce the river to a single-thread. While large flood events have been shown to significantly reduce riparian vegetation (Hering et al., 2004), long term studies of the residual impact of flood events are scarce (Ross and Shuker, 2010). Therefore, while it is obvious that flood events have the potential to regulate vegetation, there are no rigorous methods or understanding in place to evaluate a rivers' ability to naturally regulate species or general types vegetation.

Initial flood observations of the UWB's rivers have shown that flood events can be detrimental to lupins; however, the specific processes involved could not be determined through brief examination. By knowing the specific processes and thresholds that cause vegetation mortality, it could be possible to evaluate a river's ability to regulate vegetation. Based on these post-flood observations and conversations with professors and professionals, the main hypothesis of this research is that floods are capable of causing lupin mortality within a braided river floodplain, and the mechanisms responsible can be broken into three categories: sediment movement, water movement, and inundation (Figures 3.1 and 3.2). Channel and floodplain morphologic adjustments caused by large and small floods can cause lupin mortality. These include:

- lateral erosion undercutting lupins,
- sediment deposition burying lupins,
- surface erosion uprooting lupins,
- sediment transport causing detrimental trauma to lupins
- hydraulic drag alone, or in combination with erosion, could pull lupins from the substrate, and
- extended flood duration could cause lupin mortality due to anoxia and/or reduced photosynthesis.

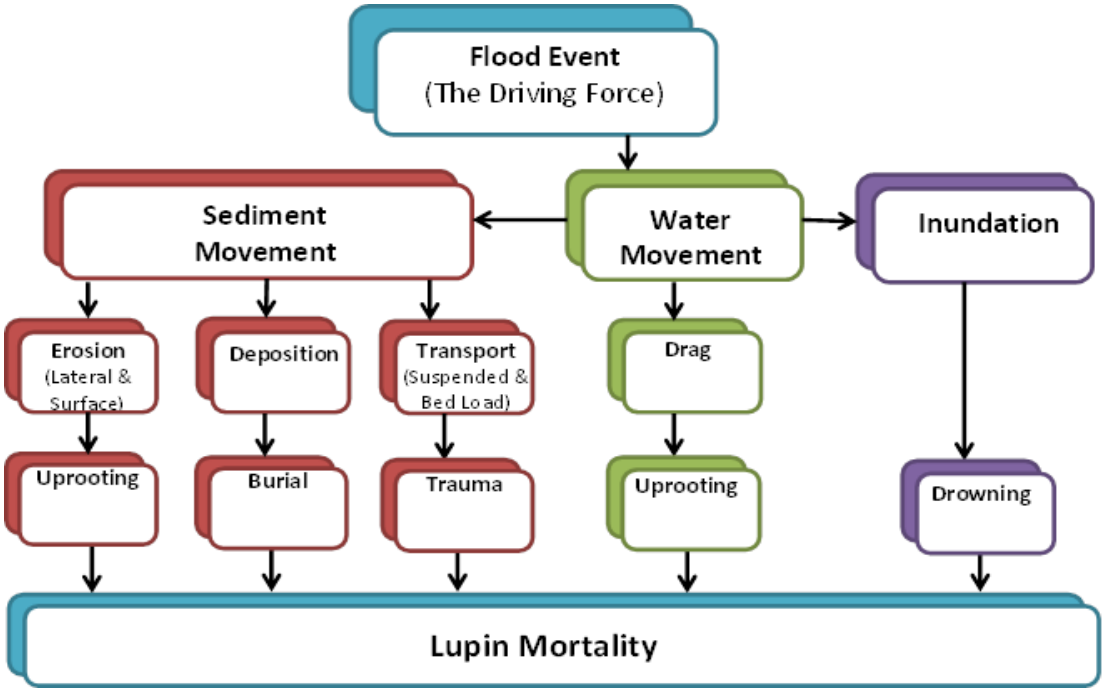

Figure 3.1: Conceptual model of flood induced processes that could cause lupin mortality.

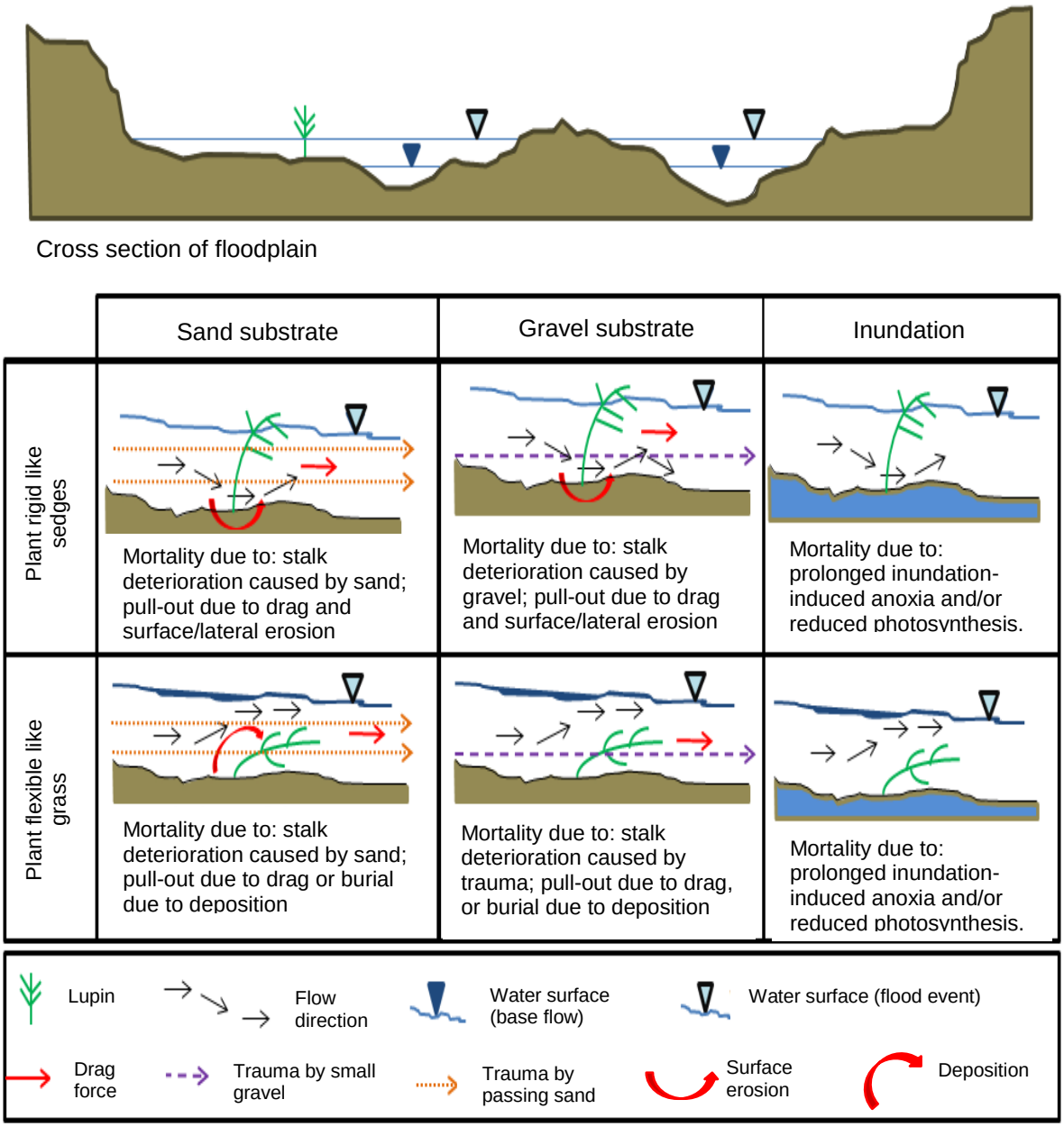

Figure 3.2: Conceptual model of lupin mortality processes occurring during flood event.

3.3 Scope

To determine i) the processes that cause vegetation mortality and ii) the ability of a river to regulate vegetation requires an interdisciplinary approach to collect, process, and synthesize all data such as hydrological, hydraulic, ecological, botanic, and geomorphological. The research objectives are presented below with an overview of the methods and scope in which this project was conducted.

3.3.1 Objective 1

Determine what flood-induced processes are responsible for lupin mortality typical of the UWB's river floodplains.

Accomplishment of this objective requires that the invasive vegetation of the UWB to be identified. As previously discussed, the four species causing most habitat degradation are crack willow (*Salix fragilis*), broom (*Cytisus scoparius*), gorse (*Ulex europaeus*), and Russell lupin (*Lupinus polyphyllus*) (DoC, 1996; Rawlings, 1993). However, of these four, Russell lupins are possibly the most aggressive and widespread within the UWB and will be the main focus of this research. Further, this research will focus on the peak flood season of the studied river, as this will result in the most likely/probable time frame for lupins to be affected by large flood events.

Based on the hypothesis, five key processes are hypothesized to cause lupin mortality: erosion, sediment deposition, trauma by abrasion, drag, and long periods of inundation. Therefore, these processes were investigated in both field monitoring and laboratory experiments with the aim to identify a threshold in terms of velocity, water depth, inundation duration, and morphological changes for the various processes that signifies when these processes become detrimental to the lupins survival. These processes are discussed in greater detail in Chapter 4, and are presented in a schematic in Appendix Figure E.1.

To assess erosion and deposition, detailed topography of the study-reach was captured using SfM and optical-bathymetric mapping both before and after a flood event to build high quality DEMs. Using these DEMs, a DoD was generated to identify the erosion and deposition burial that occurred during the flood event of interest. Assessment of the erosion and sediment deposition impacts upon lupins required a dataset of vegetation types throughout the study-reach. This was accomplished by a distributed vegetation survey and was complemented with aerial photographs in which vegetated areas were located and categorized. Knowing the extent of erosion and deposition that occurred and comparing the vegetation reduction provided by the aerial photograph inventories, the erosion and deposition processes were estimated. These potentially provide validation to the erosion and deposition mortality that were identified in the field and laboratory experiments.

Lupin extraction by drag was examined in two parts. First, the force required to extract lupins with no erosion and with varying degrees of erosion was determined to evaluate whether the drag alone can extract lupins from the substrate. Secondly, the drag force exerted on lupins in various flow depths and velocities was determined and related to the force by which the lupins were extracted in the first step. Combining the results of the required force and generated force (drag) provided thresholds for lupin extraction. The results for this were collated into a force matrix where lupin sizes and flow velocities determine lupin removal. This was later utilized to determine lupin removal based on the flow conditions simulated and spatial distribution of lupins and corresponding size.

Flood induced trauma caused by abrasion of drag and mobile sediment was studied in the field after the flood event, as this process was very difficult to re-create in the laboratory. Therefore, directly after flood levels receded, lupins in flooded areas were examined, and later revisited to determine if trauma alone caused any mortality. This was likely the most difficult process to identify a detrimental threshold value and required additional numerical model simulations to identify the hydraulics and sediment transport that occurred in specific areas.

As highlighted by Friedman and Auble (1999), vegetation mortality can occur in river systems due to long periods of inundation. Therefore, a laboratory experiment was conducted to test the inundation sensitivity of lupins. Since inundation can occur at different depths, various depths of inundation were investigated. Also, lupins were tested at their developmental and mature life stages, both of which occur during the flood season. Mortality thresholds were determined in terms of the number of days the lupins were inundated. Therefore, lupin testing was separated into 24 hour intervals, and lupins were given adequate time to recover in favorable growing conditions to ensure full mortality occurred.

Finally, a field experiment was conducted to simulate lupin burial by deposition. Prior to testing varying deposition levels for mortality, it is important to understand the lupins' flexibility and corresponding deformation during flood events. This is because the level of deformation will determine the amount of deposition necessary for full burial. Therefore, lupin deformation testing was also conducted in a field experiment where lupins were

uprooted and immediately tested in the nearby river braid. Once lupin deformation was recorded, lupins were gently deformed to the appropriate level and buried at various depths. These lupins remained buried for an adequate time period to allow regrowth or mortality. After the testing period was completed, the lupins were revisited and mortality was documented. While it is possible that lupins partially buried may die, it was hypothesized that only full burial would cause lupin mortality due to the results of previous studies (e.g. Deng et al., 2008).

3.3.2 Objective 2

To model where lupin mortality processes are likely to occur for various sized flood events.

With the processes and corresponding thresholds that cause lupin mortality identified through the efforts of Objective One, a hydrodynamic numerical model was calibrated and utilized to simulate where these processes should occur across the river bed and to relate mortality to water discharge. To accomplish this task, the open-source model Delft3D was utilized due to its ability to model the river's flow in 2D, as well as its abilities to include vegetation and simulate morphodynamics. Field data such as topography, sediment grain sizes, and vegetation mapping were utilized to help create a representative reach model in Delft3D. To achieve the best model simulations requires the model to be properly calibrated to the river of interest. This was accomplished in three steps. The first focused on calibrating the model to adequately represent the hydraulics of the river. This was conducted in a fixed-bed mode and was accomplished by matching the river's observed discharge, braiding pattern, and water depth to the simulated river. The second step was to calibrate the model's vegetation influence on local hydraulics. Vegetation presence and influence were incorporated through the use of trachytopes, which- alter the local bed roughness and flow resistance. Trachytope calibration was achieved by utilizing the data of a field experiment which quantified the lupin-altered conveyance of a particular reach. Therefore, the vegetation parameterization was adjusted until velocity and depth data best represented the observed data. Finally, the third calibration was the model's morphology. This calibration was accomplished by utilizing the studied flood event captured, and the pre- and post-flood data collected. The aim of this calibration was to achieve adequate comparison between the simulated and the observed morphologic changes identified by the DoD.

Once the model was calibrated, the flood events of interest were simulated using the morphology mode, and the results were examined to compare the areas of lupin mortality to the processes that occurred in that area (e.g. velocity, inundation extent, etc). This provided an opportunity to assess each individual process and the corresponding threshold previously identified in the first objective. Finally, this working model was then be utilized to examine the impacts of various sized flood events. However, to understand the river's capability to regulate vegetation required an understanding of historic and potential flood magnitudes. Therefore, a hydrological assessment was required for the river. Using the hydrological data such as flood frequencies, magnitudes, and duration, the probabilities of various sized future flood events and their corresponding lupin removal could be assessed. The simulations consisted of 2, 5, 10, 25, 50, 100, 200, and 500-year flood events. Comparing these results with the current vegetation of the river provided a probabilistic assessment of the river's ability to naturally regulate lupins based on the processes and thresholds identified. Refer to Appendix E.1, Figure E.2 for a schematic of the model calibration, validation, and simulations.

3.4 Limitations

Throughout this research it was necessary to place certain boundaries to narrow this project's scope in order to complete this project in a manageable time frame and to ensure proper attention was provided to the necessary areas. While additional aspects were important to consider during this research, various limitation were identified and are summarized in the following paragraphs.

While willows, broom, and gorse are invasive in the UWB, only lupins were investigated. This decision was based on the literature review that suggests the aggressive nature of the lupins' spread, as well as a visual inspection that revealed widespread lupin infestation in the study river. It was recognized that this visual inspection was impacted by the extensive willow removal conducted in the UWB by DoC's PRR. An additional aspect purposely excluded from this research was the regrowth of lupins. A tangent question to this research would be the rate of gestation and sprawl specific to lupins in the UWB, and to assess if the flood events are outpacing the ability of lupins to spread. However, to answer this question would require the investigation of smaller questions such as: gestation of lupin seeds in the

UWB, regrowth from dormant or damaged lupins, spread of lupin seeds, and typical lupin seed bank in the UWB soil. Therefore, while this question was intriguing and valuable to the overall understanding of lupin infestation, this addition would require extensive research that was out of the scope for this particular project. Finally, lupins were only evaluated during the peak flood season when they were at their mature life stages (i.e. December). While it is recognized that flood events occur during all seasons and likely cause lupin mortality, since the impacts upon lupins were likely dependent upon their maturity (e.g. canopy size and root strength) and the growing season, a specific time frame was chosen to narrow the focus of this research. This was necessary since studying flood impacts on lupins during all seasons was far too great a challenge to consider within the duration of this research.

During the course of this project numerous software programs with various parameter settings were utilized. While these programs are complex and have multiple parameters, not all programs and parameters received a detailed sensitivity testing. However, sufficient time was spent to become familiar with the various parameters and respective functions to ensure that accurate results were obtained. However, many of the programs used in this research are complex and would take enormous amounts of time to explore and perfect. Therefore, some parameter sensitivity was explored to gain an adequate and effective understanding of the programs, but time does not allow for extensive testing. This included the SfM software PhotoScan, the model Delft3D, and the DoD software Geophysical Change Detection.

In designing this project's data collection and analysis techniques to identify the processes responsible for lupin mortality, numerous potential methods were discussed. The first was to utilize the University of Canterbury's largest flume (~ 2 m x 30 m) and through custom fabrication a series of live lupins could be inserted and the processes could be studied in various simulations. Due to issues including the February 22nd earthquake, the flume was no longer an option for use and all efforts were then redirected to field data collection. While the processes could be observed and quantified from extensive field work, this would require an adequate flood event to occur in the time frame suitable for field work. Therefore, solely depending on field data was risky, and potentially limiting since large flood events are not guaranteed to happen. However, this method was pursued as it was the best option available at the time.

Some overall limitations were unavoidable. Since many of these processes were studied individually, it was impossible to consider all combinations and the respective effects of various processes occurring simultaneously, which may have a heightened or lessened overall impact. The likelihood is that the combination of various processes could cause additional mortality; however, these could not be adequately identified in field and laboratory experiments (e.g. trauma and inundation, trauma and deposition, deposition and inundation, etc.) and while these individual results provide a good reference, they are not completely representative of the natural processes. Further, these individual processes and thresholds were simulated in a numerical model, which operates under numerous assumptions and has its own intrinsic limitations.

The final limitation was the sediment supply, storage, and transportation of the river. It is important to recognize that the lupin mortality processes are heavily influenced by the combination of moving water and sediment, with the sediment movement dependent upon the sediment supply. While it would be ideal to have data to quantify these important values, this would be a very large undertaking. Therefore, the sediment transport for this study was assumed dependent upon flow rates and the study area's slope. While this was a crude approximation, it provides the necessary input for the numerical model and this method was a practical assumption given the data limitations (T. Davies, personal communication, July 6, 2011). Further, the study-reach was extended at the upstream end for numerical modeling purposes. This extended-reach was acquired for numerical modeling purposes. This data provided a buffer for the upstream boundary conditions and helped ensure that realistic hydraulic flow conditions and sediment transport occurred within the study-reach.

3.5 Study site

The Ahuriri River was chosen for this study because it is unaffected by HEP development and retains its natural flow and sediment regimes with little irrigation draw; however, its lower section was significantly affected by weed encroachment (C. Woolmore, personal communication, 2010; DoC, 2000c). Therefore, this river provided a unique opportunity to investigate the flood effects on vegetation in the field. The Ahuriri River is located in the Southern Alps of the South Island, New Zealand (Figure 3.3a). With a drainage basin area of 1,312 km^2 (Figure 3.3b) and basin-averaged annual precipitation of 1775 mm, the Ahuriri

River flows 70 km before draining into the artificial Lake Benmore (NIWA, 2007; Hicks et al., 2011). The headwaters of the Ahuriri River flow through steep and highly erodible mountains with elevations in excess of 2000 m. Additionally, high tectonic activity occurs throughout the Southern Alps with present-day uplifting estimated up to 5 mm $year^{-1}$ (Beavan, et al., 2010). Together, these geological properties and moderate precipitation provide the Ahuriri River with an abundant sediment supply of coarse schist and greywacke (DoC, 2000d) with a median surface grain diameter (D_{50}) of 30 mm. While sediment studies are scarce for the Ahuriri River, it has been estimated to yield 43,000 tonnes annually and modeled to yield 127,400 tonnes of suspended sediment annually (Griffiths, 1981; Hicks et al., 2011).

The study site is located 22 km upstream from Lake Benmore. Three reaches were defined. The *study-reach* covers an area of 1.6 x 0.65 km (1,100 m^2 – outlined in dashed red line), the *extended-reach* is 1.7 x 0.65 km and is located upstream of the study-reach (1,105 m^2 – outlined in dashed blue line), and together the two are referred to as the *full-reach* (2,275 m^2) as shown in Figure 3.3c. The study-reach is characterized by two large channels and multiple anabranches that converge at the downstream end into one large single thread, and one relatively insignificant anabranch. The full-reach starts as a single braid in the upstream section, but quickly diverges into multiple braids as it merges with the study-reach. Average gradient for the study-reach and full-reach is ~0.9 percent channel slope and upstream basin area is approximately 692 km^2 (NIWA, 2007). The study-reach is the primary focus for this study and is where all lupin processes will be examined and simulated; however, the immediate upstream topography is required for the numerical modeling mentioned in Section 1.2 and 3.3. This upstream topography was necessary for model ‘run-in’ data that improved the hydraulic simulations in the study-reach by providing fully developed simulated flow conditions at the upstream domain boundary.

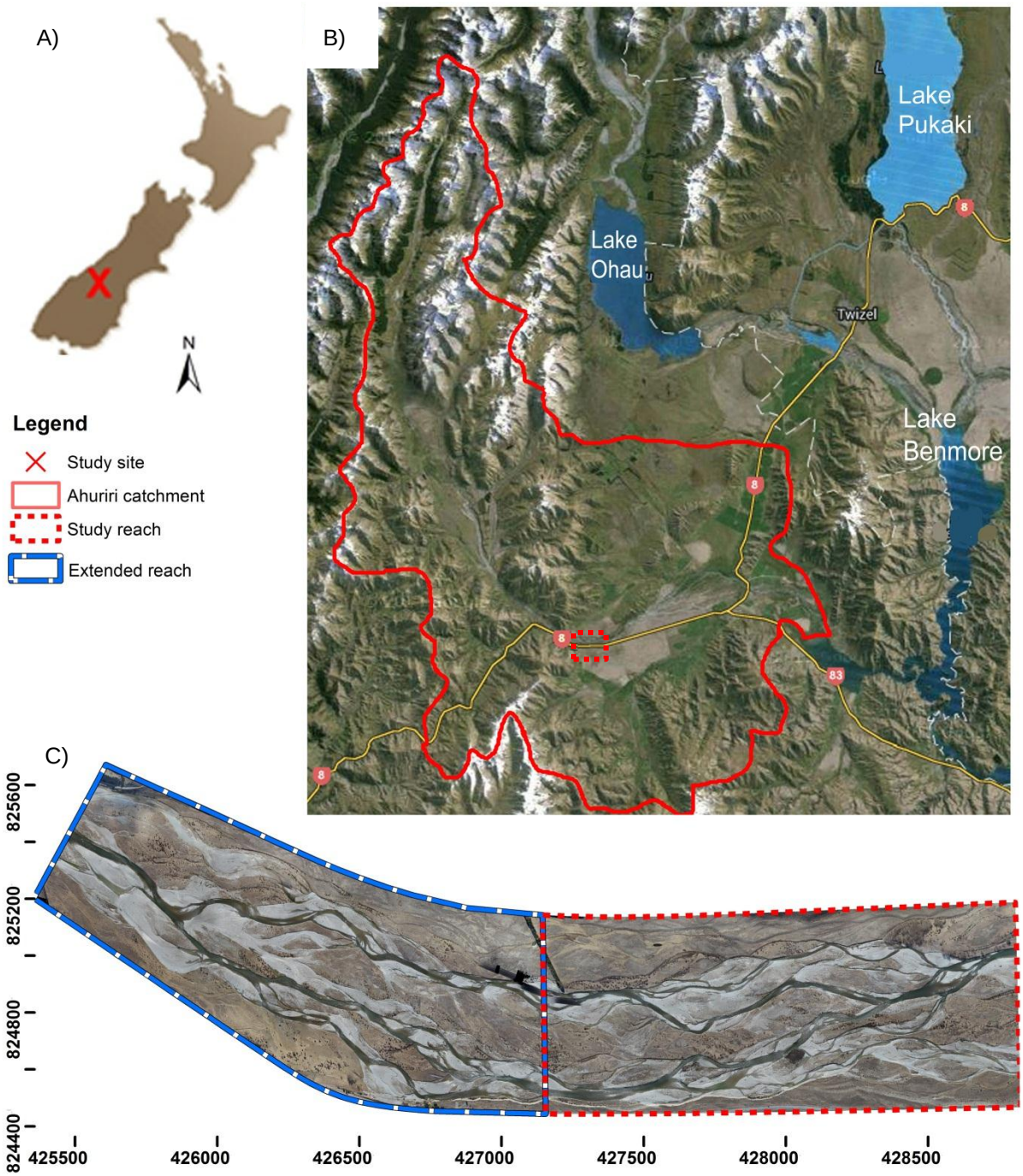

Figure 3.3: Ahuriri River: A) New Zealand study site location, B) Ahuriri catchment, and C) study-reach outlined in dashed red line and extended-reach outlined in dashed blue line.

Flow data has been recorded 9.5 km upstream of the study site by NIWA (and precursor organizations) since 1963. Originally, the data was recorded in 12 hour increments; however, since January 1965 the data has been recorded in sub-hour increments with the majority collected at 15 minute intervals. This flow data has helped determine the Ahuriri River's hydrological characteristics such as: mean flow of 23.4 m^3 s^{-1}, mean annual flood flow

(Leopold, Wolman, & Miller, 1964) of 222 $m^3 s^{-1}$; a maximum instantaneous flow of 570 $m^3 s^{-1}$, and a minimum instantaneous flow of 6.7 $m^3 s^{-1}$.

3.6 Summary

Previous relevant studies and key knowledge gaps have been presented in Chapters 1 and 2. With the new capabilities of recent advances in fluvial surveying and numerical modeling, there currently exists an opportunity to develop a deeper understanding of the hydraulic impacts of flood flows on vegetation. While the scope of this project is specific to one river and vegetation species, and subject to numerous limitations, the potential benefits of this research are fourfold. First, it has the potential to distinguish vegetation infested riparian areas that will require herbicide application from those areas that can be regulated naturally through flood events. This knowledge could help PRR better manage its limited resources (grazon and labor), apply these savings to other areas, and potentially improve public relations by reducing herbicide application. Second, the determination of flood effects and vegetation mortality can be utilized to assess the long-term effects of PRR limitations on weed eradication of the Upper Ahuriri River, Longslip Creek, and other rivers in the UWB. This could provide a risk analysis for such actions, and could be used in education and outreach activities to illustrate the problems of not allowing weed eradication in such areas. Third, this research benefits the discipline through the contribution of quantitative data relating river hydraulics to vegetation mortality, a overlooked subject. Fourth, the methods developed in this study could be used to assess the potential effects of flow regulation on other braided rivers. Together, these findings can be applied to provide insights into restoring the Ahuriri River and the remaining rivers in the Upper Waitaki Basin, as well as global river restoration projects faced with weed encroachment.

Part II

Data Collection, Experiments, and Modeling

Chapter 4

General Data Collection

4.1 Research site selection

Research concentrated on a river reach representative of the lupin infested braided Ahuriri River. This reach was the basis of all field work, laboratory work, and numerical modeling. Therefore, considerable care and time were taken to identify a reach that possessed the right attributes of lupin infestation, active mobile bed, braiding, and included two morphologic cycles that included multiple braids with major meanders to ensure a full range of river morphodynamics occurs within the reach. Initially, three potential study-reaches were identified through the use of satellite imagery available through Google Earth (Figure 4.1a). However, at the time of viewing, the most recent imagery on Google Earth for this location was 2005 (6 years old). Therefore, the first step in field work was to visit these potential study sites and to determine their suitability. On August 24th and 25th, 2011 each of the three sites was visited and extensive observations were conducted by trekking through each reach's entire length by zigzagging the width of the floodplain. This was done to: i) identify if the reach contained the appropriate morphologic cycles, ii) to identify the lupin infestation within the reach, iii) to document the braiding in the reach, iv) to determine if the reach had channels clearly active during common floods, and v) to outline any potential issues associated with the reach (e.g. forested areas causing poor GPS satellite signals).

On the 25th of August, the best reach was selected. Reach 1 was rejected due to lack of lupin infestation, and the potential for the surrounding canyons to interfere with GPS satellite communication. Reach 3 was rejected due to excessive vegetated bars and highly degraded river channels (which would suggest stable floodplains), and significant willow patches along the true left bank which could cause data satellite communication interference. Reach 2 possessed abundant lupin infestation on low-lying bars, relatively low channel degradation, an adequate morphologic cycle with sufficient braiding, and minimal areas of potential GPS

satellite blockage. Therefore, the study-reach was located within Reach 2, and was approximately 1.6 km long and 0.6 km wide as shown in Figure 4.1b outlined in blue.

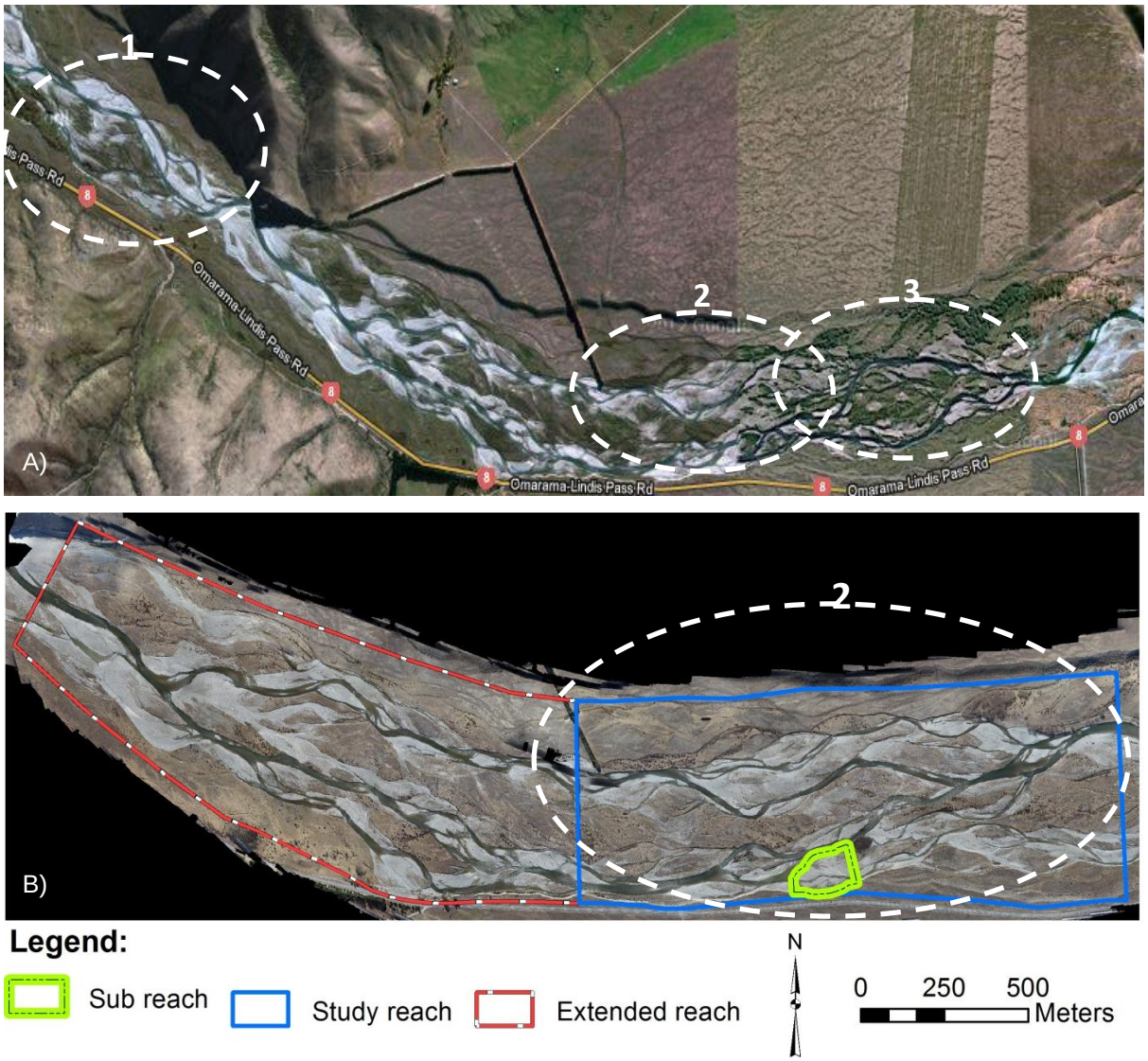

Figure 4.1: Study site identification: A) three potential research sites identified in Google Earth, and B) selected study sites.

4.1.1 Additional reaches

While the study-reach provided the necessary hydraulics and morphodynamics to properly study and model a braided river, its large size made it difficult to quantify and map the flood impacts on the vegetation prior to, during, and post flood event, and additional upstream topography would be beneficial to provide 'run-in' data for the model simulations (e.g. velocity, depth, sediment transport). Therefore, to study particular flood impacts on the

vegetation, a smaller *sub-reach* was identified within the study-reach. The ideal area would have lupins growing on a bar or bank with low vertical relief relative to the river's water surface that could easily be impacted by smaller, frequent flood events. This ideal area would also accommodate equipment such as a time lapse camera to safely document the developing vegetation and flood events. The chosen sub-reach was located approximately mid-way along the study-reach along the true right bank, as shown in Figure 4.1b and outlined in green. This area had abundant lupins growing in an area of low vertical relief within the braid plain and was within camera sight from a nearby terrace that was approximately 10 meters above the floodplain. This terrace provided an ideal location for a time lapse camera to document the sub-reach's vegetation development and the anticipated flood event impacts all while being safely elevated on the terrace. Further, this particular area was evaluated the previous year during initial site visits when organizing this research. From previous observations, it was known that flood events on the order of 300 $m^3 s^{-1}$ removed lupins in this particular area. To provide the necessary upstream run-in data for the anticipated numerical model simulations, the study-reach was extended by 1.7 km upstream, to where the river converged into one main channel as shown in Figure 4.1b. This area is outlined in red and is referred to as the *extended-reach*. Finally, combining the study-reach and extended-reach produced a 3.3 km stretch of river which will be referred to as the *full-reach*.

4.1.2 Site preparation: local network

The first field task was to create a network of checkpoints of known coordinates around the study-reach perimeter; hereafter referred to as a *local network*. This was necessary to ensure that future surveys could be compared to the current survey in the event of activity on the nearby Ostler Fault. Using a Trimble R8 GNSS system, operating RTK mode, the first coordinate surveyed was the Land Information New Zealand (LINZ) geodetic mark A3WB using NZGD 2000 coordinates with the Lindis Peak 2000 Circuit. This geodetic mark was north-east of Omarama, approximately 14 km from the study-reach. Using the Trimble equipment, the R8 reciever was placed over the center of the A3BW pin and using a *fast static* setting, the location was occupied for several hours and the recorded coordinates provided a calibration for the soon-to-be created local network and surveys conducted within the study-reach.

The next step was to set up the local network around the perimeter of the study-reach. Installing and surveying four steel posts and utlizing a previous survey's pin set in concrete, the true left side of the local network was created. The true right side of the network was created by surveying another pre-existing pin set in concrete, and three previously-installed wooden survey posts. Each of the nine network controls was surveyed using the RTK-GPS equipment's fast-static mode, and occupied for 30 minutes. When setting up the network, it was decided that the pre-existing survey pin on the left bank would serve as the '*master*' control point as it had the highest location overlooking the study-reach, was the most stable, and the small pin set in concrete offered the most precise point to start future surveys. The master point was then used for the entire field work as the location of the RTK-GPS's base station. In addition, a repeater was set up on the terrace of the left bank to ensure that the base-station's radio signal would be broadcast over the entire reach.

4.2 Hydrology

4.2.1 Introduction

Knowledge of the Ahuriri River's hydrology and sediment regime underpins all aspects of the research. The river's flood magnitude, duration, and frequency, together with its sediment supply, storage, and transport, were crucial information for conducting field work, numerical model simulations, and laboratory experiments. Therefore, as an initial step in this research, a basic hydrological assessment was conducted using the Ahuriri River's flow record collected by the National Institute of Water and Atmospheric Research (NIWA) and precursor organizations since 1963. This flow gauge is located approximately 9.5 km upstream of the study-reach and does not include the downstream Longslip Creek tributary entering the Ahuriri River between the gauge and study-reach. However, with unknown losses between the gauge and study-reach and without flow data for this tributary, its contribution was not considered and no flow scaling was conducted. This is partially justified since the mean annual flood for Longslip Creek was estimated at 17.3 $m^3 s^{-1}$ and the Ahuriri River's was determined to be 222 $m^3 s^{-1}$; thus, the Longslip Creek tributary's contribution was not significant (NIWA, 2007).

A previous hydrological assessment of the Ahuriri River was conducted by Rademaker and Balme (2010). This provided a summary of annual flow statistics and flood frequency up to a

500-year return period based on NIWA's daily mean flow records from 1963 to 2009. While this analysis provided preliminary information for the hydrological assessment, a further assessment was performed using the updated 2011 NIWA flow record. Following Environment Canterbury's hydrological year, the water year begins on June 1 and ends May 31; with the water year corresponding to the year it began (e.g. data from June 2010 to May 2011 is the 2010 water year). Initially, flow data for 1963 was recorded in 12 hour increments; however, by January 1965 the data is recorded in sub-hour increments with the majority collected at 15 minute intervals.

Once the frequency and magnitude of high flows was assessed, the final part of the hydrological assessment was to compare the duration of specific flood events for two reasons. First, flood duration was an essential part of understanding the flood impacts upon vegetation, as inundation mortality has been hypothesized as a detrimental process. Secondly, identifying a relationship between duration and magnitude aided the model simulations of various sized future flood events.

4.2.2 Methods

The raw flow data were first sorted in Microsoft Excel to produce the minima, maxima, and mean for daily and yearly flows. Using the yearly maxima, an annual maximum series (AMS) was produced for statistical analysis to determine the flood frequencies and magnitudes. Both the Weibull and Gringorten plotting methods were applied to the AMS to determine the probability and return period of each flood event (Stedinger, Vogel, & Foufoula-Georgiou, 1993). The Weibull and Gringorten methods produced similar results for smaller return periods (2 – 12 years); however, their results differed for larger events (> 20 years). In the end, the Weibull method was chosen because it is the method most frequently used (Viessman & Lewis, 2003) and provides a plotting method free of bias (Stedinger et al., 1993). It is important to note that Rademaker and Balme (2010) used the daily mean values for assessing the Ahuriri hydrological data; however, the maximum values were chosen for this assessment since the focus of this study was flood impacts.

Fitting a probability distribution to the AMS dataset was achieved by using Mathwave's EasyFit; a distribution fitting software. EasyFit can test over 55 probability distributions in a

matter of minutes and can be used as a Microsoft Excel plugin. Once the data were processed, EasyFit provides a *goodness of fit* test (GOF) that measures the compatibility of the data (flows) with the theoretical probability distribution functions. The GOF uses the Kolmogorov-Smirnov (KS) and Anderson-Darling (AD) tests as well as the Chi-Squared (CS) distribution test. The GOF results showed that many distributions fit the data relatively well. However, because each distribution had a GOF test that produced three different rankings (KS, AD, and CS), it was not clear which distribution was the best-fit. Therefore, to determine the best distribution, the rankings were averaged, and the distribution with the best averaged ranking was selected.

To examine flood duration, the raw NIWA flow record was utilized to identify flood events. However, unlike the AMS used in the frequency and magnitude section, multiple flood events could be assessed for the same water year. To filter the raw data first required the quantification of a *flood*. This was done in number of steps. First, a flood was defined and quantified as anything equal to or greater than the *mean annual flood;* which has a return period of 2.33 years (Leopold, Wolman, & Miller, 1964). The second step was to define the beginning and end of flood events. This was accomplished through the use of the *FRE3* value; which is based on the median flow of the river (over the entire dataset) multiplied by three (= 57.96 $m^3 s^{-1}$). This value has been described as a threshold for ecological disturbance (Duncan & Woods, 2004), which complements the overall goal of this project in determining flood effects on lupins. With these two restrictions, it was possible to analyze the duration of a single flood event. Using these criteria, 29 flood events were identified and analyzed for the 47 years of data.

To simulate the various sized flood events of the Ahuriri River required a generalized hydrograph that represented the unique flood characteristics. Therefore, utilizing the 29 identified flood events and corresponding hydrographs, a synthetic hydrograph was developed based on the real flood events. This was accomplished by identifying a representative hydrograph flood wave shape and single crest of the available 29 flood events (Voskresensky, n.d.). With the representative hydrograph selected, the synthetic hydrograph was produced using the curvilinear hydrograph method outlined by the Natural Resources Conservation Service of the U.S. Department of Agriculture ("SCS/NRCS Hydrographs;" Appendix D.1). Therefore, the resulting synthetic hydrograph was of the same flood wave

shape, but stretched. Using this method, synthetic hydrographs were generated for 2, 5, 10, 25, 50, 100, 200, and 500-year events.

4.2.3 Results and discussion

Based on the data for the 1963-2011 period of record utilizing EasyFit, the Log Pearson 3 (LP3) distribution was determined to be the best distribution for this river. Using the LP3 distribution, EasyFit was then utilized to forecast flood magnitudes with estimated return periods of 2, 5, 10, 25, 50, 100, 200, and 500 years with results shown in Table 4.1. This was accomplished by utilizing the cumulative distribution function and annual exceedence probability for a given event (Figure 4.2). The LP3 distribution is recommended by the United States Water Resources Council and the Australian Institute of Engineers (Stedinger et al., 1993). However, Pearson (1991) concludes that the generalized extreme value (GEV) distribution best described South Canterbury flood data, and Rademaker and Balme (2010) found that the GEV and Lognormal distributions best-fit for the Ahuriri River data set. This discrepancy could be due to the data used as Rademaker and Balme (2010) used the averaged flow data while this assessment used annual maxima. Further, it should be noted that these flood discharges were determined using the NIWA flow gauge data, which is located 9.5 km upstream of the study-reach. Therefore, the discharges that would occur in the study-reach are likely larger due to the Longslip Creek tributary and additional basin runoff. As mentioned, due to lack of flow data and unknown losses, these contributions were not included.

Table 4.1: Return period and corresponding discharge.

Return period (years)	Annual exceedence probability	Flow ($m^3 s^{-1}$)
2	0.500	218
5	0.200	325
10	0.100	403
25	0.040	507
50	0.020	596
100	0.010	687
200	0.005	784
500	0.002	923

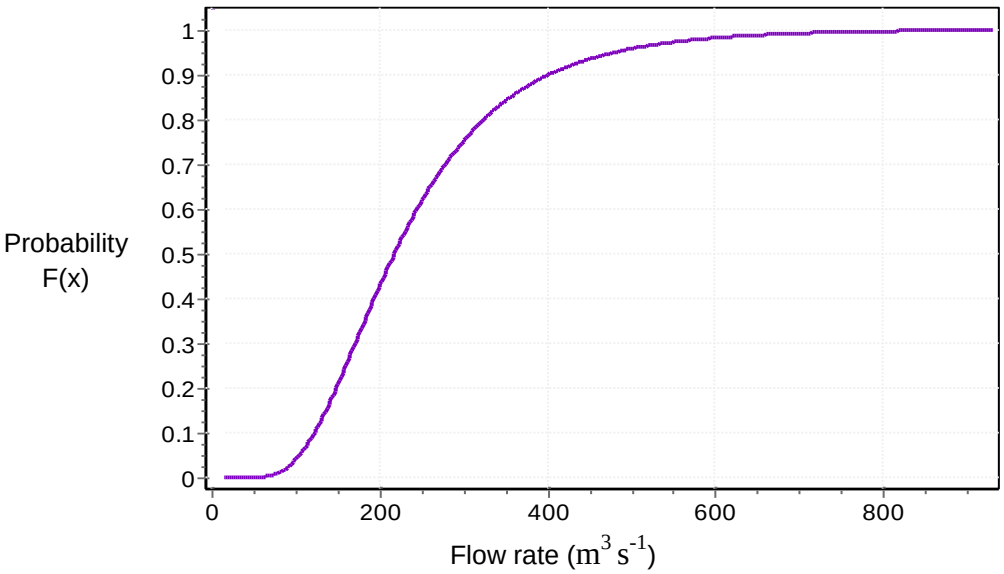

Figure 4.2: Log-Pearson 3 cumulative distribution function for Ahuriri River at South Diadem site.

The final check was to compare the Weibull distribution data with the LP3 modeled data. As shown in Figure 4.3, the two data sets compare well for the smaller frequent floods (~10 year return). For example, the two-year flood for the Weibull distribution has a flow of 220 $m^3 s^{-1}$, and the LP3 data has 218 $m^3 s^{-1}$. However, the data deviate for larger events (> 20 years). For example, the largest Weibull distribution flood was 570 $m^3 s^{-1}$ and determined to be a return period of 48 years, while the LP3 data had 568 $m^3 s^{-1}$ for a 40 year flood. While these results were not perfect, they show adequate similarity between the modeled data and the Weibull calculated data. Finally, the LP3 flood frequency and magnitude data was valuable for numerical model simulations; however, a magnitude and duration relationship was also required.

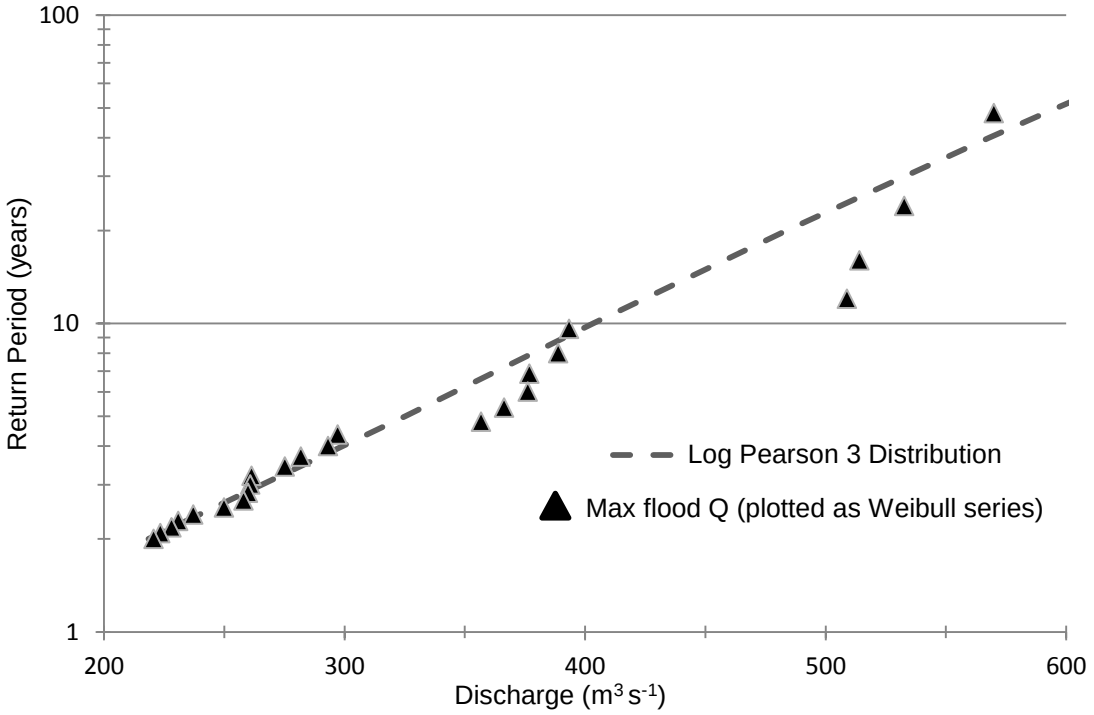

Figure 4.3: Log-Pearson 3 distribution compared to the Weibull distribution for the Ahuriri River at South Diadem site.

The duration and return period relationship for the 29 flood events was developed into a box and whisker diagram (Figure 4.4). However, no distinguishable relationship between a flood's duration and frequency could be established due to the extreme variation in duration. For example, floods with a return period of three years (T=3) had durations between 68 hours and 282 hours, while the largest flood event (T=48) had a duration of only 132 hours. Separating the 29 flood events into monthly occurrences showed that December had the highest frequency, with 7 of the 29 events (Figure 4.5).

With numerous lupin mortality processes hypothesized in Section 3.2 that required field data and experiments, it was paramount to narrow the research focus to one particular season; as varying seasons would inevitably alter the mortality processes and thresholds. Utilizing the peak flood season was a practical choice as it would document the conditions and processes most likely present during lupin mortality and corresponding flood events. Therefore, December was the time period in which all research was focused. Further, all laboratory experiments were conducted on lupin maturity typical of the Ahuriri's lupins in December and typical of flood durations.

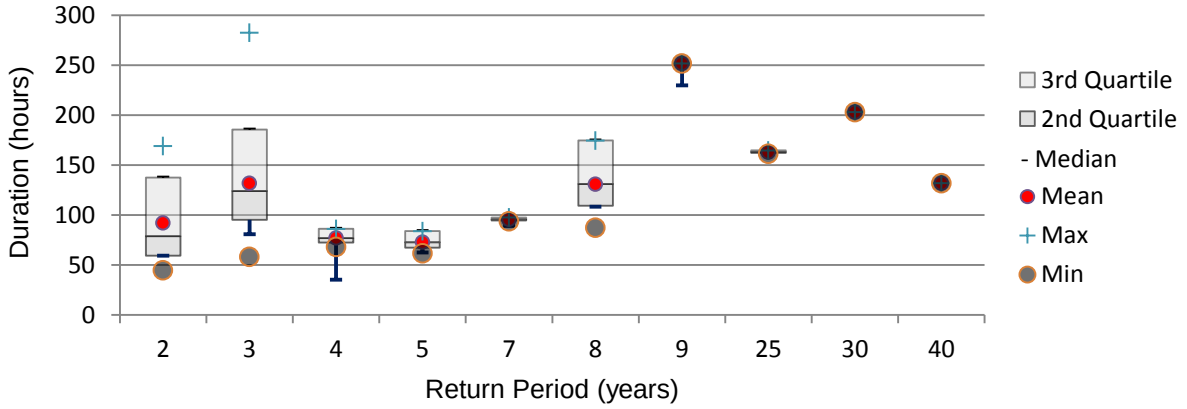

Figure 4.4: Box and whisker plot for duration vs. return period.

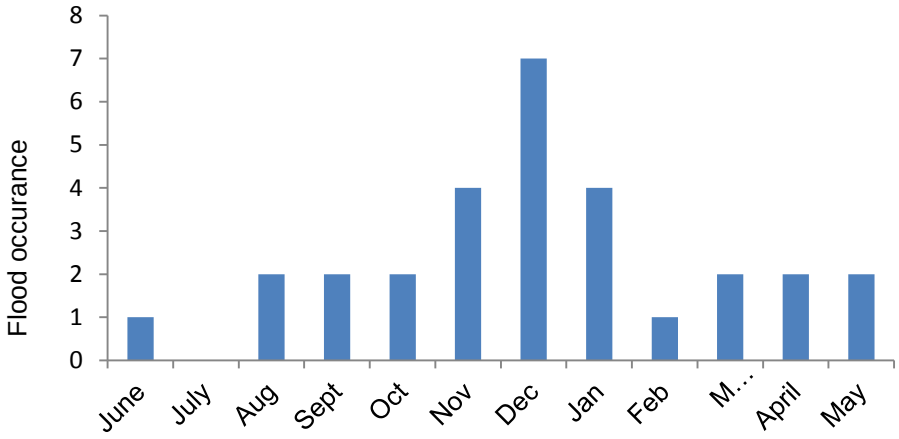

Figure 4.5: Monthly occurrence of the 29 flood events between 1963-2011.

Since a duration and magnitude relationship could not be determined from the 29 flood events, the seven December flood events were evaluated separately. As shown in Table 4.2, the seven events range from a return period of 2.7 to 33.1 years based on the previously determined LP3 data. When comparing the duration and discharge of Table 4.2, the Pearson correlation was utilized to provide a quick measure of the two variables' interdependence and produced a value of 0.9, suggesting a strong linear relationship. With the overall goal to simulate various flood magnitudes, it was necessary to determine the typical corresponding duration. Therefore, utilizing the seven events, various empirical formulas were developed in Microsoft Excel by fitting trendlines such as a linear, power, logarithmic, and polynomial functions to describe this relationship. Since multiple relationships were tested and many

provided adequate least squares regression (R^2), and due to the limited data set size, an alternative method was needed to test the fit of the estimated data compared to the measured data. Therefore, error variance, s^2, was utilized; which provided a goodness-of-fit measure. Error variance is calculated by (Hill and Tiedeman, 2007):

$$s^2 = \frac{\Sigma_p\left(\frac{Y_P - \bar{Y}_P}{s_P}\right)^2}{n_P - n_R} \qquad \text{(Eqn: 4.1)}$$

where, Y_P is the measured value, $\bar{Y}_P$ is the modeled value, S_P is the standard deviation of the measurement's uncertainty, n_P is the number of data points, and n_R is the number of parameters in the models equation (Hill and Tiedeman, 2007; Daughney, Fakih, & Châtellier, 2011). Ideally an s^2 value of 1 is achieved, which indicates the model's errors are equal to the estimated uncertainty. Values smaller than one indicate that errors are estimated and/or there are too many parameters governing the equation. Finally, s^2 values greater than one indicate a weaker model fit and values of 20 and higher indicate a poor fit (Daughney et al., 2011). Using the least squares regression and error variance, the best relationship was determined, and example calculations are shown in Appendix B.1, Table B.1. Based on the R^2 and s^2, the linear trendline and equation was determined to best-fit the seven data points with a R^2 of 0.8 and an s^2 of 1.6 (Figure 4.6). However, while Figure 4.6 revealed data well outside the trendline equation, this magnitude-duration relationship achieved significantly improved forecasting ability over all flood data, thus it provided the necessary means to forecast future December flood hydrographs. Therefore, the resulting empirical formula was utilized to determine the durations of the various sized flood events as shown in Table 4.3.

Table 4.2: December flood events.

	December flood events						
Year	1965	1969	1979	1984	1995	2000	2010
Duration (hours)	77	96	161	203	165	124	94
Discharge ($m^3 s^{-1}$)	256	332	513	532	507	281	355
Return period (T)	2.7	5	27.6	33.1	26.2	3.3	6.3

The final process was to develop a generalized synthetic hydrograph for the various flood events. Therefore, using the NIWA flow data, the seven December flood hydrographs were plotted together to have flood peaks align at zero hours of duration in Figure 4.7. As shown, the seven hydrographs were similar, with steep rising limbs, short lag times, and relatively gradual recession limbs, with multiple crests likely caused by additional precipitation. Of the seven events, the December 1995 flood event hydrograph was chosen as a representative hydrograph, and with minor smoothing (mainly for the spike in the recession limb), a flow and duration relationship was developed to describe the general hydrograph shape and applied to the flow duration data of Table 4.3 to produce the generalized and detrended future flood hydrographs of Figure 4.8. Finally, the generalized hydrographs were compared to the actual 1969 and 1984 flood events which produced good comparisons (Appendix D, Figure D.1 and D.2). These two hydrographs were chosen as they provided a check to assess how well the generalized hydrograph represented the smaller 1969 (5-year) flood event and largest 1984 (33.1-year) flood event.

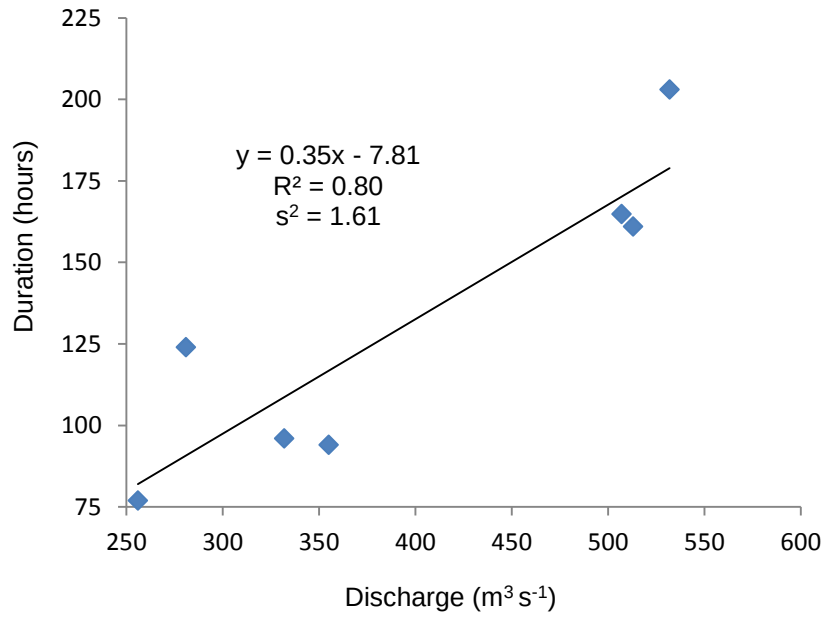

Figure 4.6: Discharge vs. duration relationship and linear trendline.

Table 4.3: Flood magnitude, frequency, and estimated duration.

Return period (year)	Flow ($m^3 s^{-1}$)	Duration (hours)
2	218	69
5	325	106
10	403	134
25	507	170
50	596	201
100	687	233
200	784	267
500	920	315

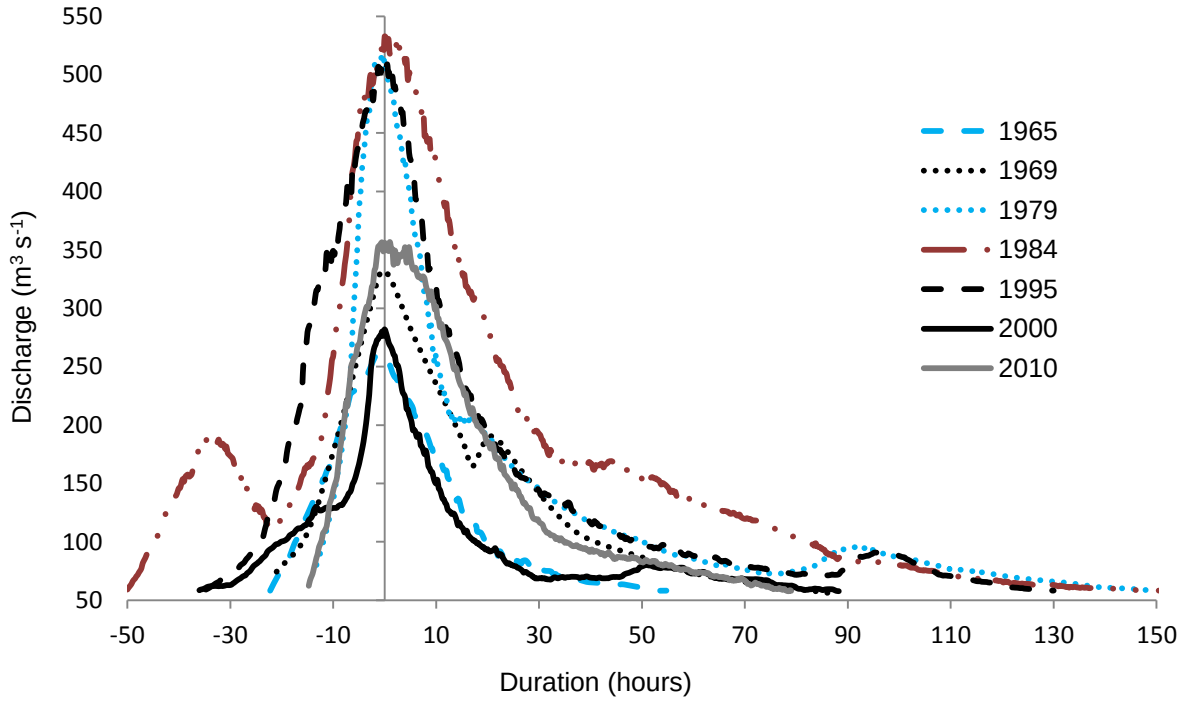

Figure 4.7: Detrended hydrographs for the seven December flood events.

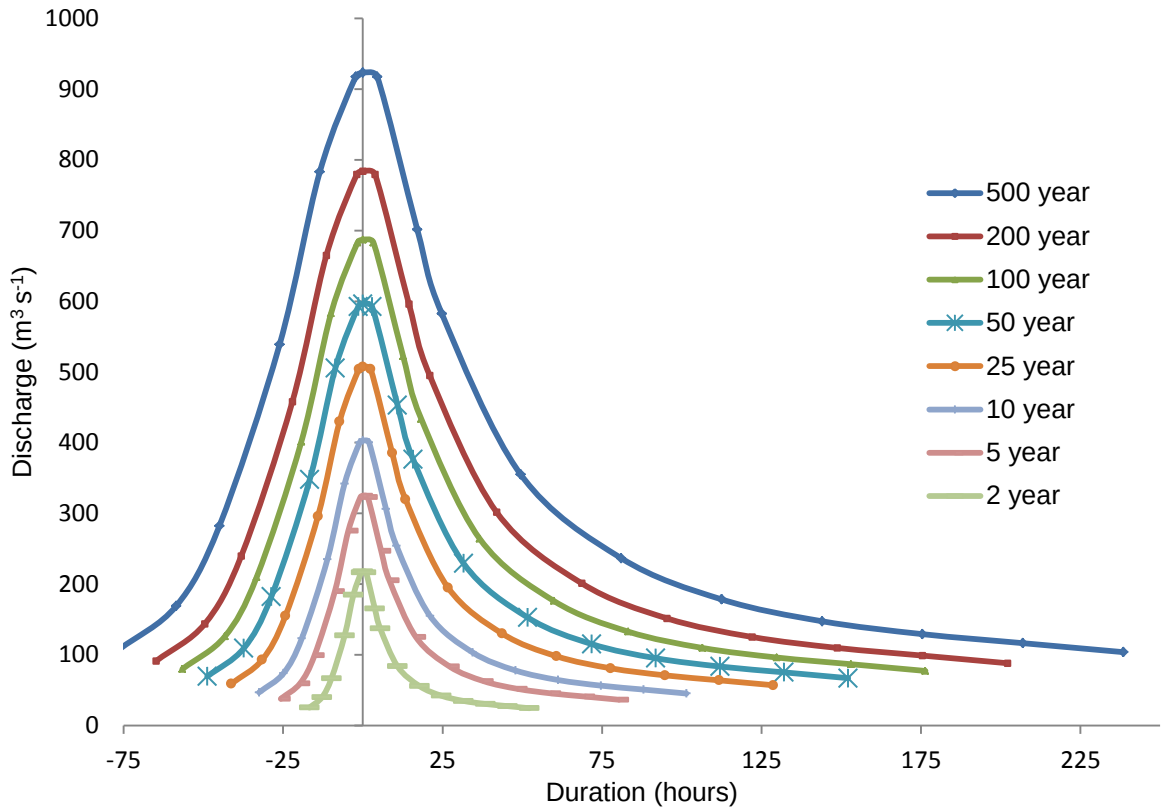

Figure 4.8: Synthetic hydrograph of forecasted floods.

4.3 Lupins: Observed data

4.3.1 Introduction

Initial field observations were conducted to investigate the hypothesized lupin mortality processes of Section 3.2. Once the study site and sub-reach were identified, the Ahuriri River was monitored for flood levels. Flood events occurred on October 26th, 2011, January 3rd, 2013, and January 10th, 2013, with peak discharges of 209 $m^3 s^{-1}$, 221 $m^3 s^{-1}$, and 288 $m^3 s^{-1}$, respectively. When flood levels receded to a safe level, field observations were conducted to identify and document the processes responsible for lupin mortality, such as removal (erosion and drag), inundation, trauma, and sediment deposition burial.

4.3.2 Methods

Combining field observations with the sub-reach time lapse imagery, qualitative assessments were made of the local vegetation before, during, and after flood events to identify lupin

removal, trauma-related mortality, and inundation-induced mortality. To investigate lupin removal, the time lapse imagery was assessed to determine vegetation extent pre- and post-flood event. To investigate trauma-related mortality, lupins with deteriorated canopies were recorded and monitored over the following six weeks, and inundation-related mortality was assessed by analyzing the time lapse images for flood inundated areas, and monitoring their health over the following six weeks. In addition to assessing the health of sub-reach lupins, additional flood-impacted areas were discovered post-flood and monitored for lupin survival. Finally, numerous lupins had been deposited throughout the floodplain from the receding flood levels. This offered the opportunity to analyze the deposited lupins throughout the sub-reach and surrounding area for clues about their removal processes.

4.3.3 Results and discussion

4.3.3.1 Trauma and inundation

Following the three flood events, field observations and follow-up time lapse imagery revealed that no lupin mortality occurred in the sub-reach from trauma or inundation due to minimal inundation extent and slow velocity. However, additional observations were carried out in various locations of the Ahuriri floodplain where areas previously covered with lupins had suffered severe flood damage. From the observations, this previously un-impacted area (hereon referred to as '*flood zone 1*') became a swift channel during the January 2013 flood events, and remaining lupins provided useful information on flood-induced trauma. As shown in Figures 4.9 and 4.10, numerous lupins in the mid-section of this flood zone 1 suffered significant flood impacts. These two images and field observations indicate that flood effects were extremely harsh on lupins' herbaceous material and caused significant trauma. As shown in Figure 4.9, the lupin's stalk was completely bent over and creased at approximately 2 cm from the substrate. Since the lupin canopies appear to be dead, a follow-up observation was undertaken 5 weeks later on Feburary 16th, 2013 to determine if these lupins experienced trauma-related mortality. Upon return, 183 lupins were recorded in the flood zone 1 and approximately one-third showed signs of regrowth. The remaining two-thirds had dead canopies and no sign of regrowth. To ensure that the lupins' regrowth was not just new seedling germination, the suspected regrowth roots were investigated. In a few cases, the growth was lupin seedlings as determined from the small and shallow roots; however, in the end, 67 of the lupins had regrowth that was directly attached to the pre-existing root structure

of the larger lupin. Pictures of this evaluation can be found in Appendix E.3, Figures E.3, E.4, E.5, and E.6. Since the 67 that did have lupin regeneration showed regrowth height above 10 cm, it was assumed that the remaining 116 lupins that showed no signs of regrowth would not regenerate their canopies. Therefore, 63.4% of the flood zone 1 lupins potentially experienced trauma-induced mortality. However, additional processes could have been fully or partially responsible for the mortality. Of the potential processes, inundation may have been a likely contributor since these lupins were inundated.

Figure 4.9: Lupins post-flood event showing: i) trauma and deformation, and ii) deposition around lupins.

Figure 4.10: Post-flood lupin trauma and deformation.

While post-flood diagnostics can be made for flood-induced trauma, inundation-induced mortality was not easily determined from initial observations. The inundation extent, depth, and duration were all important factors for lupin inundation sensitivity. Since the sub-reach time lapse image analysis showed that the area had only been inundated by shallow water, it was no surprise that the damaged and inundated lupins of the sub-reach regenerated healthy canopies over the following months. However, since no inundation-mortality was observed, an additional experiment was required to further study inundation effects on lupins. This is presented in Section 4.4.1.

4.3.3.2 Lupin removal

Time lapse imagery revealed that no sub-reach lupins were removed during any of the flood events. Following the October 2011 flood event that peaked at 209 $m^3 s^{-1}$, 65 deposited lupins were examined and a qualitative assessment found that all had suffered some trauma indicated by canopy deterioration. However, of these lupins, the vast majority (~90%) had their tap roots freshly severed (Figure 4.11a). Typical canopy heights of these lupins were greater than 40 cm, and the roots were severed between 15 and 25 cm from the base of the

stalk. The remaining lupins (~10%) had no major root damage and ranged in canopy heights (Figure 4.11b).

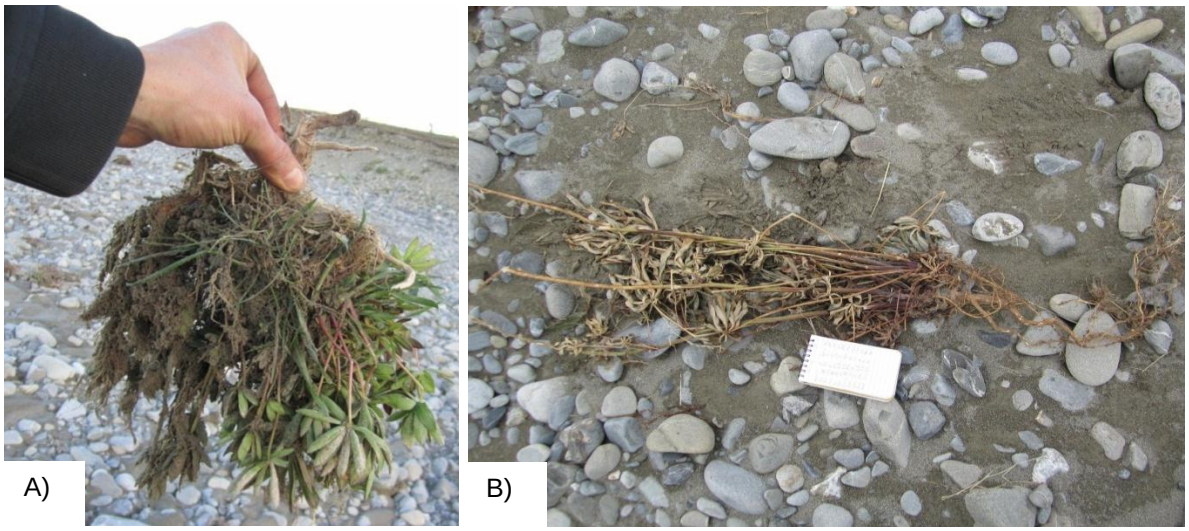

Figure 4.11: Lupins from the October flood event: A) lupin with severed root, and B) lupin with intact root.

Following the January 2013 flood events of 221 and 288 m^3 s^{-1}, deposited lupins were observed and their physical characteristics were documented (Appendix E.2, Table E.1). From the results of the 72 lupins assessed, 42 had severed roots and 30 had intact roots. Assessing the lupins with severed roots revealed that typical root depths were between 20 and 30 cm, and the canopy height exceeded 40 cm - similar to the October 2011 flood observations. The lupins with intact roots had a broader range of sizes, which also compares well with the first observed flood. The majority of the deposited lupins had significant canopy deterioration. Using the deposited lupin data, Figure 4.12 illustrates the cumulative frequency of the deposited lupins for various root diameters for the categories of severed roots, intact roots, and all root conditions. From this figure, it was apparent that severed lupins typically have larger root diameters than the lupins with intact roots. For example, comparing the R_{50} (50% of the sampled root diameters are finer) shows that the severed R_{50} = 3.9 cm, while the intact R_{50} = 3.0 cm.

These observations suggest that the lupins with severed roots were removed forcefully. Processes that could cause this are drag, and/or collisions with passing debris (sediment,

other removed vegetation, etc.). Further, the severed lupin roots occurred at varying lengths and diameters, suggesting that the lupins with short lengths experienced extensive drag or collisions while those with longer roots may have been affected by a combination of drag, erosion, and/or local soil conditions (that provided reduced binding between roots and soil). The lupins with intact roots suggest that removal was relatively gentle on the root system, which was possibly caused by erosion and/or local soil conditions. Since no major root damage was found, it was assumed that this was caused specifically by bank erosion where sections of sediment and vegetation would slough off into the river.

While it is acknowledged that local sediment conditions and spatial and temporal variation in shear stress can, and do, likely affect the lupin-mortality of the observed deposited lupins, the equipment and funding necessary to investigate these processes were well beyond this research. Further, based on the observation and results presented, the evidence implies that drag, abrasion by entrained debris, and erosion were likely processes for two reasons: First, the intact root diameter size was more variable than those of the severed lupins. This assessment was consistent with eroded lupins, as any vegetation on top of an eroded bank would be removed. Thus, vegetation removal was not dependent upon vegetation characteristics and would likely produce varying vegetation sizes. Secondly, severed root-related removal was typical of larger lupins. Because larger vegetation will naturally produce greater drag forces and increase the risk of collision with passing debris, larger lupins have a greater chance of being removed by this process.

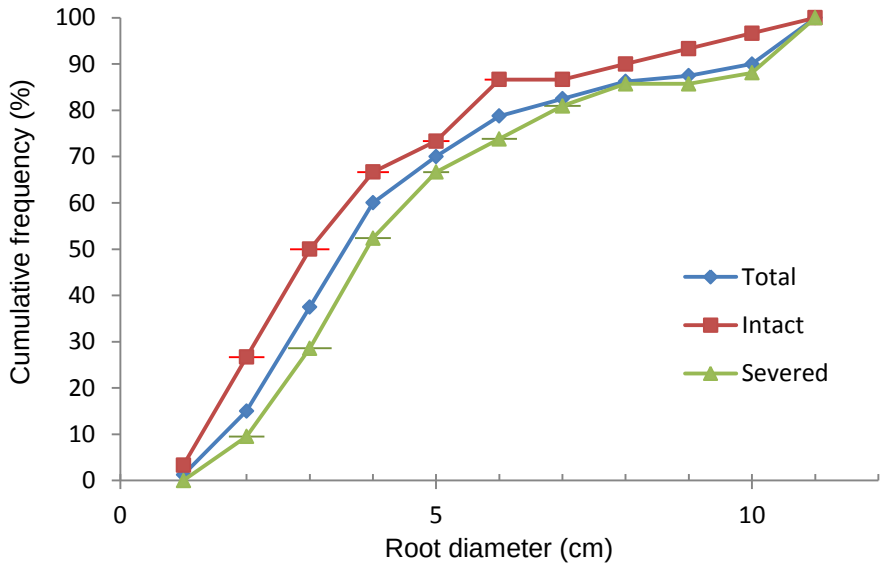

Figure 4.12: Cumulative frequency of root diameter for the deposited lupins following the two January 2013 flood events (error bars show root diameter standard deviation).

During this evaluation of deposited lupins, none were found with canopies shorter than 25 cm. Three possible reasons were hypothesized: i) small lupins were able to withstand the forces/processes (except bank erosion) that removed larger lupins, possibly due to their size, flexibility, and/or protection by surrounding larger sediment such as cobbles or boulders (Figure 4.13); ii) smaller lupins were not deposited as readily as larger and heavier lupins and were carried downstream into Lake Benmore; and iii) the lack of smaller lupins may be a local phenomenon. Observations frequently documented small lupins present in areas of obvious strong flow conditions (Figure 4.14) following flood events, indicating that smaller lupins were likely able to withstand flood conditions. However, no prior information was available for this area; therefore, it could not be assumed that large lupins were removed and small lupins remained. A likely scenario was that all, or many, lupins were removed during a large previous flood event and the present lupins were just young, re-establishing lupins. Therefore, the removal of smaller lupins was unclear at this point. However, one hypothesis was that smaller lupins may be able to withstand the processes detrimental to larger lupins due to their flexibility, smaller size (less drag and collisions), and protection by the surrounding large sediment found in the Ahuriri floodplain. This hypothesis was later re-examined in drag experiments (Section 4.4.3). However, one important observation was that while smaller lupins may be less susceptible to removal, their smaller stature makes them more susceptible to deposition burial, which could be detrimental if burial reduced sun

exposure (i.e. prevent photosynthesis). Therefore, an experiment was necessary to examine lupin sensitivity to burial by sediment deposition and is presented in Section 4.4.4.

Figure 4.13: Small lupin sheltered by large sediment typical of the Ahuriri floodplain.

Figure 4.14: Small lupins in an area following a recent flood event.

4.3.3.3 Erosion and deposition

Vegetation such as grass can encourage sediment deposition, and vegetation with leaf mass can encourage sediment transport by deflecting flow downward causing local scour around the vegetation's roots (Abt, et al., 1994; Samani & Kouwen, 2002; Leonard & Luther, 1995; Nepf & Vivoni, 2000; Freeman et al., 2000). Since lupins are flexible herbaceous vegetation with a distinct leaf mass, it was difficult to assess which effect they would produce: a local

scour due to their leaf mass and semi-rigid stalk, or if flood induced deformation would cause them to behave similarly to grass and encourage deposition. To answer these questions, the previously mentioned *flood zone 1* area provided useful information on lupin removal by erosion and burial by deposition. As shown in Figure 4.15, numerous lupins at the downstream end of flood zone 1 were not removed; however, due to eroded roots visible in Figure 4.15, it was estimated that the lupins in this area experienced bed erosion of approximately 10 cm. Based on the observations in this area, it can be concluded that lupins do not fully prevent bed erosion.

Figure 4.15: Flood impacted lupins with approximately 10 cm of bed erosion.

Through additional observations, areas in the mid-section of flood zone 1 were identified where lupins may have encouraged sediment deposition. As shown in Figures 4.9 and 4.16, fine sediment was deposited around lupins, while vegetation-free areas between the lupins consisted of larger sediment and minimal fine material. Based on the erosion and deposition of observations made for Figures 4.9, 4.15, and 4.16, lupins may have varying results on

erosion and deposition. Since the deposition only occurred around a small perimeter around lupins, and nearby areas free of vegetation had large surface sediment, it was assumed that it was not a condition of the flow causing the deposition, but rather the vegetation. However, in the previously mentioned downstream area where erosion occurred beneath lupins, there were no signs of sediment deposition. One possible reason for this was higher velocities occurred in the erosion area, which was supported by the fact that surface erosion was taking place and finer sediment was not deposited. Further, this may also be related to the local upstream supply and sediment size composition (D. M. Hicks, personal communication, October 7, 2013).

While these observations were suggestive of lupin effects on hydraulics and sediment deposition, there were no observations of lupins fully buried by deposition; thus an experiment would be required to assess deposition-induced mortality (presented in Section 4.4.4). However, before an experiment was conducted, it was necessary to determine flood-induced lupin deformation in order to determine the initial amount of deposition required to bury flood-affected lupins. Initial assessment for flood zone 1 indicated that lupin deformation was significant due to the lupin canopy height being reduced to ground level (as shown if Figure 4.9, 4.10 and 4.16). However, these results were not conclusive because at the time of image capture, the lupins' state of health would have been impacted over the days following the flood event. Due to the likely trauma inflicted and several days to further deteriorate and deform, the current state of these photographed lupins was not representative of the deformation experienced during a flood event. Therefore, while these observations were helpful, an experiment was necessary to fully document lupin deformation.

Figure 4.16: Flood impacted lupins showing signs of trauma, deformation, and sediment deposition.

4.4 Lupins: Experiments

4.4.1 Lupin inundation experiment

4.4.1.1 Introduction

As Friedman and Abule (1999) have shown, certain types of vegetation are sensitive to long periods of inundation. As determined by the hydrology assessment, flood events in the Ahuriri River have lasted up to eleven days; therefore, lupins were tested for inundation-related mortality. Knowing that lupins thrive in coarse permeable soil in the floodplain, it was hypothesized that lupins will tolerate partially submerged conditions, but mortality would occur after several days when completely submerged.

4.4.1.2 Methods

This experiment tested 80 lupins that were planted in 25-litre planter bags with substrate that was typical of the Ahuriri River. Substrate was extracted from the floodplain of the braided Waimakariri River in October 2011 (3 m^3) by Isaac's Construction gravel extraction site. The river substrate was placed in the planter bags which were filled to approximately 85%, and the remaining 15% was filled with a fine soil that Isaac's Construction had removed from settling ponds. This finer material was chosen as the top soil because it would better retain water for the critical germination period. Once the planter bags were filled, five seeds (Yates Lupin Russell Hybrids seeds) that had previously soaked overnight to improve germination were planted in each bag at a depth of about 12 mm. Following sowing, the soil was immediately watered and regular water was applied as needed thereafter.

In February 2012, the lupins were ready for inundation testing as they had reached the maturity indicative of lupins in the Ahuriri during December (roughly half flowering). The experiment consisted of three tanks at different depths: i) shallow water depth to simulate a high water table, where water was filled to the middle of the planter bag (~18 cm deep and shown in Figure 4.17), ii) medium water depth to simulate shallow inundation, where the water level reached the base of the stock of the plant, but the canopy was emergent (~33 cm deep), and iii) deep water depth to simulate full inundation, where the water level completely submerged the plant (~100 cm deep). Since flood waters can be turbid, the deep water tank was equipped with a cover to simulate sunlight reduction by turbid water. This was deemed an important aspect of the experiment because the lupins may be more sensitive to reduced sun exposure and limited photosynthesis than water-induced anoxia.

As mentioned in the hydrology section (4.2), December had the highest flood occurrence and the longest flood duration was 282 hours (~11.75 days). Therefore, December was the target month to simulate, and inundations would last up to 12 days. To ensure that the results were representative, three planter bags were tested every day in each of the three tanks, resulting in 9 lupin planter bags tested for each day of inundation. This redundancy reduced the risk of erroneous results; however, it also limited the test period to eight days due to the limited number of lupins. Limiting the test to eight days would restrict the results only if after eight days the lupins where still alive. Indeed, this was the case for tanks with shallow and medium

water levels. Therefore, at day eight, with the lupins in the shallow and medium depth tanks still alive and healthy, no plants were removed. Instead, the three remaining plants in the shallow tank and the four remaining plants in the medium tank were left for further inundation. At day 9, the lupins were alive and healthy looking in the shallow tank, but the medium tank showed significant wilting; therefore, one plant was removed from the medium tank. Days 10, 11, and 12 resulted in one plant from each tank being removed to conclude the inundation testing period of 12 days. Since mortality in the deep tank occurred starting at day 2, testing in the deep tank was not conducted past 8 days.

Figure 4.17: Inundation testing for the mature lupins in the shallow tank.

4.4.1.3 Results and discussion

Since all planter bags had five seeds planted, most bags had numerous plants growing. Therefore, some results are marked as *damaged*, which indicates that some of the plants in a specific bag died, while others lived. All plants were allowed 30 days to recover and show signs of re-growth. Following this regrowth period, plants that had experienced full mortality were examined. Table 4.4 shows that the shallow tank lupins survived the majority of the inundation with some death at day six yet the remaining survived the remaining inundation

days. The lupins in the medium depth tank all survived up to day five, but some survived from days six to ten. The lupins in the deepest tank only fully survived one full day of inundation; however, some managed to partially survive up to day five. Observing the lupins post inundation revealed that many exhibited wilted and sagging canopies. Lupins removed from the deep tank were always sagging and had wilted canopies, while lupins removed from the shallow tanks experienced this wilting and sagging after two days of inundation. While mortality for some of these lupins never occurred, canopy often took days to weeks to recover.

Table 4.4: Inundation results for the corresponding tank and planter bag removed.

	Tank 1 - Shallow Depth			Tank 2 - Medium Depth			Tank 3 - Deep Depth		
Days	**Plant 1**	**Plant 2**	**Plant 3**	**Plant 1**	**Plant 2**	**Plant 3**	**Plant 1**	**Plant 2**	**Plant 3**
1	1	1	1	1	1	1	1	1	1
2	1	1	1	1	1	1	2	2	2
3	1	1	1	1	1	1	2	2	**3**
4	1	1	2	1	1	1	2	**3**	**3**
5	1	1	1	2	2	**3**	2	**3**	**3**
6	1	2	2	1	1	**3**	**3**	**3**	**3**
7	1	1	1	2	2	**3**	**3**	**3**	**3**
8							**3**	**3**	**3**
9				2	N.A.				
10	1	N.A.		2					
11	1			**3**					
12	1			**3**					

1 = Alive
2 = Damaged (Some dead, some alive)
3 = Dead
N.A. = Not applicable

Since some of the results at a given depth in Table 4.4 were inconsistent, a further analysis was performed to assess the lupins' root size and mortality. This was accomplished by grouping the lupins into root diameter categories of 0.1 to 1 cm, 1.1 to 2 cm, and 2.1 to 3 cm, and examining the percentage of lupins that experienced mortality for the specific bags tested. These results are presented in Table 4.5, with the total number of plants (dead and alive) that were included in that particular category in parentheses.

Table 4.5: Percentage lupin mortality based on root diameter categories and inundation extent; with total lupins in the particular category (alive and dead) in parenthesis.

	Shallow Depth (18cm)			Medium Depth (33cm)			Deep Depth (100cm)		
	Root diameter (cm)			Root diameter (cm)			Root diameter (cm)		
Days	0.1 - 1	1.1 - 2.0	2.1 - 3.0	0.1 - 1	1.1 - 2.0	2.1 - 3.0	0.1 - 1	1.1 - 2.0	2.1 - 3.0
1	0 (1)	0 (4)	N.A.	0 (2)	0 (3)	0 (1)	N.A.	0 (4)	0 (1)
2	0 (1)	0 (6)	N.A.	N.A.	0 (6)	N.A.	100 (1)	25 (4)	0 (2)
3	N.A.	0 (4)	0 (2)	0 (2)	0 (2)	0 (2)	100 (1)	0 (4)	50 (2)
4	33 (3)	0 (4)	0 (1)	0 (1)	0 (5)	N.A.	100 (1)	100 (2)	0 (1)
5	0 (1)	0 (5)	0 (1)	100 (3)	25 (4)	N.A.	100 (1)	100 (3)	50 (2)
6	33 (3)	40 (5)	0 (1)	0 (1)	50 (4)	0 (1)	100 (2)	100 (5)	N.A.
7	0 (3)	0 (3)	0 (1)	N.A.	80 (5)	100 (1)	N.A.	100 (5)	100 (2)
8	N.A.	N.A.	N.A.	N.A.	N.A.	N.A.	100 (2)	100 (5)	100 (1)
9	N.A.	N.A.	N.A.	N.A.	50 (2)	N.A.	Not tested		
10	N.A.	0 (1)	N.A.	N.A.	50 (2)	N.A.			
11	0 (1)	0 (1)	N.A.	N.A.	100 (2)	N.A.			
12	N.A.	0 (2)	N.A.	N.A.	100 (2)	100 (1)			

Based on the results of Tables 4.4 and 4.5, all lupins were sensitive to various water inundation levels and durations, with smaller lupins more prone to mortality. Although the results for the shallow inundation were inconclusive, it appeared that deeper water and increased inundation duration had a greater effect on the lupins' survival for the medium and deep tanks. Based on the re-examination following the regrowth period, the dead plants' root systems had drastically withered and rotted into a soft organic material. Since these examinations did not take place until 30 days following the inundation, it was difficult to determine if this rotting was caused by the long period of inundation or just by the decay of the dead plant. However, this root decay was a clear indication that the lupins' health was severely degraded, and regrowth was highly unlikely.

4.4.2 Lupin pull-out forces

4.4.2.1 Introduction

With current-drag identified as a potential lupin removal process from initial field observations, an important research question became how much force is required to uproot

lupins during a flood event? This posed sub-questions, such as what is the force required without erosion, and what is the force required with varying levels of erosion?

Vegetation's influence on surrounding soil is similar to steel reinforcement in concrete. Since most soils are strong in compression and vegetation's roots are strong in tension, vegetation presence acts as natural soil reinforcement (Baets et al., 2008; Ali, 2010; Pollen, 2006). Recent studies (e.g. Ali, 2010) have investigated pull-out forces of various vegetation types and have found that smaller root diameters produced lower pull-out forces as well as some vegetation's tensile strength decreases with increasing root circumference. Further, Pollen (2006) discusses the importance of soil moisture, as decreasing moisture increases the frictional bond between roots and surrounding soil; thus, vegetation in dry soils requires greater pull-out forces. Pollen (2006) continues that vegetation extraction with intact roots occurs for relatively lower forces, and that a force threshold typically exists where greater forces will result in the roots shearing at shallow depths. These studies have helped shaped this experiment, and will be discussed throughout this section.

4.4.2.2 Methods

To answer the posed questions, a simple lupin pull-out lever tool was fabricated with a 4:1 mechanical advantage that allowed large forces to be produced by hand in the field. Attaching a Kern hanging digital scale to the tool and a lupin (Figure 4.18, Appendix C.1, Figures C.1 and C.2), lupins' pull-out forces were measured. Based on the soil moisture findings of Pollen (2006), and since flood events saturate the floodplain soil, it was paramount to include saturated soil conditions in the pull-out experiment. However, locating saturated soil conditions in the Ahuriri floodplain during field data collection was difficult. Eventually, one area was located where 28 lupins were extracted. With a small sample size, additional lupin data were required. While artificial saturation was attempted, the required water volume (~40 liters) and time to ensure saturation at root depths up to 1 m were not practical. Therefore, it was decided that lupins would also be extracted in dry soil conditions and a separate laboratory experiment would be conducted to validate the force relationship between dry and saturated soil conditions.

Using the lupin extraction tool, an additional 100 lupins were extracted from the dry sediment of the Ahuriri floodplain and were placed into three categories: i) no erosion simulation, ii) 10 cm erosion; where 10 cm of soil had been removed around the stalk, and iii) 20 cm erosion; where 20 cm of soil had been removed. Prior to pulling each lupin, the plant's height (flower and canopy) and frontal width were measured. Following pull-out, the maximum force required, lupin diameter (taken at the beginning of the taproot, just below where the shoots meet), and length of taproot were recorded. To ensure consistent data, each lupin was pulled by applying smooth incremental pressure and at angles of approximately 10° from the surface. While pulling the lupins at a 0° angle from the surface would best represent flood effects, this was not practical given the geometry of the lupin tool.

Figure 4.18: Lupin extraction tool and Kern digital scale attached to an erosion simulated lupin.

The laboratory pull-out experiment tested an additional 38 lupins at the University of Canterbury. Twenty of these lupins were cultivated with the same methods and during the same time as the lupins used for inundation testing, and the additional 18 were lupins that remained alive and healthy after days one, two, and three for the shallow and medium depth tanks (Table 4.4). While the previously inundated lupins remained healthy, there was concern

that use of these 'stressed' lupins would result in altered pull-out forces. Therefore, inundated and non-inundated lupins were mixed together and separated evenly into two groups of 18 where one group would be saturated and the other would remain dry for pull-out testing. The dry lupins' pull-out forces were measured and recorded in the same fashion as for the field lupins. The saturated lupins were first inundated in a tank of water with a depth of 33 cm (same as the medium tank depth for inundation) and allowed three hours to become saturated. Once properly saturated, the lupins' forces were measured and recorded in the same fashion as during field work.

Utilizing the field and laboratory pull-out data, numerous relationships were tested to identify a plant characteristic that correlated well to the pull-out force. Since lupin pull-out would ultimately be related to lupin-induced drag force (Section 4.4.3), the lupin's canopy frontal area was considered, as was root diameter based on previous studies (e.g. Pollen, 2006; Ali, 2010). Since multiple relationships were tested and many provided adequate least squares regression results, error variance (Eqn. 4.1) was utilized to provide a goodness-of-fit measure. Example calculations are shown in Appendix B.1, Table B.2. Further, residual errors were calculated to evaluate the performance of the observed data against the empirical relationships derived. Residual errors included the root mean squared error (RMSE), the absolute mean error (MAE), the mean error (ME), and the standard deviation (SDE) (Lane et al., 2010):

$$RMSE = \sqrt{\frac{\sum_i^n (Est_i - Obs_i)^2}{n}} \qquad \text{(Eqn: 4.2)}$$

$$SDE = \sqrt{\frac{\sum_i^n \left((Est_i - Obs_i) - (\overline{Est_i - Obs_i})^2\right)}{n}} \qquad \text{(Eqn: 4.3)}$$

where Est_i is the estimated value from the empirical relationships and Obs_i is the observed (measured) value.

Once adequate relationships were established using the field data, the varying erosion levels were examined to determine a force reduction relationship. Since vegetation pull-out forces are a function of soil strength and root tensile strength, it was hypothesized that erosion would reduce the required pull-out forces since less soil would be available to provide the frictional bonds between soil and roots. Therefore, to determine the force reduction, the dry soil erosion data was evaluated to identify force reduction and was related to the root exposure. Determining a specific plant's root exposure required knowledge of root lengths of varying sized lupins and was provided by the observed flood-deposited lupins of Appendix E.2. Once the relationships between lupin size vs. root length and root exposure vs. force reduction were established, it was possible to estimate the force reduction for varying levels of erosion and varying size of lupin. As a final data check, the laboratory data were evaluated to determine if the dry and saturated soil relationship was the same as the field data. While both data sets were relatively small (28 field samples and 38 laboratory samples), these data offered a partial validation to the field data.

4.4.2.3 Results and discussion

Developing a relationship between pull-out forces and lupin characteristics was first attempted using the field data. Separating the data into dry and saturated soil conditions with varying erosion categories, both root diameter and canopy area were tested for empirical relationships. Results (Table 4.6) determined that root diameter typically produced slightly higher R^2 and considerably better s^2 values. Therefore, based on these results, it was determined that root diameter better represented the lupins' pull-out resistance. Poor canopy area results were expected, as lupin canopies ranged substantially in height and density for similar pull-out forces. Using root diameters, the pull-out forces were plotted for the four data sets collected in the field (Figure 4.19). As shown, all dry soil condition datasets show a steep rise in pull-out force with root diameter for smaller lupins and then leveling-out towards a force of approximately 550 N for large diameter roots. These results were likely influenced by multiple lupins growing in clusters. Based on field observations, single lupin plants rarely exceed 8 cm root diameters while larger root diameters were frequently documented, these actually consisted of numerous lupins growing together in clusters. Naturally, these clusters could contain variation in lupin size and maturity, thereby making root structures and pull-out forces highly variable.

Table 4.6: Field data force vs. various lupin characteristic relationships.

	Force vs:	Empirical function	R^2	s^2
0cm erosion: Dry soil	Root diameter	Log	0.63	13.5
		Power	0.68	5.9
	Canopy area	Log	0.53	75.1
		Power	0.73	9.8
10cm erosion: Dry soil	Root diameter	Log	0.76	7.9
		Power	0.71	6.0
	Canopy area	Log	0.69	12.1
		Power	0.67	111.1
20cm erosion: Dry soil	Root diameter	Log	0.63	5.0
		Power	0.70	7.2
	Canopy area	Log	0.44	8.3
		Power	0.55	5.6
0cm erosion: Saturated soil	Root diameter	Log	0.53	20.8
		Power	0.59	11.1
	Canopy area	Log	0.39	23.5
		Power	0.51	21.1

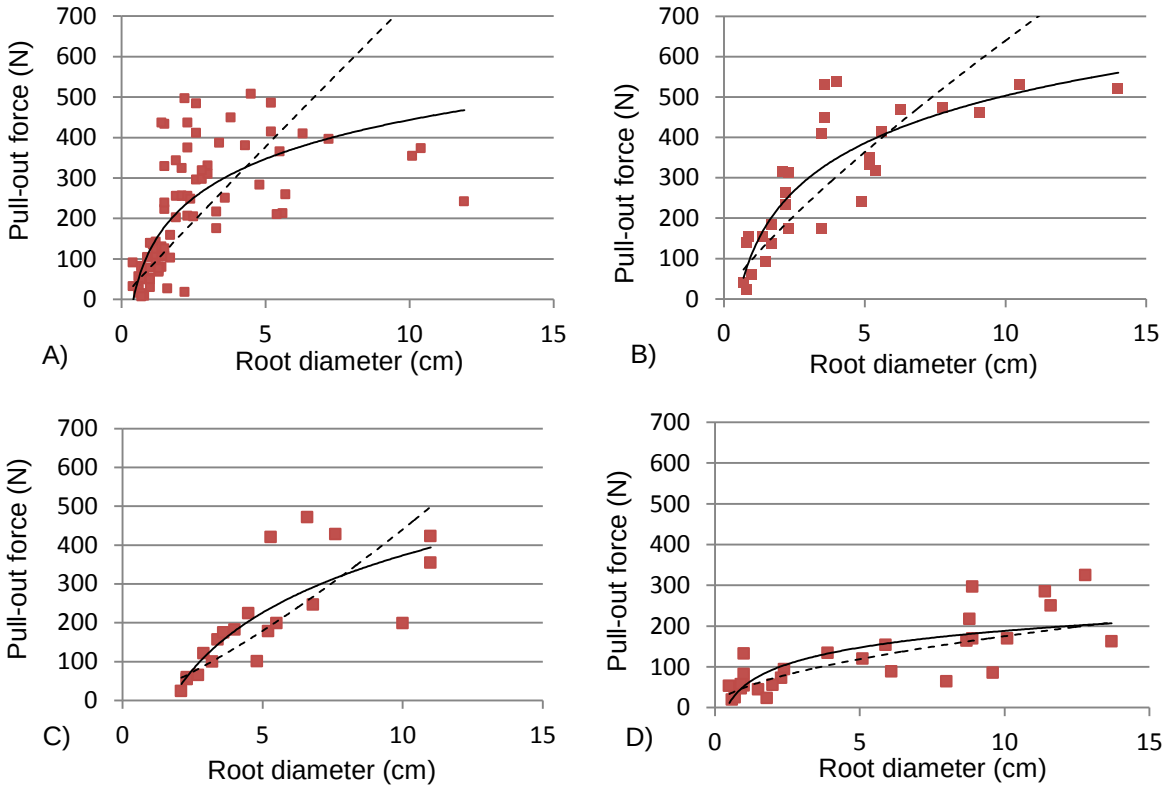

Figure 4.19: Pull-out forces for plotted against root diameter with logarithmic (solid line) and power functions (dashed line) for: A) dry soil: 0 cm erosion, B) dry soil: 10 cm erosion, C) dry soil: 20 cm erosion, and D) saturated soil: 0 cm erosion.

Assessing the results of the various empirical functions of Table 4.6, the logarithmic and power functions were plotted in Figure 4.19 along with the raw data. As shown in the dry soil condition (Figure 4.19a, b, c), the power function over-predicts pull-out forces for larger lupin root diameters, and under-predicts the pull-out forces of the smaller lupin root diameters. Conversely, the power function in the saturated soil (Figure 4.19d) tends to under-predict all pull-out forces. The logarithmic function better represented the steep rise and plateau trend; however, the dry soil forces were still drastically under-predicted for small root diameters and over-predicted for large root diameters. Further, the logarithmic function in the saturated soil performs well for the small lupin root diameters, but under-predicts the forces for larger roots. Therefore, all empirical functions would produce high residual errors (example shown for logarithmic residual errors Table 4.7). Taking into consideration the purpose of this data is to identify a predictive relationship for lupin pull-out forces for use in numerical modeling, it was a priority to have high confidence the relationship. Therefore, custom relationships were developed (Figure 4.20) by splitting the datasets into obvious steep rise and plateau force sections and utilizing maximum values.

Prior to creating custom relationships, it was noticed that no significant reduction in force was acquired with the 10 cm erosion. Therefore, this data was simply added to the dry 0 cm erosion category. This was appropriate given the similar and occasionally higher pull-out forces obtained in the 10 cm erosion dataset. Therefore, only datasets of dry 0 cm (which incorporated 10 cm erosion), 20 cm, and saturated 0 cm, were developed using the custom linear relationships (Figure 4.20). While these custom models may be unconventional, Hill (2006) states that model building is best started simple, and with complexity slowly added. Typically, this method is adequate for the level of detail needed for model forecasting, and allows the modeller to better understand the data modeled and the model's fit (Hill, 2006). Indeed, by separating the data into two categories, the added model complexity was approached simplistically and was well within the understanding of the data. Further, by developing the custom empirical relationships with a focus on the maximum values, the empirical formulas over-predicted most observed data. While this method produced higher residual errors (Table 4.8), this relationship provided added confidence in lupin pull-out prediction. This method was chosen as all empirical formulas would produce high residual errors, and this method was the only way to gain confidence in lupin removal.

Table 4.7: Example of large residual errors calculated for the pull-out forces estimated using logarithmic empirical relationships and observed data for various erosion and soil moisture categories (errors reported in Newtons).

	Dry			Saturated
	0 cm erosion	10 cm erosion	20 cm erosion	0 cm erosion
ME	0.0	0.0	0.0	0.0
MAE	75.3	65.6	57.2	41.8
RMSE	99.3	83.0	83.0	56.1
SDE	99.9	84.4	85.2	57.1
Max	225.5	150.7	175.4	110.8
Min	-266.6	-199.7	-185.8	-122.3

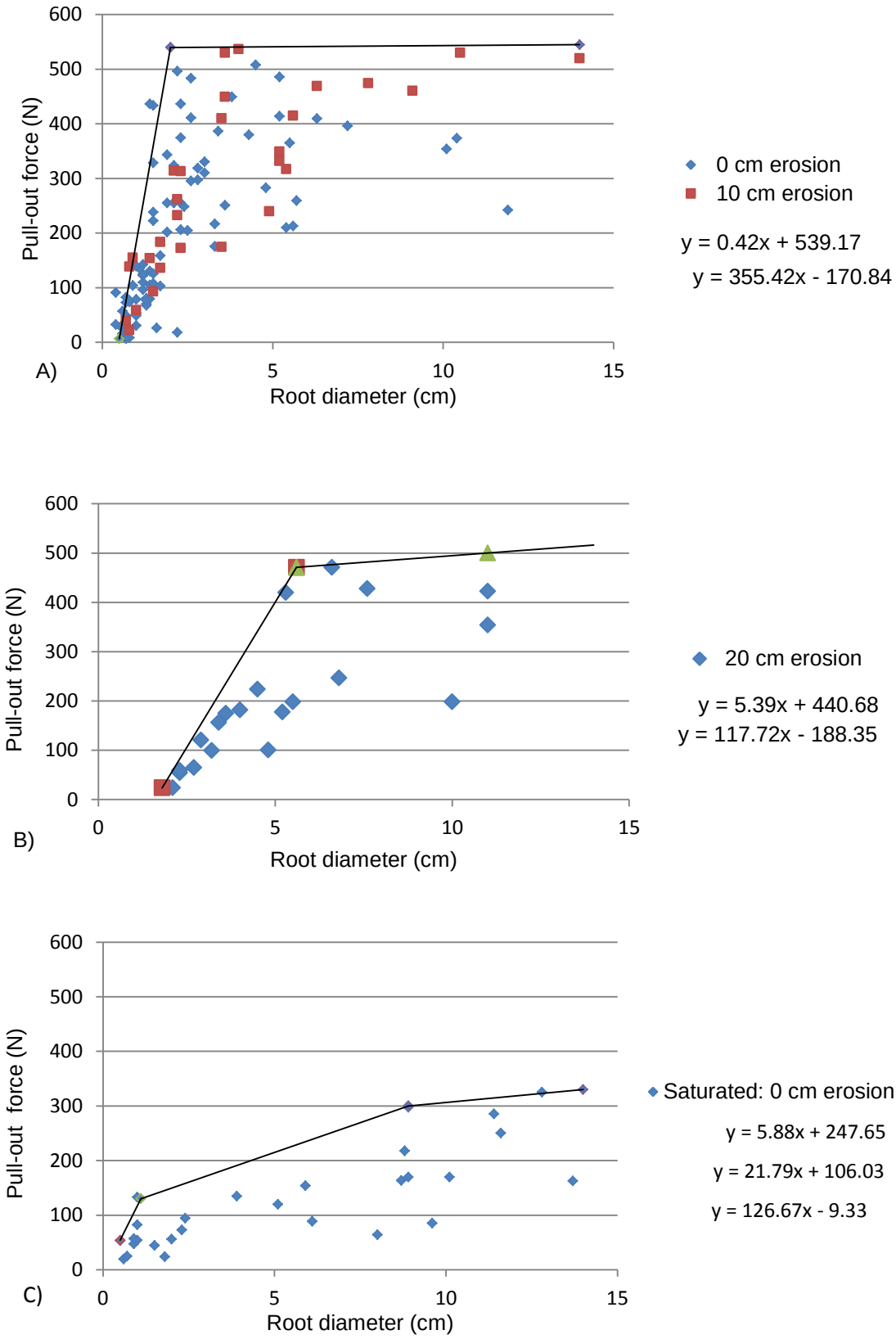

Figure 4.20: Custom empirical relationships for the: A) dry soil condition: 0 cm erosion, B) dry soil condition: 20 cm erosion, and C) saturated soil condition: 0 cm erosion.

Table 4.8: Residual errors results for custom empirical relationships and observed data (errors reported in Newtons).

	Dry		Saturated
	0 and 10 cm erosion	20 cm erosion	0 cm erosion
ME	160.12	110.97	82.59
MAE	167.41	110.97	83.82
RMSE	200.12	142.08	101.62
SDE	120.57	96.69	60.28
Max	521.84	296.66	219.10
Min	-119.91	5.39	-15.10

With the empirical relationships established for the dry and saturated soils, the dry soil conditions with varying levels of erosion were assessed for force reduction relationships. This naturally was more restricted than planned, as 10 cm erosion level showed no relationship existed. Nevertheless, the 0 cm and 20 cm erosion data was compared and results (Figure 4.21 and Table 4.9) show a considerable force reduction for smaller root diameter lupins and no reduction for the largest roots. This was likely caused by the root exposure for two reasons. First, as soil was removed from the root, the root-soil frictional bonds was reduced (Pollen, 2006); thus, the roots have less resistance to pull-out. Secondly, lupins have a distinct tap root that gradually tapers with depth. Therefore, as soil was eroded, the exposed root typically will become smaller in diameter; thus, the smaller diameter roots will fail with lower forces (supported by results of Ali (2010)). Therefore, while the relationships have been built upon root diameter, evidence in this research and previous studies suggest that force reduction caused by erosion levels was a function of root depth and root exposure.

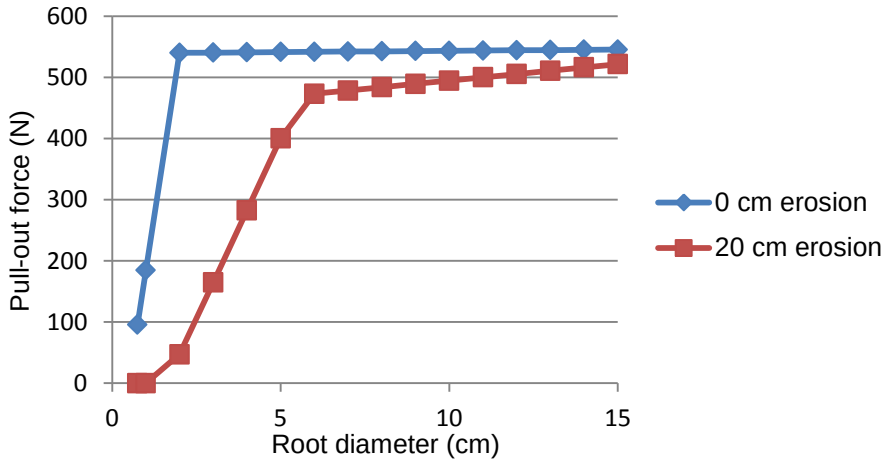

Figure 4.21: Custom empirical relationships plotted for 0 cm and 20 cm erosion levels in dry soil condition.

Table 4.9: Dry soil forces and calculated force reduction.

Root Diameter (cm)	0 cm erosion force (N)	20 cm erosion force (N)	Force reduction (%)
1	185	0	100
2	540	47	91
3	540	165	70
4	541	283	48
5	541	400	26
6	542	473	13
7	542	478	12
8	543	484	11
9	543	489	10
10	543	495	9
11	544	500	8
12	544	505	7
13	545	511	6
14	545	516	5
15	545	522	4

To investigate the root exposure and force reduction relationship first required data for the root lengths. This was available from the observed data of intact lupin root lengths and root diameters (appendix E.2). Using this data, root length averages and standard deviations were

calculated for lupins in root diameter categories of 1 cm (Table 4.10). Results show a strong trend for lupin root lengths gradually increasing in size for smaller root diameters (categories: 2 to 2.9 through 5 to 5.9 cm); however, larger root diameters revealed smaller root lengths. These results illustrate the complexity of lupins; particularly for root diameters above 8 cm being clustered roots. Using the increasing root length trend for the four categories of 2 to 2.9 cm through 5 to 5.9 cm, root diameters and corresponding root lengths were plotted and results (Figure 4.22a) show a strong linear relationship. While many empirical functions produced strong relationships, the linear relationship was chosen as it produced largest root lengths. As shown, empirical root lengths (Table 4.10) were calculated up to 200 cm; which was considerably larger than any root length observed (Appendix E.2). This conservative approach was warranted since limited data was available for root lengths as well as provided a high level of confidence for the results.

Table 4.10: Observed root length and empirically predicted root length (standard deviation only for data with two or more values).

	Observed		Empirical
Root diameter (cm)	Average root length (cm)	Standard deviation root length (cm)	Root length (cm) (Fig. 4.22A)
1 to 1.9	-	-	41.9
2 to 2.9	55.5	8.7	54.1
3 to 3.9	66.5	22.2	66.4
4 to 4.9	75.8	16.0	78.6
5 to 5.9	92.8	9.0	90.9
6 to 6.9	72.0	16.6	103.1
7 to 7.9	-	-	115.4
8 to 8.9	81.3	-	127.6
9 to 9.9	45.8	-	139.9
10 to 10.9	58.4	-	152.2
11 to 11.9	-	-	164.4
12 to 12.9	-	-	176.7
13 to 13.9	-	-	188.9
14 to 14.9	-	-	201.2
15 to 15.9	-	-	213.4

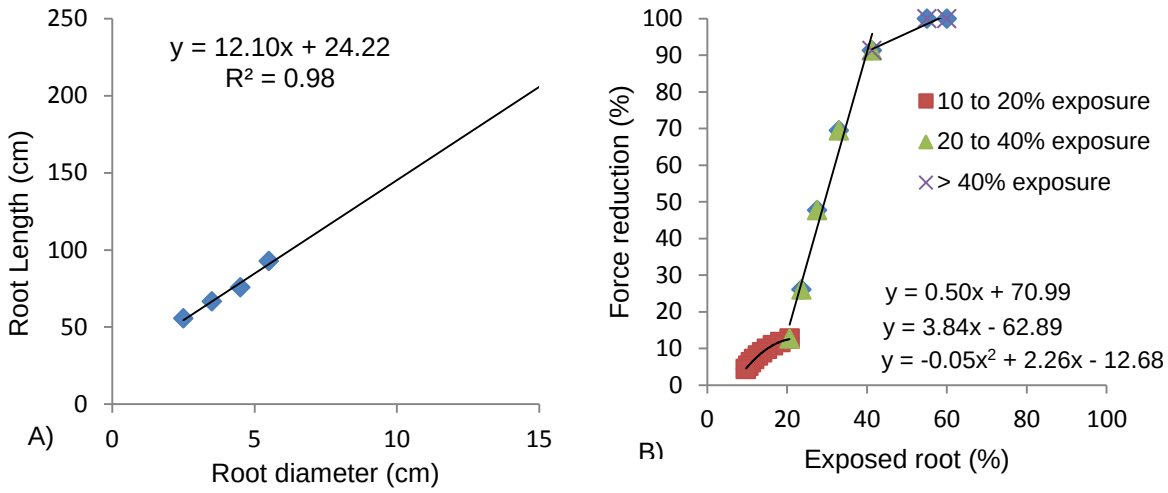

Figure 4.22: Raw and empirical relationship of: A) lupin root diameter vs root length, and B) exposed root vs. force reduction.

Using the data from Tables 4.9 and 4.10, it was possible to determine the percent root exposed and compare it to the force reduction. This was applied to the same four root diameter classes (2 to 2.9 through 5 to 5.9 cm) and was plotted; however, the resulting relationship was complicated and required custom empirical functions (Figure 4.22b). Using this data, additional erosion levels and corresponding pull-out forces for dry soil conditions were produced and tabulated in Table 4.11. Since all data utilized to derive this relationship and forecasting was conservative due to utilizing maximum pull-out forces, it was reasoned that this erosion and force reduction was also a conservative estimate. This was confirmed in comparing the original empirical relationship of 20 cm erosion (Table 4.9) with the force reduction empirical relationships for 20 cm erosion (Table 4.11). Comparing the two derived pull-out forces shows similar results. Therefore, residual errors were calculated by differencing the force reduction empirical results from the linear results; thus, positive values indicate that the force reduction relationship over-predicts pull-out forces. Results (Table 4.12) revealed a positive mean error near zero; indicating similar performance. Further examining the results of both tables revealed that the force reduction method under-predicted pull-out forces for a few root diameters, with the largest being 21 N lower. However, these differences were slight (indicated by residual standard deviation of 12 N) and since the data this was derived from used conservative methods (Table 4.9 and Figure 4.20b), these slight differences were not concerning.

Finally, using the same force reduction relationships (Figure 4.22b) and methods applied to the dry soil conditions, the force reductions for saturated soil conditions were applied to the custom empirical relationship (Figure 4.20c). Results (Table 4.13) show that erosion levels coupled with the already lower pull-out values of the saturated soil reduced the force considerably. Again, since these empirical relationships were built upon conservative methods, the final results of Table 4.13 were considered realistic and likely higher than most lupin pull-out forces.

Table 4.11: Pull-out forces for varying erosion levels in dry soil conditions.

	Pull-out force (N) (Table 4.20a and b)		Empirically predicted pull-out force (N)					
Diameter (cm)	0 cm	20 cm	20 cm	40 cm	60 cm	80 cm	100 cm	120 cm
1	185	0	3	0	0	0	0	0
2	540	47	45	0	0	0	0	0
3	540	165	194	0	0	0	0	0
4	541	283	309	8	0	0	0	0
5	541	400	391	29	0	0	0	0
6	542	473	452	45	0	0	0	0
7	542	478	478	118	8	0	0	0
8	543	484	483	195	23	0	0	0
9	543	489	489	257	35	0	0	0
10	543	495	495	310	45	8	0	0
11	544	500	501	354	89	19	0	0
12	544	505	506	393	146	29	0	0
13	545	511	511	426	195	38	0	0
14	545	516	516	455	239	45	8	0
15	545	522	521	477	277	73	17	0

Table 4.12: Residual errors for the 20 cm erosion of Table 4.9 and Table 4.11.

	Error (cm)
ME	1.6
MAE	6.3
RMSE	12.1
SDE	12.4

Table 4.13: Pull-out forces for varying erosion levels in saturated soil conditions.

Diameter (cm)	Pull-out force (N) (Fig. 4.20c) Erosion: 0 cm	Empirically predicted pull-out force (N) 20 cm	30 cm	40 cm	60 cm	80 cm	100 cm	120 cm
1	117	0	0	0	0	0	0	0
2	150	2	0	0	0	0	0	0
3	171	14	0	0	0	0	0	0
4	193	69	8	0	0	0	0	0
5	215	123	18	3	0	0	0	0
6	237	171	63	13	0	0	0	0
7	259	216	113	22	0	0	0	0
8	280	247	160	61	4	0	0	0
9	302	269	204	108	13	0	0	0
10	306	276	234	145	20	0	0	0
11	312	285	261	178	26	4	0	0
12	318	293	279	207	52	11	0	0
13	324	301	287	234	87	17	0	0
14	330	310	296	258	118	23	5	0
15	336	318	303	280	147	28	11	0

As a final data check, the lupin laboratory experiment data was evaluated and presented in Figure 4.23. Since the lupins were only grown for four months, the root development was limited and only produced small root diameters. Therefore, a full comparison between the laboratory and field data was not possible. Nevertheless, valuable results were obtained. As shown, dry soil condition pull-out forces rise steeply up to +500 N and saturated soil forces quickly rise to +200 N; comparable to the field results. Further, significant force reduction between dry and saturated soil conditions existed. Therefore, while this data and the field data for saturated soils were limited, results indicate that the field data was representative.

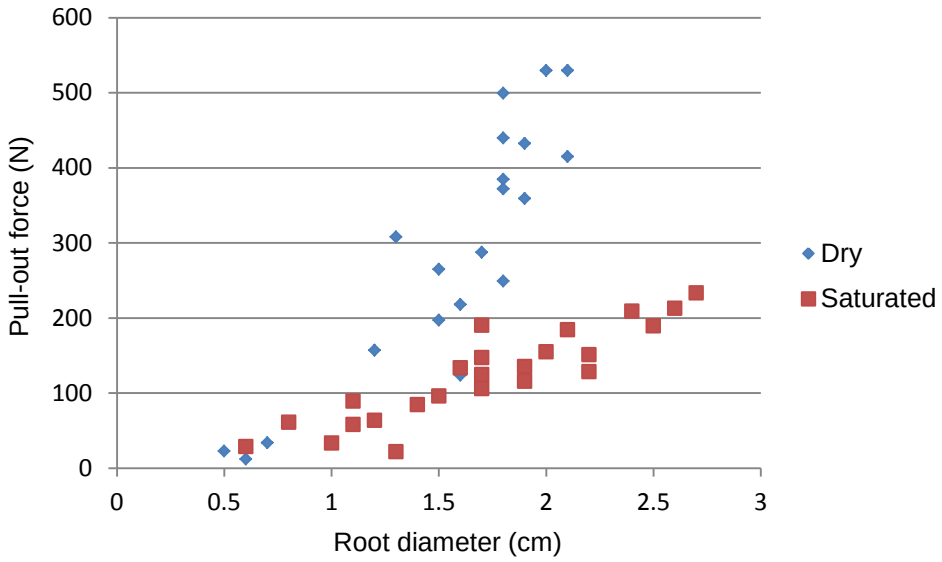

Figure 4.23: Laboratory pull-out forces for cultivated lupins

This experiment attempted to quantify the force required to extract various sized lupins during flood events and produced highly variable results with poor accuracy and precision. These results were expected given the extreme complexity and numerous conditions affecting lupin pull-out resistance (local soil composition, local soil saturation, lupin root morphology, lupin age, clustered roots, and available nutrients). However, despite these limitations custom empirical relationships were developed using lupin root diameters and the maximum pull-out forces. While this method produced large residual errors, it provided high confidence in determining lupin removal. Therefore, this data still provided useful information in lupin-mortality and was utilized in this research.

4.4.3 Drag

4.4.3.1 Introduction

To fully utilize the preceding results of lupin pull-out forces, the forces that lupins experience during flood events must first be determined. When a fluid passes an object, a force is created at the object-fluid interface and consists of i) a shear stress, τ_w, due to the viscous effects passing the object, and ii) pressure variations, p, caused by the passing flow (Munson, Young, Okiishi, & Huebsch 2009). The force acting on the object that is parallel to the upstream flow is termed drag, and the force normal to the object is termed lift. In this research, it was recognized that the net vector sum of drag and lift were acting on lupin

canopies and responsible for potential removal by pull-out; however, it was assumed that lift was minimal compared to drag. Therefore, we are only concerned about drag, and drag will be the only focus from hereon. Drag is calculated for any object using Equation 4.4 (Munson et al., 2009):

$$D = \int dF_x = \int p \cos\theta \, dA + \int \tau_w \sin\theta \, dA \qquad \text{(Eqn: 4.4)}$$

Here *D* is the drag force, θ is a function of the object's orientation to the passing fluid, τ_w is the fluid shear stress and is a function of the fluid acting along the object body's length, p is the pressure distribution along the object body, and *dA* is the differential surface area. Since these distributions are difficult to obtain for specific objects, the alternative is to define a drag coefficient (C_D) that is specific to the object in question based on the object's shape. The drag coefficient is defined in Equation 4.5 as:

$$C_D = \frac{D}{\frac{1}{2}\rho U^2 A} \qquad \text{(Eqn: 4.5)}$$

Here *D* is the drag force, ρ is the fluid density, *U* is the flow velocity, and *A* is the projected area of the object perpendicular to flow (Munson, et al., 2009). Rearranging this equation, the drag force can be calculated in Equation 4.6 as:

$$D = \frac{1}{2}\rho U^2 A C_D \qquad \text{(Eqn: 4.6)}$$

Since lupin drag coefficients cannot be found in the literature, an experiment was conducted to measure them. This was necessary to relate the lupin drag to the river's velocity, in order to determine if, and where, river velocities were high enough to remove lupins based on the previously identified lupin pull-out forces.

4.4.3.2 Methods

The drag for various sized lupins was determined by utilizing a fabricated tool shown in Figure 4.24 and Appendix C.2, Figures C.3, C.4, and C.5. As shown, lupins were attached to a pivoting arm which was attached to the Kern digital scale. The design of the lupin drag tool was such that the user positioned the tool perpendicular to the flow, then securing its position by standing on the horizontal platform. Once the tool and corresponding lupin were in the

river, the user recorded the digital scale data. To ensure that minimal flow disturbance occurred during the experiment, the user and scale were located approximately 1.5 meters away from the lupin being tested. Further, the lupin drag tool minimized erroneous drag data by connecting the lupin and scale through internal cable routing as well as securing the lupin by the roots; thus, enabling the lupin canopy to behave and deform naturally.

In addition to the lupin drag tool, a SonTek acoustic Doppler current profiler was utilized to record the depth and velocity of the tested area. Using these tools and four lupins varying in size (root diameters from 1.1 cm to 4.7 cm), the drag was determined for each lupin in three situations: i) a slow velocity and shallow depth (0.6 m/s and 0.4 m deep), a moderate velocity and moderate depth (1 m/s and 0.6 m deep), and a fast velocity and deep depth (1.7 m/s and 0.9 m deep). Each plant tested had the root diameter, canopy height, flower height, and frontal width recorded. During the drag tests, the minimum, maximum, and average forces were recorded, but the maximum simultaneous forces were utilized in relationship building.

Figure 4.24: Lupin drag tool with lupin secured to the pivoting arm (designed in collaboration with D. M. Hicks, T. R. H. Davies, and A. Stokes).

4.4.3.3 Results and discussion

The goal for this experiment was to relate the drag force generated to flow velocity and lupin size so that the lupin pull-out forces determined in earlier sections could be transformed to velocity thresholds for lupin extraction. The first approach was to determine the drag coefficient for lupins. An adequate relationship could not be calculated using Equation 4.5, since the calculated C_D values varied from 0.18 to 1.61, with an average of 0.75. Attempts were made to identify underlying relationships such as plant height, width, and flowers; however, an adequate relationship could still not be developed. Using the average C_D of 0.75, drag estimates were calculated and compared to measured drag (Figure 4.25) and revealed poor agreement. To better understand these results, mean and standard deviation residual errors were calculated by differencing the measured drag from the estimated drag; thus, negative errors indicated under-prediction and vice versa. Residual results (Table 4.14) revealed the mean errors of the 0 to 49 N drag category had the lowest mean error; however, these errors are relatively large considering the measured drag values, indicating poor accuracy. Further, standard deviation errors for the three measured drag categories were relatively large, suggesting poor precision.

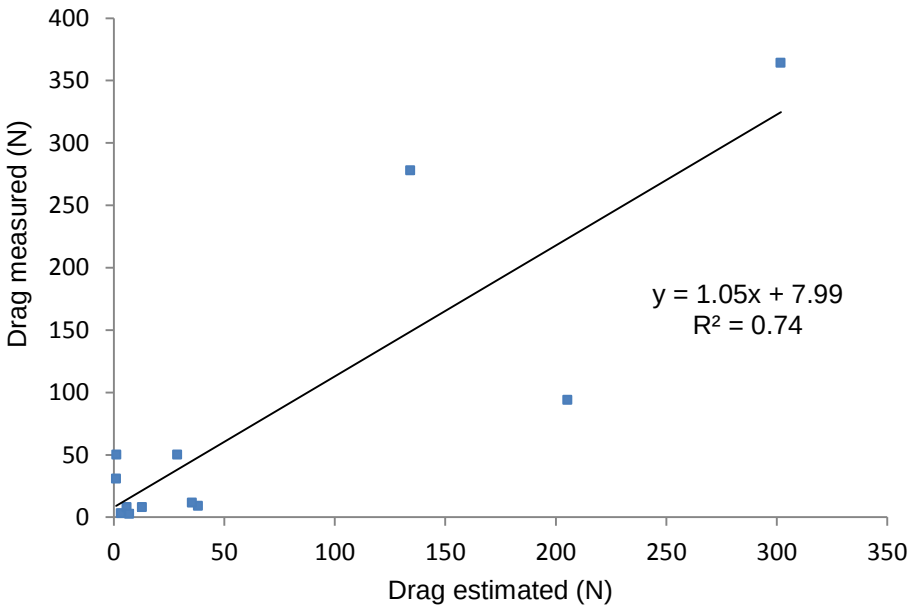

Figure 4.25: Estimated drag (solid line) using equation 4.6 vs. measured drag (blue squares).

Table 4.14: Drag residual errors.

Measured drag (N)	Residual mean error (standard deviation error) (N)
0 to 49	4 (19)
50 to 100	14 (86)
200 +	-103 (58)

With inadequate drag coefficient results, Equation 4.5 was re-examined to assess alternative methods for a relationship between the drag and lupin size. The drag equation is a function of the water density, velocity, and plant descriptors (shape and drag coefficient). Using this information, alternative methods were examined to develop a drag relationship between the lupin properties and flow conditions. Ultimately, many relationships were tested and produced adequate least squares regression fits to the data; however, since data were limited to 12 tests, it was difficult to identify the model with the best-fit. Therefore, both the least squares regression R^2 and error variance were utilized to select the most suitable option.

As previously determined during the lupin pull-out experiment, lupin root diameter produced the best relationship to pull-out forces; therefore, lupin root diameters were again considered as a lupin drag property along with the lupin frontal area, flow velocity, and water depth. These various relationships were examined and plotted with the best relationships listed in Table 4.15, and example error variance calculations can be found in Appendix B.1, Table B.3.

Table 4.15: Tested relationships for lupin drag with corresponding least squares regression coefficient and error variance values.

Measured drag compared to:	Empirical Trendline	R^2	s^2
Root diam. x velocity	Polynomial	0.87	118.9
Root diam. x depth	Polynomial	0.83	168.0
Root diam. x depth x velocity	Polynomial	0.67	309.6
Root diam. x velocity$^{1/2}$	Polynomial	0.97	14.2
	Exponential	0.94	9.9
	Combo: Linear and Poly	0.91 & 0.97	10.1
Canopy area	Polynomial	0.96	77.4
	Exponential	0.91	30.6
(Canopy area + flower height) x velocity$^{1/2}$	Linear	0.90	32.0
	Exponential	0.89	86.0

Considering both the R^2 and s^2 values, the best relationship to drag force was achieved by root diameter and the square root of the velocity. The exponential relationship (Figure 4.26) had R^2 of 0.94 and s^2 of 9.9. However, when considering lupins of larger diameter, the drag forces generated were high (up to 90 kN). Therefore, this data model was eliminated due to exaggerated forces. The polynomial relationship provided a strong R^2 of 0.97 and a moderate s^2 of 14.2 (shown in Table 4.15, and Figure 4.25). However, when plotted, this relationship produced unrealistic negative drag forces for root diameter x velocity^{½} values between 0.01 and 0.02 (a significant portion of the data). The root diameter x velocity^{½} data was divided into two categories: i) drag forces $\leq$ 11 N, and ii) drag forces $\geq$ 11 N. This custom relationship was considered because splitting the data at 11 N provided an obvious fit for two linear models. Assessments were performed on the individual curve's least squares regression R^2 and error variance for linear, power, polynomial, and exponential functions. However, the best combination was a linear fit to the data with drag forces $\leq$ 11 N and a polynomial fit for drag forces $\geq$ 11 N, which produced an s^2 of 10.1 (Table 4.15 and Figure 4.28). While this custom relationship was considered the best option due to its model fit and realistic results for all portions of the data, it was not a conventional method. Therefore, an error analysis was performed with residual errors, and the results (Table 4.16) show considerable improvement

over the previously discussed estimated drag (Table 4.14). However, these results show both the mean and standard deviation errors increased with increasing drag; indicating the relationship accuracy and precision degrades with larger data. Nevertheless, this method provided the best model fit and drastically improved the residual errors and was utilized with the lupin pull-out forces (Table 4.13) to produce a drag force and lupin pull-out matrix for the various root diameters and velocities (Table 4.17).

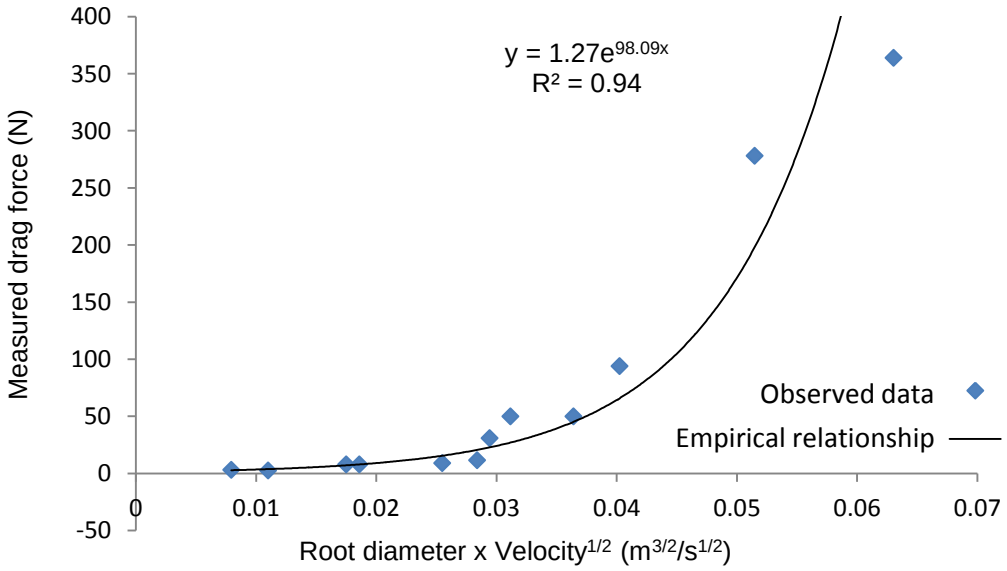

Figure 4.26: Observed data and exponential empirical relationship for drag force vs. root diameter x velocity^{½}.

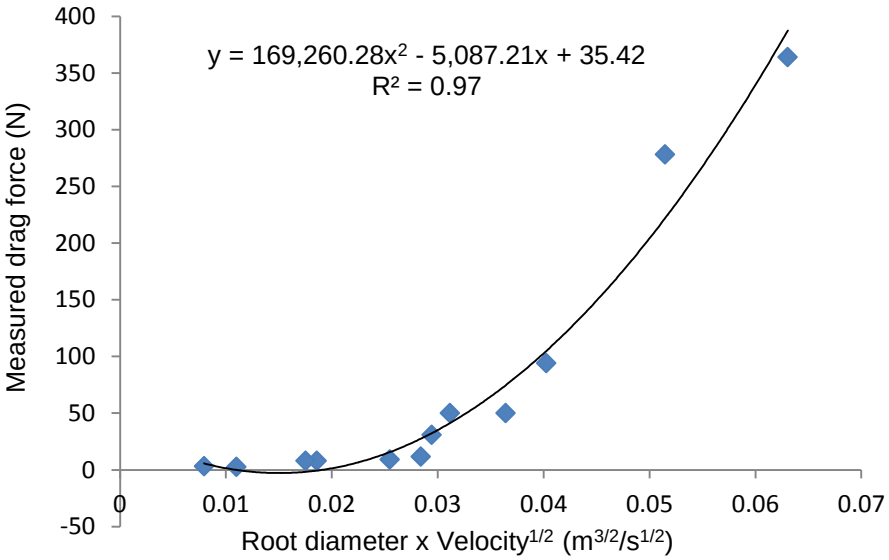

Figure 4.27: Observed data and polynomial empirical relationship for drag force vs. root diameter x velocity^{½}.

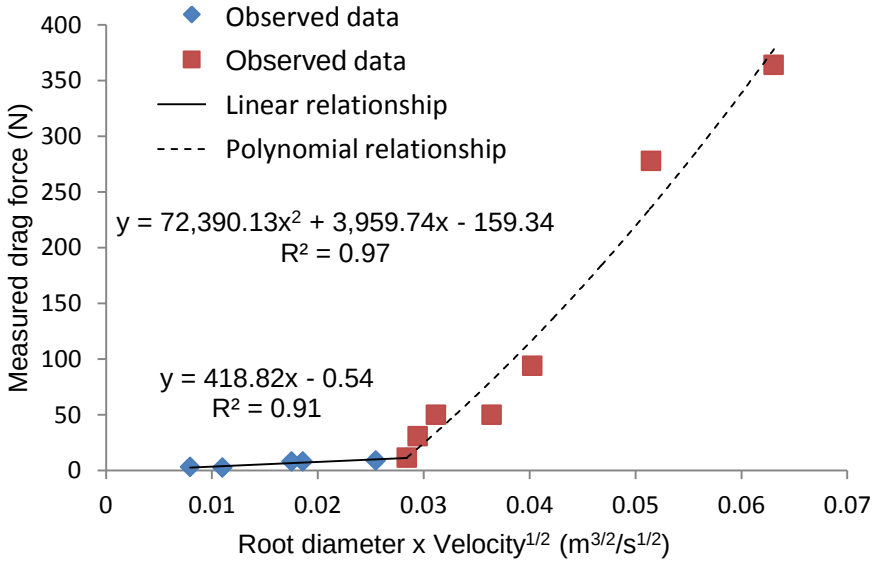

Figure 4.28: Observed data and custom (linear and polynomial) empirical relationships for drag force vs. root diameter x velocity^{½}.

Table 4.16: Drag residual errors of the custom empirical relationships (Figure 4.28).

Measured drag (N)	Residual mean error (standard deviation error) (N)
0 to 49	-2 (4)
50 to 100	8 (33)
200 +	-14 (39)

Table 4.17: Quantified lupin drag forces (N) and shaded pull-out matrix for various lupin root diameters, flow velocity, and erosion.

Root diameter (cm) \ Velocity (m/s)	0.25	0.37	0.5	0.75	1	1.25	1.5	1.75	2	2.25	2.5	2.75	3
0.75	1	1	2	2	3	3	3	4	4	4	4	5	5
1	2	2	2	3	4	4	5	5	5	6	6	6	7
1.5	3	3	4	5	6	6	7	8	8	9	9	10	10
2	4	5	5	7	8	9	10	11	11	25	38	52	65
2.5	5	6	7	9	10	8	30	51	71	91	110	129	148
3	6	7	8	10	25	55	84	112	139	165	191	217	242
4	8	10	11	65	115	163	208	253	296	339	381	422	462
5	10	28	71	148	220	288	355	419	483	545	606	667	727
6	25	82	139	242	339	432	523	611	698	783	868	951	1034
7	68	141	214	347	473	594	712	828	942	1055	1166	1276	1385
8	115	205	296	462	621	774	924	1070	1215	1358	1500	1640	1779
9	165	274	386	589	783	972	1157	1338	1517	1695	1870	2044	2217
10	220	349	483	727	961	1188	1411	1631	1848	2063	2277	2488	2698
11	277	430	587	875	1152	1423	1688	1950	2208	2465	2719	2972	3223
12	339	515	698	1034	1358	1675	1986	2293	2597	2899	3198	3495	3791
13	404	606	816	1204	1579	1945	2306	2663	3015	3365	3713	4059	4402
14	473	703	942	1385	1814	2234	2648	3057	3462	3865	4264	4662	5057
15	545	805	1075	1577	2063	2541	3011	3477	3938	4396	4852	5305	5756

Pull-out: 0 cm erosion

Pull-out: 20 cm erosion

Pull-out: 30 cm erosion

Pull-out: 40 cm erosion

While the drag coefficient was not effectively calculated by conventional equations, a strong relationship between drag, lupin size, and flow conditions was achieved between the lupin drag force and lupin root diameter x velocity^{½}. There are many potential sources of errors that may have prevented an adequate drag coefficient from being estimated. These may include

the small amount of data sampled, the freshly uprooted lupins, the arm of the lupin drag tool and the position in which it held the lupin into the flow, uncertainties in the digital scale, and operator errors. However, based on observations, lupins of the same root diameter often have drastic differences in vegetal height, width, canopy density, and flower stage development; thus making it difficult for a single drag coefficient to exist based on projected area.

The initially produced exponential and polynomial models produced adequate least squares regression R^2 values and moderate error variance; however, exaggerated projected forces or negative values for a significant portion of the utilized data were concerning. The final custom drag force model was achieved using a combination of two models and may be an unconventional choice. However, this model did achieve a competitive error variance score, had a comparable least squares regression value, produced adequate force results for the entire range of data, and most importantly produced better residual errors. While this combination model may be unconventional, the model development started simple and complexity slowly added (Hill, 2006). Nevertheless, while the custom model was chosen for good reasons, the disregarded exponential and polynomial models (Figures 4.26 and 4.27) were also utilized to generate forces vs. pull-out matrices and presented in Appendix D.2, Tables D.1 and D.2. Interestingly, similar pull-out was predicted; however, the final model results of Table 4.17 were produced with higher confidence.

Though the lupin extraction matrix provides critical information for this research, it was recognized that this data was developed through the combination of multiple empirically determined data that range from strong relationships with low residual errors (lupin drag relationship) to weak relationships with large residual errors (lupin pull-out forces). However, since the lupin pull-out forces of Section 4.4.2 were constructed with conservative data, high confidence was warranted for the pull-out force results. Nevertheless, combining these relationships to develop the lupin extraction matrix also combined errors and uncertainty. Therefore, while the matrix was a valuable tool for this research, it was recognized that the data was built upon two experiments that utilized simplistic tools and methods to determine and quantify extremely complicated processes and relationships.

4.4.4 Sediment deposition

4.4.4.1 Introduction

Based on the initial observations of the three flood events, smaller lupins (height < 40 cm) were not deposited by receding flood levels; however, numerous larger lupins were deposited. While it was possible that this was a local phenomenon and not representative of the entire river, it was hypothesized that the smaller lupins were more capable of resisting drag due to their smaller size producing less drag, shelter provided by large sediment, and their flexibility. This hypothesis was supported by the data presented in Table 4.17; where smaller lupins can only be removed with significant levels of erosion. However, as observed during post-flood events, lupins may encourage deposition in certain conditions. Since smaller lupins appear to resist pull-out, their smaller stature may make them susceptible to deposition burial; thus mortality. While most sediment burial studies have focused on wetland vegetation, relatively few have focused on fluvial environments (Lowe, Watts, Roberts, & Robertson, 2010); however, studies have found that herbaceous plants' survival diminish with increased burial and complete burial caused mortality (Lowe et al., 2010; Deng et al., 2008). Together these observations and studies suggest that sediment deposition is a likely process that results in lupin mortality. Therefore, the following experiment was conducted to determine the sensitivity of various sized lupins to burial by sediment deposition.

4.4.4.2 Methods

To determine lupin sensitivity to deposition burial required an experiment to test how various sized lupins responded to various deposition depths. It was hypothesized that when lupins were completely buried, the deposition would reach its detrimental depth dictated by reduced photosynthesis. However, from the literature review, we know that vegetation's shape can deform during hydraulic interaction. Since lupins are flexible herbaceous vegetation, it is highly unlikely that they remain upright during a flood event. However, the degree of the vegetation deformation was unclear and would impact the amount of deposition necessary to completely cover the lupins. Therefore, the first method in this deposition experiment was to determine the deformation of various sized lupins. This experiment was conducted by testing 20 lupins of various sizes placed in a river with velocity of approximately 0.6 m/s. This experiment was conducted on the Ahuriri River in December of 2012 which was consistent

with all other lupin maturity and testing. Once the site was selected, each lupin's canopy height, flower height, and root diameter were recorded and the lupin was removed from the sediment and taken directly to the nearby river braid where it was submerged. Based on observations made after the January 2013 flood events, lupin deformation was significant. As shown in Figure 4.16, lupins in a recently flooded area showed significant deformation; approximately 75% height reduction. However, the deformation photographed in Figure 4.16 was not fully representative of the deformation during a flood event because these photographed lupins had had several days following the flood event to further decay and deform.

Since flood events can last up to several days, it was assumed that lupin deformation increased with increasing inundation time. This assumption was also based on observations made during the lupin inundation experiment that showed canopy sag and wilt even in short inundation periods (1 day for submerged and 2 days for emergent). Further, due to the flow fluctuations and possible passing debris, it was assumed that the prolonged exposure to flood conditions would cause the plants' herbaceous material to fatigue and increase their deformation over time, which is supported by observed flood affected lupins (Figure 4.10). Therefore, to simulate these processes, each lupin was submerged in a local channel (velocity 0.6 m/s) where artificial deformation was simulated for approximately two minutes. This consisted of moderately dragging the lupins through the current in a 'swirling' fashion to increase the experienced velocity and condense the flood effects; however, care was taken to avoid exaggerated roughness such as bending the stalk and canopy deterioration. Once artificial flood simulation was conducted, the lupin's roots were placed on the river bed and the deformed height was measured from the base of the stalk to the top of the deformed canopy. Finally, deformation was calculated by dividing the deformed height by the original pre-testing height.

The deposition experiment was conducted in December of 2012 and utilized the findings of the deformation experiment. Identifying 20 lupins in the sub-reach, the lupin's canopy height and flower height were measured; however, the root diameter was not measured, as digging around the lupins roots could have compromised the health of the lupin and impacted the experiment. Based on the deformation findings, each of the 20 lupins was bent over by hand

to their typical deformation height and covered with nearby sediment at deposition levels of 2 cm, 5 cm, and 10 cm above the plants upper-most herbaceous material. Once buried, the locations of the lupins and lupin details were marked by survey flags, as shown in Figure 4.29, and left for a six-week period, ensuring adequate time for regrowth. After the six week period, the location was revisited and the lupins status was recorded. Unfortunately, 6 of the 20 deposition experiment lupins were impacted by the January 2013 flood event and could not be located. However, the remaining 14 were located on a slightly higher area of the floodplain and appeared to be unaffected.

Figure 4.29: Lupin deposition testing in the Ahuriri floodplain.

4.4.4.3 Results and discussion

Lupin deformation results are shown in Table 4.18. The average deformation for the canopy and flower was 50.6 % and 57.1% of the original height, respectively. These results are less drastic than the observed lupins deformation post-flood event, which was estimated to be a height reduction on average of 75%. However, the results of this experiment were likely less drastic than the deformation occurring in flood events lasting more than 12 hours. As observations from the field show (Figure 4.9 and 4.10), lupin deterioration was significant and often resulted in stripped leaf mass and bent stalks, suggesting sediment-laden water.

While the tested lupins of this experiment were moderately swirled to simulate longer durations and flood impacts, none experienced canopy deterioration. The different results between observed and tested were likely due to velocity differences experienced, duration, and possibly trauma induced by passing debris. Therefore, it was assumed that the results from this experiment were conservative, and the actual lupin deformation in the field was likely between the tested lupin deformation results and the post-flood deformation of 75% reduction, depending of course on the local water velocity, duration, and sediment/debris transport.

Table 4.18: Lupin deformation experiment results.

Diameter (cm)	Natural Height (cm)		Deformation Height (cm)		Height reduction (%)	
	Flower	Canopy	Flower	Canopy	Flower	Canopy
0.2	N.A.	7	N.A.	3	N.A.	57.1
0.3	N.A.	6	N.A.	3	N.A.	50.0
0.3	N.A.	5	N.A.	2	N.A.	60.0
0.4	N.A.	6	N.A.	2	N.A.	66.7
0.4	N.A.	7	N.A.	3	N.A.	57.1
0.6	N.A.	9	N.A.	3	N.A.	66.7
1.4	N.A.	14	N.A.	5	N.A.	64.3
1.9	30	23	14	14	53.3	39.1
1.9	N.A.	19	N.A.	9	N.A.	52.6
1.9	N.A.	18	N.A.	10	N.A.	44.4
2.0	N.A.	19	N.A.	9	N.A.	52.6
2.2	N.A.	25	N.A.	11	N.A.	56.0
2.3	N.A.	33	N.A.	20	N.A.	39.4
2.4	38	22	15	12	60.5	45.5
3.1	N.A.	30	N.A.	13	N.A.	56.7
3.6	64	42	27	35	57.8	16.7
3.6	38	20	17	14	55.3	30.0
3.8	72	37	23	18	68.1	51.4
4.6	52	30	20	13	61.5	56.7
5.8	31	33	20	16	35.5	51.5
7.1	62	37	22	19	64.5	48.6

The deposition mortality results are presented below in Table 4.19. The results of the deposition experiment show that a 50% mortality rate occurs for a 2 cm burial, but mainly on the lupins of shorter canopy height. The 5 cm deposition has a 28.5% mortality rate, but appeared to be most effective on the shorter lupins. The 10 cm deposition had a 100% mortality rate on all lupin sizes. The six flood-affected lupins that could not be located consisted of 1 cm and 10 cm deposition testing. However, while the test results were limited, they were still useful. Based on the results, the 2 cm deposition tests killed two of the four lupins tested with the dead lupins being the smallest tested in that category (canopy height ~ 20 cm). The 5 cm deposition testing resulted in two dead lupins with canopy heights of ~20 cm, while large lupins were able to regrow. However, the 10 cm deposition experiment ended with all three plants dead, including a larger lupin canopies up to a height of 32 cm. Therefore, the conclusion from these results is that 2 cm and 5 cm of deposition will cause mortality in lupins with canopy heights of 20 cm and lower, and that 10 cm of deposition will cause mortality of all lupins up to 32 cm canopy height.

Table 4.19: Deposition burial results of the flood surviving lupins.

Height (cm)		Deposition Depth (cm)	Status
Flower	Canopy		
N.A.	27	2	Regrowth
N.A.	30	2	Regrowth
18	20	2	Dead
N.A.	20	2	Dead
N.A.	17	5	Regrowth
N.A.	21	5	Regrowth
37	24	5	Regrowth
32	27	5	Regrowth
58	38	5	Regrowth
N.A.	18	5	Dead
N.A.	20	5	Dead
N.A.	18	10	Dead
25	25	10	Dead
76	32	10	Dead

4.5 Conclusion

This chapter has outlined the study site location, field observations, and the general data collected that has improved the understanding and developed quantification of the processes that cause lupin mortality. The hydrology assessment undertaken has provided valuable data to describe and model the various Ahuriri flood events' frequencies, magnitudes, and durations. Evaluating the frequency of occurrence, December was identified as the month most likely to produce the most flood events. Therefore, December was chosen as the period on which all research was focused. This narrowed the research focus and helped develop such experiments as the inundation duration and lupin maturity required for all testing. Further, this data helped identify the Ahuriri's flood characteristics and was utilized to generate synthetic hydrographs of large flood events that have not been recorded, such as 100, 200, and 500-year events, which was critical for flood simulations.

Throughout the duration of this research, periodic field observations were conducted to develop a deeper understanding of flood impacts on lupins. During these observations, insight was gained into the flood-induced trauma impacts and how lupins influence bed erosion and sediment entrainment. While it was acknowledged that the observed deposited lupins in this reach only represent one local area of the river, and that it was possible that other areas of the river have varying results that may confirm or contradict these observed results, it was assumed for this research that this observed area was representative of the study-reach. Further, these observations helped shape the research path for this project. First, erosion and drag are likely processes that caused the removal of the observed deposited lupins; therefore, these processes were studied further in laboratory experiments and will be assessed in numerical modeling. Trauma did appear to be detrimental to lupins in area flood zone 1; however, the hydraulic conditions that occurred in this section were unknown. Therefore, this area and specific flood event will be further assessed using numerical model simulations (Section 7.2.5) to determine the water depth, velocity, sediment transport, and/or shear stress that caused 63% lupin mortality rate. Finally, the flood events and extent captured by the time lapse camera did not have sufficient inundation extent or duration to cause lupin mortality. Therefore, this was further investigated in a laboratory experiment.

While the experiments presented in this chapter used simplistic approaches and methods to determine and model extremely complicated natural phenomena, the findings and relationships did improve the understanding of the processes that cause lupin mortality within the Ahuriri River. Though the resulting empirical formulas were built upon limited data with residual errors indicating poor accuracy and precision, the final lupin extraction matrix provided insight and agreement with much of the post-flood observations and vice versa. While it has been recognized throughout this chapter that the results are treated with low confidence, the agreement between empirically derived lupin mortality and field observations suggests that the lupin mortality-processes (and thresholds to an extent) were relatively accurate and realistic. Therefore, this data was considered adequate to utilize in conjunction with numerical model simulations to assess lupin mortality caused by various sized flood events.

Chapter 5

Flood Evaluation

5.1 Introduction

This chapter outlines the processes and results of the flood monitoring that took place for this research. While much can be learnt from field data collection at base flows and from laboratory experiments, nothing can replace observing the effects of an actual flood event. Therefore, in addition to the individual processes investigated in chapter 4, additional field data was collected around a specific flood event in which extensive surveys collected pre- and post-flood topography and vegetation extent. This chapter is organized into three sections. The first outlines the DEM production and resulting accuracy. In order to capture as much detail as possible, full-reach 3D point clouds were required and developed into digital elevation models (DEM) for each survey, and were later differenced to provide a DEM of difference (DoD). The second section presents the pre- and post-flood vegetation survey data and vegetation mapping. Obtaining current vegetation types and spatial distribution was needed as boundary conditions for the simulation results, thus identifying areas impacted by various flood simulations. Finally, the third section combined the DoD data and pre- and post-flood vegetation surveys to identify the type and amount of vegetation removed as well as estimate the flood processes that likely occurred in association with its removal. Using this data can potentially add further knowledge to the lupin mortality previously identified in Chapter 4, as well as serve as a valuable datum for numerical model calibration/validation.

5.2 Digital elevation model production

The following three sections (5.2.1, 5.2.2, and 5.2.3) present the workflow utilized to generate the required fluvial DEMs. This workflow utilized PhotoScan's SfM-DMVR to generate the terrain surface for dry areas, the geospatial Topographic Point Cloud Analysis Toolkit (ToPCAT) to reduce the point cloud resolution to i) improve data handling and ii) to reduce vegetation "noise", and finally optical-empirical bathymetric mapping to model the inundated terrain. Finally, the dry and wet point clouds were fused into one point cloud which was utilized to develop the required digital elevation model. The full production is presented in Figure 5.1.

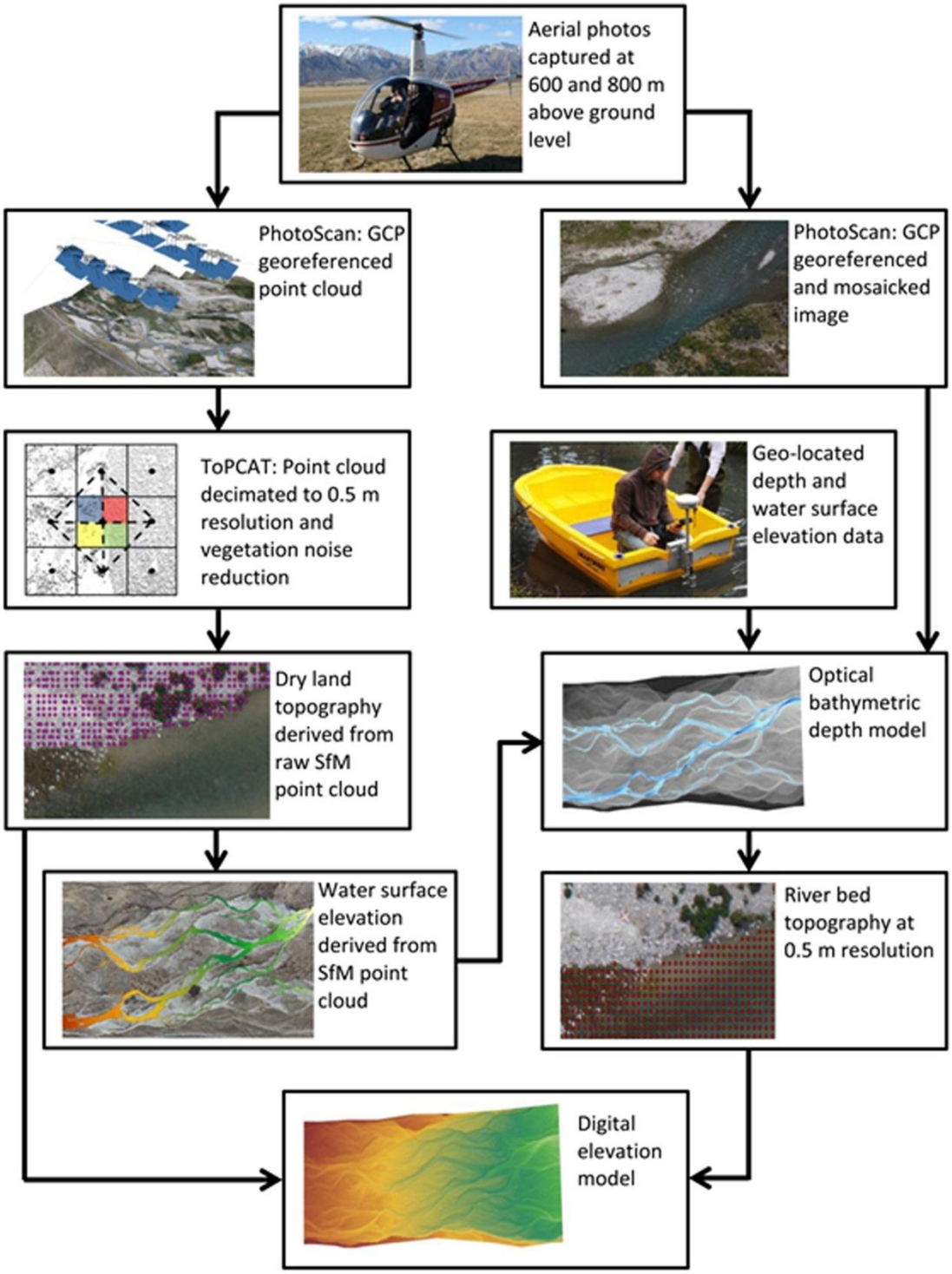

Figure 5.1: Workflow combining SfM-DMVR, ToPCAT point cloud editing, and bathymetric mapping to produce final DEMs.

5.2.1 Structure-from-Motion and Dense Multi-View Reconstruction

5.2.1.1 Introduction

In order to identify flood-induced mortality from the observed flood event, high quality vegetation and topographic surveys were necessary to detect subtle geomorphic changes as well as the corresponding vegetation impacts. Therefore, to obtain the best topography while maintaining a practical and affordable field campaign, multiple methods were assessed that were identified in the literature review such as: mass GPS surveys, photogrammetric surveys, airborne LiDAR, TLS surveys, and Structure-from-Motion (SfM). Of these techniques, all have produced adequate fluvial surveys; however, due to budget constraints, availability, and/or quality, many were excluded. For example, traditional photogrammetric surveys were considered and would have cost NZ$3,000 for 9 cm image resolution; however, this method was not chosen as the photogrammetric product would be of low resolution due to the processing software utilized. Airborne LiDAR was considered, but was estimated to cost NZ$28,000 for the study-reach. TLS equipment was not available at the time, but the oblique scanned images would have required significant post-processing to rid the topography of the Ahuriri's vegetation (J. Brasington, personal communication, July, 2011).

These limitations left a mass RTK-GPS survey and SfM as the best candidates. Since the University of Canterbury had the necessary equipment, both options were considered; however, after a day trial of GPS surveying, it was determined that a high resolution survey of the study-reach would be far too time consuming, even with four individuals surveying simultaneously. Therefore, SfM was the chosen method and offered an affordable and practical technique for obtaining a high quality survey for the study-reach's exposed topography. However, as mentioned in Section 2.2.4, SfM is incapable of collecting data below the water surface, thus leaving the inundated areas unmeasured (Brasington, et al., 2011; Snavely et al., 2006; Williams, et al., 2011). Therefore, additional methods were required and considered to map the river bed elevation. The two most practical were sonar (using an echo-sounder) and optical bathymetric mapping. Echo-sounding provided a practical alternative since the necessary equipment was available and optical-empirical mapping provided a good alternative since aerial images would already be acquired for the SfM process. However, due to the echo-sounder's required depth below the water surface of approximately 10 cm, and due to the low flow at time of the surveys, the echo-sounder was not able to map shallow sections of the river bed and was limited to the river's main channel.

Therefore, the best option was to combine this data with the aerial images that were captured just prior to the depth measurements, thus providing the necessary data required for the optical bathymetric mapping method.

While several SfM software packages were currently available and capable of producing quality DEMs (e.g. Dowling, Read, & Gallant, 2009; Fonstad et al., 2011b, Westoby et al., 2012; James & Robson, 2012), this research utilized PhotoScan (version 0.9.0) due to its user control, user-friendly GUI, inclusive transformation ability, and in part based on the exceptional results published in Doneus et al. (2011). This section presents the SfM software PhotoScan and the methods utilized to generate accurate terrain models of the exposed floodplain. This process required extensive data collection, software testing, model generation, and model improvement through noise reduction.

5.2.1.2 Observed flood event and data collection

Extensive data were required for the topography and vegetation assessment. This data collection took place twice, first as a baseline survey before a flood, and second as a post-flood survey. While the majority of the field data collection methods were identical between the two surveys, a few small differences in procedure occurred and will be discussed below. The first survey took place in late August 2011 (herein referred to as the pre-flood survey) and documented the river's topography and vegetation within the study-reach. At the time of the pre-flood survey, the Ahuriri's discharge was 13 $m^3 s^{-1}$. This provided easy river crossings and exposed river sections. On October 26, 2011, the Ahuriri River flooded to a peak discharge of 209 $m^3 s^{-1}$, which was near the mean annual flood (222 $m^3 s^{-1}$). After the flood event, it was apparent from field observations that a second survey was necessary due to the significant morphologic changes. In mid-December 2011 the second round of field work commenced.

During the lag between the pre-flood survey and the flood event, no floods occurred; only a slight discharge spike up to 25 $m^3 s^{-1}$. During the lag between the flood event and the post-flood survey, no flood event occurred; only a small rise in discharge to 69 $m^3 s^{-1}$. The delay between the flood event and subsequent survey was to allow the flow to return to a level near

that of the pre-flood survey to enable the best comparison. However, the levels never reached as low as desired (13 $m^3 s^{-1}$, likely due to snowmelt), and in December the second field survey was completed with the Ahuriri discharge at 21 $m^3 s^{-1}$. With the exception of a slight spike in discharge after the flood event, the short timeframe between surveys limits the amount of morphologic change caused by low flow. Therefore, it was assumed that the geomorphic changes that occurred outside of the inundated river channels were entirely due to the October flood event. Further, during this lag time between surveys, lupin development had nearly peaked; thus the December post-flood survey was an optimal time for vegetation surveying.

With the study site selected, field work commenced. As mentioned in Sections 3.3 and 4.1, the study-reach was the main focus of this research. Therefore extensive data collection was carried out for the study-reach, and limited data were collected for the extended-reach which would provide the required run-in data for the numerical model simulations. Prior to field work, preliminary planning was undertaken to determine the necessary equipment, equipment settings, and materials. During this planning, it was decided that near vertical aerial photographs would be acquired from a helicopter with a non-metric, high-grade digital camera. A Canon 10.1 megapixel digital SLR with adjustable focal length of 18-55 mm was utilized, and calibration tests determined that a focal length of 28 mm resulted in minimal image distortion (near 35 mm equivalent; see Appendix B.2 for further details and calculations). With a target image object space resolution of 0.1 m, and using a 28 mm focal length, it was determined that the appropriate flight elevation would be 600 m above the ground level (producing 0.12 m resolution), with additional images taken at 800 m (0.16 m resolution) to ensure sufficient image overlap and coverage.

During the pre-flood survey, 254 aerial photographs were captured covering the full-reach (187 at 600 m, and 67 at 800 m). The post-flood survey data set consisted of 1,076 images; with 705 images taken at 600 m covering both the study-reach and extended-reach, and 371 images taken at 800 m covering only the study-reach. Prior to taking aerial photographs, *ground control points* (GCPs) were distributed througout the study-reach for georeferencing purposes for both field campaigns (Figure 5.2). Each GCP was made of black polythene squares approximately 1.3 x 1.3 m with a superimposed cross made of yellow plastic strips

0.2 m wide. Target centroids were recorded with the RTK-GPS equipment, thus imparting an accuracy of approximately 0.02 m. Based on the camera settings, 95 GCPs were distributed thoroughout the study-reach in a 100 m grid to ensure a minimum of three GCPs in every photograph (as recommended by Chandler, 1999). GCPs were not distributed throughout the extended-reach; however, 10 transects were acquired and spaced at approximately 150 m and were deemed adequate for the level of accuracy and resolution required (Figure 5.3).

Figure 5.2: One of 95 distributed ground control points (GCP) in the Ahuriri floodplain.

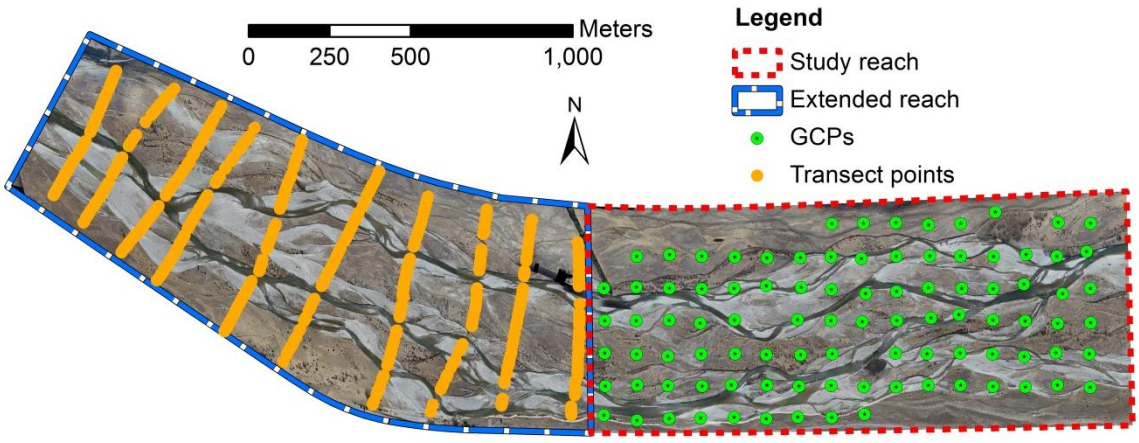

Figure 5.3: Study-reach's GCPs and the extended-reach's 10 transects.

After the aerial photographs were captured, ground truth data was collected. As outlined by Chandler (1999), ground truthing data is a collection of surveyed coordinates distributed throughout the intended study area and offers a measure of the DEM's accuracy. Ground truthing was split into two tasks: i) the study-reach, and ii) the sub-reach (Figure 4.1). Ground truth data in the extended-reach were obtained from the 10 transects (1,363 GPS points).

Ground truth data for the pre-flood survey were collected throughout the study-reach using Trimble RTK-GPS equipment, collecting survey points on roughly a 25 m spacing grid. Ground truthing in the sub-reach was accomplished by taking survey points at roughly 2 m spacings (0.25 points/m^2). This high resolution collection was performed to provide a high quality DEM of the sub-reach to accompany the time lapse camera data (mentioned in Section 4.3.2); therefore, in the event that detrimental processes occurred within the sub-reach, a high quality DEM would be acquired should the SfM provide a lesser quality. Additionally, any GPS point collected in the field could be used as a ground truthing point; therefore, surveys discussed in the preceding sections (i.e. vegetation surveys, Sections 5.3.1) also provided GPS data to utilize as ground truth data.

Combining all available GPS points collected in the pre-flood survey totaled 15,293 points for the full-reach (average of 0.0071 points/m^2). However, the points in the sub-reach were 3,361 points alone. Therefore, these points were reduced to a similar resolution spacing for the study-reach, and other redundancies were removed to provide a total of 10,622 ground truthing points for the study-reach (average 0.1 points/m^2.). The 10 transects in the extended-reach added 1,363 points (average of 0.0012 points/m^2) for a total of 11,985 ground truth points for the full-reach (average of 0.0056 points/m^2).

The ground truth data of the post-flood survey were collected in a similar manner and was divided into the study and sub-reach sections. However, since a large portion of the floodplain was not affected during the October flood event, and since landmass shift did not occur (determined from simple local network coordinate comparison), many of the ground truth points remained valid. These points were identified in ArcGIS by comparing the pre- and post-flood aerial photographs in areas of interest. By matching identifiable objects between photos, such as bushes, wood debris, and sediment patterns, certain areas could be

identified that had no flood impact. Therefore, much of the previously collected ground truth data remained valid. The post-flood ground truthing survey comprised of 5,572 points, with 4,105 points in the sub-reach alone (average of 0.10 poinst/m^2); thus leaving only 1,467 points in the greater study-reach (0.0015 points/m^2). Combining the new and reusable ground truth data and reducing the sub-reach data to a comparable resolution, a total of 10,536 points were available for the full-reach (average of 0.050 points/m^2) and 9,470 points for the study-reach (average of 0.0091 points/m^2).

Since SfM can only adequately model the visible surface, the ground truth data was split into three sets: i) a dataset utilizing all available points, ii) a dataset edited to exclude areas of tall vegetation and steep slopes, and iii) a dataset edited to include only vegetated areas. These three ground truthing data sets were frequently utilized throughout the remainder of this chapter to test the accuracy of the produced DEMs, and will be referred to as *all-ground ground-truth, bare-ground ground-truth, and vegetation-ground truth* data sets, respectively. The all-ground ground-truth data set provided an assessment of how well the SfM model performs in general, the bare-ground ground-truth data set provided an assessment of how well the SfM performs in areas where it was expected to perform well, and the vegetation-ground truth provided an assessment where the SfM was expected to perform poorly. The all-ground ground-truth data included all available points as discussed in the previous two paragraphs for a total of 11,985 pre-flood full-reach points and 10,622 study-reach points; and the post-flood full-reach had 10,536 and study-reach had 9,470 points. However the bare-ground ground-truth was reduced to pre-flood full-reach with 3,152 points (average of 0.0041 points/m^2) and study-reach with 1,985 points (average of 0.0057 points/m^2), and the post-flood full-reach had 1,797 and study-reach had 1,275 points (averages of 0.0024 and 0.0037 points/m^2, respectively). Finally, the pre-flood vegetation-ground truth consists of 134 points for the study-reach (average of 2.1×10^{-4} points/m^2) and 144 points for the full-reach (average of 1.0×10^{-4} points/m^2), and the post-flood vegetation-ground truth was 760 points for the study-reach and 902 points for the full-reach (averages of 0.0011 and 6.0×10^{-4} points/m^2, respectively). The significant difference in available vegetation-ground truth was due to the seasonal changes and resulting vegetation development between the early spring pre-flood and the mid-summer post-flood datasets.

5.2.1.3 Structure-from-Motion outputs and Topographic Point Cloud Analysis Toolkit

5.2.1.3.1 Introduction

In this research, aerial photographs and the extensive ground control mentioned in the above sections were utilized in PhotoScan to produce the topographic models of the study-reach and full-reach areas. While PhotoScan produced a 3D polygon mesh of the modeled area within the software, exported data consisted of the raw point cloud with each point having the corresponding xyz coordinates. This data was useful; however, to utilize this data outside of PhotoScan required additional editing. The point clouds exported out of PhotoScan were routinely utilized in Esri's ArcGIS 10. However, these models contained millions of points (up to 83 million) at high resolution (~0.25 m, 16 points/m^2); therefore, to improve data handling and processing time, these model's resolutions were reduced using the Topographic Point Cloud Analysis Toolkit (ToPCAT). Originally designed to analyze hyperscale point clouds produced by terrestrial laser scanners, ToPCAT overlays the point cloud with gridcells at the user specified length and width to sort and calculate statistics for the points within each gridcell (Brasington, et al., 2012). Calculated statistics of the grid contained points include the gridcell's maximum, minimum, and average elevation as well as the skewness, Kurtosis (k), standard deviation, and number of points (refer to Appendix A.2 for further details).

While reducing the resolution of the point cloud can have negative impacts on the topographic detail (e.g. undesirably smooth river banks and bar-top chutes), the statistics produced by ToPCAT can help the user preserve valuable information. For example, Brasington et al. (2012) utilized the minimum elevation (zmin) statistic for each gridcell to model the terrain surface, as this can help remove unwanted surface objects such as vegetation spikes. This is based on the assumption that the minimum local elevation in sparsely vegetated areas could have been a point that penetrated the vegetation cover and represents the terrain surface. Therefore, since the point cloud assessed for this project contains vegetated areas, the zmin was utilized to model the terrain surface.

5.2.1.3.2 Methods

Prior to utilizing ToPCAT on all models, an assessment was undertaken on the pre-flood study-reach model to determine the accuracy impact for various resolution reductions. As mentioned above, the typical SfM model had a point cloud resolution of ~0.25 m. Utilizing

ToPCAT, resolutions of 0.3, 0.5, 0.75, 1.0, 2.0, and 3.0 m were generated. Larger resolutions (e.g. > 3 m) were not evaluated due to the excessive topography smoothing that would result. Further, it was feared that anything greater than 3 m could create a negatively biased elevation model, and would result in inaccurate and excessive elevation differences and thus reducing the value of this exercise.

To assess the accuracy of the varying ToPCAT-produced resolutions and corresponding point clouds, all models were assessed independently using ArcGIS. Once the zmin point clouds were imported into ArcGIS, the point clouds were converted into digital elevation models by: i) creating a surface for the point cloud by using a Delaunay-constrained triangular irregular network (TIN), and ii) converting the TIN into a raster for surface assessment. In order to determine the model's surface accuracy, the various GPS ground truth data collected during the pre- and post-flood surveys were utilized to produce residual errors. Therefore, by subtracting the z-values of the GPS data from the modeled surface, negative values indicated that the modeled surface was too low and vice versa. To evaluate the DEM quality, the residual errors are calculated and include root mean squared error (measure of surface quality, RMSE), the mean absolute error (measure of average non-directional height differences, MAE), the mean error (as a measure of accuracy, ME), and the standard deviation (as a measure of the precision, SDE) (Chandler, 1999; Lane et al., 2010).

$$RMSE = \sqrt{\frac{\sum_{i=1}^{n}(SfM_i - Obs_i)^2}{n}} \qquad \text{(Eqn: 5.1)}$$

$$SDE = \sqrt{\frac{\sum_{i=1}^{n}\left((SfM_i - Obs_i) - \left(\overline{SfM_i - Obs_i}\right)\right)^2}{n}} \qquad \text{(Eqn: 5.2)}$$

where SfM_i is the SfM-DMVR modeled elevation and Obs_i is the observed RTK-GPS elevation. This assessment attempts to compare the modeled surface to discrete GPS data that have inherent uncertainty (~0.02 m) as well as additional sources of errors (e.g. incorrect antenna height, un-level data collection, and blunders) (Brasington et al., 2000; Brasington et al., 2003). Nevertheless, the GPS data provide an indication of the model's performance. In addition to the residual errors, cell statistics were mined from the ToPCAT zstat and underpopulated_zstat files (Appendix A.2) in order to evaluate the number of points per cell

that occurred for the various resolutions tested. As this resolution reduction would occur for every model, this assessment was only conducted on the pre-flood survey's study-reach to provide a summary of the process and a performance check.

5.2.1.3.3 Results and discussion

ToPCAT-reduced point cloud resolution and corresponding accuracy statistics are shown below in Table 5.1 for the bare-ground ground-truth and all-ground ground-truth data of the pre-flood study-reach model. Table 5.2 shows the various point clouds and statistics which provide insight into the resolution reduction and quality reduction. As shown, a resolution reduction factor of two reduced the point clouds' density by a factor of four. Therefore, even slight grid cell modifications can have large impacts on the quality of the surface model point clouds.

Interestingly, comparing the varying resolutions of Table 5.1 revealed that all resolutions produced similar accuracies when compared to the near-raw 0.3 m resolution. As shown for the bare-ground ground-truth, the RMSE only increases by 0.04 m between the 0.3 m resolution and the 3 m resolution. However, under visual observation, the topographic smoothing that occurs along the river banks and other areas of steep slopes was significantly degraded with increasing resolution reduction. Since vegetation smoothing could be beneficial in this modeling, the ideal compromise would be to find the resolution that preserves adequate topographic detail yet reduces the frequent vegetation spikes. Therefore, the resolution of choice was 0.5 m and this was chosen for its ability to preserve the topographic detail while slightly reducing the incidence of vegetation spikes and improving processing time. Throughout the remaining thesis, this method of ToPCAT edited 0.5 m resolution SfM point cloud models will be referred to as *SfM+ToPCAT*.

Table 5.1: Study-reach elevation checks for different resolution grids using only bare-ground ground-truth points and all-ground ground-truth points (for mean error (ME), root mean squared error (RMSE), mean absolute error (MAE), and standard deviation (SDE).

	ME (m)	RMSE (m)	MAE (m)	SDE (m)
Bare-ground ground-truth				
0.3m	-0.07	0.17	0.13	0.15
0.5m	-0.07	0.17	0.14	0.16
0.75m	-0.08	0.18	0.14	0.16
1.0m	-0.09	0.18	0.14	0.16
1.5m	-0.10	0.19	0.15	0.16
2.0m	-0.11	0.20	0.16	0.16
3.0m	-0.13	0.21	0.17	0.17
All-ground ground-truth				
0.3m	-0.03	0.23	0.16	0.23
0.5m	-0.03	0.23	0.16	0.23
0.75m	-0.04	0.22	0.16	0.22
1.0m	-0.05	0.22	0.17	0.21
1.5m	-0.07	0.23	0.17	0.22
2.0m	-0.08	0.23	0.18	0.22
3.0m	-0.10	0.25	0.20	0.23

Table 5.2: Various ToPCAT reduced point cloud resolutions and corresponding cell statistics.

Point cloud Resolution	Points (million)	Average points per cell	Cells with ≥1 point (%)	Cells with no points (%)
0.3 m	22.54	1	95.9	4.1
0.5 m	8.13	4	99.6	0.4
0.75 m	3.62	9	99.9	0.1
1.0 m	2.04	16	99.8	0.2
1.5 m	0.91	36	99.8	0.2
2.0 m	0.51	64	99.9	0.1
3.0 m	0.22	144	99.9	0.1

5.2.1.4 PhotoScan testing

5.2.1.4.1 Introduction

PhotoScan's point cloud generation process offers users with little photogrammetry experience a method to develop quality terrain point clouds; however, there are numerous parameter settings throughout the SfM, DMVR, and transformation stages. During the SfM image feature identification stage, the *quality* parameter setting affects camera position accuracy, with lower settings offering time savings, and the *pair selection* parameter can be utilized to speed up the image matching process through the use of subset image datasets which utilize less accurate matching algorithms. DMVR parameters are available after the SfM process has completed. Choosing the reconstruction method depends on the acquired data and intended modeled surface. PhotoScan recommends that the *height field* reconstruction be utilized for aerial photographs, as the algorithms are tailored for planer surface modeling, and that *arbitrary* reconstruction is recommended for general modeling, since the algorithms make no modeling assumptions. Additionally, reconstruction considers that geometry type and parameter settings will depend on user preferences. For example, *sharp* offers no added geometry, *smooth* fills undesired holes, and *point cloud* simply generates a generic point cloud. *Face count* offers the user the ability to limit the total faces generated in the 3D mesh and is useful to ensure that model resolution remains within the computer's capabilities. The *filter threshold* parameter filters the final mesh by removing a user-specified percent (of the total face count) of high resolution areas. The *hole threshold* is also a user-specified percent (of the total surface area) that fills in mesh holes (Agisoft, 2012a).

During the transformation process numerous parameters are available and can be categorized under the measurement accuracy parameters and the fit parameters. The measurement accuracy parameters include *camera accuracy*, *marker accuracy*, and *projection accuracy*. However, the PhotoScan user manual offers no explanation or guideline values for these parameters, other than a marker accuracy set to zero may produce slightly better results when using high precision GCPs; therefore, it is the user's obligation to experiment with various values. Internal camera calibration is available using six fit parameters which are adjusted during optimization and include: lens focal length (*fx, fy*), principle point coordinates (*cx, cy*, which calibrate lens optical axis with the camera's sensor plane), radial distortion (*k1, k2, k3*), *skew* (angle between the x and y pixel axes), tangential distortion (*p1, p2*), and *aspect* (ratio

for non-square pixels) (AgiSoft; 2012a; A. Pasumansky, personal communication, May 27, 2012). In order to achieve the best possible performance from PhotoScan, multiple preliminary parameter tests were conducted and assessment was based on the corresponding residual errors.

Since numerous tests were required to fully assess these errors and parameters, a sub-section of the study-reach was utilized to reduce processing time. This test area utilized the pre-flood data and 40 photographs with 15 GCPs and was considered equivalent to future testing of the entire reach for two reasons: i) this test region was the center of the study-reach, which provided diverse landscapes representative of the entire reach, and ii) the area utilized all available photographs for that region with significant image overlap for proper model generation. Due to the reduced test area, and since testing was performed to identify the best performance, ToPCAT resolution reduction was not utilized on these preliminary testing datasets.

5.2.1.4.2 Methods

PhotoScan has numerous parameters that may be adjusted by the user. Many of these were easily discerned from preliminary testing; however, some require a deeper assessment. The parameters identified in preliminary qualitative testing included the quality setting, face count, filter threshold, hole threshold, and optimization. These parameter settings were easily discerned based on visual observations, recommended settings, and GCP accuracy improvements. The parameters that required a deeper evaluation were the measurement accuracy parameters, fit parameters, and the reconstruction parameters. These were assessed by importing the raw point clouds in ArcGIS, generating surface rasters, and calculating residual errors between the modeled and observed surfaces. Of these parameters, the measurement accuracy parameters were the primary focus because these parameters significantly impact the overall model performance during the transformation stage.

While use of the optimization tool produced greater GCP accuracy, the PhotoScan user manual does not specify the transformation process nor does it provide details on proprietary algorithms. Therefore, to gain insight into processes, a simple assessment was performed to determine and illustrate the internal camera calibration that takes place during the various

transformation stages. This was done by examining PhotoScan's camera calibration window prior to linear transformation, post linear transformation, and post optimization.

5.2.1.4.3 Results and discussion

The qualitative results of the various quality parameter DEMs indicated that the medium and ultra-high quality settings produced 3D meshes with poor resolution and lower point densities (~9 million points over the study-reach area). The high quality setting consistently produced high resolution meshes with higher face count densities (~30 million). The results of the face count showed that 20 million had the lowest resolution, 30 million had a good quality, and the 40 million had the highest quality. However, the 40 million frequently resulted in program crashes. Finally, the filter and hole thresholds were always set to 0 to ensure that the final DEMs were unedited. Based on the observed results, the quality parameter that performed the best was the high quality setting. The face count that produced the best results was the setting of 40 million; however, due to frequent program crashes, the 30 million setting was chosen as it provided quality results without the associated problems. The program crashes may be due to the graphic card limitations, as the computer's CPU and memory were never at full capacity during the program crashes. While it was unclear why the ultra-high setting performed poorly, it was suspected to be an issue with the computer's performance and not a fault with the program itself.

The residual errors from the in-depth parameter test are shown in Tables 5.3, 5.4, and 5.5. Table 5.3 shows the results of the three measurement accuracy parameters and the best results obtained from various parameter values. Table 5.4 shows the results of the three fit parameters and the height-field vs. arbitrary reconstruction methods. The results of the projection accuracy of Table 5.3 were different than previous experience where the projection accuracy of 0.001 pix typically outperformed the 0.01 pix. Therefore, these two projection accuracy values were tested along with the reconstruction parameters, and the results are shown in Table 5.5.

Table 5.3: PhotoScan measurement accuracy parameters testing various values (residual errors are in meters).

	Camera accuracy (m)			Marker accuracy (m)				Projection accuracy (pix)		
	15	10	5	0.1	0.01	0.001	0	0.1	0.01	0.001
ME	-0.10	-0.09	-0.10	-0.09	-0.08	-0.05	-0.09	-0.09	-0.10	-0.09
RMSE	0.26	0.26	0.26	0.26	0.23	0.13	0.11	0.26	0.16	0.26
SDE	0.25	0.25	0.25	0.25	0.22	0.12	0.06	0.25	0.13	0.25
Max	0.36	0.34	0.29	0.34	0.34	0.25	0.00	0.34	0.12	0.34
Min	-0.62	-0.61	-0.61	-0.61	-0.55	-0.23	-0.17	-0.61	-0.34	-0.61

Table 5.4: PhotoScan fit parameters and reconstruction methods tested (residual errors are in meters).

	Fit: Aspect, skew, p1 & p2		Height-field vs arbitrary	
	Yes	No	Height-field	Arbitrary
ME	-0.09	-0.10	-0.09	-0.05
RMSE	0.26	0.27	0.26	0.24
SDE	0.25	0.25	0.25	0.24
Max	0.34	0.35	0.34	0.29
Min	-0.61	-0.61	-0.61	-0.47

Table 5.5: Comparing the best two options (residual errors are in meters).

	10 m (CA), 0 m (MA), 0.01 pix (PA)		10 m (CA), 0 m (MA), 0.001 pix (PA)	
	Height-field	Arbitrary	Height-field	Arbitrary
ME	-0.11	-0.02	-0.09	-0.02
RMSE	0.13	0.08	0.11	0.06
SDE	0.08	0.08	0.06	0.06
Max	0.01	0.17	0.00	0.09
Min	-0.24	-0.16	-0.17	-0.10

The results of Table 5.3 indicated that the camera accuracy had little impact on the overall model accuracy. These results were expected since the model transformation was based on the markers, and not the camera coordinates. In contrast, the marker accuracy had a

significant effect on the overall accuracy, with the setting of 0 m performing the best overall (as the PhotoScan user manual suggests). The projection accuracy results of Table 5.3 show the 0.01 pix performing the best, but no trend in performance against the changing projection values. Instead of performance improving with increasing or decreasing projection values, the best performing setting was in the middle of the values tested at 0.01 pix, with the 0.1 and 0.001 having an identical performance. However, while Table 5.3 clearly shows the 0.01 projection values performing the best, previous experience had shown that 0.001 pix typically performed the best. Therefore, additional testing was performed for the projection accuracy parameter.

The results of the fit parameters and reconstruction methods of Table 5.4 show a slight improvement with the parameters selected, but overall it appeared that these parameters had a slight effect on the model accuracy. The results of the reconstruction methods showed the arbitrary reconstruction outperformed the height-field. Due to the expectation that the 0.001 pix and height-field reconstruction would perform the best, further testing of these two parameters was undertaken with the results in Table 5.5. Based on the results of Table 5.5, the 0.001 m did outperform the 0.01 m projection accuracy, and the arbitrary outperformed the height-field. Therefore, based on the initial parameter testing of the test reach, the following parameters were used for the full scale model test: camera accuracy of 10 m, marker accuracy of 0 m, projection accuracy of 0.001 pix, fit parameters selected, and an arbitrary reconstruction. However, significant noise was created in the full scale model. Keeping all parameters the same, but switching from the arbitrary to the height-field reconstruction eliminated this noise, and produced a quality point cloud.

Assessing the internal camera parameters results (Table 5.6) during the various transformation stages, most parameters were adjusted during the first linear transformation with the exception of the skew and tangential distortion parameters p1, and p2. These results were expected, as linear (similarity) transformation does not include skew and tangential distortion. Comparing the linear and optimized parameter values revealed all were slightly adjusted, with skew having the largest relative adjustment. While these results help quantify the internal camera calibration processes, how the optimized transformation improves the GCP accuracy is still unknown. Nevertheless, due to the improved results, optimization was

utilized throughout this study. Detailed comparison between linear vs. optimized transformation GCP and surface accuracy were investigated and presented in Section 5.2.1.5. Based on these initial results, the parameter settings utilized on all generated models are shown below in Table 5.7.

Table 5.6: PhotoScan calculated camera parameters during initial, linear, and optimization transformation.

Parameter	Initial	Linear	Optimized
fx	4896.87	4823.81	4812.29
fy	4869.87	4823.81	4813.94
cx	1944.00	1966.23	1966.57
cy	1296.00	1384.03	1390.76
skew	0.00	0.00	11.05
k1	0.00	-0.11	-0.09
k2	0.00	0.25	0.12
k3	0.00	-0.27	0.08
p1	0.00	0.00	-0.0002
p2	0.00	0.00	-0.0001

Table 5.7: Final parameters utilized after preliminary testing of various PhotoScan models.

SfM parameters:	Setting
Quality	High
Pair selection	Disabled
DMVR Parameters:	
Reconstruction method	Height field - Sharp
Target quality	High
Face count	30 million
Filter threshold	0
Hole threshold	0
Transformation parameters:	
Optimization	Yes
Camera Accuracy (m)	10
Marker accuracy (m)	0.0
Projection accuracy (pix)	0.001
Aspect	Yes
Skew	Yes
p1 & p2	Yes

5.2.1.5 Model generation and accuracy assessment

5.2.1.5.1 Introduction

The SfM assessment undertaken in this research focused on the two previously mentioned surveys (pre- and post-flood) and for the mentioned reaches: the study-reach, extended-reach, and the full-reach (Section 3.5). As previously mentioned the study-reach was the main focus of this research and had extensive data collection, whereas the extended-reach had limited data collection. Therefore, the study-reach offered the best assessment for the SfM due to its dense and uniformly distributed GCPs, extensive ground truthing, and redundant image datasets. The extended-reach had less data and photo control, but was still capable of providing adequate data for a quality SfM model, which increased the quantity of topographic data compared to the acquired 10 transects. The SfM pre- and post-flood models were produced in PhotoScan using the specified parameters shown in Table 5.7 and were generated following the three-step process outlined in Section 2.2.3. The following sections were separated into the generation of pre- and post-flood models and sub categories for the study-reach and full-reach models.

5.2.1.5.2 Methods

The pre-flood model generation was performed for three separate SfM+ToPCAT models: i) the study-reach using a linear transformation, ii) the study-reach using an optimized transformation, and iii) a full-reach model using an optimized transformation. The study-reach model was generated using 147 photographs and produced a 23 million point cloud with typical point spacings of 0.25 m. Both linear (similarity) and optimized transformations were used to georeference the point cloud using the GCPs; however, as discussed by Chandler (1999), withholding a portion of the dataset provides an accuracy check. Therefore, of the 95 GCPs, 65 were utilized to transform the model and 30 were withheld. When using GCPs to set the coordinate system and apply the transformation, PhotoScan automatically calculates the difference between the model's estimated GCP coordinates (xyz) and the user supplied GPS coordinates. Utilizing these differences, residual errors of the utilized and withheld GCP coordinates offered an unbiased check on the transformation performance and were the first quality assessment. The second quality assessment compared the SfM+ToPCAT-generated surface raster against the three segmented GPS ground truth datasets (all, bare, and vegetation) to evaluate the surface accuracy.

While a comprehensive data acquisition campaign was implemented for the study-reach, a network of GCPs was not created for the extended-reach. Nonetheless, given the desirability of extending the SfM model to provide additional topography for adequate 'run-in' for hydrodynamic simulations, a sparse survey of data from 10 transects (1,363 points) across the extended-reach was analyzed in an attempt to extract viable photocontrol. In order to model this extended-reach, photographs from both the study-reach (acquired at 600 and 800 m) and extended-reach (acquired at 600 m) were combined to create a new photo set totaling 224 images. A dense reconstruction based on this entire photo archive generated a point cloud comprising over 60 million points with an average of 0.23 m point spacing.

This point cloud was transformed using the optimized setting and was accomplished by using the 95 GCPs covering the study-reach. Since no photocontrol existed for the extended-reach section, a surface accuracy assessment (Section 5.2.1.3.2) was performed in ArcGIS to evaluate how well the modeled surface compared to the surveyed surface. This was accomplished by using the GPS points of the 10 transects and a georeferenced orthophoto that was generated in PhotoScan and imported into ArcGIS. During the collection of the 10 transects in the extended-reach, the GPS points were taken at slope break points and geocoding was utilized to distinguish river channel margins ('w' for water). As shown in Figure 5.4, channel margins aligned well and breaks of slope matched clustered GPS points and thus horizontal alignment was adequate. With the horizontal alignment set, a vertical alignment was assessed by comparing the modeled surface to the surveyed surface (1,363 transect points); however, the vertical alignment had residual errors up to 30 m.

To improve the vertical alignment required additional GCPs in the extended-reach. Therefore, an additional 70 GCPs were retrofitted by identifying natural features near the transect points using aerial images. Using these features and GPS coordinates, photocontrol was gained in the extended-reach. Once the 70 additional GCPs were added with the 95 study-reach GCPs, a total of 165 GCPs were available to re-transform the full-reach model. However, as with the study-reach, approximately one-third of the points were withheld for check-points; therefore, 112 GCPs were utilized for the model's optimized transformation.

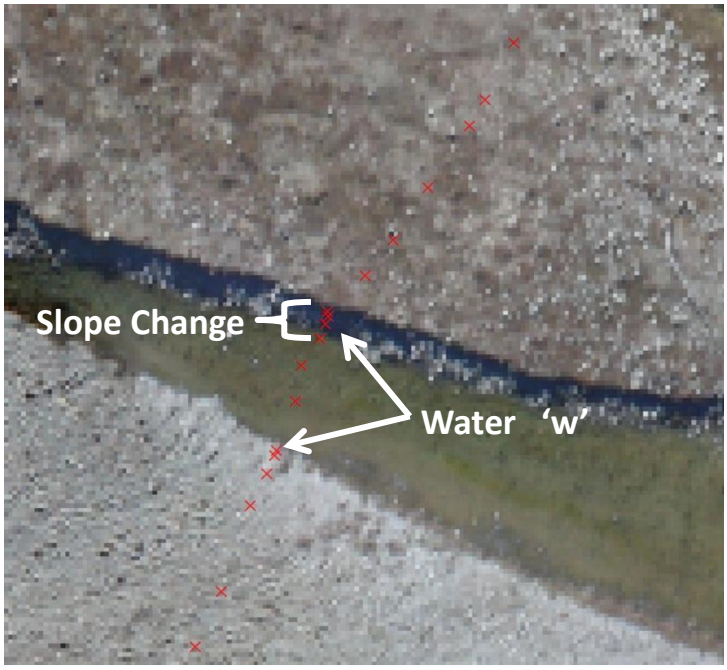

Figure 5.4: Evaluation of the extended-reach horizontal alignment.

Since the pre-flood model was generated and fully evaluated before the post-flood model, advantages were in place to fast-track the future SfM model generation. As discussed in the upcoming results and discussion sections, the model accuracy within the study-reach was improved by adding the extended-reach data; therefore, instead of generating two models (study-reach and full-reach), only the full-reach model was generated. Further, the linear transformation models were not included for the post-flood model as the results of the pre-flood optimized models were significantly improved.

Based on the impressive results from the first SfM+ToPCAT model of the pre-flood data, the post-flood full-reach model was generated using 281 photographs and produced a point cloud of over 87 million points. This model was first georeferenced using the 95 study-reach GCPs, and later refined by retrofitting an additional 56 GCPs (total 151 GCPs) in the extended-reach that were acquired using the same procedure as the pre-flood full-reach method. This model was then transformed using the optimized method with 96 GCPs utilized and 55 GCPs withheld.

5.2.1.5.3 Results and discussion

Utilizing the GCP residual errors to evaluate the transformation, and surface residual errors (referred to as ground truth errors) to assess the overall accuracy of the SfM models, the pre-flood study-reach linear transformed model results are shown in Table 5.8 and the optimized transformed model results are shown in Table 5.9. Results revealed that the optimized model outperformed the linear model in every category. The linear model results show the utilized and withheld GCPs have x- and y-errors in the decimeter range, which indicated a successful horizontal transformation. However, the z-errors were considerably higher and would not suit the objectives of most fluvial terrain models. Ground truth performance affirms the poor surface model with precision in the meter-range. While the residual errors of Table 5.8 provide valuable insight into the model performance, color-coordinated error values of the model provided a valuable visual observation that can identify issues such as spatial bias and model generation quality. Spatially presenting the GCP and all-ground ground-truth z-errors (Figure 5.5) shows a distinct pattern of positive z-errors in the upstream and downstream ends and negative z-errors in midsection. This spatial error pattern raised concern as it suggests that PhotoScan's linear transformation produces spatial bias.

The optimized model's withheld and utilized GCP residual errors show strong agreement for the x- and y-dimensions, which indicated that the horizontal transformation was successful in both areas with and without photocontrol. However, the withheld GCP z-errors produced considerably higher residuals than the utilized GCPs, which indicated the transformations dependence on photocontrol. Nevertheless, the z-errors mean and standard deviation results show considerable improvement over the linear transformation model and produced accuracies and precisions suitable for terrain modeling. Examining the ground truthing errors, the all- and bare-ground ground-truth data have similar performance in the decimeter range; however, the vegetation-ground truth errors were significantly higher. Spatially plotting these GCP and all-ground ground-truth z-errors (Figure 5.6) revealed no discernible error distribution, thus indicating a successful transformation. Interestingly, when comparing the optimized GCP z-errors with the bare-ground truth and all-ground ground-truth z-errors revealed similar performance; however, the ground truth mean errors had become negative. This result was likely caused by the use of the ToPCAT z-minimum data to represent the terrain. While a negative mean was undesirable, the overall accuracy impact of ToPCAT appears to be minimal when comparing the withheld GCP and ground truth residuals.

Nevertheless, the results of the optimized model's GCPs and ground truth suggest a successful transformation and bias-free surface model. Due to the poor results of the linear transformed model, and the superb results of the optimized models, only optimized models were evaluated from hereon.

Table 5.8: Accuracy results for the linear transformed pre-flood study-reach SfM+ToPCAT model.

		Data	n	ME (m)	RMSE (m)	MAE (m)	SDE (m)
GCPs	x	Utilized	65	0.04	0.19	0.14	0.19
		Withheld	30	0.04	0.20	0.15	0.20
	y	Utilized	65	-0.06	0.17	0.14	0.17
		Withheld	30	-0.04	0.19	0.16	0.19
	z	Utilized	65	0.40	2.00	1.52	1.97
		Withheld	30	0.46	1.96	1.53	1.93
Ground truth	z	Bare	1,985	0.42	2.27	1.75	2.23
		Veg.	134	1.71	2.69	2.16	2.08
		All	10,622	0.58	2.41	1.93	2.34

Table 5.9: Accuracy results for the optimized transformed pre-flood study-reach SfM+ToPCAT model.

		Data	n	ME (m)	RMSE (m)	MAE (m)	SDE (m)
GCPs	x	Utilized	65	0.00	0.02	0.01	0.02
		Withheld	30	0.00	0.05	0.03	0.05
	y	Utilized	65	0.00	0.02	0.01	0.02
		Withheld	30	0.00	0.04	0.04	0.04
	z	Utilized	65	0.00	0.03	0.02	0.03
		Withheld	30	0.04	0.22	0.13	0.22
Ground truth	z	Bare	1,985	-0.07	0.17	0.14	0.16
		Veg.	134	0.41	0.78	0.50	0.67
		All	10,622	-0.03	0.23	0.16	0.23

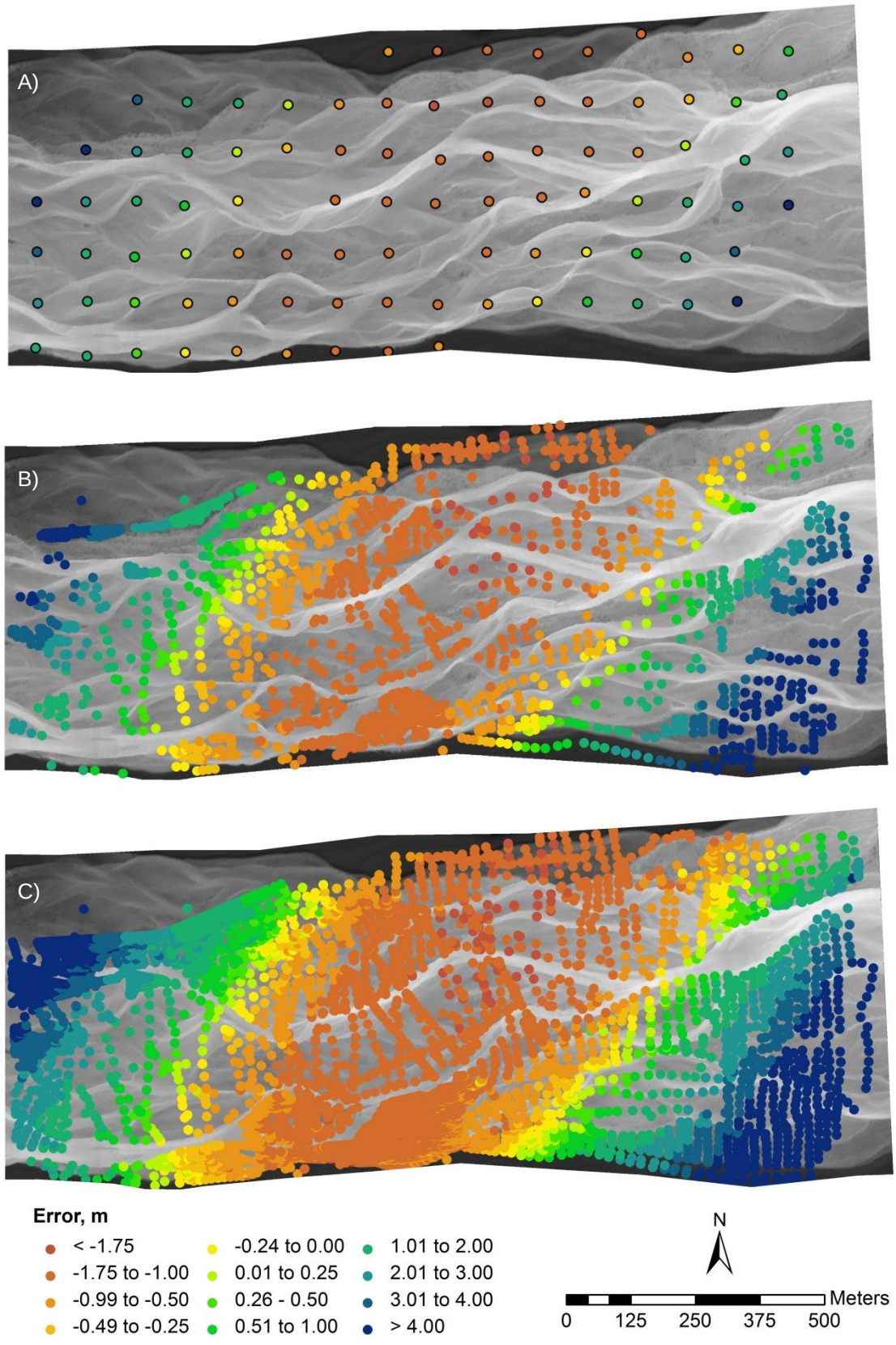

Figure 5.5: Spatial bias testing of the study-reach, pre-flood linear transformed model: A) GCPs, B) bare-ground ground-truth, and C) all-ground ground-truth.

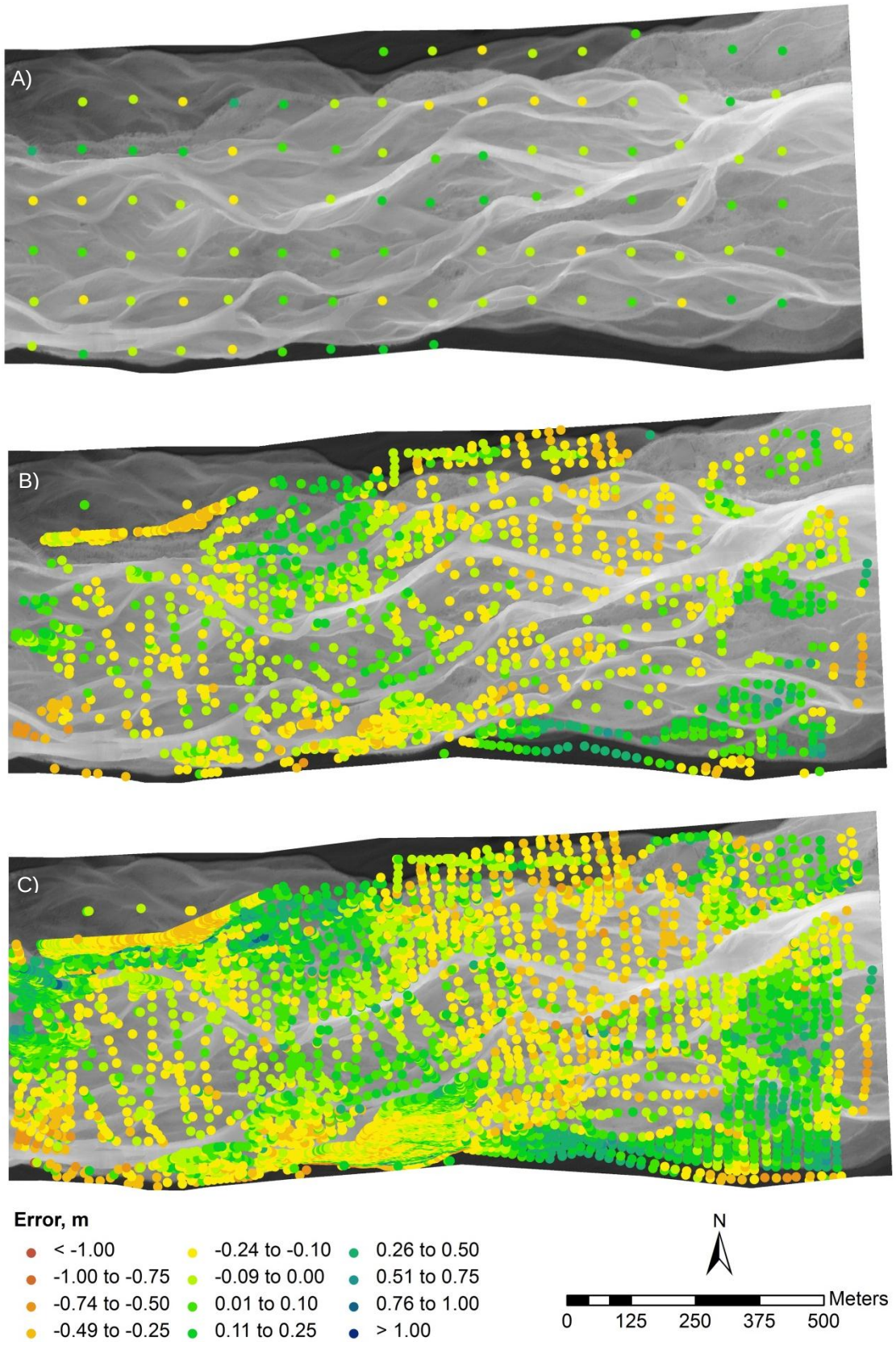

Figure 5.6: Spatial bias testing of the study-reach, pre-flood optimized transformed model: A) GCPs, B) bare-ground ground-truth, and C) all-ground ground-truth.

The study-reach and extended-reach quality assessment was separated for the pre-flood full-reach optimized model, and results are shown in Table 5.10. Similar to the optimized study-reach model of Table 5.9, the study-reach portion of the optimized full-reach model has GCP errors in the decimeter range with the z-errors slightly higher and less accurate for the withheld data. Conversely, the GCP errors of the extended-reach portion of the full-reach model had higher errors in all dimensions with only the y-errors showing agreeance between utilized and withheld data. Examining the ground truth errors of the individual reaches in Table 5.10, the study-reach outperformed the extended-reach in nearly every category. This was expected as the study-reach had significantly higher quantity and quality data utilized for transformation. Nevertheless, the overall performance of the models was promising with bare and all-ground ground-truth performing in the decimeter range. The vegetation ground truth errors were relatively high, but this performance was expected and limited to small areas. Plotting the color-coordinated residual errors, the spatial errors are shown in Figure 5.7 and depict a random order of errors, thus suggesting a successful optimization was achieved.

Table 5.10: Accuracy results for the optimized transformed pre-flood full-reach SfM+ToPCAT model.

		Data	n	ME (m)	RMSE (m)	MAE (m)	SDE (m)
Study-reach							
GCPs	x	Utilized	65	0.00	0.06	0.03	0.06
		Withheld	30	0.00	0.05	0.03	0.05
	y	Utilized	65	0.00	0.05	0.03	0.05
		Withheld	30	0.01	0.05	0.04	0.05
	z	Utilized	65	0.01	0.08	0.06	0.08
		Withheld	30	0.03	0.13	0.10	0.13
Ground truth	z	Bare	1,985	-0.05	0.13	0.10	0.12
		Veg.	134	0.41	0.69	0.52	0.53
		All	10,622	-0.01	0.21	0.14	0.21
Extended-reach							
GCPs	x	Utilized	47	0.01	0.10	0.08	0.10
		Withheld	23	0.01	0.21	0.17	0.21
	y	Utilized	47	0.01	0.13	0.09	0.13
		Withheld	23	-0.01	0.13	0.09	0.13
	z	Utilized	47	0.01	0.18	0.15	0.18
		Withheld	23	0.13	0.36	0.28	0.34
Ground truth	z	Bare	1,116	-0.03	0.29	0.23	0.29
		Veg.	10	0.37	0.72	0.61	0.66
		All	1,233	0.05	0.27	0.24	0.27

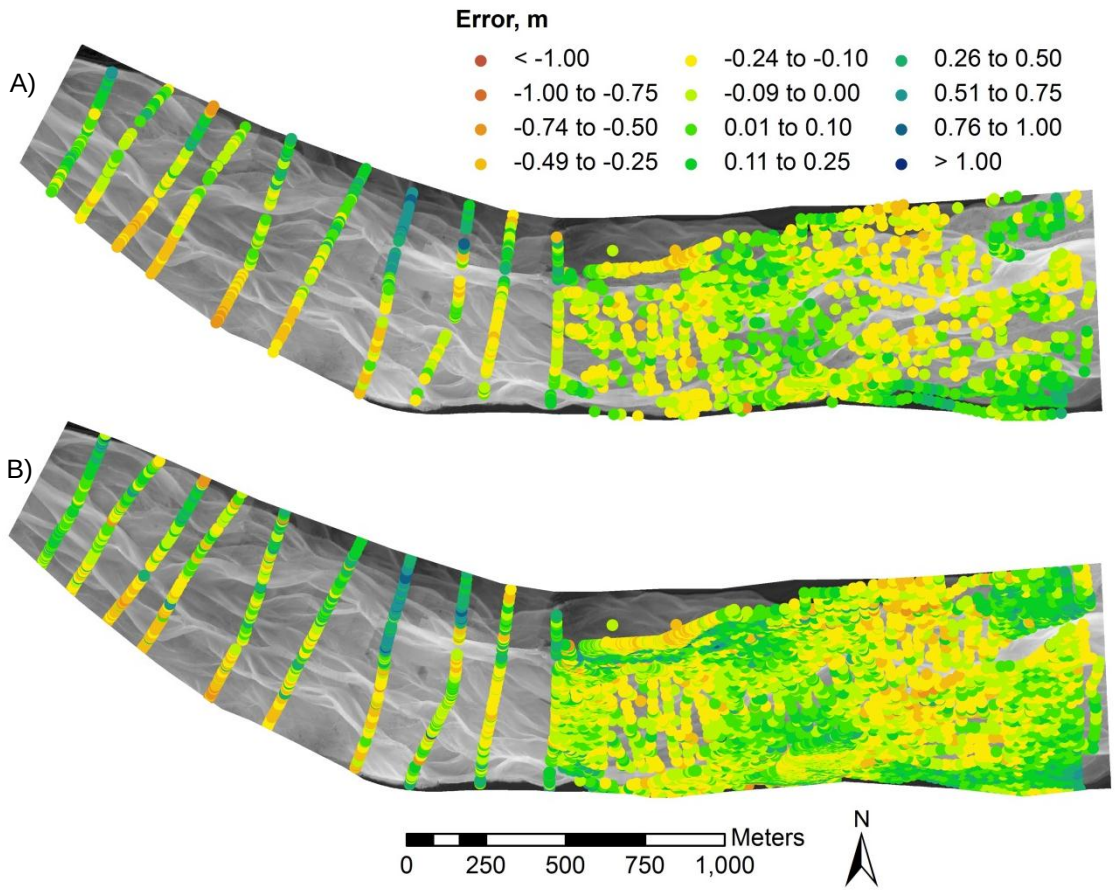

Figure 5.7: Spatial bias testing of the full-reach, pre-flood optimized transformed model: a) bare-ground ground-truth, and b) all-ground ground-truth.

Examining the results of the study-reach only model of Table 5.9 and the study-reach section of the full-reach model of Table 5.10 revealed that the full-reach model improved the performance of the study-reach residual errors. As shown in the two tables, the study-reach performance (Table 5.10) has significantly improved the GCP, bare-ground ground-truth, and all-ground ground-truth z-errors when compared to the study-reach performance of Table 5.9. This was likely due to the added photocontrol of the extended-reach, albeit less accurate. Conversely, the extended-reach performance does not reciprocate this improvement. Based on the improved results of the full-reach modeled study-reach over the single study-reach models performance, it was assumed that the poor performance of the extended-reach was not a function of the larger area modeled, but rather the limited data available for the area. Since the photocontrol for the extended-reach was retrofitted, it was subject to more sources of error and inaccuracy than the study-reach. While there are many possible sources of error, some significant causes may be the retrofitted GCPs and horizontal alignment. The greatest of these was the accuracy to which the natural GCPs can be identified and located in ArcGIS,

and then re-located in PhotoScan. First, identifying the object in ArcGIS was subject to the 12 cm image pixel resolution. Next the coordinates of the natural features were determined based on the distance to the nearby GPS transect points, and finally, the GCP was then marked on a PhotoScan 12 cm pixel image. Within these necessary steps to retrofit the extended-reach GCPs, inaccuracies already exist in the decimeter range. Further, while it was discussed and demonstrated that the extended-reach had an 'adequate' horizontal alignment, this too can cause further extended-reach inaccuracies. Since the vertical errors are calculated from taking the difference between the modeled surface and the GPS point of the surveyed surface, if these two are not perfectly aligned, then the errors are misleading and inaccurate. Therefore, it was no surprise that the extended-reach had larger errors than the study-reach.

Based on the results of the pre-flood models, understanding PhotoScan's capabilities was improved. This allowed a few changes to occur for the post-flood model generation. First, it was obvious from Tables 5.8 and 5.9 that the optimized transformation vastly outperforms the linear transformation; therefore only the optimized transformation was generated and tested for the post-flood models. Secondly, generating the full-reach model produces better results for the study-reach section than a single study-reach model; therefore only the full-reach model was produced.

The results of the post-flood model are presented in Table 5.11 and show that the study-reach GCPs produced low x- and y-errors, and the z-errors are slightly higher; thus suggesting a successful transformation. Similar to the pre-flood full-reach model, the post-flood's extended-reach produced considerably larger GCP errors than the study-reach; however, some of the z-errors show higher performance for the withheld data. Nevertheless, the GCP errors of the extended-reach were still within decimeter range and show agreeance between withheld and utilized data, suggesting a successful transformation. Examining the study-reach's bare-ground ground-truth data revealed comparable results to the pre-flood results, with low standard deviations and a slightly negative mean error, which was likely caused by the ToPCAT z-minimum values representing the terrain. However, the all-ground ground-truth errors were significantly higher. The extended-reach ground truth results were similar to the study-reach's, with bare-ground ground-truth performing well and the all-ground ground-truth having poor precision and accuracy. The difference in the vegetation and all-ground ground-truth performance was likely due to the fact that the post-flood data has significantly

greater vegetation influence (due to the summer growth) when compared to the pre-flood data taken during the early spring season. Further, as discussed for the pre-flood model, the extended-reach was subject to additional sources of errors, and therefore it was no surprise that it produced higher errors than the study-reach that had extensive photocontrol and data. Finally, the spatially plotted residual errors of Figure 5.8 depict that the errors are random and suggest that the optimized transformation was successful.

Table 5.11: Accuracy results for the optimized transformed post-flood full-reach model.

		Data	n	ME (m)	RMSE (m)	MAE (m)	SDE (m)
Study-reach							
GCPs	x	Utilized	65	0.01	0.05	0.03	0.05
		Withheld	30	0.00	0.05	0.04	0.05
	y	Utilized	65	0.00	0.06	0.04	0.06
		Withheld	30	-0.02	0.08	0.05	0.08
	z	Utilized	65	-0.01	0.14	0.10	0.14
		Withheld	30	-0.02	0.18	0.13	0.18
Ground truth	z	Bare	1,275	-0.07	0.12	0.10	0.10
		Veg.	760	1.35	2.13	1.36	1.64
		All	9,470	0.09	0.64	0.25	0.64
Extended-reach							
GCPs	x	Utilized	31	0.03	0.20	0.15	0.20
		Withheld	25	0.04	0.20	0.16	0.20
	y	Utilized	31	0.03	0.20	0.13	0.20
		Withheld	25	0.03	0.18	0.15	0.18
	z	Utilized	31	0.03	0.32	0.24	0.32
		Withheld	25	-0.01	0.28	0.23	0.29
Ground truth	z	Bare	522	0.08	0.23	0.17	0.21
		Veg.	142	1.11	1.62	1.12	1.19
		All	1,066	0.26	0.64	0.33	0.59

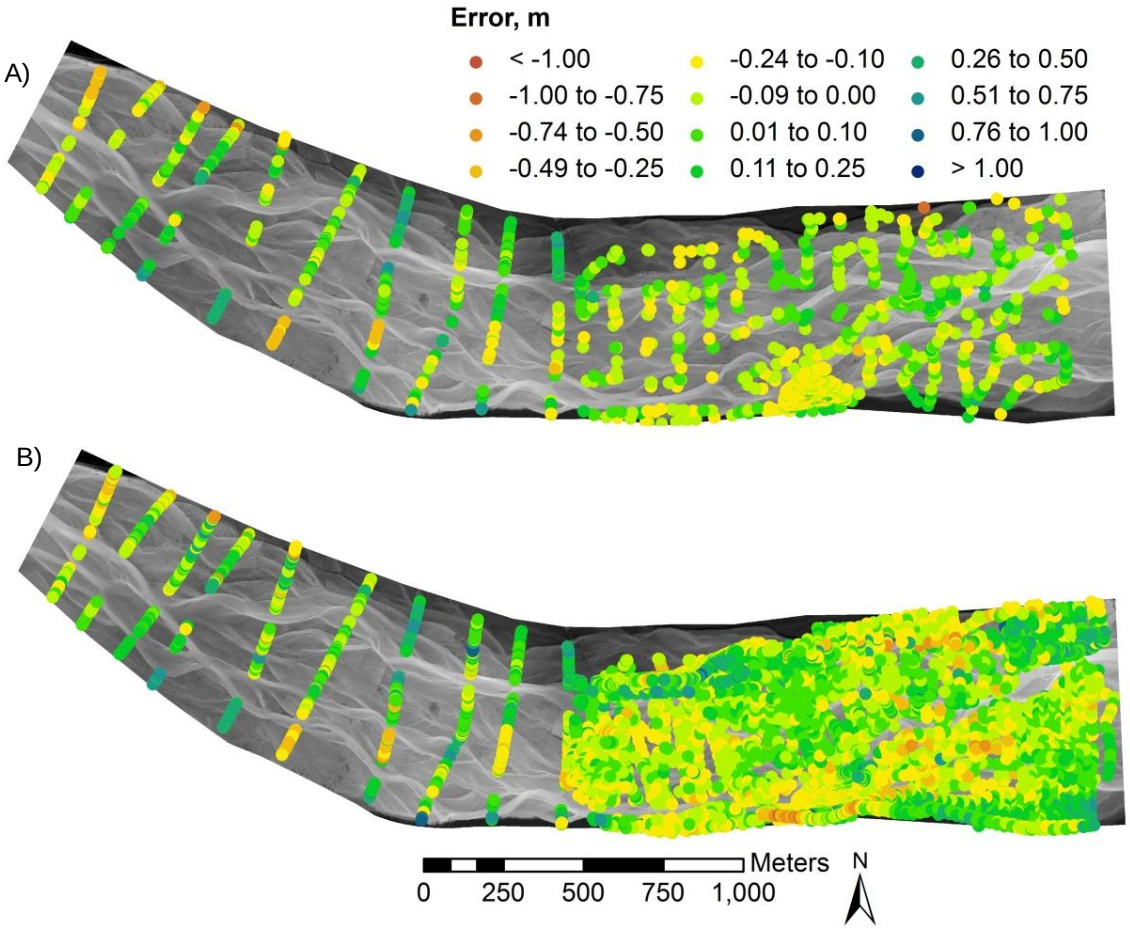

Figure 5.8: Spatial bias testing of the full-reach, post-flood optimized transformed model: A) bare-ground ground-truth, and B) all-ground ground-truth.

5.2.1.6 Model improvement

5.2.1.6.1 Introduction

With the overall goal to simulate flood events in the study-reach, the final SfM+ToPCAT model, and resulting DEM need to be representative of the ground elevation. Due to moderate weed encroachment in the study-reach and extended-reach, the resulting SfM+ToPCAT model still had significant elevation errors in vegetated areas; as shown in Tables 5.9, 5.10, and 5.11. As previously mentioned, ToPCAT is a geospatial topographic point cloud analysis toolkit utilized in this project to reduce the point cloud resolution without losing valuable elevation information for the final DEM. In addition to intelligently reducing the resolution, ToPCAT can be utilized to evaluate noise, and potentially as a tool to aid in removal of artifacts related to vegetation. Evaluating the data from Section 5.2.1.3, the resolution testing

produced similar results, yet observational analysis determined significant topographic detail reduction for the coarser resolutions (2 and 3 m).

Determining one resolution that best represents the topographic detail and adequately smoothed the unwanted vegetation is a difficult qualitative task. Therefore, instead of choosing one, a hybrid topographic point cloud was constructed in an effort to preserve the topography of low- and zero-vegetation areas, and reduce the noise in large densely vegetated areas using coarse ToPCAT point clouds. This process was relatively simple and was implemented using various tools in ArcGIS with little manual editing.

5.2.1.6.2 Methods

Creating raster maps of the varying ToPCAT resolutions (0.75, 1, 2, and 3 m) in ArcGIS, it was possible to directly compare the topography detail and vegetation influence for each resolution. Using the raster calculator tool in ArcGIS, each of the additional coarser rasters were differenced from the original SfM+ToPCAT raster, which produced an elevation difference raster. This was performed for all rasters; however, the two rasters that were chosen that best preserved the topography and best smoothed the vegetation were the 0.5 m and 3 m resolutions, respectively. Subtracting the coarser raster from the fine raster creates positive differences in areas where the fine raster had a higher elevation. Since the finer raster typically had higher elevation in areas of vegetation (due to less smoothing), this helped identify where vegetation influences occurred. However, as discussed in Brasington et al. (2012), differences are also likely to occur in areas such as steep breaks in slope (e.g. river banks); therefore, post-processing was necessary to exclude such areas. To utilize the raster differences to edit the point cloud required the ArcGIS tools Raster to Points, Select by Attributes, Aggregate Points, and Clip.

Discretizing this new calculated raster into points allows the selection of certain areas based on their values (e.g. the values of raster differences). Selecting the points based on elevation differences, a specific threshold value reasonable to identify vegetation noise was selected. In this research, vegetation that could affect the DEM primarily consists of sweet briar, crack willows, matagouri, and lupins, with lupins being the shortest. Therefore, the threshold value

of 0.4 m was qualitatively chosen, as 0.4 m was appropriate to identify lupin vegetation noise while taking into consideration larger sediment typical of the Ahuriri River and the DEMs uncertainty.

With the difference points of 0.4 m and greater selected in the discretized raster, these points were grouped together into polygons based on the user-specified vicinity using the Aggregate Points tool. These polygons were distributed throughout the reach; however, as mentioned above, these identified areas were not entirely vegetation. Therefore, post-processing was necessary and conducted by deleting polygons that were created in areas where vegetation did not exist. After this slight editing, the remaining polygons were utilized with the Clip tool in ArcGIS to cut the points from the final SfM+ToPCAT point cloud. Finally, the 3 m resolution point cloud was used to fill in the holes created from the clipped point cloud; thus producing a hybrid resolution point cloud. Once the final point cloud was produced, a raster surface model was generated and the ground truth data was utilized to compare the accuracy of the edited point cloud to the accuracy of the unedited point cloud. This final hybrid surface model will be hereafter referred to as *SfM-Veg*.

Similar to the pre-flood noise reduction, the vegetation would need to be removed from the post-flood SfM+ToPCAT model. This was accomplished in the same manner as the first data set by using ToPCAT to create a hybrid resolution model to smooth over vegetation spikes and preserve the topography in low- and zero-vegetated areas. However, since the post-flood survey was acquired in mid-summer, the vegetation density and extent was much greater than the pre-flood model, thus making a vegetation free surface model more difficult. To reduce the vegetation noise produced, significant post-processing was necessary. Since many of these areas were large (> 20 m^2), ToPCAT offered little improvement as 20 m resolutions would overly smooth the topography to an unusable level. Therefore, a simple solution was to patch in the topography of the first DEM in these newly vegetated areas.

Using the aerial photographs of the pre- and post-flood surveys, it was possible to identify areas that were not impacted by the flood event based on identifiable features such as wood debris, vegetation, and sediment patterns. By identifying areas that were not impacted by the flood, and assuming minimal changes occurred from animal disturbance, human disturbance,

and/or wind erosion, it was determined that the elevation in vegetated areas on elevated bars and banks would be constant. Therefore, all vegetated areas unaffected by the flood event were clipped form the post-flood point cloud and patched with the pre-flood point cloud to produce a (nearly) vegetation free point cloud for modeling reasons. However, since the surface models were produced by SfM, the errors within specific areas varied. Therefore, in certain areas where the pre-flood model had positive residual errors, occasionally, the post-flood point cloud had negative errors; thus producing a noticeable step in elevation where the patch took place. Often, these patch borders had relatively minor steps ($\leq$ 0.15 m); however, a few areas required additional smoothing to reduce the step influence. Fortunately, these more drastic steps (~0.3 m) all were confined to inner-floodplain areas where flow would only be influenced in large flood events. Further, these steps were always down in elevation (if traveling from upstream to downstream); therefore, in the event that water is simulated within these floodplain areas, the water will run down the step, and would not be dammed by an increase step in elevation.

5.2.1.6.3 Results and discussion

Using various ToPCAT resolutions, a simple technique was developed in ArcGIS to produce a hybrid resolution model that best represented the ground topography (illustrations provided in Appendix E.4). Using this method on the pre-flood model, approximately 1% of the total points were reduced from the 0.5 m to the 3 m resolution. To evaluate the effectiveness of the hybrid model, the accuracy of the 0.5 m resolution model (Table 5.10) was directly compared to the hybrid model accuracy (Table 5.12) using the ground truth data and results revealed that the hybrid model considerably improved the accuracy and precision of the vegetated areas for both study- and extended-reaches; however, the overall performance was still below the reach-wide SfM accuracy for both reaches. Further comparison shows the study-reach's and extended-reach's bare-ground ground-truth results were unaffected by this hybrid resolution. The study-reach's and extended-reach's all-ground ground-truth results show a slight improvement in the hybrid resolution. These results were expected, as the bare areas would not be impacted by the hybrid resolution due to lack of vegetation noise and the all-ground ground-truth data showed a slight improvement due to the inclusion of vegetated areas. With the hybrid SfM-Veg resolution showing significant improvement in terrain representation of vegetated areas, this was chosen as the final model for DEM generation.

Table 5:12: Pre-flood ToPCAT noise reduced terrain model (SfM-Veg).

	ME (m)	RMSE (m)	MAE (m)	SDE (m)
Study-reach				
Bare	-0.05	0.13	0.10	0.12
Veg.	0.20	0.37	0.32	0.33
All	-0.02	0.18	0.13	0.18
Extended-reach				
Bare	-0.03	0.29	0.23	0.29
Veg.	0.12	0.52	0.41	0.57
All	0.04	0.26	0.23	0.26

The post-flood hybrid model residual errors are shown below in Table 5.13. Comparing these results to the results of Table 5.11 illustrates the overall improvement of the hybrid resolution. Comparing the study-reach bare-ground ground-truth data, the results were nearly identical for the SfM+ToPCAT and SfM-Veg models, yet the all-ground ground-truth results were significantly improved for the SfM-Veg hybrid model. The results of the extended-reach are similar to the study-reach, with no significant improvement in bare-ground ground-truth results and a significant improvement in the vegetation-ground truth and all-ground ground-truth areas. These results were expected, as the bare areas had little or no impact of the hybrid resolution and due to the significant improvement in the vegetated areas that are included in the all-ground ground-truth data set. With the significant improvement in the terrain representation, this hybrid was the final model utilized in DEM production.

Table 5.13: Post-flood ToPCAT noise reduced terrain model (SfM-Veg).

	ME (m)	RMSE (m)	MAE (m)	SDE (m)
Study-reach				
Bare	-0.07	0.12	0.10	0.10
Veg.	0.11	0.27	0.20	0.25
All	-0.04	0.17	0.13	0.17
Extended-reach				
Bare	0.05	0.23	0.18	0.23
Veg.	0.05	0.24	0.17	0.23
All	0.06	0.26	0.19	0.25

5.2.1.7 Conclusion

Through various tests and assessments, the SfM-DMVR process was refined to produce the best models. Initial preliminary testing provided the necessary parameter settings based on a smaller test area of the study-reach. These results were then applied to the full scale models that generated study-reach and full-reaches DEMs. Through extended testing, it was determined that the larger full-reach model, with its additional photocontrol and data, did improve the accuracy results for the study-reach portion when compared to the independently produced study-reach model. Further, optimized transformation vastly outperformed the linear transformation model quality. While the extended-reach had larger errors and a greater number of sources of errors that made it difficult to evaluate the accuracy, it was clear that even with errors in the 0.3 m range, this data provided greater topographic detail for the extended-reach than the 10 transects; thus improved run-in data for the hydrodynamic model. Therefore, while greater quality models were generated with extensive control data, the extended-reach results illustrated that qualitatively convincing models can be generated from limited and retrofitted data. Finally, due to processing time and data handling issues, ToPCAT was initially used to reduce the resolution of the SfM models, but later utilized to reduce the vegetation noise. Comparing the SfM+ToPCAT produced models with the SfM-Veg hybrid resolution models showed a large quantitative improvement in accuracy, and an obvious improvement in visual observation comparing the rasters of Appendix E.4, Figure E.7C and D.

5.2.2 Bathymetric mapping

5.2.2.1 Introduction

Bathymetric mapping was required to provide the topography of the river beds, which was later combined with the SfM-Veg dry land topography to produce the final DEMs of the pre- and post-flood data sets. In order to model the river channel bathymetry, the following three steps were followed: i) develop an empirical formula to calculate the water depth based on the Red-Green-Blue bands (RGB) from the true color aerial photographs, ii) model the water surface elevation based on the river edge SfM point clouds, and iii) produce the final river channel bathymetric map by calculating the depth of the water and subtracting from the water surface's elevation. This section covers the following: i) data collection, ii) empirical development, iii) model generation, and iv) conclusion.

5.2.2.2 Data collection

The optical bathymetric mapping method utilized the same aerial photographs mentioned in Section 5.2.1.2. To recap, the photographs for the pre-flood survey captured 254 images covering the full-reach (187 at 600 m, and 67 at 800 m) and the post-flood survey captured 1,076 images with 705 images taken at 600 m, covering both the study-reach and extended-reach, and 371 images taken at 800 m covering only the study-reach. Both image datasets were captured during unfavorable sunny conditions; however, due to time restrictions and forecasted weather storms, the aerial photography proceeded.

During both the pre- and post-flood surveys, bathymetric data was recorded an hour after the aerial photographs. During the pre-flood data collection, a Tritech PA500 altimeter (echo-sounder) was utilized to map the river's bathymetry; however, the echo-sounder alone only documents the water depth. To provide geo-located depth measurements, the Trimble RTK-GPS was fixed to the echo-sounder using a custom fabricated mount, which positioned the Trimble R8 receiver directly above the echo-sounder. Further, the echo-sounder and TSC2 controller were connected, and through various TSC2 settings, it was possible to log the sounder's National Marine Electronics Association (NMEA) data string output with the synchronized GPS coordinates at one-second intervals (the sounder measures the depth 10 times per second (10 hertz)). This provided geo-located depth measurements as well as the water surface elevation. Considering the RTK-GPS elevation precision was approximately 0.03 m, and the PA500 precision was approximately ±0.025% of the depth range, the accuracy and precision of the bathymetric data was considered to be comparable to just the RTK-GPS, given the shallow water depths of the braided river.

In order to best utilize the echo-sounder and map the largest area possible in a short amount of time, the GPS and echo-sounder were attached to a small dinghy. Using a set of ropes and two people on opposite river banks, the dinghy was zigzagged down the river's main channels. However, due to the depth at which the sounder must sit below the water surface (10 cm), it was not possible to record the depths in shallow areas due to concern of damaging the sounder. Therefore, only areas of adequate depth (>20 cm) were recorded using this method. This restricted the sounder to only the deeper sections of the main channel. Therefore, additional depth measurements were acquired for the side braids and the extended-

reach manually through the GPS equipment and wading into the river. This was performed by first recording the water surface elevation along the river shoreline, and then proceeding into the river perpendicular to the flow. In total, 7,055 water depth points were recorded during the pre-flood field work, with 68 of these taken manually; however, numerous depth measurements were erroneous. If depth data were not adequately measured by the echo-sounder, a value of -50 was produced. Therefore, after deleting these measurements and any measurement that were less than 20 cm, a total of 6,567 points were available. The water surface elevation measurement was always valid even if the depth measurement was not, and this provided 7,015 measurements of the water surface. While not every stretch or braid of river was covered with bathymetry measurements, the data acquired were more than adequate to build and calibrate a depth model based on optical-empirical bathymetric mapping methods.

The post-flood bathymetric survey was conducted similarly to the pre-flood survey, with depth measurements taken an hour after the aerial photography. However, only manual spot checks were conducted using the Trimble RTK-GPS equipment. This was conducted by surveying the shoreline first to document the water surface elevation, then, proceeding perpendicular to the flow, additional survey points were taken of the river bed. In total, 474 bathymetric points were recorded; however, as with the pre-flood model, only points with depths of 20 cm and greater were utilized. This reduced the number of depth points to 300 points, yet provided 474 water surface elevation measurements.

5.2.2.3 Empirical relationship

5.2.2.3.1 Introduction

Unlike the SfM section, the bathymetric data and model generation was not divided into study-reach and extended-reach. Instead, the model was developed and applied to the entire full-reach. Therefore, data processing and results presented are for the full-reach.

As authors have shown (e.g. Williams et al., 2013; Legleiter, Roverts, Marcus, & Fonstad, 2004; Winterbottom & Gilvear, 1997), both the Lyzenga (1981) algorithms and band ratios can be an effective optical method to map river bed channels. Therefore, both methods were

tested using the data captured and described in the bathymetry field work section. However, the first task was to determine how the photographs would be utilized. Following the work of Williams et al. (2011), it was decided to test both a set of mosaicked images and a single image to develop the best technique to extract depth values from the color imagery RGB bands. Raw image resolutions were approximately 0.12 m, and while the mosaicked images were ortho-rectified, the single images were not. However, due to the low vertical relief of the braid plain, this was not a concern.

Upon investigating the aerial photographs, it was apparent that some of the photographs had significant sun interference. This significant glint was caused by the sunny conditions during image capture. While no images had the sun directly exposed, the reflection of the sun off the water caused significant glint in several images that were taken when the camera was facing towards the sun (north). Therefore, it was decided to split the photographs into two additional categories: the first would contain all photographs and the second set would separate the north- and south-facing image sets. In addition to separating the two sets of photographs, all images were slightly modified to exclude areas of severe glint. By inspecting the RGB bands separately, the blue band was identified as the band with the most sensitivity to glint, as expected by the results of Williams et al. (2013). Further assessment determined that blue band values of 140 and greater were indicative of water glint. Therefore, using the Exclude Area tool in ArcGIS, glint areas were removed from the images.

5.2.2.3.2 Methods

To produce the best empirical depth formula, multiple models were produced and assessed using the Pearson correlation coefficient to identify the relationship strength between the depth data and band variables. To ensure that the best method was chosen, the data collected were divided into two sets: i) data set consisting of approximately two-thirds of all bathymetric data that would be utilized to produce the empirical formula to calculate the water depth, and ii) the remaining one-third of the depth data to evaluate the empirical formula's performance.

Pre-flood: Mosaicked vs. single images

As found by others (e.g. Williams et al., 2011), manually mosaicking the images in ArcGIS proved unsuccessful due to obvious illumination differences between overlapping images. Previously using PhotoScan to create and export orthophotos revealed PhotoScan's ability to produce high quality mosaicked images with smooth transition between large set of overlapping images. Using PhotoScan's Export Orthophoto, the user has four options, or *modes*, to control how the pixels are utilized when mosaicking the images: Mosaic, Average, Maximum, and Minimum. Testing each of these modes, the average mode produced a mosaicked image with seamless transitions between overlapping images and pixel brightness. Therefore, PhotoScan was utilized to produce three mosaicked image sets using: all photographs, the north-facing images, and the south-facing images.

The next step was to import the orthophotos into ArcGIS. Since these were created and transformed in PhotoScan using the same coordinate system (Lindis Peak Circuit 2000), all three mosaicked image sets were pre-georeferenced. With ArcGIS having the georeferenced river images and geo-located bathymetric points, it was then possible to extract and tabulate the RGB image band values to the corresponding depth measurement. This table was then imported into Microsoft Excel where two-thirds of the data were used to calculate the Pearson correlation coefficient for the various band values (Lyzenga algorithms and band ratios) and depth measurements.

The single images were assessed in the same manner as the mosaicked image sets. Since images facing both north and south were required to cover the entire full-reach channels, both north- and south-facing single images were evaluated. Prior to testing the relationship between the images' bands and depth, the single images were georeferenced in ArcGIS using the visible GCPs as well as additional identifiable natural features. This was completed using a total of 18 tie-points that were distributed throughout the image center and edges and transformed using the spline transformation option, which is a rubber-sheet-produced transformation. Once the single images were georeferenced, the RGB image band values were extracted and tabulated to the corresponding depth measurement. This data was then imported into Excel where two-thirds of the bathymetric data were utilized to calculate Pearson correlation for the various band values and depth measurements.

Lyzenga (1981) algorithms vs. band ratios

The first step in using the Lyzenga (1981) algorithms (shown in Section 2.2.4, and Equation 2.1) was to determine the value of the DN_{max} variable. This was accomplished by locating the deepest (reasonable) depth measurement and identifying the pixel's band values at that location. This resulted in a depth of 2.04 m, and the pixel values depended upon the image(s) being examined (e.g. south-facing had Red 26, Green 45, and Blue 45 for the 2.04 m deep area). Using Equation 2.1 and the DN_{max} for the image set of interest, the value of X_i was then evaluated with the corresponding depth. By comparing the X_i term against the depth, a relationship can be assessed. This was first assessed using the Pearson correlation coefficient for depth vs. red, green, and blue bands without Lyzenga algorithms, and again for the red, green, and blue bands using Lyzenga algorithms. Once the best Pearson correlation relationship was established, the corresponding data was plotted in Excel to compare the measured depth and band value. These data were fitted with a trendline and the resulting equation was then used with the withheld dataset (one-third) of the original depth data to evaluate the empirical formula's performance.

The band ratio approach was more simplistic. Simply dividing one or more band values by another, the resulting ratios were compared against corresponding depths. Again, the Pearson correlation method was first used to assess any relationship between the depth and image bands including green-over-red, blue-over-red, and blue-over-green band ratios as well as the natural log of the green-over-red, blue-over-red, and blue-over-green band ratios. Based on the Pearson correlation coefficient, the strongest relationships were then assessed further by plotting the measured depth against the band value in Excel. As with the Lyzenga method, once the best relationship was established, a trendline was fitted to the depth vs. X_i data in Excel. This trendline's equation was then used with the withheld data to evaluate the empirical formula's performance.

Similar to the pre-flood aerial photographs, the post-flood aerial photographs were captured during sunny conditions, thus producing considerable glint in the images facing north. As done for the SfM of this research, the pre-flood data was compiled, processed, and evaluated prior to the post-flood data, thereby providing insight into the future data processing. As proven for the pre-flood bathymetric mapping techniques, and discussed below in the results

section, the aerial photographs that were separated into north- and south-facing datasets outperformed the mosaics that combined all photographs. Further, based on the results of the pre-flood data, the south-facing data set produced improved results, which was likely due to the reduced glint. Due to the increased number of aerial photographs covering the full-reach of the river (224 pre-flood vs. 281 post-flood), both the south- and north-facing image set completely covered the entire full-reach river channels; therefore, both were not required to provide full coverage. Even though the pre- and post-flood aerial photographs were both taken in sunny conditions at midday, the seasonal difference in the sun's position was noticeable in image glint, with significant glint increase in the post-flood's north-facing image set. Therefore, due to the severe glint of the post-flood north-facing photographs and based on the performance of the pre-flood's south-facing image set, only the south-facing image set was utilized for the post-flood model.

The south-facing image set was again split into the groups of mosaicked and single images and were generated using the same technique as outlined in the pre-flood methods (e.g. PhotoScan generated mosaicked images, and single images georeferenced in ArcGIS). Once the images sets were imported into ArcGIS and properly georeferenced, the RGB bands were extracted to the corresponding depth measurement. These tables were then imported into Excel, where Pearson correlation relationships were evaluated for the various band and depth relationships. With the best relationships identified, the empirical formula was developed using two-thirds of the data set, and evaluated using the withheld one-third data set.

5.2.2.3.3 Results and discussion

Using Pearson's correlation approach, the values of the RGB bands were compared to the corresponding depth and the results for the pre-flood data can be found in Table 5.14. Comparing the results of the mosaicked and single photograph sets show that the mosaicked images typically produce stronger Pearson correlation coefficients; however, the separated image sets improved in every band tested by separating the photographs into south- and north-facing, as opposed to grouping all photographs together into one mosaic. Comparing the south- and north-facing photographs of the mosaicked and single images, the mosaicked image set frequently outperformed the single images and produced the stronger Pearson correlation. Comparing the individual red, green, blue bands, Lyzenga bands, and band ratios,

the band ratios and logarithmic band ratios have the highest Pearson correlation relationships, with the green-over-red ratios having the best relationship. The Lyzenga and individual bands have mixed results, with the red band always having the best Pearson correlation relationship. Based on the results of Table 5.14, the green-over-red ratio and the natural log of the green-over-red ratio have the best results. However, light attenuation is an exponential relationship to water depth (Legleiter et al., 2004), therefore, the natural log band ratio was the appropriate selection and follows the work of Legleiter et al. (2004). This method was applied to the mosaicked photographs for the south- and north-facing image sets resulting in separate bathymetric models.

The next step was to develop an empirical relationship between the depth and log green-over-red band for the separate north- and south-facing mosaicked image sets. These results are shown in Figures 5.9a and 5.10a. Using least squares regression, the model performance was assessed for the south- and north-facing data with the south-facing photographs giving an R^2 of 0.77 and the north-facing photographs giving an R^2 of 0.70. While these results indicate mediocre relationships, they compare well to previous bathymetric studies (Table 2.1). Therefore, these results provided a relatively adequate trendline fit with the linear empirical equations developed. Using the withheld data, the empirical model was evaluated and results are shown in Figures 5.9b and 5.10b, with R^2 of 0.76 and R^2 of 0.71 for the south-facing and north-facing model evaluation, respectively. As expected, these results compare well with the empirical results of Figures 5.9a and 5.10a.

Table 5.14: Pearson correlations coefficients for the measured depth and corresponding color band for the pre-flood data.

	Red	Green	Blue	Lyzenga Red	Lyzenga Green	Lyzenga Blue	G/R	B/R	G/B	ln (G/R)	ln (B/R)	ln (B/G)
Mosaicked photographs												
All photos	0.24	0.04	0.04	0.22	0.00	0.02	0.61	0.60	0.29	0.61	0.61	0.31
South facing	0.71	0.38	0.26	0.80	0.38	0.25	0.89	0.86	0.38	0.88	0.84	0.38
North facing	0.29	0.09	0.19	0.33	0.07	0.03	0.83	0.79	0.38	0.83	0.78	0.39
Single photographs												
South facing	0.64	0.35	0.36	0.73	0.28	0.31	0.77	0.64	0.10	0.76	0.68	0.12
North facing	0.22	0.01	0.12	0.25	0.02	0.12	0.55	0.40	0.22	0.56	0.48	0.26

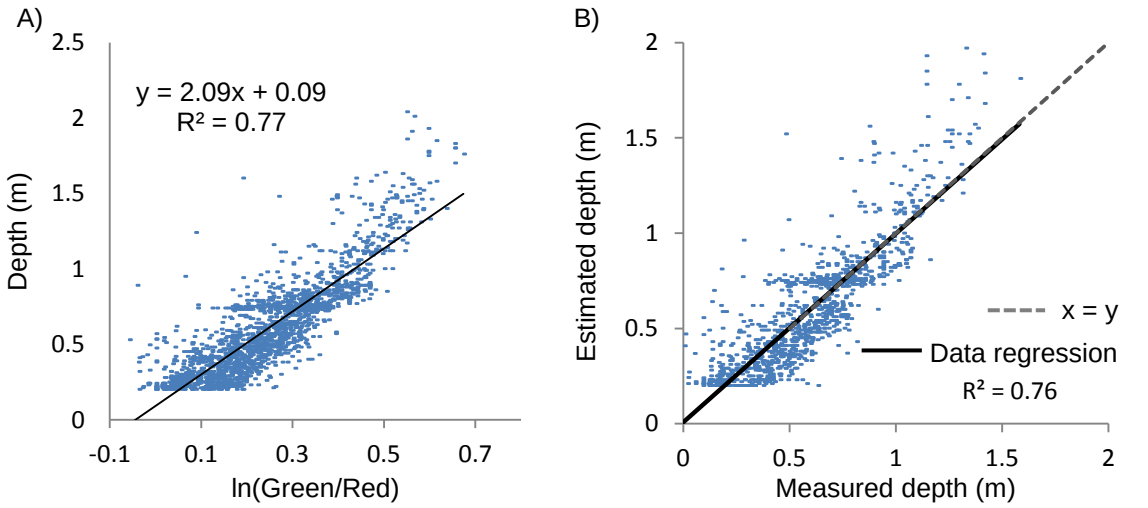

Figure 5.9: Optical-empirical bathymetric model for the pre-flood south-facing mosaicked photographs: A) empirical relationship development, and B) empirical relationship evaluation.

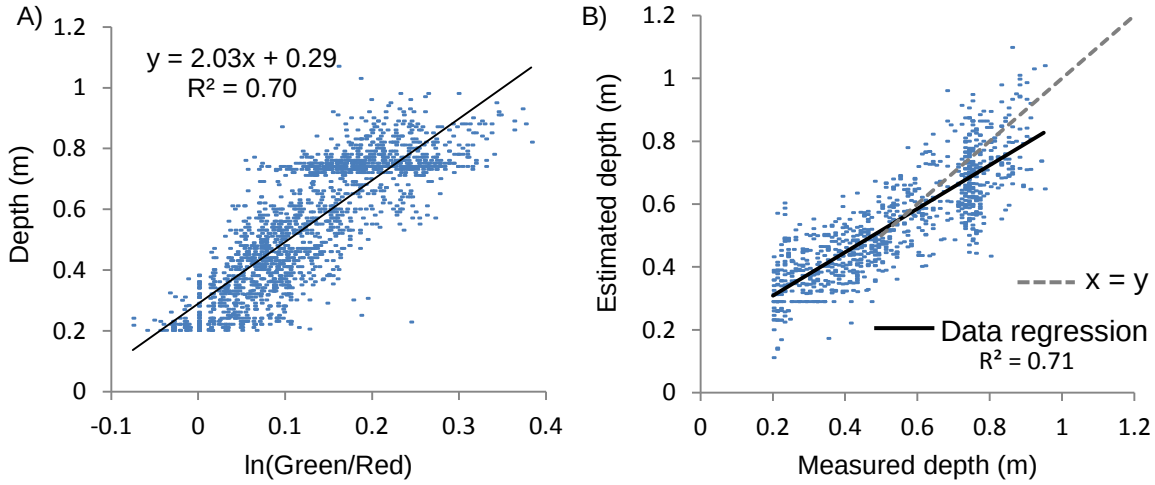

Figure 5.10: Optical-empirical bathymetric model for the pre-flood north-facing mosaicked photographs: A) empirical relationship development, and B) empirical relationship evaluation.

Finally, the empirical depth estimate was compared to the corresponding measured depth, and statistics of the residual errors are shown in Table 5.15. The south- and north-facing datasets have comparable residual errors. With mean errors near zero, and RMSE in the decimeter range, these residual errors were within the performance of the SfM residual errors. However, these errors are just the modeled depth, and are not final elevation errors.

Table 5.15: Pre-flood bathymetric mapping residual errors.

	n	ME (m)	RMSE (m)	MAE (m)	SDE (m)
South-facing	1,397	0.00	0.14	0.10	0.14
North-facing	934	0.01	0.12	0.09	0.12

The post-flood bathymetric data was developed in the same manner as the pre-flood data and the Pearson correlation coefficients of the various methods are presented in Table 5.16. As shown, the results were similar to the pre-flood results of Table 5.16, with the green-over-red band ratio and log green-over-red band ratio and mosaicked photograph image set outperforming the rest. Therefore, the log green-over-red band ratio was utilized to develop the empirical formula for the post-flood data in order to maintain consistency with the pre-flood data and is shown in Figure 5.11a. With an R^2 of 0.59, the post-flood empirical relationship was weaker than the pre-flood relationship. This was likely due to the increased sun glint caused by the seasonal difference in sun position. Nevertheless, even with lower least squares regression values, adequate depth modeling can be performed, as illustrated by Williams et al. (2011), who obtained an R^2 of 0.52 but still obtained a residual mean error of -0.01 m, a standard deviation error of 0.09 m, and a RMSE of 0.10 m, which were of the same order of magnitude as the project's TLS RMSE of Williams et al. (2011). Therefore, this data was considered sufficient to produce the depth model and was evaluated using the withheld one-third data set as shown in Figure 5.11b. As shown in Table 5.17, the residual errors of the post-flood depth model produced mean errors of 0.0 m and RMSE and standard deviation values in the decimeter range, which was comparable to the pre-flood results of Table 5.15. While these results compare well to previous studies (e.g. Table 2.1), typical errors in the decimeter range were relatively large considering that the study-reach's water depth rarely exceeds 1.5 m.

Table 5.16: Pearson correlations coefficients for the measured depth and corresponding color band for the post-flood data.

	Red	Green	Blue	Lyzenga Red	Lyzenga Green	Lyzenga Blue	G/R	B/R	G/B	ln (G/R)	ln (B/R)	ln (B/G)
Mosaicked photographs												
South facing	0.47	0.32	0.24	0.46	0.21	0.03	0.77	0.70	0.48	0.77	0.70	0.48
Single photographs												
South facing	0.33	0.13	0.05	0.34	0.12	0.40	0.63	0.49	0.22	0.63	0.50	0.22

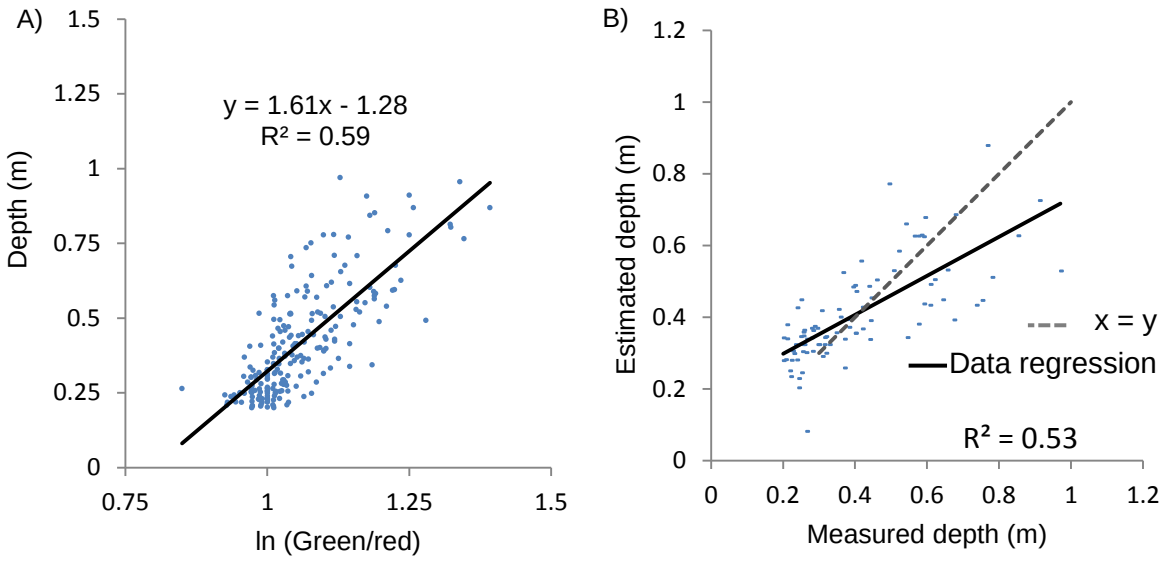

Figure 5.11: Optical-empirical bathymetric model for the post-flood south-facing mosaicked photographs: A) empirical relationship development, and B) empirical relationship evaluation.

Table 5.17: Post-flood empirical formula accuracy.

	n	ME (m)	RMSE (m)	MAE (m)	SDE (m)
South-facing	89	0.00	0.12	0.09	0.13

5.2.2.4 Model Generation

5.2.2.4.1 Introduction

In this section, a method using the SfM-Veg point cloud is presented in which the water surface elevation was modeled for the full-reach. With this water surface elevation model in place, the empirical formulas that were developed in Section 5.2.2.3 were utilized to create the final river channel bathymetric map. The quality of these data were then assessed using the water surface elevation and river bed elevation recorded during the echo-sounding and manual RTK-GPS bathymetric measurements.

5.2.2.4.2 Methods

Estimates of the water surface elevation were obtained by using the method of Williams et al. (2011) and Brasington et al. (2003) and is partially illustrated in Figure 5.12. This method

utilized point cloud datasets for the dry areas closest to the water edge, and interpolated a surface across the river channel. This was accomplished through multiple steps in ArcGIS. The first step was to map the inundated river channels of the full-reach as close to the river banks as possible. This polygon was produced for both the pre- and post-flood data and was utilized with the Clip Tool to cut the mosaicked image of the full-reach to just the river channels. This was done for the pre-flood data for the south- and north-facing mosaics, and for the post-flood south-facing mosaic, which produced three rasters at the original 0.5 m resolution.

The second step was to extend this river polygon to include the river banks. This was accomplished by using the Buffer Tool which extended the polygon by 1 m. This buffered polygon was utilized to clip the SfM-Veg point cloud to just the river margin points (Figure 5.12b). Following this, the river margin points were again clipped with the original river polygon to exclude any point cloud points within the inundated area, thus leaving only a 1 m point cloud strip along the river banks. This narrow strip was desired for three reasons. First, only a small section of point cloud was needed nearest to the river to ensure that the water surface TIN was only utilizing the points nearest to the river's edge. Secondly, this smaller dataset would allow for easier observational quality assessment, and potentially less manual editing. Finally, the SfM point cloud within the inundated river channel was excluded due to the significant noise that it produced. While it was hoped that SfM could model the water surface like any other visible surface, drastic elevation spikes occurred in most inundated areas. This was likely due to the water movement, glint, reflection, and refraction; thus the various images of a particular area have varying features, illumination, and texture, which likely caused the discrepancies in the SfM process.

Once the 1 m river channel margins were isolated, a Delaunay constrained TIN was produced to interpolate a water surface across the channels (Figure 5.12 C). This was then clipped to the inundated areas using the original river polygon. Using visual observations, the first TIN produced had an adequate surface connecting the opposite banks in area of straight channels; however, in river bends, noticeable slopes were created between opposing banks. This was due to the river bends producing high banks on the outside of the bend, referred to here as natural levees, and the inner banks having gradual slopes from the water surface elevation to

the floodplain, referred to as point bars. To improve the water surface in these locations, minor point cloud editing was performed on levee areas. This was done manually, and was prone to inaccuracies; however, two methods were developed to produce the adequate elevation editing. First, the aerial photographs and point clouds were assessed to determine the point where the levee elevation spiked. This was used to identify the last point that accurately represented the elevation for the upstream and downstream end of the levee. Using these two points, the slope between the inaccurate levee section was calculated. Secondly, since this slope could not always be fully representative of the water surface elevation, the elevation that was directly across the river (perpendicular to flow) was also considered. Since this was done manually, it took considerable time to edit these points; therefore, to improve this process, the point clouds were reduced to 2 m resolution within the inaccurate levee sections.

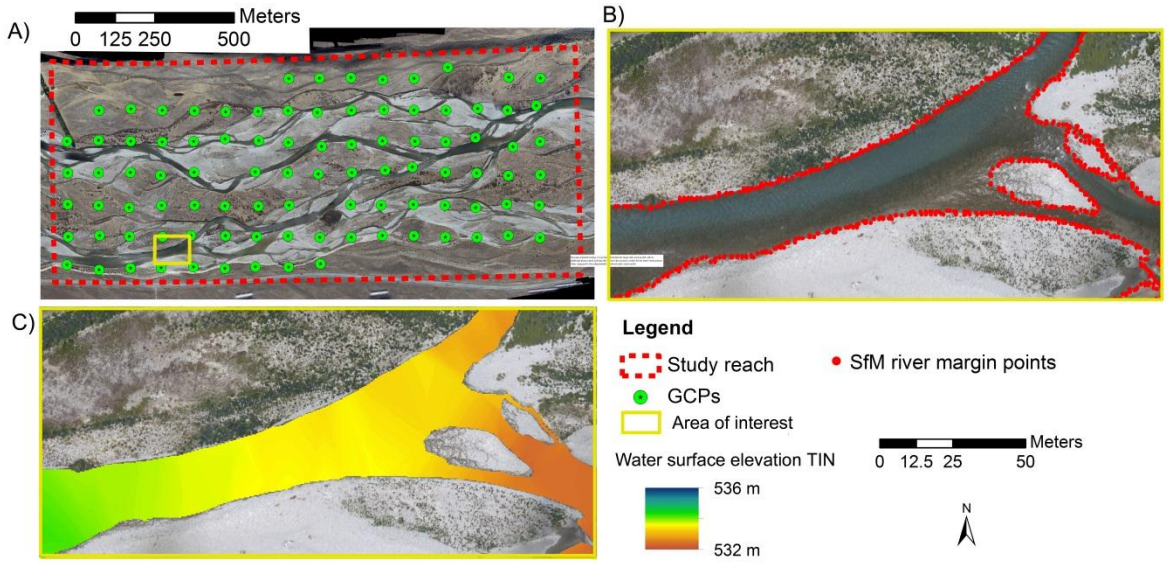

Figure 5.12: Water surface elevation model: A) study-reach with area of interest highlighted, B) SfM point cloud cropped to river margins, and C) water surface elevation model TIN.

Once this was done for the pre-flood and the post-flood full-reaches, the water surface was re-interpolated using a TIN. As previously mentioned, the echo-sounder and RTK-GPS depth measurements also recorded the water surface elevation. Therefore, this data was utilized to test the accuracy of the modeled surface against the surveyed surface. Since the water surface elevation extracted from the SfM-Veg point clouds, the full-reach can be assessed without south- and north-facing divisions.

Once the final water surface elevation TIN was created, it was developed into a raster and clipped to the inundated areas using the river polygon. This final water surface raster was then discretized at 0.5 m providing a point cloud for the bathymetry. This 0.5 m resolution was chosen to match that of the SfM-Veg point cloud resolution. Once these points were discretized, the x- and y- coordinates and RGB band values from the spatially corresponding mosaicked image sets were extracted and appended. Finally, using the ArcGIS field calculator, the empirical formulas were utilized to calculate the spatial depths, which were subtracted from the water surface elevation value; thus providing the channel bathymetric model. To assess the accuracy of this model, the measured river bed elevation was compared to the model for the full-reach data.

5.2.2.4.3 Results and discussion

The water surface elevation for the pre-flood data was assessed for both the first raster that had no levee editing, and again after the final levee modifications. The residual errors are presented in Table 5.18. As with the SfM surface assessment, these residual errors are produced by taking the difference between the modeled surface and the measured surface; thus positive errors indicate that the model was higher than the survey. As shown, the levee editing significantly improved the water surface elevation, with the mean error much closer to zero and the standard deviation reduced by nearly 45%. Since the final river channel bathymetry model combined the water surface model and the empirical depth calculations, minimizing the errors in both models was paramount as the combined models naturally combined errors. To further investigate the errors of the water surface models, the SfM-Veg point cloud residual errors are re-examined. Since the water surface was developed from the SfM-Veg point clouds, the water surface residual errors should be comparable. Further, with most of the river edges free of vegetation and since most of the bathymetry data was acquired in the study-reach, the study-reach's bare-ground ground-truth residual errors should be compared to the water surface errors. Re-examining the pre-flood data (Table 5.12) shows that the residual errors are comparable, with the water elevation having a slightly improved mean error and a slightly worse standard deviation. This error similarity suggests that the combined echo-sounder and RTK-GPS uncertainty was near that of the SfM. However, unlike the RTK-GPS measurements on land, the RTK-GPS mounted on the boat was subject to more sources of error. The greatest of these errors may be that the RTK-GPS water surface elevation was calibrated while the boat was floating in a stationary pool, yet the

measurements recorded were in fast currents with standing waves. Additionally, the elevation calibration did not consider the effects of the guide ropes. With the guide ropes controlling the dinghy from the bow, and the GPS mounted on the stern, the guide ropes likely affect the attitude of the boat; especially since the ropes were regularly managed from atop the river banks, thus raising the bow and lowering the stern and likely causing the GPS to sit lower in the water. Nevertheless, the errors produced were well within the SfM errors; therefore, these and other sources of errors were assumed minimal.

Table 5.18: Pre- and post-flood water surface elevation assessment.

	n	ME (m)	RMSE (m)	MAE (m)	SDE (m)
Pre-flood					
No editing	7,015	0.17	0.30	0.24	0.24
Edited levees	7,015	-0.03	0.14	0.11	0.13
Post-flood					
Edited levees	474	-0.10	0.14	0.12	0.10

Based on these pre-flood levee editing results, the levee editing was performed for the post-flood data set and the result are shown in Table 5.18. However, the results for the post-flood were not as accurate as the pre-flood residual errors. While the RMSE, mean absolute error, and standard deviation were comparable, the mean error at -0.10 m was considerably less accurate and suggests a negative bias. This was surprising given the pre-flood and post-flood SfM accuracies were comparable. Re-examining the SfM post-flood data (Table 5.13) shows comparable results to the water surface elevation; however, the water surface mean has become more negative and the remaining residuals are slightly higher. Again, these results show a similar range to the SfM errors, and were considered adequate for further bathymetric mapping.

While the SfM point cloud water surface interpolation provided an effective method to model the water surface of large areas, it was prone to inaccuracies. First, the accuracy of the water surface model was dependent on the SfM accuracy; thus the errors are combined to produce a less accurate final product. Secondly, the interpolated surface was flat across the river

channel; however, significant areas of this river reach have standing waves and turbulence, creating discrepancies between the surveyed data and the model.

The overall performance of the optical-empirical bathymetric mapping method was evaluated by comparing the modeled river bed elevation and the measured elevation. Taking the residual errors of the model and survey, Table 5.19 provided an accuracy assessment. As shown in Table 5.19, the pre-flood bathymetric model had a slight negative mean error and standard deviation in the 20-30 cm range. The post-flood river bed elevation assessment shows a greater negative mean error, and again has a standard deviation in the 20-30 cm range. These results were comparable to the SfM-Veg bare areas of the extended-reach. As expected, the combined errors of the empirical water depth calculations (Tables 5.15 and 5.17) and the water surface elevation (Table 5.18) produced increased errors for the river bed elevation model. While these results were higher than the study-reach SfM-Veg point cloud residual errors, they were still comparable and together produced an adequate DEM.

Table 5.19: Pre- and post-flood river bed elevation accuracy.

	n	ME (m)	RMSE (m)	MAE (m)	SDE (m)
Pre-flood					
	6,567	-0.02	0.28	0.22	0.27
Post-flood					
	300	-0.07	0.27	0.22	0.26

5.2.3 Final digital elevation model generation and digital elevation model of difference

5.2.3.1 Introduction

This section presents the workflow of the SfM and bathymetric mapping that produce the final pre- and post-flood DEMs. Using the final DEMs, the geomorphic adjustment that occurred during the October 2011 flood event was determined using the Geomorphic Change Detection Software.

5.2.3.2 Final digital elevation model

5.2.3.2.1 Introduction

The production of the final DEMs involved combining the separate SfM and bathymetric point clouds into a seamless elevation model. While this was a relatively simple task, the final DEMs offered a final quality check. Therefore, this task was not taken lightly, as it was paramount that these elevation models accurately represented the actual terrain to obtain the best numerical simulations. Only full-reach models were produced for two reasons: i) the full-reach SfM model produced more accurate study-reach model residual errors than the study-reach model, and ii) producing the complete full-reach would provide for a seamless transition between the extended and study-reaches, thus better elevation models for the numerical model simulations.

5.2.3.2.2 Methods

The final pre- and post-flood digital elevation models were produced using a workflow that combined PhotoScan's SfM-DMVR generated terrain surface for dry areas, the geospatial Topographic Point Cloud Analysis Toolkit (ToPCAT) to reduce the point cloud resolution to i) improve data handling, and ii) to reduce vegetation-related topographical noise, and finally optical-empirical bathymetric mapping to model the inundated terrain. Once these components were finalized, the dry and wet point clouds were fused into one point cloud and the surface was constructed using a Delaunay constrained TIN. The TIN was then converted into a raster of 0.5 m resolution (Figure 5.1). Finally, these rasters were clipped to the width of the active floodplain (bounded by the river's high terrace) and the 3.3 km length of the full-reach. The original DEMs were ready to be utilized in the hydrodynamic numerical model simulations of Delft3D; however, the rasters were also detrended for better vertical relief visualization. This was accomplished by creating an arbitrary planar surface with the approximate elevation and slope of the reach. Once this was created into a surface using a TIN and Raster, the raster calculator tool was used to create a new raster of elevation difference, thus taking the rasters elevation to an origin of zero.

5.2.3.2.3 Results and discussion

The final DEMs generated produced seamless transitions between the SfM and bathymetric mapping. Unlike the residual errors discussed in the SfM and bathymetry sections of this

chapter, the DEMs provided the opportunity to visually inspect the model's quality. Using the combined SfM and bathymetric point cloud, the final pre-flood full-reach DEM was generated and is presented in Figure 5.13a. As shown, the elevation decreased from the upstream end to the downstream end, with noticeable river braids. The detrended pre-flood DEM is presented in Figure 5.13b, which highlights the elevation differences between the river braids and terraces. Finally, the bathymetric mapping was laid over the black and white detrended DEM in Figure 5.13c. As shown, the river channel on the true right of the floodplain has deeper water depths, which was as expected since this was the main channel.

The pre-flood model of Figure 5.13a appears to transition well between the dry and wet areas, suggesting a successful data fusion. However, a close inspection revealed subtle anomalies in the detrended DEMs of Figures 5.13a and 5.13c (shown in Figure 5.13c). The first artifacts noticed were two elevation spikes (white circles), which were confirmed to be large vegetated areas (140 and 480 m^2) and were not detected nor removed by the ToPCAT vegetation reduction method. This was expected since ToPCAT vegetation smoothing has a resolution of 9 m^2 and would not detect such large areas.

Additional artifacts were identified by sudden illumination and/or color difference and are visible in the extended-reach section (outlined black and white boxes). Investigations using PhotoScan's 3D mesh revealed that these lines were sudden steps in elevation of approximately 1 m (black box) and 0.5 m (white box) relief. Photographs utilized in the SfM generation of these areas were of similar quality, resolution, and captured at 600 m; however, minimal overlapping photographs were available for these areas. The area identified in the white box was generated with three photographs (whereas most areas were generated with an average of 6 photographs). The area identified with the black box was generated with five photographs; however, image border alignment occurred for two of the photographs directly over the elevation step. Therefore, it appeared that the artifacts were produced by limited image data as well as the unfortunate chance of image border alignment. While these artifacts illustrate the limitations of ToPCAT vegetation removal and SfM-DMVR ability, these errors were infrequent and easily modified; therefore, the pre-flood DEM was deemed adequate for numerical modeling.

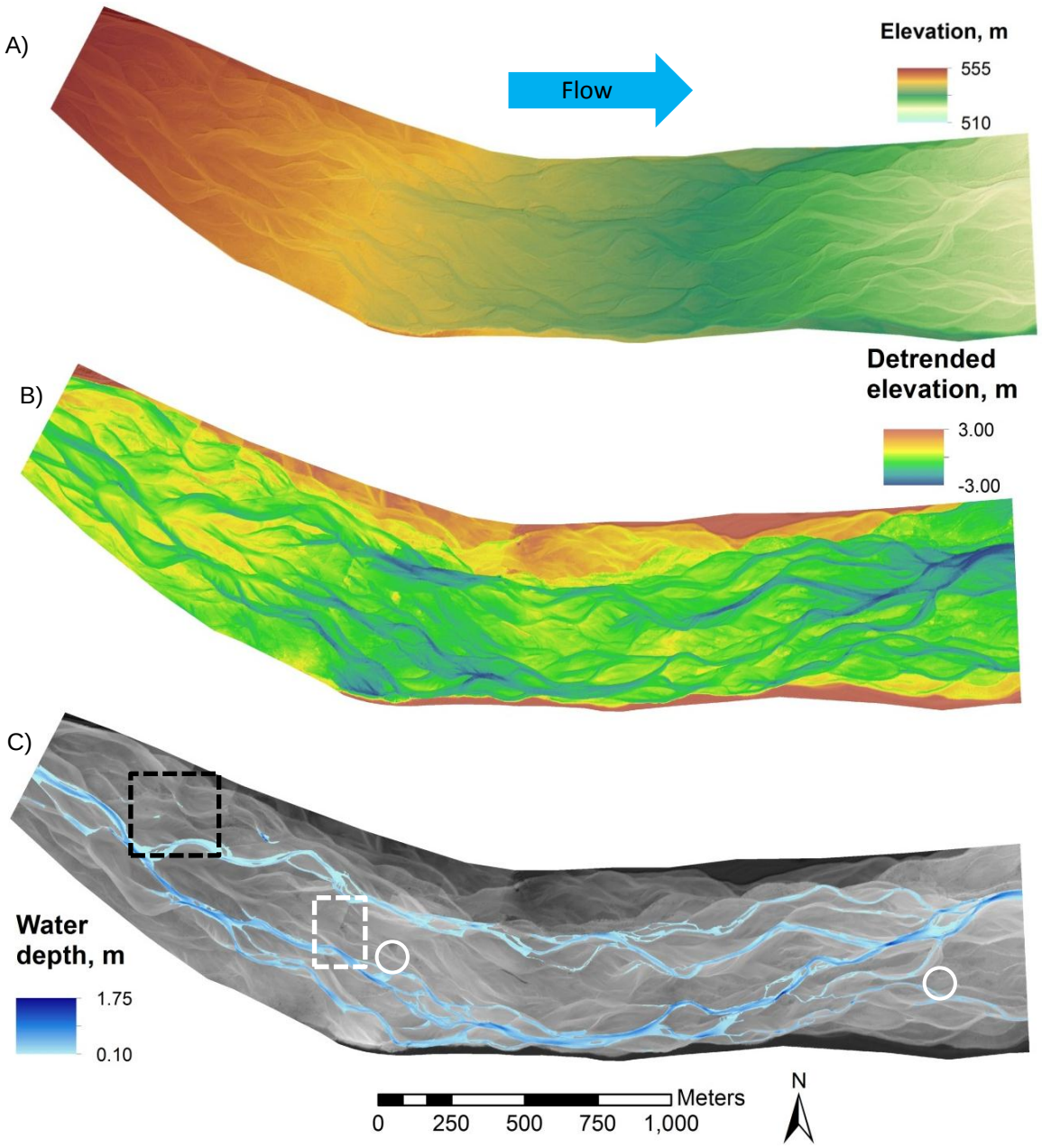

Figure 5.13: Final pre-flood DEMs: A) Original DEM, B) detrended DEM, C) mapped river depth with anomalies highlighted.

The post-flood full-reach DEM was produced using the same procedure as the pre-flood DEM and is presented in Figure 5.14a. As shown, the DEM produced smooth transitions between the SfM and bathymetric mapping division and shows a steady decrease in elevation from the upstream to the downstream section with river braids visible with the lower elevations. The detrended DEM is presented in Figure 5.14b, and the water depth is presented in Figure 5.14c. As shown in Figure 5.14c, the same artifacts are outlined that were present in the pre-flood DEM. This was due to the manual vegetation editing described in Section

5.2.1.6.2, where pre-flood topography was utilized in the post-flood DEM generation. Therefore, it was no surprise that the same artifacts were also transferred. Again, these errors were easily modified and the post-flood model provided an adequate DEM for numerical modeling.

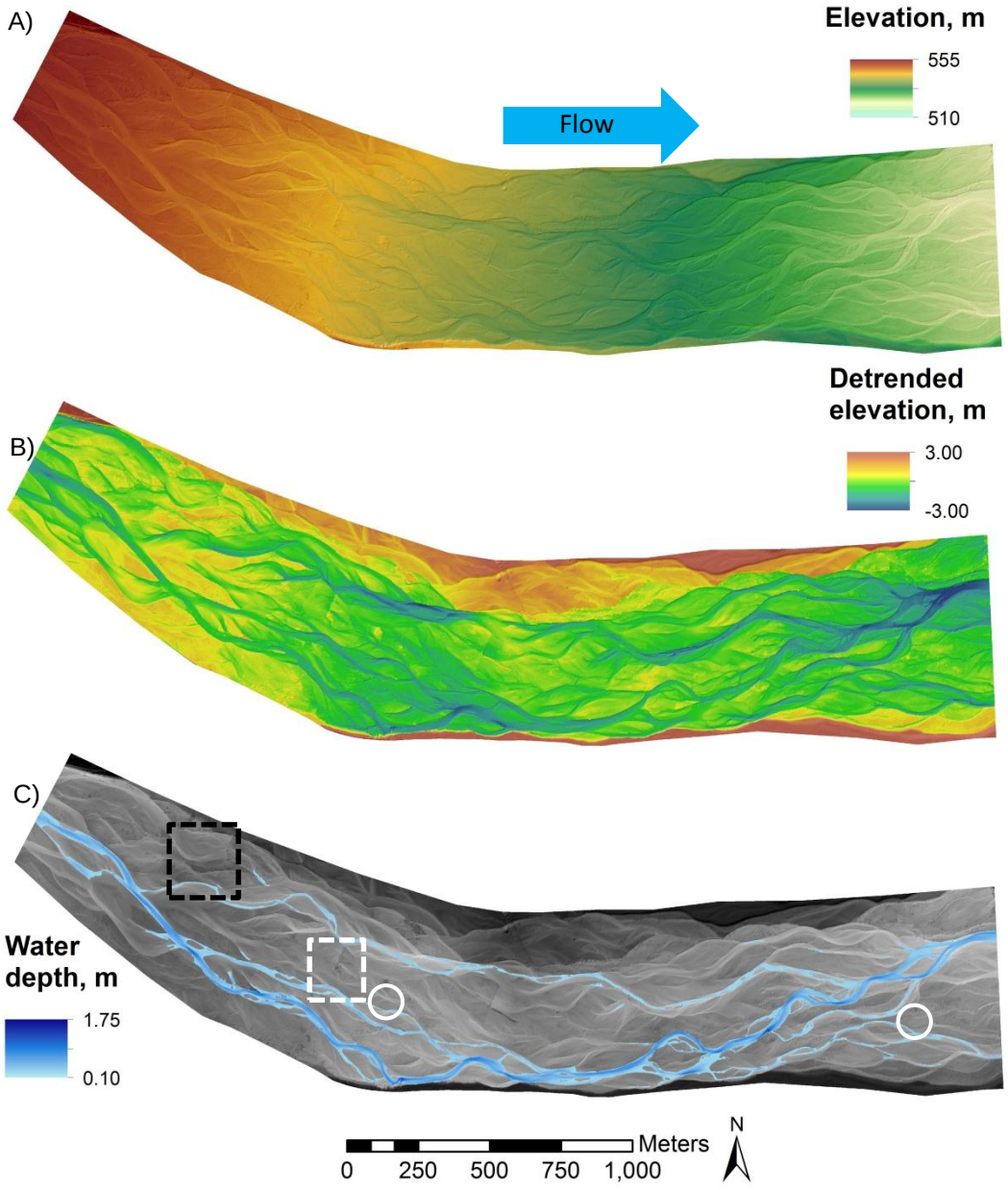

Figure 5.14: Final post-flood DEMs: A) original DEM, B) detrended DEM, C) mapped river depth.

5.2.3.3 Digital elevation model of difference

5.2.3.3.1 Introduction

While DEMs of Difference (DoDs) are widely used to determine sediment budgets from repeat topographic surveys, the DoD assessment for this thesis was conducted for two purposes: i) to identify the geomorphic adjustment that occurred during the October 2011 flood event, thus providing a calibration for the hydrodynamic numerical modeling morphology mode, and ii) to examine the flood impacts on the reach's vegetation and correlate the processes that may have occurred. This was accomplished by first identifying areas that had vegetation removed during the flood event; which was assessed using the pre- and post-flood aerial photographs. However, identifying the morphological adjustment that occurred provided insight into the processes that removed the vegetation. For example, if the vegetation was removed and deposition occurred in that location, then it was possible that deposition-induced mortality occurred. The DoD assessment in this research was produced using the Geomorphic Change Detection (GCD) software (version 5.0.24). GCD is a freely available plugin for ArcGIS that offers numerous advanced DoD assessments such as DEM uncertainty, probability confidence intervals, and Bayesian updating. Please refer to Section 2.2.5 for more information on DoDs and GCD.

5.2.3.3.2 Methods

To develop the DoD in GCD, the user must specify the two DEMs of interest and the uncertainty associated with the corresponding DEMs. This uncertainty was utilized to determine a threshold value at which geomorphic changes were considered real or noise. The most commonly used method to assess a DEM's uncertainty is to apply a uniform uncertainty value for the full DEM using the minimum level of detection (minLOD, discussed in Section 2.2.5, Equation 2.2). However, GCD offers a method of using spatially varying uncertainty. Since no method was without assumptions, and it was not clear which method produced the best and most reliable results, the uncertainty analysis methods evaluated were: i) spatially varying error propagation (SV), ii) spatially varying error propagation using a threshold of 95% confidence interval (SV 95%), and iii) spatially varying propagated errors with 95% confidence interval threshold and Bayesian updating (SV 95% BU). The spatially varying propagation methods were chosen over the uniform uncertainty based on the findings in Milan et al. (2010), and the 95% confidence interval was based on the methods of Wheaton et

al. (2010). Further, Bayesian updating was also considered due to its added ability to identify change significance by the probability of spatial geomorphic patterns (see Wheaton, 2008).

The spatially varying uncertainty raster for the pre- and post-flood DEMs was produced in ArcGIS. Using the previously calculated ground truth errors for the pre- and post-flood DEMs, an uncertainty raster was created for the corresponding DEMs. Unfortunately, while the ground truth data for the dry areas exceeded 10,000 well distributed points, the river channels were limited to the clusters of bathymetric data collection. Therefore, spatially varying uncertainty rasters could not be produced for the inundated areas; instead, the uncertainty averages of Table 5.19 were utilized to develop a uniform valued uncertainty raster of 0.22 m (taken from the average of the mean absolute errors). Therefore, the final uncertainty rasters for the pre- and post-flood DEMs were a hybrid of the spatially varying uncertainty for the dry areas and a uniform uncertainty for the inundated areas.

Since the DoD detects any elevation changes, and the SfM point cloud in vegetated areas is represented by elevation spikes, the DoD would calculate differences throughout the floodplain caused by geomorphic processes and vegetation growth or removal. Therefore, to accurately detect only the geomorphic changes, it was decided to only assess areas that were impacted by the flood event. This was done by isolating the first and second DEMs' wet areas and adding any area along the channels where water obviously, or possibly, flowed in the flood. By comparing the two sets of aerial photographs, it was possible to determine if the area was impacted by the flood based on natural objects' positions, such as sediment patterns. Once these areas were identified and isolated, they were combined into a single polygon and used to clip the DEMs and uncertainty rasters. Using these methods, DoDs were produced for both the full-reach and the study-reach. This study-reach and full-reach division was necessary because the DEM accuracy (and uncertainty) was of higher quality in the study-reach; thus providing higher quality DoD results; however, the full-reach DoD was also necessary to appreciate the overall geomorphic adjustment caused by the October flood event.

Using the three uncertainty methods discussed generated three DoDs (SV, SV 95%, and SV 95% BU), and produced varying results due to their change detection sensitivity. With no

clear indication which uncertainty method produced the best representation of the actual geomorphic change, an additional assessment was required. Therefore, a simple visual assessment was performed using the pre- and post-flood aerial photographs to identify noticeable geomorphic changes within the study-reach and to compare these changes with the varying DoD's detection. This assessment only considered the study-reach as it was the area of most concern, and provided the best accuracy as previously determined in the SfM and bathymetric sections.

5.2.3.3.3 Results and discussion

The DoD production heavily depends upon the errors and uncertainties associated with the DEMs. Therefore, insight into the expected results and accuracy of the GCD DoD can be gained by reviewing the results of the DEMs' errors reported in Tables 5.12 and 5.14. As shown, the study-reach and extended-reach bare-ground ground-truth errors for both the pre- and post-flood cases produced similar residual performance. Further, the river bed elevation errors (Table 5.19) also show the pre- and post-flood data having highly comparable results. These residual errors highlight the similarity produced by the SfM and optical-empirical bathymetric mapping techniques, as well as the consistency between the pre- and post-flood quality and accuracy. Therefore, due to the high quality and resolution of these individual DEMs, it is expected that GCD DoD should have the ability to detect geomorphic changes above 0.3 m.

Subtracting the post-flood DEM from the pre-flood DEM, the GCD DoD statistics and budget estimates for the SV, SV 95%, and SV 95% BU uncertainty analysis methods are shown below for the study-reach and full-reach in Tables 5.20 and 5.21, respectively. Examining the results, the SV 95% BU produced the highest total erosion and deposition values in both the areal and volumetric categories; however, it also produced the smallest volumetric net difference (-1,688 m^3) and the greatest uncertainty (±23,594 m^3). The SV 95% produced the lowest budget estimates and uncertainty, but also calculated the highest total volumetric net difference (-6,507 m^3 ±5,300 m^3) . In general, the GCD DoDs indicated that the study-reach degraded during the October 2011 flood event.

Interestingly, the full-reach budget estimates of Table 5.21 show that the full-reach experienced aggradation on average. Again, the SV 95% BU produced the highest total area and volumes of geomorphic change as well as uncertainty, and the SV 95% produced the most conservative estimates. In addition, the spatial geomorphic changes were presented for the study-reach and full-reach in Figures 5.15 and 5.16, respectively. Since the full-reach and study-reach data was produced by the same DEMs, the extended-reach budget estimates can be easily calculated by subtracting the study-reach data from the full-reach data. Therefore, the large amounts of aggradation are within the extended-reach, while the study-reach experienced an overall degradation. Since the DoD uncertainty considers the larger errors of the extended-reach, this aggradation may be realistic; however, this aggradation may be exaggerated since the geomorphic change detected includes the potential uncertainty. For example, in an area with a minLOD of 0.1 m, if the change detected was 0.15 m, then the 0.15 m was considered real. This has been a topic of debate (Wheaton, Brasington, Darby, & Sear, 2010) as to whether or not to include the minLOD value: should the change detected be 0.15 m or should it not include the minLOD value and be 0.05 m? Since GCD included the uncertainty in the detectable areas, this may cause some over- and under-exaggerated geomorphic changes. However, in this research it was assumed that the over- and under-exaggerations were relatively equal and eliminated the influence.

Table 5.20: GCD-calculated DoD for the first and second data set study-reach DEMs.

Attribute	Raw	Spatially varying	Spatially varying with 95% C.I.	Spatially varying with 95% C.I. and Bayesian updating
AREAL				
Total Area of Erosion (m^2)	137,065	50,938	24,128	79,022
Total Area of Deposition (m^2)	177,156	60,191	20,857	110,291
VOLUMETRIC				
Total Volume of Erosion (m^3)	30,319	23,461 (±8,591)	17,307 (±4,110)	25,512 (±18,695)
Total Volume of Deposition (m^3)	28,707	19,327 (±9,542)	10,801 (±3,346)	23,824 (±14,393)
Total Volume of Difference (m^3)	59,025	42,789 (±18,134)	28,108 (±7,457)	49,337 (±33,088)
Total Net Volume Difference (m^3)	-1,612	-4,134 (±12,840)	-6,507 (±5,300)	-1,688 (±23,594)
PERCENTAGES (BY VOLUME)				
Percent Erosion	51%	55%	62%	52%
Percent Deposition	49%	45%	38%	48%
Percent Imbalance (departure from equilibrium)	-1%	-5%	-12%	-2%

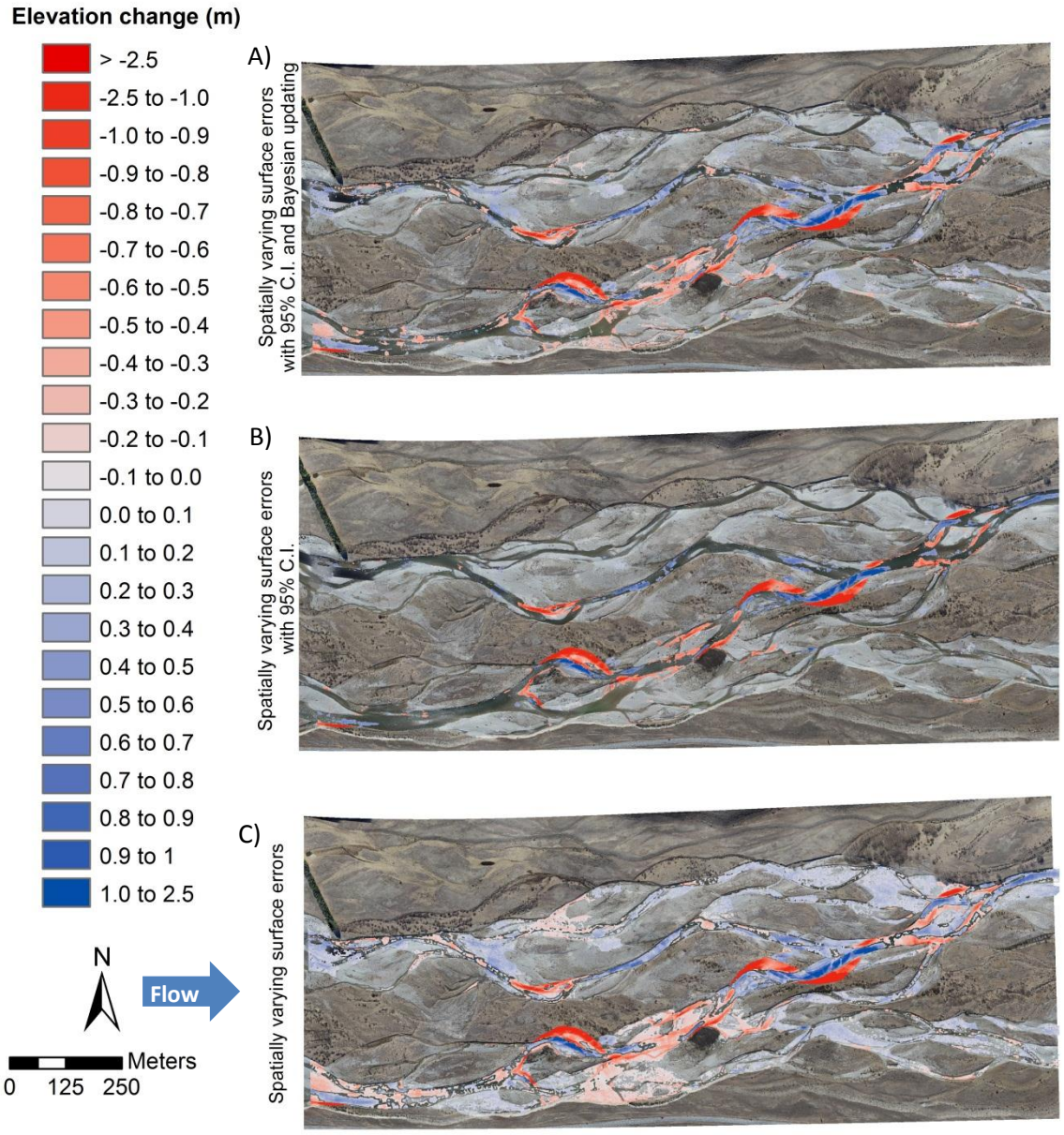

Figure 5.15: Comparison between the varying uncertainty methods for the study-reach DoD construction of: A) SV 95% BU, B) SV 95%, and C) SV.

Table 5.21: GCD-calculated DoD for the first and second data set full-reach DEMs.

Attribute	Raw	Spatially varying	Spatially varying with 95% C.I.	Spatially varying with 95% C.I. and Bayesian updating
AREAL				
Total Area of Erosion (m^2)	298,703	126,982	63,181	199,729
Total Area of Deposition (m^2)	441,974	223,729	96,530	332,412
VOLUMETRIC				
Total Volume of Erosion (m^3)	73,449	56,322 (±22,469)	40,068 (±10,852)	64,968 (±54,759)
Total Volume of Deposition (m^3)	121,810	96,927 (±45,889)	58,771 (±18,242)	112,261 (±62,237)
Total Volume of Difference (m^3)	195,259	153,249 (±68,358)	98,839 (±29,094)	177,228 (±116,996)
Total Net Volume Difference (m^3)	48,361	40,605 (±51,095)	18,703 (±21,226)	47,293 (±82,898)
PERCENTAGES (BY VOLUME)				
Percent Erosion	38%	37%	41%	37%
Percent Deposition	62%	63%	59%	63%
Percent Imbalance (departure from equilibrium)	12%	13%	9%	13%

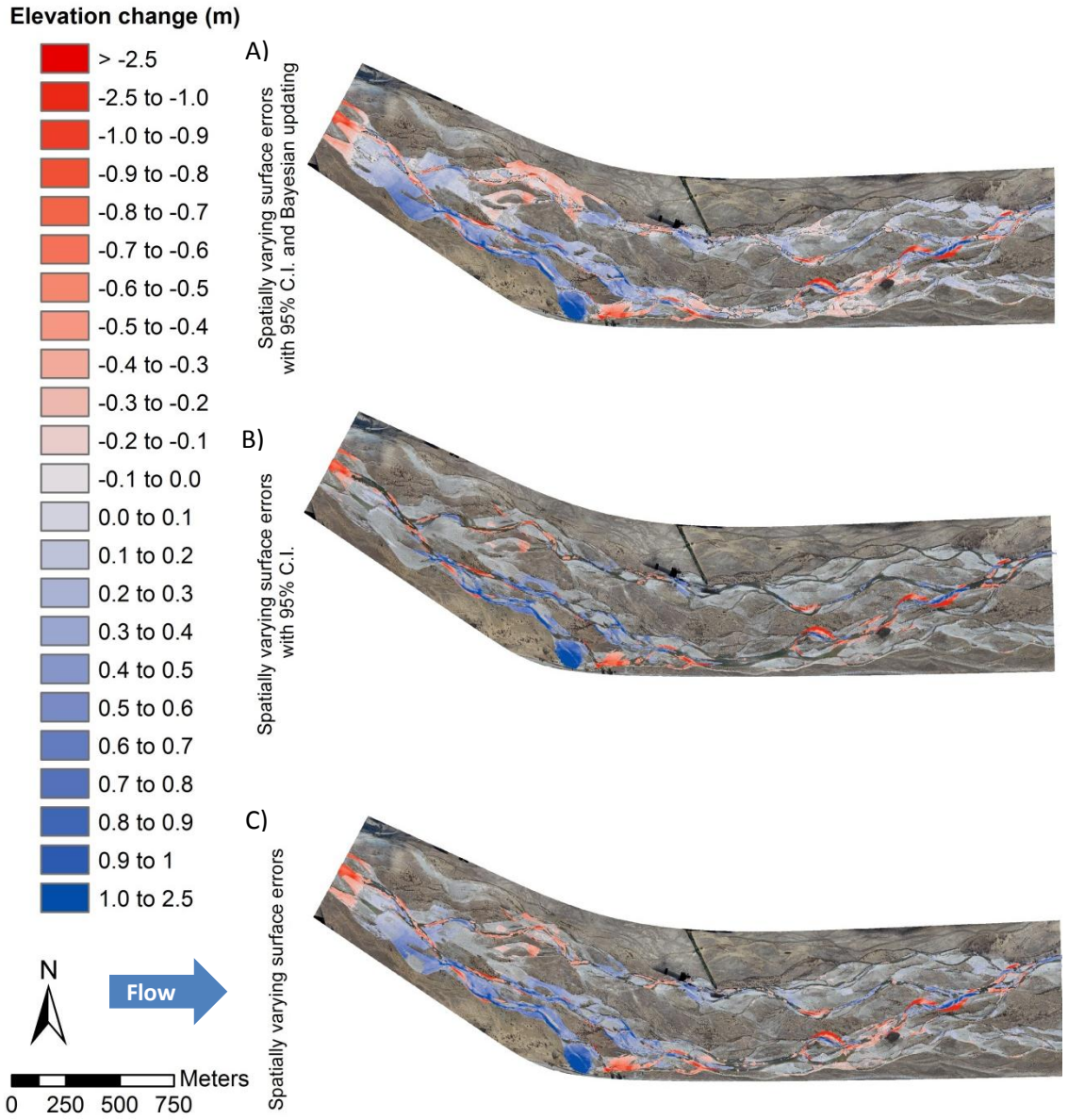

Figure 5.16: Comparison between the varying methods for the full-reach DoD construction of: A) SV 95% BU, B) SV 95%, and C) SV.

Numerous areas were found with noticeable geomorphic change between the pre- and post-flood aerial photographs, and were outlined in green polygons in ArcGIS (as shown in Figures 5.17 and 5.18). In an effort to determine which of the three methods provided the most representative results, specific areas were visually inspected using the aerial photographs and the GCD DoDs results. Of these observations, it was determined that the SV 95% was conservative and poorly represented the obvious adjustments; therefore, this method was removed from consideration. However, the SV and SV 95% BU compared well. Figures 5.17 and 5.18 demonstrate how this assessment was performed as well as show the two

observations that resulted in selection of the final uncertainty method utilized in this research. Additional comparisons are available in Appendix E.5.

As shown in Figure 5.17, the post-flood aerial photographs show a bar development. Comparing the three methods, the SV 95% only detected deposition in the downstream end of the bar, and no geomorphic change elsewhere. The SV 95% BU showed that deposition occurred on the upstream and downstream ends of the bar, but detected nothing in the center; however, the SV method detected that deposition occurred for nearly the entire bar length. Since this bar formation was within the main channel, and the post-flood survey had higher flow discharge (22 $m^3 s^{-1}$ compared to 13 $m^3 s^{-1}$) and due to a significant braid avulsion that routed greater flow through the main channel, it was reasonable to assume that this bar was actually created from the October flood event and not a result of altered flow levels. The same assumptions can be made for Figure 5.18, as this area was also within the main channel. As shown in Figure 5.18, multiple areas of geomorphic change occurred in this area; however, the horseshoe shaped erosion that occurred in the bottom right corner was of particular interest when comparing the uncertainty methods. Based on the results of uncertainty methods, only the SV method detects the erosion in this area. This was likely due to the SV 95% CI results being conservative. However, as shown in Tables 5.20 and 5.21, the SV 95% BU was the least conservative of the three methods and was expected to detect this erosion. This result illustrated a limitation of the Bayesian updating method. Since the Bayesian updating considers the neighboring cell's patterns for erosion and deposition, areas such as the horseshoe in Figure 5.18 were missed due to the deposition and erosion occurring in such close proximity. This drastic switch in geomorphic change likely caused the BU probability to consider the detected change as noise and not real change.

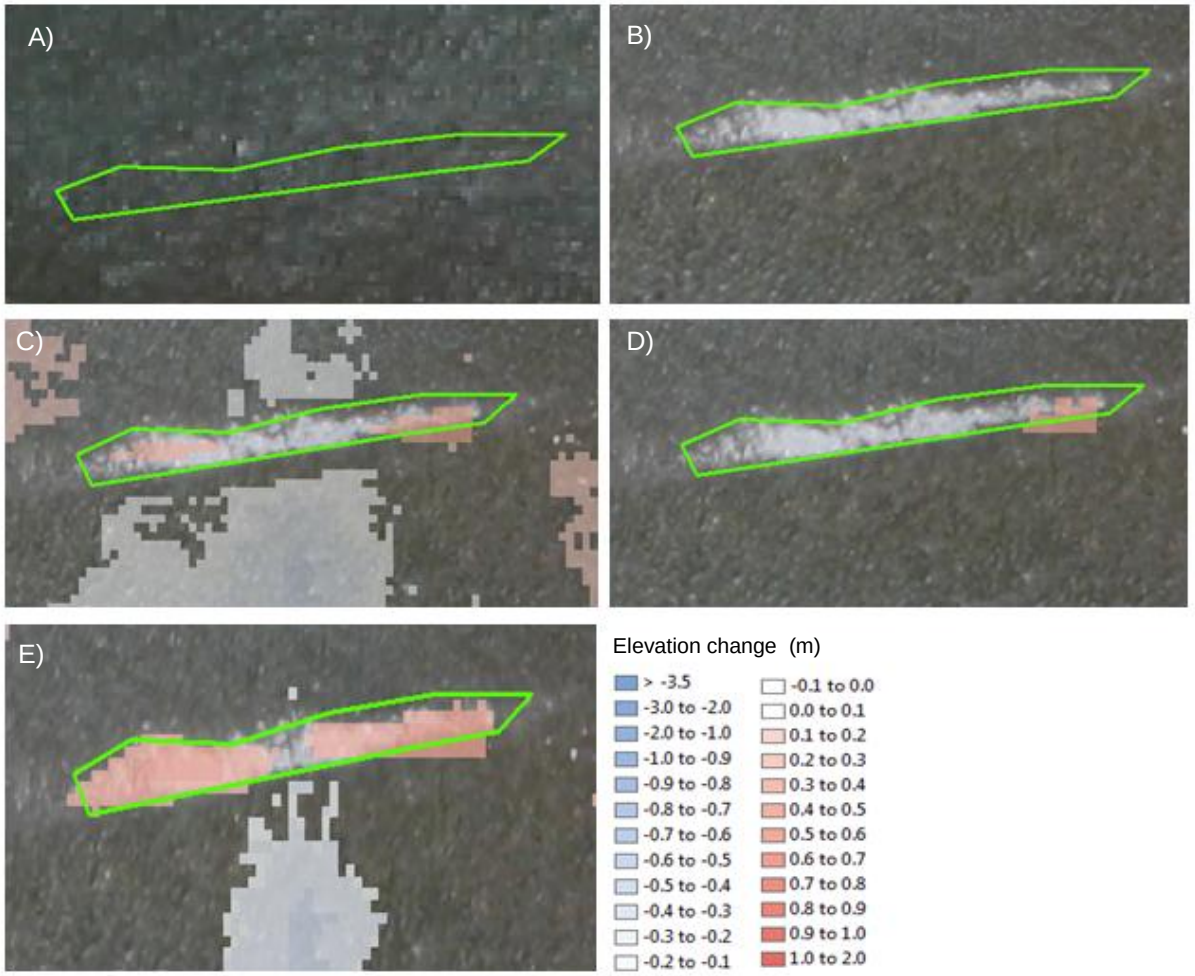

Figure 5.17: Visual comparison between the varying methods for the study-reach DoD. A) pre-flood image, B) post-flood image, C) SV 95% BU DoD results, D) SV 95% DoD results, and E) SV DoD results.

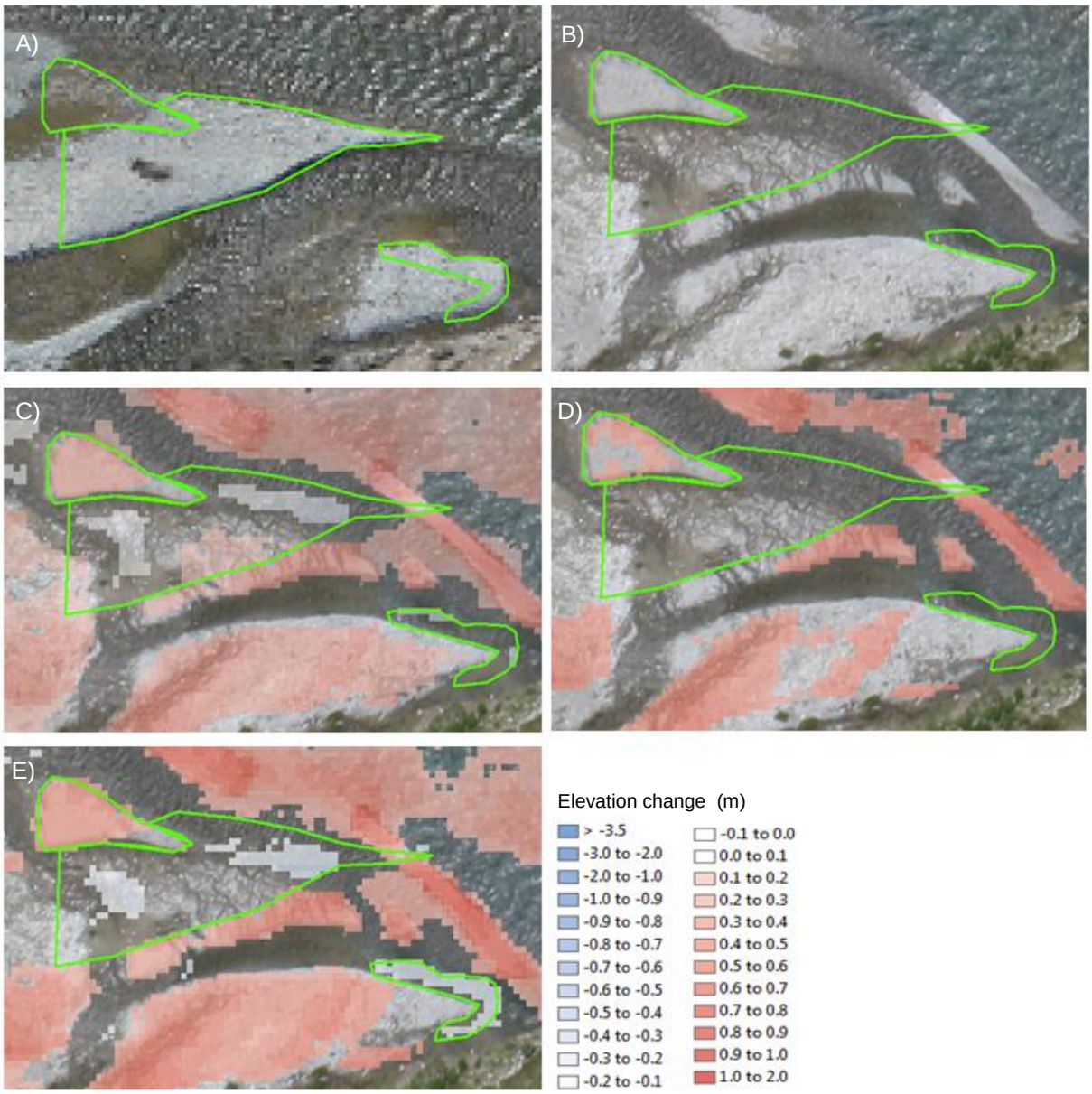

Figure 5.18: Visual comparison between the varying methods for the study-reach DoD. A) pre-flood image, B) post-flood image, C) SV 95% BU DoD results, D) SV 95% DoD results, and E) SV DoD results.

Based on these results and observations, the SV method was chosen as the best representation of observable geomorphic change. This decision was based on the visual performance of these methods presented in Figures 5.17 and 5.18 as well as in Appendix E.5. Further, based on the results of Tables 5.20 and 5.21, the SV method produces volumetric geomorphic changes and uncertainty between the SV 95% CI, and SV 95% CI w/ BU methods. Therefore, the SV method not only produced the best visual performance, but also was a median between the total detection of the two discarded methods.

5.3 Study site vegetation

5.3.1 Vegetation survey

5.3.1.1 Introduction

With the research focused on lupin mortality, it was necessary to understand the extent of lupins throughout the study-reach. To obtain the necessary data, two vegetation surveys were conducted during the pre- and post-flood surveys: i) a reach-wide survey that consisted of 95 observations taken near the GCP locations (refer to Section 5.2.1.2), and ii) a local survey of the sub-reach area that consisted of 12 transects.

5.3.1.2 Methods

The reach-wide survey was conducted for an area of 1 m^2 at 95 locations throughout the study-reach. The 95 locations were located near the GCPs which provided a well distributed survey at a 100 m grid. The pre- and post-flood reach-wide surveys were not recorded in the exact same location; instead, the pre-flood vegetation survey was taken 5 m upstream of the GCPs, and the post-flood survey was taken 5 m downstream of the GCPs. Each vegetation survey recorded the percent ground cover of the vegetation divided into the following categories: lupins, bare substrate, willows, unidentifiable vegetation (UV), grass, and bush (matagouri and sweet briar (also known as rosehip)). In addition to the vegetation recorded, the location's coordinates were surveyed using the Trimble RTK-GPS equipment.

Following the reach-wide vegetation survey, an extensive vegetation survey was conducted within the sub-reach. Through 12 transects, 397 vegetation survey points were recorded at approximately two-and-a-half meters spacing, using the same methods as the reach-wide survey to document the percent ground cover of the vegetation within 1 m^2 areas. This survey area totaled 4,140 m^2 and was chosen in the sub-reach as it provided moderate lupin infestation. As with the distributed vegetation survey, this survey was also recorded with the GPS coordinates. Initially, this sub-reach vegetation survey was taken in order to compare the amount of lupins present before and after a flood event; however, even though the flood event observed (October 26th) did not result in lupin removal, this survey and the reach-wide survey were beneficial in mapping and identifying the vegetation in the acquired aerial photographs, especially for areas of moderate lupin infestation.

Based on the results of Section 4.4.2 and 4.4.3, the forces required to uproot lupins have been related to root diameter, erosion levels, and flow velocity. Since the lupins root diameter was utilized in this research as the lupin's physical characteristic for removal, it was necessary to survey the study-reach's lupin root size distribution. Therefore, 217 lupins' root diameters were surveyed in late December, 2012 as well as their canopy height and relative location. The relative location was separated into four categories: i) flood zone in sparse vegetation, ii) flood zone in dense vegetation, iii) aggradation zone in sparse vegetation, and iv) aggradation zone in dense vegetation. Flood zone areas include areas of relief in relation to the river channels, which are likely to be affected by smaller and more frequent flood events. The aggradation zones are vegetated areas along natural levees and other areas of higher relief relative to the river channels, which are likely to be impacted by larger infrequent flood events. Further, it was decided to separate these areas by the vegetation density. Examining aerial photographs of the study-reach, areas of dense vegetation and sparse vegetation were easily identified; therefore, sparse and dense lupin data were separated for mapping purposes. With the data collected and entered into Excel, the root diameters were evaluated for the corresponding areas.

5.3.1.3 Results and discussion

The results of the vegetation surveys were split into two groups: i) to compare the vegetation total, and ii) to compare the ground cover which included substrate. These two surveys provided information on the total vegetation composition as well as the particular frequency of type and percent cover. As shown in the pre-flood data of Table 5.22, lupins were 25% of the vegetation identified in the study-reach, and 12.3% of the total ground cover. In the sub-reach, where lupin infestation was concentrated, lupins comprised 44.4% of total vegetation; however, their ground cover was only 11.2%. The post-flood data of Table 5.22 revealed similar results to the pre-flood data; however, the study-reach survey showed less lupin cover at 17.8% for total vegetation and 8.0% for ground cover. In contrast, the sub-reach showed a slight increase in lupin presence with 48.6% total vegetation and 18.8% ground cover. Finally, the ground cover results for both the pre- and post-flood surveys revealed that bare substrate was dominant.

These surveys provided local vegetation representation of the study- and sub-reaches and quantified the type and ground cover in which this invasive vegetation had spread. Using this data combined with aerial photographs enabled reach-wide vegetation mapping that was useful for both identifying the reach-wide vegetation removed during the flood event, and producing vegetation mapping for later use in the numerical model.

Table 5.22: Pre-and post-flood vegetation cover survey for the study-reach and sub-reach.

		Lupin (%)	Bare Substrate (%)	Willow (%)	U.V. (%)	Grass (%)	Bush (%)
Pre-flood							
Study-reach	Vegetation	25.0	N.A.	1.8	9.6	56.8	6.7
	Veg and Substrate	12.3	50.9	0.9	4.7	27.9	3.3
Sub-reach	Vegetation	44.4	N.A.	0.3	5.3	44.7	5.2
	Veg and Substrate	11.2	74.8	0.1	1.3	11.3	1.3
Post-flood							
Study-reach	Vegetation	17.8	N.A.	0.0	30.9	47.8	3.4
	Veg and Substrate	8.0	55.4	0.0	13.8	21.3	1.5
Sub-reach	Vegetation	48.6	N.A.	0.3	10.7	37.9	2.5
	Veg and Substrate	18.8	61.2	0.1	4.2	14.7	1.0

The lupin root diameter frequency distributions are presented in Figure 5.19. No clear relationships were visible; however, subtle relationships existed between the densely vegetated and sparsely vegetated areas, regardless of flood or aggradation zone. From Figure 5.19, it was apparent that the densely vegetated areas consist of larger root diameters than do the sparsely vegetated areas. Comparing the sparsely vegetated areas, the flood zone had a higher frequency for lupins with root diameters in the 1 to 4 cm range and a lower frequency with diameters from 13 to 16 cm. However, for root diameters between 4 and 13 cm, both the aggradation and flood zone frequencies were comparable. These trends show that the flood zone had more lupins of the smaller root diameter and less larger diameters than the aggradation zone; however, they have similar root diameters in the mid-root diameter range. Comparing the densely vegetated areas, the aggradation zone had less frequency of lupins ≤ 6 cm and greater frequency for lupins with 9 and 12 cm roots; which indicated that aggradation

zone has lupins with larger root diameters up to 12 cm, at which point the densely vegetated areas were comparable.

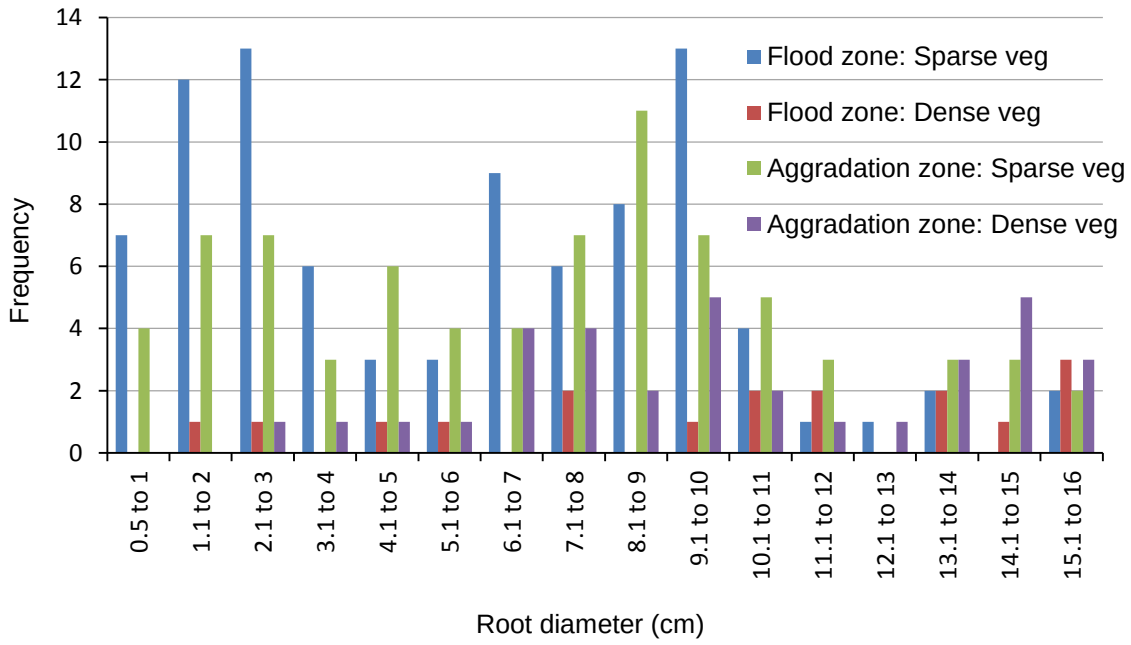

Figure 5.19: Lupin diameter and frequency histogram.

The results of the varying floodplain areas show that the densely vegetated areas have larger root diameters than the sparsely vegetated areas. These results were expected, as the densely vegetated areas were well established and should have older vegetation; thus larger root diameters. Evaluating the difference between the aggradation and flood zone areas shows that the flood zone areas contained higher frequency of smaller lupin root diameters ($\leq$ 6 cm). Again, these results were expected as the higher areas were more established and likely to have older vegetation. While subtle differences were detected between the overall lupin size compositions of the study-reach for the four areas sampled, the results of the sparsely vegetated areas and densely vegetated areas perform similarly; regardless of flood or aggradation zone. Therefore, this data was utilized to map the study-reaches vegetation, but was only separated into the two groups of sparse and dense vegetation patches.

5.3.2 Vegetation mapping

5.3.2.1 Introduction

Pre- and post-flood vegetation maps were valuable in three aspects of this research. First, combining the vegetation maps with the DoD it was possible to estimate the vegetation type that may have been removed and the corresponding morphologic process. Second, the post-flood vegetation distribution was utilized to evaluate the simulated flood events' impacts on the current vegetation. This was accomplished by comparing the DoDs of the simulated floodplain with the vegetation distribution of the post-flood map. Finally, the vegetation typical of the Ahuriri River was not only important for understanding the vegetation type and distribution, but also the influence upon the hydraulic conditions as discussed in Section 2.1.3. Since the Ahuriri River's floodplain contained moderate vegetation sprawl, it was critical that the vegetation was incorporated into the numerical model. In order to model a vegetation impact upon local hydraulics, vegetation information such as stem density, stem diameter, and vegetation height was required for the numerical model utilized in this research. Further information on the numerical model and representation of vegetation can be found in Sections 6.2 and 6.4.3.

5.3.2.2 Methods

Using aerial photographs of the study-reach and extended-reach and familiarity gained in field observations, the pre- and post-flood vegetation maps were created in ArcGIS. This was accomplished by knowing what vegetation was in certain areas, categorizing this vegetation, and then using the aerial photographs to identify and map the same image texture, color, and density. This was accomplished for nine vegetation categories: mature willow thicket, young willow thicket, juvenile willow patches, dense lupin patches, moderate lupin patches, sparse lupin patches, minimal herbaceous patches, pine trees, and bushes (comprised mostly of sweet briar, but contains some matagouri). It should be noted that all lupin patches contained other low-lying vegetation such as grass and other herbaceous vegetation (Table 5.22); however, lupins and lupin patches were easily identified in the aerial photographs. Once these lupin areas were mapped, considerable areas of low-lying herbaceous vegetation remained. These areas contain sparsely distributed grass and various low-lying groundcovers and were classified and mapped as minimal herbaceous patches. Since all areas were mapped by hand using visual inspection, the total areas generated were subjective. Therefore, there was no

method for determining the specific uncertainty created; however, great care was taken during vegetation identification and mapping to ensure high accuracy was achieved.

Once the areas were mapped in ArcGIS for the full-reach and study-reach, it was possible to calculate the surface area of the specific vegetation categories. This was done for the pre- and post-flood data of the study-reach only, as the vegetation area in the extended-reach was not of concern. However, the study-reach width extends beyond that of the active floodplain; thus included more vegetation than a flood event could impact. Therefore, the floodplain boundaries were established using field observations and assisted by the vertical relief of the corresponding DEMs. To set guidelines for consistency, the floodplain boundary was created along the outlying terraces and at a height $\geq$ 1.0 m above the highest river bar elevation of that specific transect (bank to bank, and perpendicular to flow). This boundary resulted in the high terrace on the true-right bank, and the gradual terrace along the true-left bank; thus this bound floodplain could contain a bank-full flood event of at least 1 m deep. The floodplain and study-reach perimeters are outlined in Figure 5.20 by a black border and red border, respectively.

With the various vegetation categories specified, mapped, and areas calculated, it was necessary to assess which vegetation would have the greatest impact on the hydraulics, as it was unrealistic to include and calibrate trachytopes for each of the nine vegetation categories. Naturally, lupins were the primary interest, and as shown in Section 4.4.3, lupins create significant drag due to their vegetated canopies and thus should have a significant impact on the flood hydraulics. The minimal herbaceous areas consisted of low-lying grass and groundcover with sparse density; therefore, these areas should not have a significant impact upon the flood hydraulics. While the bush areas were relatively common throughout the reach, most of the bush areas consist of sweet briar which have small stalks and lack a vegetated canopy, thus having a small impact on the hydraulics. Similar to the bush areas, the juvenile willow thickets were distributed throughout the reach, but at considerably less frequency than the bush vegetation. Similar to the bush, juvenile willows will have only their small trunk inundated in the majority of floods, and since such few areas exist with juvenile willow patches, these were eliminated from consideration. Finally, the pine trees, mature willow thicket, and young willow thickets exist in tight clusters, thus having a significant

impact on the hydraulics. However, the mature willow thicket and pine trees were located on river banks ≥ 1.3 m above the nearest braid elevation; therefore, these areas would not be inundated during most flood events. The young willow thicket was mostly confined to one area, and was likely to experience flooding, thus would certainly impact the local hydraulics. Based on this evaluation, the trachytopes to be utilized in the model were the three lupin patches and the young willow thicket. Therefore in December 2012, an additional vegetation survey was conducted throughout the study-reach that documented typical stem density, stem diameter, and vegetation height for these four vegetation categories. While the lupin stem density considered all stems of the plant, willow density only included the trunk. This was considered appropriate because only the trunk would impact flow conveyance during most flood events as the upper canopy would rarely be inundated. This provided the necessary trachytope data and was appended to the mapped and categorized vegetation.

5.3.2.3 Results and discussion

The study-reach pre- and post-flood vegetation maps are presented in Figures 5.20a and b, with the various vegetation categories color-coordinated and study-reach and floodplain area boundaries present. Using the pre- and post-flood vegetation maps, the surface area of the nine vegetation categories are presented in Table 5.23, as well as the area difference between the post- and pre-flood area. The vegetation survey data for the four trachytope categories are presented below in Table 5.24 with the corresponding average stem diameter, stem density, and average height. Finally, the four vegetation trachytopes are presented in Figure 5.21 for the study-reach and in Figure 5.22 for the full-reach.

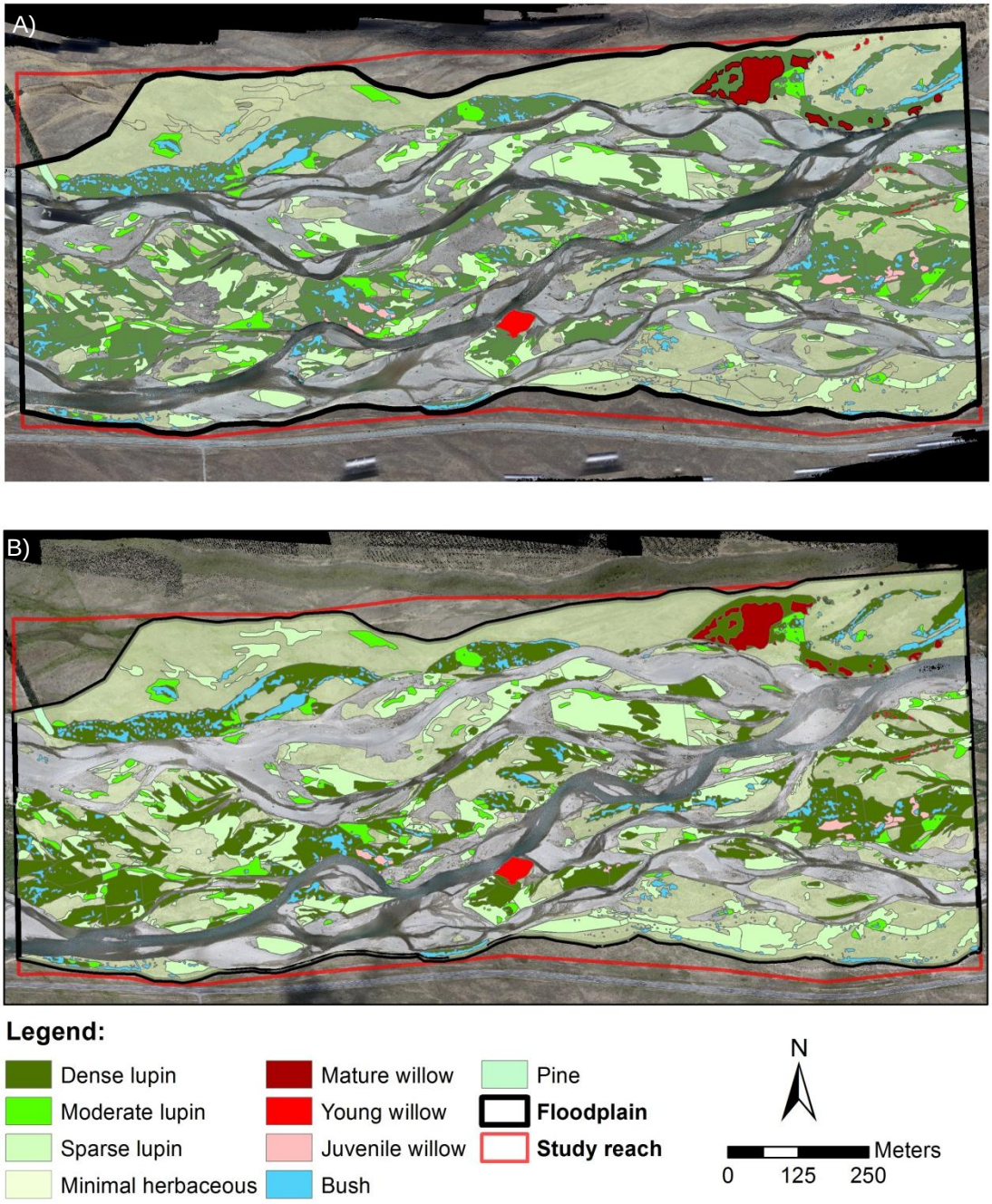

Figure 5.20: Vegetation mapping based on vegetation survey and aerial photographs for the study-reach and floodplain areas of: A) pre-flood data, and B) post-flood data.

Table 5.23: Surface area calculations for the various vegetation categories of the pre- and post-flood.

	Pre-flood vegetation area (m^2)	Post-flood vegetation area (m^2)	Difference (m^2)
Bare substrate	401,292	345,659	-55,633
Dense lupin	200,911	196,532	-4,379
Moderate lupin	33,990	32,454	-1,535
Sparse lupin	99,498	120,468	20,969
Minimal herbaceous	305,156	330,543	25,387
Mature willow	8,491	8,491	0
Young willow	2,592	2,530	-62
Juvenile willow	3,677	3,086	-591
Bush	31,534	30,929	-604
Pine	758	758	0
Total area	1,026,692	1,026,692	
Total vegetated area	625,400	681,033	55,633

Table 5.24: Physical characteristics for the various vegetation types.

	Average stem diameter (cm)	Stem density (stems/m^2)	Average height (cm)
Dense lupin	0.8	100.9	80
Moderate lupin	0.35	53.8	33.6
Sparse lupin	0.3	34.4	25.7
Young willows	2.13	17.3	400

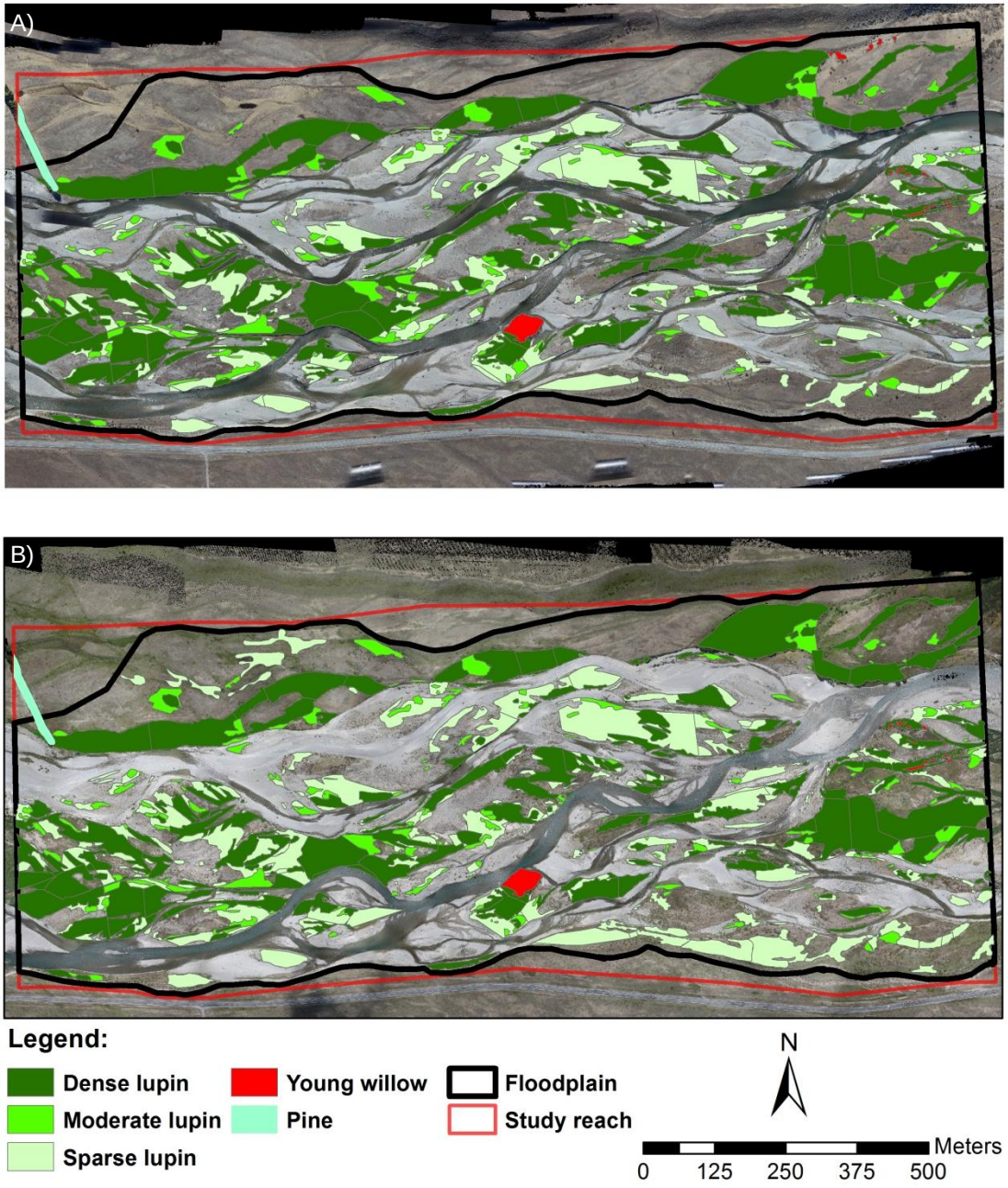

Figure 5.21: Vegetation trachytopes of the study-reach floodplain: A) pre-flood, and B) post-flood.

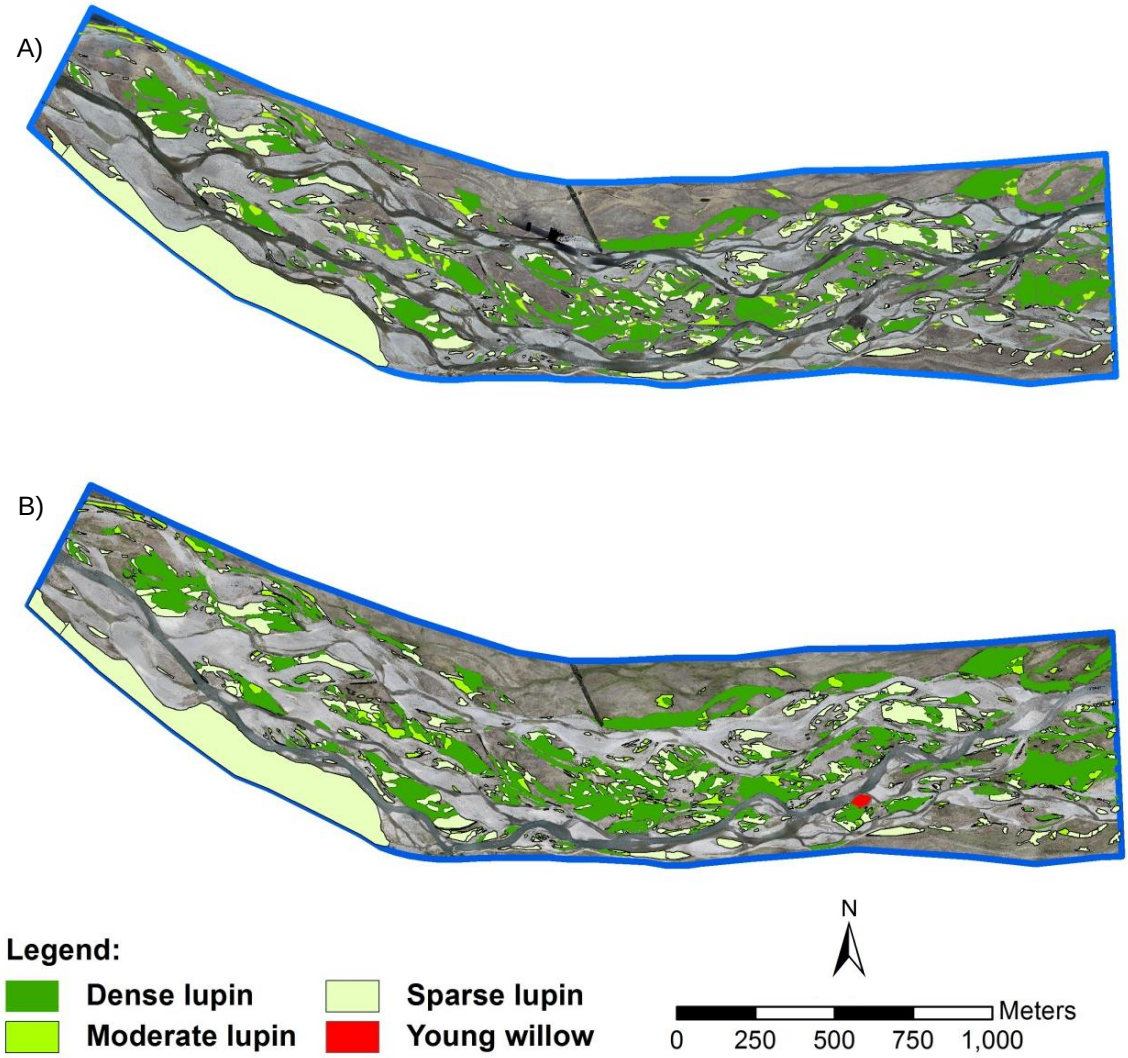

Figure 5.22: Vegetation trachytopes of the full-reach floodplain: A) pre-flood, and B) post-flood.

The vegetation mapping provided valuable information for the floodplain vegetation statistics. With a total study-reach floodplain area of 808,014 m^2, the lupins comprise 41.4% (pre-flood) and 43.2% (post-flood) of the total area and bare substrate comprises of 49.6% (pre-flood) and 42.8% (post-flood) of the total area. From the vegetation survey of Section 5.3.1, the lupin ground cover within this area was between 11 and 18%, with a significant portion of the area being bare substrate. Nevertheless, what can be confirmed was that lupin patches existed in an estimated 334,399 m^2 of the floodplain.

Reviewing the data in Table 5.23, it should be noted that the vegetation differences were not caused completely by the October flood event. Many factors affect the varying vegetation

between the pre- and post-flood event vegetation density and distribution. First, significant growth was expected between the early-spring conditions of the pre-flood data and the mid-summer conditions of the post-flood data, which impacted the herbaceous plants, but should not significantly alter the slower developing woody-vegetation. The differences between the wood-vegetation were likely due to the flood event, but this will be confirmed in Section 5.4, where the flood event and vegetation reduction was compared. Secondly, this mapping was subjective and based on visual identification. Since the vegetation in the post-flood event survey was more visible and distinguished (e.g. lupins are blooming in colors of purple, white, and pink), making it easier to identify and map the vegetation.

Finally, it should be noted that it was difficult to compare the lupin and herbaceous areas of the pre- and post-flood due to the mapping technique. Since tall vegetation canopies cover the ground beneath, there was no way to confirm the underlying vegetation; however, based on field observations, the vegetation under these areas were sparsely to moderately covered by smaller herbaceous vegetation. This issue was overcome by assuming the underlying vegetation was similar to the surrounding visible lupins and herbaceous vegetation. Therefore, in areas of bush and willows, there was an underlying ground vegetation that may be lupin patches or minimal herbaceous vegetation. However, no underlying vegetation was in the pine tree area, as this area was noted as bare from field data collection. This overlapping of vegetation explains why combining all the vegetation areas was greater than the total vegetation area provided in Table 5.23, as the total vegetated area was the area of bare substrate subtracted from the total area.

Combining the vegetation survey data of Table 5.24 with the vegetation mapping of the study-reach and full-reach produced the necessary vegetation mapping for the numerical model as shown in Figures 5.21 and 5.22. Each of the four vegetation polygons contained the vegetation type, average stem density, average stem diameter, and average height and improved the hydraulic simulations in the vegetated areas (Section 6.4.3).

5.4 Vegetation and digital elevation model of difference comparison

5.4.1 Introduction

Using the vegetation survey, vegetation mapping, and the DoD produced by spatially varying uncertainty (SV) method, an assessment was conducted on the study-reach to: i) determine what vegetation types were removed, ii) what total area of vegetation was removed, and iii) identify what geomorphic changes occurred in such areas; which can inform on the processes that were likely responsible.

5.4.2 Methods

To determine the areas impacted by the flood event, the SV DoD map of Figure 5.15 was utilized. This provided the first assessment to identify vegetation areas impacted by flood events; however, vegetation was also removed in areas without geomorphic change, so further visual observations were used to located areas of vegetation removal outside of the DoD. This was necessary to find areas that may have removed vegetation through drag alone or inundation, thus showing no signs of geomorphic change. Once the areas of vegetation removal were identified, polygons and various ArcGIS tools were used to isolate the individual vegetation types, the corresponding areas, and the geomorphic changes. Since the mapped lupin patches contained other vegetation types (i.e grass, low-lying herbaceous vegetation), it is important to note that actual lupin area of the identified location was significantly less than the reported area of occurrence. Using the data of Table 5.22, the sub-reach lupin vegetation coverage best represents mapped lupin patch coverage which was determined to have 11.2% (pre-flood) and 18.8% (post-flood) lupin composition. However, for mapping and mortality identification, all results presented herein were for areas that contain lupin presence instead of composition. This was considered adequate since lupin presence and flood-induced removal/mortality would focus on the mapped areas affected. Further, in determining lupin removal, comparing lupin total presence to reduced areas of presence would provide the same percentage removed as comparing total lupin composition to composition removed.

Using the study-reach's DoD and pre- and post-flood vegetation maps, it was possible to identify which areas experienced erosion and deposition. However, heavy consideration was given when determining the process of removal. While the DoD and pre- and post-flood

aerial photographs provided snapshots of information, the actual processes that took place were unknown. Therefore, while the DoD shows where areas have experienced erosion or deposition, the processes responsible for the vegetation removal were only considered where there was high confidence in the interpreted process. For example, in areas of channel migration and apparent bank erosion, erosion was considered with confidence. Likewise, in areas outside of channel migration and relatively unaffected topography, deposition was considered. However, areas of channel migration that developed into new bars were not considered, since there it was a matter of speculation whether erosion or deposition removed the vegetation.

5.4.3 Results and discussion

Based on the mapped areas of study-reach vegetation removal, the specific vegetation type and corresponding areas were calculated in ArcGIS and the results are presented in Tables 5.25 and 5.26. In total, 15,906 m^2 of vegetation was removed from the study-reach during the October 2011 flood event, including small willows (503 m^2), bush (737 m^2), lupin patches (11,540 m^2), and minimal herbaceous vegetation (3,126 m^2). With the pre-flood vegetated area at 625,400 m^2 and 15,906 m^2 removed, this flood event re-worked approximately 2.6% of the floodplains vegetation. Of this vegetated area, 334,399 m^2 of lupins covered the pre-flood area and 11,540 m^2 of these were removed, thus this flood removed approximately 3.5% of the floodplain lupins. Therefore, while the October 2011 flood event had significant morphologic change within the study-reach floodplain, only minimal vegetation impact occurred.

Table 5.25: Vegetation removal by type.

	Area (m^2)	Percent of total vegetation removed (%)
Total	15,906	100
Willows	503	3.2
Bush	737	4.6
Minimal herbaceous	3,126	19.7
Dense lupin	5,381	33.8
Moderate lupin	4,469	28.1
Sparse lupin	1,690	10.6
Total lupin removal	11,540	72.6

Table 5.26: Vegetation removal by area.

	Pre-flood area (m^2)	Post-flood area (m^2)	Area removed (m^2)	Difference (%)
All vegetation	625,400	681,033	15,906	2.6
Lupin	334,399	322,859	11,540	3.5

Using the SV DoD produced, the areas of vegetation removal were assessed for deposition and erosion. Of the 15,906 m^2 of vegetation removed, erosion and deposition were identified to occur within 13,934 m^2 of vegetation removal; however 202 m^2 (125 m^2 of dense lupin, and 77 m^2 of moderate lupin patches) were removed from consideration since this area was over a newly formed bar. This resulted in 13,732 m^2 assessed for erosion and deposition. Additional areas were identified to have vegetation removal without any geomorphic change detected and these results are presented in Table 5.27. The erosion, deposition and no geomorphic change assessment provided an estimate of the distribution of likely processes that caused vegetation removal. As shown in Table 5.27, it was estimated that erosion was responsible for 77.1% of the vegetation removal, deposition was responsible for 9.3% removal, and processes such as drag or inundation may have been responsible for 12.4% removal (remaining 1.2% withdrawn from consideration due to bar development). It is stressed that these results are only an estimate, as there was no way of knowing the exact removal area or processes. For instance, while erosion or deposition may have occurred in one location of vegetation removal, it was highly possible that other processes such as drag removed the vegetation before, or in combination with the morphodynamics. Further, in the areas that showed no geomorphic change, it was possible that erosion may have removed the vegetation, and then deposition occurred during the flood recession, which could show no geomorphic change.

Table 5.27: Vegetation area removal by deposition and erosion processes (all deposition occurred for herbaceous).

	Deposition	Erosion	No geomorphic change
Veg area removed (m^2)	1,472	12,260	1,972
Total (%)	9.3	77.1	12.4

Table 5.28 presents the area breakdown for the specific vegetation and geomorphic change detected as well as statistics (mean, standard deviation, maximum, and minimum) for the deposition and erosion categories. These results best illustrate the areas of the specific vegetation categories affected by the estimated process. However, the erosion and deposition categories mean, standard deviation, maximum, and minimum were calculated to determine trends. As shown in Table 5.28, the results for the deposition values for the lupins show consistent values with mean errors around 0.25 m and standard deviations around 0.1 m. These values correspond well with the deposition mortality testing of Section 4.4.4. The minimal herbaceous vegetation was expected to experience mortality at even less deposition due to the smaller vegetation; however, the results of Table 5.28 show that this vegetation may have experienced mortality at levels of 0.4 m with 0.15 m standard deviation. The erosion category had mixed results. For instance, the removed willows had a mean erosion level of 0.8 m and standard deviation of 0.42 m; while the lupins had greater erosion levels. Since the willows removed consist of young and juvenile willows between 1.5 – 4 m tall, it was expected that these would take greater erosion than the lupins. This example illustrates why these values provided no insight into the removal processes, since they provide no threshold values or indication when the vegetation was removed, but rather a snapshot of the final flood result.

Table 5.28: Areas of lupin removal by process and statistics of the associated elevation changes for the individual vegetation categories.

	Area (m^2)	Mean (m)	SDE (m)	Max (m)	Min (m)
Deposition					
Dense Lupins	3	0.22	0.08	0.35	0.13
Moderate lupins	555	0.29	0.09	0.88	0.13
Sparse lupins	591	0.27	0.08	0.48	0.12
Minimal herbaceous	323	0.42	0.15	0.85	0.14
Erosion					
Willow	503	-0.80	0.42	-0.07	-1.91
Bush	737	-1.26	0.42	-0.10	-2.13
Dense Lupins	5097	-1.17	0.40	-0.05	-2.22
Moderate lupins	3330	-0.89	0.38	-0.07	-2.01
Sparse lupins	695	-1.02	0.33	-0.07	-1.85
Minimal herbaceous	1898	-0.75	0.33	-0.05	-1.63
No elevation change					
Dense Lupins	156				
Moderate lupins	507				
Sparse lupins	404				
Minimal herbaceous	905				

5.5 Conclusion

This chapter has demonstrated the potential to generate high-quality large scale DEMs using a combination of SfM-DMVR and optical-empirical bathymetric mapping, provided that image resolution and texture and adequate ground control data is acquired. Originally, LiDAR was considered for this DEM production and was estimated at NZ$27,500, which would have provided spatial point resolutions of 1 m^2 and vertical accuracies of ±0.15 m. At an estimated cost of NZ$10,900 for initial surveys, and NZ$5,600 for additional surveys, SfM combined with optical-empirical bathymetric mapping provided a full DEM with raw point clouds generating spatial point resolutions of 0.5 m (reduced from 0.25 m to improve computer handling), and accuracies in the decimeter range, rivaling specifications for LiDAR data for one-third of the cost. These two quality DEMs were then analyzed in the ArcGIS plugin GCD, which was able to generate a DoD and sediment budget statistics. Testing various uncertainty methods, the SV propagated errors method was chosen to represent the

geomorphic change of the October 2011 flood event, as it best represented the observable changes.

Using vegetation surveys and aerial photographs, vegetation maps were created for the pre- and post-flood study-reach. This allowed for the identification and quantification of the reach's vegetation composition, distribution, and extent and was separated into nine vegetation categories. Utilizing the pre- and post-flood vegetation maps, it was possible to determine that approximately 2.6% of the floodplain's total vegetation had been removed by the October 2011 flood, which included approximately 3.5% of the total lupins in the study-reach. Combining the DoD with the spatial information on vegetation removal provided insight into the processes responsible for the vegetation removal. It was estimated that of the vegetation mortality, 77.1% was erosion related, 9.4% deposition related, and 12.4% experienced no major morphologic change; which suggested drag and/or inundation-induced mortality existed. While these results were estimates, the results compare well with the processes identified and studied in Chapter 4 in which flood-induced erosion, deposition, inundation, drag, and trauma were identified as likely causes of lupin mortality.

Chapter 6

Numerical Model Calibration

6.1 Introduction

This chapter presents the numerical model chosen to simulate the various flood-induced processes that cause lupin-mortality, and the calibration efforts to ensure realistic hydraulic and morphologic conditions were simulated. Three progressive calibrations were undertaken which built upon precursor calibrated parameters and included: i) hydraulic calibration in fixed-bed mode that focused on velocity, depth, and water extent, ii) vegetation calibration in fixed-bed mode that focused on altered hydraulic conveyance of flow through vegetated areas, and iii) a morphologic calibration using mobile-bed mode and focused on replicating the observed morphology changes. Prior to calibration, sensitivity analyses were performed using meso-reaches to determine individual parameter sensitivity and functionality. Armed with the sensitivity analyses, optimal parameterization was transferred to macro-reach (full-reach) models for further calibration. While all macro-reach simulations utilized the full-reach topographies, the main focus for results was on the simulated performance of the study-reach. However, it was recognized that accurate study-reach results require accurate upstream simulations. Therefore, the main focus of results and discussion was centered on the study-reach, but full-reach results were presented and discussed in less detail. This chapter does not provide full details on model production and model input, as this would be cumbersome and unnecessary. Instead, the reader is referred to the numerical model's user manuals for further details (Deltares, 2010).

6.2 Numerical model

Numerous numerical models are currently available and range from 1D fixed-bed to fully 3D mobile-bed capabilities. Taking into consideration the fluvial complexity and scale of the study-reach, a 1D model was not considered as it does not adequately simulate the lateral flow necessary for proper braiding or lateral channel migration. Further, 3D models were not desired given the large scale of the reach, relatively shallow depths, and the impractical simulation durations. Considering these restrictions and the model's purpose to accurately simulate vegetation influence and morphologic changes, candidate models were narrowed and Delft3D in 2D mode was chosen for this research.

Delft3D is an open-source numerical model developed by Deltares, and consists of several modules including Delft3D-FLOW, which offers both 2D and 3D hydrodynamic simulations based on non-steady, Navier-Stokes equations with shallow water and Boussinesq approximations (Deltares, 2010, Williams et al., 2013). Delft3D-FLOW, hereon referred to simply as Delft3D, is capable of simulating the hydrodynamics of coastal, estuarine, river, and lake areas as well as sediment transport and 2D-morphological changes. Of particular interest for this research, Delft3D incorporates a function called trachytopes that among other capabilities can be implemented to represent vegetation roughness upon local hydraulics in 2D depth-averaged simulations. Unlike previous methods that solely use hydraulic roughness to describe the hydraulic impacts of vegetation (Keijzer, Baptist, Babovic, & Uthurburu, 2005) which can lead to exaggerated shear stress and sediment transport (Deltares, 2010), trachytopes (using formula 154 Baptist 2) incorporate an additional momentum equation term that describes the vegetation's flow resistance (Deltares, 2010) and thus improves the flow-vegetation-sediment transport relationship.

While certain numerical models offer bedload transport and morphologic updating, their ability to accurately model floodplain morphologic changes are critically hampered by bank erosion prediction and remeshing the grid after changes occur (Rinaldi & Darby, 2008; Lane & Ferguson, 2005). While studies have tried to improve the modeling accuracy of bank erosion (e.g. Darby et al., 2007), and specifically using Delft3D (e.g. Rinaldi Mengoni, Luppi, Darby, & Mosselman, 2008), the Delft3D version (v 4.00.07) utilized in this research only implements one bank erosion parameter called ThetSd. However, this is a simplistic scheme that redistributes sediment from dry to wet cells and has shown to cause unrealistic bank erosion in straight channels (Duran, Beevers, Crosato, & Wright, 2010). An additional undocumented bank erosion parameter has been implemented by Richard Measures, of NIWA, which is referred to as *Repose.* This method determines bank erosion based on a user-defined critical slope between adjacent grid cells. This method is another simplistic approach to a complex process and can generate bank failure without the grid cells encountering flow. Nevertheless, these are the options available, and were fully explored during model calibration.

6.3 Model input and data collection

Developing flood simulations in Delft3D required a considerable amount of data. Extensive data collection and extraction has been presented in Chapters 4 and 5 and provided the majority of the data needed to perform flood simulations and evaluate potential impacts upon vegetation. These data includes flood hydrographs, vegetation mortality thresholds, vegetation mapping, topography for the pre- and post-flood surveys, as well as instantaneous boundary conditions of the pre- and post-flood surveys, such as discharge and corresponding downstream depth. However, additional data were required to ensure model calibration/validation were reasonable. These data included hydraulic roughness, eddy viscosity, and sediment grain size. Therefore, additional field data collected was undertaken during the pre-flood survey and an additional field campaign was conducted in December 2012. Together, these two data collection efforts acquired the study-reach's sediment grain size distribution and additional flow data using an acoustic Doppler current profiler (aDcp) to help calibrate the model's hydraulic roughness, eddy viscosity, and vegetation influence on hydraulics.

6.3.1 Sediment

A grain size analysis of the study-reach's surface and sub-surface material was necessary to determine the bed roughness (using White-Colebrook formula, for which Delft3D requires the Nikuradse roughness length, k_s), and provide sediment composition for the morphological module. Therefore, extensive field work was conducted during the pre-flood survey to obtain these data. The surface was sampled using the Wolman pebble count method (Wolman, 1954). Using this method, a tape measure was stretched 30 m and 100 pebbles were documented at 0.5 m intervals and measured across the intermediate axis. This was completed for 20 locations throughout the study-reach and included: five true-right bank, five true-left bank, five floodplain, and five locations along a dry river channel. Using Microsoft Excel, these data was then processed to produce a cumulative percentage 'finer than' grain size for the four areas (Figure 6.1) and all data were combined by averaging to produce a single representative distribution (Table 6.1).

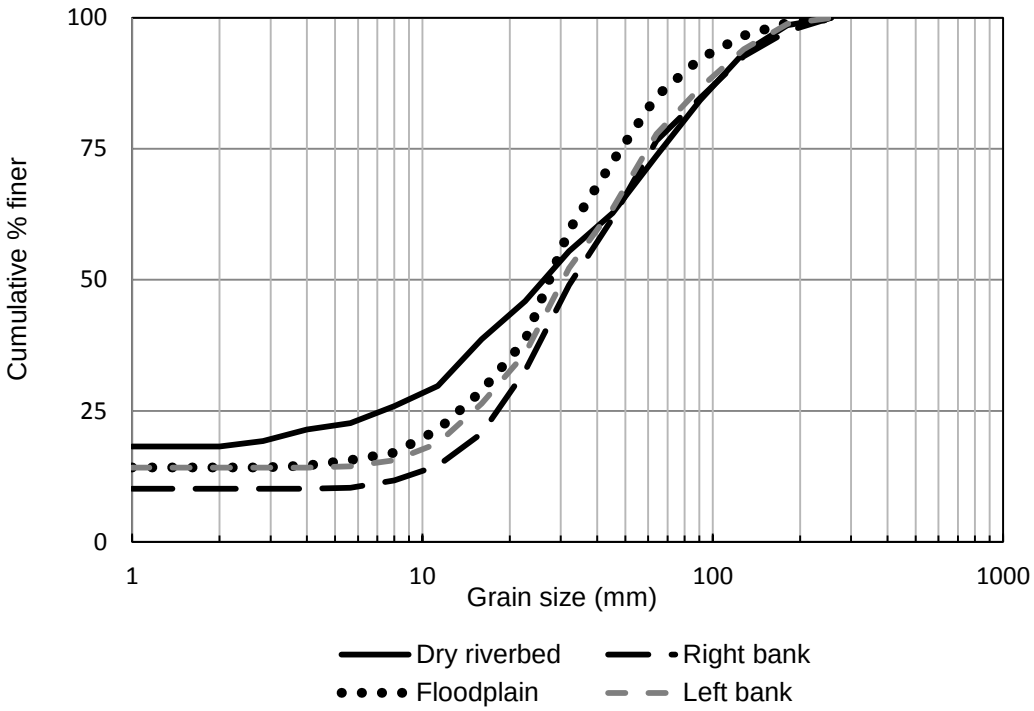

Figure 6.1: Surface sampling cumulative percentage finer than grain size.

Table 6.1: Representative surface grain size percentiles.

Percentile	mm
100	256
95	136
90	103
84	82
75	61
65	45
50	29
25	14

Sub-surface sediment sampling was performed at the study-reach's upstream and downstream ends following the Hicks/NIWA Sub-Surface Bed-Material Sampling Method (Appendix D.3). The sub-surface material was excavated and larger sediment was recorded in the field, and a sub-sample of the fine sediment was taken and processed in the lab using sieve analysis. The upstream sub-surface sample consisted of 330 kg of excavated substrate from a pit of approximately 0.62 x 0.62 x 0.4 m (length, width, depth) and the downstream sub-surface sample consisted of 644 kg of substrate excavated from a pit of approximately 0.79 x

0.79 x 0.4 m. The sediment was categorized into half-phi intervals, and tabulated into cumulative percentages (Figure 6.2) at common percentiles (Table 6.2). Results show the downstream pit with larger sediment size, which explains the smaller required sampling volume of the upstream site. Since the upstream and downstream sediment distributions show similar results, additional sub-surface sampling was not conducted. Instead, the final sub-surface sediment size was averaged to provide the necessary data for Delft3D.

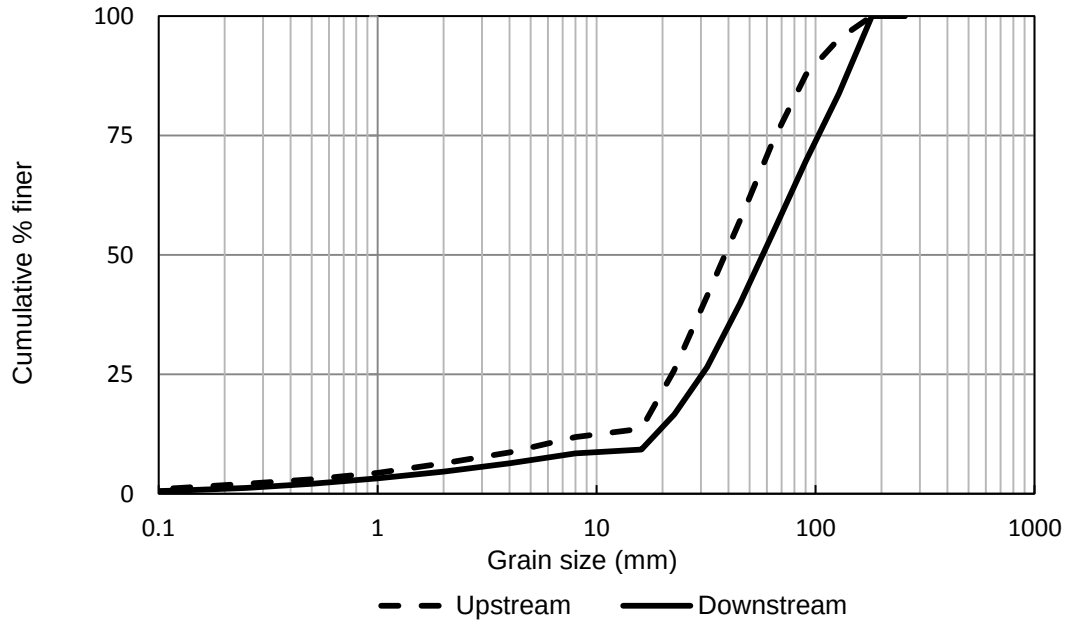

Figure 6.2: Sub-surface sampling cumulative percentage finer than grain size.

Table 6.2: Representative sub-surface grain size percentiles.

Percentile	Upstream (mm)	Downstream (mm)	Average (mm)
100	181	180	180
95	128	163	146
90	103	149	126
84	83	128	105
75	66	103	84
65	53	88	70
50	39	56	48
25	22	30	26

6.3.2 aDcp data and lupin conveyance experiment

While significant vegetation data were collected, and Delft3D's trachytopes can account for floodplain-vegetation-altered flow conveyance, no data had been collected to properly calibrate the trachytope parameters. Therefore, a simple experiment was conducted in December of 2012 on a 5-m-wide anabranch of the study-reach that took freshly uprooted lupins from the Ahuriri floodplain, and using a SonTek aDcp, the lupin-altered flow conveyance was documented. Using the SonTek aDcp S5 (four profiling and one vertical beam) system, the aDcp provided depth and velocity accuracy within ± 1.0% and ± 0.25% of the measurement, respectively. In addition, the aDcp's Differential GPS (DGPS) was utilized to provide measurement coordinates, and provides sub-1 m accuracy (Xylem Inc., 2012).

With the goal to calibrate trachytopes in Delft3D, it was decided to investigate lupin clusters instead of individual lupins, as clusters could be represented as model grid cells. Therefore, 20 lupins were attached by their roots to a wire mesh 0.5 x 6 m to simulate typical moderate lupin clusters (hereon referred to as *lupin-mesh*) (Figure 6.3, Table 6.3, and Table 5.24). The experiment surveyed various river flow conditions and was conducted twice; once without the lupin-mesh and again with the lupin-mesh. Each survey started 10 m upstream of the lupins and recorded the inflow-boundary transect. Next, the channel was surveyed in a zigzag pattern until the upstream end of the lupin-mesh was reached, at which point a transect directly in front of and behind the lupin-mesh were surveyed. This pattern was then repeated 10 m downstream of the lupin-mesh.

Figure 6.3: Lupin-mesh experiment conducted in the moderate depth and velocity reach section.

This experiment was conducted in three locations: i) a deep pool with slow velocity, ii) a riffle with fast velocity, and iii) a reach with moderate depth and velocity (Figure 6.4). For convenience, these areas are hereafter referred to as *pool-reach, riffle-reach, and moderate-reach sections*. However, due to the shallow depth of the riffle reach section, adequate depth and velocity data were not acquired and were not utilized for calibration. Further, due to time constraints, only the 20 lupins of moderate cluster density were tested. It should be noted that the lupin density was not sufficient to create a full boundary. Instead, flow was retarded behind the local lupins and channeled between lupin-free areas of the mesh. This result was desired for the model calibration, as this density was representative of the Ahuriri floodplain. Due to this density, the resulting depth and velocity data of this experiment produced only slight variations between the lupin-mesh and no mesh experiments, with typical depth

differences of 0.04 m, and velocity differences of 0.03 m/s. Therefore, calibration efforts required the ability to detect and simulate relatively small changes in flow conveyance.

Table 6.3: Physical characteristics for the lupins attached to the lupin-mesh.

	Average stem diameter (cm)	Stem density (stems/m^2)	Average height (cm)
Lupin statistics	0.43	117	49

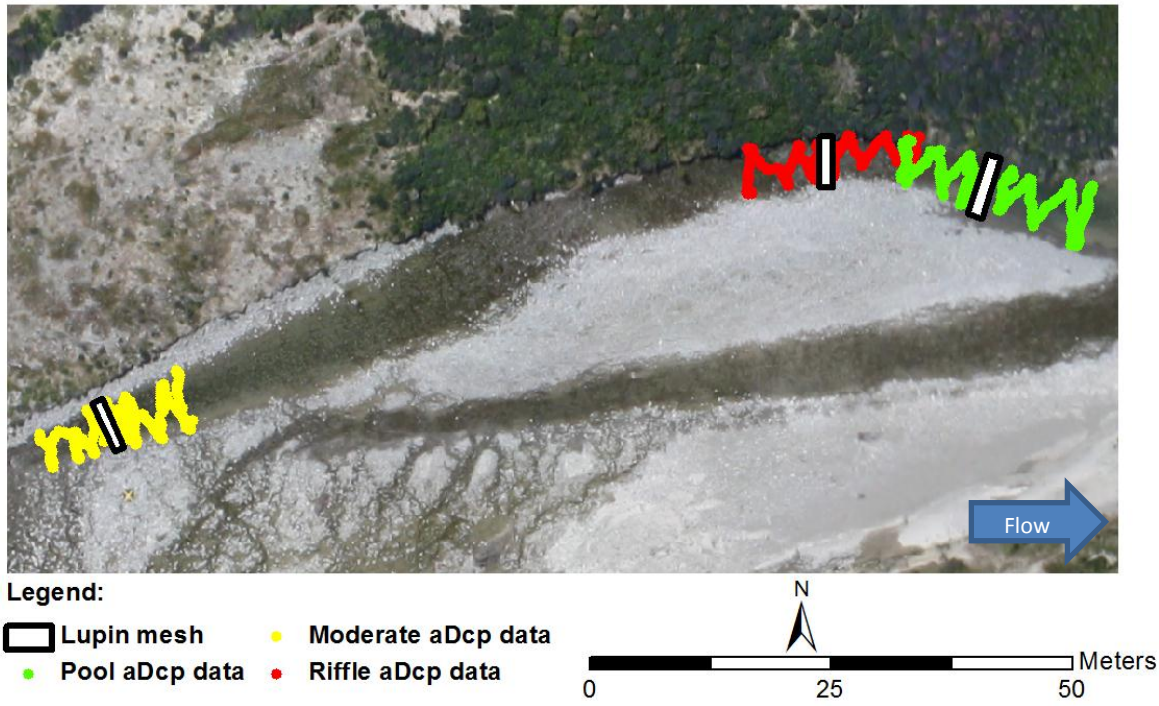

Figure 6.4: Lupin-altered flow conveyance trachytope experiment data collection.

6.4 Model calibration

6.4.1 Introduction

Although in some numerical models the processes being simulated are fully understood, the equations are still reduced for computational savings. To counter these simplifications, parameters are introduced to help control the inherent uncertainty. However, not all parameters produce measurable or desired changes in the simulated system (Hasselaar, 2012). Therefore, to achieve the best simulation results, stringent parameter calibration is required, yet achieving desirable simulation results is difficult at best. Therefore, the modeler must

calibrate based on the goals and objectives of the intended modeling purpose (R. Measures, personal communication, June 18, 2013). Based on the objectives of this research (objective 2), the purpose of this model was to identify lupin mortality for varying flood conditions based on the thresholds identified in Chapter 4. Processes identified to cause lupin mortality were high inundation depths combined with extended duration, drag causing pull-out (which was identified through the critical velocity, Table 4.17), trauma, erosion, and deposition (Table 4.19). Therefore, the parameters that govern these flow conditions were given the highest priority .

While reduced complexity models can produce convincing simulations of flow, depth, and velocity, shallow depth areas can develop local flow accelerations. Given the topographic complexity, vegetation extent, and shallow depths of braided morphology, model development required great physical detail to ensure the landscape and hydraulics were properly represented, thus in return would provide the foundation for morphological simulations (Nicholas et al., 2012, Van De Wiel et al., 2011; Williams et al., 2013). Therefore, physical details such as sediment composition, vegetation influence on hydraulic conveyance, spatially varying vegetation, and high quality SfM and bathymetric DEMs made this model data-rich. However, one aspect not included in this data-rich model was spatially-varying grain size. While these data were not collected, it may have provided valuable physical representation of bank and floodplain roughness; however, model studies that utilized uniform roughness have shown to produce accurate hydraulic conditions (e.g. Williams et al., 2013).

Model calibration was performed in three stages: i) hydraulic calibration with a fixed-bed mode, ii) vegetation calibration with a fixed-bed mode, and iii) a morphologic calibration with mobile bed mode. The hydraulic calibration used velocity, depth, and water extent data. The vegetation calibration utilized the lupin-mesh experiment and provided a calibration for trachytopes which was essential for flood events and overland flow through lupin infested areas. The final calibration used the October 2011 flood event and pre- and post-flood DEM of difference to calibrate the model's morphologic parameters. Each calibration method is presented below with a full methods review and discussion of the results.

6.4.2 Hydraulic model

6.4.2.1 Introduction

Based on the results of Chapter 4, it is evident that velocity (Section 4.4.3) and water extent combined with depth (Section 4.4.1) are important hydraulic variables when considering lupin mortality. Therefore, in determining the best hydraulic parameters, both depth and velocity must be optimized, which promotes accurate water extent. To achieve optimal parameter settings, the hydraulic model was calibrated in two stages. The first stage utilized a (meso-scale) reach and the previously described aDcp data that was collected without the lupin-mesh. These data provided velocity, depth, water extent, and discharge for both the pool-reach and moderate-reach sections (Figure 6.4). Transferring the optimized parameterization of the meso-scale, the second stage utilized the (macro-scale) full-reach pre-flood survey data and topography, which provided water extent (from aerial photographs), and depth data from the acquired bathymetric data (meso-scale represented in Figure 6.4, and macro-scale represented in Figure E.28).

6.4.2.2 Methods

Stage 1:

The first step in simulating velocity, as measured by the acquired aDcp data, was to build the meso-reach's terrain model for the numerical grid. While the aDcp data could have been utilized to develop the bathymetry and river bed elevation of the surveyed areas, the post-flood topography of this anabranch appeared to have remained constant, regardless of the two small flood events (120 and 105 $m^3 s^{-1}$) that had occurred between surveys. This consistency was highly likely given that this anabranch of interest would have only experienced a small influx in flow during the relatively small flood events. Utilizing the post-flood topography of the region provided a larger simulation reach (300 m in length) as well as having the ability to connect the moderate-reach and pool-reach sections into one simulation, thus providing necessary upstream run-in conditions. However, to ensure that the bathymetry was accurate in the aDcp areas, the post-flood riverbed elevation was manually edited to match the aDcp depth data. This was performed by comparing the aDcp and SfM water surface elevations, and differencing the local water depths. In general, in most areas the differences in water depth were $\leq$ 5 cm and that bathymetry was not altered; however, some areas in the pool-reach required modification.

Following the simulations, various statistics were taken by extracting the simulated data from the observed data locations. However, given the DGPS accuracy, additional georeferencing calibration was necessary to ensure the aDcp data was correctly located. In georeferencing the aDcp, the DGPS provided the initial coordinates of the data; however, the path along which the aDcp travels was recorded using the bottom-tracking setting, which calculates the path based on the river bed. This method was used as the low-flow conditions and large sediment size of the anabranch ensured minimal sediment transport and thus the most accurate tracking. Therefore, while the relative location of the aDcp was fairly accurate (in the centimeter range; J. Brasington, personal communication, January, 2013), initial starting coordinates required slight adjustment to ensure the data points were in the correct location. This was done by simply fitting the aDcp's track within the narrow anabranch planform. Given the sub-1 m starting accuracy, and the limited options for the aDcp's path to fit the planform, final data location was assumed adequate for the modeling purpose and provided useful hydraulic calibration data, albeit less accurate than the RTK-GPS data of the pre- and post-flood surveys.

Prior to any simulation, a grid was required. Considering the first calibration would be performed on the meso-reach's 5 m-wide anabranch, it was desired to represent the width with at least 2 grid cells; thus, a 2.5 m grid was developed. Additionally, based on the results of Williams et al. (2013) who produced good hydraulic results with a 2 m grid, a finer grid was desired. Therefore, a 1.5 m grid was also developed, which provided three grid cells to simulate the anabranch channel width. Using the aDcp calculated flow rate of 0.44 $m^3 s^{-1}$, various simulations were conducted to calibrate the hydraulics. The first objective in the model calibration was to determine the sensitivity of the various hydraulic parameters, which included bed roughness, horizontal eddy viscosity (V_H), and horizontal eddy diffusivity (K). Therefore, using the 1.5 m grid, a sensitivity analysis was performed with typical parameter values initially adjusted by factors of ten to establish sensitivity. Following this assessment, the sensitive parameters were again tested and fine-tuned for both a 1.5 m and 2.5 m grid resolution.

Bed roughness was simulated in Delft3D using the White-Colebrook roughness formula, which uses the Nikuradse equivalent roughness size, k_s (m) (Garcia, 2008):

$$k_s = \alpha_s \text{ x } D_x \qquad \text{(Eqn: 6.1)}$$

$$k_s = 2.0 \text{ x } 0.103 \text{ m} = 0.206 \text{ m} \qquad \text{(Eqn: 6.2)}$$

Where D_x is the sediment size (m) and α_s is the ratio of Nikuradse roughness and sediment size. Using the Kamphuis (1974; cited from Garcia, 2008) empirical relationship, D_x was set to D_{90} and α_s is 2.0. Using the average D_{90} sediment size of Table 6.2, k_s was calculated at 0.21 m (Eqn: 6.2). Eddy viscosity and diffusivity were initially set to Delft3D default values of 1 and 10, respectively.

Stage 2

Once optimal hydraulic parameterization was achieved for the meso-reach's 1.5 m and 2.5 m grids, parameter values were transferred to the (macro-) full-reach simulations using the pre-flood topography and corresponding boundary data. Transferring the parameterization was considered appropriate given that the hydrodynamic model calibration was based primarily on the grain roughness and protrusion (Nikuradse roughness length), both reaches have similar water depths, and both models were developed with the same grid sizes (Williams et al., 2013).

To assess the accuracy of the simulation and fine tune the hydraulic parameters, three performance measures were utilized. The first evaluates the velocity and depth residual errors between the observed and the simulated data. The second and third methods assessed the simulations inundation and river routing compared to the observed using i) the *effective width, (Fit_{We})* and ii) the *congruent fit* ($Fit_{congruent}$) (Smith, Isacks, Bloom, & Murray, 1996; Ashmore & Sauks, 2006; Williams et al., 2013):

$$Fit_{We} = \frac{We_{sim}}{We_{obsv}} \qquad \text{(Eqn: 6.3)}$$

$$Fit_{congruent} = \frac{IA_{obs} \cap IA_{sim}}{IA_{obsv} \cup IA_{sim}} \qquad \text{(Eqn: 6.4)}$$

Where We_{sim} and We_{obsv} are the simulated and observed reach averaged widths respectively, and the IA_{obs} and IA_{sim} are the total areas of simulated and observed results. These areas were determined in ArcGIS by mapping and calculating the wetted area of the aerial photographs and Delft3D predicted inundated cells. However, a direct comparison between the simulated wet cells and the observed was not initially possible because the simulated wet areas were represented as single points located in the grid cell center. Therefore, in order to fully represent the simulated wet area, the 1.5 m grid water extent was extended by 0.75 m, and the 2.5 m grid water extent was extended by 1.25 m to account for the full simulated water extent.

6.4.2.3 Results and discussion

Sensitivity results (Table 6.4) indicated that eddy diffusivity had minimal to no impact on the hydraulic conditions simulated. Eddy viscosity results showed minimal difference between 0.01 $m^2\ s^{-1}$ and 0.1 $m^2\ s^{-1}$, but moderate difference between 0.1 m^2/s and 1 m^2/s. As shown, increasing the eddy viscosity value increased the flow depth and lowered the velocity. Finally, the sensitivity analysis of the Nikuradse roughness length showed that higher k_s values increased depth and decreased velocity, as expected, by increasing bed roughness.

Utilizing the results of Table 6.4, and starting with the initially calculated k_s of 0.21 m, *eddy* viscosity of 0.01 m^2/s, and diffusivity of 1 m^2/s, additional tests were performed on the meso-reach and simulation results are shown in Table 6.5. Results indicate that the bed roughness (k_s) of 0.21 m was appropriate, and the diffusivity of 1 m^2/s and viscosity of both 0.15 and 0.10 m^2/s produced good results for the 1.5 m grid. However, the larger 2.5 m grid's optimal roughness was determined to be an increased 0.35 m. These results were confirmed when applied to the full-reach model (Table 6.6), which revealed the 1.5 m grid optimal roughness of 0.21 m, eddy viscosity at 0.15 m^2/s, and diffusivity at 1 m^2/s, and the 2.5 m grid optimal bed roughness of 0.35 m, but the same eddy viscosity and diffusivity values. The increased k_s for the 2.5 m grid may have been necessary due to greater topographic smoothing. In general,

increased smoothing causes lower elevation spikes and higher troughs; which is one explanation why the simulated flow depth was too low and the velocity was too fast.

Comparing the 1.5 m and 2.5 m grids, depth results produced mean errors (ME) of zero for the full-reach and near zero for the meso-reach, which indicated high accuracy. With the average depth in the meso-reach at 0.37 m, the standard deviation error (SDE) residual indicated relatively poor precision. These limitations are also evident in the full-reach data, where depths rarely exceed 1.5 m. The meso-reach velocity results show ME just below zero for the 1.5 m grid, and just above zero for the 2.5 m grid; both of which are near enough to zero to indicate relatively good accuracy. However, examining the SDE residuals shows errors in the decimeter range. With meso-reach velocities averaging 0.24 m/s, these results are relatively poor.

Table 6.4: Meso-reach hydraulic parameter sensitivity analysis for the 1.5 m grid (errors in meters).

	k_s	1.6	1.6	1.6	1.6	1.6	1.6	0.1	0.5	1.0	1.6
	v_H	0.1	0.1	0.1	0.01	0.1	1.0	0.1	0.1	0.1	0.1
	K	0.01	1.0	10.0	10.0	10.0	10.0	1.0	1.0	1.0	1.0
Depth	ME	0.06	0.06	0.06	0.05	0.06	0.09	-0.04	0.00	0.03	0.06
	MAE	0.11	0.11	0.11	0.11	0.11	0.13	0.09	0.09	0.09	0.11
	RMSE	0.13	0.13	0.13	0.13	0.13	0.15	0.11	0.11	0.11	0.13
	SDE	0.12	0.12	0.11	0.12	0.11	0.12	0.10	0.11	0.11	0.12
	Max	0.29	0.29	0.29	0.28	0.29	0.31	0.20	0.23	0.26	0.29
	Min	-0.32	-0.32	-0.30	-0.32	-0.30	-0.35	-0.38	-0.36	-0.33	-0.32
Velocity	ME	-0.07	-0.06	-0.07	-0.06	-0.07	-0.08	0.00	-0.04	-0.05	-0.06
	MAE	0.13	0.12	0.13	0.12	0.13	0.14	0.11	0.11	0.12	0.12
	RMSE	0.16	0.16	0.16	0.15	0.16	0.18	0.14	0.14	0.15	0.16
	SDE	0.15	0.15	0.15	0.14	0.15	0.16	0.14	0.13	0.14	0.15
	Max	0.22	0.22	0.22	0.19	0.22	0.26	0.71	0.27	0.24	0.22
	Min	-0.55	-0.55	-0.55	-0.53	-0.55	-0.67	-0.44	-0.44	-0.49	-0.55

Table 6.5: Final hydraulic parameters for the meso-reach 1.5 and 2.5 m grids (errors in meters).

		1.5 m grid				2.5 m grid		
	k_s	0.15	0.21	0.21	0.25	0.21	0.35	0.50
	v_H	0.10	0.10	0.15	0.15	0.15	0.15	0.15
	K	1.0	1.0	1.0	1.0	1.0	1.0	1.0
Depth	ME	-0.03	-0.02	-0.02	0.06	-0.05	-0.01	-0.01
	MAE	0.09	0.08	0.08	0.11	0.09	0.08	0.08
	RMSE	0.11	0.11	0.11	0.13	0.12	0.11	0.11
	SDE	0.11	0.11	0.11	0.12	0.12	0.11	0.11
	Max	0.23	0.21	0.21	0.27	0.19	0.18	0.19
	Min	-0.37	-0.37	-0.37	-0.35	-0.46	-0.44	-0.43
Velocity	ME	-0.02	-0.02	-0.02	-0.07	0.04	0.01	0.00
	MAE	0.10	0.10	0.10	0.14	0.15	0.13	0.14
	RMSE	0.13	0.13	0.13	0.18	0.20	0.18	0.17
	SDE	0.13	0.13	0.13	0.17	0.20	0.18	0.17
	Max	0.36	0.32	0.30	0.32	0.78	0.69	0.65
	Min	-0.43	-0.44	-0.44	-0.69	-0.52	-0.51	-0.55

Table 6.6: Final full-reach hydraulic calibration results for pre-flood depth data for the 1.5 and 2.5 m grids (errors in meters).

		1.5 m grid			2.5 m grid		
	k_s	0.20	0.21	0.25	0.21	0.35	0.50
	v_H	0.15	0.15	0.15	0.15	0.15	0.15
	K	1.0	1.0	1.0	1.0	1.0	1.0
Depth	ME	-0.01	0.00	0.03	-0.02	0.00	0.03
	MAE	0.13	0.13	0.14	0.14	0.14	0.15
	RMSE	0.17	0.16	0.17	0.18	0.18	0.18
	SDE	0.17	0.16	0.16	0.18	0.18	0.18
	Max	0.50	0.49	0.53	0.51	0.53	0.59
	Min	-1.14	-0.69	-0.67	-1.13	-1.10	-1.09

Using the best parameters determined for the 1.5 and 2.5 m grids, the hydraulic simulations were performed, and effective width and $Fit_{congruent}$ were calculated for both the study-reach and full-reach. Results of the study-reach (Figure 6.5) show the 1.5 m grid's effective width

was considerably more accurate than the 2.5 m grid. Further, a $Fit_{congruent}$ improvement (+3%) demonstrates an overall improvement in modeling accuracy with the finer grid resolution. Results of the full-reach models (Figure 6.6) were encouraging with the Fit_{we} of the 1.5 m grid slightly under-predicting inundation and the 2.5 m grid slightly over-predicting inundation. The lower accuracy of the $Fit_{congruent}$ results highlighted the model's limitations to accurately predict water extent and braid routing. Visual inspection of Figures 6.5 and 6.6 show both grid sizes failed to model small anabranches and over-predicted wet cells in similar places. Based on the statistics as well as visual observation, grid size difference between 1.5 and 2.5 m seemed to have relatively minimal effect on general model performance. Considering the shallow water depth, complex braidplain, and inherent SfM terrain uncertainty, the results of Table 6.6 and fit results of Figure 6.5 and 6.6 show reasonably good results. Further, these results were comparable to previous braided river water extent studies (i.e Williams et al., 2013), which further suggests that an adequate hydraulic calibration was achieved.

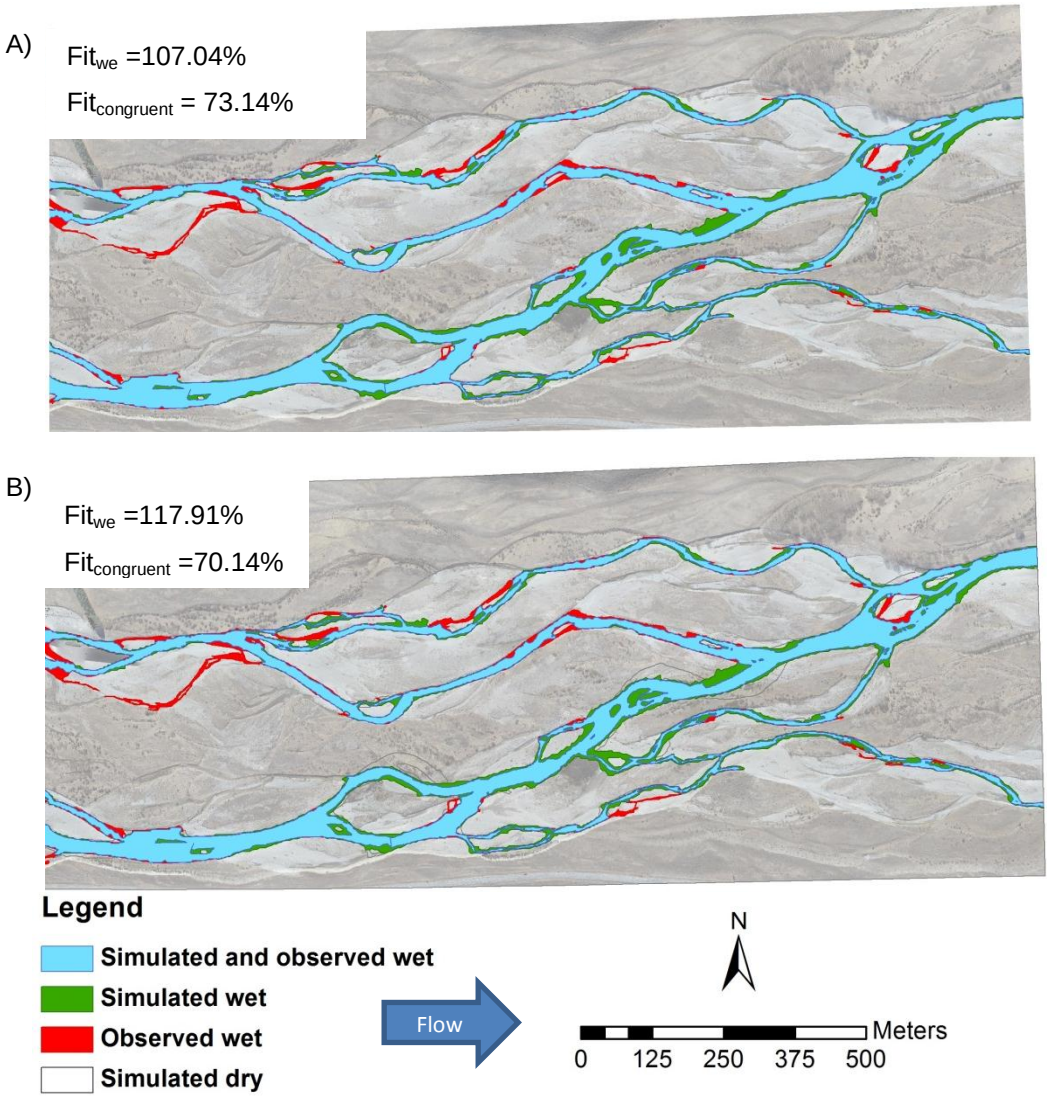

Figure 6.5: Pre-flood study-reach simulation with effective width and congruent fit for A)1.5 m grid, and B) 2.5 m grid.

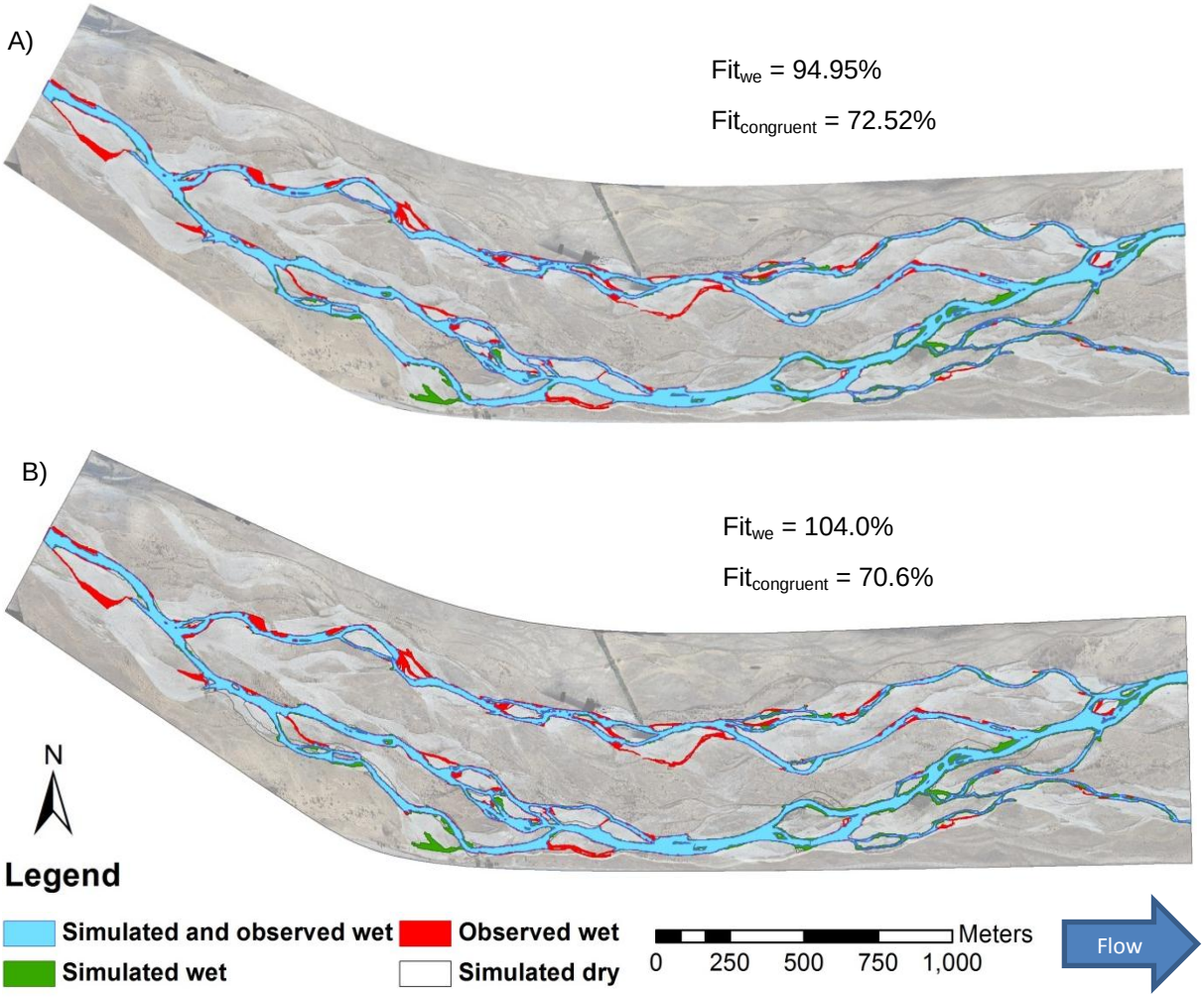

Figure 6.6: Pre-flood full-reach simulation with effective width and congruent fit for A)1.5 m grid, and B) 2.5 m grid.

6.4.3 Vegetation calibration

6.4.3.1 Introduction

The Delft3D trachytope function offers a method to model spatially varying bed roughness, which is converted into the representative bed roughness (in this case the Nikuradse roughness length, k_s). Three classes of trachytopes are available, however, only the area class with vegetation sub-class was considered. In the vegetation sub-class, four formulas are available to represent vegetation roughness; however, only formula 154 Baptist 2 includes a momentum equation that allows the flow resistance and bed roughness to be separated for non-submerged vegetated areas. In submerged vegetated areas, the two cannot be entirely separated. Instead, the local shear stress is calculated using the velocity within the vegetation layer and the user supplied 'real' bed roughness, C_b (Deltares, 2011). These alterations make

it possible to increase the flow resistance within vegetated areas without increasing sediment transport rates.

While the trachytopes available in Delft3D offer a convenient method to include vegetation influence on flood conveyance, the trachytopes modeled do not simulate additional hydraulic or soil conditions typically influenced by vegetation. For instance, soil reinforcement and bank stability (through root structure) are not considered, nor is local erosion and deposition influenced by vegetal canopies. Based on the results of Section 4.3.3.3 and various studies (e.g. Samani & Kouwen, 2002; Leonard & Luther, 1995; Nepf & Vivoni, 2000; Freeman et al., 2000) lupins in flood events may cause local scour due to their moderately rigid stalk and upper canopy, as well as cause additional deposition once they have deformed. While the trachytope simulation does not account for any such condition nor does the 2D depth-averaged model allow for these conditions to be evaluated, the trachytopes inclusion will alter bed roughness and flow resistance in vegetated areas causing reduced velocities; thus, potentially increasing deposition. Despite these limitations, the trachytopes' ability to alter the flood conveyance was still a valuable tool in increasing the accuracy of the hydraulics simulated and was utilized in this research.

6.4.3.2 Methods

Using the same meso-scale simulation reach as the stage 1 hydraulic calibration, and with trachytope formula 154 Baptist 2 chosen, trachytope parameterization was undertaken to match the flow condition with the lupin-mesh that was surveyed with the aDcp. To simulate results from this experiment, the lupin-mesh location was designated in representative grid cells of the 1.5 m and 2.5 m grids. Using Baptist 2 formula, parameters were initially set to the lupin-mesh statistics (Table 6.3) and additional trachytope parameters were set to default values (Table 6.7). Using nine parameters, a sensitivity analysis was undertaken using the 1.5 m grid to determine the sensitive parameters and general influence on the modeled depth and velocity. Once this was accomplished, the best parameters were applied and tuned until optimal results were achieved for both the 1.5 m and 2.5 m grids. This was conducted separately for the moderate- and pool-reach sections. To determine the performance of each model, the aDcp data were divided into upstream and downstream of the lupin-mesh, which

provided greater insight into the lupin-altered conveyance and the model's ability to replicate such conditions.

Table 6.7: Initial values of the nine trachytope parameters tested during vegetation sensitivity analysis.

Variable	Description	Initial values
Baptist 2 parameters		
h_v	Vegetation height (m)	0.49
n	Stems density x stem diameter (1/m)	0.51
C_D	Vegetation drag coefficient (-)	0.75
C_b	Real bed roughness (-); *H* is local water depth $C_b = 18^{10}\log\left(\frac{12H}{k_s}\right)$	27.6
General trachytope parameters		
Area Fraction	Percentage of gridcell with vegetation	1
TrtDt	Time step of roughness and resistance updating (minutes)	1
TrtClu	Trachytope calibration factor (u-direction)	1 (uniform)
TrtClv	Trachytope calibration factor (v-direction)	1 (uniform)
TrtMnH	Min. water depth in roughness computation (m)	0.1

6.4.3.3 Results and discussion

Using the 1.5 m grid and the aDcp data of the pool-reach section, the sensitivity analysis determined that the only parameter to influence the depth and velocity conditions was the trachytope calibration factor (TrtClu and TrtClv). All other parameters showed little to no influence, and while the mean error occasionally changed by one centimeter, the remaining residual errors were unchanged. Therefore, full results of the sensitivity analysis will not be discussed, but are tabulated in Appendix E.6. The trachytope calibration factor did show considerable sensitivity (Table 6.8). As shown, the factor value of 1 was the default value and produced the same results as the remaining parameter testing of Appendix E.6. Reducing the value to 0.1 effectively reduced the trachytopes influence, and similarly increasing the value

magnified the influence. As shown, the increase from 1 to 100 had minimal influence on the depth errors, but greater influence on velocity; however, the increase from 100 to 1000 had significant influence on both the depth and the velocity. As expected and desired, the trachytopes only significantly influenced the upstream flow data.

Table 6.8: Trachytope calibration factor values and simulated results for the pool-reach and corresponding upstream and downstream aDcp data. Additional parameters were held constant (h_v = 0.49, n=0.51, C_D = 0.75, and C_b = 27.6, Area Frac = 0.3, Dt =1, and TrtMnh = 0.1).

	TrtClu & TrtClv	0.1		1		100		1000	
		Up	**Down**	**Up**	**Down**	**Up**	**Down**	**Up**	**Down**
Depth	ME	-0.03	-0.01	-0.02	0.01	-0.01	0.01	0.24	0.00
	MAE	0.06	0.09	0.06	0.10	0.06	0.10	0.24	0.10
	RMSE	0.07	0.11	0.08	0.11	0.07	0.11	0.25	0.11
	SDE	0.07	0.11	0.07	0.11	0.07	0.11	0.08	0.11
	Max	0.13	0.27	0.14	0.27	0.15	0.27	0.41	0.27
	Min	-0.33	-0.33	-0.33	-0.22	-0.32	-0.22	-0.03	-0.24
Velocity	ME	0.00	0.01	-0.01	0.01	-0.01	0.01	-0.16	0.01
	MAE	0.12	0.10	0.12	0.10	0.12	0.09	0.19	0.10
	RMSE	0.16	0.11	0.15	0.11	0.16	0.11	0.23	0.11
	SDE	0.16	0.11	0.15	0.11	0.16	0.11	0.17	0.11
	Max	0.33	0.17	0.27	0.17	0.31	0.15	0.14	0.15
	Min	-0.38	-0.30	-0.38	-0.30	-0.39	-0.30	-0.57	-0.35

Without multiple parameters to calibrate the trachytope performance, calibration became simplistic and the trachytope capability became limited. For example, without the vegetation height (h_v) having sensitivity, the ability for the trachytope to behave differently in submerged and emergent vegetation was effectively void. Since the vegetation of the moderate-reach section had emergent lupins, and the pool-reach section had submerged lupins, it was hoped to establish a numerical difference between the two flow conditions. This limitation forced the calibration to compromise optimal results for the two flow conditions of submerged and emergent vegetation. With this limitation in mind, and only the calibration factor to alter the trachytopes, the hydraulic parameters previously calibrated were re-tested in an effort to produce optimal results.

Testing the 1.5 m grid with various trachytope calibration factors, bed roughness, viscosity, and diffusivity were re-tested on the moderate- and pool-reaches with the best results given in Table 6.9 and Table 6.10, respectively. Results showed that the previously determined k_s of 0.21 m still produced the best results for the 1.5 m grid and was not altered. However, altering the viscosity for the pool-reach caused slight modification in the upstream and downstream results, with higher viscosities producing closer depth results for upstream and downstream, and increased the gap between upstream and downstream velocity. However, the moderate-reach results did not fully mimic this relationship. Therefore, bed roughness and viscosity values previously determined remained the best choice, and only the trachytope calibration factor was adjusted. Similar results (Table 6.11 and Table 6.12) for the 2.5 m grid determined the k_s of 0.35 m remained the best representation and viscosities were adjusted with minimal results.

In determining optimal trachytope calibration factors, priority was given to the upstream data. This was considered appropriate because: i) the upstream data was more representative of the vegetation-altered hydraulics, ii) as shown in Table 6.8, the trachytope does not significantly alter the downstream flow, and iii) downstream flow will eventually return to equilibrium; therefore, it is of little importance in trachytope calibration. With priority given to the upstream data, results determined the optimal trachytope calibration factor of 10 for both the moderate- and pool-reaches using the 1.5 m and 2.5 m grids. This was chosen for both grids based on the slightly improved results of both the pool-reach and moderate-reach data. Therefore, the final parameter settings were left at the initial settings of Table 6.7, with the exception that the calibration factor was set to 10.

Table 6.9: Trachytope calibration results of the pool-reach with 1.5 m grid.

	k_s	0.21		0.21		0.21		0.21		0.21		0.21	
	v_H	0.1		0.2		0.3		0.1		0.15		0.2	
	TrtClu & v	0.1		0.1		0.1		10		10		10	
		Up	**Down**	**Up**	**Down**	**Up**	**Down**	**Up**	**Down**	**Up**	**Down**	**Up**	**Down**
Depth	ME	-0.03	-0.01	-0.02	0.01	-0.01	0.01	-0.03	0.00	-0.02	-0.01	-0.02	0.01
	MAE	0.06	0.09	0.06	0.10	0.06	0.10	0.06	0.10	0.06	0.09	0.06	0.10
	RMSE	0.07	0.11	0.07	0.11	0.07	0.11	0.07	0.11	0.07	0.11	0.07	0.11
	SDE	0.07	0.11	0.07	0.11	0.07	0.11	0.07	0.11	0.07	0.11	0.07	0.11
	Max	0.13	0.27	0.14	0.27	0.14	0.27	0.13	0.26	0.14	0.27	0.14	0.27
	Min	-0.33	-0.33	-0.32	-0.22	-0.32	-0.22	-0.33	-0.23	-0.32	-0.33	-0.32	-0.22
Velocity	ME	0.00	0.01	-0.02	0.01	-0.03	0.01	0.00	0.01	-0.01	0.01	-0.02	0.01
	MAE	0.12	0.10	0.12	0.10	0.12	0.10	0.12	0.10	0.12	0.10	0.12	0.10
	RMSE	0.16	0.11	0.15	0.11	0.15	0.11	0.16	0.11	0.15	0.11	0.15	0.11
	SDE	0.16	0.11	0.15	0.11	0.15	0.11	0.16	0.11	0.15	0.11	0.15	0.11
	Max	0.33	0.17	0.26	0.17	0.23	0.16	0.34	0.17	0.29	0.17	0.26	0.16
	Min	-0.38	-0.30	-0.39	-0.31	-0.39	-0.31	-0.37	-0.29	-0.39	-0.30	-0.39	-0.31

Table 6.10: Trachytope calibration results of the moderate-reach using 1.5 m grid.

	k_s	0.21		0.21		0.21		0.21		0.21	
	v_H	0.1		0.3		0.1		0.15		0.3	
	TrtClu & v	0.1		0.1		10		10		10	
		Up	**Down**	**Up**	**Down**	**Up**	**Down**	**Up**	**Down**	**Up**	**Down**
Depth	ME	-0.06	-0.05	-0.04	-0.03	-0.04	-0.05	-0.03	-0.05	-0.02	-0.04
	MAE	0.07	0.07	0.06	0.06	0.07	0.07	0.06	0.07	0.06	0.07
	RMSE	0.09	0.09	0.08	0.08	0.08	0.09	0.07	0.09	0.07	0.08
	SDE	0.07	0.08	0.07	0.07	0.07	0.07	0.07	0.07	0.07	0.08
	Max	0.09	0.14	0.10	0.15	0.10	0.14	0.11	0.14	0.12	0.15
	Min	-0.24	-0.28	-0.22	-0.27	-0.21	-0.28	-0.21	-0.28	-0.20	-0.27
Velocity	ME	0.03	0.02	0.02	-0.01	0.00	0.02	0.00	0.01	-0.01	-0.01
	MAE	0.16	0.11	0.16	0.11	0.17	0.11	0.15	0.11	0.15	0.11
	RMSE	0.19	0.15	0.19	0.14	0.20	0.14	0.18	0.14	0.18	0.14
	SDE	0.19	0.14	0.20	0.15	0.20	0.14	0.19	0.15	0.19	0.15
	Max	0.38	0.31	0.40	0.26	0.39	0.31	0.38	0.29	0.37	0.26
	Min	-0.26	-0.41	-0.26	-0.45	-0.28	-0.41	-0.26	-0.42	-0.26	-0.45

Table 6.11: Trachytope calibration results of the pool-reach with 2.5 m grid.

	k_s	0.35		0.35		0.35		0.35	
	V_H	0.15		0.25		0.15		0.25	
	TrtClu & v	0.10		0.10		10.0		10.0	
		Up	**Down**	**Up**	**Down**	**Up**	**Down**	**Up**	**Down**
Depth	ME	-0.02	-0.06	-0.02	-0.07	-0.01	-0.06	-0.02	-0.07
	MAE	0.10	0.12	0.10	0.12	0.10	0.12	0.10	0.12
	RMSE	0.11	0.15	0.11	0.15	0.11	0.15	0.11	0.15
	SDE	0.11	0.14	0.11	0.14	0.11	0.14	0.11	0.14
	Max	0.23	0.21	0.22	0.20	0.23	0.21	0.22	0.20
	Min	-0.29	-0.38	-0.30	-0.39	-0.29	-0.38	-0.30	-0.39
Velocity	ME	-0.01	0.02	-0.01	0.02	-0.01	0.02	0.00	0.02
	MAE	0.17	0.09	0.18	0.09	0.17	0.09	0.17	0.09
	RMSE	0.23	0.10	0.23	0.10	0.23	0.11	0.23	0.10
	SDE	0.23	0.10	0.24	0.10	0.23	0.10	0.24	0.10
	Max	0.72	0.17	0.73	0.17	0.71	0.17	0.72	0.17
	Min	-0.45	-0.30	-0.46	-0.31	-0.46	-0.30	-0.45	-0.30

Table 6.12: Trachytope calibration results of the moderate-reach with 2.5 m grid.

	k_s	0.35		0.35		0.35		0.35	
	V_H	0.15		0.25		0.15		0.25	
	TrtClu & v	0.1		0.1		10		10	
		Up	**Down**	**Up**	**Down**	**Up**	**Down**	**Up**	**Down**
Depth	ME	-0.01	-0.04	-0.01	-0.04	0.00	-0.04	0.01	-0.04
	MAE	0.06	0.06	0.06	0.06	0.06	0.06	0.06	0.06
	RMSE	0.07	0.08	0.08	0.08	0.07	0.08	0.07	0.08
	SDE	0.07	0.07	0.07	0.07	0.07	0.07	0.07	0.07
	Max	0.13	0.12	0.13	0.13	0.15	0.13	0.15	0.14
	Min	-0.25	-0.24	-0.24	-0.23	-0.23	-0.24	-0.23	-0.23
Velocity	ME	-0.02	-0.02	-0.03	-0.04	-0.01	-0.03	-0.02	-0.04
	MAE	0.18	0.12	0.18	0.12	0.18	0.12	0.18	0.12
	RMSE	0.22	0.14	0.22	0.15	0.22	0.14	0.22	0.15
	SDE	0.22	0.14	0.22	0.14	0.22	0.14	0.22	0.14
	Max	0.45	0.19	-0.41	0.19	0.43	0.19	0.42	0.19
	Min	-0.33	-0.41	-0.31	-0.43	-0.31	-0.43	-0.32	-0.43

As a final measure of trachytope calibration and trachytope effectiveness, the aDcp depth and velocity data with the lupin-mesh were compared to simulations with and without the inclusion of trachytopes. Focused on the upstream data, the 1.5 m grid shows the pool-reach had mixed results (Table 6.13), but in general the residual errors showed slight improvement with the trachytope inclusion. The moderate-reach showed greater improvement with both the depth and velocity showing more accurate mean errors (+3%) and improved RMSE. However, the moderate-reach SDE showed no change for the velocity. The 2.5 m grid results (Table 6.14) with trachytope inclusion show slight general improvement in the pool-reach's depth and velocity errors. However, the mean error of the moderate-reach's velocity was improved (+6%). Comparing the no trachytope results of the 1.5 m and 2.5 m grid revealed that the 2.5 m grid typically produced improved results without trachytope inclusion; thus, less room to improve. The cause of this was not entirely clear, but it was speculated that the increased k_s value of the 2.5 m grid may have influenced this result. As trachytopes alter the bed roughness, the increased bed roughness of the 2.5 m grid may have increased the vegetation simulation accuracy without trachytopes. Further, the larger grid size and less bathymetric detail may have caused the depth and velocity to be more homogenous.

Results for both grid sizes indicated that the trachytope inclusion did not significantly improve the hydraulic depth and velocity precision; instead, the errors were merely shifted and provided more accurate mean errors. Regardless, both simulated grids slightly improved from including the trachytopes. Considering the slight differences in measured depth (0.04 m) and velocity (0.03 m/s) with and without the lupin-mesh and only one sensitive parameter, the results demonstrated that a successful calibration was achieved.

Table 6.13: Flow simulation results of lupin mesh aDcp data and the use of trachytopes using 1.5 m grid (errors in meters).

		Pool-reach				Moderate-reach			
		No Trachytope		Trachytope		No Trachytope		Trachytope	
		Up	Down	Up	Down	Up	Down	Up	Down
Depth	ME	-0.02	0.00	-0.02	-0.01	-0.06	-0.06	-0.03	-0.05
	MAE	0.07	0.09	0.06	0.09	0.07	0.08	0.06	0.07
	RMSE	0.08	0.11	0.07	0.11	0.10	0.11	0.07	0.09
	SDE	0.08	0.11	0.07	0.11	0.08	0.09	0.07	0.07
	Max	0.16	0.28	0.14	0.27	0.09	0.14	0.11	0.14
	Min	-0.35	-0.23	-0.32	-0.33	-0.46	-0.40	-0.21	-0.28
Velocity	ME	-0.04	0.01	-0.01	0.01	0.03	0.00	0.00	0.01
	MAE	0.11	0.10	0.12	0.10	0.16	0.12	0.15	0.11
	RMSE	0.15	0.11	0.15	0.11	0.19	0.16	0.18	0.14
	SDE	0.14	0.11	0.15	0.11	0.19	0.16	0.19	0.15
	Max	0.25	0.17	0.29	0.17	0.38	0.31	0.38	0.29
	Min	-0.38	-0.36	-0.39	-0.30	-0.26	-0.47	-0.26	-0.42

Table 6.14: Flow simulation results of lupin mesh aDcp data and the use of trachytopes using 2.5 m grid (errors in meters)..

		Pool-reach				Moderate-reach			
		No Trachytope		Trachytope		No Trachytope		Trachytope	
		Up	Down	Up	Down	Up	Down	Up	Down
Depth	ME	-0.02	-0.07	-0.01	-0.06	-0.01	-0.04	0.01	-0.04
	MAE	0.10	0.12	0.10	0.12	0.06	0.06	0.06	0.06
	RMSE	0.12	0.15	0.11	0.15	0.07	0.08	0.07	0.08
	SDE	0.11	0.13	0.11	0.14	0.07	0.07	0.07	0.07
	Max	0.21	0.20	0.23	0.21	0.11	0.13	0.15	0.13
	Min	-0.31	-0.39	-0.29	-0.38	-0.26	-0.24	-0.23	-0.24
Velocity	ME	0.01	0.02	-0.01	0.02	0.07	-0.03	-0.01	-0.03
	MAE	0.17	0.10	0.17	0.09	0.18	0.12	0.18	0.12
	RMSE	0.24	0.11	0.23	0.11	0.23	0.14	0.22	0.14
	SDE	0.24	0.11	0.23	0.10	0.22	0.14	0.22	0.14
	Max	0.74	0.18	0.71	0.17	0.52	0.19	0.43	0.19
	Min	-0.43	-0.30	-0.46	-0.30	-0.27	-0.42	-0.31	-0.43

6.4.4 Morphology

6.4.4.1 Introduction

Due to the model calibration progression from hydraulic, to vegetation, and finally to morphologic, the final parameterizations of the precursor models were included into the morphological calibration efforts. Due to the previous calibration efforts, realistic hydraulic conditions were achieved in model simulations for both the 1.5 m and 2.5 m grids. Generally, the 1.5 m grid produced slightly better performance; however, the 2.5 m grid offered considerably less simulation time (reduced by factor of 4) and increased model stability. Therefore, due to the morphological model's numerous parameters requiring evaluation and the added complexity (mobile bed with numerous sediment layers), only the 2.5 m grid was utilized.

Enabling the sediment transport and bank erosion in Delft3D allows the model to simulate morphological changes. At a minimum, the user must supply sediment data (median sediment diameter(s), specific density, dry bed density, initial sediment thickness), supply desired morphology characteristics (bathymetric updating, sediment effect on fluid density, sediment concentration entering the system, etc.), and select the desired sediment transport formula. In addition to these settings, numerous parameters are also available for bed slope, morphological acceleration, and many more. Therefore, to determine the best morphological representation, the 2.5 m grid was utilized to provide an initial sensitivity analysis using a (meso-) 500 m reach that experienced extensive morphological change during the October 2011 flood event.

Once parameter sensitivity and functionality were determined, the (macro-) full-reach morphology was simulated with various parameter settings and compared to the available DoD (Section 5.2.3). As mentioned in Section 6.2, morphological simulations are hampered by inaccurate representation of bank erosion; therefore, while it was ideal to recreate identical morphological changes, the expectation was to produce a model that best represented lupin mortality processes. To keep the model fit for the purpose of vegetation impacts, the morphological model was optimized to reproduce observed bank erosion, sediment deposition, and total transport for trauma purposes.

6.4.4.2 Methods

To identify sensitive parameters and their functionality, a sensitivity analysis was performed for the parameters identified by Williams, Measures, Hicks, and Brasington (2012b) and Hasselaar (2012). Parameters and values tested are shown in Table 6.15 and were easily manipulated in the model; however, the various sediment compositions were developed (Appendix D.4) using the sediment data collected. To process the sensitivity analysis in a timely manner, a 500 m reach of the main channel (within the study-reach) was utilized in simulations. This reach was chosen for the complex morphology and extensive bank erosion and channel morphologic changes that occurred during the October flood event. Initial sensitivity simulations lasted three hours with discharge increasing linearly from 13 to 75 m^3 s^{-1} with the primary focus to determine parameter sensitivity; thus, a simple hydrograph was considered adequate. In total, 25 simulations were tested and generated into DoD's by differencing the evolved and starting (original) topography with Geomorphic Change Detection software. This process was identical to Section 5.2.3.3; however, terrain uncertainty was not included in the DoD production, as all changes were model generated. Using the DoD and corresponding sediment volumetric changes, qualitative analysis was performed to determine the various parameters' sensitivity.

Table 6.15: Morphological calibration parameters and values tested (bold values were the baseline values).

Parameter	Values tested (**Baseline**)
Bed composition	
Active layer thickness (m)	(**0.25**), 0.1, 0.5
Base layer thickness (m)	(**2**), 0.1, 0.25, 0.5
Sediment composition	(**2 phi interval**), 1 phi interval, and Sand-gravel-cobbles
Bank erosion	
ThetSd	(**0**) 0.1, 0.5, 0.9
Repose	(**0.4**), 0.1, 1
Bed material transport	
Bedload transport component	(**Central**), Upwind
Transport formulas	(**Gaueman et al.**), Meyer-Peter-Muller, Wilcock and Crowe, and Modified Wilcock and Crowe
Transport calculations	
Morphology factor, (MorFac)	(**1**), 2.5, 10
Bed slope effects (**not included in baseline**)	
Longitudinal bed gradient factor (AlfaBs)	0.1, 1, 10
Transverse bed gradient factor (AlfaBn)	0.1, 1.5, 10

Following sensitivity analysis, the pre-flood full-reach topography was utilized with the October 2011 flood hydrograph, and parameterization attempted to replicate the observed morphologic changes of the DoD (Section 5.2.3.3). In order to maintain consistency between model calibration and future forecasting, flood-duration relationships were bound by the FRE3 (3 x the median flow) discharge of 58 m^3 s^{-1} (Section 4.2.2). Therefore, it was imperative that the simulated October 2011 flood event adhere to these standards. Bound by the FRE3 restrictions, the flood duration lasted approximately 41.5 hours, with the peak discharge of 209 m^3 s^{-1} at 13.5 hours. However, a 41-hour simulation period was time consuming for calibration efforts; therefore, the hydrograph was condensed to produce the same flood in 21 hours. Due to the condensed hydrograph and shorter simulation, the morphological acceleration factor (MorFac) was tested to ensure representative changes occurred. In total, 77 simulations were tested with varying settings and examined to identify the best morphological representation of the October flood event.

To test the simulated morphological performance, both qualitative and quantitative methods were applied. The first step in model evaluation was through visual observation of where the simulated morphologic change occurred compared to the observed changes in the study-reach. This was initially viewed and evaluated in Delft3D's Quickplot, which provided a simple method to view the simulated water depth, depth-averaged velocity, and total sediment transport at various time-steps throughout the simulation. Since Quickplot does not specifically identify morphologic changes, morphologic changes were identified by comparing depth changes and channel position for the various time-steps. This preliminary method was sufficient as numerous simulations generated obvious undesirable results (Sutherland, Peet, & Soulsby, 2004). If the simulation results were free of severe discrepancies, the data were further developed into a DoD using ArcGIS and GCD software, and was qualitatively compared to the observed DoD. However, as calibration progressed and model performance increased, quantitative comparisons were required. Therefore, two methods were used to determine optimal parameterization. The first method to quantify the morphological performance was to compare the bias, accuracy, and skill of the model (Sutherland et al., 2004). The bias was calculated by taking the mean error of simulated and observed data, and provides a measure of the models central tendency. The accuracy was assessed using the mean absolute error and provides a measure of the average difference between the simulated and observed results. Finally, the skill was similar to the accuracy, but provides a non-dimensional measure of how well a model performs relative to the baseline model (using the mean absolute error), with positive values indicating better performance, and vice versa. Together, the bias, accuracy, and skill quantitative method are hereafter referred to as the *Sutherland method*.

Due to the small morphological changes that occurred in most areas, spatial residual statistics provided from the bias and accuracy of the Sutherland method produced elevation errors in the decimeter range. With seemingly low errors generated, this had the potential to imply the model's performance was better than actual. Therefore, a second method was developed to quantify the fit between simulated morphologic processes and the observed erosion and deposition processes. This method builds from the categorical assessment of Sutherland et al. (2004) as well as the congruent fit (Egn 6.4) in the hydraulic calibration section. Essentially, this method separates the simulated morphological processes into the categories of erosion, deposition, and no simulated change (void), and directly compares occurrence to the areas of

observed erosion and deposition. Thus, by calculating the areas of accurate, inaccurate, and void predictions, an assessment was provided of how well the simulation predicts local processes. This method was hereafter referred to as the *MOR_{fit} method*.

Once the parameterization was refined through the preliminary qualitative assessment, Sutherland results, and MOR_{fit} results, a full qualitative analysis was conducted to assess the overall quality of the simulated results and calibration. The majority of the results and discussion was centered on the study-reach, as the objective of the calibration was to maximize the morphological performance of the study-reach. However, it was recognized that proper morphological rendering of the study-reach was dependent upon the upstream morphology. Therefore, full-reach performance was considered throughout the process, but was only fully discussed for the final model.

6.4.4.3 Results and discussion

Sensitivity analysis

The sensitivity analysis determined that all parameters tested (Table 6.15) except ThetSd provided measureable and noticeable changes. Due to the numerous simulations and large quantity of figures and results, all sensitivity results are documented in Appendix E.7. Evaluating the results, both active and base sediment layers revealed that increasing the layer thickness produced increased total sediment transport and net erosion. However, visual inspection of both the active and base layer thickness indicate this variable appeared to have no influence on morphology patterns. Assessing the sediment composition revealed mixed results for the total erosion and deposition volumes. However, morphology patterns and net volume differences between the simulations were near identical. This result was surprising, given that the simplified, three component sand-gravel-cobbles (SGC) sediment composition performed essentially the same as the more detailed one-phi interval composition in both morphology pattern and total volumetric difference. The bank erosion parameter repose showed significant sensitivity in both observable and statistical results. Increasing the repose value from 0.1 to 1 clearly reduced the total bank erosion as well as total transport. However, repose is a function of bank slope and does not require the bank erosion to take place in wetted cells. As shown in Figure E.15, the repose of 0.1 had significant deposition along the southern bank, which was not caused by fluvial erosion. While this result taints the statistics

of this particular simulation, this occurrence demonstrates the limitations of repose as well as the simulated topography that one must consider.

The bedload transport conditions using the central and upwind numerical schemes produced similar erosion statistics, but the upwind scheme had slightly higher deposition statistics and less total net volume difference. Examining the morphology pattern showed slight variations in channel morphology; thus, additional full-reach calibration testing was required to determine optimal morphology patterns. Transport formulas showed significant differences in total sediment transport statistics as well as morphology patterns. In order of decreasing sediment transport, the four formulas were ordered as: Meyer-Peter-Muller, Gaueman et al., Wilcock and Crowe, and Modified Wilcock and Crowe. All formulas produced negative net sediment volume difference except the Modified Wilcock and Crowe, which determined zero net difference. Of the formulas, Meyer-Peter-Muller and Gaueman et al. appeared to induce the greatest bank erosion. The morphology acceleration factor, *MorFac,* did accelerate changes in both the bed and bank morphology. However, the factor did not produce linear results. For example, increasing the factor by 10 increased the erosion and deposition by nearly a factor of two. The net differences however, remained nearly constant between the two simulations. Interestingly, the factor of 2.5 produced a larger negative net difference, which indicated that the similar net difference between the factor of 1 and 10 was a coincidence. Examining the longitudinal (AlfaBs) and transverse (AlfaBn) bed slope gradient factors revealed that increasing these values produced slightly greater volume eroded and decreased the volume deposited, thus increasing the values generated greater channel degradation. Visual inspection revealed that increased AlfaBs caused deeper and narrower channels. Conversely, increased AlfaBn caused wider channels with more uniform depth.

Full-reach modeling

The sensitivity analysis provided insight into parameter function and useful starting values for the full-reach model. Based on this analysis, the full-reach model would utilize the SGC sediment composition, as it produced near identical results to the more complex composition with the benefit of substantially reducing simulation time and increasing model stability. Further, only Repose would be utilized to model bank erosion. Despite this progression in model development, optimal settings for all parameters were not determined; thus, additional

testing was performed for transport components (upwind and central), transport formula, and bed slope parameters. Of the 77 simulations, only 33 were developed into DoDs based on the initial examination with Quickplot. While the remaining 44 were qualitatively determined undesirable, they provided valuable insight and shaped the parameterization process by limiting the available options. Due to the extensive results, a full presentation of the calibration is not presented or discussed as this would be a cumbersome and unnecessary process. Instead, the results and figures are presented in Appendix E.8, and the discussion below focusses on the general findings that led to the final parameter settings.

Since the simulated hydrograph was condensed by a factor of two, the first calibration focus was on the MorFac parameter to ensure that adequate morphological changes occurred. Therefore, MorFac values of 1, 2, and 3 were tested. To determine adequate MorFac values, the observed sediment volumetric change was compared with the simulation results; however, it must be considered that the observed results utilized the uncertainty of the terrain surfaces, and therefore only provide an approximation. Testing revealed that MorFac = 1 produced comparable volumetric change statistics and was the initial choice (Figure E.21).

The second calibration focused on three sediment transport formulas: Gaueman et al., Meyer-Peter-Muller, and Wilcock and Crowe. However, these results were only qualitatively assessed because Gaueman et al. was the obvious best choice due to morphological accuracy and model stability. Meyer-Peter-Muller was not evaluated further as the morphology changes caused anabranches in the study-reach to turn into the main channel. Wilcock and Crowe was disregarded as it only simulated minor morphological changes (Figure E.22) as well as drastically decreased model stability (Wilcock and Crowe produced 1137 warnings, a 50% increase over Gaueman et al.). Modified Wilcock and Crowe was not considered due to the substantially under-predicted sediment transport during the sensitivity analysis.

The third calibration focus was on the bed component schemes. Using the Gaueman et al. transport formula, both the upwind and central schemes were tested (Figure E.23). While both show similar agreement with the general observed morphology, the central scheme was chosen as it outperformed the upwind scheme in several areas. For example, the upwind

scheme inaccurately produced occasional deposition along the river banks as well as channel erosion where deposition was observed (highlighted areas in Figure E.23a).

Repose was the fourth calibration focus, and values of 0.2, 0.3, and 0.4 were tested. Results revealed that a repose value of 0.2 produced exaggerated bank erosion along all banks, while a repose value of 0.4 grossly under-predicted bank erosion in critical areas (Figure E.24). Therefore, 0.3 was initially chosen as a compromise. Additional testing was conducted on MorFac, AlfaBs, AlfaBn, and an altered SGC sediment composition in an attempt to increase the bank erosion accuracy. Of the tested parameters, MorFac, AlfaBn, and altered sediment compositions did increase bank erosion. Testing various altered SGC sediment compositions showed that increased total sand content naturally increased bank erosion, but produced undesirable channel morphology. Conversely, decreasing the sediment composition's sand content caused less bank erosion, but also slightly improved channel morphology and model stability. Therefore, based on these qualitative results, parameter settings had been narrowed and additional calibration testing continued with slight variations in repose, MorFac, AlfaBn, and sediment composition. Various qualitative testing determined four simulations (Table 6.16) that produced the best results (Figure E.25), and these were further assessed using the Sutherland and MOR_{fit} quantitative methods.

Table 6.16: Parameter settings of the four best (qualitatively determined) simulations.

Simulation	Repose	MorFac	AlfaBn	Sediment composition
v74	0.25	5	1.5	SGC: less sand (-8% active, -1% in base layer)
v75	0.30	3	1.5	SGC - normal
v76	0.30	3	1.2	SGC - normal
v77	0.30	4	1.2	SGC - normal

Using the Sutherland method, and v75 as the baseline model against which others were compared, Table 6.17 shows the results for: i) all areas that experienced morphologic changes (including channel and overland morphology), ii) morphology changes that occurred from overland flow, and iii) the overland morphology that was documented in areas of vegetation mortality (identified using results of Section 5.4). As shown, the all morphology area category had the lowest residual errors, which indicates that the channel morphology was

more accurately simulated than the morphology from overland flow. Further, erosion was simulated with less bias and more accuracy for the 'all morphology' category; however, deposition had better results for the overland flow and vegetation mortality areas. Comparing the models, v74 had the best performance for both all morphology and overland flow morphology areas, and v75 had the best for all and erosion categories of the vegetation mortality areas.

Assessing the four models using the MOR_{fit} method, all morphology results (Table 6.18) show that all models accurately predicted erosion and deposition in approximately 54% of the observed areas. Conversely, inaccurately predicted data of all morphology area shows deposition occurred in approximately 37% of the observed erosion area, and erosion was inaccurately predicted in approximately 28% of observed deposition areas. When comparing the 'all morphology', 'overland flow', and 'vegetation mortality' areas for the specific models, a general trend was revealed across these categories where the accurately predicted erosion increased, the accurately predicted deposition decreased, and less morphology was simulated in total (void area increased). These results indicated that overland flow typically had erosion more accurately predicted than deposition and simulations missed significant areas of observed overland morphologic changes.

Table 6.17: Sutherland method results for various morphology areas and the final four models (errors in meters).

		All			Erosion			Deposition		
		Bias	Accuracy	Skill	Bias	Accuracy	Skill	Bias	Accuracy	Skill
All morphology	v75 (baseline)	0.06	0.30		-0.04	0.30		0.15	0.29	
	v74	0.05	0.27	0.08	-0.01	0.27	0.10	0.09	0.27	0.07
	v76	0.05	0.29	0.03	-0.04	0.29	0.03	0.12	0.28	0.03
	v77	0.05	0.29	0.03	-0.04	0.30	0.02	0.14	0.28	0.04
Overland flow morphology	v75 (baseline)	0.14	0.35		0.35	0.41		-0.22	0.24	
	v74	0.16	0.34	0.03	0.37	0.40	0.02	-0.22	0.23	0.04
	v76	0.16	0.34	0.01	0.37	0.41	0.00	-0.21	0.23	0.04
	v77	0.15	0.35	0.00	0.36	0.41	0.00	-0.21	0.23	0.04
Vegetation mortality morphology	v75 (baseline)	0.43	0.62		0.55	0.66		-0.34	0.34	
	v74	0.55	0.68	-0.11	0.65	0.72	-0.09	-0.32	0.32	0.06
	v76	0.50	0.66	-0.07	0.61	0.74	-0.03	-0.32	0.33	0.03
	v77	0.48	0.66	-0.07	0.59	0.70	-0.06	-0.33	0.33	0.03

Table 6.18: MOR_{fit} method results for various morphology areas and the final four models (percent coverage).

	All morphology		Overland flow		Veg mortality	
	Erosion observed	Deposition observed	Erosion observed	Deposition observed	Erosion observed	Deposition observed
v75 - Baseline						
Erosion	54.2	28.3	56.1	31.8	64.1	49.6
Deposition	37.8	54.6	32.7	34.2	12.8	35.0
Void	8.0	17.1	11.1	34.1	23.1	15.4
v74						
Erosion	54.3	28.6	56.9	33.1	56.4	28.1
Deposition	36.2	53.5	29.5	32.4	12.8	28.4
Void	9.5	17.9	13.7	34.5	30.8	43.4
v76						
Erosion	52.4	29.0	54.2	30.1	58.9	39.4
Deposition	38.8	54.0	32.8	34.9	13.1	29.0
Void	8.8	17.0	13.0	35.0	27.9	31.6
v77						
Erosion	53.6	28.5	54.1	29.6	59.6	37.1
Deposition	37.3	54.5	33.0	35.5	14.0	31.0
Void	9.1	16.9	12.9	34.9	26.4	31.9

Based on the initial qualitative assessments and the results of Tables 6.17 and 6.18, all four models under-predicted local erosion and deposition and over-predicted general erosion and deposition. These results revealed the inability of the morphological model to accurately simulate local morphologic-induced lupin mortality. While these results were discouraging, the model could still provide valuable insight into lupin mortality as long as the erosion and deposition processes were representative of the specific flood event and the resulting morphology was realistic. Therefore, the final assessments were to determine the parameter settings that best generated realistic river characteristics (e.g. pools, riffles, etc.) as well as produced representative erosion and deposition.

Comparing the individual model results of Tables 6.17 and 6.18, the data show that all models perform similarly. With the model's purpose to predict flood-induced lupin mortality and the model's inability to reproduce local conditions, the overland flow areas were treated

as the primary focus. As previously identified, v74 had the best performance for overland flow morphology areas, and v75 had the best for all and erosion categories of the vegetation mortality areas of Table 6.17. Assessing Table 6.18 showed v75 produced the best erosion in vegetation mortality areas and v74 typically produced the lowest inaccuracy results. Therefore, v74 and v75 would be further evaluated using in-depth qualitative and quantitative assessments. The qualitative assessment compared v74 and v75 models DoDs to the observed DoD, as well as evaluating the simulations final bathymetry, bank erosion, overland flow deposition, and general river characteristics.

Guided by the observed morphologic changes, v74 and v75 were assessed qualitatively (Figure 6.7). Comparing v74 to the observed DoD revealed the model's inability to replicate the areas of significant bank erosion (areas a1 and a3 compared to observed areas 2, 3, and 4) and over-predicted bank erosion (areas a4 and a5). Channel erosion was also inaccurately predicted (area a2) and under-predicted the erosion of observed area 1. Comparing the volumetric sediment changes revealed good agreement for both erosion and deposition; however, the observed data's net volume difference had greater reach degradation by 57%. Comparing v75's DoD showed innaccurate channel erosion (area b2), exaggerated bank erosion (b1 and b3), and under-predicted bank erosion of the observed areas 2, 3, and 4. Similar to v74, v75 under-predicted channel and bank erosion in the observed area 1. Comparing the sediment volume change showed that v75 over-predicted the erosion and deposition, and the observed data's net volume difference had greater reach degradation by 68%.

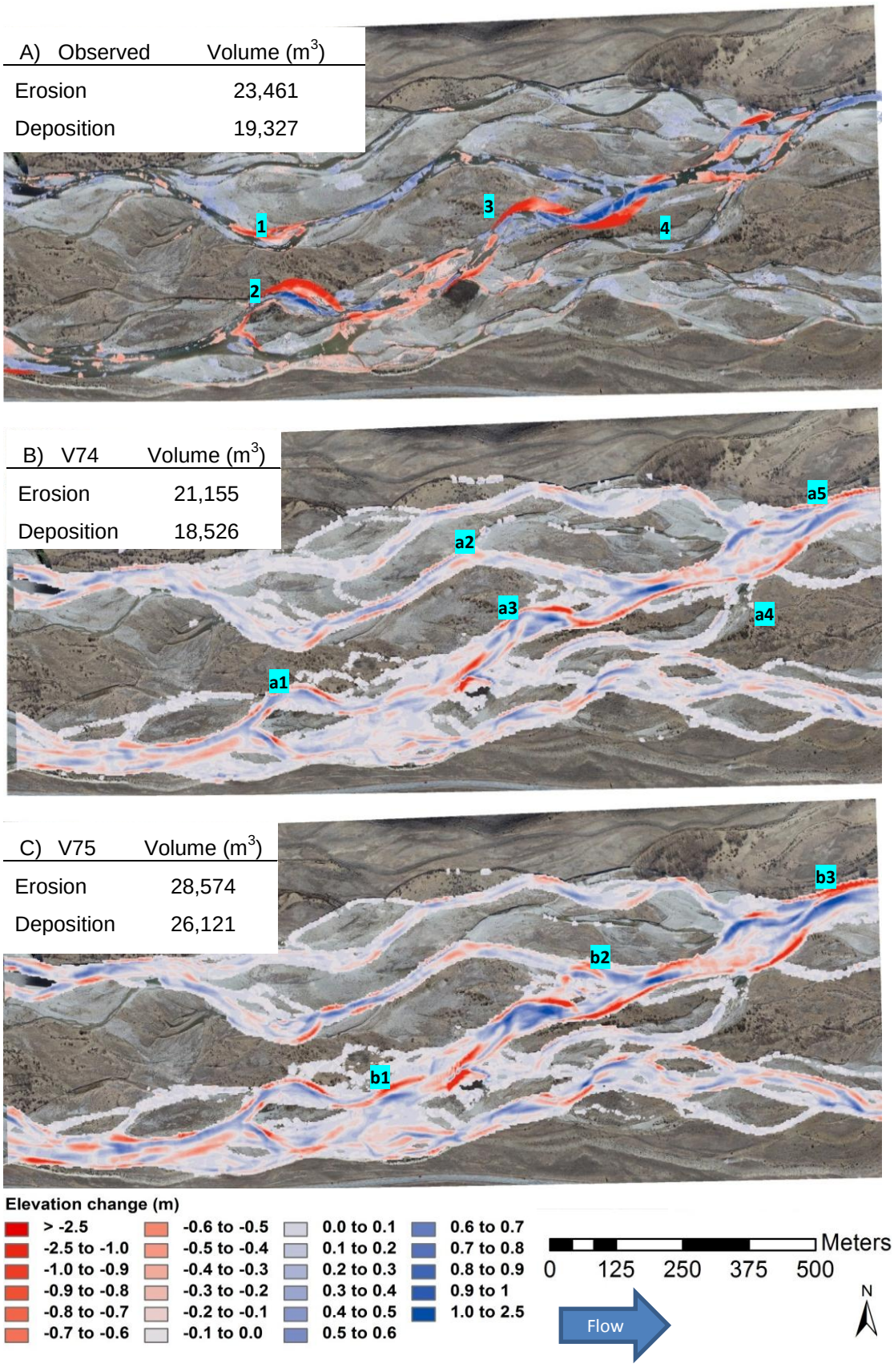

Figure 6.7: Final DoD comparison for A) observed, B) v74, and C) v75.

Comparing the simulated final channel bathymetry to the actual post-flood channel bathymetry provided insight into the model's abilty to replicate the morphological processes as well as provided a method to assess its general ability to represent the complex river characteristics such as pools, riffles, and channel width-depth relationships. Taking the Quickplot water depth animations for the: i) pre-flood, ii) v74 post-flood, iii) v75 post-flood, and iv) observed post-flood simulated at 58 $m^3 s^{-1}$ provided a method to assess the channel bathymetry. Comparing the initial observed and final bathymetry (Figure 6.8a and d, respectively) showed that the anabranch of the true-left floodplain had reduced flow after the flood event. This is also apparent in both the v74 and v75 simulation results (Figures 6.8b and c, respectively, and confirmed using velocity data for v75 in Figures E.28 and E.29). Assessing the model's and observed data, numerous areas show comparable water depths such as where pools occur (v74: c5, c6, v7, c11; v75: d6, d7). However, some areas appear too deep (v74: c1; v75: d5, d12) with other areas appearing too shallow (v74: c9, c10; v75: d10, d11). Both models produced unobserved riffles that appeared as bathymetric gaps in the main channel (v74: c3; v75: d3). The flood event produced minimal bar developments; however, neither model represented this well (v74: c3; v75: d3). Finally, both models produced undesirable symmetric channel width-depth relationships in one particular area (v74: c4; v75: d4), instead of greater depths on the outer-left bank and shallower depths on the inner-right bank. While both simulations have advantages and disadvantates, v74 had a slighltly greater advantage due to its ability to reproduce pools, lack of significant unobserved channel erosion (v75 area b2), and more accurate sediment volume data.

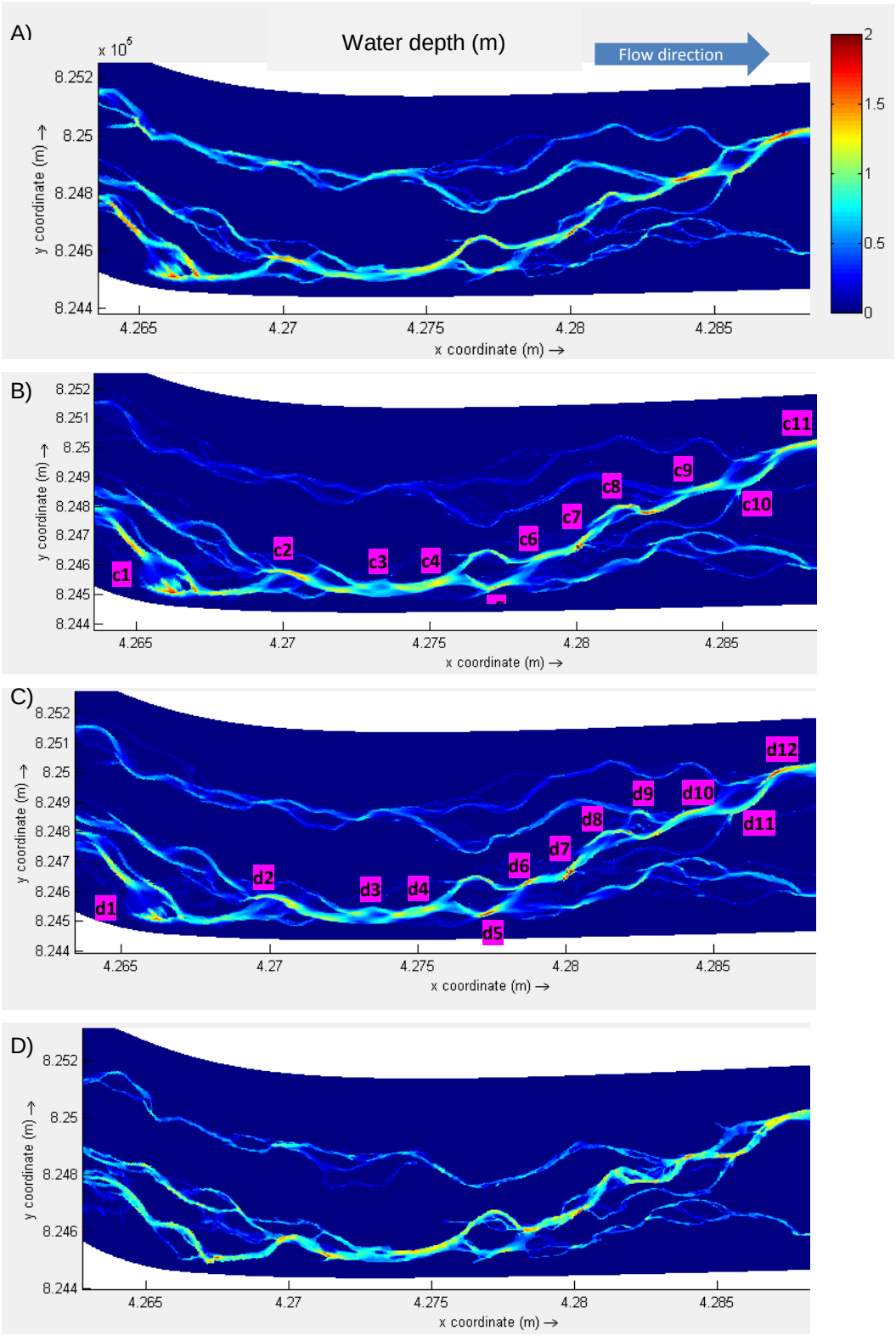

Figure 6.8: Delft3D simulated (58 $m^3 s^{-1}$ discharge) water depth for A) initial bathymetry (pre-flood), B) v74 model flood-evolved bathymetry, C) v75 model flood-evolved bathymetry, and D) actual flood-evolved bathymetry (post-flood).

Evaluation of the model's deposition using two observed braid bar morphological changes revealed the model's inability to replicate general braid bar deposition. As shown in Figure 6.9, deposition occurred at the bar's upstream end (bar-head) and erosion occurred along the true-left side and downstream end. Both v74 and v75 produced slight erosion at the bar-head and failed to produce erosion along the left side. Figure 6.10 revealed a second braid bar developed deposition at the bar-head and along the true-right side and erosion along the true-left yet both v74 and v75 produced bar-top erosion and deposition along the true-left bank. However, both did produce slight deposition along the true-right, with v74 having slightly better performance. These results indicated the model's inability to replicate deposition along instream braid bars. While these results were not critical for determining areas of lupin mortality during smaller flood events, extreme flood events will treat larger islands in a similar manner. Therefore, it was speculated that simulated deposition accuracy would be poorly predicted for extreme events.

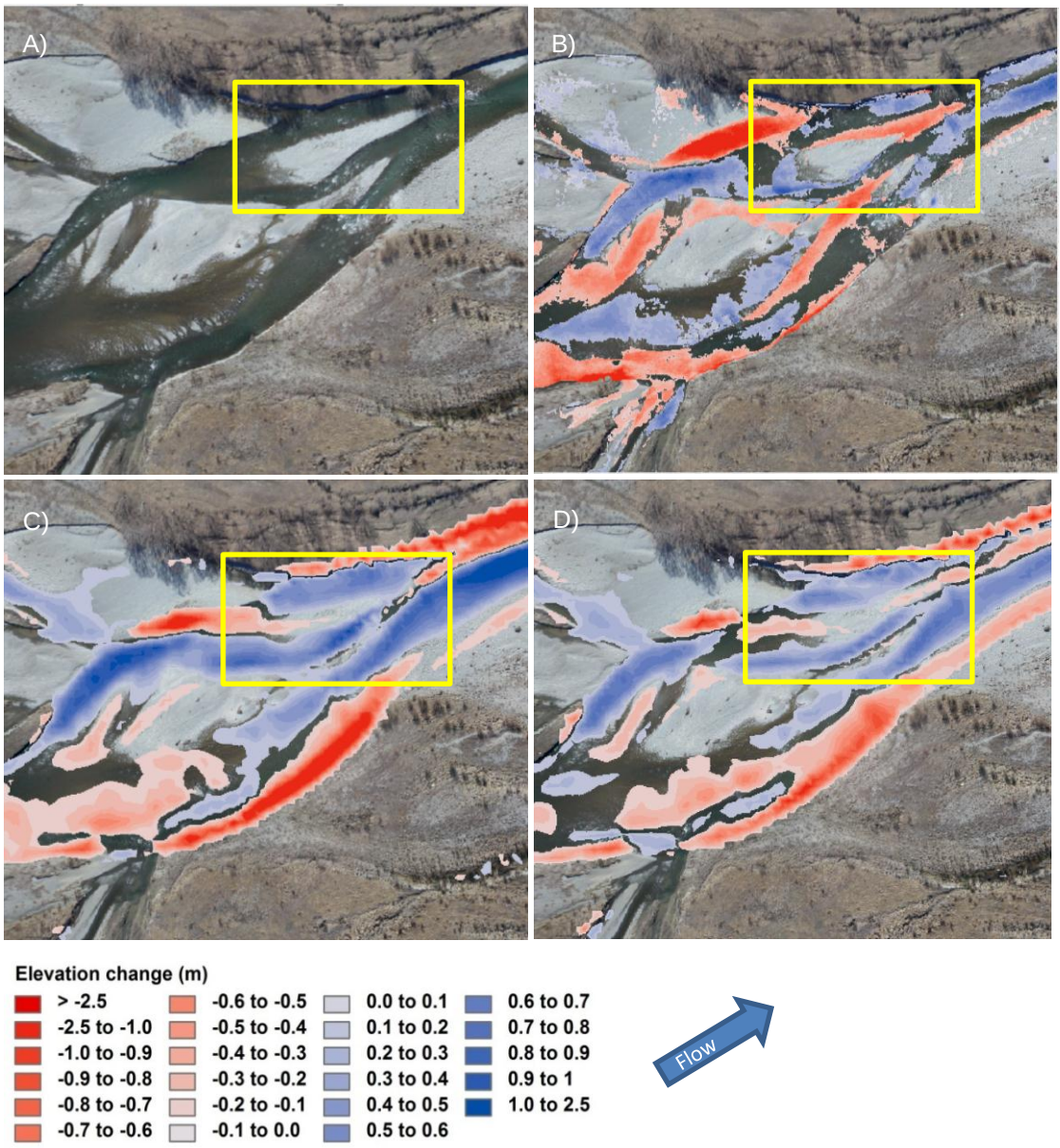

Figure 6.9: Qualitative assessment of the bar-top erosion and deposition: A) area of interest 1, B) observed DoD, C) v75 DoD, and D) v74 DoD.

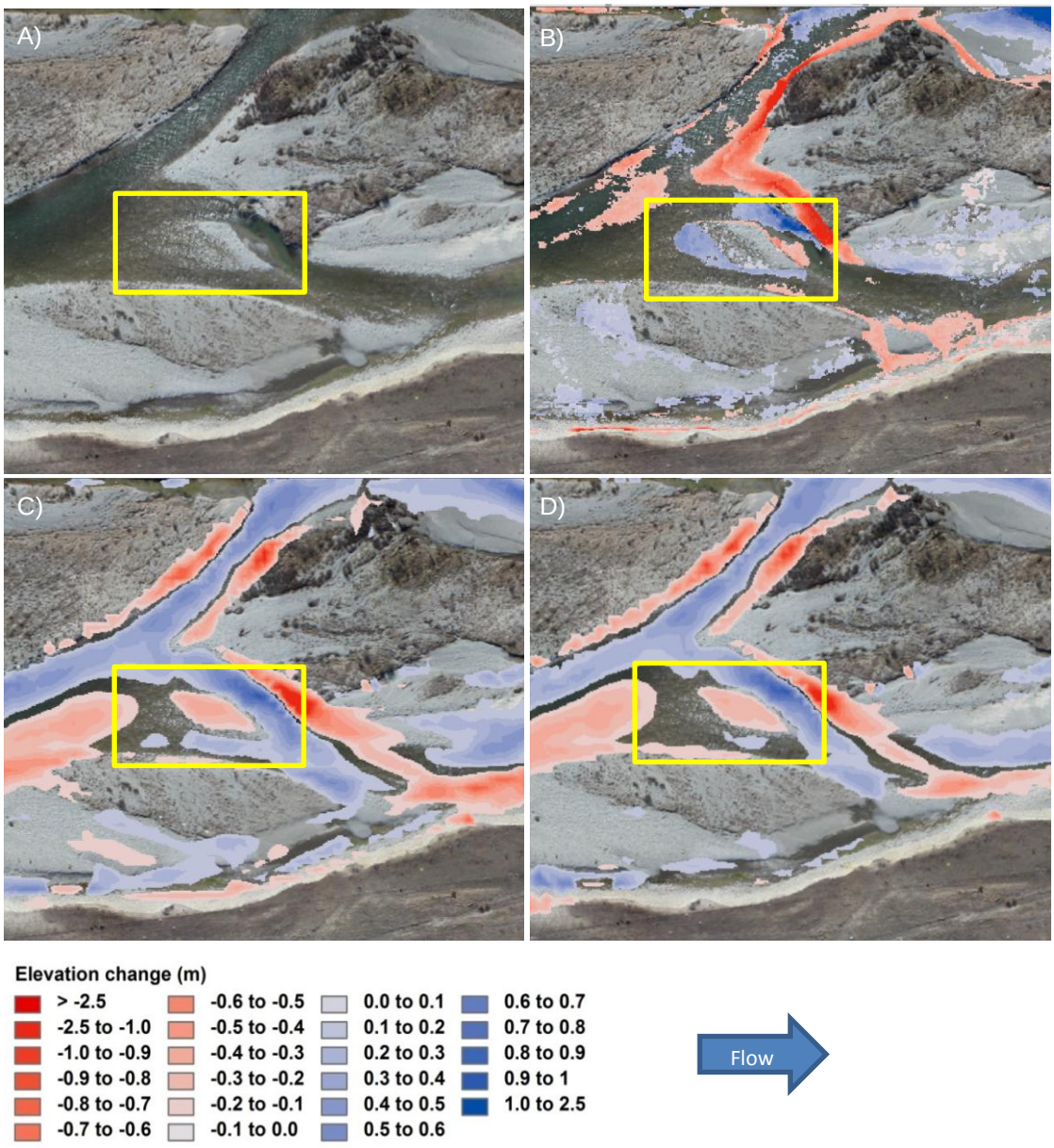

Figure 6.10: Qualitative assessment of the bar-top erosion and deposition: A) area of interest 2, B) observed DoD, C) v75 DoD, and D) v74 DoD.

Final quantitative assessment focused on the total bank erosion and deposition that was simulated. Total bank erosion was mapped and calculated in ArcGIS using the observed, v74, and v75 DoD results. While numerous areas along the river's edge experienced erosion, only areas with obvious banks were considered. Mapped bank erosion only consisted of areas that experienced bank retreat and that showed an obvious bank prior to the October flood event. Results (Table 6.19) revealed that v74 and v75 simulated areal bank erosion with 89.3% and 99.0% agreement to the observed data, respectively.

Table 6.19: Total areal bank erosion for the observed flood event and simulated v74 and v75.

	Bank erosion area (m^2)
Observed DoD	12,272
v74	10,962
v75	12,148

To evaluate total erosion and deposition, additional DoD's were generated that excluded the inundated channel (Figure E.26). By only assessing the initially dry areas of the pre-flood DEM, the morphologic changes that occurred to vegetated areas could be assessed. This was done in ArcGIS by simply removing the wetted channels from the differenced rasters and regenerating the DoDs using GCD software. Results for the observed, v74, and v75 cases are presented in Table 6.20. However, these results were processed slightly differently than the previous simulated DoD's. With lupin-mortality-induced deposition and erosion being the primary concern, the DoD's were assessed for the thresholds identified to induce mortality. As shown in Table 4.13, erosion can greatly affect lupin mortality, and Table 4.19 shows that lupins completely buried with an additional ≥ 2 cm can cause mortality. Therefore, erosion and deposition levels of ≥ 10 cm were evaluated, which reduced the insignificant morphologic changes. Since the observed DoD incorporated the SfM uncertainty, the results represent morphologic changes of differences approximately ≥ 10 cm (due to SfM uncertainty); thus, limiting the simulated DoDs to ≥ 10 cm provided a better comparison to the observed results. Results (Table 6.20) show that the simulated areal extents of erosion far exceeded the observed, while the deposition was comparable, but slightly under-represented. Volume results show both models produce comparable erosion and deposition as well as net difference. Dividing the volume by the area, an average erosion/deposition depth can be calculated and offers a further comparison. As shown, deposition depth for both models compared well to the observed data and both models under-predicted erosion depth by approximately 50%. Comparing the two models, v75 produced better agreement with the observed results for areal deposition and volumetric deposition, as well as average erosion depth yet v74 produced closer net difference and deposition average depth.

Table 6.20: DoD statistics for overland flow erosion and deposition with ≥ 10 cm threshold.

minLoD: Propagated errors

A)		Area (m^2)	Volume (m^3)	Average depth (m)
Observed DoD	Observed			
	Eros.	35,523	18,007	0.51
	Deps.	27,898	5,554	0.20
	Diff.	-	-12,453	-

minLoD: ≥10 cm

B)		Area (m^2)	Volume (m^3)	Average depth (m)
v74 DoD	v74 DoD			
	Eros.	69,387	14,715	0.21
	Deps.	15,260	3,050	0.20
	Diff.	-	-11,665	-
v75 DoD	v75 DoD			
	Eros.	74,537	20,606	0.28
	Deps.	23,154	5,255	0.23
	Diff.	-	-15,351	-

Based on the qualitative and quantitative results, all models struggled to reproduce the observed morphological changes. However, the final models v74 and v75 both produced realistic river characteristics and representative areal and volumetric erosion and deposition. Despite v74's slightly improved bathymetry, increased stability, and generally higher skill, v75 best represents the October 2011 flood event's total areal and volumetric erosion and deposition (based on results of Table 6.19 and 6.20). Thus v75 was considered better suited for the modeling to identify lupin mortality. Final parameterization for v75 is shown in Table 6.21.

Table 6.21: Final morphology parameter values of v75.

Parameter	Values
Bed composition	
Active layer thickness (m)	0.25
Base layer thickness (m)	2
Sediment composition	Sand-gravel-cobbles
Bank erosion	
ThetSd	0
Repose	0.3
Bed material transport	
Bedload transport component	Central
Transport formulas	Gaueman et al.
Transport calculations	
Morphology factor	3
Bed slope effects	
Longitudinal bed gradient factor	1
Transverse bed gradient factor	1.5

Full-reach assessment

While the calibration results were focused on the study-reach, the simulated results on the full-reach were also considered qualitatively. Examining the simulation results of v75 (Figure E.27) revealed that the sediment volumetric change of the observed data was comparable to that simulated for erosion, but considerably larger than simulated for deposition. With nearly a 25% increase in deposition and relatively similar erosion, the observed data had nearly four times the material added to the system. While these results were less agreeable than the study-reach, it is important to restate that due to the SfM uncertainty, the statistics of the observed data were approximations. Considering the larger uncertainty in the terrain modeling of the extended-reach, it was highly possible that the observed volumetric changes were exaggerated. However, the simulated and observed study-reach determined a negative net difference, and full-reach observed and simulated determined positive net differences, which suggested that simulations were modeling the general processes. Further, as a result of the October 2011 flood event, the first braid divergence in the upstream end of the full-reach

experienced avulsion and thus reduced the flow in the left braid (outlined in Figure E.28). Interestingly, the final four simulations produced similar avulsion in the same location, causing greater flow into the right channel. As shown in Figure E.28 and Figure E.29, the initial depth and velocity of v75 were greater than the resulting water depth and velocity of v75. Given this morphological process and the ability for both the full-reach and study-reach to produce general sediment volume change tendencies, evidence suggests that the model represented the morphology with reasonably good results.

6.5 Model validation

6.5.1 Introduction

Model validation is presented in the following sections for the hydraulic and vegetation models utilizing the calibrated parameters. Validation considered only new independent data that was not utilized in model calibration, as only independent data can offer insight into how well the model performs the calibrated-intended task. However, a model's validation is site, space, and time specific, and validation only produces high confidence for situations where the model was tested (Refsgaard, 2004). With only one observed mean annual flood event, true model validation only applies to similar scenarios. Therefore, the term model validation will be used loosely and it should be recognized that only similar scenarios are validated. Nevertheless, these models and results were useful in evaluating larger than validated flood events, but the inherent uncertainty must be considered (Section 7.3).

6.5.2 Hydraulic model

6.5.2.1 Introduction

Hydraulic validation was necessary to provide full assessment of the calibration efforts as well as to provide confidence in the model's ability to accurately replicate similar, but different events. Therefore, validation tested low-, medium-, and high-flow conditions. While these flow rates were relative to the October flood event and would not provide validation for extreme flood events (e.g. 100+ year flood events), results provided insight into the realistic nature of the hydraulics simulated and thus provided an assessment into the overall usefulness of the hydraulic simulations for larger events. It should be noted that the high flow simulations presented did not account for vegetation influence on the hydraulic conveyance. Given the moderate overland flow that existed through vegetated areas, it was assumed that

the flood inundation simulated in this section was not fully representative of the observed. However, these conditions are fully evaluated in Section 6.5.3.

6.5.2.2 Methods

Using the post-flood topography and a discharge of 19.5 $m^3 s^{-1}$, the calibrated parameters were utilized to model the observed low-flow conditions. As with the calibration testing, the various bathymetric depth measurements (474 points) were utilized to provide residual errors of the model's performance. Further, utilizing the aerial photographs and simulated results, the effective width and $Fit_{congruent}$ were calculated for overall model water routing and braid inundation performance.

Time lapse images of the October flood event captured various discharges and corresponding inundation extents for the sub-reach (Section 4.1.1) and these were utilized to calculate the Fit_{we} and $Fit_{congruent}$. While the sub-reach only offered insight into the model's performance of one relatively small area, this area experienced moderate inundation of shallow overland flow, which provided insight into Delft3D's sensitivity to small topographic and flood conveyance differences. With time lapse images and the NIWA flow gauge data available at 15 minute intervals, numerous discharges were available for model validation. However, prior to determining the flow rate of various images, the lag time between NIWA's gauging station record and the flow captured in time lapse images (9.5 km downstream) had to be determined. Therefore, time lapse images were examined to determine the peak water extent and depth, which was determined to occur at 1300 on the 26th of October. Reviewing the NIWA flow gauge records, the peak discharge was recorded at 1100 on the 26th of October. Therefore, a lag time of approximately 2 hours was determined, which resulted in a realistic mean velocity of 1.3 m/s at the flood peak.

With the goal to use the pre- and post-flood topographies to simulate various high-flow conditions, the evolving morphology had to be considered. To ensure that the available topographic datasets adequately represented time-specific morphology and water extent, the time lapse images were visually assessed for initial, evolved, and final morphology. Examining the pre-peak discharge pictures, the last available image of the 25th October

documented the flood at approximately 45 $m^3 s^{-1}$, and the first image on the morning of October 26th documented 181 $m^3 s^{-1}$. Naturally, the 45 $m^3 s^{-1}$ flow and inundation extent did not provide adequate overland flow for the high-flow simulation, nor did it meet the FRE3 required 58 $m^3 s^{-1}$. Conversely, the 181 $m^3 s^{-1}$ provided adequate flow conditions and appeared to have only minor morphological changes (Figure E.30a and b). Therefore, the 181 $m^3 s^{-1}$ was simulated with the pre-flood topography and fixed-bed mode and represents the high-flow condition. Examining the post-peak discharge images provided more options, and an image that recorded the flow at approximately 77 $m^3 s^{-1}$ was utilized as it was the first image to represent the final morphology and provided moderate inundation extent (Figure E.30C and D). Thus that image was considered appropriate to use with a simulation of medium-flow conditions using the post-flood topography.

To test the Fit_{we} and $Fit_{congruent}$ performance first required the ability to quantify the flood extent captured in the medium- and high-flow time lapse images. The obvious method to do this was to rectify the images using the pre-existing GPS points captured in the images as well as the extensive ground truthing. However, attempts to rectify these images using various software packages (ArcGIS, PhotoScan, MapWarper, Meta Carta's Map Rectifier, and GRASS GIS) all produced erroneous results. Therefore, a meticulous manual attempt to map water extent was performed using the post-flood aerial photographs, the time lapse image before the flood event, medium-flow condition image, and high-flow condition image (Appendix E.9, Figures E.31-E.34). This was accomplished by comparing the low-flow time lapse image and the time lapse images of interest to identify the landmarks near the floodline, and then identify the landmarks in the aerial photographs (example procedure in Appendix D.5). Since aerial photographs of the sub-reach were captured at 300 m above ground level, the 0.06 m image resolution provided great detail to help identify unique vegetation or sediment patterns.

Rarely were points identified along the actual floodline. Instead, most areas were just below or above the floodline, and interpolation was required to locate the floodline and extent. Using this method, 160 and 198 flood extent points were identified and connected into the corresponding floodline for the 181 and 77 $m^3 s^{-1}$, respectively. The reduced points of the 181 $m^3 s^{-1}$ were due to the greater inundation, which required less floodline mapping (Figure

E.32). Through great effort all points were placed with high confidence; however, retrofitted data, interpolated floodlines, and coordinate accuracy degradation with increasing distance from the camera reduced the waterlines to approximations. Therefore, while the time lapse images captured water inundation well outside of the sub-reach, only the close-range sub-reach was utilized in performance evaluation to maintain high confidence in floodline mapping (Figure E.34). Further, main channel inundation was not included in mapping and fit calculations because the main channel was always simulated with flow; therefore, inclusion of the main channel in the fit calculations would only inflate the simulation's performance. While the water extent only offered an approximation of the observed flow, this data added valuable insight into the model performance and sensitivity.

6.5.2.3 Results and discussion

The low-flow simulation depth results for the study-reach (Table 6.22) show the 1.5 m and 2.5 m grids both produced mean errors near zero and standard deviation errors in decimeter range. This accuracy and precision indicate that the model's Nikuradse roughness length and eddy viscosity were properly calibrated and produced comparable accuracy and precision to the SfM and bathymetric data. The water extent for the low-flow simulation showed the study-reach (Figure 6.11) 1.5 m and 2.5 m grids had Fit_{we} or 95% and 120%, respectively. These results indicate that the 1.5 m grid predicted water extent was close to the observed, and the 2.5 m grid over-predicted total water extent by 20%. Evaluating the $Fit_{congruent,}$ the 1.5 m grid had better performance which suggested more accuracy at predicting actual water extent.

Evaluating the full-reach results (Figure 6.12) showed the Fit_{we} for both grids near 100%, with the 1.5 m grid slightly under-predicting and the 2.5 m over-predicting the total water extent. The $Fit_{congruent}$ of the full-reach showed that the two grids performance were more comparable; however, the 1.5 m grid still outperformed the 2.5 m grid. Visual observation of the study- and full-reach (Figures 6.11 and 6.12) highlighted the greater extent simulated for the 2.5 m grid, with the abundance of green areas mapped. However, both the 1.5 m and 2.5 m grids revealed that both models failed to simulate similar narrow anabranches, which contributed to the lower $Fit_{congruent}$ results.

Table 6.22: Hydraulic validation depth results (study-reach only) for the 1.5 m and 2.5 m grid low-flow simulations.

		1.5 m grid	2.5 m grid
k_s		0.21	0.35
V_H		0.15	0.15
K		1.0	1.0
Depth	ME	-0.01	0.02
	MAE	0.12	0.13
	RMSE	0.15	0.17
	SDE	0.15	0.16
	Max	0.39	0.42
	Min	-0.50	-0.59

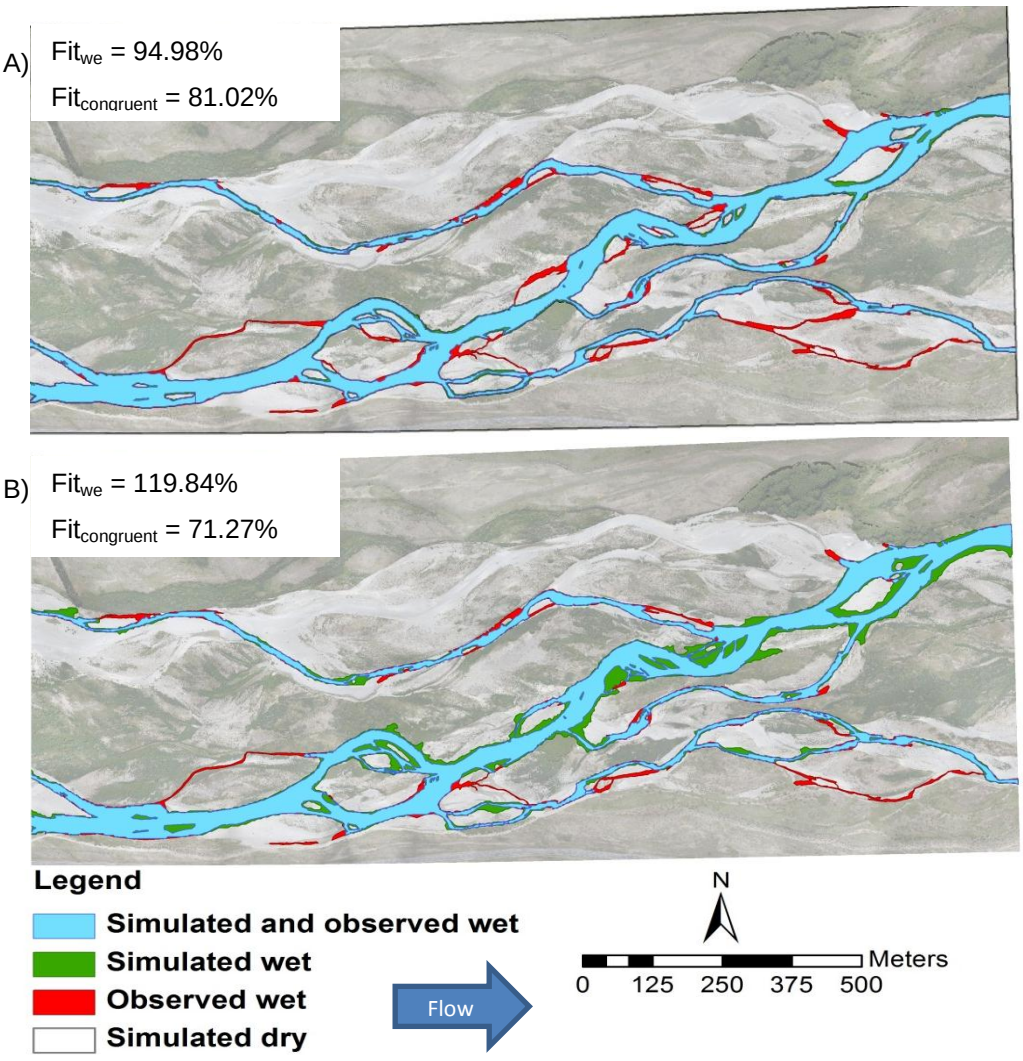

Figure 6.11: Post-flood study-reach simulation with effective width and congruent fit for A) 1.5 m grid, and B) 2.5 m grid.

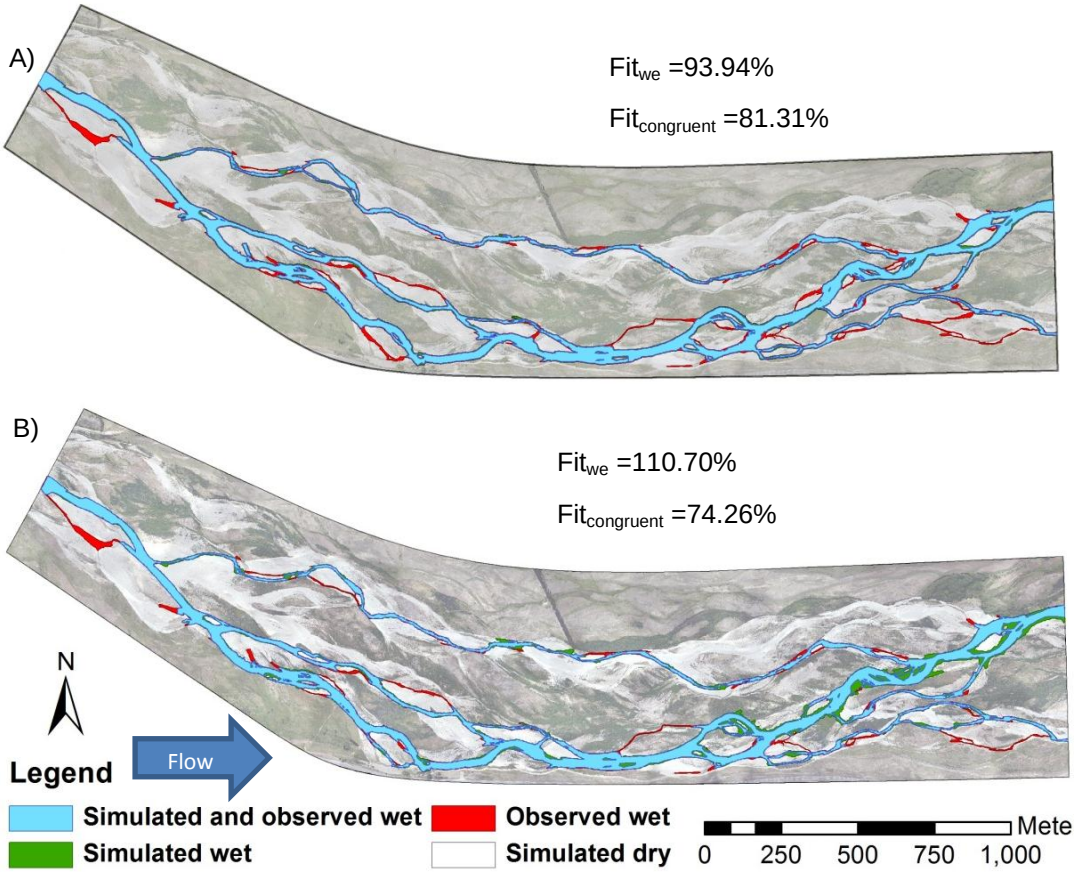

Figure 6.12: Post-flood full-reach simulation with effective width and congruent fit for A) 1.5 m grid, and B) 2.5 m grid.

Evaluating the high-flow simulation results (Figures 6.13 and 6.14) revealed that the high-flow condition produced more accurate $Fit_{congruent}$ than the medium-flow condition results. This was likely caused by the greater water extent and deeper depths produced in the high-flow simulation, thus requiring less sensitivity for Delft3D's ability to simulate the overland flow as well as less accuracy required for the SfM topography. Nevertheless, the results of the medium-flow simulation still produced comparable fit results to the study- and full-reach low-flow water extent results. Interestingly, the 2.5 m grid had higher performance in this sub-reach. Since these flood conditions did not yet incorporate vegetation influence, it was speculated that the higher k_s of the 2.5 m grid may be one reason why this occurred, which was the same theorized explanation for the 2.5 m grid's better initial performance for the no trachytope simulations of Section 6.4.3.3.

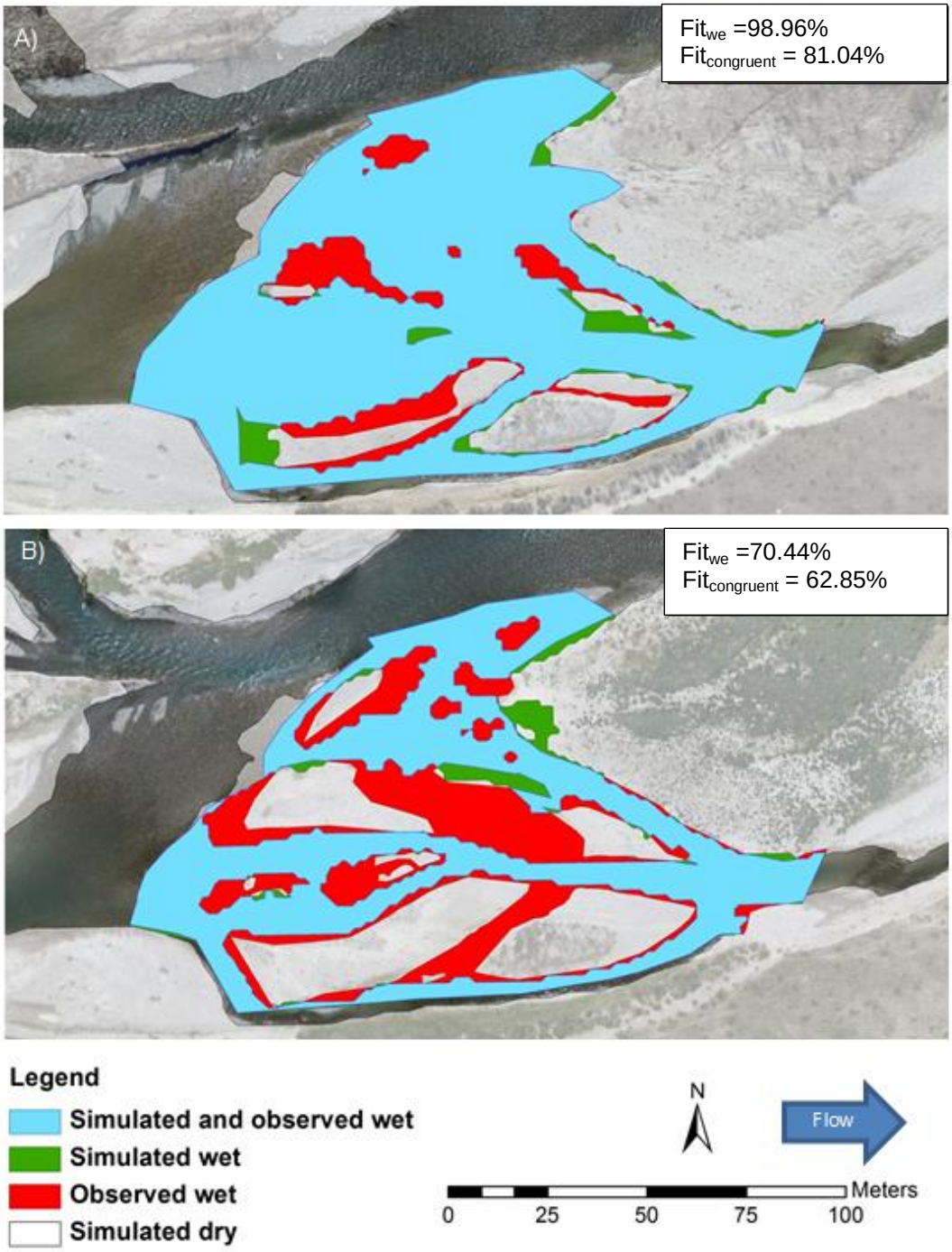

Figure 6.13: Observed and 1.5 m grid simulated inundation extent for sub-reach A) high-flow (181 $m^3 s^{-1}$), and B) medium-flow (77 $m^3 s^{-1}$).

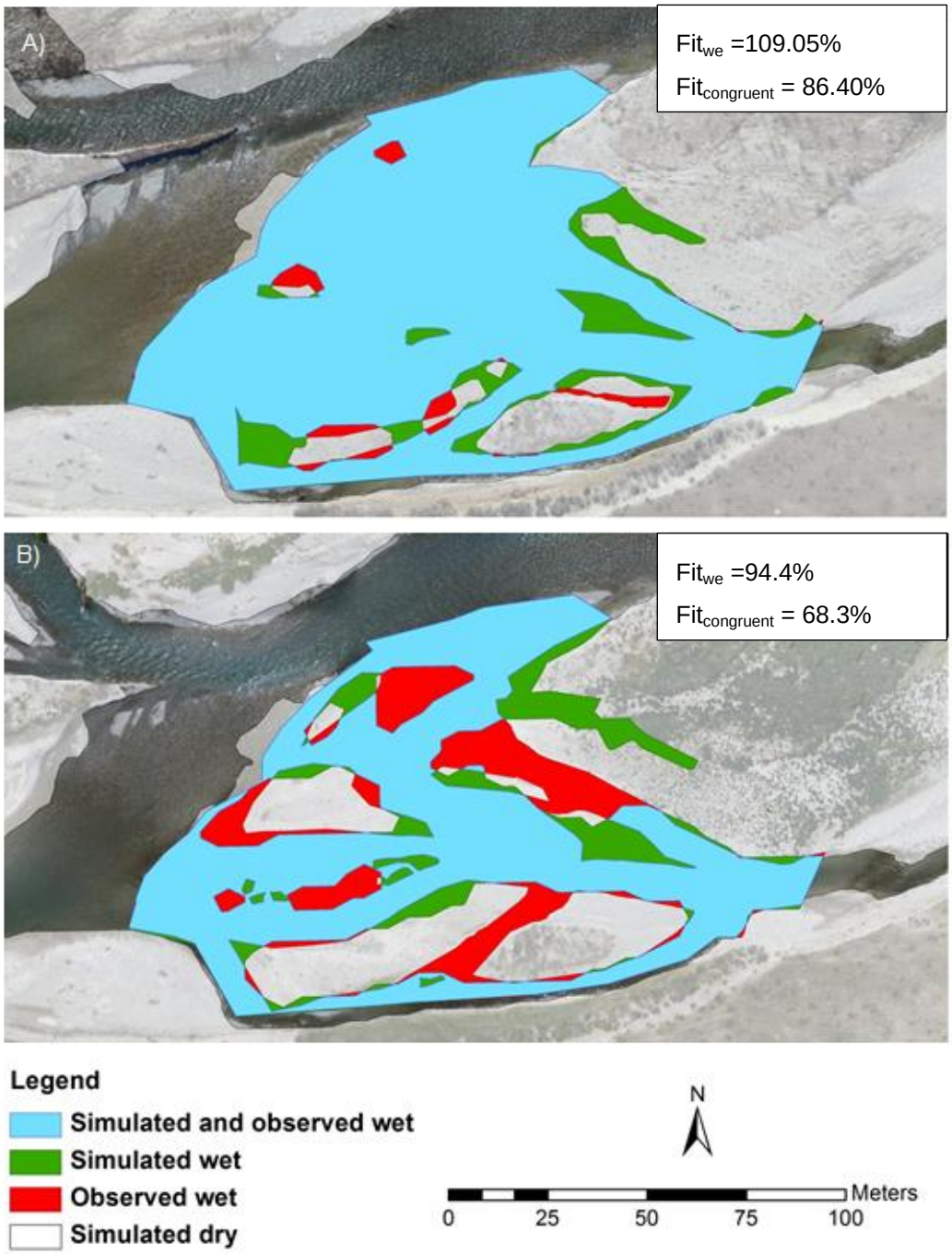

Figure 6.14: Observed and 2.5 m grid simulated inundation extent for sub-reach A) high-flow (181 $m^3 s^{-1}$), and B) medium-flow (77 $m^3 s^{-1}$) conditions.

Comparing the low-flow results for the validation and calibration simulations revealed the depth accuracy and precision were comparable for both 1.5 m and 2.5 m grids. With mean errors near zero, and standard deviation errors around 0.16 m, both produce errors near the SfM topographic uncertainty. Further, considering only the study-reach, the results of the calibration compared to the validation shows that post-flood 1.5 m grid simulation validation

Fit_{we} was more accurate (Fitwe + 2% and the $Fit_{congruent}$ + 8%) and the 2.5 m grid had nearly identical performance. These results were encouraging, given that validation results are typically less accurate than calibration results (Refsgaard, 2004). However, these results may reflect the reduced braiding complexity of the post-flood river morphology.

Validation results of the 2.5 m grid medium-flow simulation produced fit performance comparable to the study-reach and full-reach results. However, the 1.5 m grid under-predicted total inundation (Fit_{we}) and produced poor $Fit_{congruent}$. These results were unexpected, as the smaller 1.5 m grid should have greater representation of the topography and would provide increased accuracy. The high-flow conditions of both grid sizes had improved effective width and congruent fit results compared to the low-flow conditions. This was likely caused by the greater depth simulated requiring less model sensitivity to accurately braid as well as less topographic accuracy to produce accurate overland flow. While the 2.5 m grid high-flow had less accurate Fit_{we}, the $Fit_{congruent}$ was more accurate. Results with the 2.5 m grid outperforming the 1.5 m grid mimic previous discrepancies (Section 6.4.3.3), that suggested the increased k_s value of the 2.5 grid had improved simulation representation of the unaccounted vegetation influence. However, in the tested conditions of this section, these results were likely caused by the increased bed roughness, which produced slower and deeper flows and thus provided greater water extent.

While the depth and water extent data provided valuable insight into the model's performance and validation, additional velocity data would have been ideal. Nevertheless, based on the depth and water extent results providing strong agreement with observed results, velocity was considered to be represented adequately. The results of the validation show strong agreement to the results of the calibrated model and perform well within the uncertainty of the topography. Therefore, these results were encouraging and suggest that the hydraulic calibration was successful. Further, these results provided high confidence in the model's ability to simulate and identify lupin-mortality based on velocity, depth, and inundation extent.

6.5.3 Vegetation

6.5.3.1 Introduction

The lupin-mesh experiment provided calibration for the hydraulics of overland flow through the vegetated floodplain. Since flood events are typically the only time lupins alter flow conveyance, the vegetation calibration parameterization was directly applicable to high-flow conditions. Therefore, the validation of such data would be using a high-flow event in which floodplain vegetation altered the flow conveyance. However, direct overland flood flow depth and velocity data (during flood flow conditions) were never obtained; thus, there was no direct validation for this model's calibration. However, the medium- and high-flow water extent data utilized in Section 6.5.2 does provide flood conditions that have both local and regional overland flow through various vegetation densities. This naturally altered the flood conveyance which affected both flow introduced to the sub-reach and within the sub-reach. Therefore, comparing the water extent accuracy of the medium- and high-flow conditions with and without trachytope inclusion provided a partial validation.

6.5.3.2 Methods

Using the full-reach vegetation mapping of Figure 5.22, trachytopes were developed in both the 1.5 m and 2.5 m grid models. However, the lupin-mesh experiment only tested moderate lupin density (Table 6.3) and parameterization determined that a trachytope calibration factor of 10 best represented the conditions. However, various lupin densities were mapped in the reaches and required representative calibration factors. Therefore, calibration factors were linearly interpolated for the sparse and dense lupin clusters as a ratio of their densities compared to the moderate lupin density. For example, the sparse lupin cluster density was 65% of the moderate density; thus 65% of 10 provided the calibration factor of 6.5. Using this simple linear technique, the dense lupin cluster and willows were represented by calibration factors of 20 and 3.2 respectively. It is acknowledged that this simple linear interpolation was not the ideal method to model the various vegetation types and densities. However, this method was utilized as it provided a consistent and unbiased interpolation. With the vegetation mapped and trachytope parameters set, the medium- and high-flow simulations were re-simulated and water extent was mapped for the corresponding discharges of 181 and 77 $m^3 s^{-1}$ using the pre-flood and post-flood topography, respectively.

6.5.3.3 Results and discussion

Simulations with incorporated spatial trachytopes are shown below for the 1.5 m grid (Figure 6.15) and the 2.5 m grid (Figure 6.16). Comparing the 1.5 m grid results to the high-flow without trachytopes of Figure 6.15 revealed that the trachytope improved three of the four fit performance measures. The unimproved Fit_{we} of the high-flow condition dropped by a minimal 1%. However, this difference was dismissed given the approximated floodline locations and inherent uncertainty of the mapped water extent. However, the 4.5% improvement in the high-flow $Fit_{congruent}$, and the 14% and 12% improvements in the medium-flow simulation's Fit_{we} and $Fitc_{ongruent}$, are considerable differences and indicate actual improvement was achieved. Thus, trachytope inclusion in the 1.5 m grid was assumed to increase the simulated hydraulic performance.

Evaluating the results (Figure 6.16) of the 2.5 m grid trachytope simulation compared to the no trachytope simulations shows less significant improvement. While the high-flow simulation's Fit_{we} and $Fit_{congruent}$ and the medium-flow simulation's Fit_{we} improved by approximately 1%, these minimal results were dismissed. While the 2.5 m grid results did not increase with trachytope inclusion, it should be noted that the 2.5 m grid results without trachytopes were higher than the 1.5 m grid and thus had less room for improvement. Comparing the 1.5 m and 2.5 m grids for the trachytope inclusion revealed that the medium-flow had considerably higher Fit_{we} than the 1.5 m grid (+11%), and that the high-flow $Fit_{congruent}$ of the two grids were nearly identical. The only major difference was the 2.5 m grid's medium-flow simulation's $Fit_{congruent}$ which was 8% less. Therefore, while the 2.5 m grid did not show significant improvement for the trachytope inclusion, the final water extent performance was comparable for the two grids.

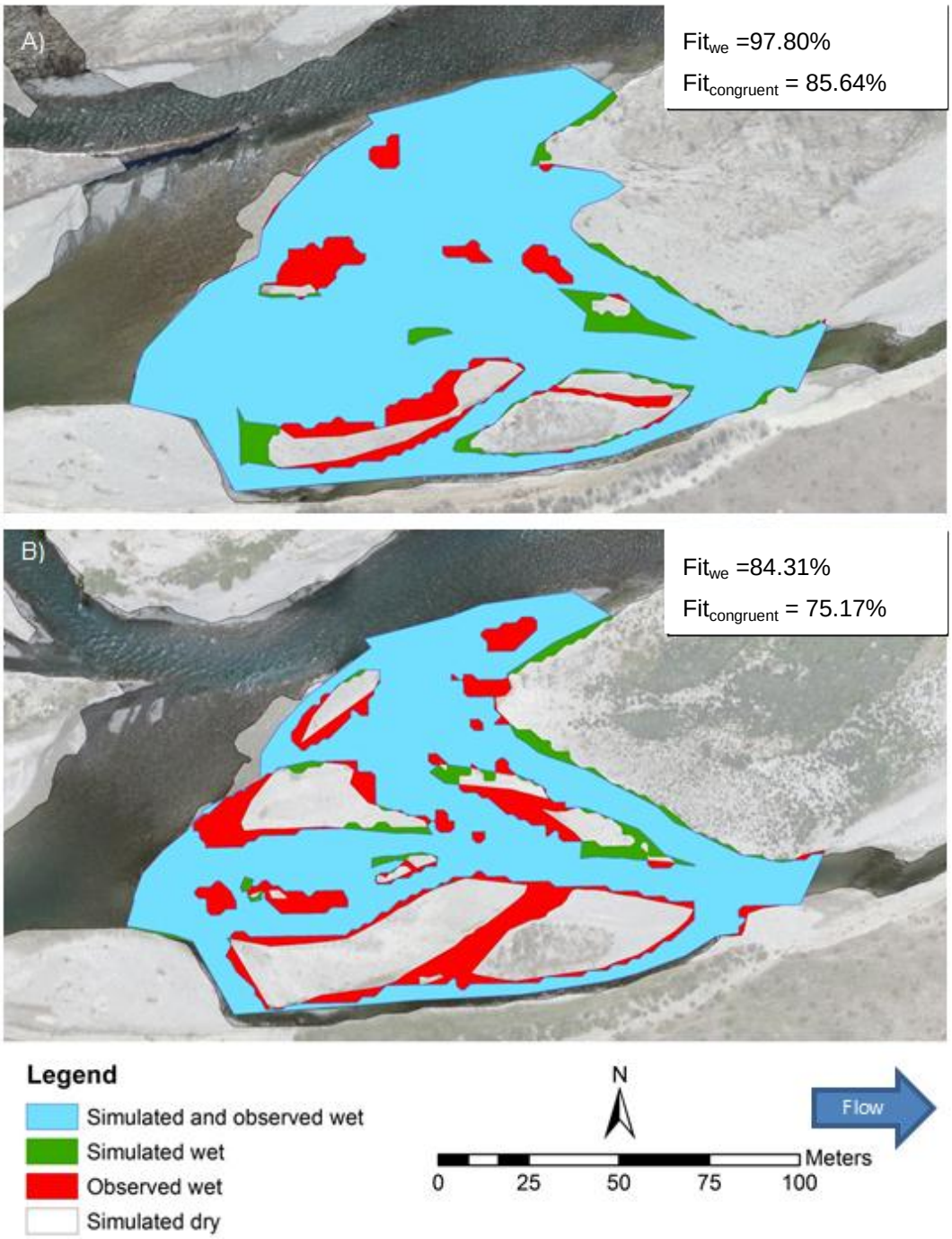

Figure 6.15: Observed and simulated (1.5 m grid) inundation extent with vegetation trachytope inclusion for sub-reach A) 181 $m^3 s^{-1}$, and B) 77 $m^3 s^{-1}$.

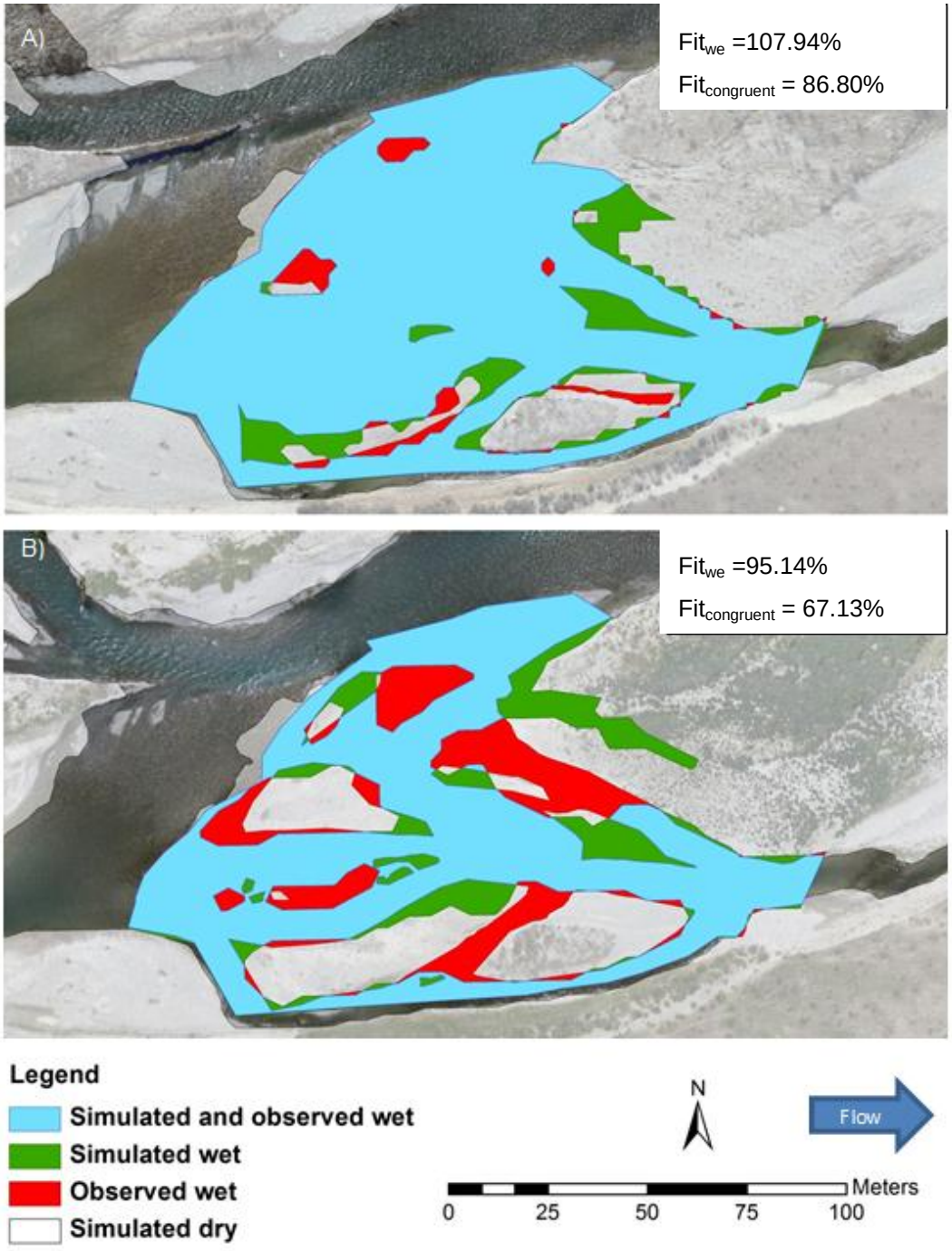

Figure 6.16: Observed and simulated (2.5 m grid) inundation extent with vegetation trachytope inclusion for sub-reach A) 181 $m^3 s^{-1}$, and B) 77 $m^3 s^{-1}$.

6.6 Conclusion

This chapter has presented the calibration methods and results undertaken to ensure realistic hydraulics and morphodynamics were simulated, which was paramount in assessing the various sized flood event's impacts upon vegetation. Hydraulic calibration efforts were successful in providing models that accurately simulated water depth and extent, with

validation results equivalent and often better. Calibrating vegetation influence on the hydraulics was a difficult task due to the limited functioning parameters as well as the slight variation in depth and velocity for vegetated and vegetation free observed data. Nevertheless, the trachytope calibration was able to produce improved simulation results, and validation using the medium- and high-flow conditions showed that the inclusion of the vegetation did improve some aspects of the Delft3D model's performance in flood extent accuracy. However, these results represent only one local area, and without observed data for various locations, validation was limited.

In determining the optimal grid size, evidence revealed that the 1.5 m grid typically outperformed the 2.5 m grid, and that trachytope inclusion in the 1.5 m grid showed obvious simulation enhancement; thus, suggesting that the 1.5 m grid was more representative and sensitive. However, the 2.5 m grid's hydraulic performance was comparable in every category, and while trachytope inclusion produced little to no simulation enhancement, the final fit performance was also comparable. Therefore, while the 1.5 m grid may have provided better foundation for the morphological model simulations due to its sensitivity and additional detail, the 2.5 m grid model was the practical choice given the similar hydraulic performance, reduced simulation run times, and increased model stability.

Calibration of the morphologic model was extensive and moderately successful. Areas considered successful were general channel morphology, sediment volume changes, and total erosion and deposition that were representative of the October flood event. However, areas of extensive bank erosion were under-predicted and general bank erosion was over-predicted. With bank erosion often considered the weakness of morphological models, these results were anticipated.

Validations of the hydraulics and vegetation representation have been presented and discussed. However, should these results be trusted? Due to their application to limited events, the answer is: i) yes, high confidence should be given to these models for the specific site, conditions, and purpose tested, and ii) no, low confidence should be given to simulations that are outside the validated conditions. Without validation data available for the morphological model, low confidence will be given to all simulated morphology results.

Nevertheless, the morphological model was built upon the hydraulic and vegetation calibrated and validated parameterization; therefore, the morphological model was capable of adequately simulating realistic hydraulics and can provide valuable insight for larger than validated flood events and vegetation mortality forecasting. However, it was acknowledged that all forecasting simulations will need to consider the model's uncertainty determined during model testing.

Part III

Data Synthesis

Chapter 7

Simulated Flood Events and Corresponding Mortality

7.1 Introduction

This chapter presents the synthesis of data from Part II of this thesis, which was utilized to simulate forecasted flood events of 2, 5, 10, 25, 50, 100, 200, and 500-year return periods with the objective to identify corresponding lupin mortality. This was accomplished using the hydrologic data, synthetic hydrographs, and lupin mortality processes identified in Chapter 4. Chapter 5 contributed the topography for the numerical model simulations, the vegetation extent, densities, and type, as well as vegetation removed during the observed flood event. Chapter 6 provided the numerical model that was specifically calibrated for the study-reach and associated hydraulics, vegetation, and morphology.

While Chapter 4 provided the foundation to identify the flood-induced processes responsible for lupin mortality, additional preparation was required for direct application to the simulated flood results. Further, while lupin mortality caused by inundation, drag, erosion, and sediment deposition were identified with high confidence, trauma mortality required additional assessment. Therefore, field observations were combined with flood simulations in an effort to gain insight into the conditions that potentially caused mortality in flood zone 1 (Section 4.3.3.1). As discussed throughout this thesis, because lupins produced variable results in all statistical analyses, all relationships developed to predict lupin characteristics and mortality inevitably had inherent uncertainty. Therefore, uncertainty of each lupin mortality process was estimated as well as the numerical model uncertainties associated with mortality identification.

With mortality thresholds and uncertainties estimated, the simulated flood results were assessed and lupin mortality was identified. To best represent the results, a map of each flood

event was developed to show the various areas and processes of mortality. Further, these mapped mortality areas were calculated and presented in a corresponding table along with the process uncertainty, associated model uncertainty, total area removed, and the percentage of the total floodplain lupins removed.

This chapter is organized into three sections. The first discusses the various mortality processes and methods necessary for practical application to the simulated flood results. This section includes the trauma assessment and the methods utilized. The second section presents the uncertainty assessment and the methods utilized to estimate the mortality processes and numerical model uncertainties. The third section presents the flood simulations, mortality results, and final discussion.

7.2 Data preparation

7.2.1 Introduction

Lupin mortality experiments presented in Chapter 4 identified thresholds of individual processes and provided the foundation for this chapter. However, the data were not easily applied to the numerical model flood results for mortality identification. Therefore, slight modifications were performed on the existing data to allow simple application to identify such mortality thresholds using Delft3D data. This section focuses on the individual processes of inundation, drag, erosion, deposition, and trauma as well as the methods applied. However, prior to data preparation, it was necessary to determine the method to quantify lupin removal. With many of the process mortalities related to root diameter, and with the varying lupin density categories (Figure 5.19) having varying root diameter frequencies, it was necessary to consider each lupin mortality process separately for each lupin density category. Therefore, by determining the threshold of interest, a lupin mortality based on root size could be determined, and using the frequency it was possible to determine the percentage of lupin mortality that occurred for the area of interest. However, the frequency of lupin root diameters of Figure 5.19 only consisted of sparse and dense areas. Therefore, a cumulative distribution plot of these data was developed for the sparse and dense lupin densities, and a moderate density cumulative distribution was produced by averaging the sparse and dense distributions (Figure 7.1).

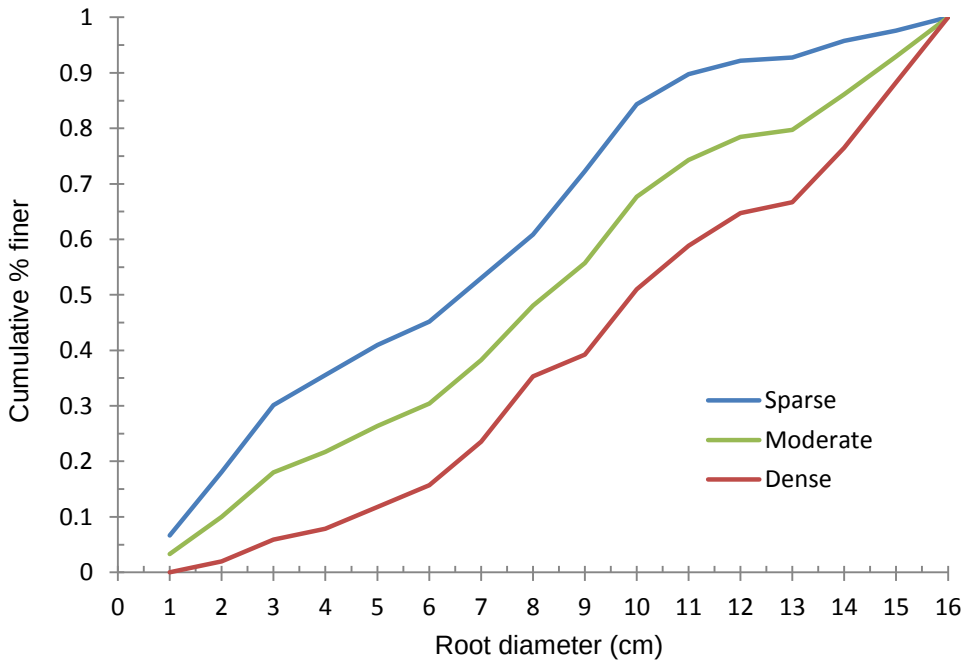

Figure 7.1: Cumulative frequency for sparse, moderate, and dense lupin.

7.2.2 Inundation

Inundation-induced mortality results (Table 4.5) revealed that inundation mortality was a function of the lupin's root diameter, inundation duration, and water depth. However, results were limited since these cultivated lupins only grew to root diameters of 3 cm. Therefore, using the results of Table 4.5, root diameter was related to mortality for diameters ≤ 3 cm, and mortality for larger root diameters was extrapolated based on this relationship. This was done for the medium depth and deep depth only (hereafter referred to as emergent and submerged conditions, respectively) since shallow depth produced no consistent mortality rates. Further, the emergent and submerged datasets had varying mortality rates since multiple plants were in the same planter bag. Therefore, the emergent and submergent data were further divided into 100% and 50% mortality conditions. The 50% mortality was developed by plotting the inundation duration against the root diameter ranges for the first day that ≥ 50% lupin mortality occurred in Table 4.5. This was repeated for the 100% mortality, and using best-fit linear relationships, trendlines were developed for forecasting larger lupin mortality thresholds (Figures 7.2 and 7.3). These empirical relationships are collated in Table 7.1. However, the inundation duration empirical formulas created two issues. First, as shown in Table 7.1 under the submerged category, the 50% mortality

condition required longer inundation than the 100% mortality. Secondly, the submergent mortality was estimated to occur at longer inundation periods than the corresponding emergent data for root diameters above 8 cm. Based on data and observations, the 50% mortality occurred at lower durations than the 100% mortality and the submerged lupins perished at shorter inundation durations than the emergent lupins. Therefore the submerged duration thresholds for the 1 cm root diameter were altered to the observed data of 2 days inundation and the submerged durations above 8 cm were lowered to match that of the emergent. Typically in this research, conservative approaches were taken when developing lupin mortality relationships, which would assume that the submerged would remain at the initial estimate and the emergent duration would be raised. However, lowering the submerged duration mortality was an appropriate method since lupin root diameters above 8 cm were typically clusters, consisting of smaller lupins that would have perished at shorter inundation durations. Therefore, Table 7.2 shows the final data used to identify inundation mortality thresholds, and the percentage of lupin removal was calculated using the root diameters and Figure 7.1 for the corresponding densities.

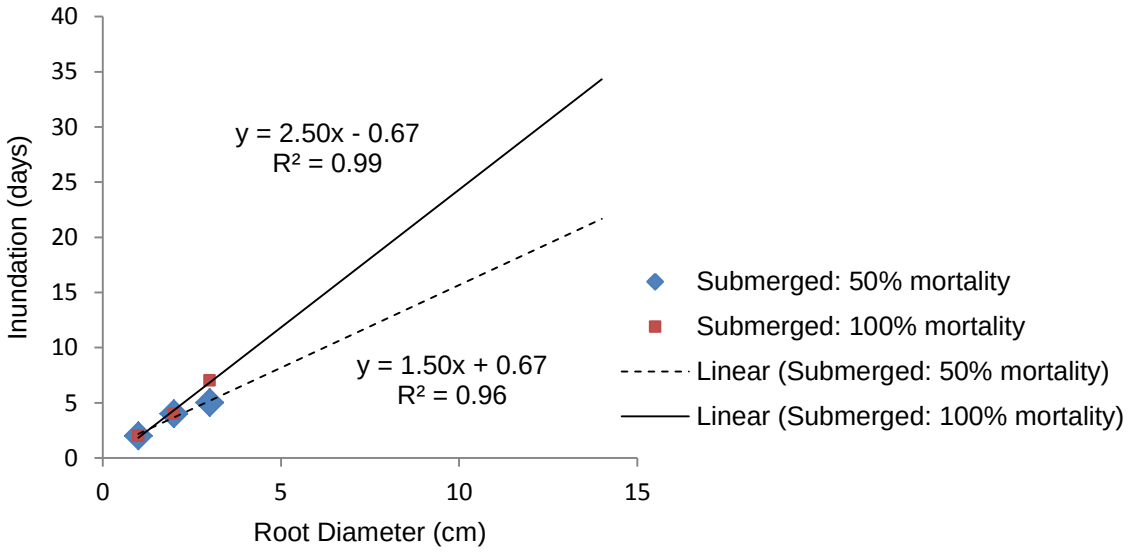

Figure 7.2: Submerged mortality threshold relationship for 50% and 100% mortality conditions.

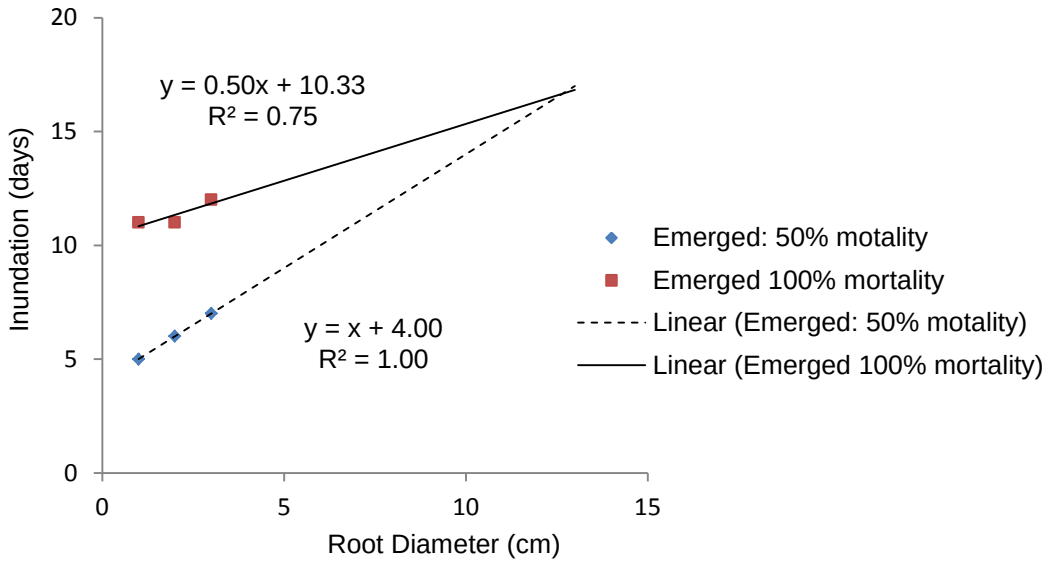

Figure 7.3: Emergent mortality threshold relationship for 50% and 100% mortality rate conditions.

Table 7.1: Initial mortality thresholds for inundation duration.

Root diameter (cm)	50% mortality	100% mortality	50% mortality	100% mortality
	Submerged (days)		Emergent (days)	
≤ 1	2.2	1.8	5.0	5.8
≤ 2	3.7	4.3	6.0	9.3
≤ 3	5.2	6.8	7.0	12.8
≤ 4	6.7	9.3	8.0	16.3
≤ 5	8.2	11.8	9.0	19.8
≤ 6	9.7	14.3	10.0	23.3
≤ 7	11.2	16.8	11.0	26.8
≤ 8	12.7	19.3	12.0	30.3
≤ 9	14.2	21.8	13.0	33.8
≤ 10	15.7	24.3	14.0	37.3
≤ 11	17.2	26.8	15.0	40.8
≤ 12	18.7	29.3	16.0	44.3
≤ 13	20.2	31.8	17.0	47.8
≤ 14	21.7	34.3	18.0	51.3
≤ 15	23.2	36.8	19.0	54.8

Table 7.2: Final mortality thresholds for inundation duration and corresponding lupin removal.

Root diameter (cm)	50% mortality	100% mortality	50% mortality	100% mortality	Lupin mortality (%)		
	Submerged (days)		Emergent (days)		Sparse	Moderate	Dense
≤ 1	2.0	2.0	5.0	5.8	7	3	1
≤ 2	3.7	4.3	6.0	9.3	18	10	2
≤ 3	5.2	6.8	7.0	12.8	30	18	6
≤ 4	6.7	9.3	8.0	16.3	36	22	8
≤ 5	8.2	11.8	9.0	19.8	41	26	12
≤ 6	9.7	14.3	10.0	23.3	45	30	16
≤ 7	11.0	16.8	11.0	26.8	53	38	24
≤ 8	12.0	19.3	12.0	30.3	61	48	35
≤ 9	13.0	21.8	13.0	33.8	72	56	39
≤ 10	14.0	24.3	14.0	37.3	84	68	51
≤ 11	15.0	26.8	15.0	40.8	90	74	59
≤ 12	16.0	29.3	16.0	44.3	92	78	65
≤ 13	17.0	31.8	17.0	47.8	96	80	67
≤ 14	18.0	34.3	18.0	51.3	98	88	93
≤ 15	19.0	36.8	19.0	54.8	100	100	100

7.2.3 Drag and erosion

Processing field data determined that drag alone and drag in combination with varying levels of erosion ≥ 20 cm can remove lupins of various sizes. However, to best utilize the lupin pull-out and drag force thresholds with the numerical results, specific velocity thresholds were required. These were determined by using the empirically developed lupin pull-out forces (Table 4.13) and the custom empirical formulas (Figure 4.28) to determine the velocity threshold for various sized root diameters and erosion levels of 0, 20, and 30 cm. Erosion levels > 30 cm were not evaluated for velocity thresholds since 40 cm of erosion removed all lupins with velocities of ≥ 0.25 m/s (Table 4.17). Finally, the lupin removal percentages were calculated for the various lupin clusters using the root diameters and Figure 7.1, and the results for the 0, 20, and 30 cm erosion levels are presented in Tables 7.3, 7.4, and 7.5, respectively. As shown in Table 7.3, velocities ≥ 0.74 m/s can remove all lupins with root diameters of 6 cm and greater. However, smaller lupins (< 6 cm) were not estimated to be removed since their smaller canopies would not generate the critical drag force for pull-out.

Table 7.4 and Table 7.5 show that all root diameters can be removed, including smaller lupins due the erosion-reduced pull-out forces requiring less drag force.

Table 7.3: 0 cm erosion and velocity thresholds.

Root diameter removed (cm)	Velocity (m/s)	0 cm erosion: % mortality		
		Sparse	Moderate	Dense
≥ 6	≥ 0.74	58	72	86
≥ 7	0.59	54	68	81
≥ 8	0.48	46	60	72
≥ 9	0.41	38	49	60
≥ 10	0.33	26	41	55
≥ 11	0.28	14	28	42
≥ 12	0.24	8	21	33
≥ 13	0.21	6	16	27
≥ 14	0.18	5	15	24
≥ 15	0.16	2	8	13

Table 7.4: 20 cm erosion and velocity thresholds.

Root diameter removed (cm)	Velocity (m/s)	20 cm erosion: % mortality		
		Sparse	Moderate	Dense
All	≥ 0.92	100	100	100
≤ 2, ≥ 4	0.78	88	92	96
≤ 2, ≥ 5	0.67	82	88	93
≤ 2, ≥ 6	0.58	77	83	89
≤ 2, ≥ 7	0.51	72	78	84
≤ 2, ≥ 8	0.43	64	70	76
≤ 2, ≥ 9	0.37	56	59	63
≤ 2, ≥ 10	0.31	45	51	58
≤ 2, ≥ 11	0.26	32	38	45
≤ 2, ≥ 12	0.22	24	27	30
≤ 2, ≥ 13	0.20	24	25	28
≤ 2, ≥ 14	0.17	20	18	17
≤ 2, ≥ 15	0.16	19	10	3
≤ 2	0.10	7	3	1

Table 7.5: 30 cm erosion and velocity thresholds.

Root diameter removed (cm)	Velocity (m/s)	30 cm erosion: % mortality		
		Sparse	Moderate	Dense
All	0.35	100	100	100
≤ 4, ≥ 6	0.33	95	82	96
≤ 4, ≥ 8	0.31	75	74	73
≤ 4, ≥ 9	0.3	64	66	69
≤ 4, ≥ 10	0.27	52	54	57
≤ 3, ≥ 10	0.26	46	48	49
≤ 3, ≥ 11	0.24	40	44	47
≤ 3, ≥ 12	0.22	38	40	41
≤ 3, ≥ 13	0.19	34	38	39
≤ 3, ≥ 14	0.17	32	30	13
≤ 3, ≥ 15	0.15	30	18	6

7.2.4 Deposition

The results of burial by deposition mortality (Table 4.19) revealed that lupin mortality occurred at varying levels of burial above the lupins' canopies. While the dataset was small, these results were useful and considered adequate for this study since they agree with other studies of riparian herbaceous vegetation burial mortality (e.g. Deng et al., 2008). However, the results of Table 4.19 were not directly applicable to the numerical model simulations. As discussed in Section 4.4.4, the amount of deposition that causes lupin mortality depends on the height of the plant canopy, which was dependent upon the amount of deformation experienced during the flood event. However, since lupin mortality of the study-reach would be assessed using the cumulative frequency of Table 7.1, it was necessary to correlate the lupin canopy heights to lupin root diameters. This was accomplished by plotting the available data for both canopy height and root diameter (Figure 7.4), and similar to previous methods, the maximum values were utilized to develop a custom empirical relationships (solid lines). Using the data of Table 4.18, the lupin height had an average reduction of 50.6% due to deformation during the experiment. Therefore, this reduction was applied to the custom empirical relationship and was represented in Figure 7.4 with a dashed line.

With the deformed lupin height and root diameter relationship established, deposition mortality was developed. Using the results of Table 4.19, the deposition burial depth and

largest canopy heights that perished were plotted, but no relationship was established due to the limited dataset and results with repeated values. Therefore, a deposition mortality threshold was developed based on the results that showed 10 cm of deposition (above canopy burial) killed all lupins up to 32 cm canopy. Using this deposition burial and the deformation data of Figure 7.4, a deposition mortality relationship was developed (Table 7.6) and mortality percentages were calculated for the varying lupin density clusters. This relationship assumed that all plants with 10 cm of deposition were killed, and while this deposition amount was only observed to kill a 32 cm canopy, the results of Table 7.6 were considered conservative due to the maximum values used to develop the canopy height and root diameter relationship as well as the deformation observed in the field was much greater (average of 75% reduction) than the average 50.6% reduction utilized.

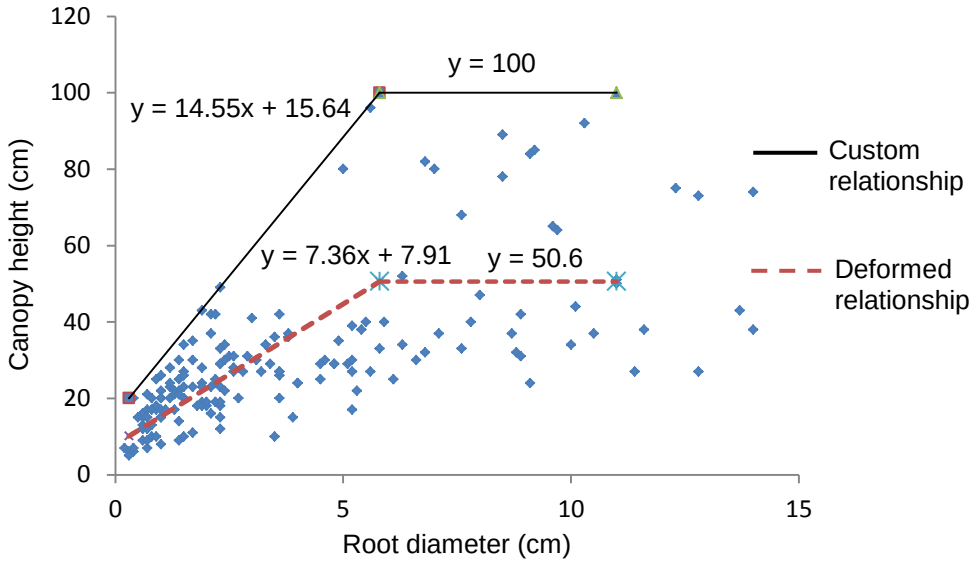

Figure 7.4: Canopy height and root diameter relationship for undisturbed lupins and flow-deformed lupins.

Table 7.6: Deposition burial mortality thresholds and lupin mortality for sparse, moderate, and dense lupin cluster densities.

Root diameter (cm)	Deformed canopy height (cm)	Deposition mortality threshold (cm)	Lupin mortality (%)		
			Sparse	Moderate	Dense
≤1	13	23	7	3	1
≤2	22	32	18	10	2
≤3	31	41	30	18	6
≤4	40	50	36	22	8
≤5	49	59	100	100	100
>5	49	59	100	100	100

7.2.5 Trauma

Trauma was a suspected flood-induced process that could cause lupin mortality (Section 4.3.3.1); however, only field data were collected. While it was acknowledged that the best method to investigate trauma-induced mortality was a hydraulic laboratory flume experiment, this was not possible due to the circumstances following the February 2011 earthquake that left the flume inoperable. Thus, trauma mortality was only assessed through field observations after actual flood events. However, without trauma mortality occurring in the sub-reach for time lapse imagery support, the ability to gain insight into this mortality process had diminished. Nevertheless, the area referred to as flood zone 1 (Section 4.3.3.1) showed signs of trauma-induced mortality, but this mortality was potentially caused by other processes such as inundation.

To investigate the processes that occurred in flood zone 1, the flood event that potentially caused the mortality was simulated. However, identifying the flood responsible was not obvious since two floods of similar magnitude occurred within a short time span (January 3rd, 2013 with 209 $m^3 s^{-1}$, and January 10th, 2013 with 288 $m^3 s^{-1}$). Since both flood events were identified to inundate flood zone 1, the flood-induced processes of an individual flood, or the combined events, could have caused the mortality. Further complicating the simulation was the significant increase in lupin density and maturity in flood zone 1, as well as the uncertainty in upstream morphologic changes during the time between the last topography and vegetation survey (post-flood).

Despite these issues, a simulation was performed; however, a few considerations and assumptions were required. With only the post-flood data available to simulate the flood event, only the smaller January 3rd flood could be adequately represented with this topography. However, the January 10th flood event's greater discharge had the greater potential to cause lupin mortality and it was assumed that any mortality process that would have occurred during the smaller flood event would have also happened during the larger flood event. Therefore, as a conservative measure, the January 10th flood was simulated using the post-flood topography. This method and assumption were partly justified based on time lapse imagery showing minor morphologic changes immediately downstream of flood zone 1 as well as similar inundation patterns for the two flood events. Therefore, it was assumed that the upstream morphologic changes were also minimal, or at least had minimal effect on inundation patterns at higher flow rates.

To account for the undocumented vegetation development within the numerical model, trachytopes were included in flood zone 1 and were mapped using the photographs taken during field observations (e.g. Figure 4.9). Naturally, these assumptions and vegetation retrofitting were prone to sources of error that were compounded by Delft3D's limitations to accurately model morphologic changes. Utilizing the simulation results, the inundation duration of flood zone 1 was assessed. However, the areas with documented mortality were inundated for 21 hours, which was significantly lower than the lowest required mortality threshold (Table 7.2). Therefore, inundation did not appear to be responsible for the observed mortality. In evaluating trauma, sediment transport was evaluated for the peak discharge (288 $m^3 s^{-1}$); however, the model did not identify a measurable amount of transport within the area. Finally, the shear stress at peak discharge was examined and the Delft3D results (Figure 7.5) revealed that areas of observed mortality typically had higher shear stress (average 26.5 Pa) than areas of observed regrowth (average 16.1 Pa).

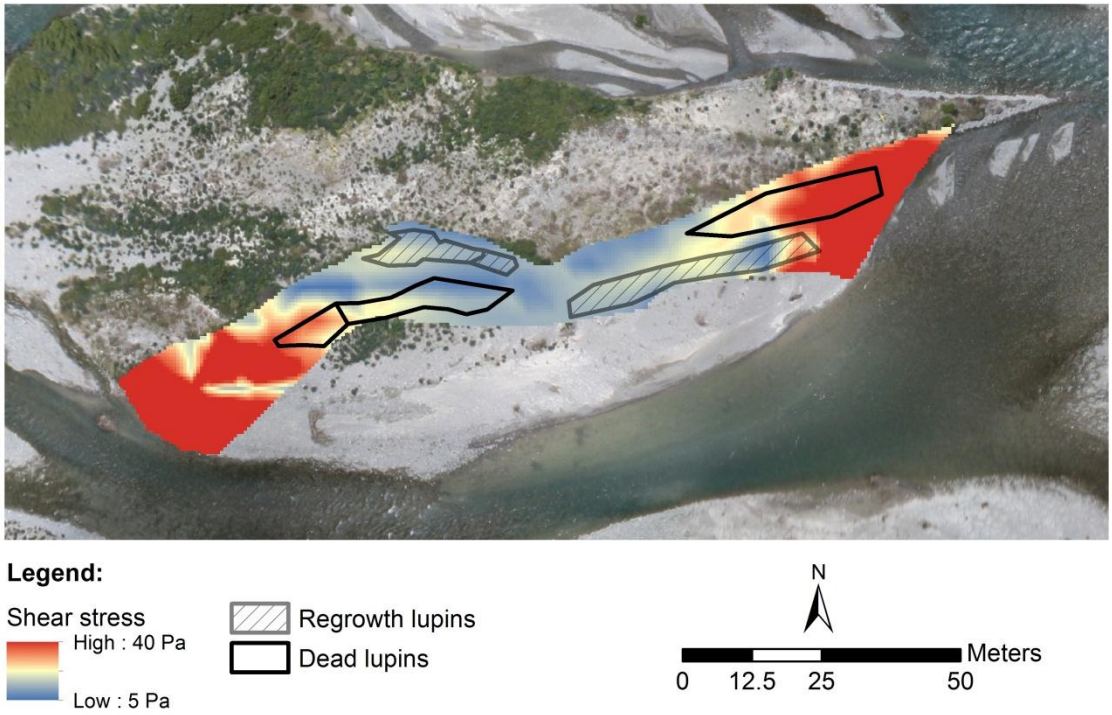

Figure 7.5: Flood zone 1 shear stress simulated at 288 $m^3 s^{-1}$ and with retrofitted mapped areas of observed lupin mortality.

While this shear stress relationship was seemingly predictive of flood-induced trauma, two concerns exist in addition to the already discusses potential errors. First, the mapped areas of mortality and regrowth were based on inaccurate methods of observations, notes, and photographs. Secondly, while the modeled shear stress provided an estimate of the potential for local sediment mobility, the overall cause of trauma was likely more complicated and a function of upstream mobility, upstream debris/sediment transport, and the flow routing into the affected areas. Therefore, while the shear stress provided some insight into trauma and lupin mortality, these results were estimates, subjective, and at their best only explain part of the overall processes that would be required. Therefore, due to low quality and large potential errors, trauma mortality was separated from the high confident mortality processes of inundation, drag, erosion, and deposition. However, trauma mortality mapping was included and identified using a shear stress mortality threshold of 30 Pa, but for discussion purposes only (Section 7.4).

7.3 Uncertainty estimation

7.3.1 Introduction

Prior to quantifying the mortality-induced by the various flood-induced processes, the uncertainty of the processes and numerical model were estimated. While most methods utilized to estimate lupin mortality were approached conservatively, the relationships were frequently developed utilizing relatively small datasets and/or custom empirical relationships. Despite these issues, uncertainty can still be estimated and quantified, which ultimately provided perspective for the complexity and uncertainty inherent in vegetation characteristics and mortality thresholds.

Uncertainty estimation is "neither a routine task nor a purely mathematical one" and depends on measurement procedure as well as individuals' understanding and critical assessment of the value (Ellison, Rosslein, & Williams, 2000, pg. 22). In assessing uncertainty associated with this research, the three categories of measurement uncertainty, process relationship uncertainty, and numerical modeling uncertainty were considered. Measurement uncertainty includes the uncertainty associated with the specific tools utilized during data collection as well as user errors. For example, these include (but are not limited to) the uncertainty in the Kern digital scale (± 1 N, utilized for pull-out force and drag force data), caliper measurements (± 1 mm for root diameters), echo-sounder (±1.0% depth and ±0.25% velocity of the range detected), RTK-GPS (±2-5 cm xyz), and river discharge which did not include the Longslip Creek tributary (estimated to be 7% for mean annual flood). Larger uncertainties include user errors as well as the subjective measuring techniques utilized for root diameter, plant height, and plant deformation; however, these user error uncertainties were not quantifiable.

Process relationship uncertainty includes the uncertainties associated with the methods utilized in identifying mortality thresholds based on field and laboratory data. These include inundation, drag, erosion, and deposition uncertainty. Due to numerous sources of error and low confidence associated with trauma, this uncertainty was not evaluated. Numerical modeling uncertainties were the uncertainties associated with the numerical model predictions. Since various flood events were simulated in an effort to identify lupin mortality, it was important to estimate the model's overall performance, and the potential uncertainty in

simulation results. These uncertainties include simulated inundation extent, water depth, velocity, and morphologic changes of erosion and deposition.

In estimating the total uncertainty, only the process and numerical model uncertainty were evaluated. Since measurement uncertainties from the digital scale, caliper, echo-sounder, and river discharge uncertainty were below 7%, these estimates were dwarfed by the process and numerical uncertainties. However, GPS uncertainty could have been higher. Considering elevation errors could have been as high as 5 cm, and average erosion and deposition changes were between 0.51 and 0.20 m (Table 6.20); thus, GPS uncertainty could have been between 10% and 25% for DoD detection. However, this uncertainty was utilized with the DoD generations in determining the minLoD. Further, measurement uncertainties due to user errors were not quantifiable. Therefore, due to these relatively low, previously incorporated, or undefinable measurement uncertainties, these were not included in total uncertainty estimates.

A valuable addition to the uncertainty evaluation that was not conducted would have been to assess each component's error influence to the overall accuracy of the final model goal (i.e. flood-induced mortality simulations). This could be accomplished through error budgets, where each component (e.g. simulated flow velocity, simulated inundation extent, etc.) could have been randomly generated within its typical uncertainty values (presented in Section 7.4.3), and evaluated based on the model's results. By quantifying the associated uncertainty of each model component and how it affects the accuracy of the overall goal, insight could have been gained into which model components are the greatest influence on the predictive uncertainty. Knowing these components, the modeler can then target the sensitive components and spend greater time constraining their influence during model calibration. While error budgets offer great insight into the model's ability, quantification would have been outside the scope of this project. Individual assessment of the model components and corresponding errors would have been labor and time intensive; however, the greatest challenge would be to couple the interdependent components (James Brasington, personal communication, January 10, 2014). For example, quantifying an error budget for topographic uncertainty would have been practical; however, because multiple and interdependent model components are linked together (e.g. bed roughness, grid resolution, etc.), this exercise would

have become extremely difficult and inherent uncertainty would have still developed. Therefore, error budgets were not attempted.

7.3.2 Inundation

7.3.2.1 Introduction

Inundation mortality was best assessed by separating the data into the four discussed conditions (submerged 50% and 100% mortality rates and emergent 50% and 100% mortality rates). With each condition developed using individual data and empirical relationships, each was assessed and resulted in unique uncertainty estimates. The methods and results for each condition are discussed in the sections below.

7.3.2.2 Methods

Limited by small datasets, estimating the potential uncertainty range was based on the understanding of the data and judgment (Ellison et al., 2000). Therefore, an acceptable approach was to develop upper and lower boundaries to cover areas of data uncertainty (Bell, 1999). Using the data of Figures 7.2 and 7.3, the best-fit linear relationship was considered the upper boundaries for the corresponding data. This was considered an appropriate choice since the data points utilized to develop these relationships met the mortality threshold, and all longer durations produced the same mortality rate or higher; thus, providing high confidence. Lower boundaries for the 100% mortality conditions were simply the upper boundary of the 50% mortality rate of similar submerged or emergent condition. This was considered appropriate given the high confidence that 50% mortality rate occurred; thus, the 100% mortality rate could potentially fall anywhere between the two relationships. The lower boundaries of the 50% mortality rates were developed by assessing Table 4.5 and determining the first duration in which any mortality occurred. With data only available up to 3 cm root diameter, the lower boundary was held constant using the 3 cm root diameters first observed mortality.

Once the boundaries were in place, it was possible to estimate the uncertainty. However, as will be discussed in Section 7.4, numerous mortality processes were identified and likely to combine mortality within specific areas. Therefore, combined uncertainty of the separate

processes (components) must be considered. In order to combine the uncertainty of multiple components, all uncertainty must be expressed using standard uncertainty. Standard uncertainty (SDU) was obtained by using standard deviation, which provided the same confidence level (one standard deviation, 68% confidence assuming data was close to a normal distribution (See Appendix D.6)) (Bell, 1999). In combining process uncertainties, one has to determine the relationship between processes. In cases where the processes were satisfied with addition or subtraction, the combined uncertainty was calculated using the root sum of the squares (Bell, 1999):

$$U_{Total} = \sqrt{a^2 + b^2 + i^2} \qquad \text{(Eqn: 7.1)}$$

where *a* and *b* are separate components' estimated uncertainties and the process was repeated for *i* number of components.

Calculating the uncertainty using upper and lower bounds was done in two stages. First, the standard deviation was calculated using the upper and lower boundary values for specific root diameters. However, as will be discussed in Section 7.4.2.1, inundation mortality was only up to 9 cm. Second, with the objective to simulate where inundation mortality occurs for various flood conditions, the final product of each simulation would be represented as an area affected. Therefore, the original units of duration in determining uncertainty would not suffice, so the uncertainty estimated was calculated as a percentage in order to utilize this uncertainty for all simulated flood events. Uncertainty percentages were calculated by dividing the difference between the upper and lower boundary values by the upper boundary value, and multiplying by 100. In this method, the uncertainty estimated was a percentage of the upper boundary value, which was appropriate given that the upper boundary values were utilized as inundation mortality thresholds for flood simulations. Further, since the upper boundary was utilized as mortality thresholds, and since all uncertainty was below the predicted, all uncertainties estimated suggest that lower inundation could cause mortality. Therefore, while typical uncertainty is represented as plus/minus (±) sign convention, the percentages for inundation uncertainty were presented as negative.

Finally, while it was acknowledged that relatively limited information was gained from calculating the standard deviation with only two values, the resulting value provided approximately 70% of the range. While it has been discussed that standard deviation of two variables typically underestimates the population's standard deviation, the difference is minimal when "compared to random variability inherent in collecting tiny data sets" ("Statistics with n=2," 2013), and thus sufficient for the uncertainty estimation in this research.

7.3.2.3 Results and discussion

In determining the lower boundary for the submerged 50% mortality rate condition, the earliest identified mortality rates occurred during two days of inundation duration for the 1 cm and 2 cm root diameters, and three days for the 3 cm roots. Therefore, these limits were plotted for the corresponding lower boundary of the observed data (Figure 7.6a). Further, with a three day duration the last identified lowest mortality, this value was utilized for the forecasted larger root diameters. The lower bound of the emergent 50% mortality rate condition was identified using the same methods, and the earliest mortality rates were identified as day 5, 5, and 7 for the root diameters of 1, 2, and 3 cm, respectively (Figure 7.6b).

Uncertainty for every root diameter was calculated using boundaries for the four inundation mortality conditions and results are shown in Table 7.7. As shown, each of the four conditions have varying results with uncertainties between zero (where the upper and lower boundary were identical) and -54%. With the exception of the emergent 100% mortality rate condition, all of the conditions produced increasing uncertainties for larger root diameters. This result was expected given that the larger root diameter's mortality was extrapolated and thus less known. In the case of the emergent 100% mortality rate, the uncertainty decreased with increasing root diameter. While this result was undesirable, this developed due to the slopes estimated for the best-fit linear relationships. Nevertheless, since the uncertainty did not decrease to zero, the uncertainty was still considered adequate.

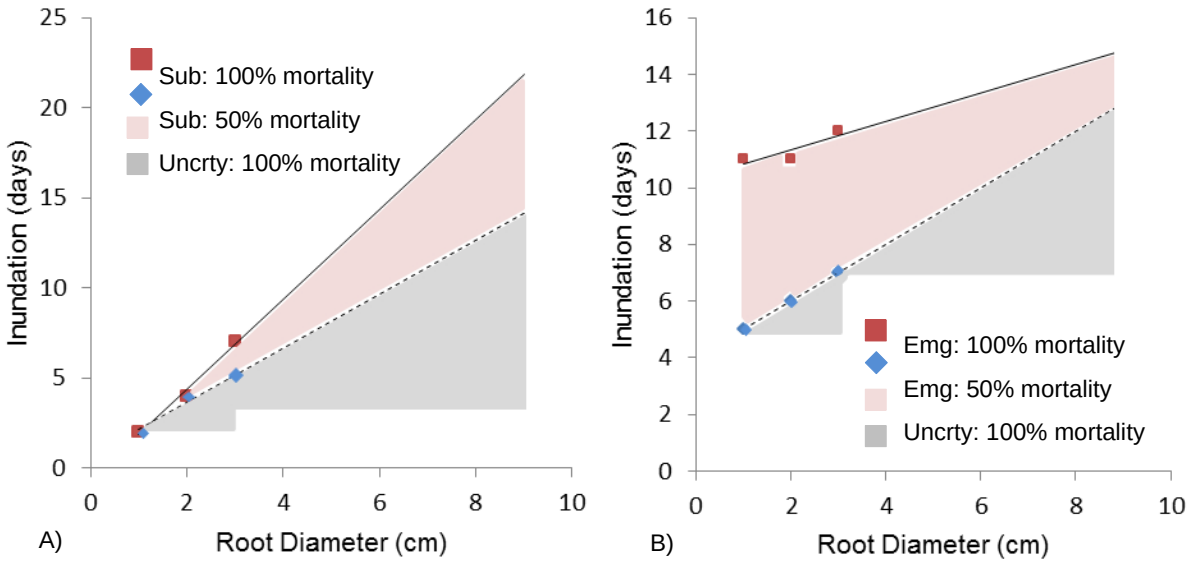

Figure 7.6: Mortality from inundation for the A) submerged conditions and B) emergent conditions.

Table 7.7: Inundation mortality uncertainty for the four inundation conditions.

Root diameter (cm)	50% mortality: Submerged			100% mortality: Submerged			50% mortality: Emerged			100% mortality: Emerged		
	Upper	Lower	Difference (%)	Upper	Lower	Difference (%)	Upper	Lower	Difference (%)	Upper	Lower	Difference (%)
1	2.0	2.0	0.0	2.0	2.0	0.0	5.0	5.0	0.0	11.0	5.0	-38.6
2	4.0	2.0	-35.4	4.3	4.0	-5.4	6.0	5.0	-12.0	11.0	6.0	-32.1
3	5.0	3.0	-28.3	6.8	5.0	-19.0	7.0	7.0	0.0	12.0	7.0	-29.5
4	6.7	3.0	-39.0	9.3	6.7	-19.9	8.0	7.0	-9.0	12.3	8.0	-24.7
5	8.2	3.0	-44.8	11.8	8.2	-21.7	9.0	7.0	-16.0	12.8	9.0	-21.0
6	9.7	3.0	-48.8	14.3	9.7	-22.9	10.0	7.0	-21.0	13.3	10.0	-17.5
7	11.0	3.0	-51.4	16.8	11.0	-24.5	11.0	7.0	-26.0	13.8	11.0	-14.3
8	12.0	3.0	-53.0	19.3	12.0	-26.8	12.0	7.0	-29.0	14.3	12.0	-11.4
9	13.0	3.0	-54.4	21.8	13.0	-28.6	13.0	7.0	-33.0	14.8	13.0	-8.6

7.3.3 Drag and pull-out forces

7.3.3.1 Introduction

Lupin removal from drag force alone was a potential mechanism of lupin mortality (Table 4.17). However, drag removal was estimated as a function of both the pull-out force required and drag force generated. Therefore, uncertainty for both datasets must be considered and combined.

7.3.3.2 Methods

Using the maximum values to establish custom empirical relationships for pull-out force relationship and root diameter (Figure 4.20c), all observed data values were at or below the custom linear relationships, and thus considerable uncertainty existed. Since observed data were available for most lupin diameters, single sample uncertainty was utilized and estimated for individual root diameter classes using a five-step method:

- First, data estimated from custom relationships (i.e. estimated data) and observed data were separated into root diameter intervals of 1 cm classes (e.g. 1 to 1.9 cm, 2 to 2.9 cm, etc.).
- Second, the standard uncertainty (SDU) was calculated using the observed and estimated data force values for each observed data point.
- Third, the average SDU and average estimated force were calculated for each root diameter class.
- Fourth, the average SDUs were divided by the corresponding average estimated force values; thus producing the uncertainty percent for each class.
- Fifth, the uncertainty for the root diameters without data was provided by using the greatest uncertainty estimated. This was considered the best approach as this uncertainty represented the potential range and provided a lower or upper boundary.

With all observed data for the pull-out forces below the estimated relationship values, only negative uncertainty percentages were estimated.

Drag uncertainty was estimated using the same five-step method. However, drag data was only available for root diameters up to 4 cm. Therefore, larger lupin root diameters were given the largest uncertainty. Since observed data were frequently above and below the estimated values (Figure 4.28) both positive and negative differences were calculated, and thus the percent differences were represented with plus/minus sign convention. With the uncertainties of drag and pull-out estimated, the final combined uncertainty was calculated using Equation 7.1. However, positive and negative values have no affect when combining uncertainties using Equation 7.1; therefore, the final combined uncertainties were designated with a negative value. This was considered appropriate given the large negative uncertainties estimated for the pull-out forces and due to negative uncertainties inherent in the drag forces.

Further, treating both values as a negative only increased the uncertainty range; thus this method was conservative.

7.3.3.3 Results and discussion

Pull-out force uncertainty results (Table 7.8) included the average force estimated, the average SDU, the initial uncertainty percentage, and the final uncertainty percentage that compensated for missing data (utilizing the greatest uncertainty value of -51%). Drag force uncertainty results (Table 7.9) showed lower uncertainty percentages than the pull-out forces, which was expected given the best-fit relationships that were utilized. Since uncertainty was only calculated for root diameters up to 4 cm, the maximum drag uncertainty of ±21% was utilized for the extrapolated larger root diameters uncertainty. Combined total uncertainty results are shown in Table 7.10 and produced larger uncertainties.

Table 7.8: Pull-out force uncertainty for 0 cm erosion condition.

	Average force (N)		Uncertainty (%)	
Root diameter class (cm)	Estimated	SDU	Calculated	Final
< 1	82	29	-36.0	-36.0
1 to 1.9	127	47	-36.7	-36.7
2 to 2.9	155	57	-36.8	-36.8
3 to 3.9	191	40	-21.0	-21.0
4 to 4.9	-	-	-	-50.9
5 to 5.9	226	63	-27.9	-27.9
6 to 6.9	239	107	-44.6	-44.6
7 to 7.9	-	-	-	-50.9
8 to 8.9	295	79	-27.0	-27.0
9 to 9.9	304	155	-50.9	-50.9
10 to 10.9	307	97	-31.6	-31.6
11 to 11.9	315	34	-10.7	-10.7
12 to 12.9	323	1	-0.5	-0.5
13 to 13.9	328	117	-35.7	-35.7
14 to 14.9	-	-	-	-50.9
≥ 15	-	-	-	-50.9

Table 7.9: Drag force uncertainty.

	Average force (N)		Uncertainty (%)	
Root diameter class (cm)	Estimated	SDU	Calculated	Final
< 1	-	-	-	±20.6
1 to 1.9	6	0.8	±12.5	±12.5
2 to 2.9	9.4	0.3	±3.3	±3.3
3 to 3.9	57.2	11.8	±20.6	±20.6
4 to 4.9	158.6	25.7	±16.1	±16.1
5+	-	-	-	±20.6

Table 7.10: Combined uncertainty for drag pull-out in 0 cm erosion conditions.

	Uncertainty (%)		
Diameter (cm)	Pull-out	Drag	Total
< 1	-36.0	±20.6	-41.7
1 to 1.9	-36.7	±12.5	-39.2
2 to 2.9	-36.8	±3.3	-37.1
3 to 3.9	-21.0	±20.6	-29.7
4 to 4.9	-50.9	±16.1	-53.5
5 to 5.9	-27.9	±20.6	-35.5
6 to 6.9	-44.6	±20.6	-49.7
7 to 7.9	-50.9	±20.6	-55.2
8 to 8.9	-27.0	±20.6	-34.2
9 to 9.9	-50.9	±20.6	-55.2
10 to 10.9	-31.6	±20.6	-38.3
11 to 11.9	-10.7	±20.6	-23.7
12 to 12.9	-0.5	±20.6	-21.0
13 to 13.9	-35.7	±20.6	-43.4
14 to 14.9	-50.9	±20.6	-55.2
≥ 15	-50.9	±20.6	-55.2

With seemingly large uncertainties estimated for the custom empirical relationships for pull-out forces, it was questioned whether an alternative method using a best-fit relationship would have less uncertainty. As discussed in Section 4.4.2.3, the logarithmic function was identified to best represent the overall pull-out data; therefore, the uncertainties of the custom empirical relationships were compared to the uncertainties of the best-fit logarithmic function (Figure 7.7). Using the same five-step methods, the uncertainties of the logarithmic function were calculated and the results (Table 7.11) were directly compared to the custom

relationship uncertainties. As shown, the logarithmic uncertainty was typically lower; however, due to the observed data above and below the function, the plus/minus sign convention was required. Therefore, while the logarithmic uncertainty value was typically lower, it is important to note that the uncertainty ranges were often greater. However, this evaluation did not consider the biased nature of the custom empirical relationships developed (caused by utilizing the maximum values); therefore, a true comparison would have been complex. Nevertheless, this comparison demonstrated that the uncertainties developed from custom relationships were slightly higher, but comparable in range.

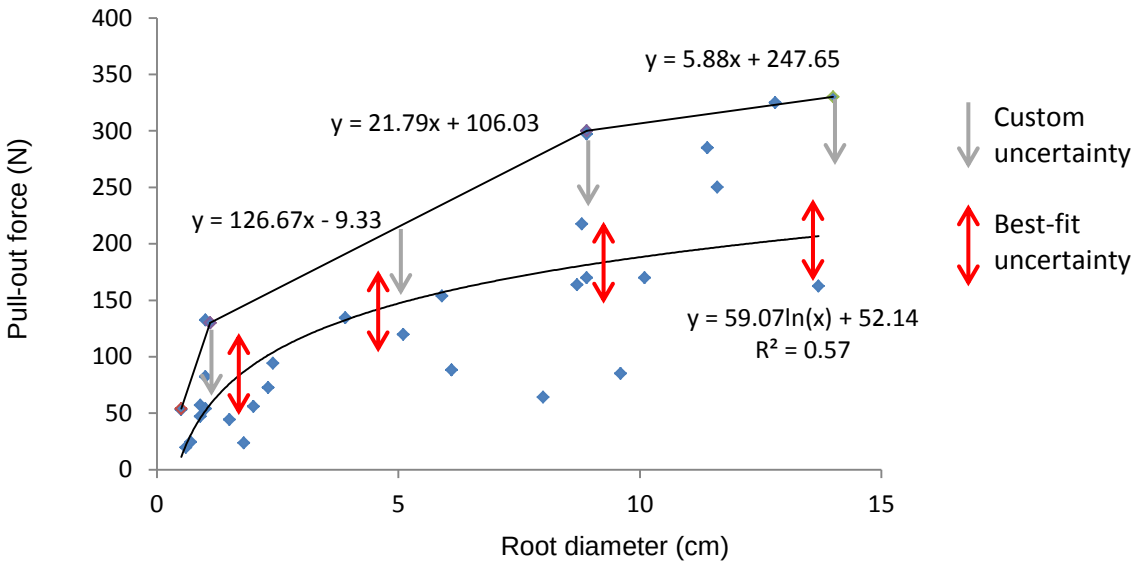

Figure 7.7: Pull-out force estimated using custom empirical and logarithmic relationships.

Table 7.11: Uncertainty comparison between custom and logarithmic relationships.

	Uncertainty (%)	
Root diameter class (cm)	Custom	Logarithmic
< 1	-36.0	±28.4
1 to 1.9	-36.7	±46.0
2 to 2.9	-36.8	±17.9
3 to 3.9	-21.0	±1.0
4 to 4.9	-50.9	±46.0
5 to 5.9	-27.9	±7.4
6 to 6.9	-44.6	±31.4
7 to 7.9	-50.9	±46.0
8 to 8.9	-27.0	±22.9
9 to 9.9	-50.9	±38.3
10 to 10.9	-31.6	±7.1
11 to 11.9	-10.7	±25.6
12 to 12.9	-0.5	±42.6
13 to 13.9	-35.7	±15.1
14 to 14.9	-50.9	±46.0
≥ 15	-50.9	±46.0

7.3.4 Drag pull-out with erosion

7.3.4.1 Introduction

Erosion combined with drag force was identified as a likely lupin removal process (Table 4.17) in cases where drag alone was not sufficient. With varying erosion levels produced using various data and relationships, separate uncertainty estimations were required. Since all lupins can be extracted with erosion levels of ≤ 40 cm and minimal velocities (Table 4.17), only erosion levels of 20, 30, and 40 cm were assessed.

7.3.4.2 Methods

Estimating uncertainty for lupin removal caused by drag/pull-out combined with erosion of 20 cm was approached similarly to drag and pull-out described in Section 7.3.3. This included calculating the uncertainty for pull-out forces with 20 cm of erosion and combining the uncertainty of drag. Therefore, using the data of Figure 4.20b, the pull-out force for 20 cm of erosion was estimated using the described five-step method. However, these data were collected in dry soil conditions, unlike the saturated soil conditions for 0 cm erosion. Nevertheless, the uncertainty estimated was considered adequate due to comparable

uncertainties estimated for the 0 cm saturated (Table 7.8) and 0 cm dry soil conditions (Table 7.14). Once the 20 cm erosion uncertainty was estimated it was combined with the drag uncertainty of Table 7.9.

Pull-out forces for erosion levels of 30 and 40 cm were slightly more complicated to estimate. While 20 cm of erosion data was collected, greater levels of erosion were extrapolated using the relationship between force reduction between the dry soil conditions 0 cm and 20 cm erosion data, as well as the relationship between root diameters to root lengths that were utilized to determine the erosion levels corresponding effect on root exposure (Section 4.4.2.3). Since all erosion levels of 30 and 40 cm were forecasted using the same data and relationships, it was assumed that all would have the same uncertainty. Therefore, this method was referred to as the uncertainty for erosion levels of 30+ cm. In estimating the uncertainty for 30+ cm erosion, it was necessary to combine the uncertainties of the dry soil 0 cm pull-out force, the dry soil 20 cm pull-out force, drag, and root-length to root diameter. Using the previously estimated drag uncertainty and the pull-out with 20 cm of erosion uncertainty of this section, only the 0 cm erosion for dry soil and the root-length to root diameter uncertainties were required. Therefore, using the described five-step method and data of Figure 4.20a, the uncertainty of 0 cm erosion in dry soil was estimated and the root length was estimated using the data of Figure 4.22a.

7.3.4.3 Results and discussion

Uncertainty estimation for the dry soil 20 cm erosion data (Table 7.12) produced slightly lower uncertainties than the saturated soil 0 cm erosion (Table 7.8). However, given that the 20 cm erosion had less available data to develop the relationship and thus uncertainty estimates, these lower values may not be fully representative. Nevertheless, the lower boundary was established for the root classes with missing data and utilized the largest uncertainty of -42%, which was comparable to the saturated 0 cm lower bound. Combining this data with Table 7.9, the final total estimated uncertainty was developed (Table 7.13) and produced comparable results to the final uncertainty of saturated 0 cm (Table 7.10).

Table 7.12: Pull-out uncertainty for dry soil 20 cm erosion.

	Average force (N)		Uncertainty (%)	
Root diameter class (cm)	Estimated	SDU	Calculated	Final
< 1	-	-	-	-42.4
1 to 1.9	-	-	-	-42.4
2 to 2.9	101	26	-25.8	-25.8
3 to 3.9	212	49	-22.9	-22.9
4 to 4.9	334	117	-35.0	-35.0
5 to 5.9	443	126	-28.4	-28.4
6 to 6.9	477	84	-17.5	-17.5
7 to 7.9	482	38	-7.9	-7.9
8 to 8.9	-	-	-	-42.4
9 to 9.9	-	-	-	-42.4
10 to 10.9	495	210	-42.4	-42.4
11 to 11.9	500	79	-15.8	-15.8
12 to 12.9	-	-	-	-42.4
13 to 13.9	-	-	-	-42.4
14 to 14.9	-	-	-	-42.4
≥ 15	-	-	-	-42.4

Table 7.13: Combined uncertainty for 20 cm erosion pull-out and drag.

	Uncertainty (%)		
Root diameter class (cm)	Pull-out	Drag	Total
< 1	-42.4	±20.6	-47.0
1 to 1.9	-42.4	±12.5	-44.0
2 to 2.9	-25.8	±3.3	-26.2
3 to 3.9	-22.9	±20.6	-31.1
4 to 4.9	-35.0	±16.1	-38.5
5 to 5.9	-28.4	±20.6	-35.0
6 to 6.9	-17.5	±20.6	-27.7
7 to 7.9	-7.9	±20.6	-22.5
8 to 8.9	-42.4	±20.6	-47.0
9 to 9.9	-42.4	±20.6	-47.0
10 to 10.9	-42.4	±20.6	-47.0
11 to 11.9	-15.8	±20.6	-26.4
12 to 12.9	-42.4	±20.6	-47.0
13 to 13.9	-42.4	±20.6	-47.0
14 to 14.9	-42.4	±20.6	-47.0
≥ 15	-42.4	±20.6	-47.0

Estimated uncertainty results for the dry soil 0 cm erosion pull-out (Table 7.14) produced comparable uncertainty ranges when compared to the saturated soil 0 cm erosion pull-out. Root diameter and length uncertainty results (Table 7.15) showed relatively small uncertainty compared to other relationship uncertainties. Combining the uncertainties of Tables 7.13, 7.14, 7.15, and drag of Table 7.9, the total uncertainty for 30+ cm erosion is shown in Table 7.16 with the various components that contributed to the final uncertainty. Comparing the results to the 20 cm erosion shows that the 30+ cm erosion had considerably larger uncertainty. These results were expected and the largest contributions came from the pull-out force uncertainties.

Table 7.14: Dry soil 0 cm erosion pull-out uncertainty.

	Average force (N)		Uncertainty (%)	
Root diameter class (cm)	Estimated	SDU	Calculated	Final
< 1	102.6	30.5	-29.7	-29.7
1 to 1.9	321.8	130.6	-40.6	-40.6
2 to 2.9	539.6	173.6	-32.2	-32.2
3 to 3.9	539.6	144.8	-26.8	-26.8
4 to 4.9	539.6	106.2	-19.7	-19.7
5 to 5.9	539.6	144	-26.7	-26.7
6 to 6.9	539.6	70.9	-13.1	-13.1
7 to 7.9	539.6	73.8	-13.7	-13.7
8 to 8.9	-	-	-	-40.6
9 to 9.9	539.6	55.8	-10.3	-10.3
10 to 10.9	539.6	85.3	-15.8	-15.8
11 to 11.9	539.6	210.3	-39	-39
12 to 12.9	-	-	-	-40.6
13 to 13.9	-	-	-	-40.6
14 to 14.9	539.6	13.9	-2.6	-2.6
≥ 15	-	-	-	-40.6

Table 7.15: Root diameter to root length relationship uncertainty.

	Root length (cm)		Uncertainty (%)	
Root diameter class (cm)	Estimated	SDU	Calculated	Final
< 1	-	-	-	±20.6
1 to 1.9	6	0.8	±12.5	±12.5
2 to 2.9	9.4	0.3	±3.3	±3.3
3 to 3.9	57.2	11.7	±20.6	±20.6
4 to 4.9	158.6	25.6	±16.1	±16.1
5+	-	-	-	±20.6

Table 7.16: 30+ cm erosion uncertainty and the corresponding components.

	Average uncertainty (%)				
Root diameter class (cm)	Pull-out (0 cm erosion)	Pull-out (20 cm erosion)	Drag	Root length	Total
< 1	-29.7	-42.4	±20.6	±2.6	-55.6
1 to 1.9	-40.6	-42.4	±12.5	±2.6	-59.9
2 to 2.9	-32.2	-25.8	±3.3	±1.3	-41.5
3 to 3.9	-26.8	-22.9	±20.6	±0.1	-41.1
4 to 4.9	-19.7	-35	±16.1	±2.6	-43.3
5 to 5.9	-26.7	-28.4	±20.6	±1.5	-44.0
6 to 6.9	-13.1	-17.5	±20.6	±2.6	-30.7
7 to 7.9	-13.7	-7.9	±20.6	±2.6	-26.4
8 to 8.9	-40.6	-42.4	±20.6	±2.6	-62.1
9 to 9.9	-10.3	-42.4	±20.6	±2.6	-48.1
10 to 10.9	-15.8	-42.4	±20.6	±2.6	-49.6
11 to 11.9	-39.0	-15.8	±20.6	±2.6	-47.2
12 to 12.9	-40.6	-42.4	±20.6	±2.6	-62.1
13 to 13.9	-40.6	-42.4	±20.6	±2.6	-62.1
14 to 14.9	-2.6	-42.4	±20.6	±2.6	-47.1
≥ 15	-40.6	-42.4	±20.6	±2.6	-62.1

As a final measure of the methods utilized, the custom relationship's uncertainties for the dry 0 cm erosion pull-out and dry 20 cm erosion pull-out were compared to the uncertainty estimated from best-fit logarithmic functions and shown in Figures 7.8 and 7.9, respectively. Using the same five-step methods, the uncertainty for the logarithmic functions were estimated, and the comparisons for the 0 cm erosion are presented in Table 7.17 and the 20 cm comparisons are shown in Table 7.18. Table 7.17 shows that the uncertainties were

comparable, with the logarithmic function's uncertainty typically lower. Similar results were found for the 20 cm results; however, the required plus/minus sign convention for the logarithmic data created ranges with occasionally larger uncertainty than the custom relationship.

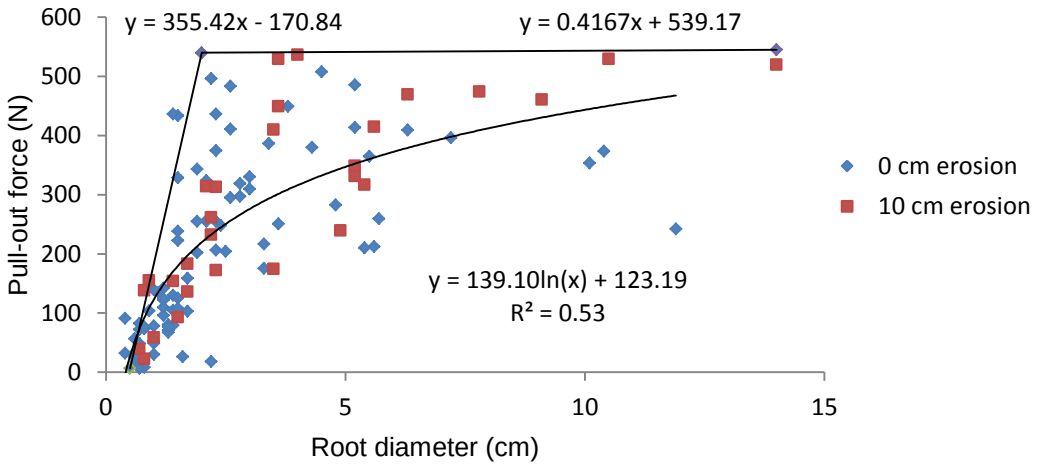

Figure 7.8: Dry soil 0 cm erosion pull-out force with custom and logarithmic relationships.

Table 7.17: Uncertainty comparison between the custom and logarithmic relationships for the dry 0 cm erosion pull-out condition.

	Uncertainty (%)	
Root diameter class (cm)	Custom	Logarithmic
< 1	-29.7	±30.3
1 to 1.9	-40.6	±30.8
2 to 2.9	-32.2	±25.5
3 to 3.9	-26.8	±25.6
4 to 4.9	-19.7	±26.1
5 to 5.9	-26.7	±14.2
6 to 6.9	-13.1	±11.2
7 to 7.9	-13.7	±5.8
8 to 8.9	-	-
9 to 9.9	-10.3	±5.0
10 to 10.9	-15.8	±13.0
11 to 11.9	-39	±34.1
12 to 12.9	-	-
13 to 13.9	-	-
14 to 14.9	-2.6	±4.3
≥ 15	-	-

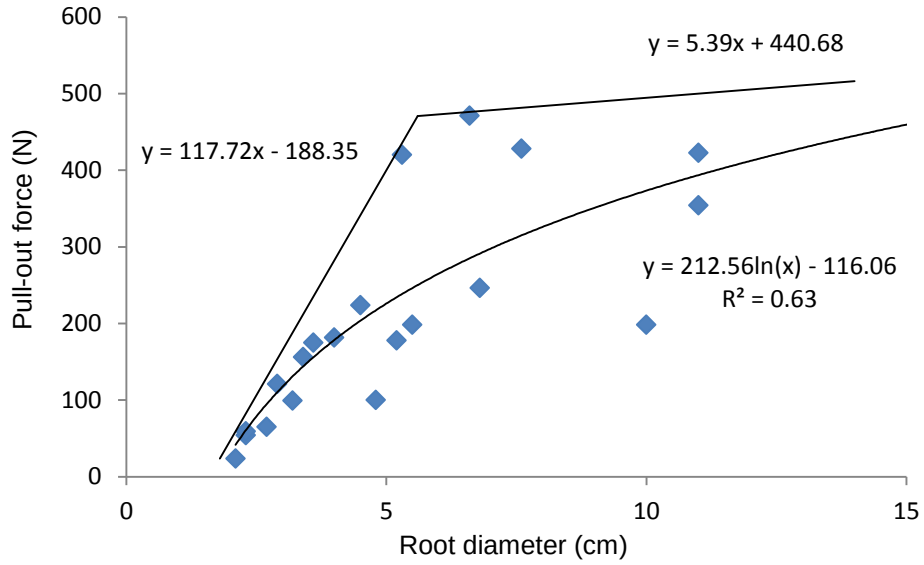

Figure 7.9: Dry soil 20 cm erosion pull-out force with custom and logarithmic relationships.

Table 7.18: Uncertainty comparison between the custom and logarithmic relationships for the dry 20 cm erosion pull-out condition.

	Uncertainty (%)	
Root diameter class (cm)	Custom	Logarithmic
< 1	-	-
1 to 1.9	-	-
2 to 2.9	-25.8	±13
3 to 3.9	-22.9	±10
4 to 4.9	-35	±17
5 to 5.9	-28.4	±28
6 to 6.9	-17.5	±28
7 to 7.9	-7.9	±25
8 to 8.9	-	-
9 to 9.9	-	-
10 to 10.9	-42.4	±33
11 to 11.9	-15.8	±6
12 to 12.9	-	-
13 to 13.9	-	-
14 to 14.9	-	-
≥ 15	-	-

7.3.5 Deposition

7.3.5.1 Introduction

Deposition mortality thresholds were identified and created using various data and relationships. While frequently throughout this research the experiment and results of Section 4.4.4 were referred to as deposition, this section will refer to that specific data as deposition burial and the term deposition uncertainty was designated to describe the total combined uncertainty of the individual components of canopy height, canopy deformation, and deposition burial.

7.3.5.2 Methods

During data preparation for deposition mortality threshold identification (Section 7.2.4), the canopy height to root diameter data were utilized and the estimated canopy heights were based on custom empirical relationships using the maximum values. Therefore, the uncertainty associated with canopy height was determined using the five-step process to estimate the uncertainty as a percentage. In estimating the required deposition for total burial, the plants height deformation data were utilized, and was estimated using the determined average deformation of 50.6% (Table 4.18); however, this assumption also has inherent uncertainty. To estimate the deformation uncertainty, the same five-step process was applied using the estimated deformation value of 50.6% of the canopy height against the observed value of Table 4.18.

The amount of deposition burial required to cause mortality was assessed. Since limited data was available for deposition burial, an upper boundary was established using the maximum documented burial that caused mortality (complete burial + 10 cm), the lower boundary was the lowest burial to cause mortality (complete burial + 2 cm), and the standard uncertainty was estimated for the specific root diameter classes. Finally, the total uncertainty was determined by combining the three components of canopy height, deformation, and deposition burial using Equation 7.1.

7.3.5.3 Results and discussion

Canopy height uncertainty results (Table 7.19) revealed the greatest uncertainty was -50%, which was used as the lower boundary for missing data. The deformation results (Table 7.20) revealed relatively small uncertainty percentages as well as a significant variation between the classes. With limited data available for deformation, the largest uncertainty of ±22.2% was utilized to fill missing data as well as forecasted data. The deposition burial uncertainty results (Table 7.21) produced a trend with larger uncertainties for smaller root diameters, which gradually decreased with larger root diameters. This lower uncertainty for forecasted data was seemingly unjustified; however, considering that smaller root diameters were found to have mortality at the lower bound of 2 cm, and the larger diameters were only found to have mortality at 10 cm, this uncertainty trend was accurate for the smaller observed data. Further, the deposition burial uncertainty of Table 7.21 was only one aspect of the overall deposition uncertainty for mortality threshold identification. Once the total uncertainty of each component was combined (Table 7.22), these were observed to be well balanced across all root diameter classes.

Table 7.19: Canopy height uncertainty

	Average height (cm)		Uncertainty (%)	
Root diameter class (cm)	Estimated	SDU	Calculated	Final
< 1	25	8	-33.0	-33.0
1 to 1.9	36	10	-28.4	-28.4
2 to 2.9	50	16	-32.7	-32.7
3 to 3.9	67	26	-49.8	-49.8
4 to 4.9	81	38	-46.2	-46.2
5 to 5.9	94	38	-40.7	-40.7
6 to 6.9	100	41	-40.7	-40.7
7 to 7.9	100	34	-34.2	-34.2
8 to 8.9	100	35	-34.7	-34.7
9 to 9.9	100	25	-25.2	-25.2
10 to 10.9	100	34	-34.1	-34.1
11 to 11.9	100	41	-41.4	-41.4
12 to 12.9	100	29	-29.5	-29.5
13 to 13.9	100	40	-40.3	-40.3
14 to 14.9	100	31	-31.1	-31.1
≥ 15	-	-	-	-46.2

Table 7.20: Canopy height deformation uncertainty.

	Average deformation (cm)		Uncertainty (%)	
Root diameter class (cm)	Estimated	SDU	Calculated	Final
< 1	3.4	0.5	±14.8	±14.8
1 to 1.9	9.4	1.1	±11.2	±11.2
2 to 2.9	12.5	1.1	±9.1	±9.1
3 to 3.9	16.3	3.6	±22.2	±22.2
4 to 4.9	15.2	1.5	±10.2	±10.2
5 to 5.9	16.7	0.5	±3.0	±3.0
6 to 6.9	-	-	-	±22.2
7 to 7.9	18.7	0.2	±1.0	±1.0
8+	-	-	-	±22.2

Table 7.21: Deposition burial uncertainty.

Root diameter (cm)	Deformed canopy height (cm)	Upper (cm)	Lower (cm)	SDU (cm)	Uncertainty (%)
< 1	8	18	10	5.7	-31.6
1	13	23	15	5.7	-24.8
2	22	32	24	5.7	-17.8
3	31	41	33	5.7	-13.9
4	40	50	42	5.7	-11.4
5	49	59	51	5.7	-9.7
6	49	59	51	5.7	-9.7
7	49	59	51	5.7	-9.7
8	49	59	51	5.7	-9.7
9	49	59	51	5.7	-9.7
10	49	59	51	5.7	-9.7
11	49	59	51	5.7	-9.7
12	49	59	51	5.7	-9.7
13	49	59	51	5.7	-9.7
14	49	59	51	5.7	-9.7
15	49	59	51	5.7	-9.7

Table 7.22: Total uncertainty of the combined components.

Root diameter (cm)	Uncertainty (%)			
	Canopy height	Deposition	Deformation	Total
< 1	-33.0	-31.6	±14.8	-47.6
1	-28.4	-24.8	±11.2	-39.2
2	-32.7	-17.8	±9.1	-38.6
3	-49.8	-13.9	±22.2	-47.8
4	-46.2	-11.4	±10.2	-48.4
5	-40.7	-9.7	±3.0	-42.2
6	-40.7	-9.7	±22.2	-47.7
7	-34.2	-9.7	±1.0	-35.5
8	-34.7	-9.7	±22.2	-42.6
9	-25.2	-9.7	±22.2	-34.9
10	-34.1	-9.7	±22.2	-41.8
11	-41.4	-9.7	±22.2	-47.7
12	-29.5	-9.7	±22.2	-37.9
13	-40.3	-9.7	±22.2	-46.8
14	-31.1	-9.7	±22.2	-39.4
15	-46.2	-9.7	±22.2	-52.0

During the deposition uncertainty estimation, both the canopy height and deformation methods utilized custom relationships instead of best-fit functions. Comparing the custom and best-fit functions of the two datasets, the canopy height results (Figure 7.10 and Table 7.23) showed that the logarithmic uncertainties were typically lower, and the deformation height results (Table 7.24) show that the custom relationship-derived uncertainties were lower. However, the deformation height uncertainties using the logarithmic function revealed a decreasing trend, and given the greater variability in the custom method, the logarithmic uncertainties were likely to produce smaller uncertainties for the undocumented larger root diameter classes, which would be unjustified. Therefore, considering the range of uncertainty, the logarithmic uncertainty was likely comparable, and often larger than the custom relationships that were utilized.

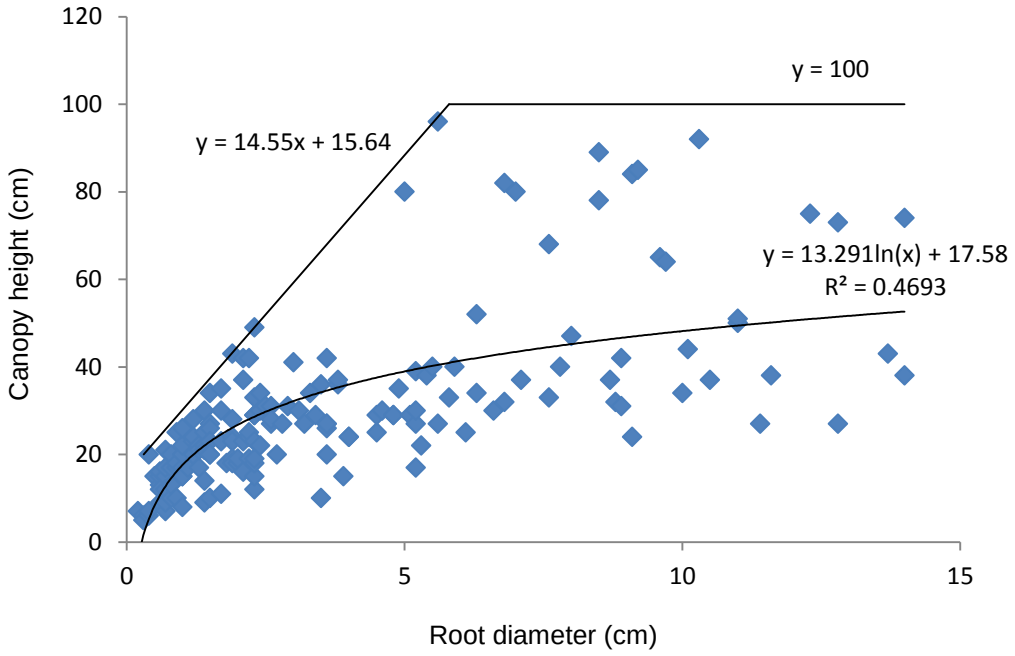

Figure 7.10: Canopy height and root diameter custom and logarithmic relationships.

Table 7.23: Root diameter and canopy height relationship uncertainty.

	Uncertainty (%)	
Root diameter class (cm)	Custom	Logarithmic
< 1	-33.0	±28.9
1 to 1.9	-28.4	±16.3
2 to 2.9	-32.7	±17.3
3 to 3.9	-49.8	±16.2
4 to 4.9	-46.2	±17.9
5 to 5.9	-40.7	±26.5
6 to 6.9	-40.7	±27.0
7 to 7.9	-34.2	±26.6
8 to 8.9	-34.7	±26.4
9 to 9.9	-25.2	±39.3
10 to 10.9	-34.1	±26.9
11 to 11.9	-41.4	±13.2
12 to 12.9	-29.5	±32.2
13 to 13.9	-40.3	±12.7
14 to 14.9	-31.1	±24.2
≥ 15	-	-

Table 7.24: Root diameter and lupin canopy height deformation uncertainty.

	Uncertainty (%)	
Root diameter class (cm)	Custom	Logarithmic
< 1	±14.8	±44.8
1 to 1.9	±11.2	±19.1
2 to 2.9	±9.1	±18.7
3 to 3.9	±22.2	±27.8
4 to 4.9	±10.2	±17.7
5 to 5.9	±3.0	±10.1
6 to 6.9	-	-
7 to 7.9	±1.0	±2.9
8+	-	-

7.3.6 Hydrodynamic model uncertainty

7.3.6.1 Introduction

Due to extensive datasets and model calibration and validation assessments in Chapter 6, estimating the model uncertainty required less assessment and relationship coupling than the process uncertainties. Therefore, all numerical model uncertainty is presented in this section. Numerical model uncertainty was estimated for the five components of water inundation extent, depth, velocity, sediment erosion, and deposition. In estimating the specific components, data were utilized that best represented flood conditions, since the uncertainties associated were applied to the various large flood simulations. Therefore, the choice of which data provided the best estimation of uncertainty was critical, and the methods and procedure for each component is presented in the section below.

7.3.6.2 Methods

Inundation extent uncertainty was best represented by the effective width (Fit_{we}). While this value does not represent local water extent accuracy, it provided a quantitative field measure of total water extent and can be thought of as representing the water surface width using infinite cross sections (Williams et al., 2013). When considering the uncertainty associated with modeling various large flood events that were simulated with the 2.5 m grid, only the two effective widths calculated during the validation stage (Section 6.5.2) were of particular interest as they represented high and moderate flow conditions with moderate overland flow and were the results of the fully calibrated model. However, the calculated effective widths

were represented as area percentages and not standard uncertainty. While all other methods have utilized the standard uncertainty, it was not utilized for inundation extent. With only one value to assess the uncertainty, the best method was to assume the uncertainty could exist within the full range of error (Bell, 1999). Therefore, the uncertainty was assumed to be represented by the effective width results.

Depth accuracy was regularly calculated throughout the numerical model calibration and validation. Unfortunately, no depth data were collected during high flow rates; however, extensive depth data were collected in the main channel for the bathymetric mapping at low flows. Because flood conditions were the primary interest, depths of ≥ 0.3 m were chosen (supported and discussed in Section 7.4.2.1) and separated from the echo-sounder data and manual RTK-GPS depth data, and compared to the simulated depths of corresponding areas (same data as used in Tables 6.6 and 6.22) to estimate uncertainty. Using the raw data, the uncertainty for both pre- and post-flood data was estimated by calculating the standard uncertainty of the measured and modeled depths values for all locations, and then dividing the SDU by the estimated depth; thus providing an uncertainty percentage in relation to the estimated depth. Depth uncertainty for the pre-flood was estimated using 5,787 points that had an average depth of 0.62 m, and the post-flood uncertainty was estimated with 126 points with an average depth of 0.53 m. Since both pre- and post-flood datasets were utilized, the average uncertainty was taken as the final.

Velocity data were collected using only the aDcp, and were limited to the moderate-reach and pool-reach sections (Section 6.3.2). However, while the best representation for velocity would have been from high flow rates, this data was reasonably appropriate given the pool-reach provided data for deeper conditions and the moderate-reach would likely provide faster velocities. Therefore, both the moderate- and pool-reaches uncertainties were estimated. Utilizing the raw data and the simulated results, the uncertainty was estimated by calculating the SDU of the observed velocity and modeled velocity for all locations, and calculating the percent uncertainty by dividing the average SDU by the average modeled velocities. This was appropriate as this was a percentage of the modeled velocity, which was the value of interest (same data utilized to calculate Table 6.11 and 6.12 depths).

Morphologic changes were divided into erosion and deposition categories. In determining the uncertainty for each morphologic process, the MOR_{fit} data of Table 6.18 was utilized for the model v75 results (which was the calibrated model utilized in all model simulations of Chapter 7). This data provided correctly, incorrectly, and void-predictions as a percentage of area occurrence for the morphological model calibration. Incorrect predictions were the result of erosion simulated where deposition was observed, and vice versa. Void predictions were areas where no morphologic change was indicated by simulations, yet changes were observed. Similar to the inundation uncertainty, uncertainty estimation was limited to the outcome of one particular value. Therefore, the incorrect and void prediction errors were considered the full potential of uncertainty and thus, final uncertainty was estimated by adding the percentages of incorrect and void predictions for erosion, and this method was repeated for deposition.

7.3.6.3 Results and discussion

Numerical model uncertainties for the individual components were estimated and results are presented in Table 7.25. Inundation uncertainty was estimated using the same data that developed the effective widths of Figure 6.16. With the high flow conditions having an effective width of 107.94%, the total simulated inundation was over-predicted by +7.9%. Further, the medium flow conditions produced an effective width of 95.1%, thus the simulation inundation was under-predicted by -4.9%. Given that the high flow condition was more representative of the forecasted flood conditions simulated, the value of +7.9% uncertainty was utilized. However, since the effective widths were shown to both over- and under-predict the inundation extent, the final uncertainty was estimated using the plus/minus sign convention (±7.9%).

Depth uncertainties for the pre- and post-flood data were ±22.2% and ±33.7%, respectively. Averaging these two values, the final uncertainty was estimated at ±28.0%. A simple average was taken instead of a weighted average because the larger pre-flood dataset depth measurements were in clusters, while the smaller post-flood dataset was well distributed. Therefore, considering both had comparable area of coverage, the two were considered equal representation of the simulation uncertainties.

The velocity data was only assessed using the upstream data of the moderate-reach and pool-reach (justified in Section 6.4.3.3). The velocity of the moderate-reach produced an average uncertainty of ±26.7% with an average velocity of 0.48 m/s, and the pool-reach had an uncertainty estimated at ±34.9% with an average velocity of 0.57 m/s. Since the pool-reach had deeper depths and faster velocities, it was more representative of the flood conditions of interest (depth ≥ 0.3 m). Therefore, the ±34.9% result was utilized, which was adequate given that it was also conservative. Finally, the erosion and deposition uncertainty results were taken from Table 6.18 for the overland flow category. Overland flow data was determined the appropriate choice since i) it represented the total area that was subjected to vegetation removal, and ii) it was more representative of the larger forecasted flood events modeled.

Table 7.25: Numerical model uncertainties for the individual components.

	Uncertainty (%)	
Process:	Calculated	Final
Inundation extent		
High flow	+7.9%	±7.9
Moderate flow	-4.9%	
Depth		
Pre-flood	±22.2	±28.0
Post-flood	±33.7	
Velocity		
Moderate-reach	±26.7	±34.9
Pool-reach	±34.9	
Erosion	43.9	±43.9
Deposition	65.8	±65.8

7.4 Mortality mapping

7.4.1 Introduction

Using the forecasted flood event simulations and the mortality thresholds of Section 7.2, lupin mortality mapping is presented in this section. However, due to the constantly changing morphology and hydraulic conditions through the flood simulations, additional methods were developed to affectively and practically map the corresponding mortality. Further, mortality processes frequently overlapped one another for specific areas; therefore, methods were

developed to assess multiple-process mortality as well as for mortality mapping priorities where multiple-processes were not necessary (due to 100% mortality rates). These methods were applied to inundation, drag, erosion, and deposition processes. However, trauma was not included due to the low confidence associated with the methods and results. Instead, areas identified with potential trauma-induced mortality (using a threshold of 30 Pa) were only offered as a potential process, and not included in final lupin mortality analysis.

7.4.2 Methods

7.4.2.1 Inundation

Inundation mortality was the most difficult process to identify and map. The first challenges were to establish what simulated conditions were required to achieve inundation mortality. While section 7.2.2 provided the inundation duration thresholds that can cause lupin mortality, additional considerations were simulated water depth, plant height, plant height deformation, and lupin presence in affected areas. Further, once these issues were resolved, identifying the inundation duration of local vegetated areas was difficult due to the ever changing morphology, water extent, and water depths. The ideal way to assess the areas affected would be to consider each recorded flood condition simulated (time-step); however, this approach was not realistic given the 500- and 200-year flood events produced well over 100 time-steps. Therefore, in order to keep the methods accurate and practical, two simplifications were utilized: i) additional mapping thresholds were applied, and ii) temporal bounds were developed.

Additional mapping thresholds were necessary since inundation mortality was a function of root diameter, plant height, water depth, and duration; thus, the original mortality thresholds of inundation duration could not solely identify mortality. Therefore, to account for specific root diameter mortalities, the three lupin density areas (dense, moderate, and sparse) were considered separately and root diameter frequency was determined for the corresponding areas (Figure 5.20b) using Table 7.1. Plant height and water depth were considered together since plant height deformation was dependent on the localized flow and water depth. Dividing water depth and plant height requirements into the two categories of submerged and emergent was necessary (Section 7.2.2) as mortality rates differed. The first attempt to simplify the submerged conditions was to assume that all plants in a submerged condition

would be ≤ 0.5 m tall; therefore water depths ≥ 0.5 m were only considered and provided a practical data simplification. This assumption utilized the previous data that lupin height deformation was on average 50.6%, which was determined in an experiment using flow with 0.6 m/s velocity. However, this inundation mortality proved too restrictive and unnecessary since inundation duration rarely caused mortality to lupins with root diameters > 3 cm; whose heights were occasionally below the 0.5 m restriction. Therefore, this depth threshold was revised to ≥ 0.3 m. This threshold assumed that the majority of plants to experience mortality (≤ 3 cm root diameters) would have deformed canopies ≤ 0.3 m tall to ensure submerged condition. This assumption was satisfied by the data of Table 7.6. Further, this assumed that water depths of 0.3 m could cause the average 50.6% plant height deformation. This assumption was satisfied through a simple evaluation using study-reach characteristics and Manning's equation (Eqn 7.2) (Munson et al., 2009):

$$v = \frac{1}{n} R_h^{\frac{2}{3}} S_o^{\frac{1}{2}} \quad \rightarrow \quad v = \frac{1}{0.05}\left(\frac{100\ m\ x\ 0.3\ m}{0.3\ m + 0.3\ m + 100\ m}\right)^{\frac{2}{3}} 0.009^{\frac{1}{2}} = 0.84\ m/s \qquad \text{(Eqn: 7.2)}$$

where n is Manning's coefficient of roughness, v is the flow velocity (m/s), R_h is the hydraulic radius (equal to the wetted area divided by wetted perimeter (m)), and S_o is the river's channel gradient. With the study-reach's average channel gradient estimated at 0.9%, utilizing a roughness coefficient of 0.05 (value for floodplains with light brush and heavy vegetation; Munson et al., 2009), and hydraulic radius calculated with a width of 100 m and water depth of 0.3 m, velocity was determined to equal 0.84 m/s; which was above the 0.6 m/s velocity that caused an average height reduction of 50.6%. Further, substituting smaller channel widths produced larger velocities and thus, the assumption that lupins susceptible to inundation mortality were completely submerged at 0.3 m water depth was justified. Therefore, in identifying areas of inundation mortality for the various simulated flood events, submerged areas were initially identified with water depths of ≥ 0.3 m (mapping threshold 1). Emergent inundation conditions were simply mapped by depths of ≥ 0.02 m and greater since emergent conditions only required water depths up to the base of the lupin stalk. Therefore, inundation depths of ≥ 0.02 m ensured local inundation existed (mapping threshold 2).

To limit the extensive available data to essential data required additional temporal considerations. This was accomplished using two methods. The first method utilized the flood hydrographs (Figure 4.8) and identified the duration in which various flood discharges were maintained or exceeded. This information was then combined with the mortality thresholds identified (Table 7.2) and provided the ability to reduce the data to specific time-steps (of specific discharges) that met the duration mortality thresholds. For example, the 500-year flood event's (discharge of 923 $m^3 s^{-1}$) total duration lasted 17.8 days; however, the highest discharge during this event that met the minimum duration mortality of 2.0 days was 600 $m^3 s^{-1}$; therefore, the area inundated at 600 $m^3 s^{-1}$ had the potential to cause inundation mortality. This process was repeated to identify the various discharges that met the duration mortality thresholds (e.g. 3.7, 4.3, 5.0 days, etc.).

The second method was to consider the updating morphology and changing discharges that altered the water depth and water extent. These issues were addressed by assessing specific discharges that met inundation mortality thresholds (identified in the first method). Using the 500-year flood example, the 600 $m^3 s^{-1}$ met a mortality threshold, therefore using the water depth and extent of the simulated 600 $m^3 s^{-1}$ during rising- and falling-limbs time-steps, areas inundated during both were identified as potential areas for inundation duration mortality. To ensure this duration was maintained during the time elapsed between rising- and falling-limb discharges of interest, the peak discharge data was also considered, but will not be further discussed since it always produced agreeable results (due to the increased discharge and greater inundation extent). Using the rising- and falling-limb time-steps data, the areas with inundation agreement (intersection) were determined and mapped and utilized as the area of interest. This procedure was repeated for all discharges found to meet the mortality thresholds. These considerations substantially reduced the required assessments as well as reduced the need to assess the smaller flood events of 2 and 5 year flood events as durations did not meet these requirements.

With the goal to determine and map the total area of lupin inundation mortality, each mortality rate and duration were assessed and mapped separately. Naturally, some of these areas overlapped. Using the 500-year flood as an example, all areas inundated at 200 $m^3 s^{-1}$ were typically inundated during the 600 $m^3 s^{-1}$; however, the 200 $m^3 s^{-1}$ duration was

considerably longer; thus causing mortality in larger root diameter lupins as well as greater total mortality. Therefore, the areas that caused the greatest mortality were given priority, and the lower priority mortality areas were excluded from the overlapping area to avoid 'double-counting' the data. Once the areas were mapped that met the depth requirements and duration requirements, the areas of inundation mortality were clipped and separated into the categories of bare areas and lupin densities of sparse, moderate, and dense.

Using the mortality rate (Table 7.2), the root diameter mortality based on duration (Table 7.2), and the area of occurrence (dense, moderate, or sparse lupin density), the percentages of lupins that could have experienced mortality were determined. For example, an area with submerged lupins for a duration of 3.7 days would have had a 50% mortality rate for root diameter $\leq$ 2 cm, and a 100% mortality rate for lupins with root diameters $\leq$ 1 cm. Using Figure 7.1, it can be deduced that the $\leq$ 2 cm root diameter lupins comprised 2% of dense lupin patches, 10% of moderate, and 18% of sparse lupin patches (also shown in Table 7.2). Using the calculated area of occurrence, the mortality rate percentage, and the percentage of lupin removal, the final total area of mortality was calculated. This is best explained by continuing the 3.7 day inundation example with the addition of ArcGIS mapping determined that 100 m^2 of moderate lupin density was submerged. Using Table 7.2, it can be determined that the 1 cm root diameters with 100% mortality rate for moderate density had a 3% removal, and the $\leq$ 2 cm root diameters had a 10% removal. Therefore, in calculating the total area of removed lupins, the 100% mortality rate would have a total of 3 m^2 (i.e. 100 m^2 x 3%). Additionally, the area also experienced a 50% mortality rate lupin mortality for lupins $\leq$ 2 cm root diameter. However, since all the lupins $\leq$ 1 were already accounted for, only the lupin root diameters between 1 cm and 2 cm needed to be considered. Therefore, the initial 50% removal was updated to account for this and would have been 7% removal (i.e. 10% - 3%). Therefore, the final 50% mortality rate for that same area would have been 3.5 m^2 (i.e. 100 m^2 x 50% x 7%) and the total mortality would have been 6.5 m^2.

Utilizing the simulated results and knowledge of lupin mortality, bare areas during the simulated flood event were also considered for inundation-induced mortality. This inclusion was important as it provided an assessment of the bare area's preservation. With bare areas determined from aerial images that had the capability to identify lupin canopies of 20 cm

width, it was reasoned that the vegetation present in these areas comprised mostly small and juvenile plants; thus lupins would have small root diameters. Assuming that all lupin roots were small, it was reasonable that they consist of mostly ≤ 1 cm root diameters, since lupins with > 1 cm root diameters typically have large enough canopies to be identified in aerial photographs. Therefore, the bare areas were assessed for such lupin root sizes, and mortality was mapped based on the required inundation thresholds. It was important to note that bare areas vegetation was not specifically surveyed, and that this inclusion was primarily based on qualitative observations.

7.4.2.2 Erosion

Estimating lupin extraction from the simulated results was done through means of drag and erosion thresholds discussed in Section 7.2. Considering that drag and erosion mortality were functions of water depth, plant height, plant deformation, velocity, and corresponding erosion levels, additional requirements for identifying extraction from the simulated results were necessary. Similar to the inundation section, the first mapping threshold was to only consider areas of water depth ≥ 0.5 m (mapping threshold 3); thus accounting for all lupins. This ensured that all inundated areas mapped provided enough depth to apply drag on the plant's entire canopy as well as a submerged flow condition; thus providing consistency with the methods in which the drag data were collected. Naturally, this was restrictive as it was likely that smaller lupins would have been extracted at lower water depths; however, as the experiment results (Table 4.17) indicated, drag alone removes only larger plants. Therefore, this assumption was considered appropriate.

The second consideration was the water velocity that was occurring in the mapped ≥ 0.5 m water depth areas. Since velocity was a crucial element in determining lupin extraction for all erosion levels (Tables 7.3, 7.4, and 7.5), velocity data was appended to the areas of intersecting depth; thus, providing the initial area of interest for potential lupin removal. The third consideration was to include the effects of the changing topography, which utilized the initial topography, peak discharge topography, and final topography to generate DEMs of difference for the peak and final conditions to assess erosion (and deposition, discussed in Section 7.4.2.3). However, due to changing morphology, it was likely that peak and final velocities and topographies did not fully represent the lupin removal. Therefore, additional

velocities were assessed (including the velocities at 80% of the peak discharges on the rising- and falling-limb), and were compared to the peak velocity. Therefore, significant changes in morphology that caused additional areas to experience lupin removal were included. However, this will not be discussed further since these additional checks showed insignificant changes from the peak discharge (Appendix E.10, Figure E.35).

Using the data from Table 7.4 and 7.5, it was estimated that lupins of all sizes were removed if the erosion was ≥ 20 cm and velocity was ≥ 0.92 m/s, and all lupins were removed if erosion was ≥ 30 cm and velocity was ≥ 0.35 m/s. Due to the depth requirement of ≥ 0.5 m, and using Equation 7.2, the velocities in areas of ≥ 0.5 m depths were expected (and later confirmed) to meet or exceed these 100% removal thresholds. Therefore, while the initial assessment showed that erosion levels of ≥ 40 cm can extract all lupins, due to the applied mapping threshold techniques, erosion of ≥ 20 cm removed all lupins. Using this information and the DoD developed using the peak topography, erosion + velocity mortality was mapped. Again, these areas were divided into the bare and vegetated areas. However, since all lupins were removed for erosion ≥ 20, sparse, moderate, and dense lupin clusters were not considered separately.

These processes were repeated using the final topography DoD; however, since water depth had receded back to 58 $m^3 s^{-1}$, the final topography was only assessed using erosion values and removal was only considered in areas with ≥ 40 cm erosion. To develop the final amount of lupin removal, the lupin removal mapped for peak and final DoDs were combined. Bare areas were assessed using the estimate that ≥ 20 cm of erosion removed all lupins with root diameters ≤ 2 cm (Table 4.17). Using the same assumption as the inundated bare area assessment, bare areas may consist of small and sparse density lupins; thus erosion levels of ≥ 20 cm could effectively removal all lupins in bare areas.

7.4.2.3 Deposition

Deposition mortality was determined to be a function plant height, plant deformation, burial duration, and sediment deposition. Therefore, additional mortality requirements were developed to identify and map corresponding mortality. Since the deposition experiment conducted allowed for a six week burial/regrowth period, the deposition mortality identified

from the simulated floods could only identify potential deposition mortality utilizing the final topography, which would provide extended burial. The second consideration was the plants' height and deformation and was presented in Section 7.2.4. Using the estimated deformed canopy heights and corresponding deposition mortality thresholds (Table 7.6) with the final topography DoD, potential mortality areas were identified using deposition depths. Using these guidelines, deposition mortality was assessed for the various flood events and accounted for the varying vegetation categories of sparse, moderate, and dense clusters as well as bare areas. Vegetated areas were assessed based on the corresponding lupin root diameter to experience mortality as well as the local lupin density. Therefore, determining the total area of occurrence, root diameter mortality, and lupin density category, the representative area of mortality was determined. Bare areas were determined with the assumption that only small lupin root diameters were present. Therefore, deposition of ≥ 0.23 m was considered to cause 100% mortality in bare areas (Table 7.6).

7.4.2.4 Drag

Drag in combination with varying erosion levels has been estimated to effectively remove lupins (Section 7.4.2.2); however, drag in areas without erosion had not been considered. Drag was determined to be a function of velocity, depth, and root diameter (Figure 4.27). As described in Section 7.4.2.2, the first consideration in identifying drag with erosion was the water depth and plant deformation and the second consideration was velocity. Using these same considerations, water depth of ≥ 0.5 m (mapping threshold 3) was utilized to determine the area of interest, and velocity during peak discharge was appended to provide lupin removal thresholds (Table 7.3). With drag forces of varying erosion levels focused on erosion levels ≥ 20 cm, drag alone was assessed for areas where erosion was < 20 cm. Further, drag had the potential to remove lupins in areas that experience mild deposition; therefore, drag was also considered in areas with deposition < 23 cm (Table 7.6). This effectively bound the drag process between erosion and deposition.

As mentioned previously, assessments did originally consider additional smaller discharges (Figure E.35), but these determined that minimal velocity change occurred. Therefore, only the peak discharge data was utilized for drag assessment. With these conditions, the areas of interest were mapped and categorized for sparse, moderate, and dense lupin clusters. With the

area of potential drag identified within the vegetation classes, the data were evaluated using the velocity to determine the size of lupins removed using the corresponding vegetation class to determine the root diameter frequency. Using these data, the total area of lupin removal was determined for the site specific thresholds. For example, if 100 m^2 of moderate lupin clusters were identified to have a velocity of 0.48 m/s, this would remove an estimated 52% of the lupins within this particular class (Table 7.3). Therefore, the final calculated total removal would be 52 m^2 (i.e. 100 m^2 x 52%). Bare area preservation was not assessed using drag, as drag alone was only estimated to remove larger lupins.

7.4.2.5 Combined processes and final mapping

Due to various processes affecting lupins of varying root diameter sizes, and with processes frequently overlapping specific areas, combined mortality was considered. As discussed in this chapter, inundation rarely caused mortality in lupins with root diameters ≥ 3 cm (Section 7.4.2.1), drag alone only potentially caused removal of lupins with root diameter ≥ 6 cm (Table 7.3), and deposition below 50 cm only killed lupins with root diameters ≤ 4 cm (Table 7.6). Therefore, these three processes were considered separately as well as in areas of overlap. While inundation and deposition both affect small root diameters, the general mortality by deposition ranged between 16% for sparse areas and 3% for dense areas, and inundation-mortality ranged between 11% for sparse and 2% for dense lupin clusters; thus both processes could be experienced within a small area. However, since both could occur in a given area, care was taken to separate-out the individual effects. For example, if a particular sparse lupin cluster experienced 16% mortality due to deposition, this would leave only 84% of the area that could experience additional mortality by inundation processes; thus, total lupin removal was not inflated (i.e. the lupins could not be killed more than once by different processes). Deposition mortality did not occur frequently, which limited the areas of intersection of inundation, deposition, and drag. However, intersection areas of inundation and drag were considered using the same technique to avoid inflating the total lupin removal. For example, in mapping the final lupin removal, areas that had erosion levels of ≥ 20 cm frequently were also susceptible to inundation; however, erosion was estimated to kill 100% of the lupins. Therefore, it was not necessary to consider overlapping datasets with erosion of ≥ 20 cm, nor deposition of ≥ 59 cm. Since each process had different mortality rates, the processes were prioritized during the mapping with higher priority given to the processes with highest mortality. The processes with 100% mortality were erosion with ≥ 20 cm and

deposition with ≥ 59 cm burial. Processes with less than 100% mortality in decreasing order were the combined inundation-deposition-drag at 50%, inundation-drag at 41%, drag at 37%, deposition at 9%, and inundation at 4%. Due to the specific processes occurring in different vegetated areas, and with every flood producing unique results, these percentages were only an approximate average and vary for both area and flood events.

The methods presented in this section were first applied to the observed October 2011 flood event and then applied to the simulated flood events of 2, 5, 10, 25, 50, 100, 200, and 500-year return periods. The observed flood event offered an evaluation of the methods of mortality identification, as observed lupin removal provided an independent check dataset to compare against the estimated lupin removal. The observed flood event was simulated by utilizing the pre-flood DEM, the observed hydrograph, and the model calibration parameters of v75. Following the simulation, lupin removal was assessed using the prescribed techniques and directly compared to the observed and documented lupin removal (Table 5.26). Once this was evaluated, the described forecasted flood events were simulated and assessments on lupin removal were undertaken.

7.4.2.6 Uncertainty inclusion

Uncertainty estimation for the various mortality processes were all developed in relation to the lupin root diameter (Section 7.3), and mortality identification of simulated results were all identified based on root diameters; therefore, determining the corresponding uncertainty for each process and each flood event was relatively simple. However, due to the three vegetation densities of dense, moderate, and sparse each having different root diameter frequency distributions, and due to each flood having unique mortality occurrence, uncertainty was unique for every lupin density, for every process, and for every flood event. Therefore, simplification was required to effectively represent this extensive amount of data into one uncertainty value per process.

Once all the process uncertainties were calculated for individual processes, the first method to simplify the uncertainty into a single representative value was to condense the data for each specific area. For example, the 500-year flood event had 11,970 drag uncertainty values for dense lupin areas. Therefore, the uncertainty was averaged into one representative value.

Since final mapping did not represent the area mortality for each density (see Table 7.30 for reference), but rather individual processes, the average values for the dense, moderate, and sparse areas were combined into one value. This was accomplished by calculating the weighted mean based on sample size. A weighted mean is similar to an arithmetic mean; however, instead of the values being represented equally, the weighted mean accounts for varying influences or weights (Hewlett-Packard, n.d.):

$$\overline{X_w} = \frac{\sum_{i=1}^{n} W_i X_i}{\sum_{i=1}^{n} W_i} \qquad \text{(Eqn: 7.3)}$$

where X_i represents the individual value and W_i is the corresponding weight (or occurrence of X_i). Since the number of occurrences could differ for the three vegetation densities, the weighed mean was the best representation of a final uncertainty for each process for a specific flood event. This was done for all individual processes and for all flood events. Further, the uncertainties were combined when necessary. For example, as mentioned in the section above (7.4.2.5), processes frequently overlapped and the total mortality was considered. Therefore, areas where inundation, drag, and deposition were considered for total mortality, the total uncertainty combined these components using Equation 7.1. Please refer to Appendix E.11 for full uncertainty details.

With each process for each flood event producing a unique uncertainty, the uncertainties were presented along with the total areas of mortality in the results and discussion section. Model uncertainty was also included for each flood event. This simply utilized the results of Section 7.3.6; however, since various model components were utilized to identify the individual process mortalities, each processes corresponding model uncertainty was determined. For example, the process of drag removal for 30+ cm erosion levels was identified in flood results by assessing simulated inundated extent, depth of ≥ 0.5 m, velocity data, and erosion. Therefore, each of these model components' uncertainties were combined using Equation 7.1 to provide the total uncertainty. This assessment was repeated for all mortality processes, and was also presented along with the total areas of mortality in the results and discussion section below.

7.4.3 Results and discussion

7.4.3.1 Process and model uncertainty

Each flood event in this section was presented with the best approximation of process and model uncertainties. Process uncertainty results for all floods are shown in Table 7.26, model uncertainty results are shown in Table 7.27, and DoD data are in Appendix E.12. To be consistent with mortality mapping, the uncertainty results were organized with the highest priority (highest mortality rate) mortality processes at the top of the table, and decreasing priority in descending order. To gain perspective on the total simulated uncertainty associated with identifying lupin mortality, the model and process uncertainties were combined by both addition and subtraction to represent the ± sign convention, which represents the minimum and maximum total uncertainty, respectively. Minimum combined uncertainty results are shown in Table 7.28, maximum combined uncertainty results are shown in Table 7.29, and minimum and maximum combined uncertainties are plotted together in Figure 7.11.

Table 7.26: Process uncertainty for each flood event.

	Flood event and associated uncertainty (%)							
Process:	500 yr	200 yr	100 yr	50 yr	25 yr	10 yr	5 yr	2 yr
Erosion (20+ cm)	-50.9	-50.3	-47.8	-50.2	-46.7	-46.6	-45.5	-49.6
Deposition (59+ cm)	-42.0	-42.0	-42.0	-42.0	-42.0	-42.0	-42.0	-42.0
Inundation, deposition, drag	-62.9	-62.6	-61.6	-60.5	-44.7	-60.2	-	-
Inundation and drag	-46.9	-46.4	-45.4	-43.7	-15.8	-43.3	-	-
Drag only	43.2	-43.2	-43.1	-43.1	-13.1	-42.9	-42.9	-42.6
Deposition only	-42.0	-42.0	-41.7	-41.8	-41.8	-41.8	-41.7	-41.6
Inundation only	-18.2	-17.1	-14.2	-7.2	-8.8	-6.0	-	-

Table 7.27: Model uncertainty for each process mapped.

	Model uncertainty (%)					
Process:	Inundation	Depth	Velocity	Erosion	Deposition	Total
Erosion (40+ cm)	±7.9	-	-	±43.9	-	±44.6
Erosion + Velocity	±7.9	±28.0	±34.9	±43.9	-	±63.2
Deposition (>0.59 m)	±7.9	-	-	-	±65.8	±66.3
Inundation, deposition, drag	±7.9	±28.0	±34.9	-	±65.8	±80.0
Inundation and drag	±7.9	±28.0	±34.9	-	-	±45.4
Drag only	±7.9	±28.0	±34.9	-	-	±45.4
Deposition only	±7.9	-	-	-	±65.8	±66.3
Inundation only	±7.9	±28.0	-	-	-	±29.1

Table 7.28: Total minimum combined uncertainty for process and model components.

	Process uncertainty added with model uncertainty (minimum uncertainty)								
Process:	500 yr	200 yr	100 yr	50 yr	25 yr	10 yr	5 yr	2 yr	Average
Erosion (20+ cm)	-6.3	-5.7	-3.2	-5.6	-2.1	-2.0	-0.9	-5.0	-3.9
Deposition (59+ cm)	24.3	24.3	24.3	24.3	24.3	24.3	24.3	24.3	24.3
Inundation, deposition, drag	17.1	17.4	18.4	19.5	35.3	19.8	-	-	21.3
Inundation and drag	-1.5	-1.0	0.0	1.7	29.6	2.1	-	-	5.2
Drag only	2.2	2.2	2.3	2.3	32.3	2.5	2.5	2.8	6.1
Deposition only	24.3	24.3	24.6	24.5	24.5	24.5	24.6	24.7	24.5
Inundation only	10.9	12.0	14.9	21.9	20.3	23.1	-	-	17.2

Table 7.29: Total maximum combined uncertainty for process and model components.

	Process uncertainty minus model uncertainty (maximum uncertainty)								
Process:	500 yr	200 yr	100 yr	50 yr	25 yr	10 yr	5 yr	2 yr	Average
Erosion (20+ cm)	-95.5	-94.9	-92.4	-94.8	-91.3	-91.2	-90.1	-94.2	-93.1
Deposition (59+ cm)	-108.3	-108.3	-108.3	-108.3	-108.3	-108.3	-108.3	-108.3	-108.3
Inundation, deposition, drag	-142.9	-142.6	-141.6	-140.5	-124.7	-140.2	-	-	-138.8
Inundation and drag	-92.3	-91.8	-90.8	-89.1	-61.2	-88.7	-	-	-85.7
Drag only	-88.6	-88.6	-88.5	-88.5	-58.5	-88.3	-88.3	-88.0	-84.7
Deposition only	-108.3	-108.3	-108.0	-108.1	-108.1	-108.1	-108.0	-107.9	-108.1
Inundation only	-47.3	-46.2	-43.3	-36.3	-37.9	-35.1	-	-	-41.0

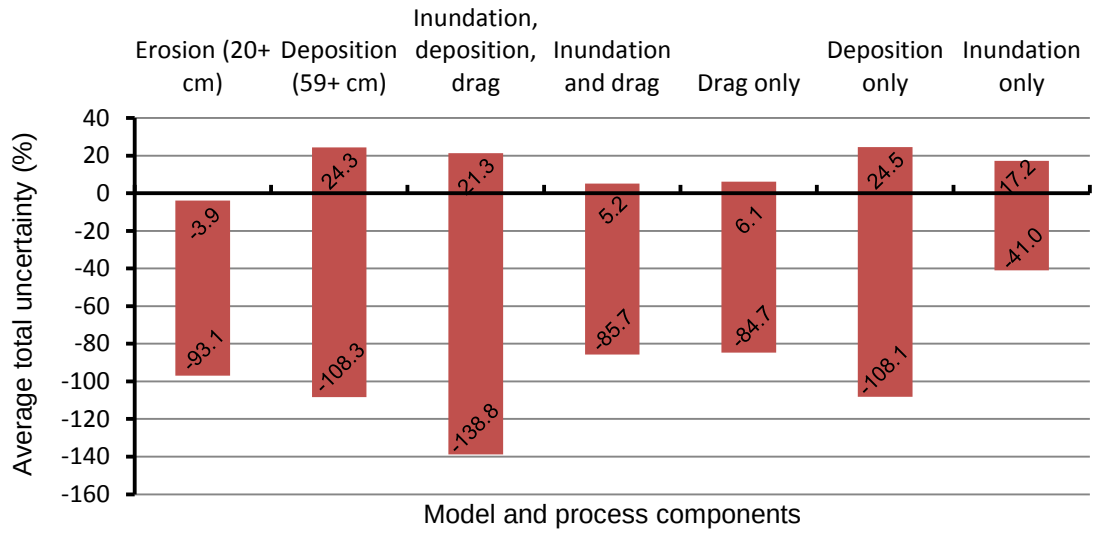

Figure 7.11: Total average uncertainty for the process and model components.

In determining the best representative uncertainties for each process (additional tables in Appendix E.11), all process uncertainties varied for the specific flood events except for deposition above ≥ 59 cm. This variation was due to unique flood simulations and varying areas and varying root diameters affected. However, deposition with ≥ 59 cm did not change since this condition was estimated to kill 100% of all lupins. This result was also expected for erosion ≥ 20 cm; however, examining the raw data showed that erosion between 20 cm and 29 cm killed approximately 98.5% of all lupins while erosion of 30+ cm caused 100% mortality; thus slight variation in uncertainties existed for the erosion of 20+ cm category. Further, process uncertainty results (e.g. Table 7.10, 7.13) were initially calculated with negative sign convention which indicated that the process mortality threshold could have happened at lower rates (i.e. forces, root lengths, days, etc.). However, when using these processes and applying the uncertainties to mortality mapped areas, the uncertainties indicate that greater area could have been affected than were mapped. Therefore, the uncertainties were best presented with a positive sign convention when applied to areas of mortality.

Model uncertainty results (Table 7.27) presented the individual components of inundation, depth, velocity, erosion, deposition as well as the combined total uncertainty. Similar to Table 7.26, the processes were listed in order of priority; however, as shown not every model uncertainty component was applicable to the corresponding process. For example, in

determining the total uncertainty for erosion of 40+ cm, the uncertainty of water inundation and erosion were only considered, as these were the simulation results utilized in determining this mortality process. However, for mortality caused by erosion and velocity thresholds (i.e. drag), the uncertainties of the modeled inundation, depth, velocity, and erosion had to be considered and were combined into the total uncertainty using Equation 7.1. These multi-process and multi-component requirements created large total uncertainties. However, these high uncertainties were anticipated given the large errors illustrated throughout the calibration and validation results of Chapter 6 and the individual uncertainties estimated in Section 7.3.6.

7.4.3.2 October flood event simulation

The first flood simulated was the observed October, 2011 flood event. The mapped mortality results for this flood are shown on Figure 7.12 and calculated affected areas are shown in Table 7.30. However, it should be noted that the observed flood event was utilized to calibrate the model's morphological behavior (Section 6.4.4). Therefore, this assessment was not meant as a hydraulic model validation. Instead, this assessment was purely performed for the purpose of validating the methods developed for identifying mortality based on model results.

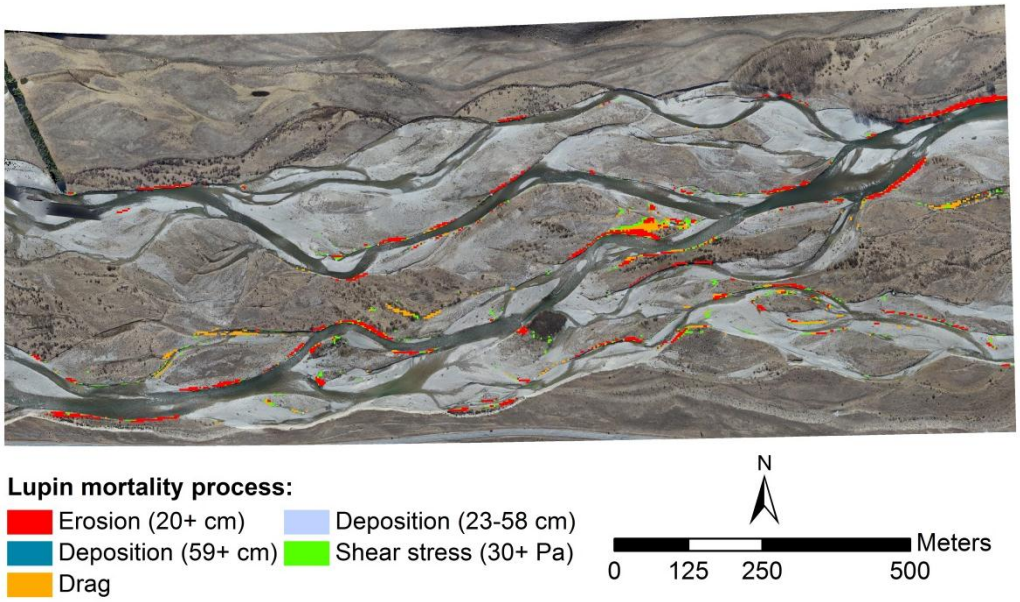

Figure 7.12: Observed October, 2011 flood event and predicted mortality processes.

Table 7.30: Predicted lupin mortality and associated uncertainties for the October 2011 flood event.

	Lupin mortality		Uncertainty (%)	
Process	Area (m^2)	Mortality area (%)	Process	Model
Erosion (40+ cm)	6,936	51.8	+52.0	±44.6
Erosion (20+ cm) + Velocity	4,927	36.8	+49.6	±63.2
Deposition (>0.59 cm)	26	0.2	+42.0	±66.3
Inundation, deposition, drag	0	0.0	-	-
Inundation and drag	0	0.0	-	-
Drag only	1,482	11.1	+42.6	±45.4
Deposition only	19	0.1	+41.6	±66.3
Inundation only	0	0.0	-	-
Total floodplain removal:	**13,391**	**4.2**		
Trauma (occurrence)	9,167			
Trauma (exclusive)	3,908			

Examining the mapped results, all mortality occurred along or near the river banks, with erosion responsible for 88.6% of removal, drag at 11.1%, and the remaining 0.3% of the areal removal caused by deposition. Comparing the total area results (13,391 m^2) to the observed results (Table 5.24: 11,540 m^2) revealed the simulated results compared well to the observed lupin removal, with the simulated removal over-predicted by 16%. The observed results of Table 5.26 show the estimated processes of deposition, erosion, and no morphologic change for all vegetation removed for the observed flood event. While the observed data contain lupins, bush (matagouri and sweet briar), and willow tree removal, the bush and willow removal only comprised approximately 3.2% and 4.6% of the total removal, respectively. Therefore, while not fully comparable to the simulated results that only accounted for lupin removal, Table 5.26 and the individual process area estimation provided perspective into the accuracy of the mortality thresholds that were developed.

Comparing Table 7.30 to Table 5.26, the simulated flood produced similar total erosion (96.8% agreement), but deposition showed poor agreement (3.1%). However, these poor deposition results were somewhat anticipated given the model's inability to re-create bar-top deposition (pg 238, and Table 6.18). Nevertheless, this inaccuracy was larger than expected given the agreement in deposition results (Table 6.20) which revealed similar area, volume,

and average deposition depth simulated; thus, reach-wide deposition seemed representative. Therefore, while the true cause was unknown, it was speculated that the deposition mortality threshold may have been too restrictive. However, no modification to the deposition threshold was attempted since the results of Table 5.26 for deposition were merely speculative, and thus there was no way of knowing with any confidence that other mortality processes had not removed the lupins prior to final deposition. Therefore, the deposition thresholds were maintained.

The observed lupin removal estimated that 1,972 m^2 occurred for areas with 'no morphologic change' in topography. However, it was possible that morphologic change occurred during the flood event and were either reworked to an undetectable level or that the changes were simply not detected by the DoD. However, with the assumption that no morphologic change occurred, this would leave drag, inundation, and/or trauma as potential processes. Examining the simulation results for the corresponding areas of no morphologic change revealed both velocity and shear stress values capable of drag pull-out (0.74+ m/s for velocity, Table 7.3; 30+ Pa for shear stress, Section 7.2.5) were predicted to occur at the peak discharge. However, inundation duration for these corresponding areas was between 10 and 14 hours; thus, inundation was not a likely process (Table 7.2). Therefore, drag and/or trauma-induced mortality were the most likely processes based on the simulation results, which was noted to have inherent inaccuracies. With drag mortality thresholds resulting in 1,482 m^2 of lupin removal for the simulated flood event and trauma estimated between 9,167 and 3,908 m^2, either process or a combination of the two could have been responsible for the mortality. However, because trauma mortality threshold was based on limited and observed data combined with model simulations using retrofitted vegetation mapping, and given that drag mortality was based on moderate data and conservative relationships, only drag can be truly be considered. Nevertheless, since drag was a likely process and given that the conditions causing drag were simulated for the corresponding areas, the process that occurred in the no morphologic change area suggests drag was a likely process, which was further supported by the agreement between the estimated and observed areas. Therefore, these results indicated that erosion was represented well, and drag was potentially represented well.

7.4.3.3 Simulated 2-year flood event

The 2-year flood event was simulated with a peak discharge of 218 $m^3 s^{-1}$ and duration of 30 hours. Mapped lupin mortality results are shown in Figure 7.13 and area calculations and uncertainties are presented in Table 7.31. As shown in the mapped mortality, most areas occurred near the river channel margins with little floodplain area affected. Interestingly, this simulated flood event had similar hydrograph shape and maximum discharge to the observed October flood event (209 $m^3 s^{-1}$). However, the differences in total lupin mortality and morphological change were remarkable. Comparing Table 7.30 and 7.31, the 2-year flood event had considerably less total lupin area mortality (71% less) and mortality was mainly due to drag process instead of erosion. With similar duration, hydrograph, and peak discharges, this difference in total mortality area was seemingly unjustified. However, visually comparing the mortality areas mapped in Figures 7.12 and 7.13, one can conclude that the two simulations produced relatively comparable affected areas; however, the processes identified were different. With the 2-year flood event having mostly drag mortality (approximate mortality rate of 37%) and the October 2011 flood event having mostly erosion (approximately mortality rate of 100%), the discrepancy was mostly due to the varying processes that were simulated. However, the reasons why similar flood events caused such marked differences in processes was not fully understood, but likely caused by two factors. First, the topographies utilized were different. The observed flood event was simulated using the pre-flood DEM topography, and all forecasted flood events were simulated with the post-flood topography in order to assess the most current conditions of the river and vegetation mortality. Therefore, the altered morphology between simulations could be in part responsible for the varying results. Secondly, the vegetation extent and densities were different for the two simulations, with the post-flood having greater overall floodplain lupin presence (due to the growing season and corresponding development), but reduced near-channel lupin presence due to the October flood event. Therefore, one reason that erosion was less significant in the simulated 2-year flood could have been that the recent October flood removed most lupins susceptible to erosion. Nevertheless, the 2-year flood was estimated to remove approximately 1.2% of the total floodplain lupins (Table 5.25: 322,859 m^2).

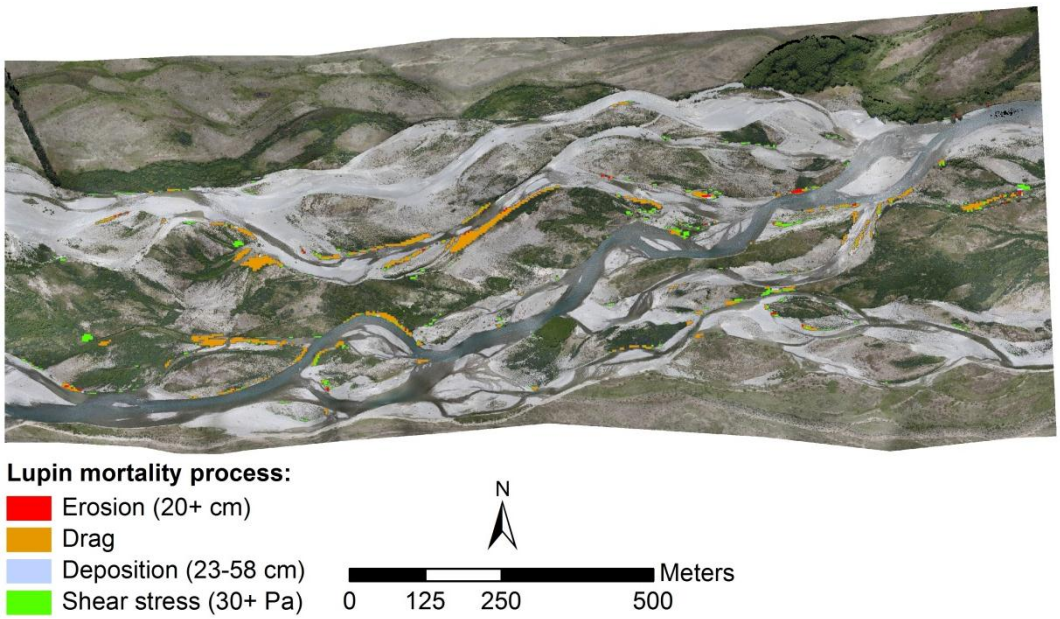

Figure 7.13: Simulated 2-year flood event and predicted mortality processes.

Table 7.31: Predicted lupin mortality and associated uncertainties for the 2-year flood event.

	Lupin mortality		Uncertainty (%)	
Process	Area (m^2)	Mortality area (%)	Process	Model
Erosion (40+ cm)	473	12.1	+52.0	±44.6
Erosion (20+ cm) + Velocity	220	5.6	+49.6	±63.2
Deposition (59+ cm)	0	0.0	-	-
Inundation, deposition, drag	0	0.0	-	-
Inundation and drag	0	0.0	-	-
Drag only	3,188	81.7	+42.6	±45.4
Deposition (23-58 cm)	22	0.6	+41.6	±66.3
Inundation only	0	0.0	-	-
Total floodplain removal:	**3,904**	**1.2**		
Trauma (occurrence)	4,443			
Trauma (exclusive)	3,127			

Assessing the simulated flood effects on the bare areas, mortality mapping results (Figure 7.14) only include areas affected that were not initially inundated. As shown, only areas near the river had potential for bare area preservation, which was due to the water inundation extent being relatively restricted for the small flood event. Total area results (Table 7.32)

showed considerable total area preserved with erosion being the greater process. Comparing the total area preserved with the total estimated bare area (Table 5.22: 345,659 m^2), this flood event preserved approximately 6.8% of the floodplains current bare area.

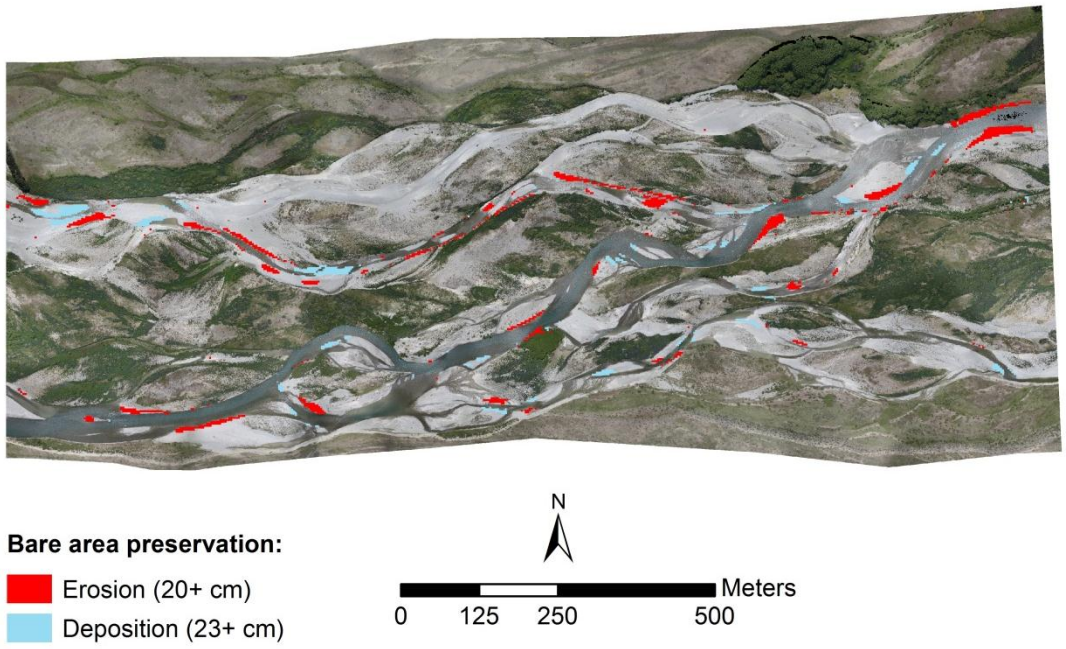

Figure 7.14: Simulated 2-year flood event and predicted bare area preservation.

Table 7.32: Predicted bare area preservation and associated uncertainties for the 2-year flood event.

	Lupin mortality		Uncertainty (%)	
Process:	Area (m^2)	Mortality area (%)	Process	Model
Erosion	16,980	72.7	+52.0	±44.6
Deposition	6,384	27.3	+42.0	±66.3
Inundation	-	-	-	-
Total	**23,365**	**6.8**		

7.4.3.4 Simulated 5-year flood event

The 5-year flood event was simulated with a peak discharge of 325 $m^3 s^{-1}$ and duration of 70 hours. Assessing the simulation mortality mapping results (Figure 7.15) showed considerably greater floodplain mortality and the calculated areas (Table 7.33) revealed drag as the largest

contributing process, with erosion (25.5%) and deposition (0.4%) contributions. As expected, this flood caused greater mortality than the smaller 2-year flood event, and removed 4.5% of the floodplain lupins. Bare area preservation mapping (Figure 7.16) also revealed greater preservation than the 2-year flood event and results (Table 7.34) showed an estimated 13.1% of the bare areas were preserved.

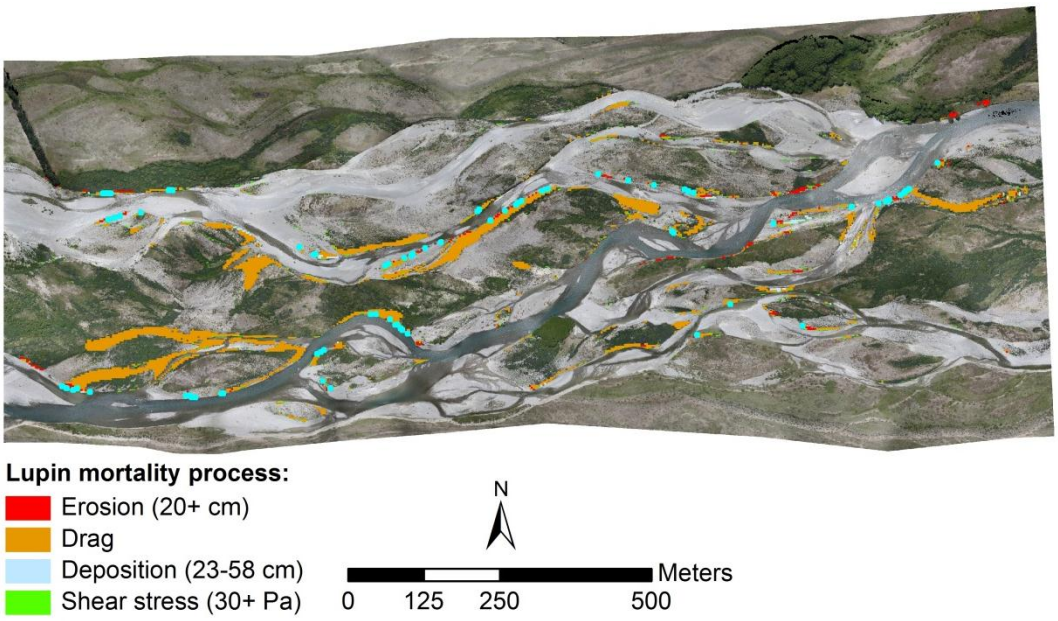

Figure 7.15: Simulated 5-year flood event and predicted mortality processes.

Table 7.33: Predicted lupin mortality and associated uncertainties for the 5-year flood event.

	Lupin mortality		Uncertainty (%)	
Process	Area (m^2)	Mortality area (%)	Process	Model
Erosion (40+ cm)	1,772	12.2	+52.0	±44.6
Erosion (20+ cm) + Velocity	1,942	13.3	+45.5	±63.2
Deposition (59+ cm)	0	0.0	-	-
Inundation, deposition, drag	0	0.0	-	-
Inundation and drag	0	0.0	-	-
Drag only	10,795	74.1	+42.9	±45.4
Deposition (23-58 cm)	58	0.4	+41.7	±66.3
Inundation only	0	0.0	-	-
Total floodplain removal:	**14,566**	**4.5**		
Trauma (occurrence)	12,277			
Trauma (exclusive)	4,630			

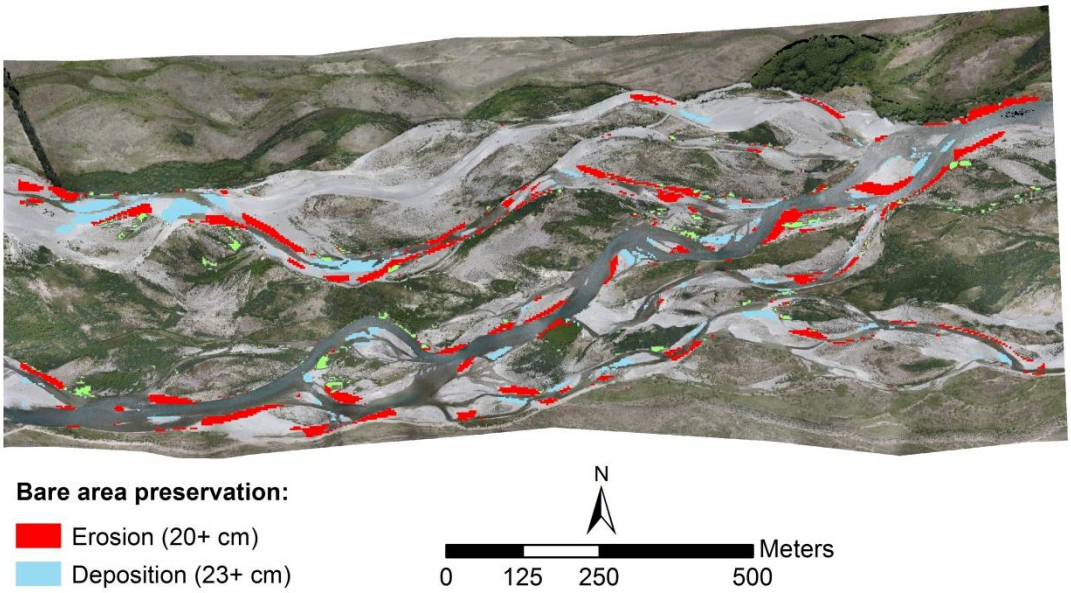

Figure 7.16: Simulated 5-year flood event and predicted bare area preservation.

Table 7.34: Predicted bare area preservation and associated uncertainties for the 5-year flood event.

	Lupin mortality		Uncertainty (%)	
Process:	Area (m^2)	Mortality area (%)	Process	Model
Erosion	30,048	66.3	+52.0	±44.6
Deposition	15,247	33.7	+42.0	±66.3
Inundation	-	-	-	-
Total	**45,295**	**13.1**		

7.4.3.5 Simulated 10-year flood event

The 10-year flood event was simulated with a peak discharge of 403 $m^3 s^{-1}$ and duration of 104 hours and was the smallest flood event wherein areas of inundation-induced mortality overlapped with areas experiencing deposition and drag-induced mortality. However, as shown in the mortality mapping (Figure 7.17), these areas were sparse and small compared to the areas affected by drag and erosion. As expected, greater floodplain areas were affected than during the smaller flood events, and the greater total removal occurred for an estimated 7.6% of floodplain lupins (Table 7.35). Bare area preservation also included inundation

(Figure 7.18). In contrast to the vegetated floodplain, bare area inundation mortality was a significant contribution (30.8%) to the overall bare area preservation at an estimated 26.9% of the total floodplain (Table 7.36).

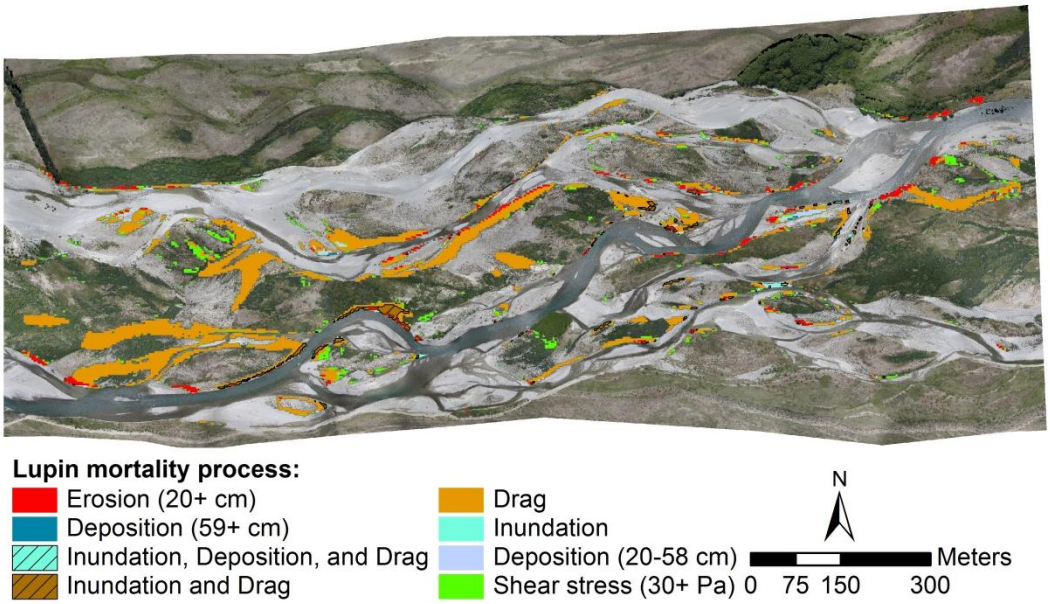

Figure 7.17: Simulated 10-year flood event and predicted mortality processes.

Table 7.35: Predicted lupin mortality and associated uncertainties for the 10-year flood event.

	Lupin mortality		Uncertainty (%)	
Process	Area (m^2)	Mortality area (%)	Process	Model
Erosion (40+ cm)	2,864	11.7	+52.0	±44.6
Erosion (20+ cm) + Velocity	2,675	10.9	+46.6	±63.2
Deposition (>0.59 cm)	108	0.4	+42.0	±66.3
Inundation, deposition, drag	77	0.3	+60.2	±80.0
Inundation and drag	1,261	5.2	+43.3	±45.4
Drag only	17,290	70.6	+42.9	±45.4
Deposition only	165	0.7	+41.8	±66.3
Inundation only	42	0.2	+6.0	±29.1
Total floodplain removal:	**24,483**	**7.6**		
Trauma (occurrence)	18,832			
Trauma (exclusive)	9,308			

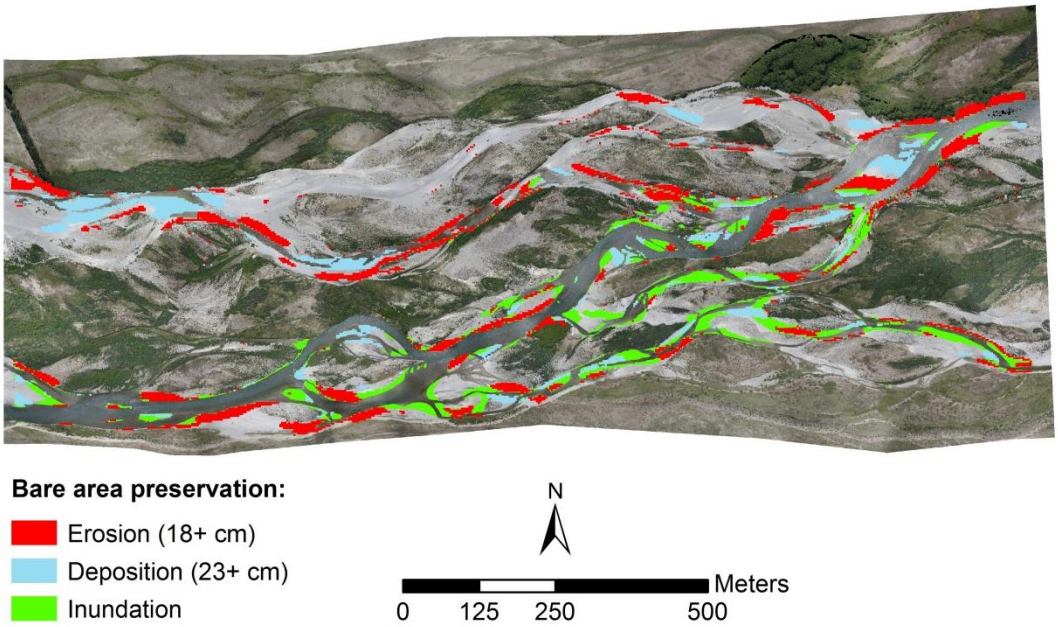

Figure 7.18: Simulated 10-year flood event and predicted bare area preservation.

Table 7.36: Predicted bare area preservation and associated uncertainties for the 10-year flood event.

	Lupin mortality		Uncertainty (%)	
Process:	Area (m^2)	Mortality area (%)	Process	Model
Erosion	40,060	43.1	+52.0	±44.6
Deposition	24,271	26.1	+42.0	±66.3
Inundation	28,617	30.8	+6.0	±29.1
Total	**92,947**	**26.9**		

7.4.3.6 Simulated 25-year flood event

The 25-year flood event was simulated with a peak discharge of 507 m^3 s^{-1} and duration of 170 hours. As expected, this flood event progressively inundated greater floodplain area than the proceeding smaller events, and the results (Figure 7.19 and Table 7.37) revealed drag and erosion were the greatest mortality processes. However, inundation contributed to a larger percentage of total mortality and the combined total lupin mortality was estimated to remove 16.6% of the floodplain lupins. Bare area preservation (Figure 7.20 and Table 7.38) nearly doubled the 10-year flood event results, with an estimated 50.0% preserved. However, the contributing processes of erosion, deposition, and inundation were relatively balanced.

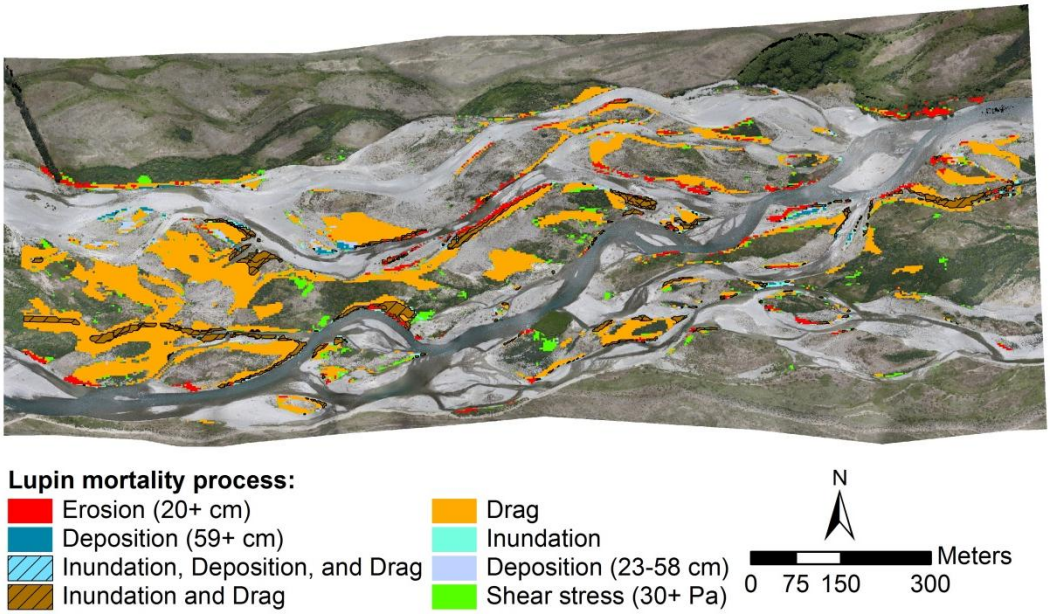

Figure 7.19: Simulated 25-year flood event and predicted mortality processes.

Table 7.37: Predicted lupin mortality and associated uncertainties for the 25-year flood event.

	Lupin mortality		Uncertainty (%)	
Process	Area (m^2)	Mortality area (%)	Process	Model
Erosion (40+ cm)	5,806	10.8	+52.0	±44.6
Erosion (20+ cm) + Velocity	4,955	9.2	+46.7	±63.2
Deposition (>0.59 cm)	1,502	2.8	+42.0	±66.3
Inundation, deposition, drag	203	0.4	+44.7	±80.0
Inundation and drag	7,085	13.2	+15.8	±45.4
Drag only	33,563	62.6	+13.1	±45.4
Deposition only	329	0.6	+41.8	±66.3
Inundation only	148	0.3	+8.8	±29.1
Total floodplain removal:	**53,592**	**16.6**		
Trauma (occurrence)	36,975			
Trauma (exclusive)	10,215			

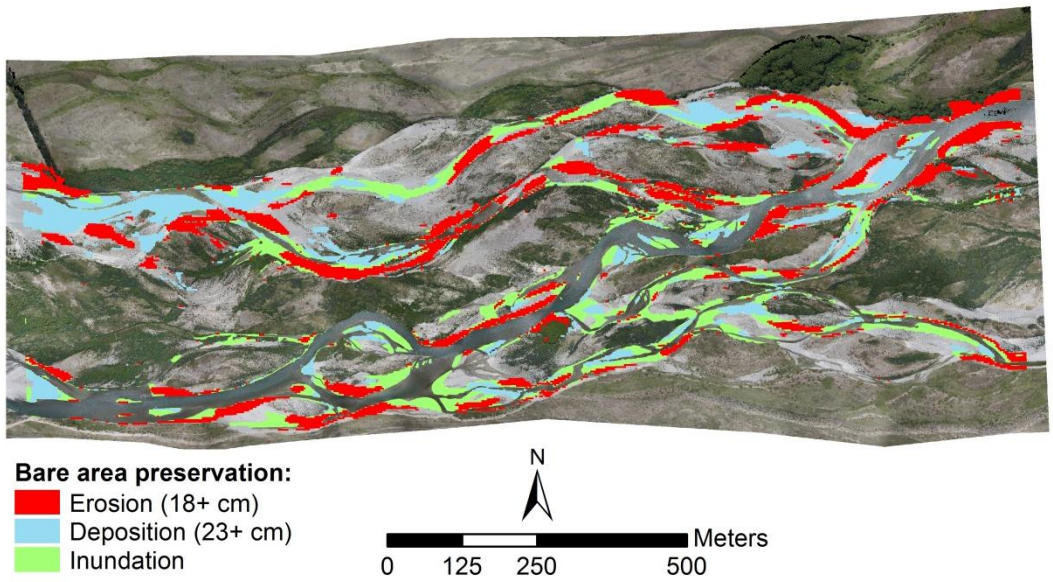

Figure 7.20: Simulated 25-year flood event and predicted bare area preservation.

Table 7.38: Predicted bare area preservation and associated uncertainties for the 25-year flood event.

	Lupin mortality		Uncertainty (%)	
Process:	Area (m^2)	Mortality area (%)	Process	Model
Erosion	69,003	39.9	+52.0	±44.6
Deposition	46,367	26.8	+42.0	±66.3
Inundation	57,599	33.3	+6.0	±29.1
Total	**172,969**	**50.0**		

7.4.3.7 Simulated 50-year flood event

The 50-year flood simulation had a peak discharge of 596 m^3 s^{-1} and total duration of 226 hours. Mortality mapping results (Figure 7.21) showed a considerable increase in the combined mortality of inundation and drag as well as considerably larger areas of erosion. Assessing the calculated area results (Table 7.39), drag and drag with inundation had the largest contribution to mortality and a total floodplain lupin removal estimated at 17.8%. Bare area preservation mapping and area results (Figure 7.22 and Table 7.40) revealed inundation was responsible for half of the estimated 68.6% bare area preservation.

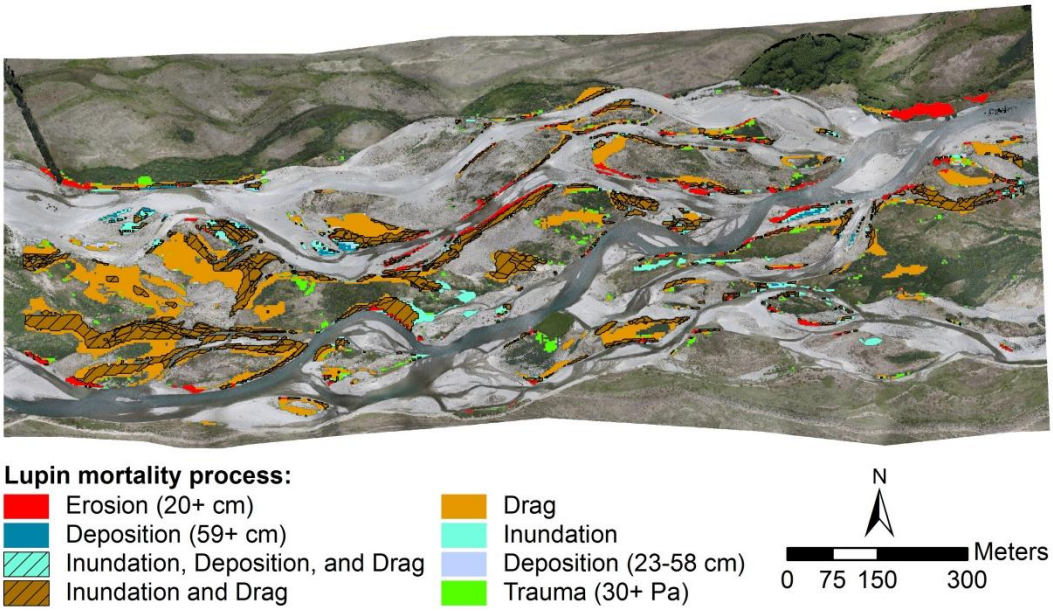

Figure 7.21: Simulated 50-year flood event and predicted mortality processes.

Table 7.39: Predicted lupin mortality and associated uncertainties for the 50-year flood event.

	Lupin mortality		Uncertainty (%)	
Process	Area (m^2)	Mortality area (%)	Process	Model
Erosion (40+ cm)	7,646	13.3	+52.0	±44.6
Erosion (20+ cm) + Velocity	2,791	4.9	+50.2	±63.2
Deposition (>0.59 cm)	1,493	2.6	+42.0	±66.3
Inundation, deposition, drag	692	1.2	+60.5	±80.0
Inundation and drag	22,807	39.8	+43.7	±45.4
Drag only	21,250	37.1	+43.1	±45.4
Deposition only	170	0.3	+41.8	±66.3
Inundation only	465	0.8	+7.2	±29.1
Total floodplain removal:	**57,314**	**17.8**		
Trauma (occurrence)	37,430			
Trauma (exclusive)	6,313			

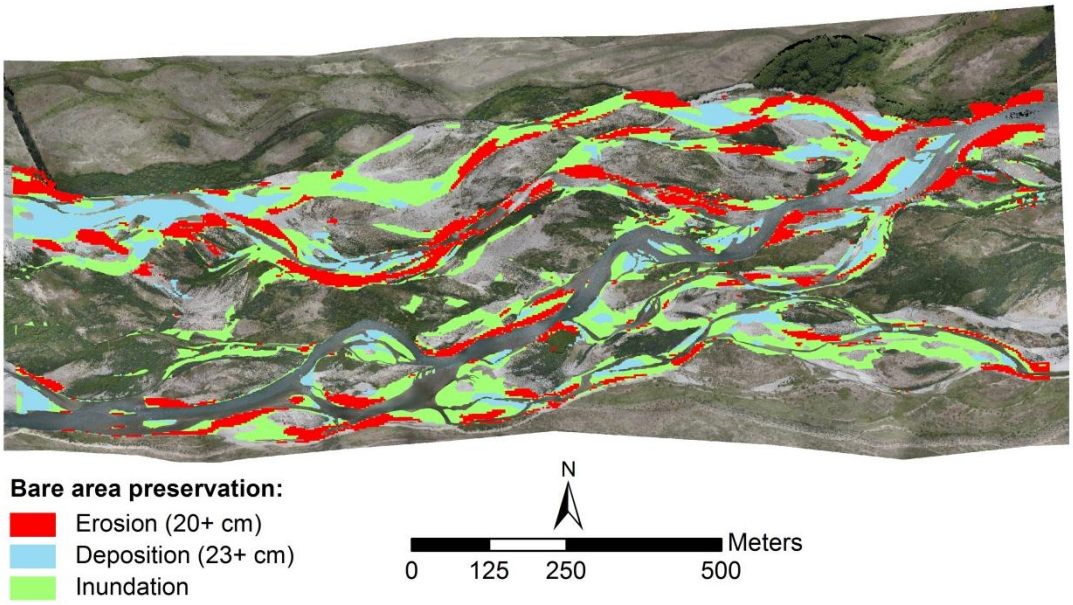

Figure 7.22: Simulated 50-year flood event and predicted bare area preservation.

Table 7.40: Predicted bare area preservation and associated uncertainties for the 50-year flood event.

	Lupin mortality		Uncertainty (%)	
Process:	Area (m^2)	Mortality area (%)	Process	Model
Erosion	69,624	29.4	+52.0	±44.6
Deposition	46,348	19.5	+42.0	±66.3
Inundation	121,210	51.1	+6.0	±29.1
Total	**237,183**	**68.6**		

7.4.3.8 Simulated 100-year flood event

The 100-year flood event had a peak discharge of 687 $m^3 s^{-1}$ and total duration of 284 hours. Similar to the 50-year flood event, the combined processes of inundation and drag became a dominant process as well as drag alone (Figure 7.23 and Table 7.41). However, erosion mortality increased and became a greater total contribution to the total mortality than the 50-year and 25-year flood events. Further, for the first time, deposition (≥ 59 cm) was identifable in the mortality mapping and provided an estimated 3.0% of the total mortality. All processes contributed to the lupin mortality and the total lupin mortality was estimated to remove 24.9% of the floodplain lupins.

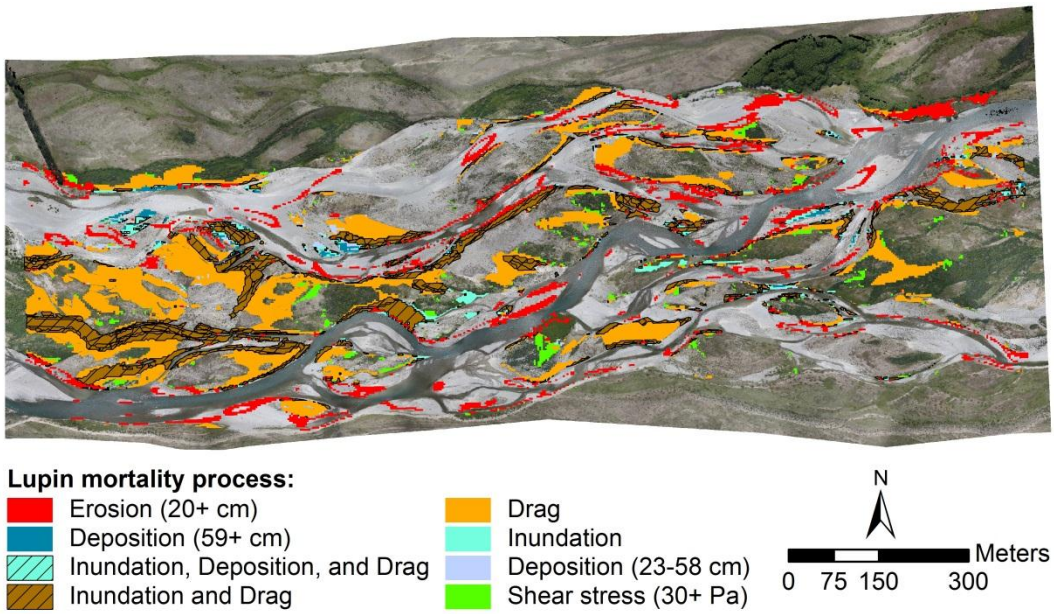

Figure 7.23: Simulated 100-year flood event and predicted mortality processes.

Table 7.41: Predicted lupin mortality and associated uncertainties for the 100-year flood event.

	Lupin mortality		Uncertainty (%)	
Process	Area (m^2)	Mortality area (%)	Process	Model
Erosion (40+ cm)	9,596	11.9	+52.0	±44.6
Erosion (20+ cm) + Velocity	12,227	15.2	+47.8	±63.2
Deposition (59+ cm)	2,383	3.0	+42.0	±66.3
Inundation, deposition, drag	724	0.9	+61.6	±80.0
Inundation and drag	22,526	28.0	+45.4	±45.4
Drag only	32,246	40.1	+43.1	±45.4
Deposition only	314	0.4	+41.7	±66.3
Inundation only	441	0.5	+14.2	±29.1
Total floodplain removal:	**80,457**	**24.9**		
Trauma (occurrence)	49,626			
Trauma (exclusive)	7,930			

Bare area preservation produced a slight reduction in total preservation when compared to the 50-year flood event. Comparing Tables 7.40 and 7.42, the 100-year flood event preserved 68.4%, which was 0.4% less than the 50-year flood event. While the composition of processes varied, the 100-year mortality process were evenly distributed. However, this would have no affect on the totaled mortality, as bare area mortality was always 100%

mortality rates due to the small lupins that were assummed to exist. Further, with mortalities mapped based strictly on model results, subjective mapping was avoided. Therefore, this descrepancy, and the reasosns why the 100-year area preserved was not relatively larger than the 50-year event was not fully understood, but could be due to varying morphologic changes experienced by the individual and unique simulations.

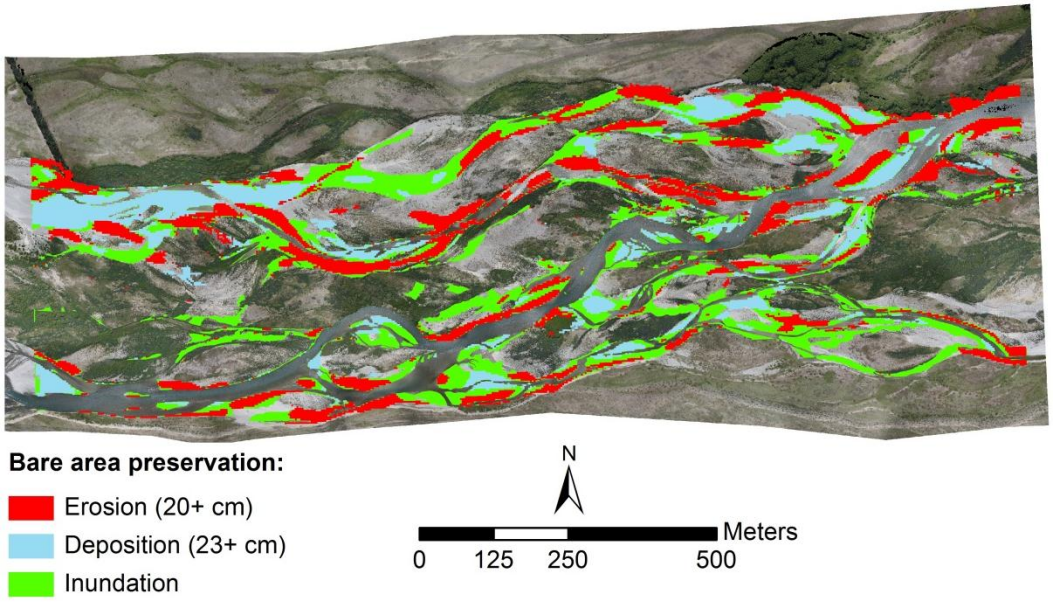

Figure 7.24: Simulated 100-year flood event and predicted bare area preservation.

Table 7.42: Predicted bare area preservation and associated uncertainties for the 100-year flood event.

	Lupin mortality		Uncertainty (%)	
Process:	Area (m^2)	Mortality area (%)	Process	Model
Erosion	79,831	33.8	+52.0	±44.6
Deposition	55,180	23.3	+42.0	±66.3
Inundation	101,517	42.9	+6.0	±29.1
Total	**236,528**	**68.4**		

7.4.3.9 Simulated 200-year flood event

The 200-year flood event was simulated with a peak discharge of 784 $m^3 s^{-1}$ and duration of 348 hours. Evaluating the mortality results (Figure 7.25 and Table 7.43), combined inundation and drag and drag alone were the greatest mortality processes; however, all processes contributed and 34.0% of the total floodplain lupins were estimated to be removed.

Bare area mortality (Figure 7.26 and Table 7.44) revealed a significant increase in bare area preservation over the 100-year flood event results; thus the discrepancy discussed for the 100-year event was an isolated event. Nevertheless, the 200-year flood event effectively removed significant lupin areas and preserved an estimated 80.1% of the total bare area.

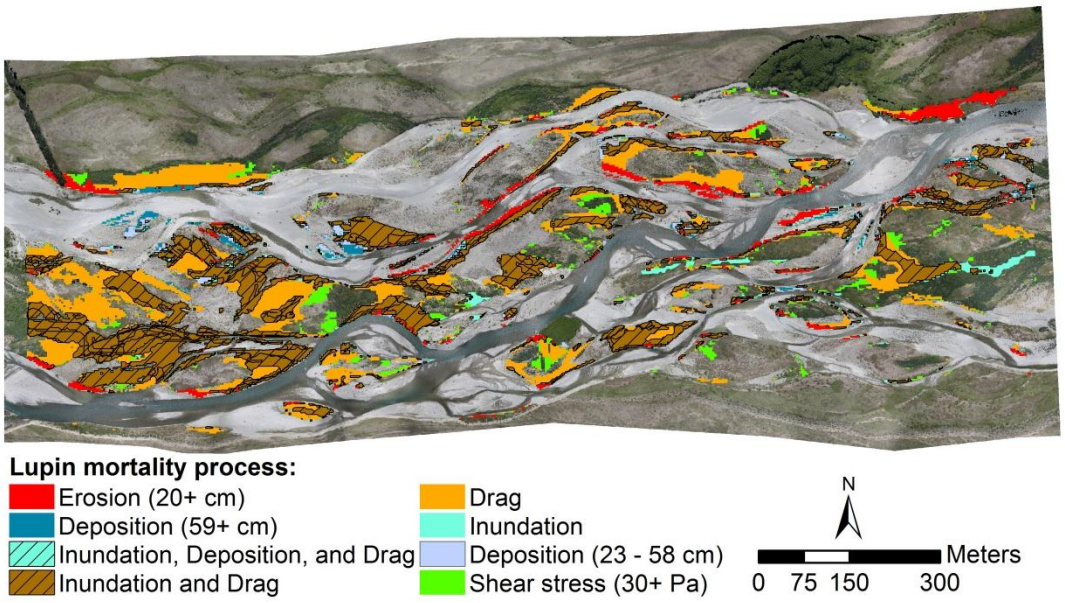

Figure 7.25: Simulated 200-year flood event and predicted mortality processes.

Table 7.43: Predicted lupin mortality and associated uncertainties for the 200-year flood event.

	Lupin mortality		Uncertainty (%)	
Process	Area (m^2)	Mortality area (%)	Process	Model
Erosion (40+ cm)	13,088	11.9	+52.0	±44.6
Erosion (20+ cm) + Velocity	2,861	2.6	+50.3	±63.2
Deposition (59+ cm)	3,053	2.8	+42.0	±66.3
Inundation, deposition, drag	1,102	1.0	+62.6	±80.0
Inundation and drag	43,035	39.2	+46.4	±45.4
Drag only	44,210	40.3	+43.2	±45.4
Deposition only	1,022	0.9	+42.0	±66.3
Inundation only	1,344	1.2	+17.1	±29.1
Total floodplain removal:	**109,715**	**34.0**		
Trauma (occurrence)	66,343			
Trauma (exclusive)	11,299			

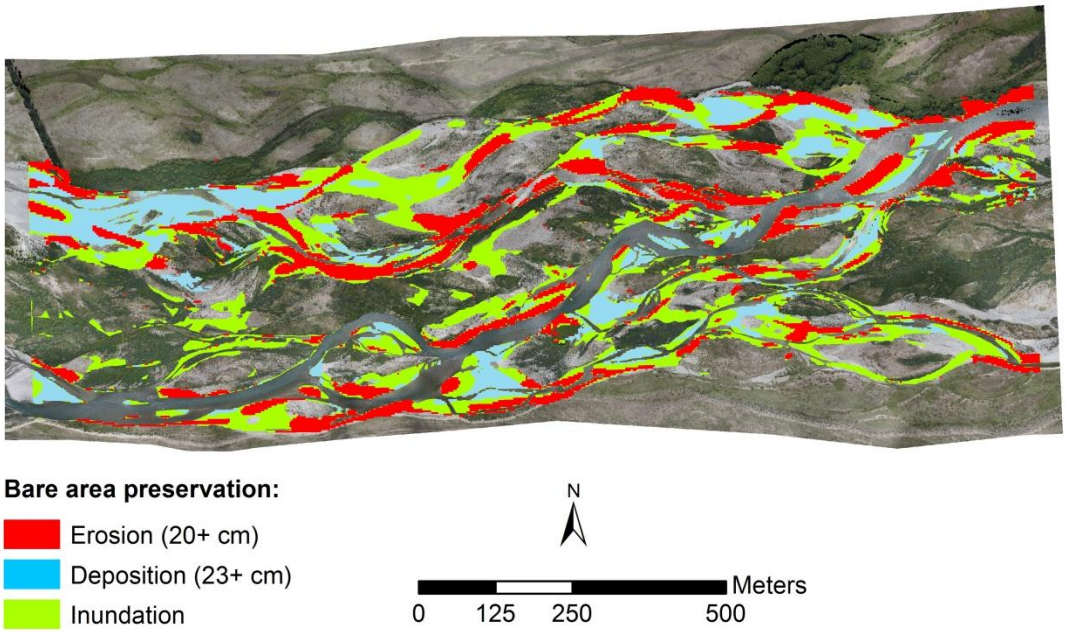

Figure 7.26: Simulated 200-year flood event and predicted bare area preservation.

Table 7.44: Predicted bare area preservation and associated uncertainties for the 200-year flood event.

	Lupin mortality		Uncertainty (%)	
Process:	Area (m^2)	Mortality area (%)	Process	Model
Erosion	89,344	32.3	+52.0	±44.6
Deposition	65,023	23.5	+42.0	±66.3
Inundation	122,419	44.2	+6.0	±29.1
Total	**276,786**	**80.1**		

7.4.3.10 Simulated 500-year flood event

Finally, the 500-year flood event was simulated with a peak discharge of 923 $m^3 s^{-1}$ and a duration of 430 hours. Mortality process results (Figure 7.27 and Table 7.45) revealed that the combined mortality of inundation and drag far exceeded all other processes (65.4%), with drag and erosion providing the majority of the remaining mortality. However, all processes did contribute to the total mortality area, and total floodplain lupin removal was estimated at 62.4%. Bare area mortality was mostly caused by inundation, however, all three processes contributed at relately comparable percentages for a total area preservation estimated at 99.5%.

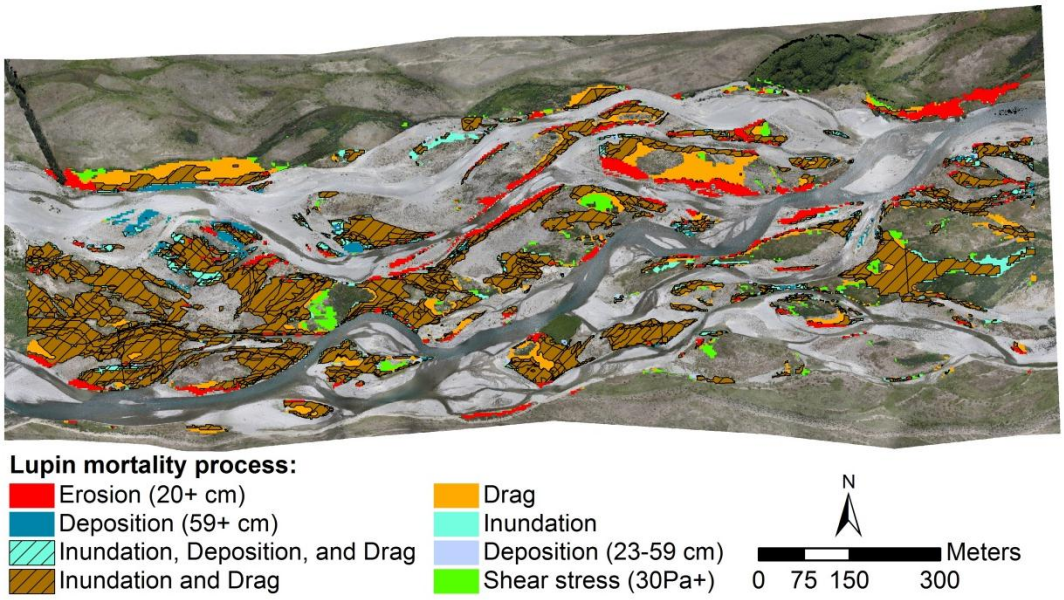

Figure 7.27: Simulated 500-year flood event and predicted mortality processes.

Table 7.45: Predicted lupin mortality and associated uncertainties for the 500-year flood event.

	Lupin mortality		Uncertainty (%)	
Process	Area (m^2)	Mortality area (%)	Process	Model
Erosion (40+ cm)	21,062	10.5	+52.0	±44.6
Erosion (20+ cm) + Velocity	4,155	2.1	+50.9	±63.2
Deposition (59+ cm)	4,933	2.4	+42.0	±66.3
Inundation, deposition, drag	9,839	4.9	+62.9	±80.0
Inundation and drag	131,731	65.4	+46.9	±45.4
Drag only	28,039	13.9	+43.2	±45.4
Deposition only	253	0.1	+42.0	±66.3
Inundation only	1,469	0.7	+18.2	±29.1
Total floodplain removal:	**201,483**	**62.4**		
Trauma (occurrence)	81,373			
Trauma (exclusive)	9,221			

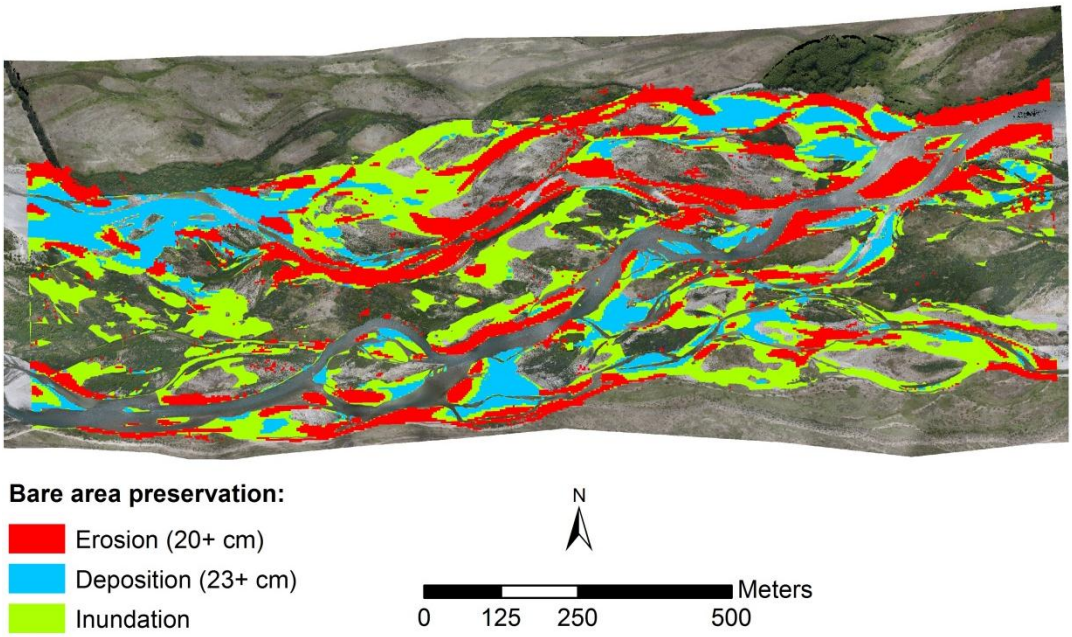

Figure 7.28: Simulated 500-year flood event and predicted bare area preservation.

Table 7.46: Predicted bare area preservation and associated uncertainties for the 500-year flood event.

	Lupin mortality		Uncertainty (%)	
Process:	Area (m^2)	Mortality area (%)	Process	Model
Erosion	123,830	36.0	+52.0	±44.6
Deposition	72,775	21.1	+42.0	±66.3
Inundation	147,182	42.9	+6.0	±29.1
Total	**343,787**	**99.5**		

7.4.3.11 Final discussion

The results of assessing flood events with increasing discharges showed that larger floods caused greater mortality and the dominant mortality processes fluctuated. In general, the mortalities of smaller floods were dominated by erosion and drag, and the mortalities of larger floods were dominated by drag and inundation. Further, erosion caused the greatest removal near river channels, and drag and inundation (when present) caused the greatest floodplain mortality. These results were seemingly realistic given vegetated river banks were vulnerable to bank erosion, and that surface erosion was unlikely to develop in the relatively flat and vegetated floodplains due to the increased flow resistance. However, the degree to

which dense floodplain vegetation would reduce conveyance and velocity was not well understood. While the lupin-mesh experiment (Section 6.3.2) did investigate lupin-altered conveyance, it only accounted for a single strip of lupins; however, greater vegetation density and vegetation orientation can affect the overall drag and flow resistance (Poggi, 2003; Nepf, 1999 as cited by Righetti & Armanini, 2002). Therefore, while floodplain vegetation and corresponding hydraulic affects were included in the Delft3D simulations, the true accuracy of trachytope inclusion was not known. However, with the restriction of drag assessment only in areas of water depths ≥ 0.5 m, the likelihood that large enough velocities existed can be justified by the results shown with Equation 7.2, which accounts for vegetated floodplains and calculated velocity thresholds necessary. Further, the depth of ≥ 0.5 m utilized was highly likely to cause submerged conditions which would promote drag forces acting on the lupins' entire canopy. Thus, drag results were seemingly realistic for the floodplain areas identified.

Deposition was shown to be a minimal process in mortality identification, but as illustrated by the observed flood simulation results and comparing mortalities, deposition was found to be under represented; thus the mortality threshold was potentially too restrictive. However, as illustrated in Section 7.3.6, simulated deposition was inaccurate and had the highest associated uncertainty of any single component. Therefore, had deposition significantly contributed to the overall mortality, its contribution would have been treated with lower confidence. However, with erosion mortality mapping methods supported by the observed and simulated comparison, and with drag and inundation mortality developed with methods promoting high confidence and relatively low uncertainties, the final results were considered to be reasonably good and were treated with high confidence.

7.5 Conclusion

This chapter has presented the data synthesis of Part II of this thesis in order to simulate various sized flood events and corresponding flood-induced lupin mortality. Known prior to this chapter, the mortality processes of inundation, drag, erosion, and deposition all had high confidence in mortality threshold identification through means of conservative methods, supporting evidence of recent flood events, and/or relevant research. However, trauma proved a difficult process to identify and predict. While it is acknowledged that the best method to

investigate trauma-induced mortality would have been a hydraulic laboratory flume experiment or an in-depth field study supported by time lapse images, neither of these were obtainable. This led to the approach that relied upon field observation and numerical simulation, and as demonstrated, this produced results based on simplified processes and with extensive sources of error. Therefore, trauma could not be considered with confidence and was only discussed as a potential mortality process.

While the mortality thresholds of inundation, drag, erosion, and deposition were developed with high confidence, large inherent uncertainty existed due to extreme variation in lupin characteristics and poor statistical relationships. Indeed, in combining all contributing components of specific mortality processes, the final uncertainty results were large. However, these results were anticipated given that many processes required multiple data and relationships as well as considering highly variable lupin characteristics and the attempts to predict mortality based on simple experiments and relationships. In addition to vegetation uncertainty, the numerical model also produced large uncertainty estimates. Again, these results were anticipated given the large errors illustrated throughout the calibration and validation results of Chapter 6. Whenever possible, the custom relationships and associated uncertainties were compared to alternative methods using the best-fit logarithmic relationships. These comparisons often revealed that the best-fit relationships produced lower estimated uncertainties; however, considering that the custom relationships were only of negative sign convention and the logarithmic relationships required plus/minus sign convention, the full range of uncertainties were often comparable. Nevertheless, the true benefit of utilizing the custom relationships derived from maximum values was the resulting high confidence that lupin mortality existed.

Utilizing the calibrated Delft3D numerical model, the observed October, 2011 flood event was simulated and the corresponding mortality was compared to the observed lupin mortality as an assessment of the developed mortality identification. Results revealed a strong agreement for erosion mortality, poor results for the deposition mortality, and potentially good results for the drag mortality. However, since the results of the observed flood event mortality were merely speculative due to only having the final DoD as a snapshot of the flood event, it was not possible to conclusively determine the accuracy of the mortality mapping

methodology. Nevertheless, this void was filled by the uncertainties associated with each mortality process and associated modeled process.

In evaluating the forecasted flood events and corresponding lupin mortality areas, the processes of inundation, drag, and erosion had the greatest influence. With erosion mortality mapping methods supported by the observed and simulated comparison, and with drag and inundation mortality developed with methods promoting high confidence and relatively low uncertainties, the final results were considered to be reasonably good. Further, the final mortality results were considered to be of high confidence and any uncertainty associated was likely only to be conservative in that if anything it would add to the total areas affected. Therefore, the calculated total area of mortality was likely the representation of the minimum lupin removal. These minimum values provide baselines for flood-induced lupin mortality and may be valuable for conservation efforts such as those of DoC and PRR.

Chapter 8

Summary, Conclusions, and Recommendations

8.1 Summary

The braided rivers of the UWB provide critical habitat for endangered fauna such as the black stilt. However, this habitat has been degrading due to introduced predators, hydropower operations, and invasive weeds (e.g. Russell lupins, crack willow, rosehip, broom, and gorse). While efforts have been made to restore these habitats through weed control, predator control, and artificial habitats, flood events may provide a natural method to re-create habitat lost to invasive vegetation. Although much research has focused on the effects of vegetation on flow hydraulics, little is understood about the feedback of the hydraulic effects on vegetation.

During the past decade, advances in survey and sensor technology and three-dimensional morphologic analysis have been partially driven by the need for high resolution topography for physical and numerical fluvial modeling and have in return created new opportunities to investigate and model the structure and dynamics of fluvial systems. Although progress has been made in modeling braided river hydraulics, there was not enough information available before this study to quantify or model vegetation mortality due to flood events in braided rivers such as those of the UWB. However, with new technologies offering affordable, sub-meter resolution terrain models with decimeter accuracy, and numerical models capable of simulating hydraulics and morphology of large-scale braided river reaches, the opportunity was created for this study to identify and model the flood-induced processes that cause vegetation mortality; thus, benefiting habitat conservation and restoration.

Russell lupins were chosen as the vegetation of focus for this study as they were widespread throughout the UWB and identified as one of the most aggressive weeds in terms of sprawl and ability to thrive in minimal nutrient soils. Thus, the objectives of this research were to i) identify the various flood-induced processes that cause Russell lupin mortality and ii) simulate various sized flood events and estimate the corresponding lupin mortality. To achieve the first objective, lupin mortality processes were investigated using a combination of field and laboratory experiments as well as observations following flood events. To achieve

the second objective, a hydrological assessment was conducted, study-reach topography and vegetation surveys were conducted, and an extensive model parameterization was conducted. In combination, these studies provided the necessary tools and understanding to simulate and assess flood-induced mortality. A summary of the specific experiments, methods, and results are presented in the sections below.

8.1.1 Lupin mortality processes

Field investigations following floods identified that the processes causing lupin mortality were prolonged inundation, current drag, erosion, and sediment deposition. However, to identify the mortality thresholds for specific processes, experiments and field data were required. Inundation mortality was assessed using three tanks of varying water depth to simulate flood conditions of i) root saturation, ii) inundated stalk, but emergent canopy, and iii) full submerged canopy. These experiments determined that fully submerged and emergent lupin stalk conditions caused mortality. Lupin removal by current drag was assessed by first determining the pull-out forces required to extract lupins, and then by determining the lupin-generated current drag forces. Combining these data provided a method to determine lupin removal as well as indicating that the velocity thresholds for lupin extraction also depended on associated fluvial processes. In particular, bank erosion and floodplain surface erosion were suspected to decrease pull-out forces, thus causing greater lupin removal during flood events. To determine this force reduction, erosion levels were simulated (10 and 20 cm) during the pull-out data collection. However, only the 20 cm erosion level was identified to reduce pull-out forces. Combining the pull-out forces of no simulated erosion and the simulated erosion-reduced pull-out forces, a force reduction relationship for varying levels of erosion was developed. These data were utilized with the previously described drag data to determine various velocity thresholds capable of removing lupins.

Field observations following flood events showed only large lupins deposited along the river floodplain. This led to the hypothesis that smaller lupins were resistant to removal by current drag, but by virtue of their smaller stature, they should also be more vulnerable to mortality by sediment deposition. Therefore, a two-part experiment was devised to determine i) the height deformation that lupins experience during flood events, and ii) the required amount of sediment deposition that would be required to bury deformed lupin canopies. Various

deposition depths were tested, and the results showed smaller lupins experienced mortality with lesser deposition, and larger lupins were killed with greater deposition. While trauma by flood flows was suspected of causing lupin mortality in one location of the study-reach, the only evidence that the area had been inundated was from time lapse camera images. Therefore, additional investigation was required and partially satisfied using a calibrated numerical model (discussed further in Section 8.1.4).

8.1.2 Observed flood event

While the lupin mortality experiments offered insight into flood-induced mortality, nothing could replace the processes of an actual flood event. Therefore, to document a flood event and corresponding lupin mortality, vegetation and topography surveys were conducted initially in September 2011 and again in December 2011 following the near-mean annual flood event of 209 m^3 s^{-1} in October. Utilizing the ground survey data, aerial photographs, and bathymetric surveys, pre- and post-flood digital elevation models were generated using a workflow combining Structure-from-Motion, optical bathymetric mapping, and point cloud filtering to remove floodplain vegetation noise. DEMs were subjected to quality assessments, and results revealed vertical surface errors of 0.10 m in non-vegetated areas.

Utilizing pre- and post-flood vegetation survey data with corresponding aerial photographs, vegetation presence, density, and type were mapped and later utilized to identify the vegetation removed during the observed October flood event. Further, differencing the pre- and post-flood DEMs, elevation differences due to morphologic changes were detected. These morphological changes combined with vegetation removal provided the necessary data to assess and estimate the mortality processes associated with erosion, deposition, and no morphologic change. Results revealed that the areas identified with erosion had the greatest lupin removal, while the areas associated with deposition and no morphologic change were comparable in size, but significantly less lupin removal compared to the eroded areas.

8.1.3 Numerical model calibration and validation

Delft3D was the numerical model chosen to simulate the study-reach and the various flood events. In order to best simulate the study-reach, extensive data were utilized to provide

accurate representation as well as full parameterization. The model's topography grid was developed and tested using cell sizes of 1.5 and 2.5 m. However, the 2.5 m grid was ultimately chosen for its comparable performance, increased stability, and practical simulation times. Further, vegetation presence was included using the vegetation surveys and mapping data and model calibration was accomplished for hydraulics, vegetation, and morphology.

Hydraulic calibration was achieved using various bathymetric data (depth, velocity, and water extent from aerial photographs). Vegetation inclusion in Delft3D was possible utilizing a function called 'trachytopes,' which can represent vegetation roughness and flow resistance. To best represent lupin effects on flow conveyance, an additional experiment was conducted utilized freshly uprooted floodplain lupins attached to a wire mesh, inserting this mesh into a reach of interest, and using an aDcp to record the resulting altered depths and velocities. Utilizing this data and the trachytope function, vegetation calibration was achieved.

Morphologic calibration was achieved by simulating the observed October 2011 flood event and adjusting the available parameters until the simulated morphologic changes best represented the observed morphologic changes identified from the DEM of Difference (DoD). With the second objective to simulate flood events, it was important to assess the calibrated model's ability to replicate flood events. Therefore, time lapse camera images that captured high flow events were utilized with the simulated inundation extent to identify the model's inundation accuracy and overland flow.

Ultimately, the results of these calibrations determined that hydraulics were well represented, vegetation inclusion often improved the model's water inundation extent accuracy at high flows, but the modeled morphology struggled to replicate local erosion and deposition. However, poor simulation of morphology was expected since bank erosion is often poorly predicted in numerical models. Nevertheless, modeled and observed total bank erosion for the study-reach were comparable, and realistic river characteristics (riffles, pools, channel width) were produced. Therefore, the model was considered adequate to represent general flood effects, but the inherent uncertainty still had to be considered.

8.1.4 Data synthesis

The results discussed in Sections 8.1.1, 8.1.2, and 8.1.3 were combined to meet the objectives of this research. While the first task of determining the processes that cause lupin mortality was nearly completed using previous data, evaluation of trauma required additional assessment. Utilizing the latest available topography (post-flood DEM), the calibrated numerical model, and field observations, the flood event that was associated with suspected trauma-induced mortality was simulated. This simulation revealed that the inundation (the other likely mortality process) threshold for mortality was not reached. Therefore, trauma was assumed to be the likely mortality process, but could not be confirmed. Additionally, simulated sediment transport and high shear stress were evaluated; however, only shear stress was identified in the area of interest. Therefore, combining the simulated shear stress data with observed areas of lupin mortality and lupin regrowth, an attempt was made to identify mortality relationships. Results showed that areas of lupin mortality had higher average shear stress (26 Pa) than areas that had lupin regrowth (16 Pa). However, while a weak relationship between shear stress and lupin mortality was found, the methods that led to this identification were simple and had multiple sources of error. Therefore, trauma mortality could not be identified with any level of confidence, and only drag, erosion, deposition, and inundation mortality were determined to be flood-induced mortality processes.

To achieve the second objective, an uncertainty assessment was performed for all mortality processes and corresponding thresholds as well as all numerical model components of simulated inundation extent, water depth, velocity, erosion, and deposition. Combining the mortality processes thresholds with the calibrated numerical model, flood events were simulated and corresponding mortalities were mapped and presented with the estimated uncertainties. As expected, the flood simulation results revealed that larger flood events caused greater mortality. However, the processes that dominated mortality varied for different flood sizes. For example, for smaller flood events lupin mortalities were dominated by erosion and drag, while for larger floods lupin mortality was dominated by drag and inundation. Further, erosion caused the greatest removal near channels, drag and inundation (when present) caused the greatest mortality on floodplains, and deposition mortality was shown to be a minimal mortality process.

8.2 Conclusions

Identification and numerical modeling of the processes causing flood-induced lupin mortality, as presented in this research, have provided greater understanding of the complex relationship of vegetation mortality, flood events, and fluvial morphology and their interdependent feedback. In particular, this research has concluded and contributed the following to science:

In the course of identifying processes causing lupin mortality, the contributions can be divided into three categories. First, lupin mortality experiments have concluded that inundation, drag, erosion, and deposition can cause lupin mortality, while field observations have shown that trauma may cause mortality. Further, mortality thresholds for these processes (previously unknown) have been identified for Russell lupins, which is a finding valuable for any river affected by lupin encroachment, especially the braided UWB rivers. Secondly, the methods devised to determine mortality are novel, as are the relationships developed to identify thresholds. These methods extend other methods previously utilized in other research studies, but in general add to the overall potential methods available. Third, these data and methods added to the limited research investigating the feedback between flood effects on vegetation. These are valuable as they have proved the ability to assess the potential flood effects on riparian vegetation. Further, combining these methods with flood frequency, flood magnitude, and vegetation sprawl, other studies could determine the flows needed to naturally control riparian vegetation of braided rivers elsewhere.

Combining lupin mortality data with the calibrated numerical model, simulated flood events were utilized to identify varying flood effects on lupin mortality. This information was important for three reasons. First, it confirmed that the identified mortality thresholds relating to velocity, inundation duration, and morphologic changes were passed during floods. While these thresholds were assumed to be present near the active river braids, the thresholds within vegetated floodplains were not well understood yet results revealed flood events were likely a natural method to re-create habitat lost to invasive vegetation. Secondly, these data illustrated that lupin mortality associated with smaller and larger flood events experiences a gradient of mortality processes. Third, the total floodplain lupin mortality was calculated for a range of

flood sizes. This was valuable in providing an estimate of total potential lupin removal and lupin regulation in relation to flood frequency.

In requiring a low cost yet high quality DEM of the study site, the relatively new and un-documented photogrammetric technique of Structure-from-Motion (SfM) with dense multi-view reconstruction (DMVR) was utilized to model the dry floodplain topography. This was combined with optical bathymetric mapping, as well as the point cloud filtering tool ToPCAT, to provide a workflow combination to effectively provide a terrain model of the study-reach with reduced vegetation noise. This workflow combination was important as it offers non-experts a highly automated method to produce quality fluvial terrain models with minimal data acquisition costs and moderate (initial surveys) to minimal (repeat surveys) field labor. In contrast to previous studies, this assessment also provided a rigorous quality assessment of the SfM-DMVR performance, which demonstrated that this method could deliver high quality terrain datasets suitable for geomorphic change detection competitive with those obtained with significantly more expensive laser scanning. Further, in utilizing the derived pre- and post-flood DEMs for numerical modeling, the results indicated that this method was indeed fit for the purpose of numerical modeling.

In preparing for numerical model calibrations, the lupin-mesh experiment to quantify the lupin-altered conveyance was a unique experimental method that provided additional information for vegetation parameterization within Delft3D. Further, the results were utilized to calibrate flood events that had moderate overland flow through vegetated areas. Ultimately, these data were important as they provided a method to calibrate the vegetation influence which was shown to increase the numerical model's accuracy for high discharge simulations. These data were unprecedented in three ways. First, vegetation-altered conveyance has not been documented with such methods. Secondly, Delft3D's trachytope function has rarely been discussed in detail in previous studies, and no known studies have presented trachytope parameterization. Third, the results of the numerical model simulation showed improved results with trachytope inclusion during high discharges and moderate overland flow. These results are encouraging, and suggest vegetation-induced bed roughness and flow resistance were significant factor during flood flows over braided river beds.

The lupin mortality mapping presented in this study is valuable for conservation efforts in three areas. First, the results showed that floods provide a natural mechanism for lupin regulation. Lupins on near-channel floodplains can be frequently regulated by small and frequent flood events. However, lupins on floodplain areas more distal from channels are only regulated by infrequent and large floods. Conservation efforts can utilize this information for Ahuriri River herbicide application, and apply herbicide over distal floodplain areas only. This method is not intended to eradicate lupin presence, as this would require upstream seed source eradication which is currently a complex and contentious issue. Nevertheless, herbicide application to distal floodplain areas will: i) reduce floodplain stability, helping larger flood events to naturally mobilize these areas and thus minimizing accelerated floodplain aggradation; ii) create more open gravel areas for endangered ground nesting bird habitats; and iii) limit herbicide application which will save time and money and will improve relations with river enthusiasts who oppose near-river herbicide application. Second, based on the flood simulation and mortality mapping results, the 500-year flood event was not estimated to remove all floodplain vegetation. This finding was important as it highlights the need for continued conservation efforts in lupin regulation. Third, this study has demonstrated methods for estimating flood-induced mortality and how numerical models can be utilized to simulate and identify areas of potential removal. Although this study has shown how this information is valuable for conservation efforts in unregulated rivers, these methods could also be utilized for flow-regulated rivers to identify what flood magnitudes and frequencies are needed to retain some level of natural control of riverbed vegetation.

8.3 Recommendations

This research has provided new and useful methods and data, and enhanced the understanding of the role natural flood events play in preserving riparian and floodplain ecosystems. However, throughout the process of completing the two research objectives, numerous sub-questions have arisen that would add to the overall understanding of these processes, but were outside the scope of this project. These additional questions and potential research studies are presented below in the following sections.

8.3.1 Lupin root structures

During the development of lupin mortality relationships, lupins with root diameters greater than 8 cm were occasionally observed, but these often had lower-than-expected mortality thresholds. This was explained by the wider rooted plants actually consisting of several lupins growing in clusters with entangled roots. However, this relationship was not considered until data processing, and field and laboratory observations did not distinguish clusters from single lupin root plants. Therefore, an important question that arose in this research concerns the true impact of lupins growing in clusters as opposed to single root plants. Since both single and clustered lupins were utilized in the same data and relationship development, this assumption likely over simplified the true and complex nature of the relationships. Based on data and observations, clustered lupins often had denser and larger canopy widths, yet root lengths comparable to smaller lupins with single roots. Therefore, it was hypothesized that these clustered lupins would have been more susceptible to drag (due to larger canopies yet disproportional root lengths) and more susceptible to inundation (due to smaller lupins contributing to the total cluster); thus treating clustered lupins like single root plants was likely a conservative approach. Nevertheless, additional research could provide greater insight into lupin mortality by exploring the vulnerability of larger clustered lupins, which were more prevalent in densely vegetated floodplain areas.

8.3.2 Lupin mortality and flume experiments

Lupin field and laboratory experiments significantly improved knowledge of flood-induced mortality; however, two additional areas were identified with the potential to increase overall knowledge. First, greater understanding of trauma-induced mortality could be gained in flume experiments with mobile sediment. Using cultivated lupins of various root diameters, different sediment loads could test trauma and potentially identify thresholds. Alternatively, insight into trauma could be obtained with time lapse imagery of observed trauma and utilizing Delft3D in mobile bed mode to re-create the conditions. Further, utilizing 3D mode during these simulations could potentially add insight into the vertical momentum exchanges occurring around the lupins' canopy; thus providing knowledge specifically to lupin-altered hydraulics. Secondly, drag, erosion, deposition, and inundation could be investigated to a greater extent using flume experiments. This could be a valuable method to test the cumulative effects of multiple processes as well as the potential for combined processes to lower mortality thresholds. Unfortunately, such experiments were side-lined during the

present study due to an inoperable flume following the February 2011 Christchurch earthquake.

8.3.3 Lupin regrowth

This research focused on lupin mortality and removal; however, at what rate the lupins can reoccupy areas of mortality is unknown. Knowing this regrowth and spread rate could enhance the overall understanding of the ability of flood events to regulate encroaching vegetation. By combining lupin growth/spread rate data with the mortality data presented in this research, a study could simulate the river's ability to self-regulate lupins. Such data could be useful not only for the assessment of the Ahuriri River, but could also be applied to other braided and UWB rivers. These data with the modeling approach could potentially be utilized to design scheduled flow releases from dams to preserve bare floodplains over downstream braided rivers.

8.3.4 Seasonal effects and additional vegetation

While lupins were only assessed during the peak flood season, which corresponded to the peak growing season, additional assessments on various seasons would be of great interest since flood events happen year-round. Naturally, varying seasons affect the lupins' physical properties with lupins becoming dormant during late-fall, winter, and early-spring months. Based on field observations, dormant lupins have reduced canopies and rigid stalks. These characteristics alone would greatly influence the lupins' resistance to drag pull-out and the required amount of deposition for burial. However, their dormant state may make them more or less sensitive to inundation and possibly trauma. These unknowns could be addressed through additional field and laboratory mortality studies on lupins during the spring, fall, and winter seasons and could be very beneficial to the overall understanding of the Ahuriri's ability to regulate lupins. Further, while lupins were the dominant exotic vegetation in the study-reach of the Ahuriri River, other species included rosehip (sweet briar) and limited willow thickets (willows had been significantly reduced by DoC efforts). Additional research could therefore consider flood effects on these other exotic species. Since rosehip bushes are typically 1 to 2 m tall, woody, and have sparse canopy density, they would likely be more resistant to the mortality processes identified in this research. While their removal has been noted and observed in this research, the process thresholds and associated frequencies-of-

occurrence are yet unknown. Further, if larger flood events did remove considerable amounts of lupins, the ability of rosehip or other exotic vegetation to establish a presence is unknown, but they could become the dominant species given lupin removal. Answering such questions should provide greater understanding of the complexities of vegetation encroachment in the Ahuriri River and other UWB rivers.

Part IV

Appendices and References

Appendices

Appendix A

Additional Data

A.1: Darcy-Weisbach and Manning's Relationship

According to Soto and Madrid-Aris (1994, pg. 1), "flow resistance is related with the physical shape and [river] bed roughness of a channel, which both control the depth, width, and discharge of the flow in the channel. The three most common resistance coefficients are Manning's (n), Chezy (c), and Darcy-Weisbach (f). These are related to each other by:

$$\sqrt{\frac{8}{f}} = \frac{c}{\sqrt{g}} = \frac{R^{\frac{1}{6}}}{n \cdot \sqrt{g}} \qquad \text{Eqn: A.1}$$

Where:

g = acceleration due to gravity

R = hydraulic radius

A.2 ToPCAT

The ToPCAT workflow can be viewed in Figure A.1, and further details can be found in Brasington et al. (2012). ToPCAT produces five useful files: filename.ini, filename_zmin.txt, filename_zmax.txt, filename_zstat.txt, and filename_underppopulated_zstat.txt. The filename.ini gives simple statistics such as total number of observation, maxima, minima, etc. The zmax and zmin text files record the x- and y-coordinates of the decimated data and the corresponding minimum or maximum elevation for the gridcells. The zstat records z-coordinate data only for cells with four or more observations. The underpopulated_zstat contains the data for cells that do not meet the four observation requirement. The zstat documents contain the coordinates of the decimated data and corresponding elevation average, range, standard deviation, standard deviation detrended, skewness, skewness-detrended, kurtosis, kurtosis-detrended, averaged detrended, and number of observations per cell (n). If gridcells only contain two or three points, statistics such as the standard deviation detrended, skewness, skewness detrended, Kurtosis, Kurtosis detrended, are not calculated; however, the cells still contain the minimum, maximum, average, range, and standard deviation. In the case where only one point is within the gridcell, it becomes the minimum, maximum, and average and the range and standard deviation are not calculated.

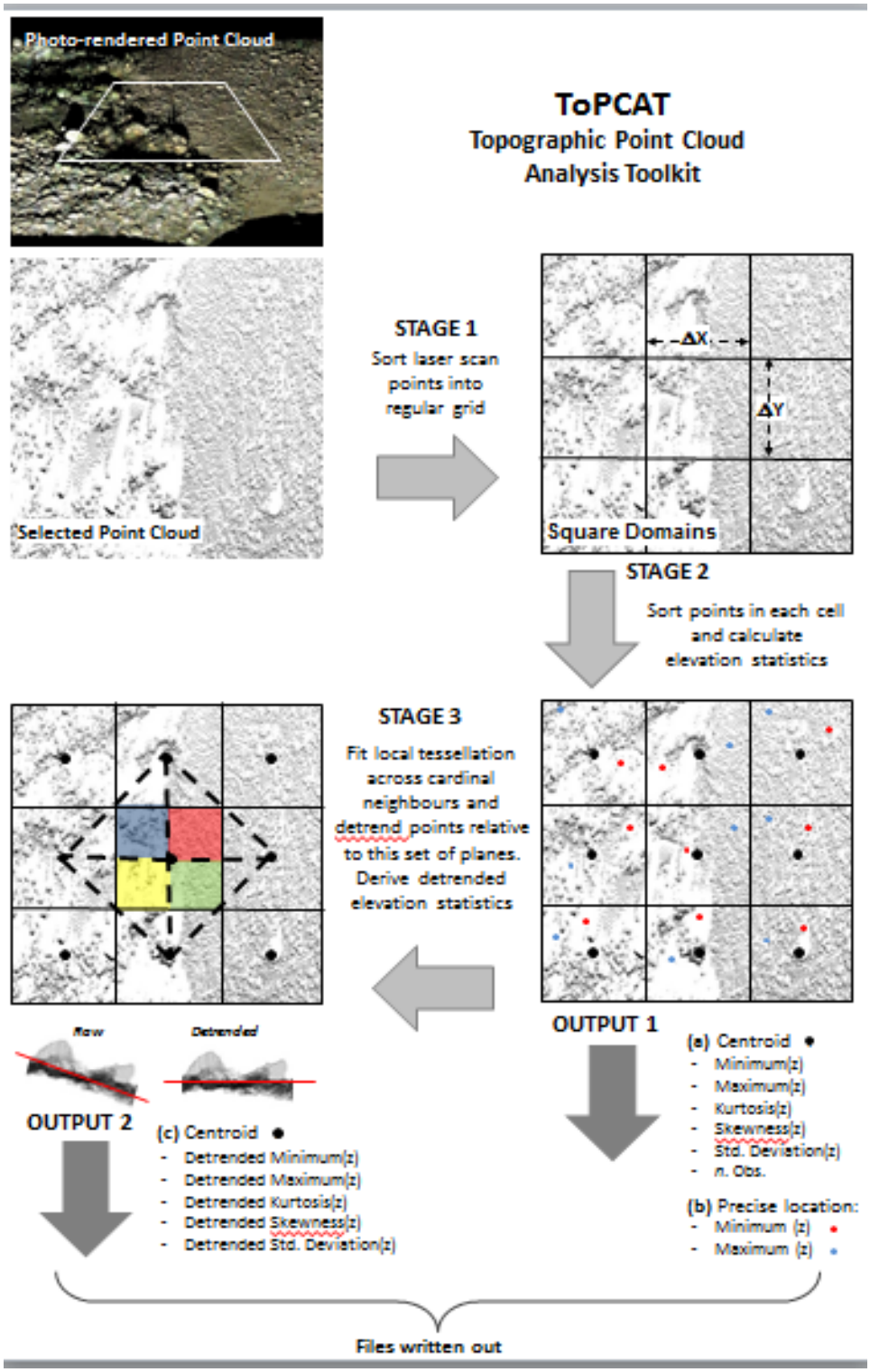

Figure A.1: ToPCAT workflow and outputs (as cited in Brasington et al., 2012).

Appendix B

Sample Calculations

B.1: Error variance

Calculating the error variance required the measurement standard deviation; however, this was not known for all data. For example, in determining the error variance for the discharge and duration relationship, the duration uncertainty was not easily determined since 15 minute interval flow data was utilized. Further, the measured uncertainty in recorded discharge was also unknown. Therefore, only an estimate could be made. Considering the recorded flow data utilized for both discharge and duration came from the flow gage upstream of the Longslip Creek tributary, and any losses between the flow recorded and the study reach could have existed, an estimated ±10% uncertainty was utilized for the measured value and the standard deviation was taken. For example, +10% of the measured 256 hour of duration produced 281 hours, and the -10% produced 230 hours, and the standard deviation was calculated at 36.2.

Table B.1: Error variance sample calculation for discharge vs. duration relationship

Measurement Standard Deviation	Measured Value	Calculated Value	Difference	Diff/SD	$(Diff/SD)^2$
36.2	256	272.4	-16.4	-0.45	0.21
39.7	281	379.7	-98.7	-2.48	6.17
47.0	332	315.8	16.2	0.35	0.12
50.2	355	311.2	43.8	0.87	0.76
71.7	507	472.8	34.2	0.48	0.23
72.5	513	464.1	48.9	0.67	0.45
75.2	532	560.0	-28.0	-0.37	0.14

Number of adjustable parameters =	2
Calculated error variance =	1.61

Table B.2: Example calculation of error variance for pull-out force.

Measurement Standard Deviation	Measured Value	Calculated Value	Difference	Diff / SD	Squared
50.76	348.92	387.84	-38.92	-0.77	0.59
43.32	317.01	400.46	-83.45	-1.93	3.71
85.85	474.12	547.12	-73.00	-0.85	0.72
66.72	410.06	277.17	132.89	1.99	3.97
42.63	313.92	179.67	134.25	3.15	9.92
106.89	536.61	310.42	226.18	2.12	4.48
68.10	414.96	413.01	1.95	0.03	0.00
152.45	653.32	704.09	-50.77	-0.33	0.11
31.91	261.93	186.91	75.02	2.35	5.53
78.15	449.30	283.87	165.42	2.12	4.48
26.56	232.50	186.91	45.59	1.72	2.95
84.30	469.21	456.42	12.78	0.15	0.02
42.41	312.94	194.09	118.85	2.80	7.85
18.80	183.45	150.18	33.27	1.77	3.13
17.29	172.66	194.09	-21.44	-1.24	1.54
27.82	239.68	368.76	-129.08	-4.64	21.53
81.62	460.62	623.58	-162.96	-2.00	3.99
46.68	331.74	387.84	-56.10	-1.20	1.44
104.46	529.74	283.87	245.87	2.35	5.54
147.28	641.05	898.78	-257.73	-1.75	3.06
17.56	174.62	277.17	-102.55	-5.84	34.10
5.59	58.86	95.73	-36.87	-6.60	43.55
12.71	136.36	150.18	-13.82	-1.09	1.18
4.35	39.24	70.73	-31.49	-7.23	52.29

Number of Adjustable Parameters =	**2**
Calculated Error Variance =	**9.8**

Table B.3: Example calculation of error variance for drag force.

Measurement Standard Deviation	Measured Value	Calculated Value	Difference	Diff / SD	Squared
1	3.20	2.79	0.4	0.41	0.17
4	8.00	7.25	0.8	0.19	0.04
2	30.80	19.93	10.9	5.43	29.51
6	50.00	80.77	-30.8	-5.13	26.29
1	2.60	4.07	-1.5	-1.47	2.16
3	8.00	6.79	1.2	0.40	0.16
6	50.00	34.29	15.7	2.62	6.86
24	278.00	236.43	41.6	1.73	3.00
2	9.00	10.13	-1.1	-0.57	0.32
2	11.60	11.48	0.1	0.06	0.00
16	94.00	117.31	-23.3	-1.46	2.12
55	364.00	378.19	-14.2	-0.26	0.07

Number of Adjustable Parameters =	**5**
Calculated Error Variance =	**10.1**

B.2: Normal lens calculations

In order to produce the best image reconstruction, PhotoScan requires the focal length of the camera's lens. Typically, the digital image contains EXIF data which includes the captured images' focal length, pixels (width and height), among other details which PhotoScan automatically determines. However, in the event that this EXIF data is missing, PhotoScan assumes that the image was of 35 mm equivalent at 50 mm focal length (Agisoft, 2012a), which results in a diagonal field of view (FOV) of 47°. Human vision has a diagonal FOV of approximately 53°, and in photography is often referred to a 'normal' lens setting (Strait, 2004). Therefore, for the aerial photographs of this research, it was determined that a diagonal FOV within the 47-53° range would produce images with minimal distortion and would provide for the best image reconstruction in PhotoScan.

To determine the focal length that would produce this FOV, simple calculations were performed using Equating B.1 and are shown below (Figure B.1). With the Canon 10.1 megapixel CCD sensor dimensions of 22.2 x 14.8 mm, the diagonal dimension was 26.68

mm. Using this value and varying the focal length, the FOV can be determined and results for a focal length of 28 mm produced a diagonal FOV of 50.1°; thus within the targeted range. Next, with an object space resolution target of 0.1 m, calculations were made to determine the necessary flight height. As a result, a flight height of 600 m would produce an image resolution of 0.12 m, and an 800 m flight height would produce an image resolution of 0.16 m.

$$FOV = \frac{\frac{CCD\ dimension\ (mm)}{2}}{focal\ length\ (mm)} \qquad \textbf{Egn. B.1}$$

Example calculations:

$$\frac{\frac{26.68mm\ ccd\ diagonal\ length}{2}}{28mm\ focal\ length} = 2\tan(\alpha) \rightarrow\ \alpha = FOV = 50.95°$$

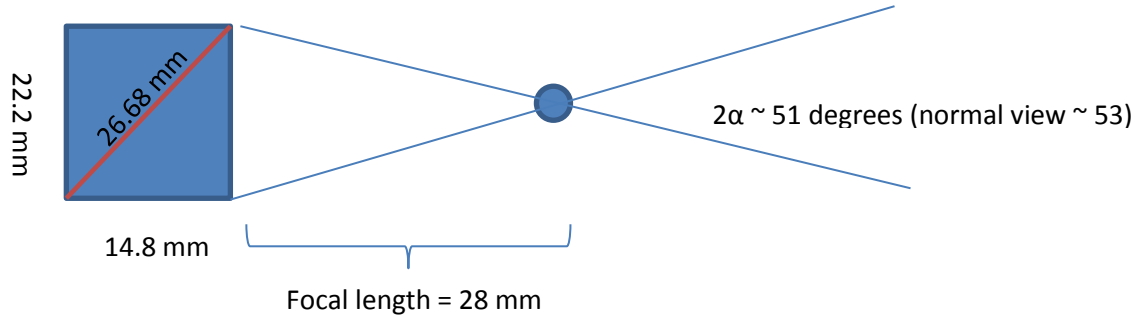

Figure B.1: Field of view calculation using CCD dimensions and focal length

Appendix C

Instruments

C.1: Lupin force tool

The lupin force tool is shown below in Figure C1 with the attached Kern digital scale and shown in Figure C2 with a lupins connected to the digital scale.

Figure C.1: Lupin extraction tool with Kern digital scale.

Figure C.2: Lupin extraction tool attached to a lupin, post pull-out.

C.2: Lupin drag tool

The lupin drag tool drawings with various views are shown in Figure C.3, use in the field in Figure C.4, and detailed photographs in Figure C.5.

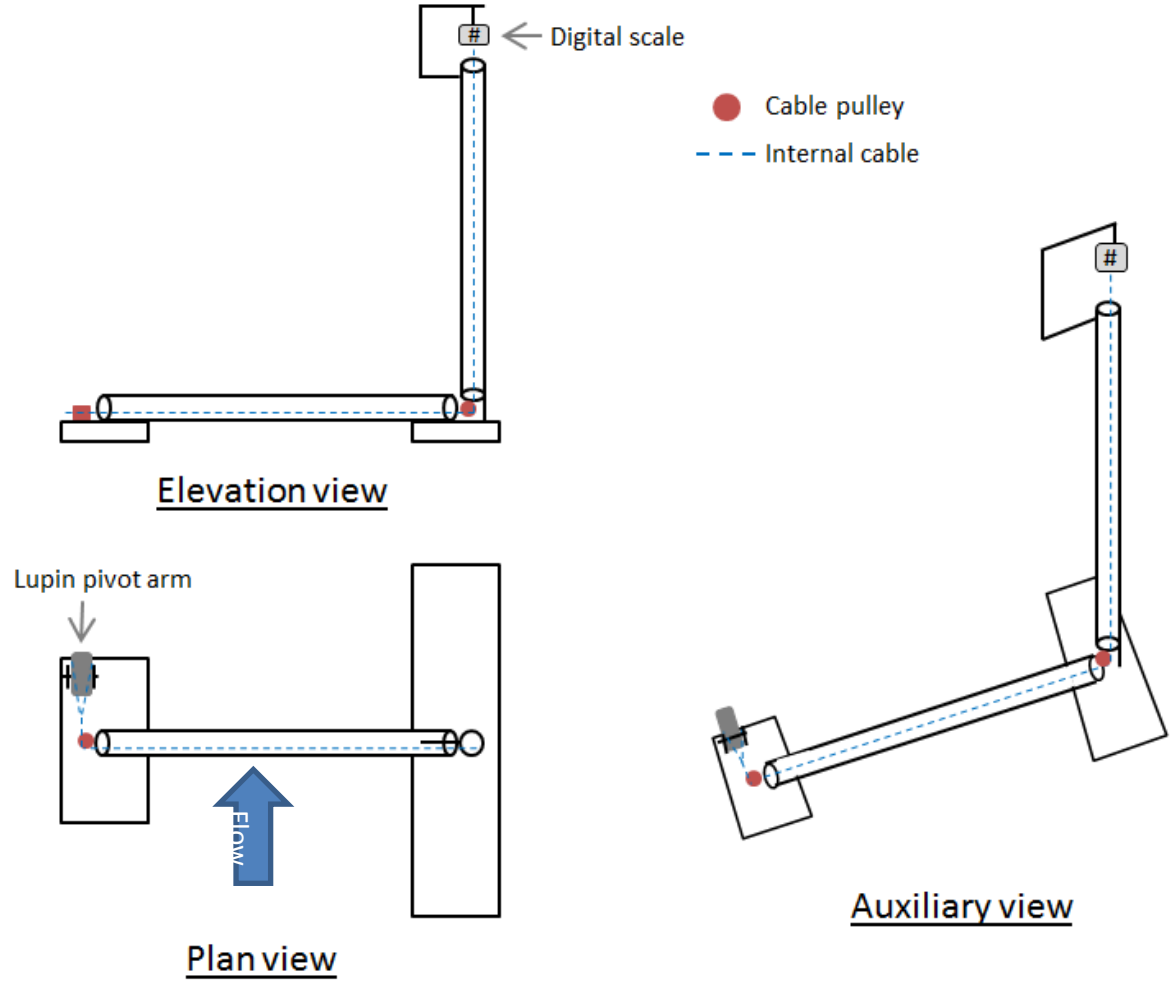

Figure C.3: Lupin drag tool illustration with multiple projections.

Figure C.4: Lupin drag tool: A) with lupin attached to pivot arm and kern digital scale through internal routing, and B) close-up of lupin attached to pivot arm.

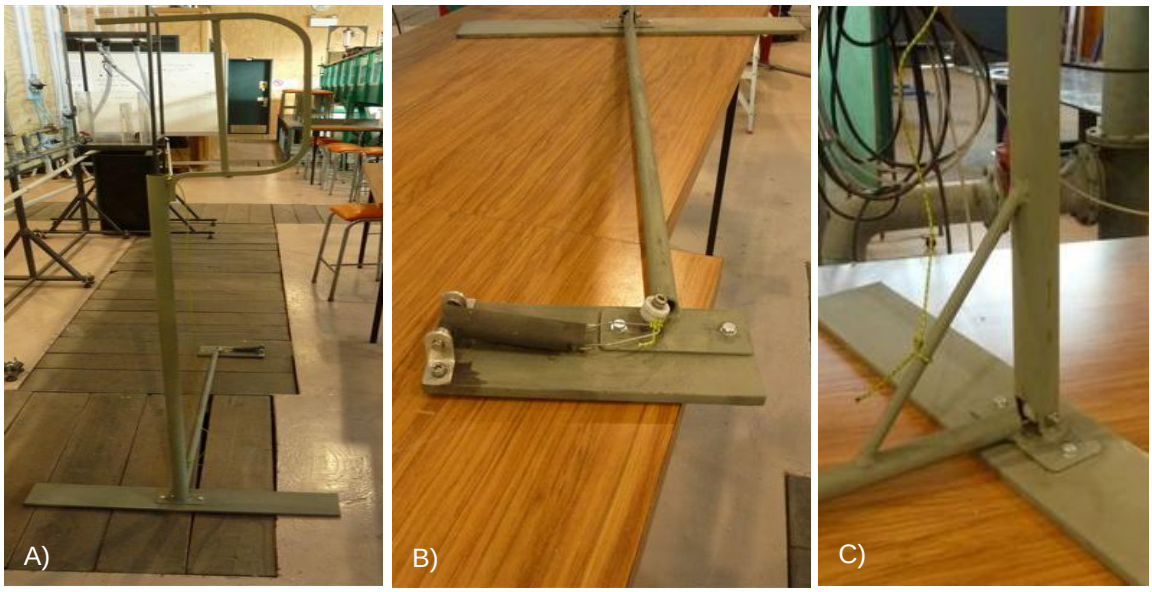

Figure C.5: Lupin drag tool shown: a) full extent, b) pivot arm and internal cabling, and c) additional internal cabling transition horizontal to vertical.

Appendix D

Procedures

D.1: Generalized synthetic hydrographs

Below are the guidelines utilized to generate the synthetic hydrographs, two comparisons utilizing the synthetic hydrographs against actual December flood events (Figures D.1 and D.2), and the final synthetic hydrographs (Figure D.3).

SCS/NRCS Hydrographs

The Soil Conservation Service (SCS) of the U.S. Department of Agriculture has published a significant catalog of hydrologic methods over several decades. (The name of the agency was changed to the Natural Resources Conservation Service (NRCS) in 1994). Two synthetic hydrographs are described here.

Two hydrograph shapes: triangular and curvilinear. Both shapes use the following parameters:

Time to peak, t_p (hrs): $$t_p = \frac{t_r}{2} + 0.6 \cdot t_c \quad \left(= \frac{t_r}{2} + t_L \right)$$

Peak discharge, Q_p (cfs): $$Q_p = \frac{484 \cdot A}{t_p} \cdot RO$$
[*RO* is Runoff Depth (in)]

Base time, t_b (hrs): $$t_b = \frac{8}{3} t_p$$

The Triangular Hydrograph is drawn as:

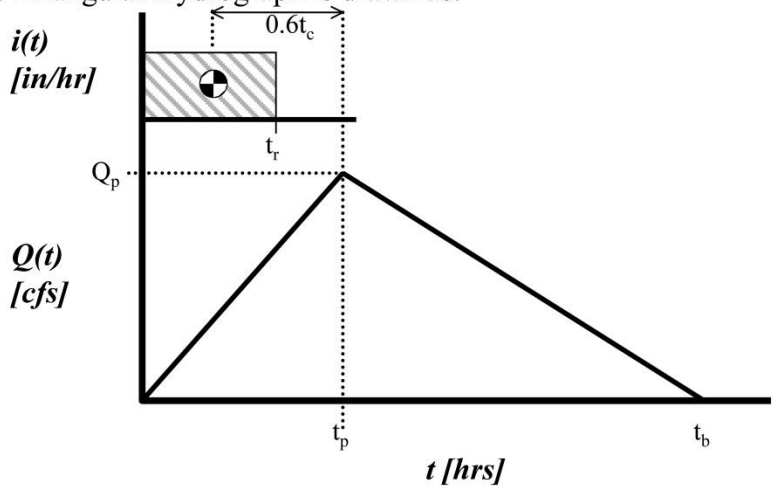

SCS/NRCS synthetic hydrographs (cont.)

The Curvilinear (or "Dimensionless") Hydrograph is tabulated as:

t/t_p	Q/Q_p	t/t_p	Q/Q_p
0	0	1.7	0.460
0.1	0.030	1.8	0.390
0.2	0.100	1.9	0.330
0.3	0.190	2.0	0.280
0.4	0.310	2.2	0.207
0.5	0.470	2.4	0.147
0.6	0.660	2.6	0.107
0.7	0.820	2.8	0.077
0.8	0.930	3.0	0.055
0.9	0.990	3.2	0.040
1.0	1.000	3.4	0.029
1.1	0.990	3.6	0.021
1.2	0.930	3.8	0.015
1.3	0.860	4.0	0.011
1.4	0.780	4.5	0.005
1.5	0.680	5.0	0.000
1.6	0.560		

To draw the hydrograph, the t/t_p values are multiplied by t_p and the Q/Q_p values are multiplied by Q_p to yield a set of 33 points to be plotted. Thus the hydrograph shape is always the same but is "stretched" by t_p and Q_p:

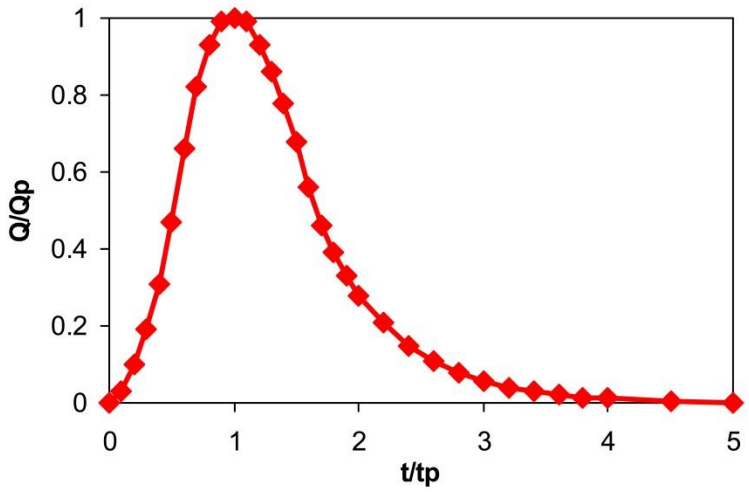

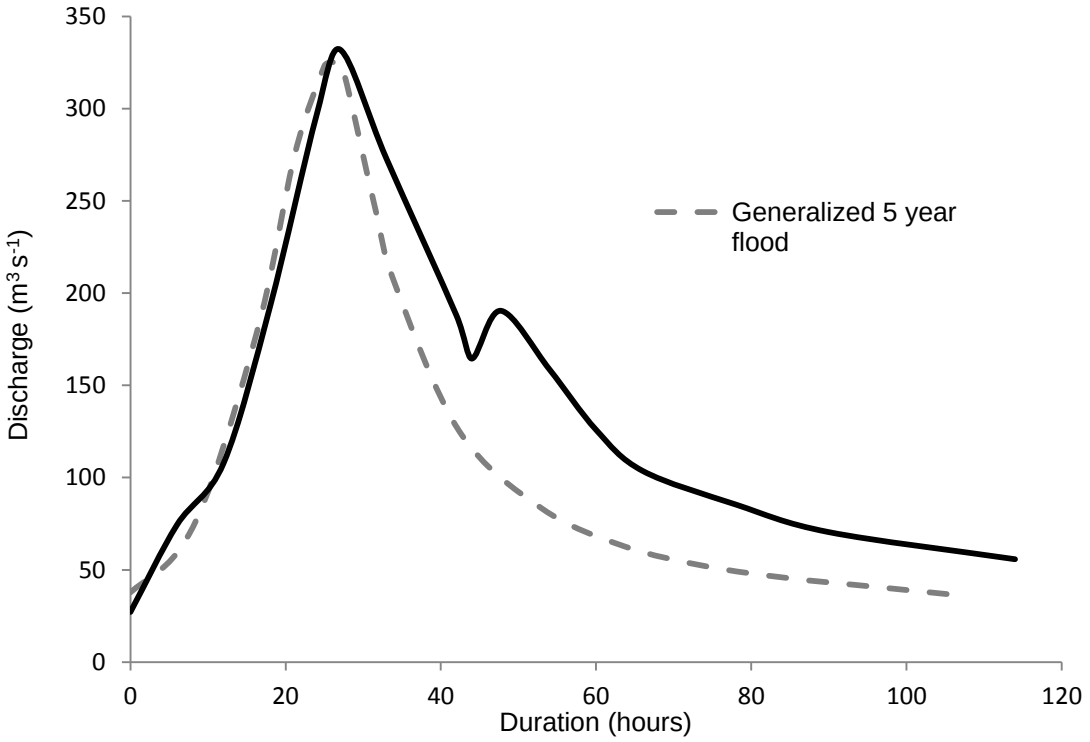

Figure D.1: Comparing the December 1969 5 year flood hydrograph to the generalized 5 year hydrograph.

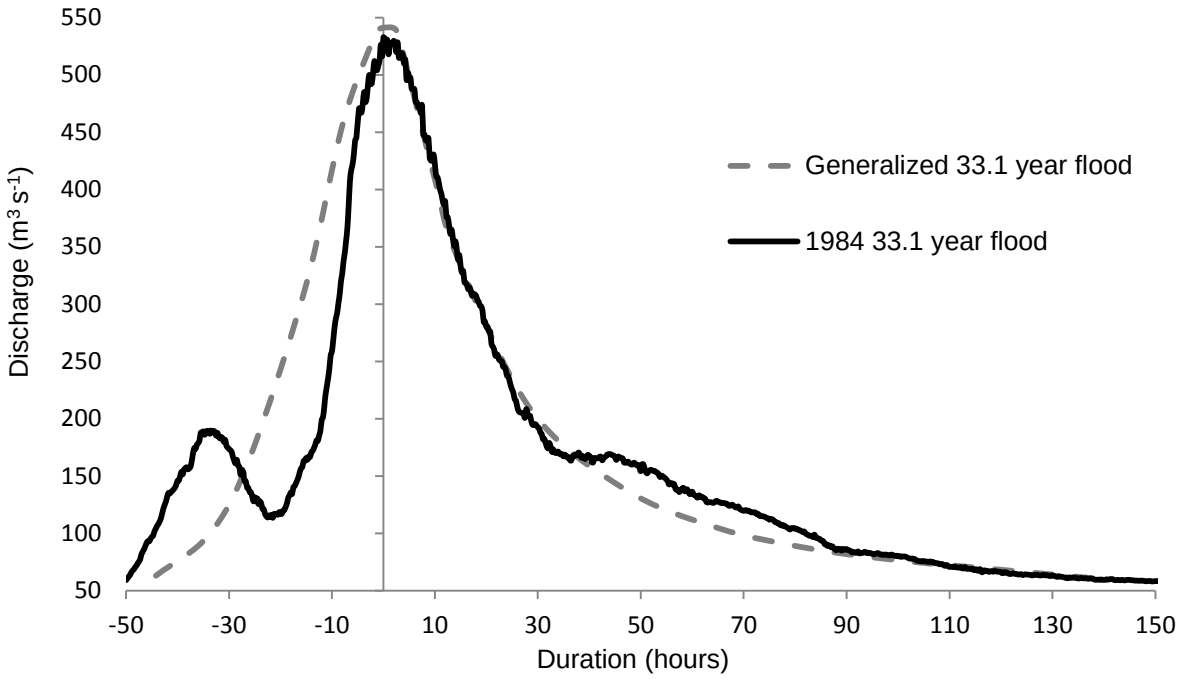

Figure D.2: Comparison between the generalized and 1984 33.1 year flood event.

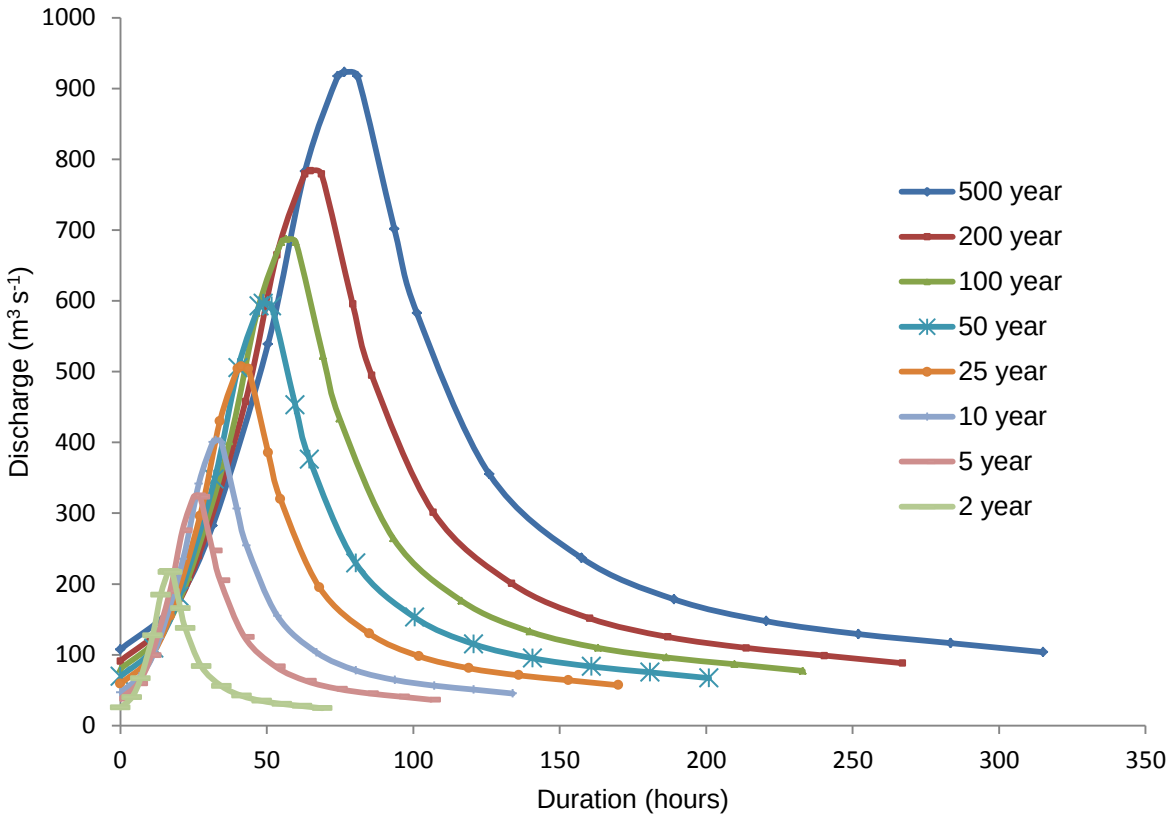

Figure D.3: Generalized hydrographs for the simulated flood events.

D.2: Various pull-out forces of other formulas

All additional pull-out matrices are shown below in Table D.1 and D.2 and revealed similar pull-out occurrences for similar velocity and root diameter relationships.

Table D.1: Exponential model produced pull-out matrix.

	Velocity (m/s)											
	0.25	0.50	0.75	1.00	1.25	1.50	1.75	2.00	2.25	2.50	2.75	3.00
0.75	2	2	2	3	3	3	3	4	4	4	4	5
1	2	3	3	3	4	4	5	5	6	6	6	7
1.5	3	4	5	6	7	8	9	10	12	13	15	16
2	3	5	7	9	11	14	17	20	24	28	33	38
2.5	4	7	11	15	20	26	33	41	50	61	74	89
3	6	10	16	24	34	47	62	81	105	133	167	208
4	9	20	38	64	102	155	228	326	457	628	850	1135
5	15	41	89	171	306	516	834	1306	1989	2961	4324	6208
6	24	81	208	457	915	1714	3054	5229	8663	1.4E+04	2.2E+04	3.4E+04
7	39	163	485	1218	2739	5700	1.1E+04	2.1E+04	3.8E+04	6.6E+04	1.1E+05	1.9E+05
8	64	326	1135	3248	8202	1.9E+04	4.1E+04	8.4E+04	1.6E+05	3.1E+05	5.7E+05	1.0E+06
9	105	653	2655	8663	2.5E+04	6.3E+04	1.5E+05	3.4E+05	7.2E+05	1.5E+06	2.9E+06	5.6E+06
10	171	1306	6208	2.3E+04	7.4E+04	2.1E+05	5.5E+05	1.3E+06	3.1E+06	6.9E+06	1.5E+07	3.0E+07
11	280	2613	1.5E+04	6.2E+04	2.2E+05	7.0E+05	2.0E+06	5.4E+06	1.4E+07	3.3E+07	7.5E+07	1.7E+08
12	457	5229	3.4E+04	1.6E+05	6.6E+05	2.3E+06	7.4E+06	2.2E+07	5.9E+07	1.5E+08	3.8E+08	9.1E+08
13	746	1.0E+04	7.9E+04	4.4E+05	2.0E+06	7.7E+06	2.7E+07	8.6E+07	2.6E+08	7.2E+08	1.9E+09	5.0E+09
14	1218	2.1E+04	1.9E+05	1.2E+06	5.9E+06	2.6E+07	9.9E+07	3.5E+08	1.1E+09	3.4E+09	9.9E+09	2.7E+10
15	1989	4.2E+04	4.3E+05	3.1E+06	1.8E+07	8.5E+07	3.6E+08	1.4E+09	4.9E+09	1.6E+10	5.0E+10	1.5E+11

0 cm erosion | 20 cm erosion | 40 cm erosion | 60 cm erosion

Table D.2: Polynomial model produced pull-out matrix.

	Velocity (m/s)											
	0.25	0.50	0.75	1.00	1.25	1.50	1.75	2.00	2.25	2.50	2.75	3.00
0.75	19	13	10	7	5	3	2	1	0	-1	-2	-2
1	14	8	4	1	0	-1	-2	-3	-3	-3	-2	-2
1.5	7	1	-2	-3	-2	-1	1	4	7	10	14	18
2	1	-3	-2	1	6	12	19	27	35	44	53	62
2.5	-2	-2	5	14	25	38	52	67	83	99	115	133
3	-3	4	18	35	55	77	100	124	149	175	201	228
4	1	27	62	103	146	192	240	289	340	391	443	495
5	14	67	133	204	280	359	439	522	606	691	777	864
6	35	124	228	340	456	576	698	822	949	1076	1205	1335
7	65	198	349	509	674	843	1016	1191	1367	1546	1726	1907
8	103	289	495	712	934	1162	1393	1626	1862	2100	2340	2580
9	149	397	667	949	1237	1531	1829	2130	2433	2739	3046	3355
10	204	522	864	1219	1582	1951	2324	2701	3081	3463	3846	4232
11	268	664	1087	1524	1970	2422	2879	3340	3804	4271	4740	5210
12	340	822	1335	1862	2400	2944	3493	4047	4604	5164	5726	6290
13	420	998	1608	2235	2872	3516	4166	4821	5480	6141	6805	7471
14	509	1191	1907	2641	3386	4139	4899	5663	6431	7203	7977	8754
15	606	1400	2231	3081	3943	4813	5691	6573	7460	8350	9243	10139

0 cm erosion | 20 cm erosion | 40 cm erosion | 60 cm erosion

D.3: Sediment data collection

Sub-surface sediment sampling was performed following the Sub-surface bed-material sampling – Hicks/NIWA method. This method is presented below and Figure D.4 is an image captured for the downstream sampling site.

1. **Where?** A sub-surface sample must be collected below the level of the largest surface clast and from within one layer (don't sample into an armoured sub-stratum- so dig around a bit to check the local stratigraphy). Make a sketch and take photos of the sample location – zoom in for detail and out for context.
2. **How much?** Select the largest clast visible on the surface layer over the sample site. Measure it's a,b,c axes or simply weigh it (w, kg). Usually, the sample mass (M, kg) should be at least 100x the weight of the coarsest clast, but in some circumstances 20 X is permissible. Use the following formula to work out the matching sample volume (assuming a bulk density of 1800 kg/m^3): V (m^3) ~ 77abc ~ b^3 (where a,b,c are in m) or V ~ M/1800 [For 20 X criteria, use V ~ abc ~ 15 b^3]
3. **Decide a sample depth** (h, m) appropriate to the local stratigraphy, then work out the side-length of the sample square (L, m): $L = (V/h)^{½}$

   Example, For 20 X criteria, largest clast has b = 0.3 m and w = 37.5 kg, so M =750 kg, V = 0.42 m^3, say h = 0.40 m, then L = 1.0 m.
4. **Mark out the sampling square** (with spray paint)
5. **Remove the surface layer** (down to depth of largest clast on surface)
6. **Dig out** the sample, passing it **through** the **stack of large sieves**. You will need to process the total volume in stages.

7. For clasts larger than the sieves, sort them into separate size piles either by passing through the Wolman grid or for boulders by measuring the b axis. Continue to use 0.5 phi intervals to separate classes – s : 64, 91, 128, 181, 256, 362, 512, 723, 1022, 1446 mm, etc
8. Spread out tarps and add each fraction to a separate pile.
9. When done, weigh each fraction using the scales and a handy bucket/box. Count lithologies if doing a lithology count. If the largest boulders are too big to weigh, measure the a, b, and c axes of each.
10. Weigh the **intermediate fractions** (caught on the finer sieves).
11. With the **fines fraction** (passing the finest sieve), split the pile by quartering (use spade, then fold tarp up through splits to separate – don't lose any from the trap! Weigh, bag, and label one quarter for taking back to the lab for further sieving. Make sure that there is at least 4.5 kg (if using a 32 mm sieve in 6 above) – if not, then you may need to keep half of the sample. Weigh the rest of the sample and discard.
12. Add up the total weight and **check** that the largest mass (M) has been met reasonably.

What you'll need in the field

- Bulk bed material sample forms and pencil
- Camera
- Shovel
- Hand-held GPS
- Clear plastic ruler
- Calculator
- 2-3 tarps
- 1 -2 weighing buckets/boxes
- Portable scales (~ k0 kg range) and spare batteries
- Plastic sample bags
- Marker pen
- Wolman template
- Large sieves (0.5 m diameter with 22, 32, and 45 mm mesh)
- Knee pads
- Spray paint

Figure D.4: Downstream sub-surface material sampling with sediment separated into 0.5 phi intervals.

D.4: Delft3D sediment composition

Utilizing the sediment data collected in the field, additional sediment classifications were developed and utilized in Delft3D numerical modeling simulations. These included the one phi-interval (Table D.3), the two phi interval (Table D.4), the sand, gravel, cobbles composition (Table D.5), and the altered sand, gravel, cobbles composition (Table D.6).

Table D.3: One phi interval sediment composition for surface and sub-surface layers.

	One phi interval Surface		One phi interval Sub-surface	
Phi	Size (mm)	Frequency (%)	Size (mm)	Frequency (%)
> 0	N.A.	0.00	0.31	1.33
0	1.00	14.19	1.00	0.73
-1	2.41	0.25	2.00	1.00
-2	4.83	1.31	4.00	1.15
-3	10.21	5.37	8.00	1.47
-4	19.90	17.18	21.50	6.37
-5	37.40	26.87	39.39	18.22
-6	74.84	21.74	78.20	28.16
-7	147.28	11.53	158.29	41.55
-8	256.00	1.55	N.A.	0.00

Table D.4: Two phi interval sediment composition for surface and sub-surface layers.

	Two phi interval Surface		Two phi interval Sub-surface	
Phi	Size (mm)	Frequency (%)	Size (mm)	Frequency (%)
≥ 0	N.A.	0.00	0.56	2.06
-1 to -2	1.48	15.75	3.00	2.15
-3 to -4	17.37	22.55	19.22	7.84
-5 to -6	54.21	48.61	63.01	46.39
-7 to -8	156.34	13.08	158.29	41.55

Table D.5: Sand, gravel, and cobbles sediment composition for surface and sub-surface layers.

	Sand, gravel, & cobbles Surface		Sand, gravel, & cobbles Sub-surface	
Class	Size (mm)	Frequency (%)	Size (mm)	Frequency (%)
Sand	1.00	14.19	1.03	3.06
Gravel	34.63	64.05	43.13	40.09
Cobbles	128.13	21.76	140.45	56.85

Table D.6: Altered sand, gravel, and cobbles sediment composition for surface and sub-surface layers (v74).

	Sand, gravel, & cobbles Surface		Sand, gravel, & cobbles Sub-surface	
Class	Size (mm)	Frequency (%)	Size (mm)	Frequency (%)
Sand	1.00	6.19	1.03	2.06
Gravel	34.63	67.05	43.13	37.59
Cobbles	128.13	26.76	140.45	60.35

D.5: Time lapse imagery extent mapping.

Evaluating post-flood time lapse image (Figure D.5), flood images (77 $m^3 s^{-1}$, Figure D.6), and aerial photographs (Figure D.7), identifiable objects were easily marked near the observed flood line. For example, large identifiable sediment (point 1) were easy objects to identify along water extent, areas that were submerged offered assistance to the later line depth (Points 2, 3, 6) and areas that were just above the water line helped to determine the water extent (points 4 and 5). In all, it was rare to find pints that were exactly along the water line, but in most cases areas just below or above the water line offered adequate data to interpolate the flood line. Further, with the aerial images providing 0.06 m resolution, it was possible to identify subtle differences that aided in the accuracy of marker identification and location. While the retrofitted data and coordinate accuracy degradation with increasing distance from the camera reduce the waterlines to mere approximations, this data adds valuable insight into the model performance.

Figure D.5: Time lapse image at low flow post-flood, with water line points marked for the 77 $m^3 s^{-1}$ image and GCPs visible (just below point 1).

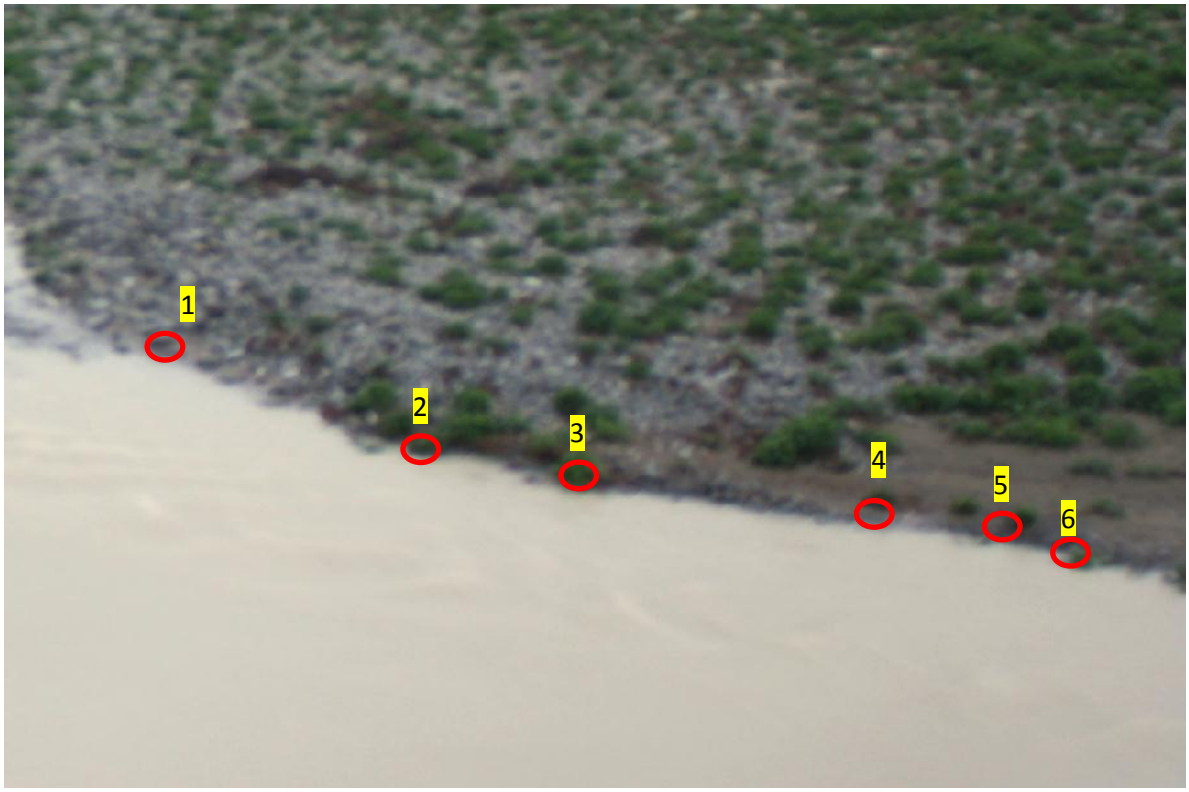

Figure D.6: Flood event at 77 $m^3 s^{-1}$ with points identifying water line.

Figure D.7: 77 $m^3 s^{-1}$ image waterline points identified in aerial image taken at low flow conditions.

D.6: Data analysis for normal distribution

Throughout this research, various statistics were taken from the field and laboratory data. In assessing the uncertainty, standard uncertainty was estimated using one standard deviation, which would provide 68% confidence level. However, this assumed the datasets were of a normal distribution. Therefore, in order to satisfy this assumption, the various datasets normality were assessed in Microsoft Excel. This was performed by taking the dataset and generating a normal probability plot and assessing if the plotted data was near-linear. Distributions and data analysis are provided below for the various data sets approximated distribution. This includes: drag (Figure D.9), pull-out force for 0 and 10 cm erosion of dry soil (Figure D.10), pull-out for 20 cm erosion and dry soil (Figure D.11), pull-out for 0 cm erosion and saturated soil (Figure D.12), lupin canopy height (Figure D.13), and lupin height deformation (Figure D.14).

Assessing the results, the drag dataset normal probability plot (Figure D.8) showed a relatively linear relationship. This indicated that the data was near-normal. However, the plot also showed a slight S-shape that starts above the linearly fitted line and appears to be heading below the linear-line towards the upper normal scores. This relationship is known as a short tail (light tail), and indicates that less variance occurred than expected for a normal distribution (SkyMark, 2013). Similar plots were developed for the 0 and 10 cm erosion pull-out forces (Figures D.9). However, opposite curved S-shapes were identified for the 20 cm dry soil, 0 cm saturated soil, and lupin canopy height datasets (Figures D.10, D.11, and D.12) which is known as a long tails, and indicates more than expected variance in a normal distribution. Finally, the lupin height deformation dataset plot (Figure D.13) showed starting and ending points below the linear-line, which indicated a left skew of the normal distribution. Since these datasets and corresponding normal probability plots were developed with small datasets, it was difficult to speculate the true distribution of the population. Nevertheless, all datasets show a near-normal distribution, which was sufficient for the purpose of this research assumption that one standard deviation is roughly 68% confidence level.

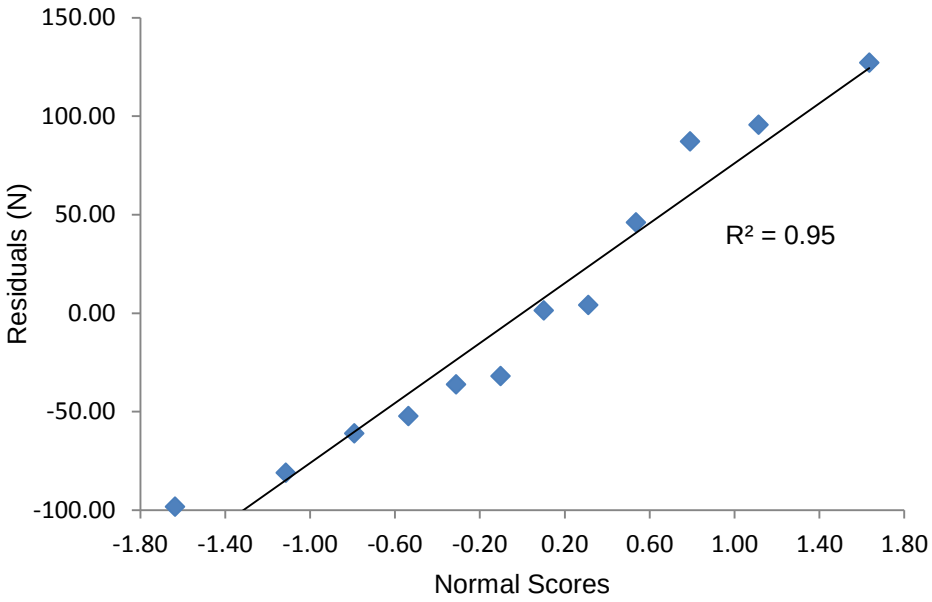

Figure D.8: Drag force data distribution among the one standard deviation bins for: A) observed data, and B) randomly generated data.

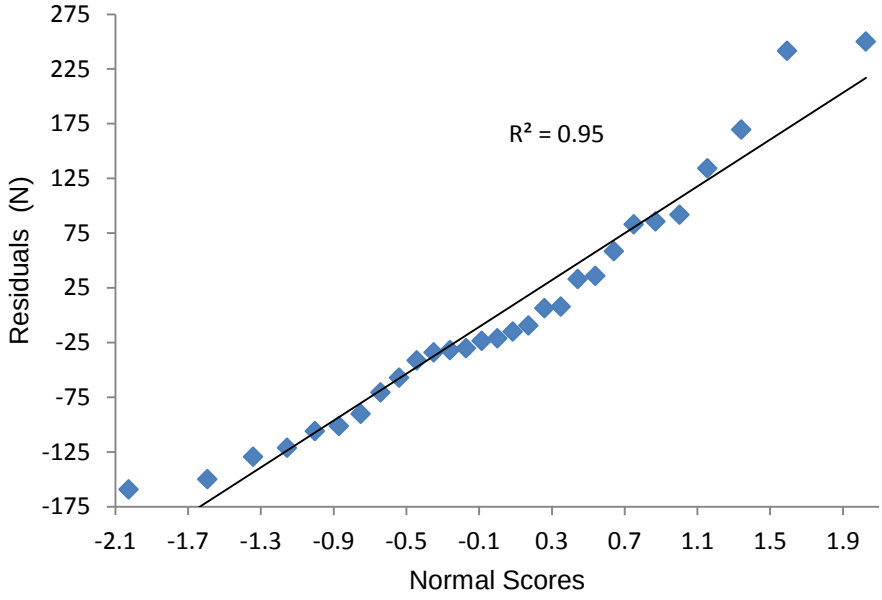

Figure D.9: Pull-out force for 0 and 10 cm erosion in dry soil conditions distribution for: A) observed data, and B) randomly generated data.

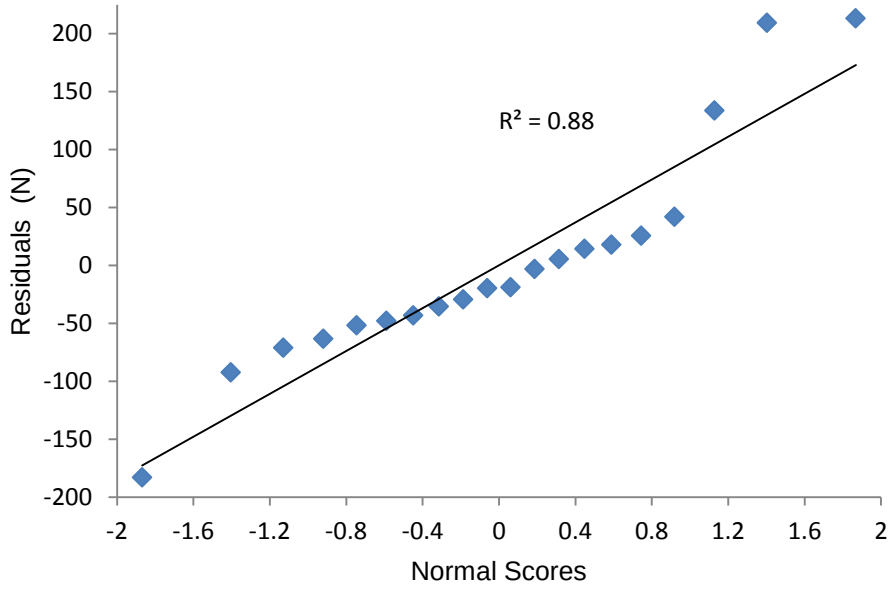

Figure D.10: Pull-out force for 20 cm erosion in dry soil conditions distribution for: A) observed data, and B) randomly generated data.

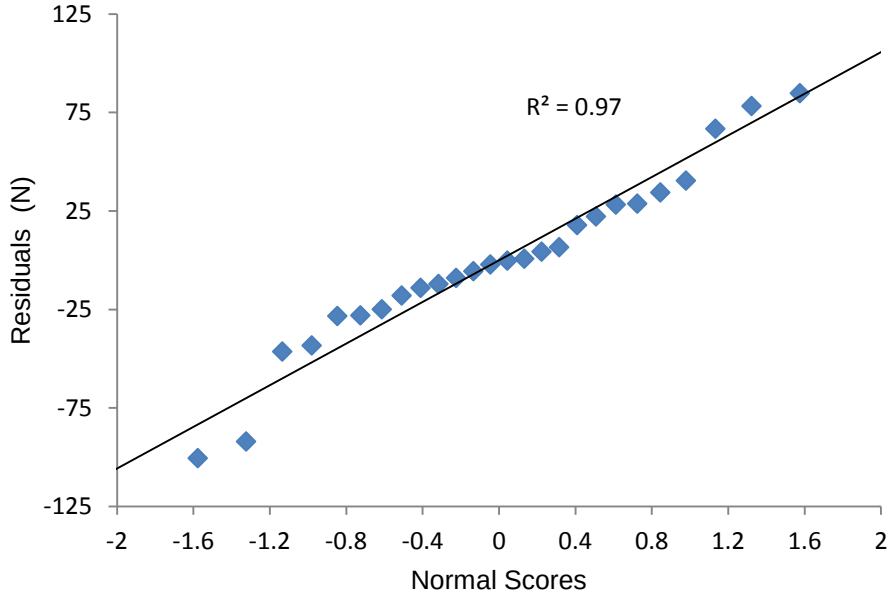

Figure D.11: Pull-out force for 0 cm erosion in saturated soil conditions distribution for: A) observed data, and B) randomly generated data.

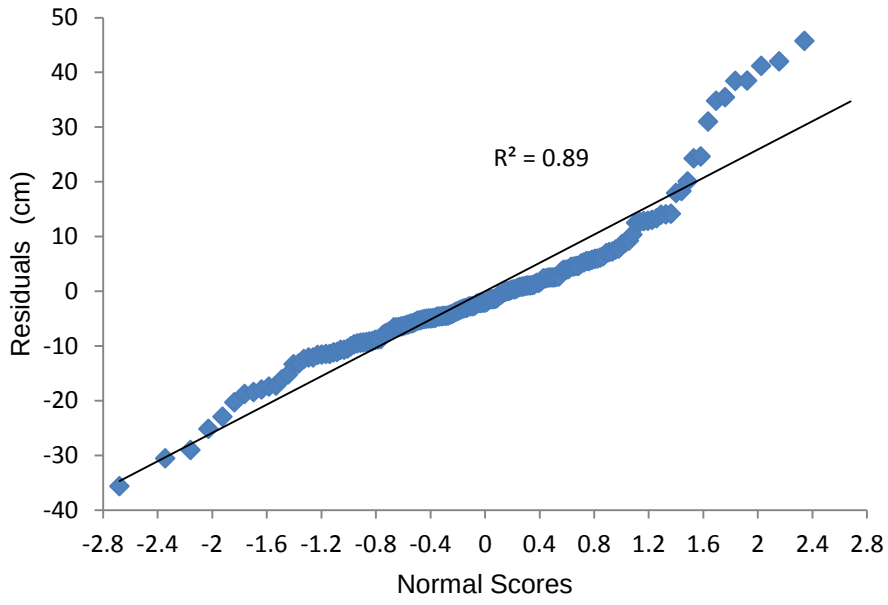

Figure D.12: Lupin canopy height distribution for: A) observed data, and B) randomly generated data.

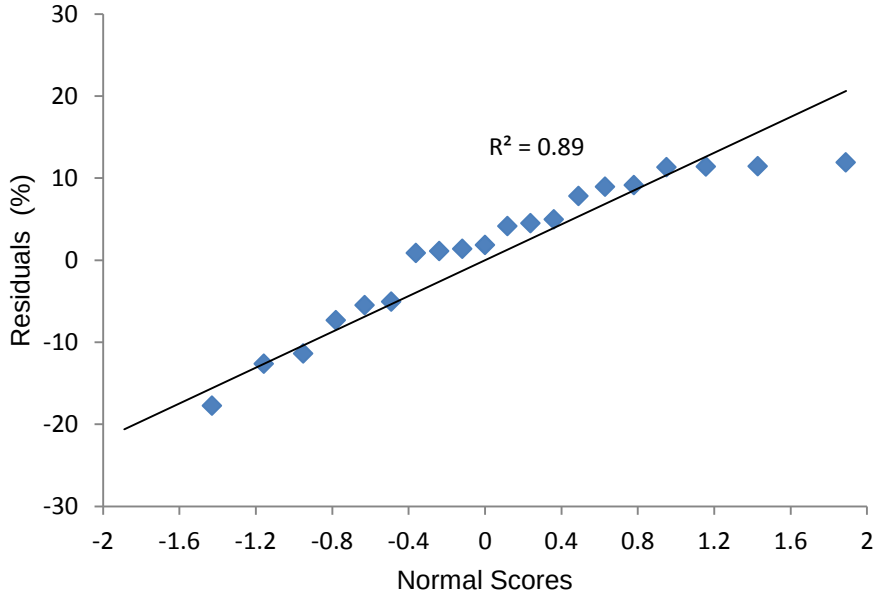

Figure D.13: Lupin height deformation distribution for: A) observed data, and B) randomly generated data.

Appendix E

Additional Figures and Tables

E.1: Lupin mortality experiments and thresholds

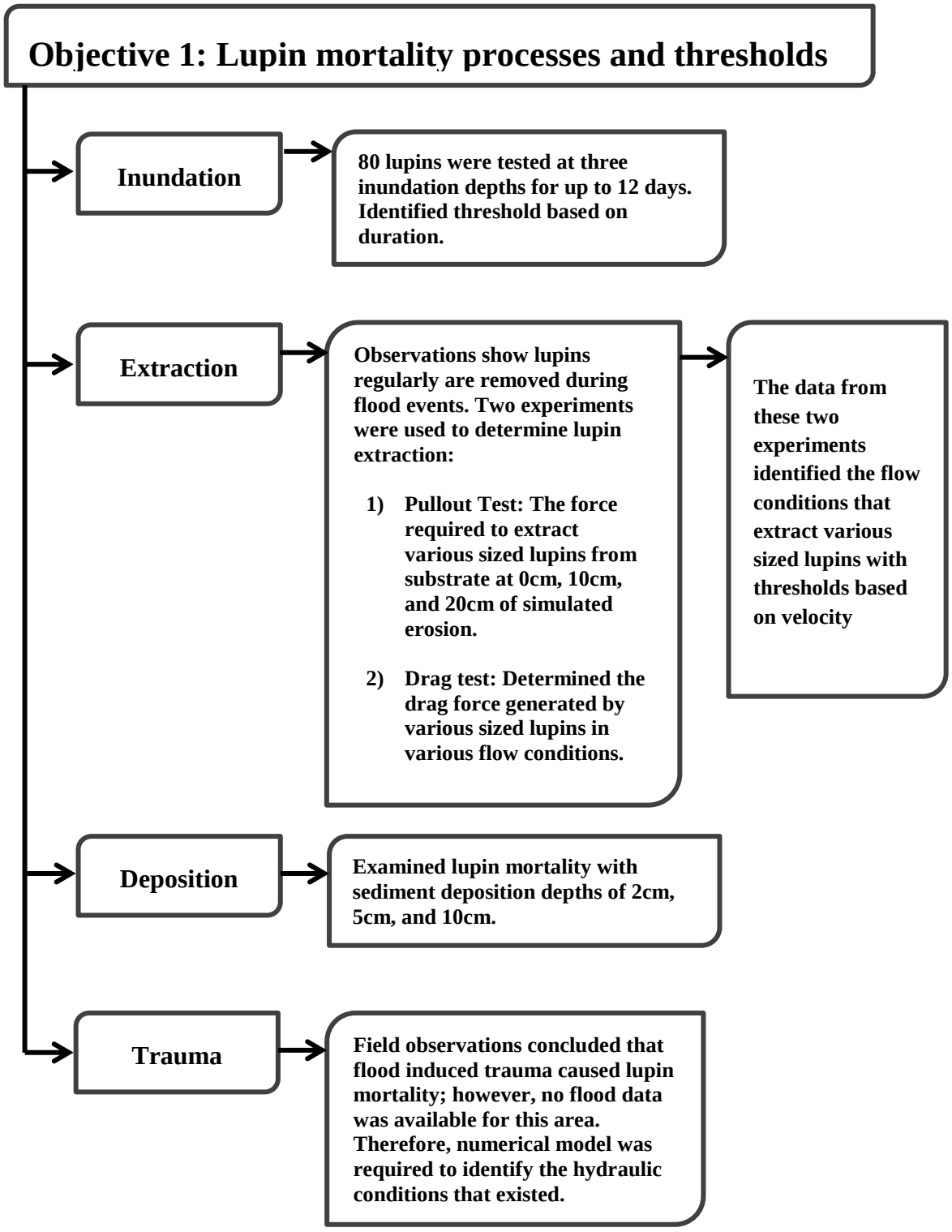

Figure E.1: Lupin experiments conducted to satisfy objective 1.

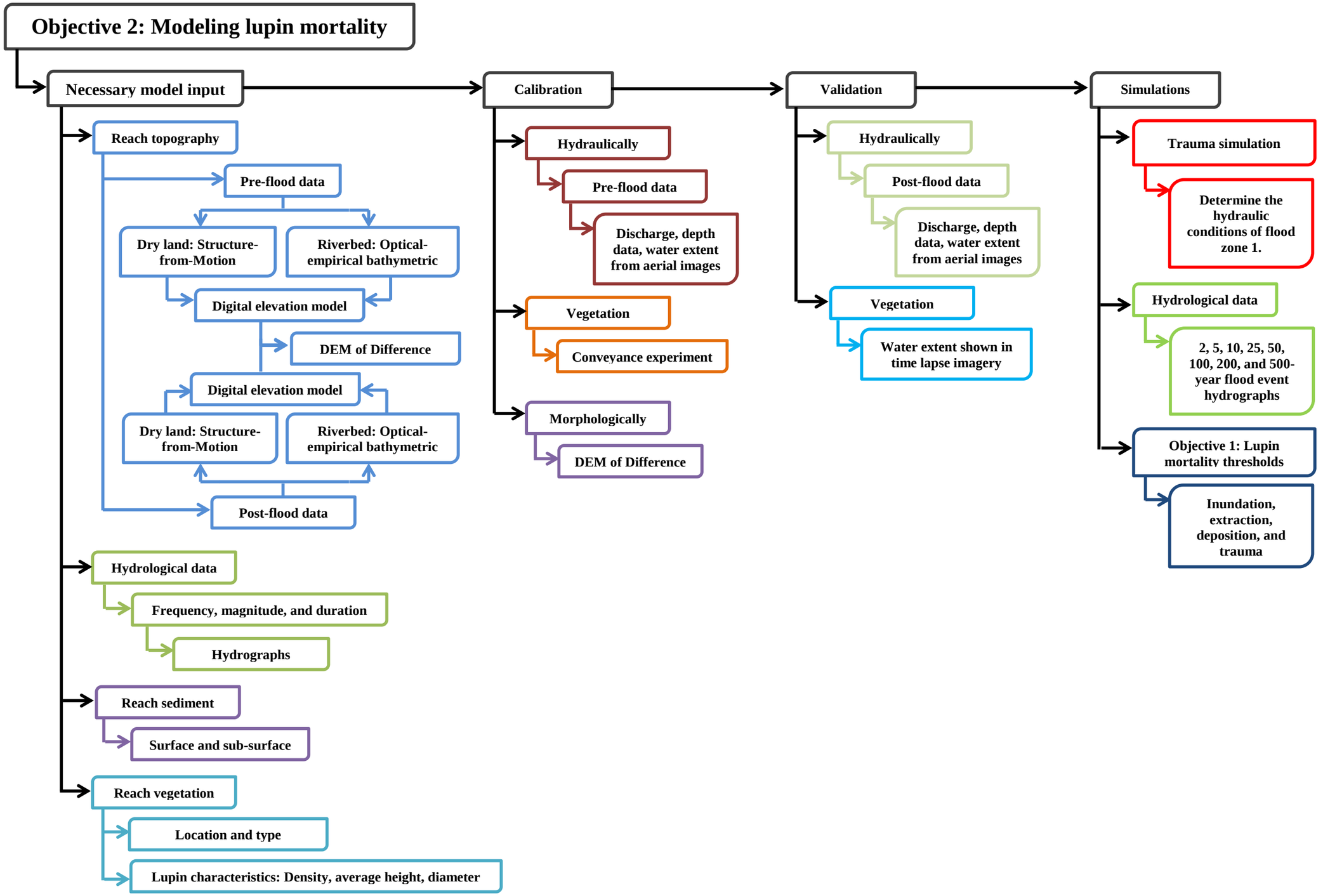

Figure E.2: Lupin mortality experiments conducted to satisfy objective 2.

E.2: Deposited lupin data

Table E.1: Observations made after the 221 cumec flood of Jan 2013. Drag determined if roots were sheared, and erosion if roots intact. Note: the canopy measured for deposited lupins was from the base of the lupin stalk to the highest part of the lupin. Since lupins were deposited, gravity no longer was weighing down the canopy; thus, these canopies heights were higher than typical.

Root Condition	Canopy Height (cm)	Diameter (cm)	Root Depth (cm)	Canopy Condition
Intact	61.0	1.4	27.9	Bad
Intact	45.7	2.0	68.6	Bad
Intact	63.5	2.3	50.8	Moderate
Intact	104.1	2.4	55.9	Both
Intact	50.8	2.5	58.4	Poor
Intact	83.8	2.5	45.7	Bad
Intact	38.1	2.8	63.5	Bad
Intact	81.28	2.8	45.72	Moderate
Intact	81.28	3.0	60.96	Poor
Intact	83.8	3.2	61.0	Poor
Intact	73.66	3.2	109.22	Moderate
Intact	55.9	3.3	50.8	Bad
Intact	91.4	3.5	68.6	Bad
Intact	N.A.	3.8	N.A.	N.A.
Intact	25.4	3.8	48.26	Ok
Intact	73.7	4.0	83.8	Bad
Intact	93.98	4.0	55.88	ok
Intact	N.A.	4.2	60.96	N.A.
Intact	N.A.	4.5	88.9	Poor
Intact	96.5	4.5	88.9	Bad
Intact	109.2	5.2	86.4	Bad
Intact	N.A.	5.5	99.1	N.A.
Intact	99.1	6.0	76.2	Poor
Intact	83.82	6.0	48.26	N.A.
Intact	88.9	6.4	87.2	Ok
Intact	139.7	6.4	76.2	Ok
Intact	N.A.	8.5	81.28	N.A.
Intact	91.44	9.2	45.72	ok

Intact	88.9	10.0	58.42	Moderate
Intact	111.76	Large cluster	88.9	Moderate
Severed	119.4	2.2	30.5	Ok
Severed	68.6	2.6	22.9	Bad
Severed	76.2	2.8	22.9	Bad
Severed	66.04	2.8	17.78	Bad
Severed	81.3	3.0	12.7	Bad
Severed	N.A.	3.0	43.18	N.A.
Severed	88.9	3.3	71.1	Bad
Severed	N.A.	3.5	N.A.	N.A.
Severed	71.1	3.6	17.8	Bad
Severed	73.66	3.7	33.02	Poor
Severed	94.0	3.8	20.3	Poor
Severed	78.7	3.9	15.2	Bad
Severed	N.A.	4.0	15.24	N.A.
Severed	76.2	4.0	17.78	Moderate
Severed	N.A.	4.0	50.8	N.A.
Severed	N.A.	4.1	53.34	N.A.
Severed	139.7	4.2	30.5	Bad
Severed	114.3	4.2	55.9	Bad
Severed	N.A.	4.4	22.86	N.A.
Severed	N.A.	4.5	15.24	N.A.
Severed	73.7	4.6	12.7	Bad
Severed	N.A.	4.8	7.62	N.A.
Severed	101.6	5.0	27.9	Bad
Severed	104.1	5.0	27.9	Moderate
Severed	N.A.	5.0	N.A.	N.A.
Severed	N.A.	5.0	33.02	N.A.
Severed	53.34	5.0	25.4	Poor
Severed	86.4	5.5	25.4	Bad
Severed	N.A.	6.0	10.16	N.A.
Severed	76.2	6.5	22.86	Bad
Severed	N.A.	6.5	25.4	N.A.
Severed	N.A.	7.0	17.78	N.A.
Severed	109.22	7.0	30.48	Poor
Severed	N.A.	7.5	12.7	N.A.
Severed	N.A.	8.3	17.78	N.A.
Severed	N.A.	8.5	20.32	N.A.
Severed	104.1	10.5	27.9	Bad

Severed	N.A.	Large cluster	50.8	Bad
Severed	N.A.	Large cluster	33.02	N.A.
Severed	109.2	Large cluster	N.A.	Bad
Severed	N.A.	Large cluster	60.96	N.A.
Severed	N.A.	Large cluster	25.4	N.A.

E.3: Trauma impacted lupins

Lupin trauma of the flood zone 1 taken on Feb 16th to investigate the mortality. Observations revealed that 67 of the 183 lupins showed regrowth.

Figure E.3: Flood zone 1: Lupin six weeks after the January 2013 flood event with 10 cm of root exposure and no signs of regrowth. This lupin was also pictured in Figure 4.14.

Figure E.4: Regrowth of a deteriorated lupin.

Figure E.5: Example of lupin regrowth determined by larger root structure attached to pre-existing lupin roots. Easily misleading since herbaceous material looks like a juvenile lupin.

Figure E.6: Initial observations indicated this was regrowth of a traumatized lupin; however, upon closer inspection, this was a new lupin seedling that was growing amongst the dead lupins.

E.4: SfM-Veg: Hybrid point cloud resolution model

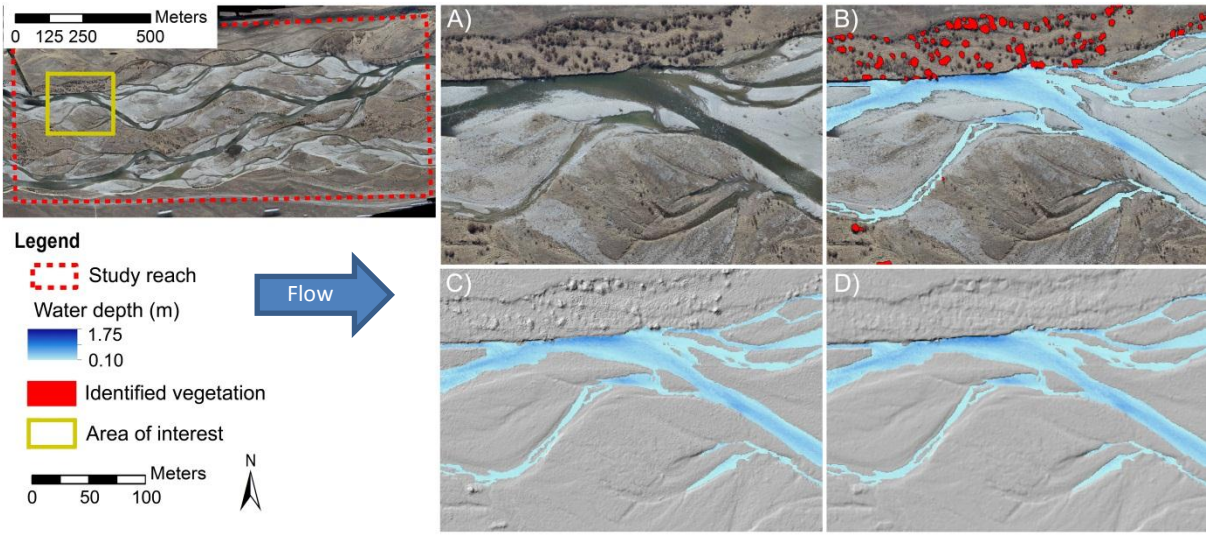

Figure E.7: ToPCAT vegetation noise reduction: A) Example area, B) threshold generated polygons that identify vegetation noise, C) topography before ToPCAT hybrid resolution, D) topography after ToPCAT hybrid noise reduction.

E.5: Additional DoD observations

Numerous areas were found with noticeable geomorphic change between the pre- and post-flood aerial photographs, and were outlined in green polygons in ArcGIS (as shown in Figure E.8). The three figures below (Figures E.8, E.9, and E.10) were utilized in conjunction with Figures 5.16 and 5.17 in an effort to determine which geomorphic detection method provided the most representative results.

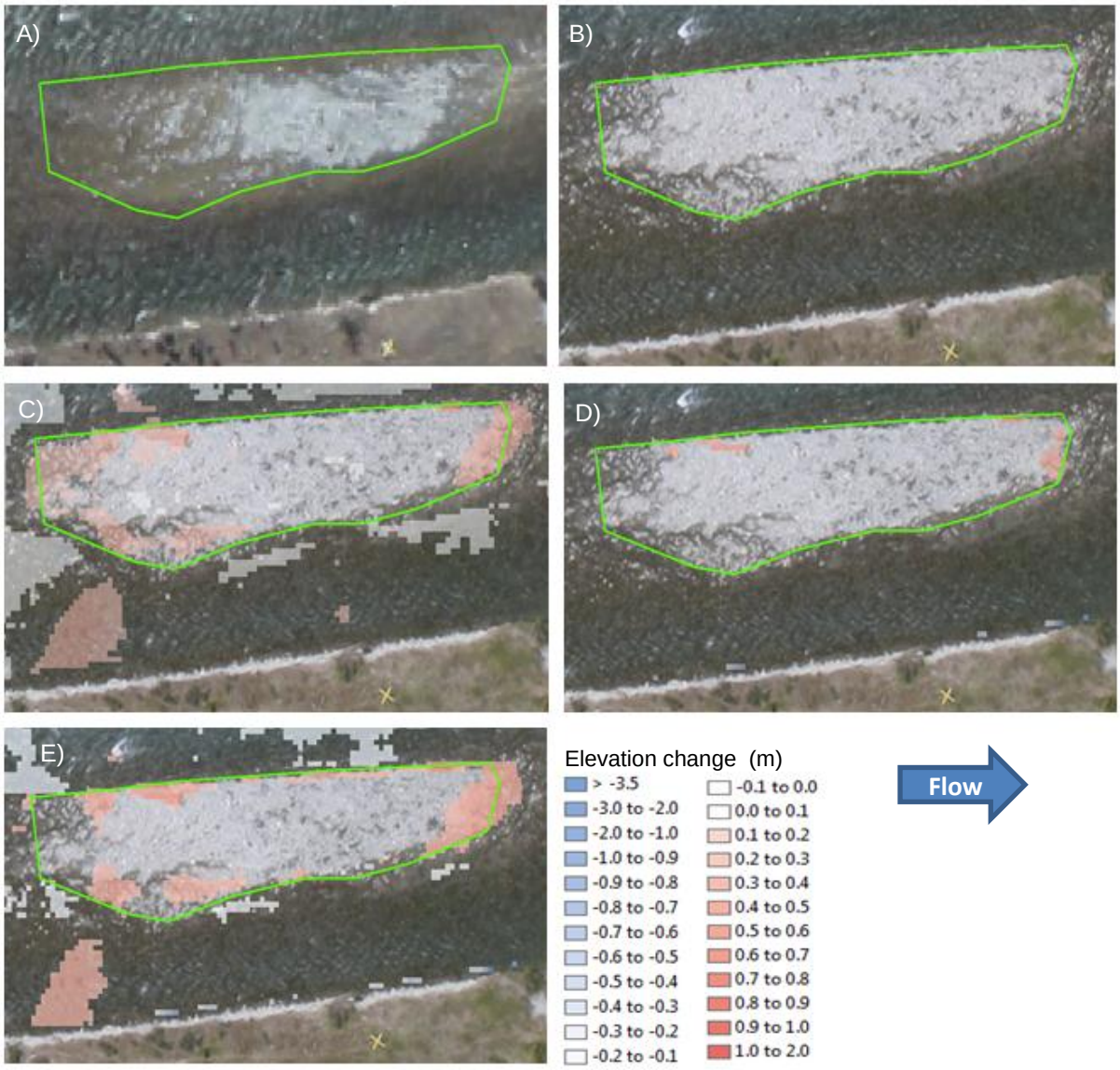

Figure E.8: Visual comparison between the varying methods for the study reach DoD. A) pre-flood image, B) post-flood image, C) SV 95% BU DoD results, D) SV 95% DoD results, and E) SV DoD results. Of the various uncertainty methods, the SV 95% BU performs better on the upstream end than the SV method, and the SV 95% method does not detect the obvious differences.

.

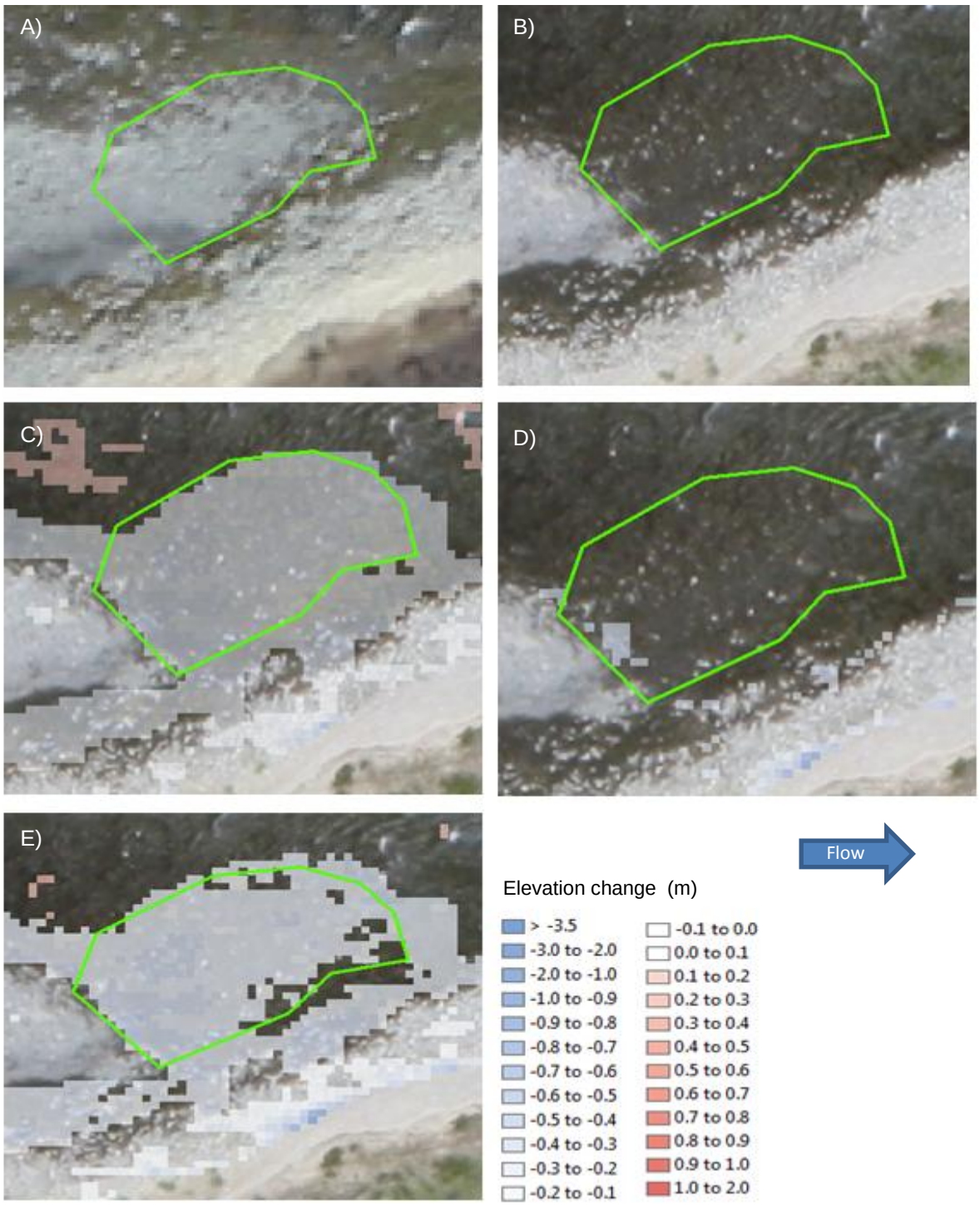

Figure E.9: Visual comparison between the varying methods for the study reach DoD. A) pre-flood image, B) post-flood image, C) SV 95% BU DoD results, D) SV 95% DoD results, and E) SV DoD results. As shown, the SV 95% BU performs well as it detected erosion in most areas that are obviously eroded. The SV method also performs well, with erosion detected in most areas. However, the SV 95% method does not detect any geomorphic change except for a small area on the left side.

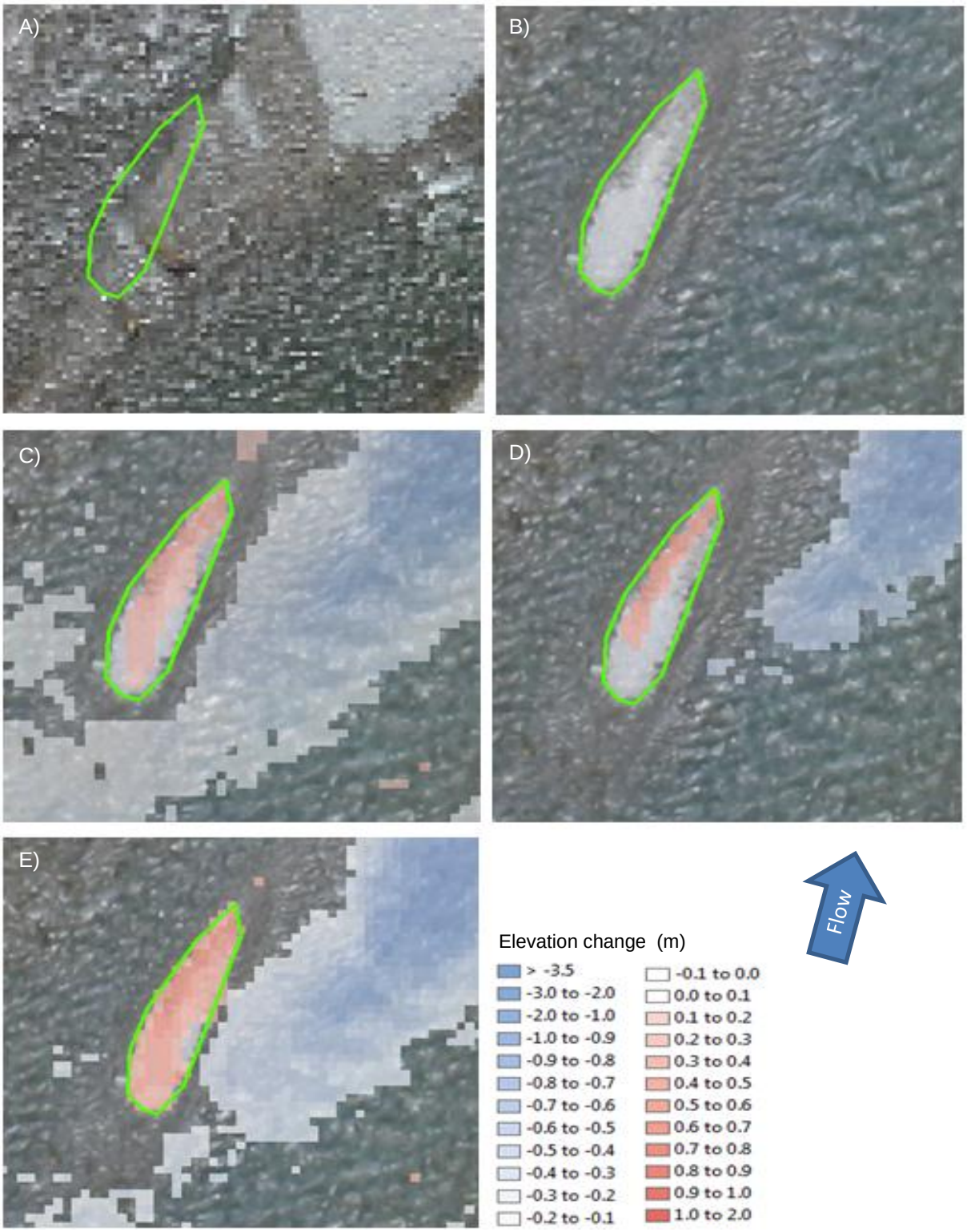

Figure E.10: Visual comparison between the varying methods for the study reach DoD. A) pre-flood image, B) post-flood image, C) SV 95% BU DoD results, D) SV 95% DoD results, and E) SV DoD results. As shown, the SV 95% detects geomorphic change in most areas; however missess along the bar edges. The SV detects change in almost all areas, and the 95% misses most of the change that occurred.

E.6: Additional trachytope calibration tables

Table E.2: Trachytope calibration results for hv and Cb.

	hv	0.49		1		0.49		0.49		0.49		0.49	
	n	0.51		0.51		0.51		0.51		0.51		0.51	
	Cd	0.75		0.75		0.75		0.75		0.75		0.75	
	Cb	27.6		27.6		0.1		1		27.6		100	
		Up	**Down**	**Up**	**Down**	**Up**	**Down**	**Up**	**Down**	**Up**	**Down**	**Up**	**Down**
Depth	Mean	-0.02	0.01	-0.02	0.01	-0.02	0.00	-0.02	0.01	-0.02	0.01	-0.02	0.01
	Abs Mean	0.06	0.10	0.06	0.10	0.06	0.10	0.06	0.10	0.06	0.10	0.06	0.10
	RMSE	0.08	0.11	0.08	0.11	0.07	0.11	0.07	0.11	0.08	0.11	0.07	0.11
	Std	0.07	0.11	0.07	0.11	0.07	0.11	0.07	0.11	0.07	0.11	0.07	0.11
	Max	0.14	0.27	0.14	0.27	0.13	0.27	0.14	0.27	0.14	0.27	0.14	0.27
	Min	-0.33	-0.22	-0.33	-0.22	-0.32	-0.22	-0.32	-0.22	-0.33	-0.22	-0.32	-0.22
Velocity	Mean	-0.01	0.01	-0.01	0.01	-0.01	0.01	-0.01	0.01	-0.01	0.01	-0.01	0.01
	Abs Mean	0.12	0.10	0.12	0.10	0.12	0.10	0.12	0.10	0.12	0.10	0.12	0.10
	RMSE	0.15	0.11	0.15	0.11	0.15	0.11	0.15	0.11	0.15	0.11	0.15	0.11
	Std	0.15	0.11	0.15	0.11	0.15	0.11	0.15	0.11	0.15	0.11	0.15	0.11
	Max	0.27	0.17	0.27	0.17	0.27	0.17	0.27	0.17	0.27	0.17	0.27	0.17
	Min	-0.38	-0.30	-0.38	-0.30	-0.38	-0.30	-0.38	-0.30	-0.38	-0.30	-0.38	-0.30

Table E.3: Trachytope calibration results for n and C_D.

	hv	0.49		0.49		0.49		0.49		0.49		0.49	
	n	0.51		3.5		1000		0.51		0.51		0.51	
	Cd	0.75		0.75		0.75		0.1		0.75		1.5	
	Cb	27.6		27.6		27.6		27.6		27.6		27.6	
		Up	**Down**	**Up**	**Down**	**Up**	**Down**	**Up**	**Down**	**Up**	**Down**	**Up**	**Down**
Depth	Mean	-0.02	0.01	-0.03	0.00	-0.02	-0.01	-0.02	0.01	-0.02	0.01	-0.03	0.00
	Abs Mean	0.06	0.10	0.06	0.09	0.06	0.10	0.06	0.10	0.06	0.10	0.06	0.10
	RMSE	0.08	0.11	0.07	0.11	0.07	0.11	0.08	0.11	0.08	0.11	0.07	0.11
	Std	0.07	0.11	0.07	0.11	0.07	0.11	0.07	0.11	0.07	0.11	0.07	0.11
	Max	0.14	0.27	0.13	0.26	0.13	0.26	0.14	0.27	0.14	0.27	0.13	0.26
	Min	-0.33	-0.22	-0.32	-0.23	-0.32	-0.31	-0.33	-0.22	-0.33	-0.22	-0.32	-0.23
Velocity	Mean	-0.01	0.01	-0.01	0.01	-0.02	0.01	-0.01	0.01	-0.01	0.01	-0.02	0.01
	Abs Mean	0.12	0.10	0.11	0.10	0.11	0.10	0.12	0.10	0.12	0.10	0.11	0.10
	RMSE	0.15	0.11	0.14	0.11	0.14	0.11	0.15	0.11	0.15	0.11	0.14	0.11
	Std	0.15	0.11	0.15	0.11	0.14	0.11	0.15	0.11	0.15	0.11	0.14	0.11
	Max	0.27	0.17	0.26	0.17	0.23	0.15	0.27	0.17	0.27	0.17	0.25	0.17
	Min	-0.38	-0.30	-0.37	-0.34	-0.38	-0.34	-0.38	-0.30	-0.38	-0.30	-0.37	-0.36

Table E.4: Trachytope calibration results for area fraction, time step (DT), and minimum water detph (TrtMnH). Remaining parameters were held constant at: hv = 0.49, n=0.51, CD = 0.75, and Cb = 27.6.

	Area Frac	0.3		1		0.3		0.3		1		1	
	Dt	1		1		0.1		1		1		1	
	TrtMnh	0.1		0.1		0.1		0.1		0.1		0.3	
		Up	**Down**	**Up**	**Down**	**Up**	**Down**	**Up**	**Down**	**Up**	**Down**	**Up**	**Down**
Depth	Mean	-0.02	0.01	-0.02	0.00	-0.02	0.01	-0.02	0.01	-0.02	0.00	-0.02	0.01
	Abs Mean	0.06	0.10	0.06	0.10	0.06	0.10	0.06	0.10	0.06	0.10	0.06	0.10
	RMSE	0.08	0.11	0.07	0.11	0.08	0.11	0.08	0.11	0.07	0.11	0.07	0.11
	Std	0.07	0.11	0.07	0.11	0.07	0.11	0.07	0.11	0.07	0.11	0.07	0.11
	Max	0.14	0.27	0.13	0.27	0.14	0.27	0.14	0.27	0.13	0.27	0.14	0.27
	Min	-0.33	-0.22	-0.32	-0.22	-0.33	-0.22	-0.33	-0.22	-0.32	-0.22	-0.33	-0.22
Velocity	Mean	-0.01	0.01	-0.01	0.01	-0.01	0.01	-0.01	0.01	-0.01	0.01	-0.01	0.01
	Abs Mean	0.12	0.10	0.12	0.10	0.12	0.10	0.12	0.10	0.12	0.10	0.12	0.10
	RMSE	0.15	0.11	0.15	0.11	0.15	0.11	0.15	0.11	0.15	0.11	0.15	0.11
	Std	0.15	0.11	0.15	0.11	0.15	0.11	0.15	0.11	0.15	0.11	0.15	0.11
	Max	0.27	0.17	0.27	0.17	0.27	0.17	0.27	0.17	0.27	0.17	0.27	0.17
	Min	-0.38	-0.30	-0.38	-0.30	-0.38	-0.30	-0.38	-0.30	-0.38	-0.30	-0.38	-0.30

E.7: Morphological sensitivity testing

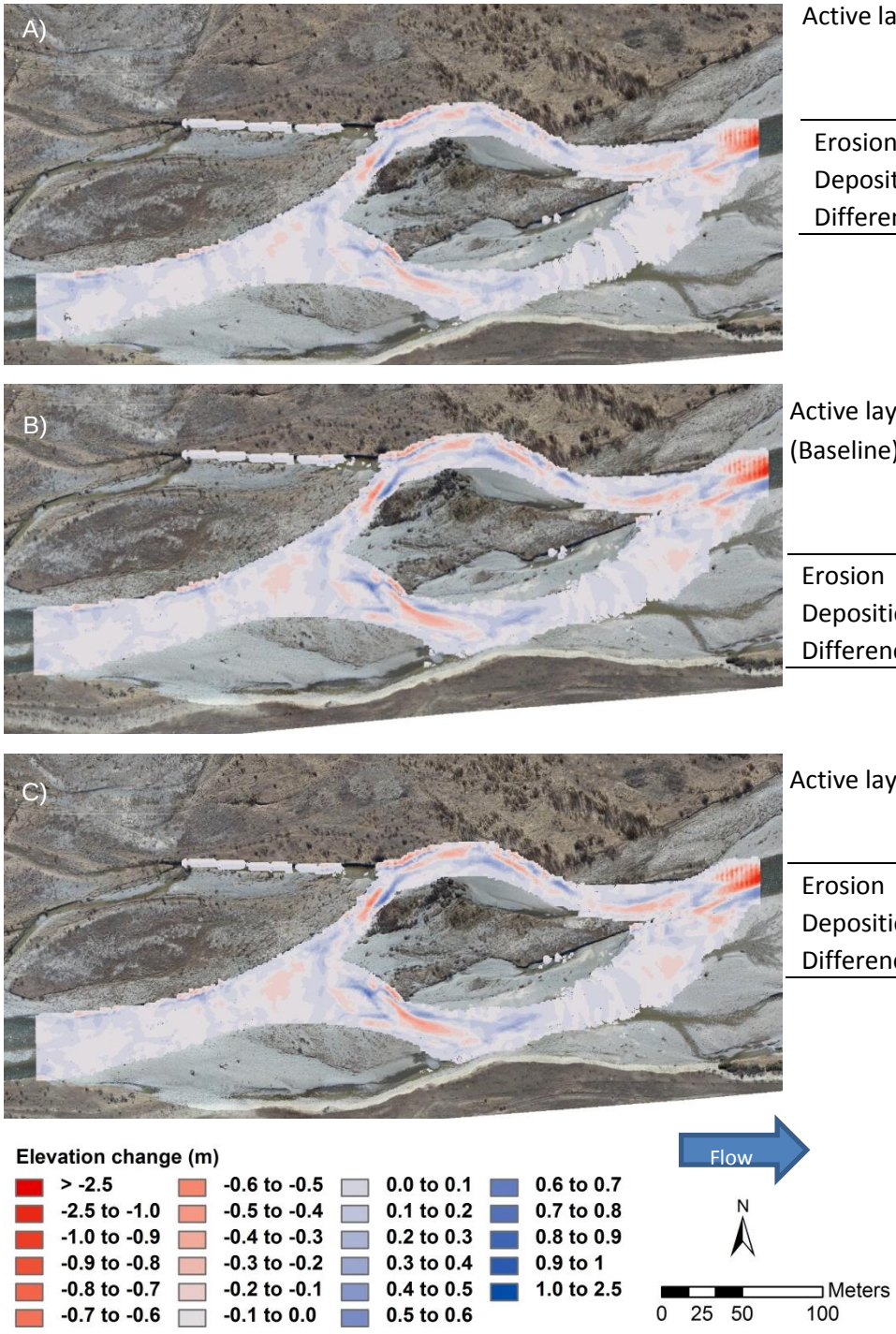

Active layer: 0.1 m

	Volume (m^3)
Erosion	828
Deposition	688
Difference	-140

Active layer: 0.25 m (Baseline)

	Volume (m3)
Erosion	1,068
Deposition	855
Difference	-213

Active layer: 0.5 m

	Volume (m3)
Erosion	1,095
Deposition	873
Difference	-222

Figure E.11: Active layer sensitivity analysis: A) 0.1 m, B) 0.25 m, and C) 0.5 m.

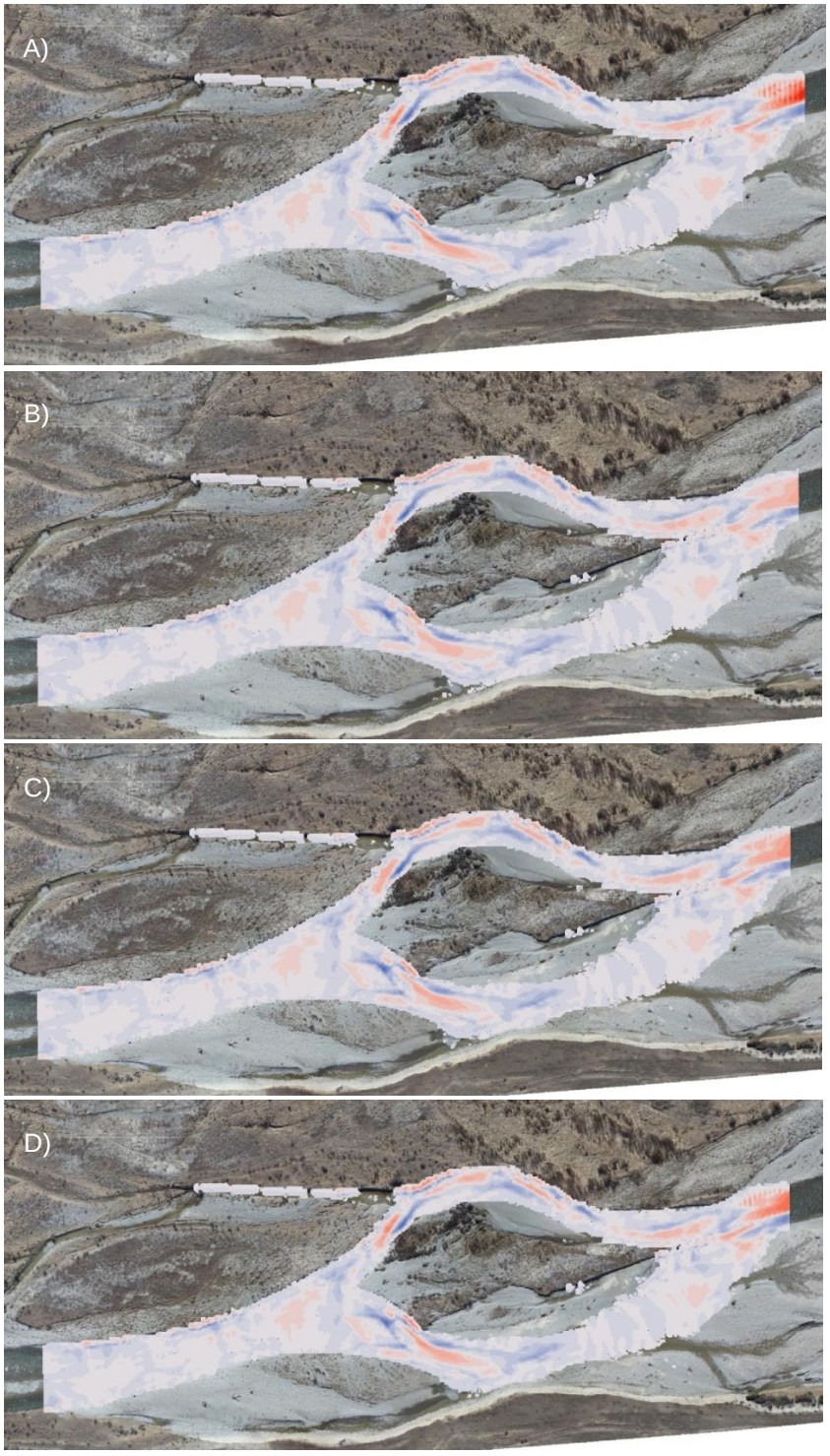

Base layer: 2 m (Baseline)

	Volume (m^3)
Erosion	1,068
Deposition	855
Difference	-213

Base layer: 0.1 m

	Volume (m3)
Erosion	963
Deposition	825
Difference	-138

Base layer: 0.25 m

	Volume (m3)
Erosion	1,006
Deposition	846
Difference	-160

Base layer: 0.5 m

	Volume (m3)
Erosion	1,038
Deposition	856
Difference	-182

Figure E.12: Base layer sensitivity analysis for: A) 2 m, B) 0.1 m, C) 0.25 m, and D) 0.5 m.

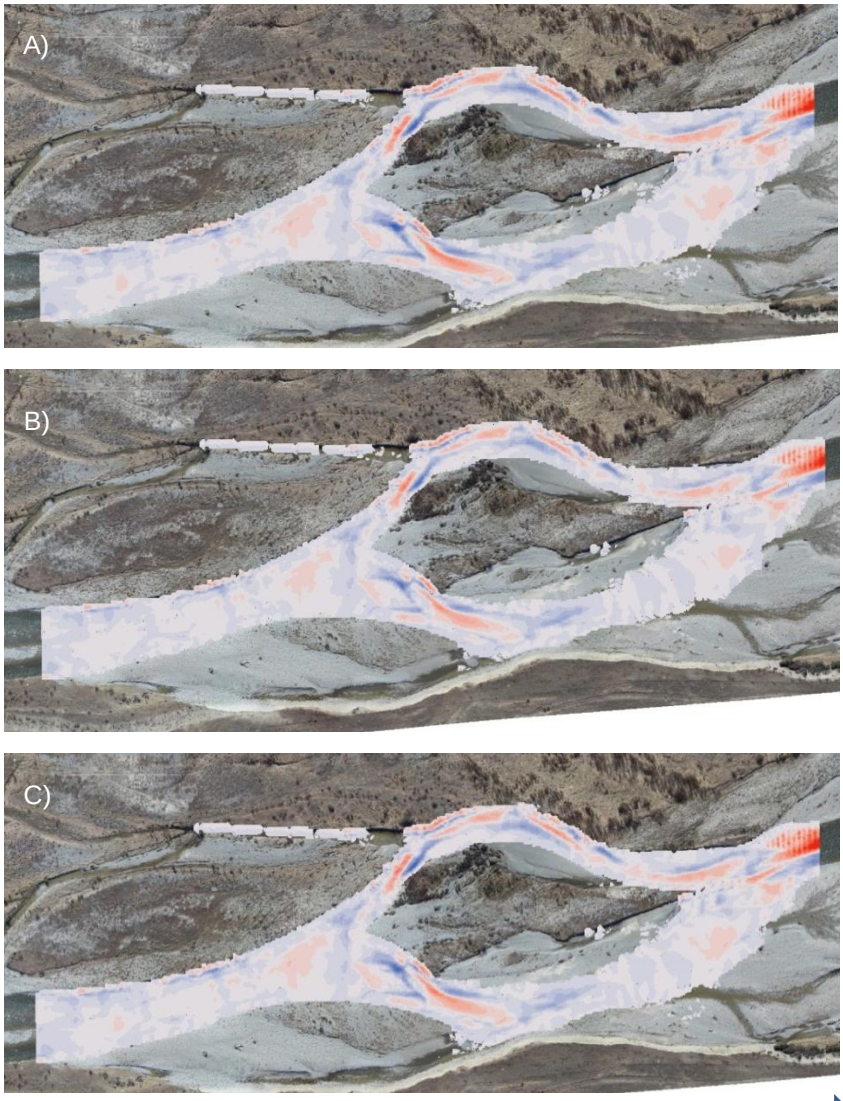

Bed composition: 1 phi interval

	Volume (m^3)
Erosion	1,263
Deposition	1,038
Difference	-225

Bed composition: 2 phi interval (baseline)

	Volume (m3)
Erosion	1,068
Deposition	855
Difference	-213

Bed composition: Sand, gravel, cobbles

	Volume (m3)
Erosion	1,223
Deposition	997
Difference	-226

Figure E.13: Bed composition sensitivity analysis for: A) 1 phi interval, B) 2 phi interval, and C) sand, gravel, and cobbles composition.

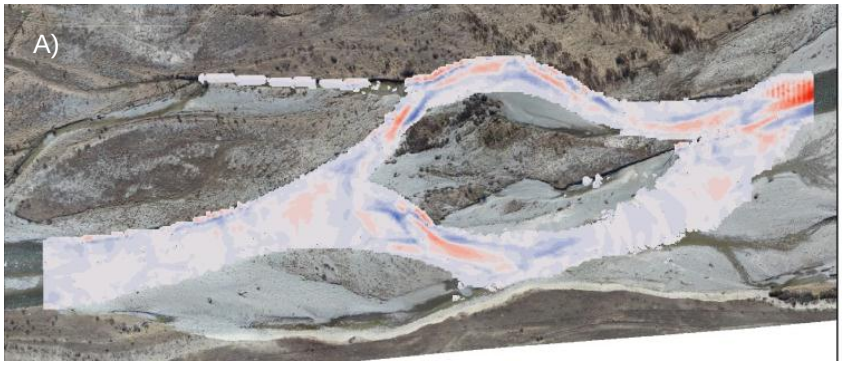

ThetSd: 0 (Baseline)

	Volume (m^3)
Erosion	1,068
Deposition	855
Difference	-213

ThetSd: 0.1

	Volume (m3)
Erosion	1,004
Deposition	784
Difference	-220

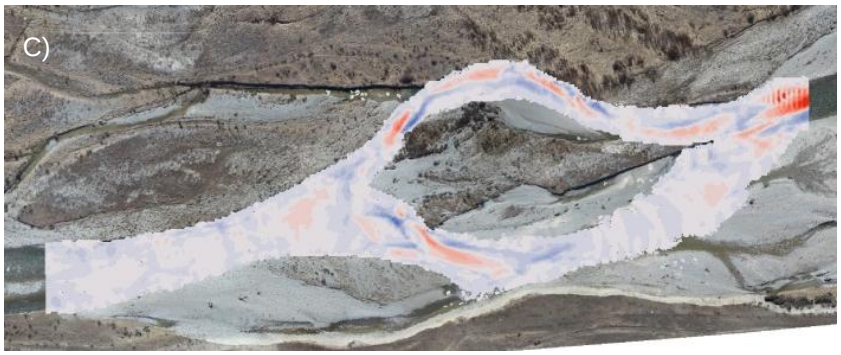

ThetSd: 0.5

	Volume (m3)
Erosion	1,004
Deposition	785
Difference	-219

ThetSd: 0.9

	Volume (m3)
Erosion	1,004
Deposition	787
Difference	-217

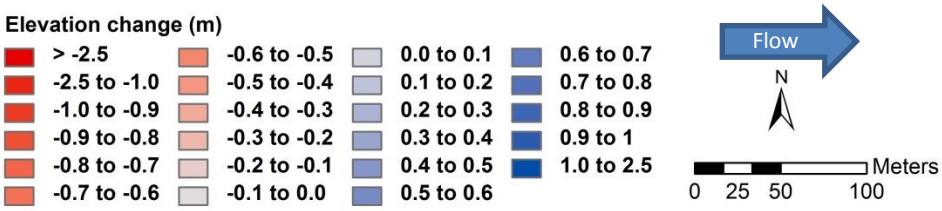

Figure E.14: Bank erosion using ThetSd sensitivity analysis for: A) 0, B) 0.1, C) 0.5, and D) 0.9.

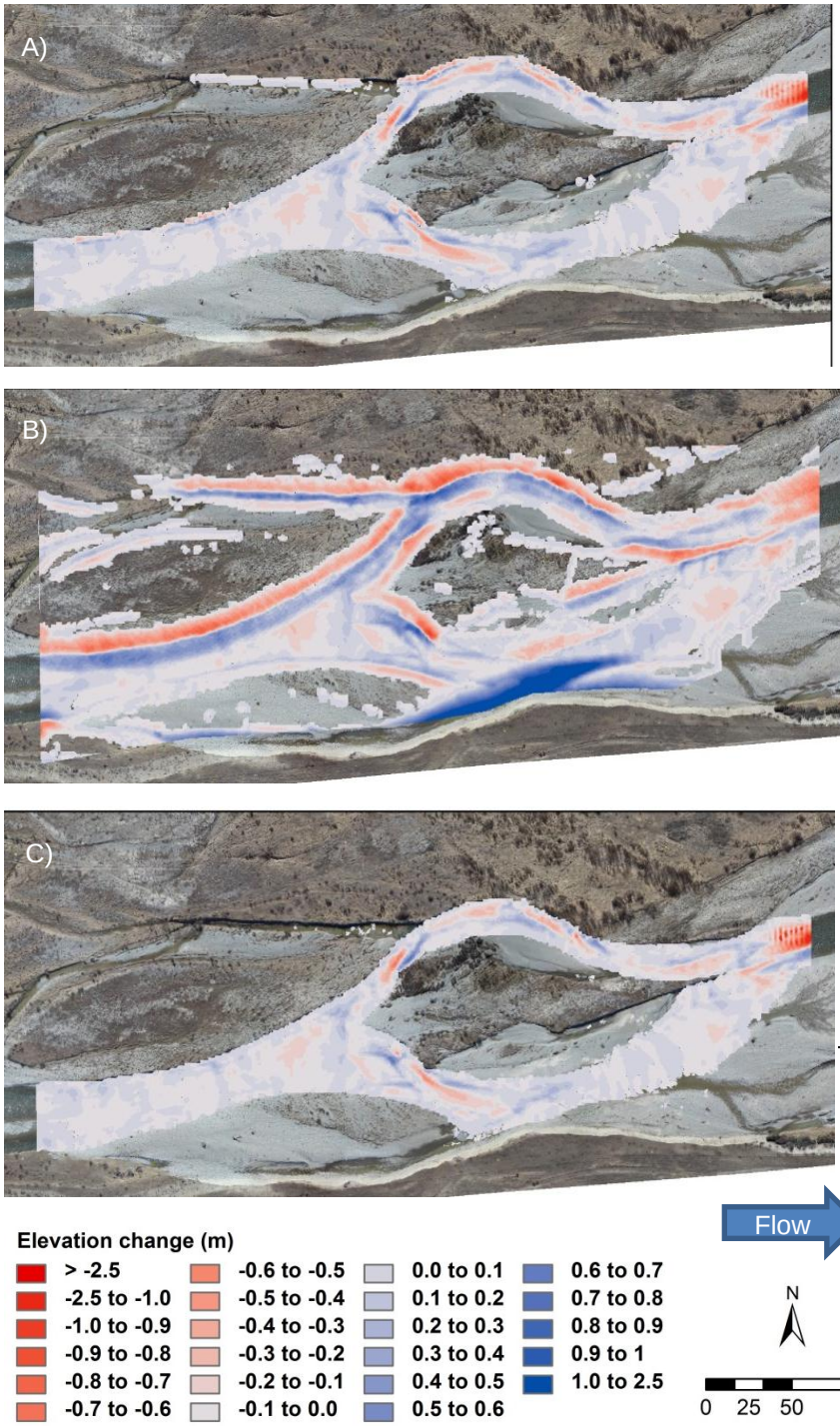

Repose: 0.4 (Baseline)

	Volume (m^3)
Erosion	1,068
Deposition	855
Difference	-213

Repose: 0.1

	Volume (m3)
Erosion	3,341
Deposition	5,131
Difference	1,791

Repose: 1.0

	Volume (m3)
Erosion	899
Deposition	696
Difference	-203

Figure E.15: Bank erosion using Repose sensitivity analysis for: A) 0.4, B) 0.1, and C) 1.0.

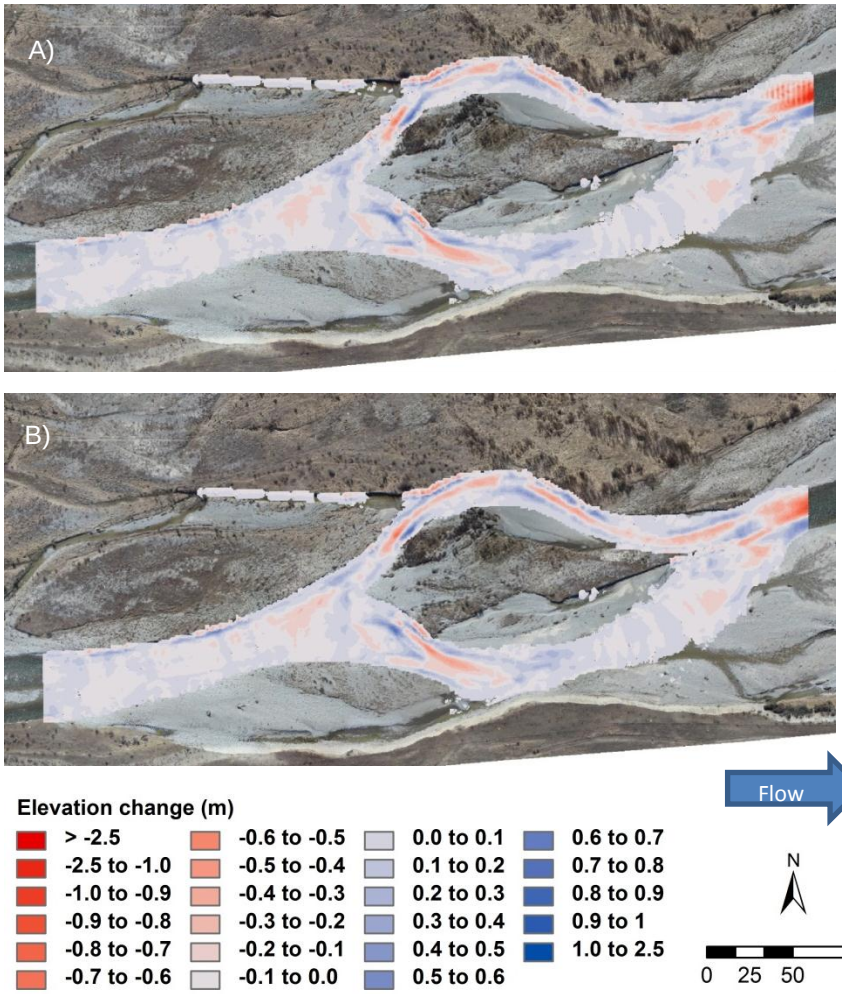

Transport component: Central (Baseline)

	Volume (m^3)
Erosion	1,068
Deposition	855
Difference	-213

Transport component: Upwind

	Volume (m3)
Erosion	1,088
Deposition	935
Difference	-153

Figure E.16: Transport condtions sensitivity analysis for: A) central scheme, and B) upwind scheme.

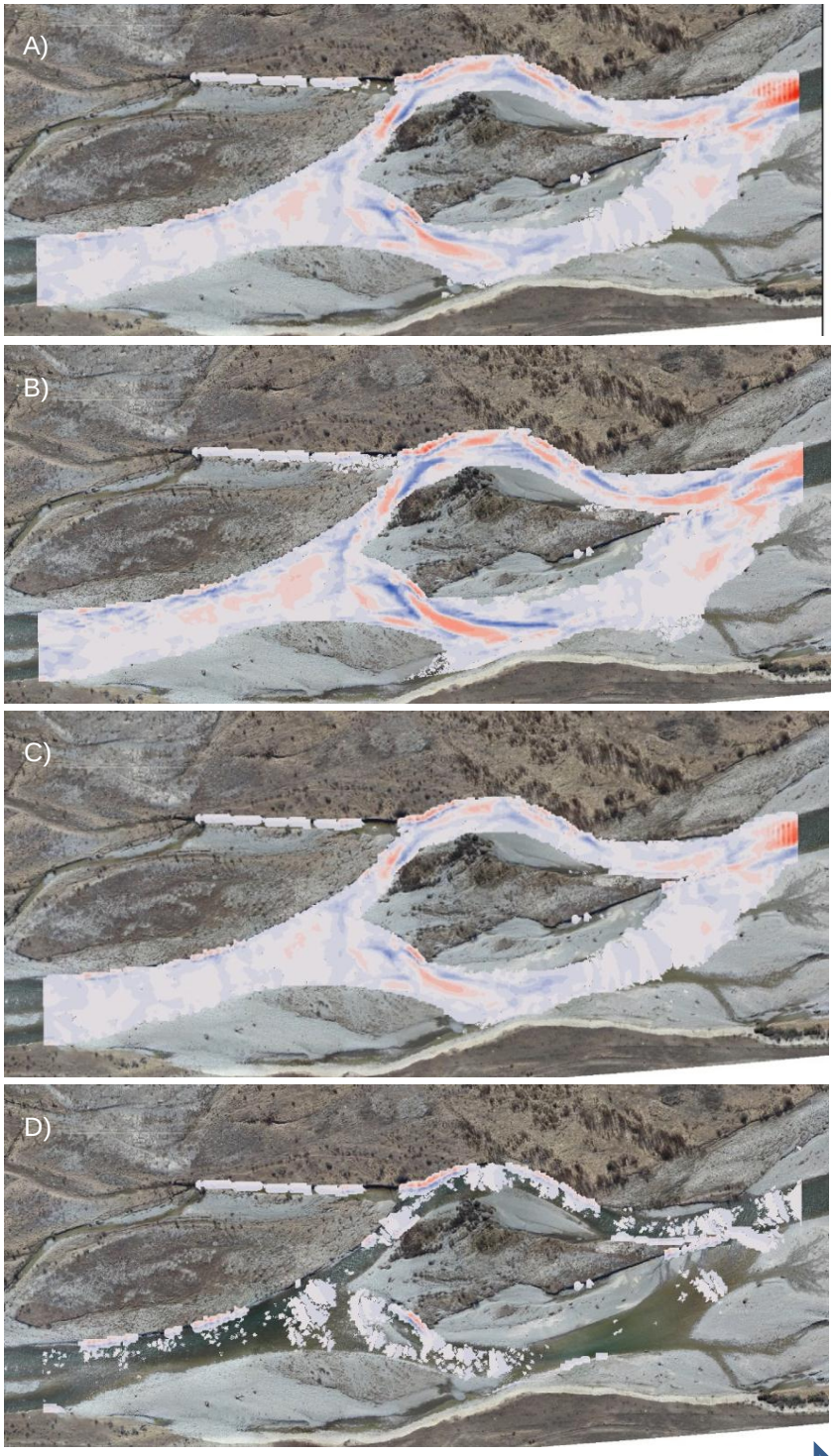

Transport formula: Gaueman et al. (Baseline)

	Volume (m^3)
Erosion	1,068
Deposition	855
Difference	-213

Transport formula: Meyer-Peter-Muller

	Volume (m3)
Erosion	1,425
Deposition	1,244
Difference	-180

Transport formula: Wilcock and Crowe

	Volume (m3)
Erosion	792
Deposition	637
Difference	-155

Transport formula: Modified Wilcock and Crowe

	Volume (m3)
Erosion	117
Deposition	117
Difference	0

Figure E.17: Transportation forumal sensitivity analysis for: A) Gaueman et al., B) Meyer-Peter-Muller, C) Wilcock and Crowe, and D) Modified Wilcock and Crowe.

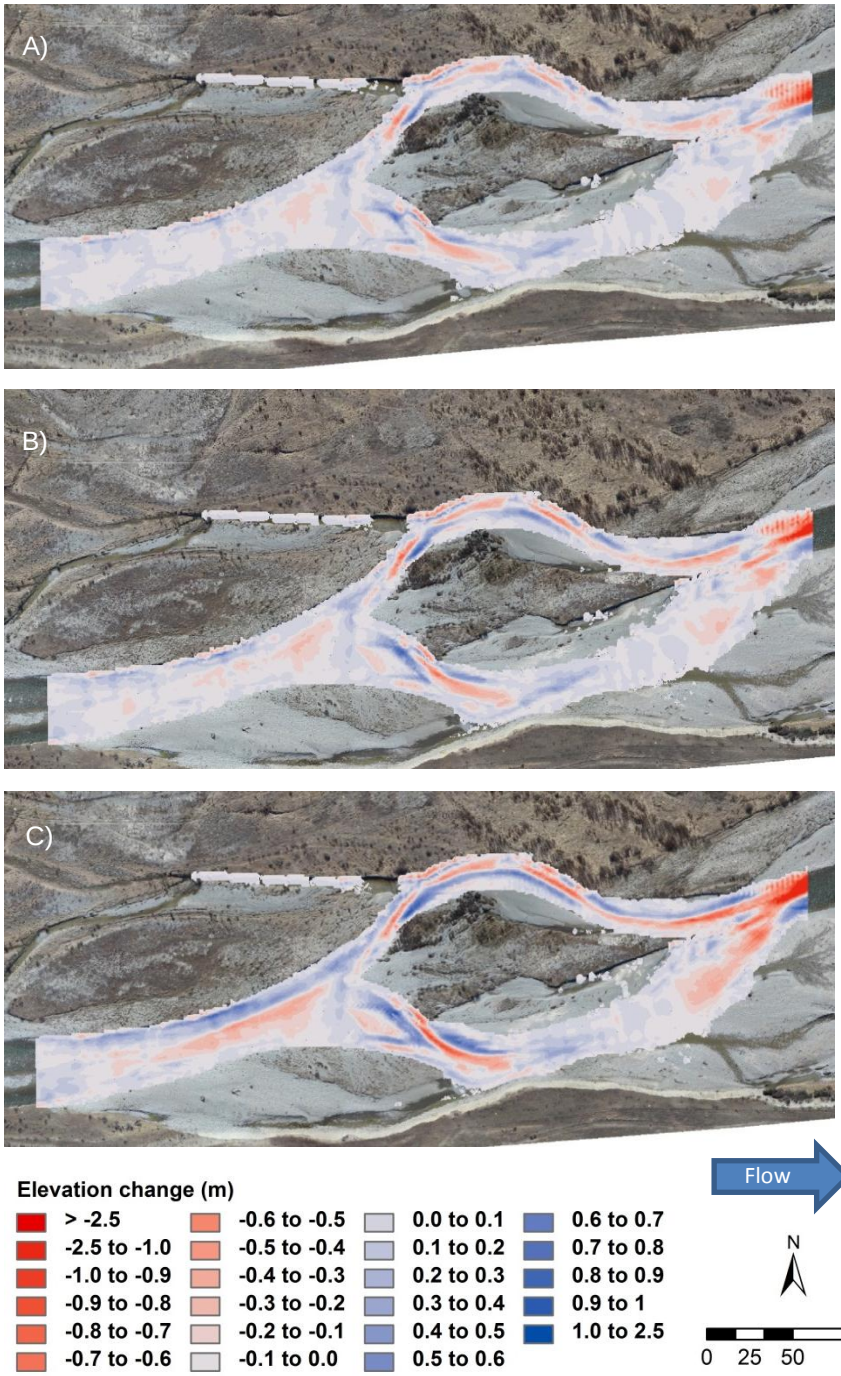

Morphology factor: 1 (Baseline)

	Volume (m^3)
Erosion	1,068
Deposition	855
Difference	-213

Morphology factor: 2.5

	Volume (m3)
Erosion	1,436
Deposition	1,122
Difference	-314

Morphology factor: 10

	Volume (m3)
Erosion	2,100
Deposition	1,881
Difference	-219

Figure E.18: Morphological acceleration factor sensitivity analysis for: A) 1, B) 2.5, and C) 10.

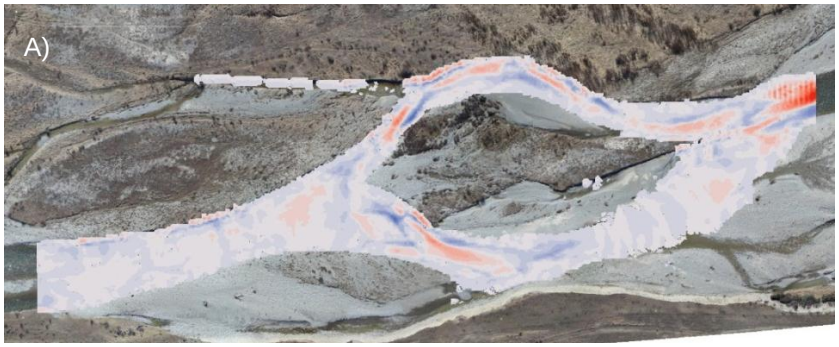

Bed slope: none (Baseline)

	Volume (m^3)
Erosion	1,068
Deposition	855
Difference	-213

Bed slope: AlfaBs 0.1, AlfaBn 1.5

	Volume (m3)
Erosion	1,098
Deposition	824
Difference	-274

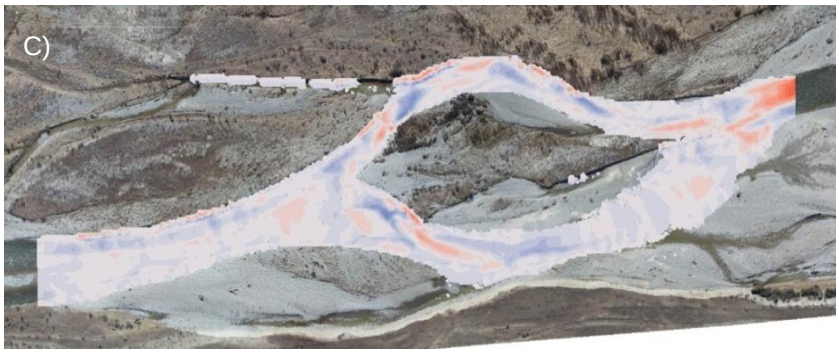

Bed slope: AlfaBs 1, AlfaBn 1.5

	Volume (m3)
Erosion	1,102
Deposition	817
Difference	-286

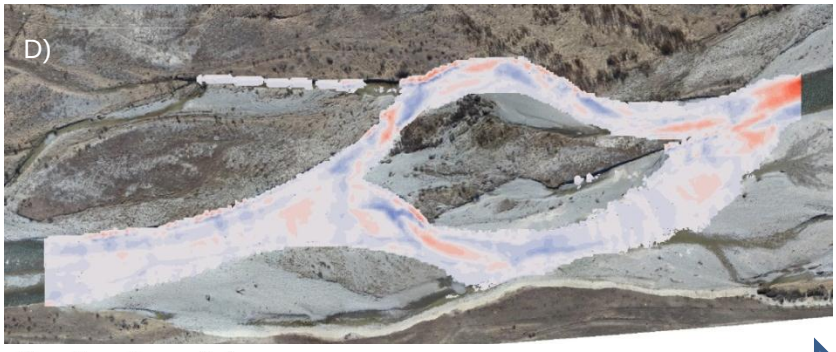

Bed slope: AlfaBs 10, AlfaBn 1.5

	Volume (m3)
Erosion	1,112
Deposition	790
Difference	-322

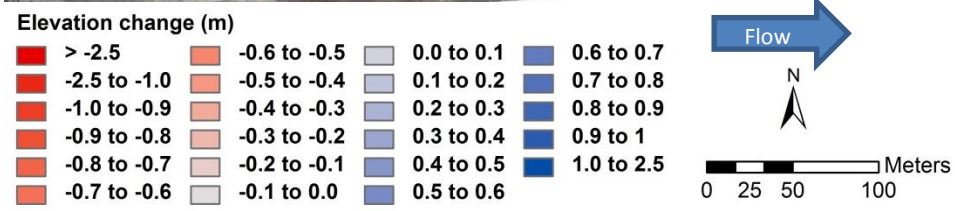

Figure E.19: Longitudinal bed slope gradient factor (AlfaBs) sensitivity analysis for: A) none, B) AlfaBs 0.1 and AlfaBn 1.5, C) AlfaBs 1 and AlfaBn 1.5, and D) AlfaBs 10 and AlfaBn 1.5.

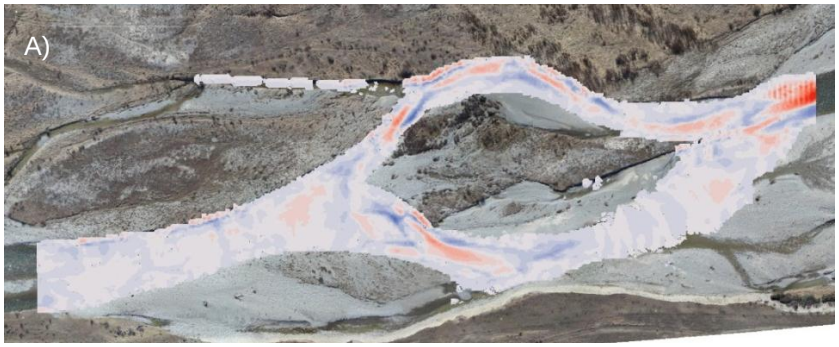

Bed slope: none (Baseline)

	Volume (m^3)
Erosion	1,068
Deposition	855
Difference	-213

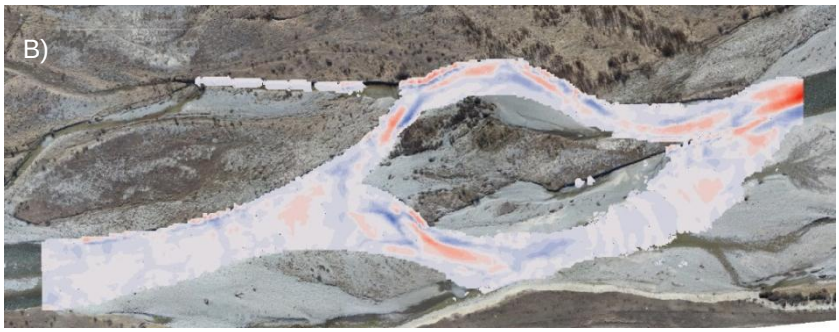

Bed slope: AlfaBs 1, AlfaBn 0.1

	Volume (m3)
Erosion	1,071
Deposition	840
Difference	-231

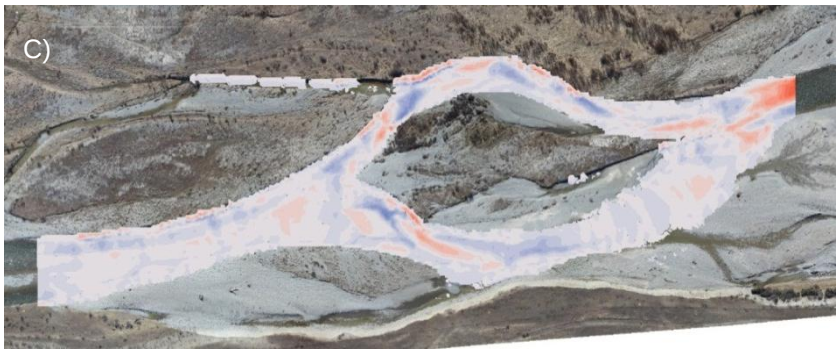

Bed slope: AlfaBs 1, AlfaBn 1.5

	Volume (m3)
Erosion	1,102
Deposition	817
Difference	-286

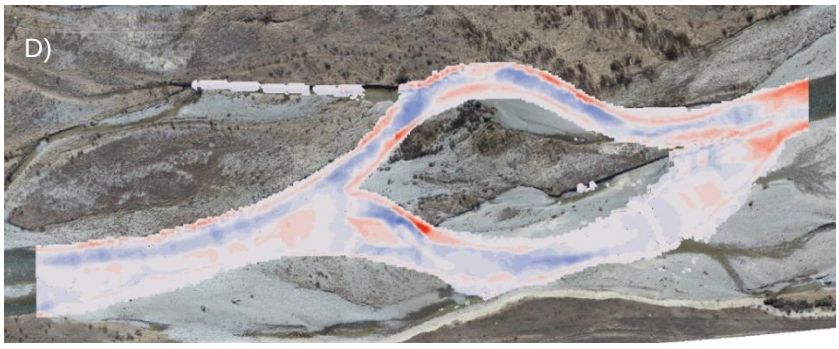

Bed slope: AlfaBs 1, AlfaBn 10

	Volume (m3)
Erosion	1,611
Deposition	1,210
Difference	-401

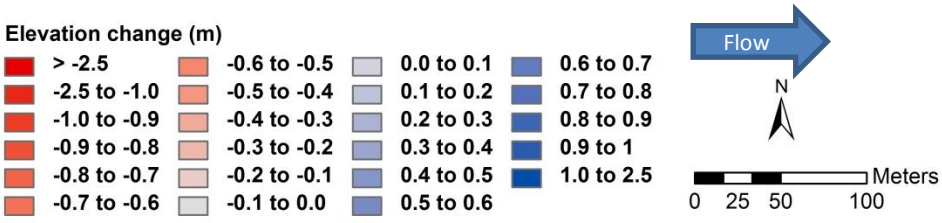

Figure E.20: Transverse bed slope gradient factor (AlfaBn) sensitivity analysis for: A) none, B) AlfaBs1 and AlfaBn 0.1, C) AlfaBs 1 and AlfaBn 1.5, and D) AlfaBs 1 and AlfaBn 10.

E.8: Full reach morphological calibration

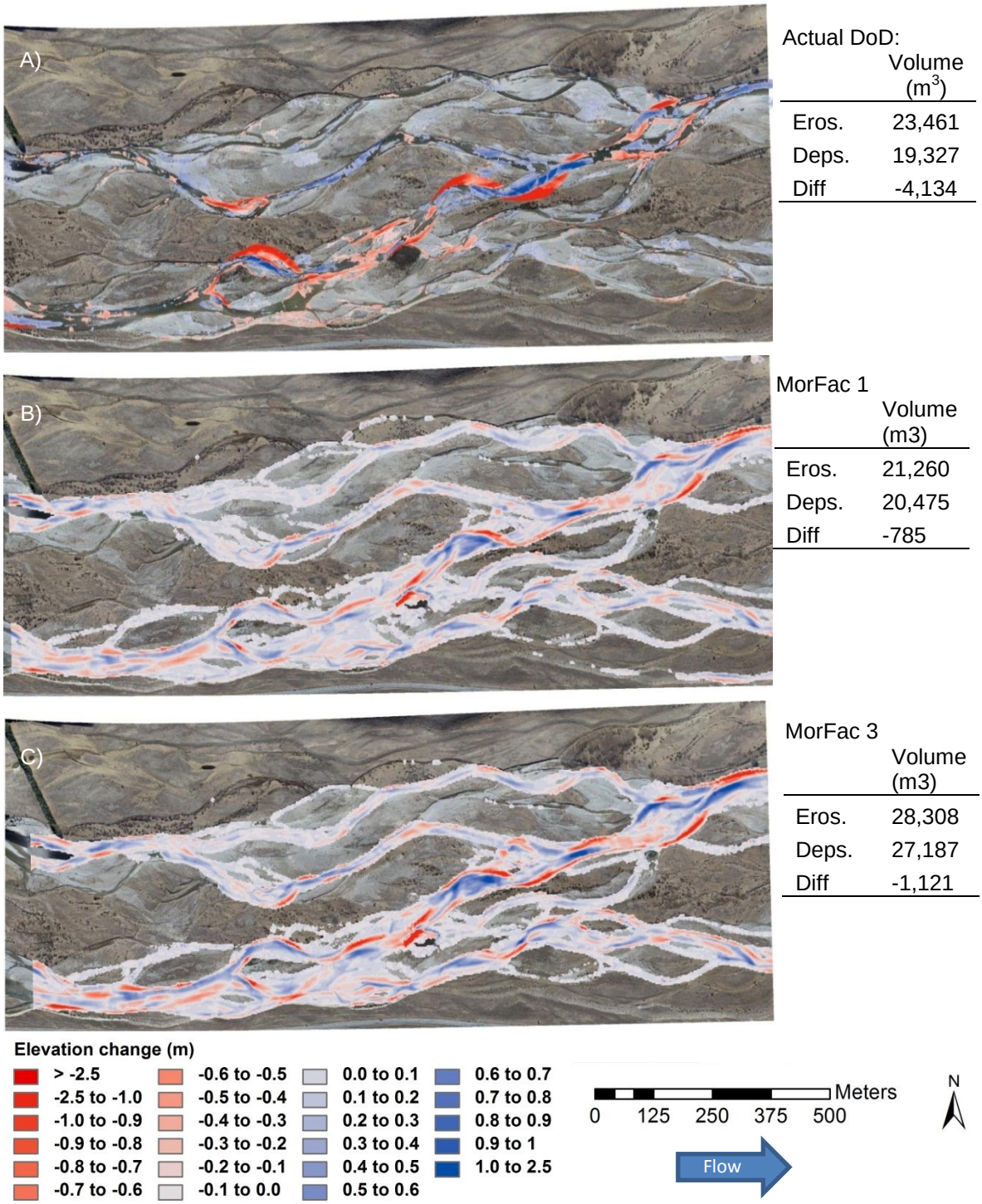

Figure E.21: DoD results for: A) observed October, 2011 flood event, B) morphology acceleration factor (MorFac) 1, and C) MorFac 3.

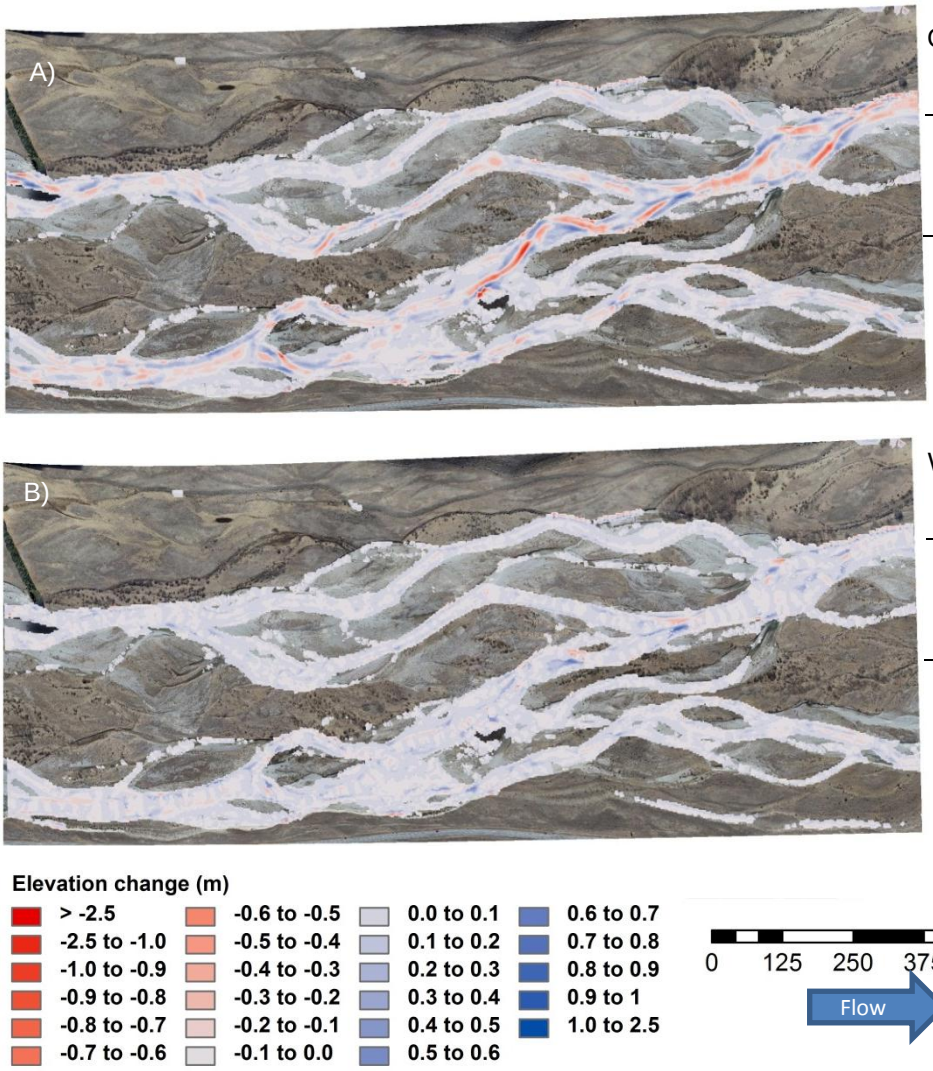

Figure E.22: Sediment tranpsort forumula results for: A) Gaueman et al., and B) Wilcock and Crowe.

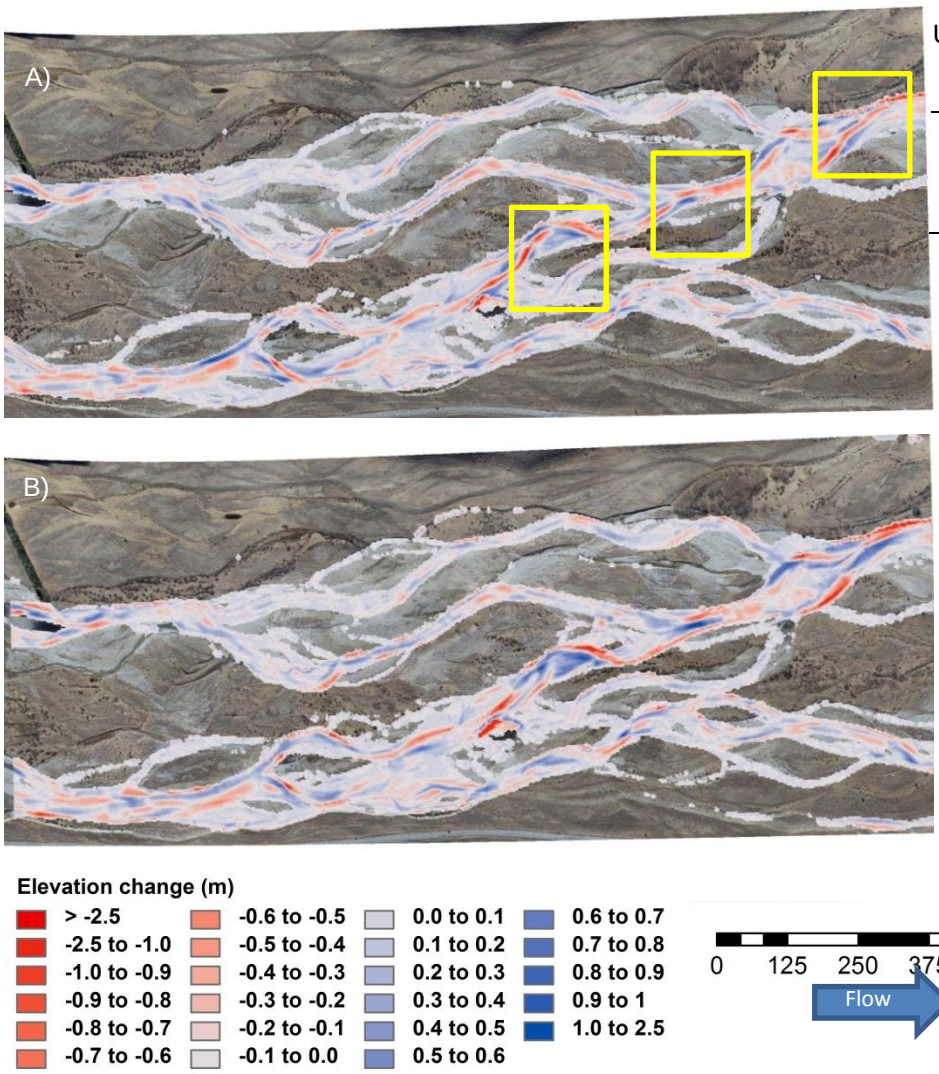

Figure E.23: Bed component scheme testing results for: A) upwind (with descrepancies outlined in yellow boxes), and B) central.

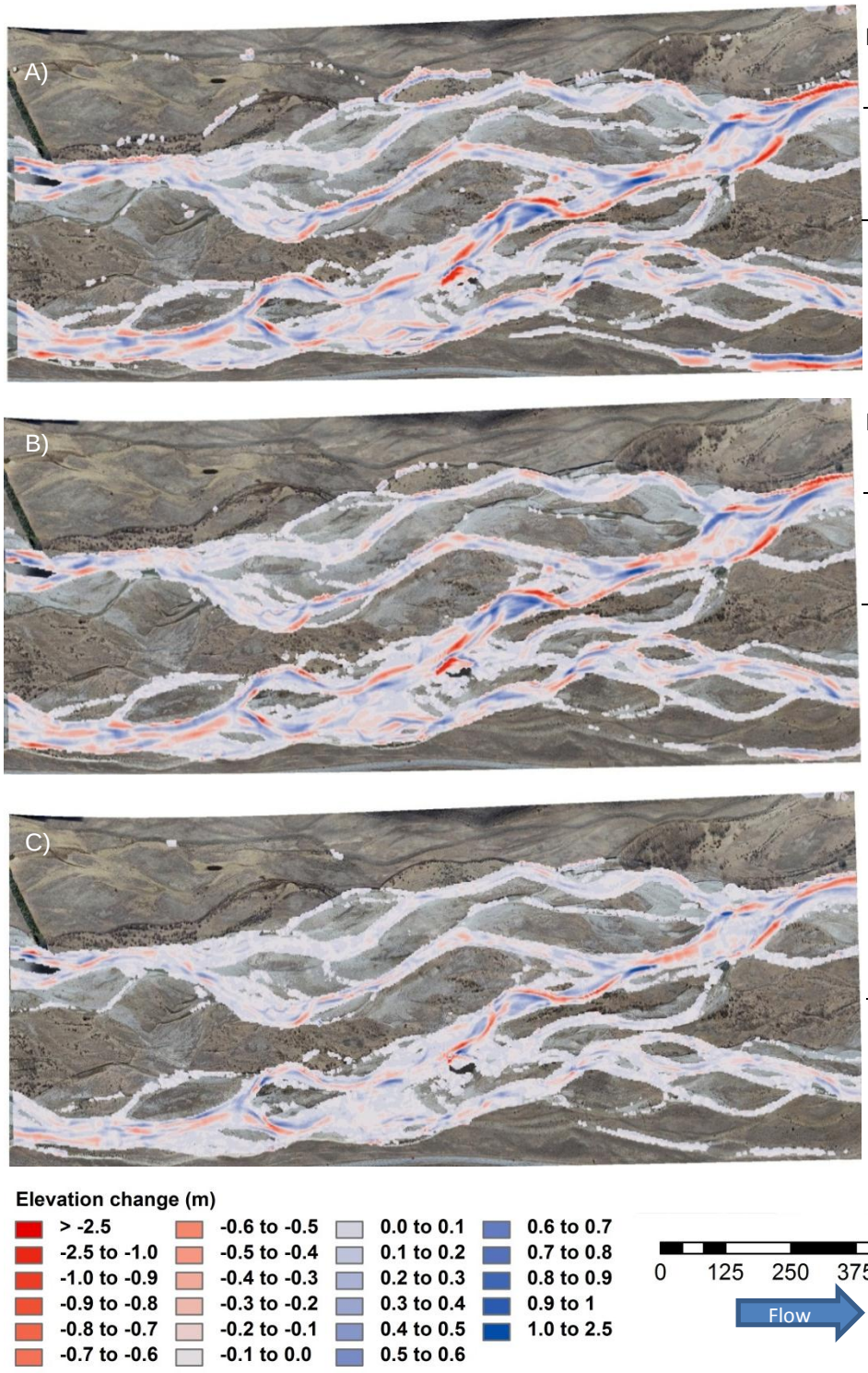

Repose 0.2

	Volume (m3)
Eros.	26,985
Deps.	26,071
Diff	-914

Repose 0.3

	Volume (m3)
Eros.	21,260
Deps.	20,475
Diff	-785

Repose 0.4

	Volume (m3)
Eros.	12,441
Deps.	12,330
Diff	-112

Figure E.24: Repose testing results for: A) repose 0.2, B) repose 0.3, and C) repose 0.4.

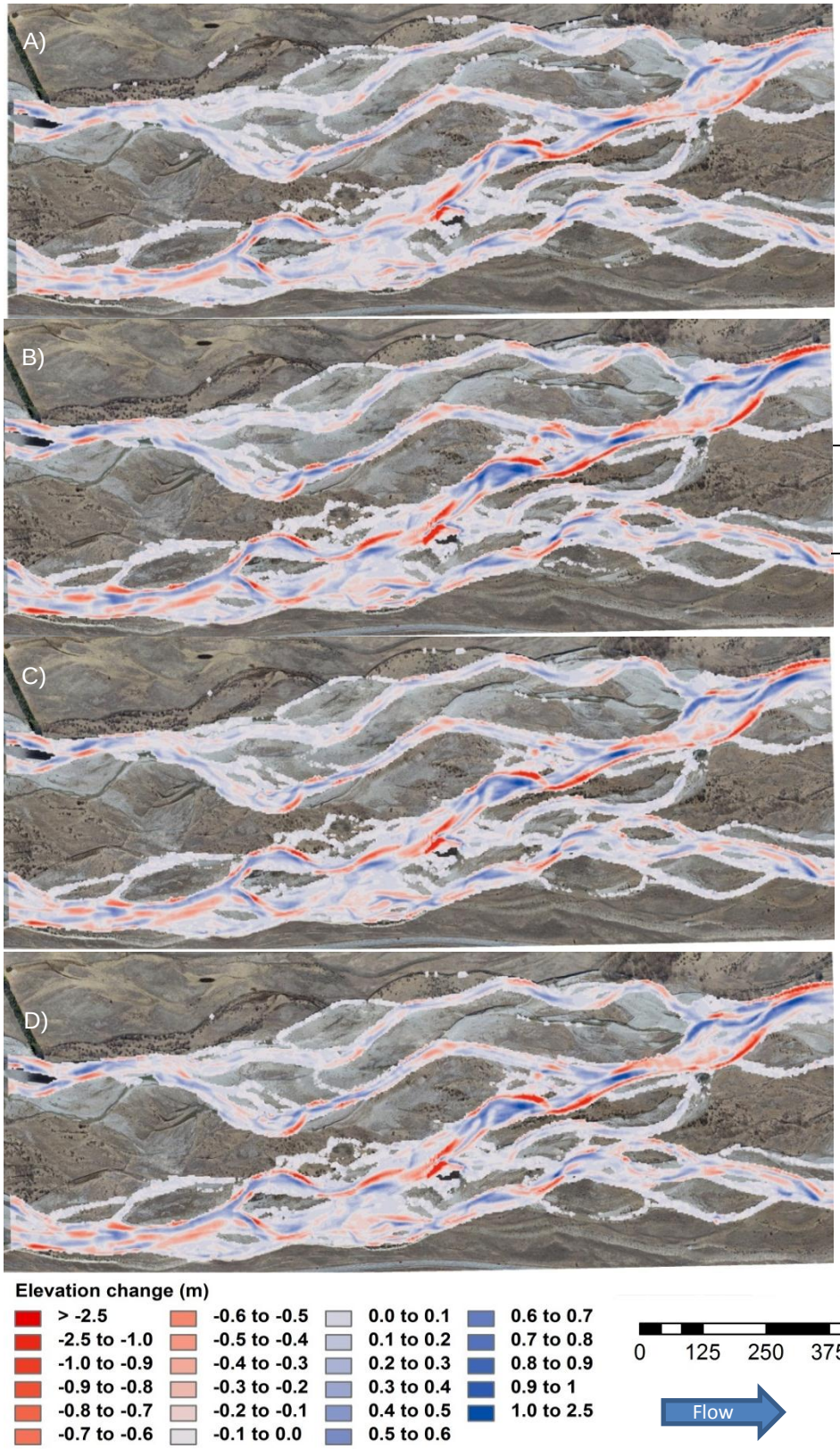

V74	Volume (m3)
Eros.	21,155
Deps.	18,526
Diff	-2,629

V75	Volume (m3)
Eros.	28,574
Deps.	26,121
Diff	-2,453

V76	Volume (m3)
Eros.	23,960
Deps.	21,856
Diff	-2,104

V77	Volume (m3)
Eros.	25,726
Deps.	23,495
Diff	-2,231

Figure E.25: DoD for simulations A) v74, B) v75, C) v76, and D) v77.

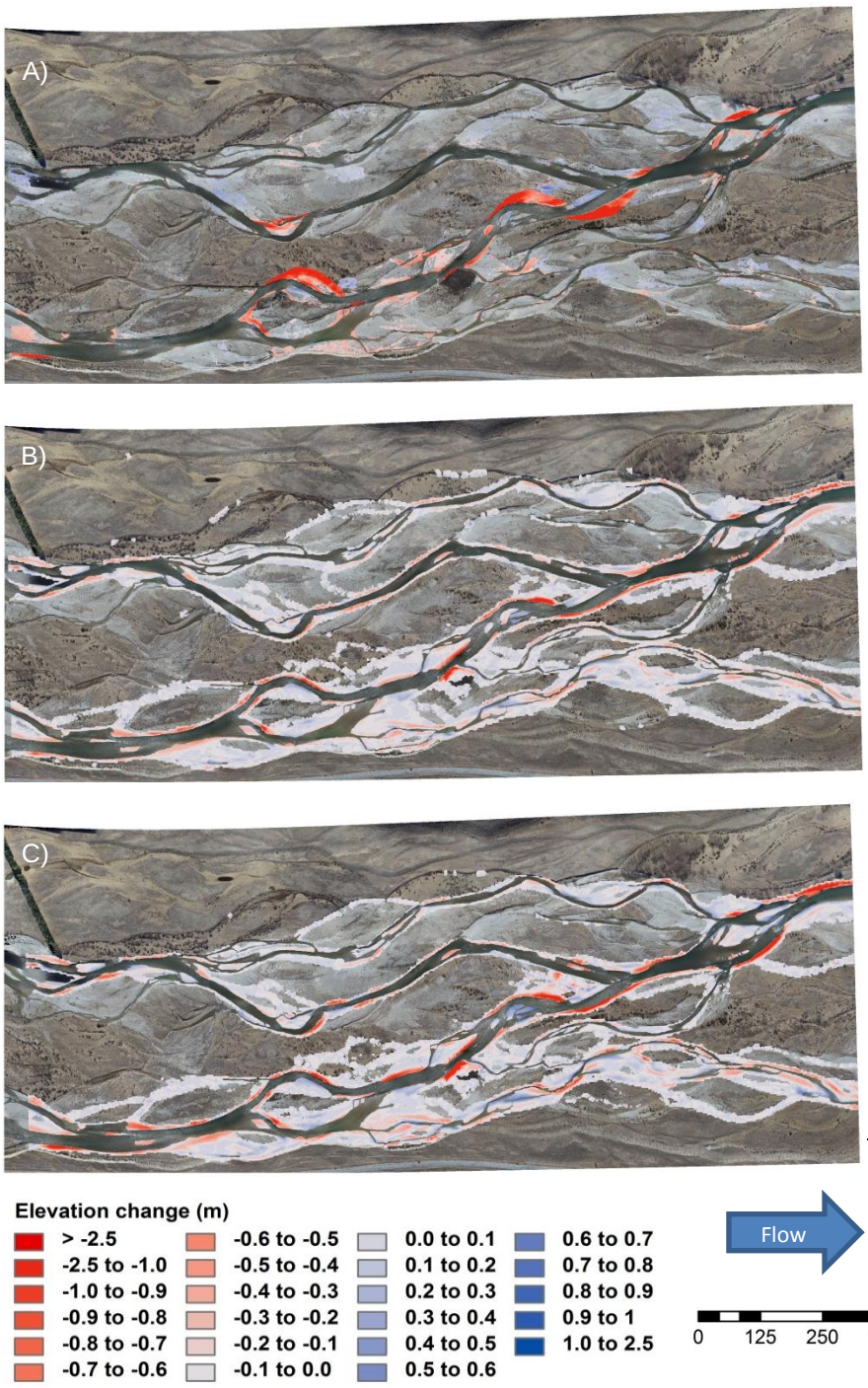

Observed DoD

	Area (m2)
Eros.	35,523
Deps.	27,898
	Volume (m3)
Eros.	18,007
Deps.	5,554
Diff.	-12,453

V74: minLOD ≥10 cm

	Area (m2)
Eros.	69,387
Deps.	15,260
	Volume (m3)
Eros.	14,715
Deps.	3,050
Diff.	-11,665

V75: minLOD ≥10 cm

	Area (m2)
Eros.	74,537
Deps.	23,154
	Volume (m3)
Eros.	20,606
Deps.	5,255
Diff.	-15,351

Figure E.26: Overland morphology DoD for: A) observed, B) v74, and C) v75.

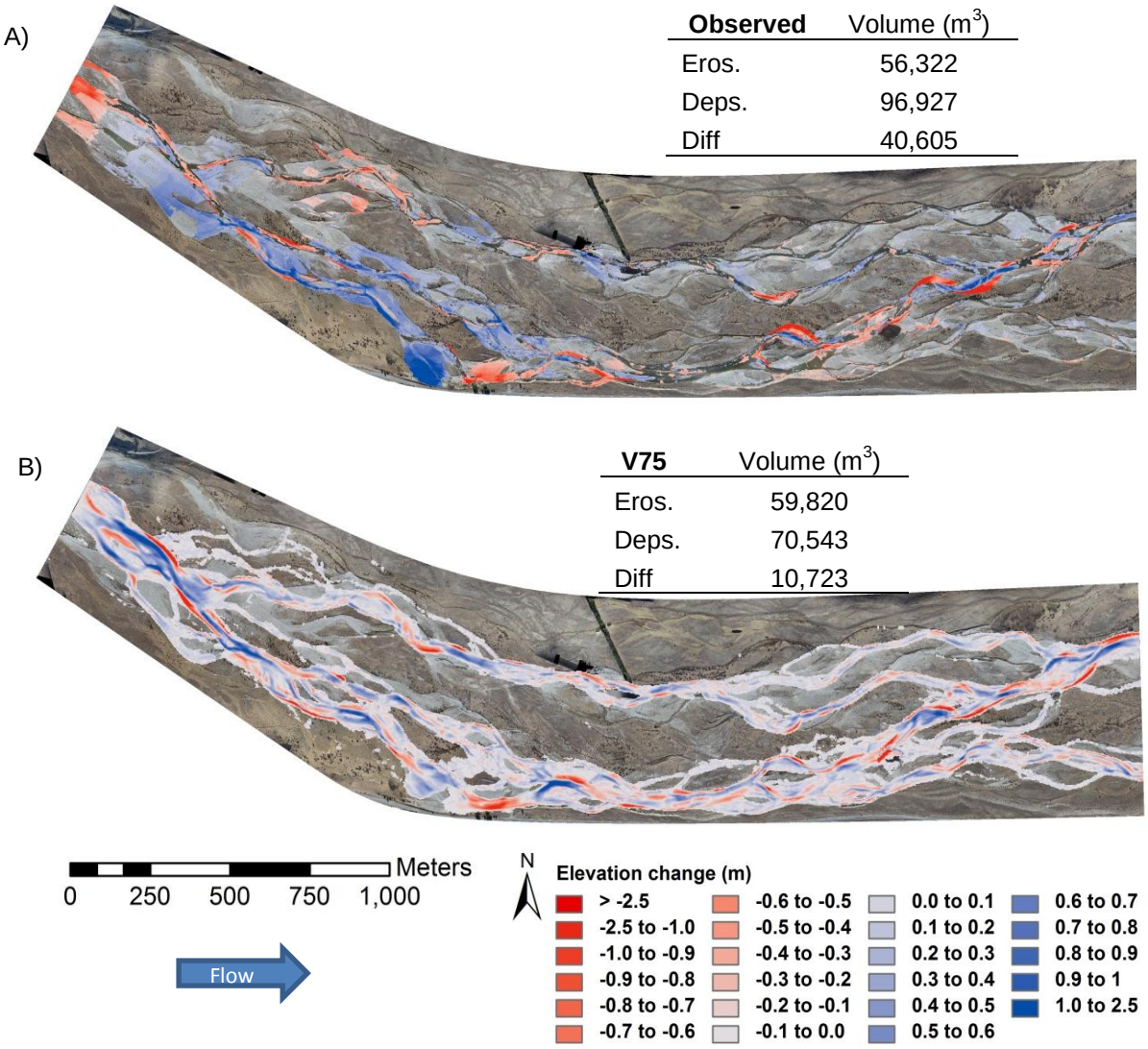

Figure E.27: Full reach morphologic changes for: A) observed data, and B) v75 simulation.

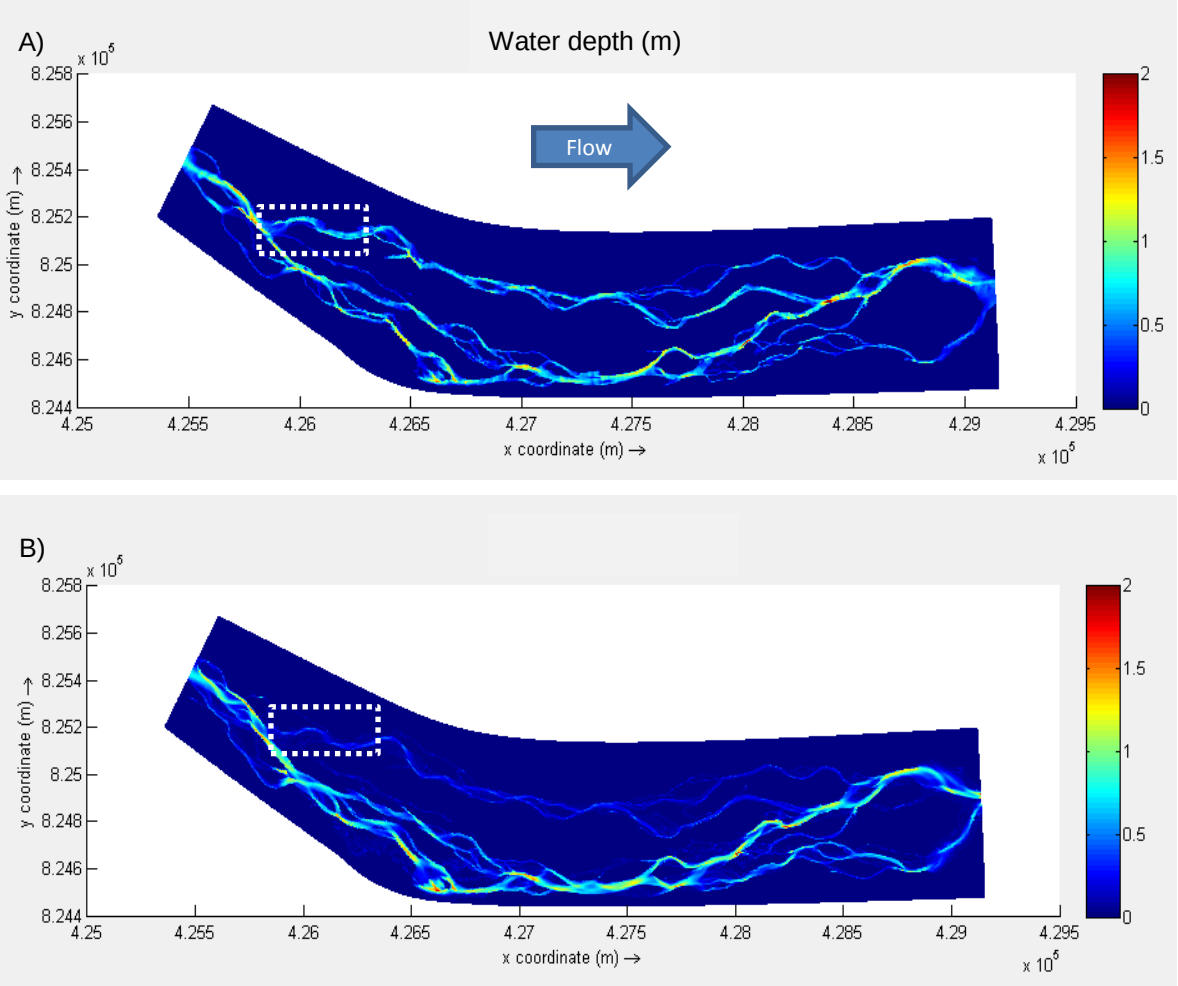

Figure E.28: V75 full reach simulation: A) starting morphology and water depth at 58 $m^3 s^{-1}$, and B) ending morphology and water depth at 58 $m^3 s^{-1}$.

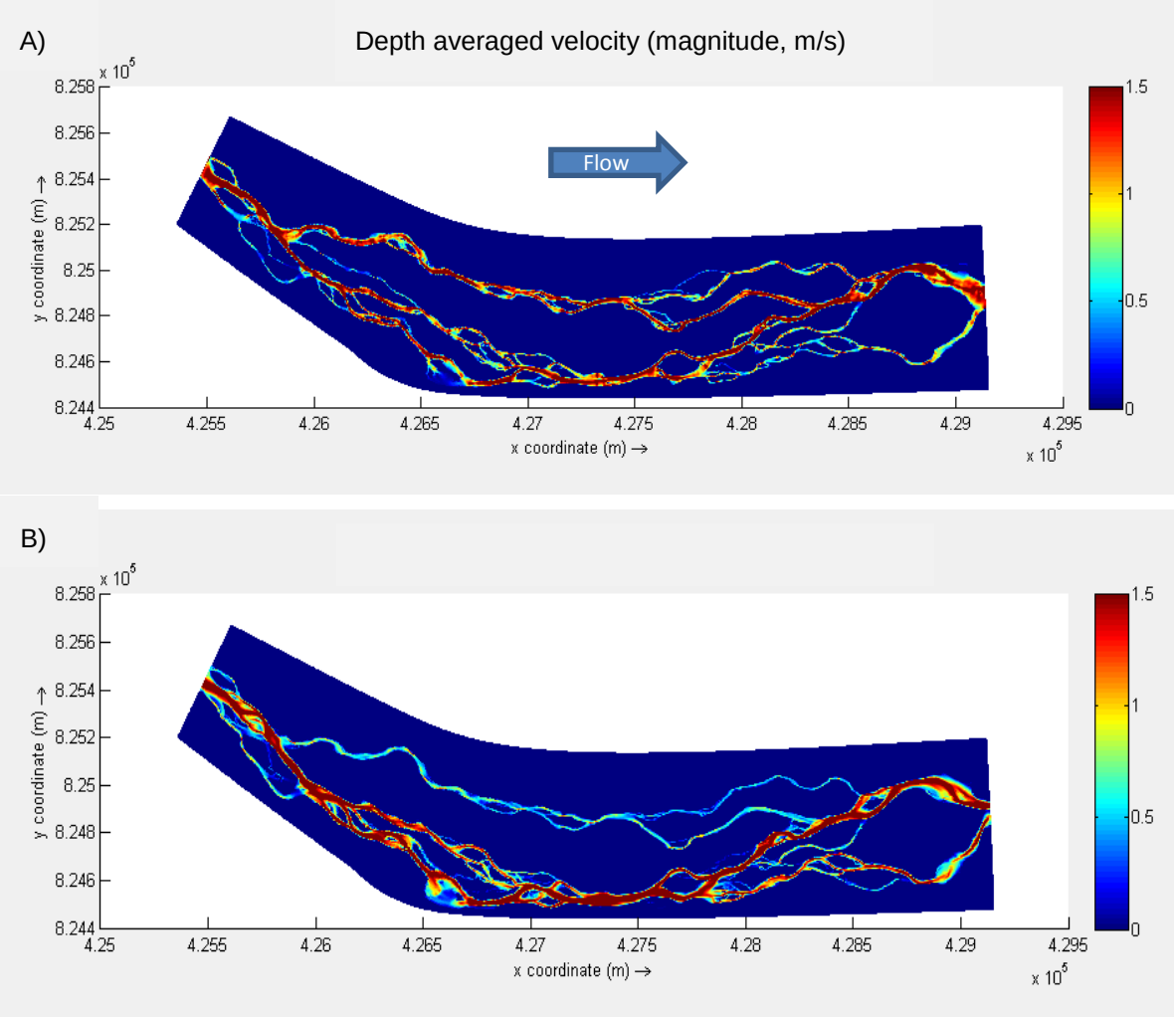

Figure E.29: V75 full reach simulation: A) starting morphology and velocity at 58 $m^3 s^{-1}$, and B) ending morphology and velocity at 58 $m^3 s^{-1}$.

E.9: Time lapse flood images

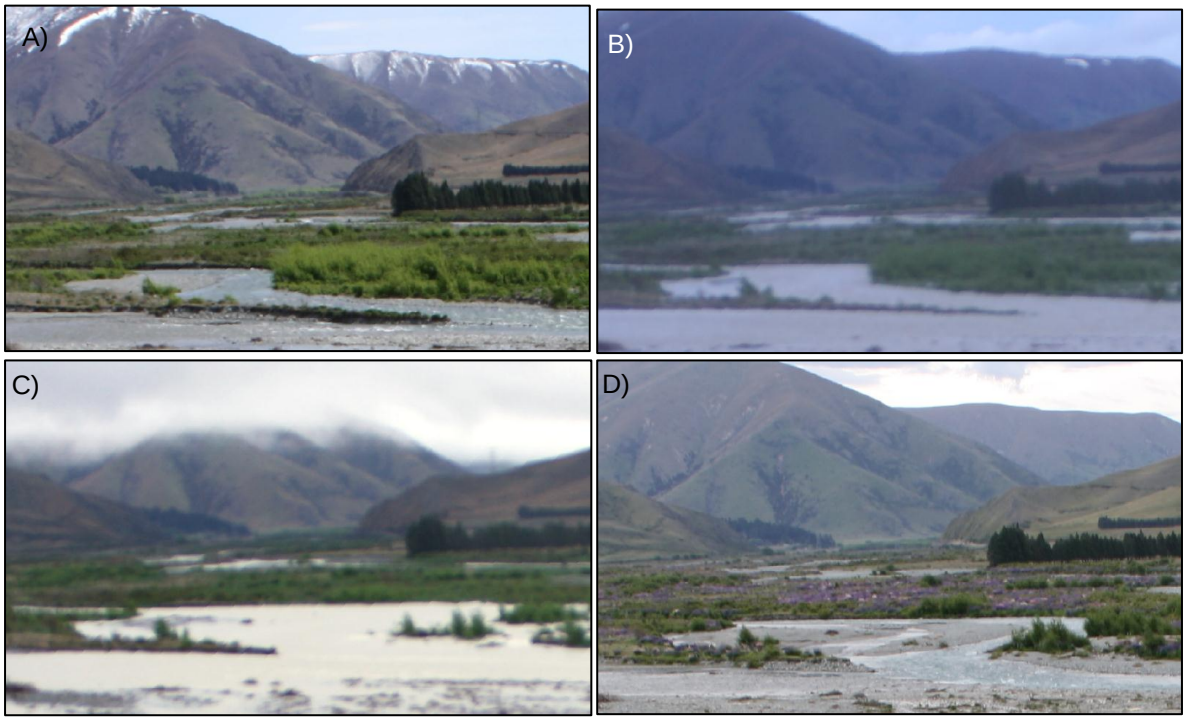

Figure E.30: Time lapse photos revealing the morphologic changes: A) pre-flood low flow conditions, B) pre-peak discharge at 181 $m^3 s^{-1}$, C) post-peak discharge at 77 $m^3 s^{-1}$, and D) post-flood low flow conditions.

Figure E.31: Time lapse image days before the October 2011 flood event.

Figure E.32: Time lapse image used to map the water extent for the 181 $m^3 s^{-1}$.

Figure E.33: Time lapse image used to map the water extent for the 77 $m^3 s^{-1}$.

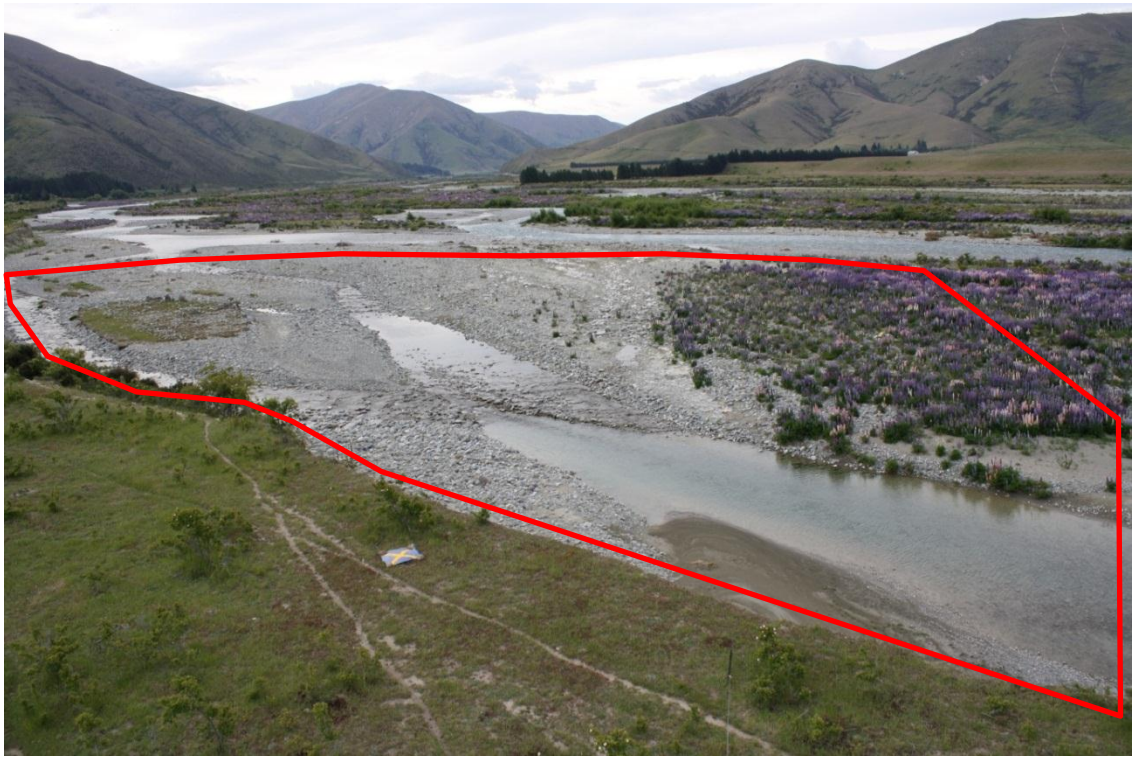

Figure E.34: Post-flood time lapse image capturing low flow conditions with visible GCPs, and area of interest outlined in red.

E.10: Mortality mapping methods

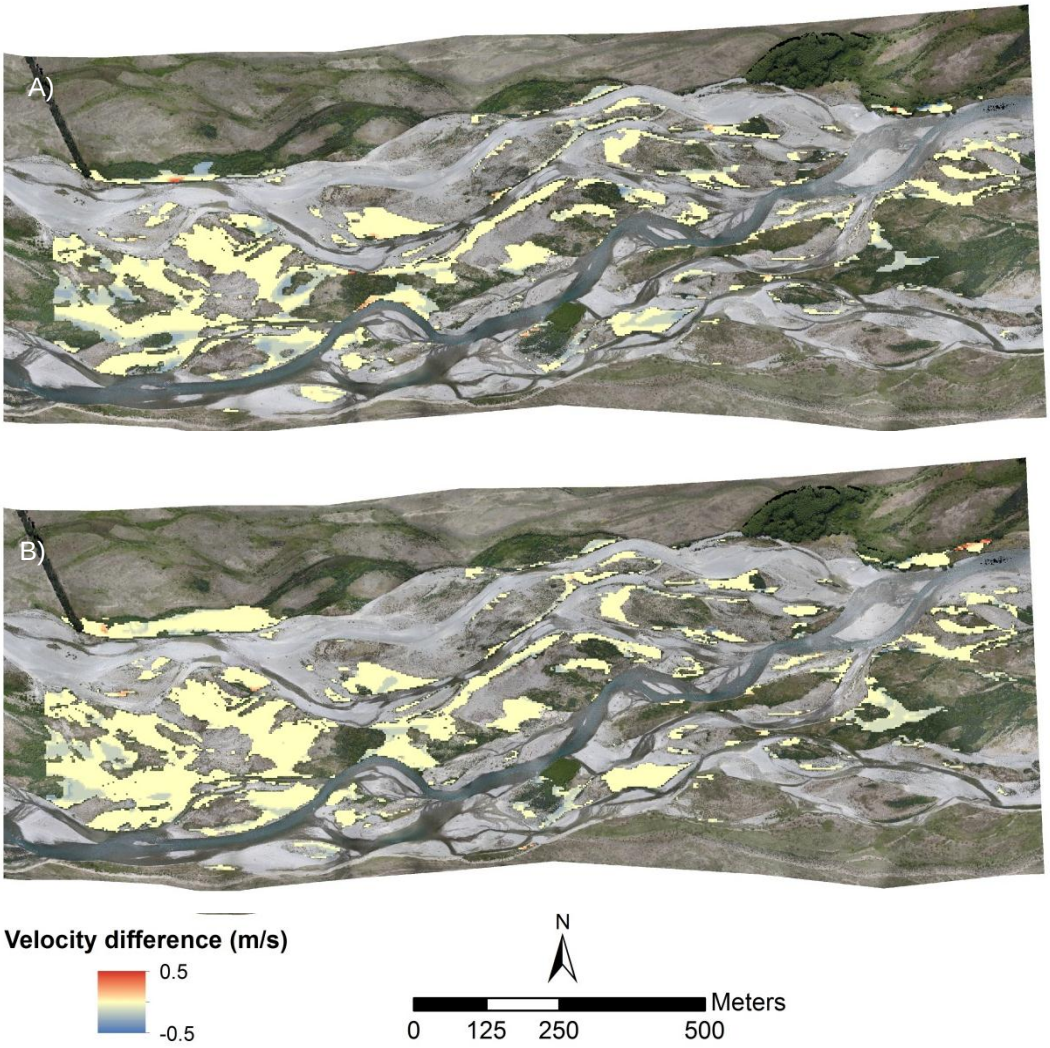

Figure E.35: Spatial velocity differences in vegetated areas for the 500-year flood event peak discharge compared to: A) 80% pre-peak discharge, and B) 80% post-peak discharge.

E.11: Uncertainty inclusion for mortality mapping

Table E.5: Root diameter and corresponding frequency for the vegetation densities.

Root diameter (cm)	Frequency (%)		
	Sparse	Moderate	Dense
1	6.8	3.4	1.0
2	11.7	7.0	2.2
3	12.3	8.4	4.4
4	5.6	3.9	2.2
5	5.6	5.0	4.4
6	4.3	4.4	4.4
7	8.0	8.5	8.9
8	8.0	10.7	12.8
9	11.7	8.1	4.4
10	12.3	12.8	13.3
11	5.6	7.2	8.9
12	2.5	4.6	6.2
13	0.6	1.4	2.2
14	3.1	7.1	11.1
15	1.9	7.6	13.3

Table E.6: Root diameter and corresponding uncertainty (average mean) of the vegetation densities for drag and pull-out 0 cm erosion condition.

Velocity (m/s)	Root diameter removed (cm)	Uncertainty (%)		
		Sparse	Moderate	Dense
0.74	≥6	-43.6	-43.1	-43.0
0.59	≥7	-43.0	-42.7	-42.6
0.48	≥8	-40.9	-40.9	-41.1
0.41	≥9	-42.4	-42.4	-42.6
0.33	≥10	-36.7	-39.9	-41.6
0.28	≥11	-35.6	-40.8	-42.7
0.24	≥12	-43.6	-46.7	-47.8
0.21	≥13	-53.7	-53.9	-54.0
0.18	≥14	-55.0	-55.0	-55.0
0.16	≥15	-55.0	-55.0	-55.0

Table E.7: Root diameter and corresponding uncertainty (average mean) of the vegetation densities for drag and pull-out 20 cm erosion condition.

Velocity (m/s)	Root diameter removed (cm)	Uncertainty (%)		
		Sparse	Moderate	Dense
0.92+	All	-39.1	-39.0	-39.0
0.78	≤ 2, ≥ 4	-38.7	-39.4	-40.2
0.67	≤ 2, ≥ 5	-38.9	-39.7	-40.4
0.58	≤ 2, ≥ 6	-38.6	-39.4	-40.2
0.51	≤ 2, ≥ 7	-40.1	-40.9	-41.6
0.43	≤ 2, ≥ 8	-42.6	-43.7	-44.6
0.37	≤ 2, ≥ 9	-41.5	-41.5	-41.6
0.31	≤ 2, ≥ 10	-43.3	-42.7	-42.3
0.26	≤ 2, ≥ 11	-44.5	-43.1	-42.5
0.22	≤ 2, ≥ 12	-46.2	-45.6	-45.2
0.20	≤ 2, ≥ 13	-44.2	-41.2	-39.0
0.17	≤ 2, ≥ 14	-44.9	-39.8	-35.7
0.16	≤ 2, ≥ 15	-39.7	-41.8	-43.3
0.10	≤ 2	-32.6	-31.9	-31.6

Table E.8: Root diameter and corresponding uncertainty (average mean) of the vegetation densities for drag and pull-out 30+ cm erosion condition.

Velocity (m/s)	Root diameter removed (cm)	Uncertainty (%)		
		Sparse	Moderate	Dense
0.35+	All	-51.6	-51.6	-51.6
0.33	≤ 4, ≥ 6	-47.2	-45.6	-44.1
0.31	≤ 4, ≥ 8	-51.3	-50.6	-49.9
0.30	≤ 4, ≥ 9	-52.6	-50.0	-47.4
0.27	≤ 4, ≥ 10	-54.8	-52.2	-50.0
0.26	≤ 3, ≥ 10	-54.7	-53.7	-53.0
0.24	≤ 3, ≥ 11	-55.4	-54.6	-54.2
0.22	≤ 3, ≥ 12	-55.4	-54.7	-54.1
0.19	≤ 3, ≥ 13	-54.4	-50.2	-46.2
0.17	≤ 3, ≥ 14	-51.9	-51.7	-51.1
0.15	≤ 3, ≥ 15	-50.2	-53.3	-57.5

Table E.9: Root diameter and corresponding uncertainty (average mean) of the vegetation densities for varying deposition levels.

Deposition (cm)	Root diameter removed (cm)	Uncertainty (%)		
		Sparse	Moderate	Dense
23	≤1	-43.4	-42.0	-42.0
32	≤2	-38.8	-38.8	-38.8
41	≤3	-42.4	-42.8	-44.0
50	≤4	-43.3	-43.8	-45.0
≥59	All	-41.8	-42.4	-43.1

Table E.10: Root diameter and corresponding uncertainty (average mean) of the vegetation densities for submerged inundation condition with 50% mortality.

Root diameter (cm)	50% mortality: Submerged		
	Sparse	Moderate	Dense
≤1	0.0	0.0	0.0
≤2	-22.4	-23.8	-24.4
≤3	-24.7	-25.8	-26.6
≤4	-26.9	-28.1	-29.4
≤5	-29.3	-31.1	-34.2
≤6	-31.1	-33.5	-37.7
≤7	-34.1	-37.3	-42.1
≤8	-36.6	-40.6	-45.6
≤9	-39.4	-42.4	-46.4

Table E.11: Root diameter and corresponding uncertainty (average mean) of the vegetation densities for submerged inundation condition with 100% mortality.

Root diameter (cm)	100% mortality: Submerged		
	Sparse	Moderate	Dense
≤1	-6.0	-6.0	-6.0
≤2	-5.8	-5.8	-5.7
≤3	-11.1	-11.7	-13.4
≤4	-12.4	-13.1	-14.9
≤5	-13.7	-14.7	-17.0
≤6	-14.5	-15.8	-18.4
≤7	-16.0	-17.6	-20.4
≤8	-17.4	-19.5	-22.4
≤9	-19.2	-20.8	-23.0

Table E.12: Root diameter and corresponding uncertainty (average mean) of the vegetation densities for emergent inundation condition with 50% mortality.

Root diameter (cm)	50% mortality: Emergent		
	Sparse	Moderate	Dense
≤1	0.0	0.0	0.0
≤2	-7.6	-8.1	-8.3
≤3	-4.6	-4.5	-3.5
≤4	-5.2	-5.2	-4.7
≤5	-6.7	-7.2	-8.2
≤6	-8.0	-9.1	-11.2
≤7	-10.7	-12.6	-16.0
≤8	-13.0	-16.0	-20.1
≤9	-16.2	-18.3	-21.4

Table E.13: Root diameter and corresponding uncertainty (average mean) of the vegetation densities for emergent inundation condition with 100% mortality.

Root diameter (cm)	100% mortality: Emergent		
	Sparse	Moderate	Dense
≤1	-39.0	-39.0	-39.0
≤2	-34.5	-34.2	-34.1
≤3	-32.5	-32.1	-31.4
≤4	-31.3	-30.8	-29.9
≤5	-29.9	-29.1	-27.2
≤6	-28.8	-27.5	-24.9
≤7	-26.6	-24.7	-21.5
≤8	-24.7	-22.0	-18.3
≤9	-22.1	-20.1	-17.3

E.12: Simulated flood events DoD statistics

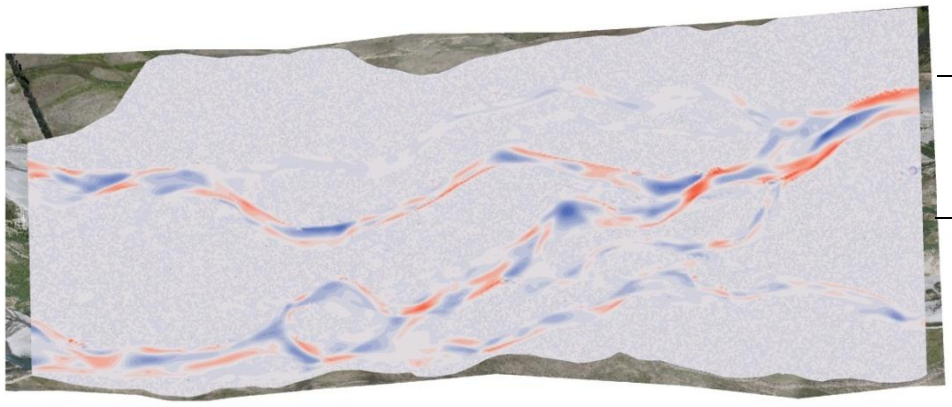

	Volume (m^3)
Eros.	18,266
Deps.	17,346
Diff.	-920

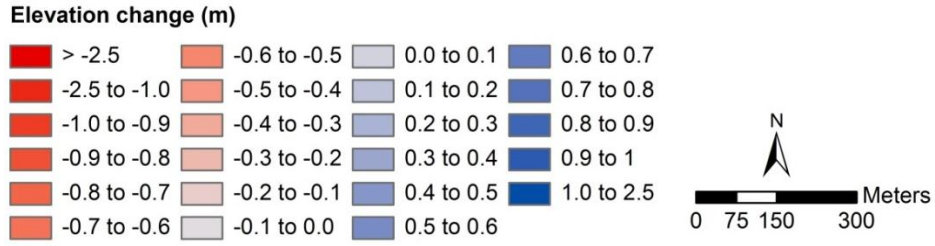

Figure E.36: DEM of Difference of final topography of the 2-year simulated flood event.

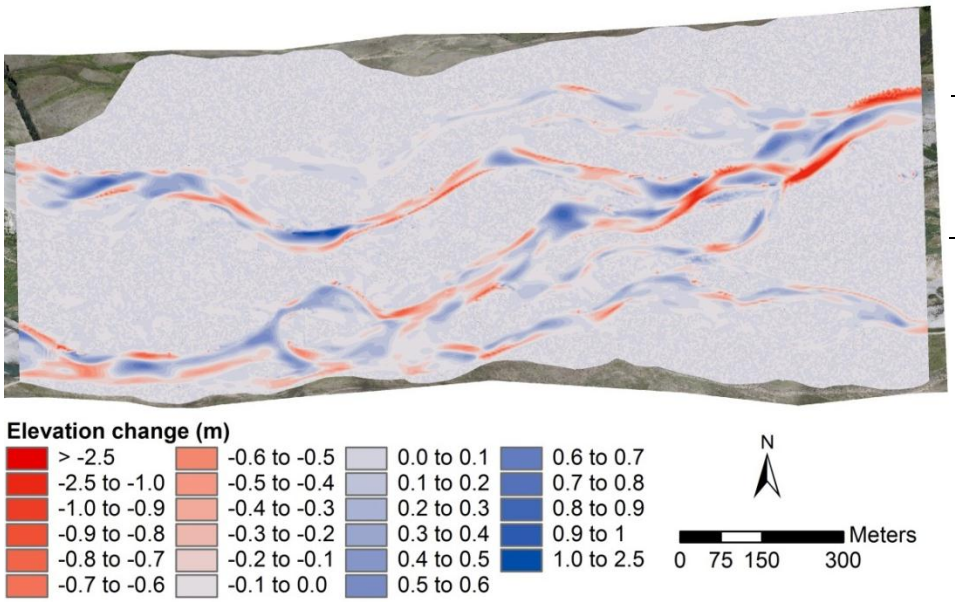

	Volume (m^3)
Eros.	29,527
Deps.	27,931
Diff.	-1,596

Figure E.37: DEM of Difference of final topography of the 5-year simulated flood event.

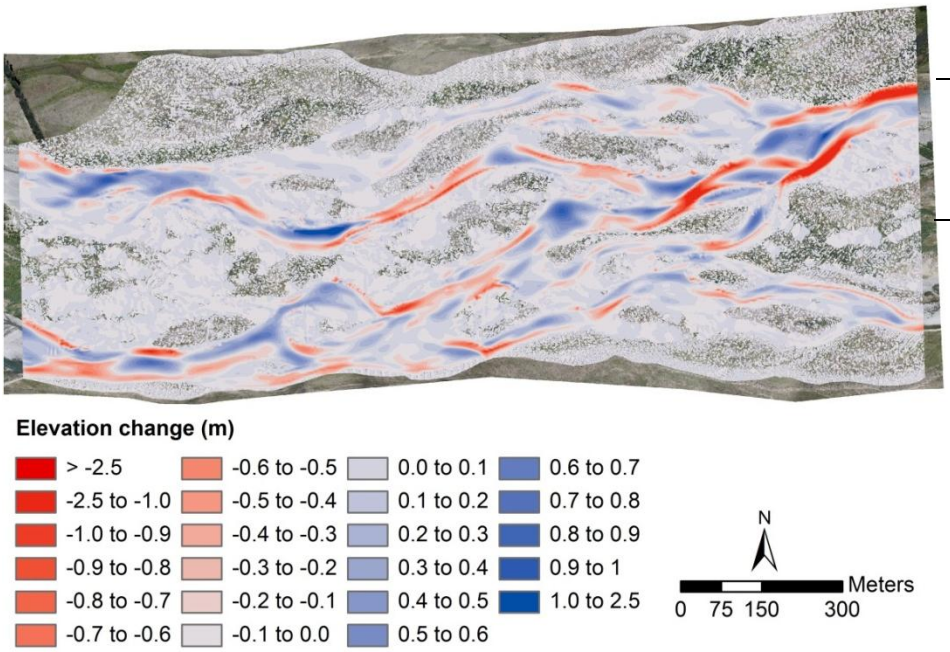

	Volume (m^3)
Eros.	37,858
Deps.	35,598
Diff.	-2,260

Figure E.38: DEM of Difference of final topography of the 10-year simulated flood event.

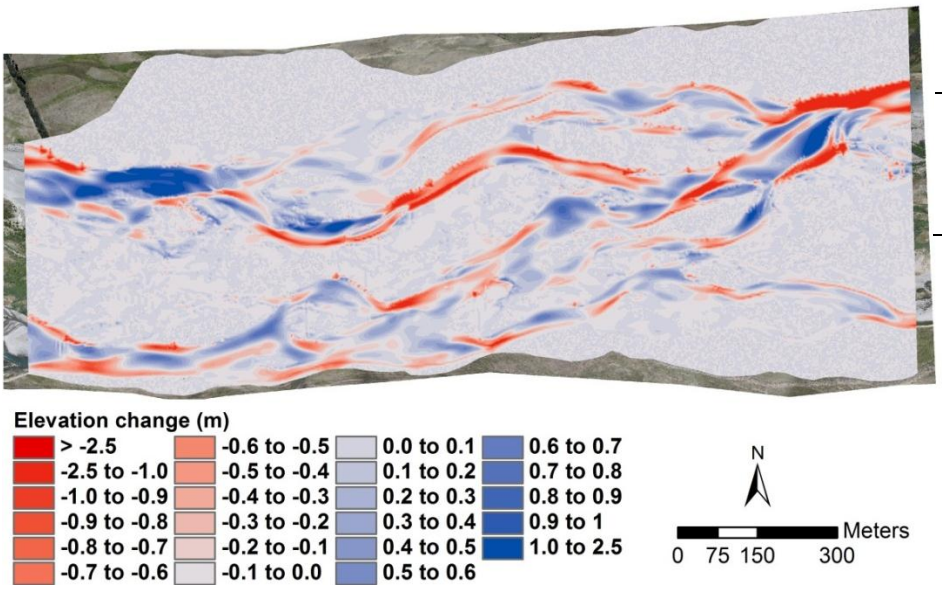

	Volume (m^3)
Eros.	61,926
Deps.	60,434
Diff.	-1,492

Figure E.39: DEM of Difference of final topography of the 25-year simulated flood event.

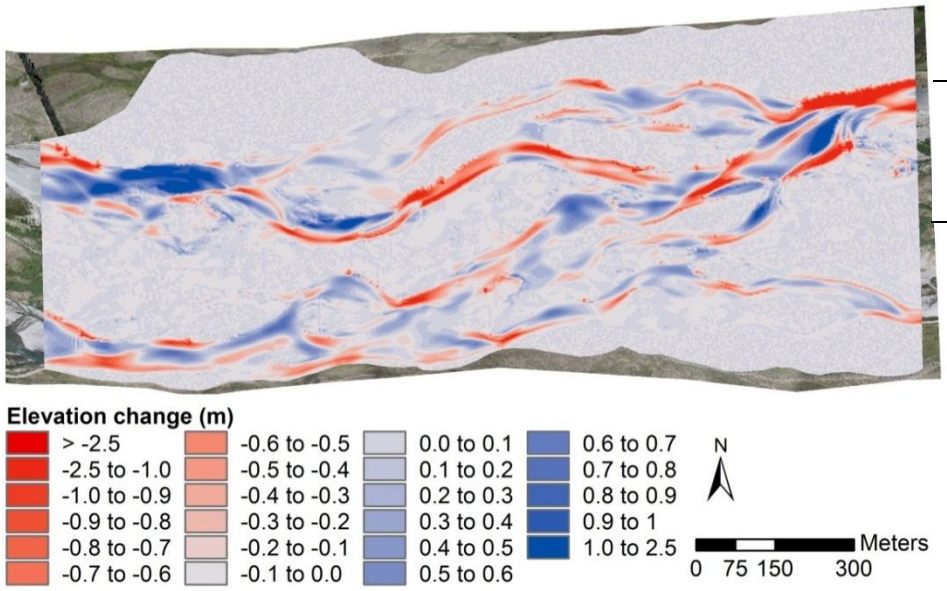

	Volume (m^3)
Eros.	61,895
Deps.	60,319
Diff.	-1,576

Figure E.40: DEM of Difference of final topography of the 50-year simulated flood event.

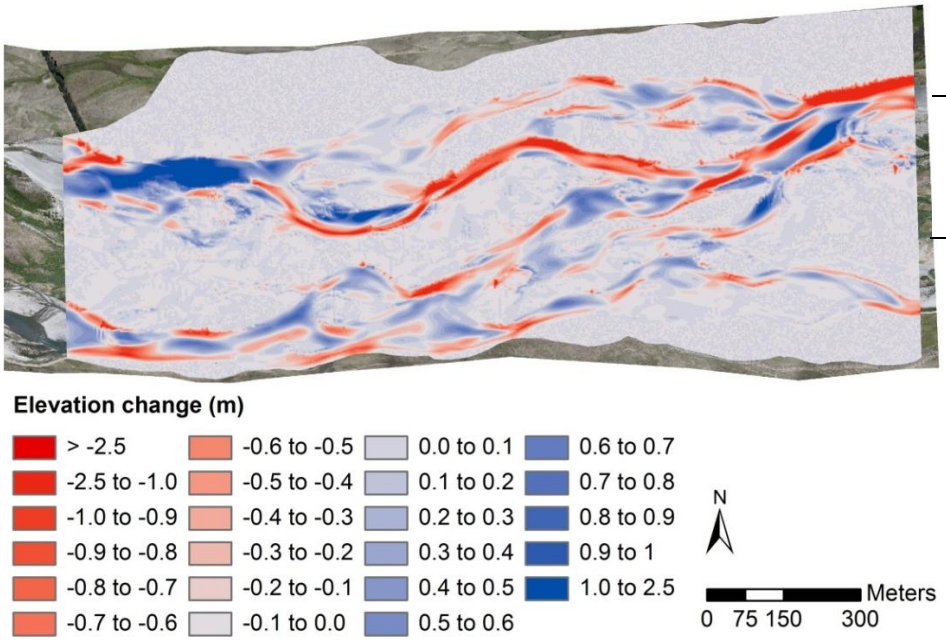

	Volume (m^3)
Eros.	73,834
Deps.	70,642
Diff.	-3,192

Figure E.41: DEM of Difference of final topography of the 100-year simulated flood event.

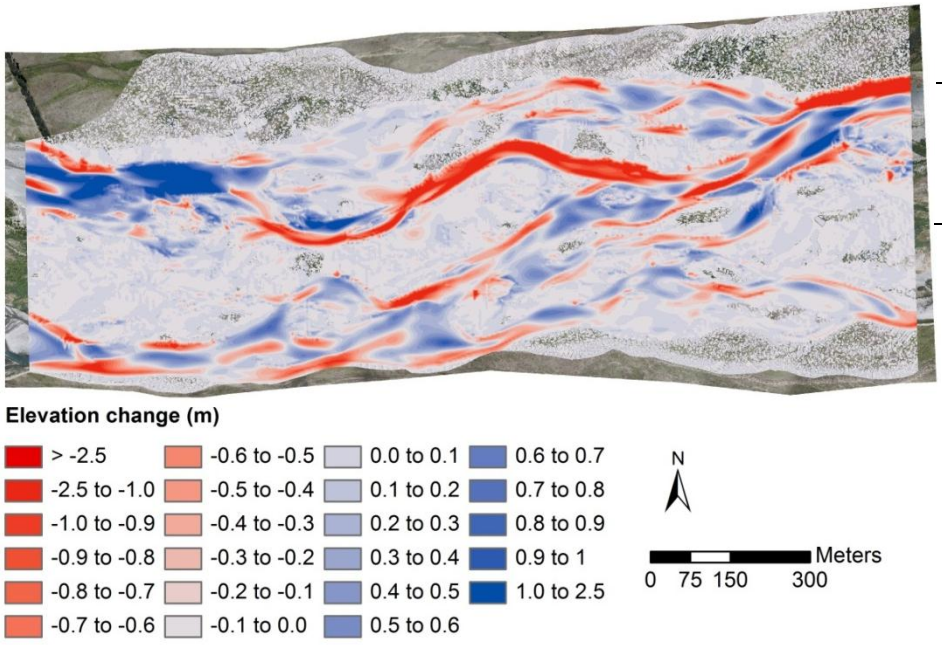

	Volume (m^3)
Eros.	87,944
Deps.	81,435
Diff.	-6,509

Figure E.42: DEM of Difference of final topography of the 200-year simulated flood event.

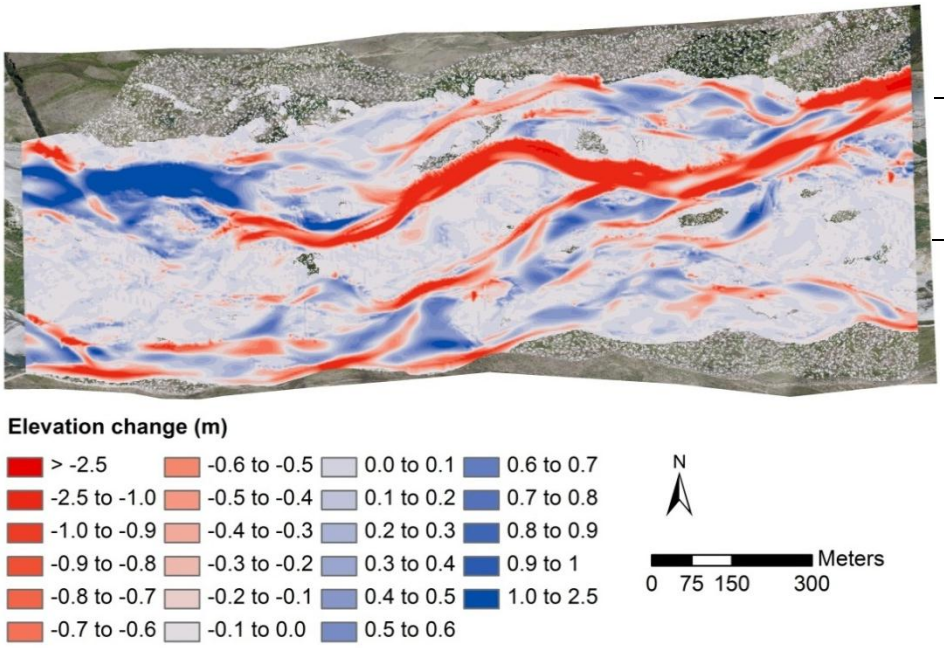

	Volume (m^3)
Eros.	128,150
Deps.	91,731
Diff.	-36,419

Figure E.42: DEM of Difference of final topography of the 500-year simulated flood event.

References

Abt, S. R., Clary, W. P., & Thornton, C. I. (1994). Sediment deposition and entrapment in vegetated streambeds. *Journal of Irrigation and Drainage Engineering, 120*(6), 1098-1111.

AgiSoft LLC. (2010). AgiSoft PhotoScan professional edition. Retrieved from http://www.agisoft.ru/products/photoscan/

AgiSoft LLC. (2012a). Agisoft PhotoScan User Manual: Professional Edition, Version0.8.5. Retrived June 15, 2012 from http://www.agisoft.ru/products/photoscan/professional/

AgiSoft LLC. (2012b). Agisoft PhotoScan Changelog. Retrieved June 15, 2012 from http://downloads.agisoft.ru/pdf/photoscan_changelog.pdf

Ali, F. (2010). Use of vegetation for slope protection: Root mechanical properties of some tropical plants. *International Journal of Physical Sciences, 5*(5), 496-506.

Antonarakis, A.**S.,** Richards, K.S., Brasington, J., & Bithell, M. (2009). Leafless roughness of complex tree morphology using terrestrial lidar, *Water Resources Research*, 45, W10401. doi:10.1029/2008WR007666

Ashmore, P., & Sauks, E. (2006). Prediction of discharge from water surface width in a braided river with implications for at-a-station hydraulic geometry. *Water Resources Research, 42*(3), W03406. doi: 10.1029/2005wr003993

Astre, H., (2010). SFMToolkit. Retrieved from http://www.visual-exeriments.com/demos/sfmtoolkit. (pp. 398).

Baets, S., Poesen, J., Reubens, B., Wemans, K., Baerdemaeker, J., & Muys, B. (2008). Root tensile strength and root distribution of typical Mediterranean plant species and their contribution to soil shear strength. *Plant and Soil, 305*(1-2), 207-226. doi: 10.1007/s11104-008-9553-0

Baltsavias, E. P. (1999). A comparison between photogrammetry and laser scanning. ISPRS *Journal of Photogrammetry and Remote Sensing, 54*(2–3), 83-94.

Baptist, M. J. (2005). Modeling floodplain biogeomorphology. Ph.D. thesis, Delft University of Technology.

Beavan, J., Denys, P., Denham, M., Hager, B., Herring, T., Molnar, P. (2010). Distribution of present-day vertical deformation across the Southern Alps, New Zealand, from 10 years of GPS data. *Geophysical Research Letters. 37*(5).

Bell, S. (1999). A beginner's guide ot uncertainty of measurement. Measurement good practice guide No. 11, (1), 41. Retrieved from http://www.wmo.int/pages/prog/gcos/documents/gruanmanuals/UK_NPL/mgpg11.pdf

Bennett, S. J., Pirim, T., & Barkdoll, B.D. (2002). Using simulated emergent vegetation to alter stream direction within a straight experimental channel. *Geomorphology*, *44*, 115-126.

Bertoldi, W., Gurnell, A., Surian, N.;, Tockner, K., Zanoni, L., Ziliani, L., & Zolezzi, G., (2009). Understanding reference processes: Linkages between river flows, sediment dynamics and vegetated landfroms along the Tagliamento River, Italy. *River Research and Applications. 25*, 501-516. doi: 10.1002/rra.1233

Best, J. (2008). Collaborative research: A field and numerical study of the morphology, flow, sediment processes, and stability of sand-bed fluvial bifuractions. Retrieved March 27, 2011 from http://www.geosc.psu.edu/people/faculty/personalpages/rslingerland/NSFFINALBIF2008Proposal.pdf

Brasington, J., Rumsby, B. T., & McVey, R. A. (2000). Monitoring and modeling morphological change in a braided gravel-bed river using high resolution GPS-based survey, *Earth Surface Processes and Landforms*, *25*(9), 973-990.

Brasington, J., Langham, J., & Rumsby, B. (2003). Methodological sensitivity of morphometric estimates of coarse fluvial sediment transport. *Geomorphology 53*, 299-316.

Brasington, J., Hicks, D. M., Vericat, D., Batalla, R., Williams, R., Goodsell, B., Rennie, C., Smith, M., & Wheaton, J. (2009, May). ReesScan: Hyperscale modeling of the Rees River. Retrieved from http://www.reesscan.org/Home

Brasington, J., & Vericat, D. (2010). Recent developments in geomatics applied to Geomorphology. Trabajos Geomorfología en España, 2008-2010. SEG, 167-187.

Brasington, J., Vericat, D., & Rychkov, I. (2012). Modeling river bed morphology, roughness, and surface sedimentology using high resolution terrestrial laser scanning. *Water Resources Research, 48*(11), W11519. doi: 10.1029/2012wr012223

Brookes, C.J., Hooke, J.M., & Mant, J., (2000). Modeling vegetation interaction with channel flow in river valley of the Mediterranean region. *Catena 40*, 93-118.

Brown, K. P., & Sanders, M. D. (1999). Project River Recovery strategic plan 1998-2005. Unpublished Project River Recovery Report 99/12, Department of Conservation, Twizel, New Zealand.

Brown, K. P., & Sanders, M. D. (2001). Project River Recovery annual report 1 July 2000-30 June 2001. Unpublished Project River Recovery Report 00/13, Department of Conservation, Twizel, New Zealand.

Butler, J. B., Lane, S. N., Chandler, J. H. (1998). Assessment of DEM quality characterizing surface roughness using close range digital photogrammetry. *Photogrammetric Record 16*(92), 271-291.

Carbonneau, P. E., Lane, S. N., & Bergeron, B. (2006). Feature based image processing methods applied to bathymetric measurements from airborne remote sensing in fluvial environments. *Earth Surface Processes and Landforms*, *31*(11), 1413-1423.

Carollo, F. G., Ferro, V., & Termini, D. (2002). Flow Velocity Measurements in Vegetated Channels. *Journal of Hydraulic Engineering, 128*(7), 664-673.

Caruso, B. (2006). Project River Recovery: Restoration of Braided Gravel-Bed River Habitat in New Zealand's High Country. *Environmental Management, 37*(6), 840-861.

Chandler, J. (1999). Effective application of automated digital photogrammetry for geomorphological research. *Earth Surface Processes and Landforms, 24*, 51-63.

Corenblit, D., Tabacchi, E., Steiger, J., & Gurnell, A. M. (2007). Reciprocal interactions and adjustments between fluvial landforms and vegetation dynamics in river corridors: A review of complementary approaches. *Earth-Science Reviews, 84*(1-2), 56-86. doi: 10.1016/j.earscirev.2007.05.004

Coulthard, T. J., Hicks, D. M., & Van De Wiel, M. J. (2006). Cellular modeling of river chatchments and reaches: Advantages, limitations and prospects. *Geomorphology, 90*, 192-207.

Coulthard, T., & Van De Wiel, M. (n.d.). The cellular automaton evolutionary slope and river model (CAESAR). Retrieved from http://www.coulthard.org.uk/downloads/ CAESAR_instructions2.pdf

Darby, S. E., Alabyan, A. M., & Van de Wiel, M. J. (2002). Numerical simulation of bank erosion and channel migration in meandering rivers. *Water Resources Research, 38*(9), 1163. doi: 10.1029/2001wr000602

Daughney, C. J., Fakih, M., & Châtellier, X. (2011). Progressive sorption and oxidation/hydrolysis of Fe(II) affects cadmium immobilization by bacteria-iron oxide composites. *Geomicrobiology Journal*, 28(1), 11-22. doi:10.1080/ 01490451003614989

Deltares (2010). *Delft3D-Flow: User manual.* Rotterdamseweg: Deltares.

Deng, Z., An, S., Zhao, C., Chen, L., Zhou, C., Zhi, Y., & Li, H. (2008). Sediment burial stimulates the growth and propagule production of Spartina alterniflora Loisel. *Estuarine, Coastal and Shelf Science, 76*(4), 818-826. doi:10.1016/ j.ecss.2007.08.008

DHI Water and Environment (2004). *Mike 21C river morphology: A short description.* Retrieved March 22, 2011 from http://mikebydhi.com/upload/dhisoftwarearchive /shortdescriptions/wr/m21c _short_2004.pdf

DoC. (1996). A directory of wetlands in New Zeland. The Department of Conservation, Wellington, New Zealand. (pp. 393).

DoC. (2000a). Project River Recovery's predator research. The Department of Conservation, Wellington, New Zealand.

DoC. (2000b). Project River Recovery's wetland construction. The Department of Conservation, Wellington, New Zealand.

DoC. (2000c). High Country DOC: Summer newsletter. The Department of Conservation, Twizel, New Zealand.

DoC (2000d). Ben Avon conservation resources report. The Department of Conservaton, Twizel, New Zealand.

DoC. (2007). Russell lupin – problem weed. Project River Recovery's predator research. The Department of Conservation, Twizel, New Zealand.

DoC. (2009). River life: Explore the ecology of braided rivers in the Mackenzie Basin. In Department of Conservation (Ed.), *Canterbury Conservancy*. Christchurch.

Doneus, M., Verhoeven, G., Fera, M., Briese, C., Kucera, M., & Neubauer, W. (2011). From deposit to point cloud – A study of low cost computer vision approaches for the staigtforward documentation of archaeological excavations. Proceedings of the XXIIIrd International CIPA Synposium, Prague, Czech Republic, Septermber 12-16, 2011.

Dowling, T. I., Read, A. M., & Gallant J.C. (2009). Very high resolution DEM acquisition at low cost using a digital camera and free software. *18th World IMACS/MODSIM Congress Transactions on*, 2479-2485.

Duncan, M., & Bind, J. (2009). Waiau River instream habitat based on 2-D hydrodynamic modeling. National Institute of Water & Atmospheric Research Ltd. (NIWA), Christchurch. Report CHC2008-176.

Duncan, M. J., & Woods, R. A. (2004). *Freshwaters of New Zealand.* Harding, J., Mosley, M. P., Pearson, C. P. & Sorrell, B. K. (eds.). Wellington:New Zealand Hydrological Society and New Zealand Limnological Society, (pp. 7.1-7.14).

Duran, R., Beevers, L., Crosato, A., & Wright, N. (2010). Bank retreat study of a meandering river reach case study: River Irwell. Proceedings of 7th International Synposium on Ecohydraulics, Concepcion, Chile.

Electricity Authority. (2010). Electricity in New Zealand. Retrieved from www.ea.govt.nz/document/12098/download/...us/documents-publications/

Ellison, S., Rosslein, M., & Williams, A. (Eds.). (2000). *Second edition of the EURACHEM Guide Quantifying Uncertainty in Analytical Measurement* (Vol. 5): Springer-Verlag.

Emerson, J., Esty, D., Kim, C., Srebotnjak, T., Levy, M., Mara, V., Jaiteh, M. (2010). Environmental Performance Index 2010. Retrieved January, 30, 2011, from http://epi.yale.edu/

Enggrob, H. G., & Tjerry, S. (1999). Simulation of morphological characteristics of a braided river. *International Association for Hydraulics, 2*, 585-594.

Environment Canterbury. (2011). Upper Waitaki Committee Membership. Retrieved November, 4th, 2011, from http://ecan.govt.nz/get-involved/canterburywater/committees /upper-waitaki/Pages/membership.aspx

Erber, K., Kambergs, P., Lampe, V., & Reich, M. (1997). Die bedeutung der abfluβdynamik für die vegetationsentwicklung in umlagerungsstrecken der oberenn Isar. *Laufener Seminarbeiträge 4/97*, 63-72.

Fathi-Maghadam, M., & Kouwen, N. (1997). Nonrigid, nonsubmerged, vegetative roughness on floodplains. *Journal of Hydraulic Engineering, 123*(1), 51-57.

Fonstad, M., Dietrich, J., Courville, J., Jensen, B., & Carbonneau, P. (2011a). Topographic structure from motion. Proceedings from the American Geophysical Union. San Francisco, CA.

Fonstad, M., Dietrich, J., Courville, B., Jensen, J., Carbonneau, P. (2011b). High resolution, low cost 3D riverscape mapping using field photography. Proceedings from the American Fisheries Society Annual Meeting, Seattle, WA.

Fonstad, M. A., & Marcus, W. A. (2005). Remote sensing of stream depths with hydraulically assisted bathymetry (HAB) models. *Geomorphology, 72*(1–4), 320-339.

Freeman, G. E., Rahmeyer, W. J., & Copeland, R. R. (2000). Determination of resistance due to shrubs and woody vegetation, Coastal Hydraulic Lab. Rep. ERDC/CHL TR-00-25, 33 pp., U.S. Army Eng. Res. and Dev. Cent., Vicksburg, Mississippi.

Friedman, J. M., & Auble, G. T. (1999). Mortality of riparian box elder from sediment mobilization and extended inundation. *Regulated Rivers: Research and Management 15*, 463–476.

Friend, A. P., & Sanders, M. D. (2000). Production, density, attrition, and depth distribution of Russell lupin seeds in the Ahuriri and Tasman Rivers. *Project River Recovery Report, 99/16.*

Furukawa, Y., Curless, B., Seitz, S.N. and Szeliski, R. (2010). Clustering views for multi-view stereo, Proceedings from the IEEE Conference on Computer Vision and Pattern Recognition (CVPR), San Francisco, (pp. 1434-1441).

Furukawa, Y., & Ponce, J. (2010). Accurate, dense, and robust multiview stereopsis. Pattern analysis and machine intelligence, *IEEE Transactions on*, *32*(8), 1362-1376.

Gabites, S., & Horrell, G. (2005). Seven day mean annual low flow mapping of the tributaries of the Waitaki River: Environment Canterbury.

Gao, J. (2009). Bathymetric mapping by means of remote sensing: methods, accuracy and limitations. *Progress in Physical Geography, 33*(1), 103-116. doi: 10.1177 /0309133309105657

Garcia, M. H. (2008). Sediment transport and morphodynamics. In M. H. Garcia (Ed.), Sedimentation Engineering: Processes, measuremnets, modeling, and practice (21 - 146). Reston, Virginia 20191: American Society of Civil Engineers.

Geodetic Systems (2012). The basics of photogrammetry. Retrieved from http://www. geodetic.com/v-stars/ what-is-photogrammetry.aspx

Gran, K., & Paola, C. (2001). Riparian vegetation controls on braided stream dynamics. *Water Resources Research, 37*, 3275-3283.

Gray, D., & Harding, S. (2007). Braided river ecology: A literature review of physical habitats and aquatic invertebrate communities. Science and Technical Publishing. Department of Conservation, Wellington, New Zealand.

Griffiths, G. A. (1979). High sediment yields from major rivers of the Western Southern Alps, New Zealand. *Nature*, *282*(5734), 61-63. doi: 10.1038/282061a0

Gyssels, G., Poesen, J., Bochet, E., & Li, Y. (2005). Impact of plant roots on the resistance of soils to erosion by water: a review. *Progress in Physical Geography*, *29*(2), 189-217.

Hasselaar, R. W. (2012). Development of a generic automated instrument for the calibration of morphodynamic Delft3D model applications. Masters thesis, Delft University of Technology.

Helmiö, T. (2002). Unsteady 1D flow model of compound channel with vegetated floodplains. *Journal of Hydrology*, *269*(1-2), 89-99. doi: 10.1016/S0022-1694(02)00197-X

Heppelthwaite, S. (1999). Restoring Braided Rivers. *Forest and Bird*, 38-41.

Hering, D., Gerhard, M., Manderbach, R., & Reich, M. (2004). Impact of a 100-year flood on vegetation, benthic invertebrates, riparian fauna and large woody debris standing stock in an alpine floodplain. *River Research and Applications*, *20*(4), 445-457.

Hewlett-Packard. (n.d.). Statistics - Weighted mean. *hp calculators*, 5. Retrieved from hp calculators website: http://h20331.www2.hp.com/Hpsub/downloads/HP12Cweighted.pdf

Hickin, E. J., & Sichingabula, H. M. (1988). The geomorphic impact of the catastrophic October 1984 flood on the planform of Squamish River, southwestern British Columbia. *Canadian Journal of Earth and Science*, *25*, 1078 – 1087.

Hicks. D. M., Westaway, R., & Lane, S. (2003). A bird's-eye assessment of gravel movement in large braided rivers. *Water & Atmosphere*. *11*(1), 21-23.

Hicks, D. M., Duncan, M. J., Lane, S. N., Tal, M., & Westaway, R. (2008). Contemporary morphological change in braided gravel-bed rivers: new developments from field and laboratory studies, with particular reference to the influence of riparian vegetation. In H. P. Helmut Habersack & R. Massimo (Eds.), *Developments in Earth Surface Processes* (Vol. 11, pp. 557-584): Elsevier.

Hicks, D. M., Shankar, U., McKerchar, A. I., Basher, L., Lynn, I., Page, M. & Jessen, M. (2011). Suspended sediment yields from New Zealand rivers. *Journal of Hydrology, 50* (1), 81-142.

Hill, M. C. (2006). The pactical use of simplicity in developing ground water models. *Ground Water, 44*(6), 775-781. doi: 10.1111/j.1745-6584.2006.00227.x

Hill, M.C., & Tiedeman, C.R. (2007). *Effective groundwater model calibration: With analysis of data, sensitivities, predictions, and uncertainty*. Hoboken, New Jersey: Wiley and Sons.

Hong, L.E. B. A., & Davies, T. R. H. (1979). A study of stream braiding: Summary. *Geological Society of America bulletin. 90*(12), 1094. doi: 10.1130/0016-7606(1979)90

Hughey, K., & Warren, A. (1997). Habitat restoration for wildlife nesting on degraded braided riverbeds in New Zealand. I*n* Hale, P., & Lamb, D. (Eds), Conservation Outside Nature Reserves (pp. 334-343). Centre for Conservation Biology, University of Queensland, Australia.

James, C. S., Birkhead, A. L., Jordanova, A. A., Kotschy, K. A., Nicolson, C. R., & Makoa, M. J. (2001). Interaction of reed distribution, hydraulics and river morphology. Rep NO 856/1/01, Water Research Commission, South Africa.

James, M. R., & Robson, S. (2012). Straightforward reconstruction of 3D surfaces and topography with a camera: Accuracy and geoscience application. *Journal of Geophysical Research., 117*(F3), F03017. doi: 10.1029/2011jf002289

Järvelä, J. (2002). Flow resistance of flexible and stiff vegetation: a flume study with natural plants. *Journal of Hydrology, 269*(1-2), 44-54.

Jordan, D. C., & Fonstad, M. A. (2005). Two dimensional mapping of river bathymetry and power using aerial photography and GIS on the Brazos River, Texas. *Geocarto International, 20*(3), 13-20.

Jordanova, A. A., James, C. S. (2003). Experimental study of bedload transport through emergent vegetation. *Journal of Hydraulic Engineering, 129*(6), 474-478. doi: 10.11061

Keijzer, M., Baptist, M., Babovic, V., & Uthurburu, J. R. (2005). *Determining equations for vegetation induced resistance using genetic programming*. Paper presented at the Proceedings of the 2005 conference on Genetic and evolutionary computation, Washington DC, USA.

Kjellman, E. (2012). From 2D to 3D: A photogrammetric revolution in archaeology. (Masters thesis). Retrieved from Academia.edu. University of TromsØ.

Kollmann, J., Vieli, M., Edwards, P. J., Tockner, K., & Ward, J. V. (1999). Interactions between vegetation development and island formation in the alpine river Tagliamento. *Applied Vegetation Science, 2*(1), 25-36.

Kouwen, N., & Li, R. M. (1980). Biomechanics of vegetative channel linings. *Journal of Hydraulics Division, ASCE, 106*(6), 1085-1103.

Kouwen, N., Unny, T. E., & Hill, H. M. (1969). Flow retardance in vegetated channels. *Journal of Irrigation and Drainage Division, ASCE, 95*(2), 329 – 342.

Kouwen, N., & Unny, T. E., (1973). Flexible roughness in open channels. *Journal of the Hydraulics Division, ASCE* 99 (5), 713 –728.

Kraus, K. (2007). Photogrammetry: Geometry from images and laser scans. New York: Walter De Gruyter.

Lane S. N. (1998). The use of digital terrain modeling in the understanding of dynamic river channel systems. In Landform Monitoring,Modeling & Analysis, Lane SN, Richards KS, Chandler JH (eds), (pp. 311-342). John Wiley & Sons: Chichester.

Lane, S. N., Chandler, J. H., & Richards, K. S. (1994). Developments in monitoring and modelling small-scale river bed topography. *Earth Surface Processes and Landforms, 19*(4), 349-368. doi: 10.1002/esp.3290190406

Lane, S. N., James, T. D. & Crowell, M. D. (2000). Application of digital photogrammetry to complex topography for geomorphological research. *Photogrammetric Record, 16*(95): 793-434 821.

Lane, S. N., & Ferguson, R. I. (2005). Modeling reach-scale fluvial flows computational fluid dynamics (pp. 215-269). John Wiley & Sons, Ltd.

Legleiter, C. J., Roberts, D. A., Marcus, W. A., & Fonstad, M. A. (2004). Passive optical remote sensing of river channel morphology and in-stream habitat: Physical basis and feasibility. *Remote Sensing of Environment, 93*(4), 493-510.

Lejot, J., Delacourt, C., Piégay, H., Fournier, T., Trémélo, M. L., & Allemand, P. (2007). Very high spatial resolution imagery for channel bathymetry and topography from an unmanned mapping controlled platform. *Earth Surface Processes and Landforms, 32*(11), 1705-1725.

Lesser, G. R., Roelvink, J. A., van Kester, J. A. T. M., & Stelling, G. S. (2004). Development and validation of a three-dimensional morphological model. *Coastal Engineering, 51*, 883-915.

Leonard, L. A., & Luther, M. E. (1995). Flow hydrodynamics in tidal marsh canopies. *Limnology and Oceanography, 40*(8), 1474-1484.

Leopold, L. B., Wolman, M.G., & Miller, J.P. (1964). *Fluvial processes in geomorphology*. San Francisco, California: W.H. Freeman.

Li, R. M., & Shen, H.W. (1973). Effect of tall vegetations on flow and sediment. *Journal of the Hydraulics Division, ASCE, 99* (5), 793–814.

Lowe, D., 2004. Distinctive image features from scale-invariant keypoints. *International Journal of Computer Vision, 60*(2), 91-110.

Lowe, B. J., Watts, R. J., Roberts, J., & Robertson, A. (2010). The effect of experimental inundation and sediment deposition on the survival and growth of two herbaceous riverbank plant species. *Plant Ecology, 209*(1), 57-69. doi: 10.1007/s11258-010-9721-1

Lyzenga, F. R. (1981). Remote sensing of bottom reflectance and water attenuation parameters in shallow water using aircraft and Landsat data. *International Journal of Remote Sensing*, 2, 71-82.

Maloney, R. F., Rebergen, A. L., Nilsson, R. J., & Wells, N. J. (1997). Bird density and diversity in braided river beds in the Upper Waitaki Basin, South Island, New Zealand, 44, 210–232.

Manning, R. (1891). On the flow of water in open channels and pipes. Transactions, vol. 20. *Institution of Civil Engineers of Ireland*, 161-207.

Marcus, W. A., & Fonstad, M. A. (2008). Optical remote mapping of rivers at sub-meter resolutions and watershed extents. *Earth Surface Processes and Landforms, 33*(1), 4-24.

Mathwave (2012). EasyFit – Distribution fitting made easy. Retrieved from http://www.mathwave.com/

Meridian Energy Limited (2008). Discover the Waitaki hydro scheme. Retrieved January 22, 2011 from http://www.meridianenergy.co.nz/NR/rdonlyres/B496C006-3F64-4F0E-8305-C22CAE732A4E/24505/0104MEDWaitakiwebBro12.pdf

Merrett Survey Partnership. (2007). Lidar terrestrial. Retrieved April 14, 2011 from http://www.laserscanning.co.uk/Index.htm

Meurk, C. D., & Williams, P. A. (1989). Plant ecology of braided rivers in Canterbury. Unpublished report. Botany Division, DSIR, Christchurch, New Zealand.

Milan, D. J., Heritage, G. L., Large, A. R. G., & Fuller, I. C. (2011). Filtering spatial error from DEMs: Implications for morphological change estimation. *Geomorphology, 125*(1), 160-171. doi: http://dx.doi.org/10.1016/j.geomorph.2010.09.012

Mosley, M. P. (1982). Analysis of the effect of changing discharge on channel morphology and instream uses in a braided river, Ohau River, New Zealand. *Water Resources Research*, 18(4), 800-812.

Mosley, M. P. (1983). Response of braided rivers to changing discharge. *Journal of Hydrology*. *22*(1), 18-67.

Morisawa, M. (1985). Rivers: Form and process. New York: Longman Group Ltd, (pp. 222).

Murray, A. B., & Paola, C. (1994). A cellular model of braided rivers. *Nature, 371*(6492), 54-54.

Munsun, B. R., Young, D. F., Okiishi, T. H., & Huebsch, W. W. (2009). *Fundamentals of fluid mechanics* (6 ed.). Hoboken, NJ: Don Fowley.

Murray, A. B., & Paola, C. (1994). A cellular model of braided rivers. *Nature, 371*(6492), 54-54.

Murray, A. B., & Paola, C. (1997). Properties of a cellular braided-stream model. *Earth Surface Processes and Landforms, 22*(11), 1001-1025. doi: 10.1002

Murray, A. B., & Paola, C. (2003). Modeling the effect of vegetation on channel pattern in bedload rivers. *Earth Surface Processes and Landforms, 28*(2), 131-143. doi: 10.1002/esp.428

Myers, W. R. C., & Elsawy, E. M. (1975). Boundary shear in channel with flood plain. *Journal of The Hydraulics Division, ASCE, 101(7)*, 933-945.

Nepf, H. M., & Vivoni, E. R. (2000). Flow structure in depth-limited, vegetated flow. *Journal of Geophysical Research, 105*, 28547-28557.

Nicholas, A. P. (2010). Reduced-complexity modeling of free bar morphodynamics in alluvial channels. *Journal of Geophysical Research, 115*(F4).

Nicholas, A. P., Sandbach, S. D., Ashworth, P. J., Amsler, M. L., Best, J. L., Hardy, R. J., Szupiany, R. N. (2012). Modeling hydrodynamics in the Rio Paraná, Argentina: An evaluation and inter-comparison of reduced-complexity and physics based models applied to a large sand-bed river. *Geomorphology, 169–170*(0), 192-211. doi: http://dx.doi.org/10.1016/j.geomorph.2012.05.014

Niethammer, U., James, M. R., Rothmund, S., Travelletti, J., & Joswig, W. (2012). UAV-based remote sensing of the Super Sauze landslide: Evaluation and results. *Engineering Geology, 128*, 2-11.

NIWA. (2007). Water Resources Explorer NZ. Retrieved October, 20, 2013, from http://wrenz.niwa.co.nz/webmodel/

Palmer, V. J. (1945). A method for designing vegetated waterways. *Agricultural Engineering 26*, 516-520.

Palmer, P., & Petrie, M. (1989). Upper Waitaki Catchment: An historical perspective on conservation value impacts. The Department of Conservation, Christchurch.

Patterson, R. (2001). River life: An environmental education resource. Dunedin College of Education, Dunedin.

Pearson, C. P., 1991. New Zealand regional flood frequency analysis using L-Moments. *Journal of Hydrology*, *30*(2), 53-64.

Peat, N., & Patrick, B. (2001). Wild rivers. University of Otago Press, Dunedin, New Zealand.

Petryk, S., & Bosmajian, G. B. (1975). Analysis of flow through vegetation. *Journal of the Hydraulics Division, ASCE 101 (7)*, 871 –884.

Petts, G., & Kennedy, R. (2005). Emerging concepts for integrating human and environmental water needs in river basin management. U.S. Army Corps of Engineers, Washington DC. Retrieved March 11, 2011 from http://el.erdc.usace.army.mil/elpubs/pdf/trel05-13.pdf

Pickrill, R. A., & Irwin, J. (1986). Circulation and sedimentation in Lake Benmore, New Zealand. *New Zealand Journal of Geology and Geophysics. 29, 83-97.*

Poggi, D., Porporato, A., Ridolfi, L., Albertson, J. D., & Katul, G. G. (2004). The effect of vegetation density on canopy sub-layer turbulence. *Boundary-Layer Meteorology, 111*(3), 565-587.

Pollen, N. (2006). Temporal and spatial variability in root reinforcement of streambanks: Accounting for soil shear strength and moisture. *Catena,* (69), 197-205. doi: 10.1002/esp.1085

Prosser, I. P., Dietrich, W. E., & Stevenson, J. (1995). Flow resistance and sediment transport by concentrated overland flow in a grassland valley. *Geomorphology, 13*, 71-86.

Pyle, C. J., Chandler, J. H., Richards, K. S. (1997). Digital photogrammetric monitoring of river bank erosion. *Photogrammetric Record. 15*, 753-764.

Rademaker, M., & Balme, A. (2010). Understanding the hydrology of the Ahuriri River, Upper Waitaki Basin, New Zealand. Unpublished report. University of Canterbury, Christchurch, New Zealand.

Rawlings, M. (1993). Lupins, willows and river restoration in the Upper Waitaki. *Forest and bird*, 10-15.

Refsgaard, J. C., & Henriksen, H. J. (2004). Modeling guidelines – terminology and guiding principles. *Advances in Water Resources, 27*(1), 71-82. doi: http://dx.doi.org/10.1016/j.advwatres.2003.08.006

Resources and Networks Branch (2005, December 19, 2005). Sustainable energy: Creating a sustainable energy system for New Zealand Retrieved January 30, 2011, from http://www.med.govt.nz/templates/MultipageDocumentTOC_10124.aspx

Rhee, D. S., Woo, H., Kwon, B. A., & Ahn, H. K. (2008). Hydraulic resistance of some selected vegetation in open channel Flows. *River Research and Applications, 24*(5), 673-687. doi: 10.1002/rra.1143

Righetti, M., & Armanini, A. (2002). Flow resistance in open channel flows with sparsely distributed bushes. *Journal of Hydrology, 269*(1–2), 55-64. doi: http://dx.doi.org/10.1016/S0022-1694(02)00194-4

Rinaldi, M., & Darby, S. E. (2008). Modeling river-bank-erosion processes and mass failure mechanisms: Progress towards fully coupled simulations. In H. Habersack, H. Piegay & M. Rinaldi (Eds.), Gravel-Bed Rivers VI (Vol. 11, pp. 837): Elsevier Science.

Robertson, D. P., & Cipolla, R. (2009). Structure from Motion. In Varga, M., (Ed.), Practical Image Processing and Computer Vision, John Wiley, 2009.

Ross, A., & Shuker, C. J. (2010). Impact of river flows on exotic vegetation in the Ahuriri River. Unpublished report. University of Canterbury, Christchurch, New Zealand.

Rumsby, B. T., Brasington, J., Langham, J. A., McLelland, S. J., Middleton, R., & Rollinson, G. (2008). Monitoring and modeling partical and reach-scale morphologic change in gravel-bed rivers: Applications and challenges. *Geomorphology, 93*, 40-54. doi: 10.1016/j.geomorph.2006.12.017

Rychkov, I., Brasington, J., & Vericat, D. (2012). Computational and methodological aspects of terrestrial surface analysis based on point louds. *Computers and Geosciences, 42,* 64-70.

Samani, J. M. N., & Kouwen, N. (2002). Stability and erosion in grassed channels. *Journal of Hydraulic Engineering, ASCE, 128,* 40-45.

Sanders, M. D. (2003). Project river recovery annual report 1 July 2001 - 30 June 2002. Unpublished Project River Recovery Report 2002/03, DoC.

Sanders, M. D., & Maloney, R. F. (2002). Causes of mortality at nests of ground-nesting birds in the Upper Waitaki Basin, New Zealand: A five-year video study. *Biological Conservation, 106,* 225-236.

Schuurman, F., & Klienhans, M. G. (2010). Self-formed meandering and braiding channel patterns in a numerical model. Proceedings of the American Geophysical Union Fall Conference, San Francisco, CA, December 2010. Retrieved March 12, 2011 from http://adsabs.harvard. edu/abs/ 2010AGUFMEP51C0561S

SCS/NRCS Hydrographs. Retrieved January 22, 2012, from https://ceprofs.tamu.edu /kbrumbelow/CVEN463/NRCS_Hgraphs.pdf

Semyonov, D. (2011, May 3). Algorithms used in Photoscan [Msg 2]. Message posted to www.agisoft.ru/forum/index.php?topic=89.0

Shaffner, P., Heisler, R., Krosley, L., Kottenstette, J., & Wright, J. (2009). Characterization of dam foundation blocks using digital photogrammetric mapping and borehole geophysical logging to create comprehensive 3D foundation models. Retrieved from http://www.aerialproducts.com/aerial-photography-systems/aerial-balloon-photogrammetry.html

Sheridan, M. (1995). Dam dwellers - End of an era. Sheridan Press, Twizel.

SkyMark. (2013). Excel data analysis: Normal test plot. Retrieved September, 19, 2013, from http://www.skymark.com/resources/tools/normal_test_plot.asp

Smith, L. C., Isacks, B. L., Bloom, A. L., & Murray, A. B. (1996). Estimation of discharge from three braided rivers using synthetic aperture radar satellite imagery: Potential application to ungaged basins. *Water Resources Research, 32*(7), 2021-2034. doi: 10.1029/96wr00752

Snavely, N., Seitz, S. M., & Szeliski, R. (2006). Photo tourism: Exploring photo collections in 3D. *ACM Transactions of Graphics, 25*(3), 835-846.

Snavely, N., Seitz, S., & Szeliski, R. (2008). Modeling the world from internet photo collections. *International Journal of Computer Vision, 80*(2), 189-210.

Soto, A. U., & Madrid-Aris, M. (1994). Roughness coefficient in mountain rivers. In A. U. Soto & M. Madrid-Aris (Eds.), Hydraulics engineering. New York: American Society of Civil Engineers. Retrieved from http://www.madrid-aris.com/ Publications/PapersPDF /Roughness.PDF.pdf

Statistics with n=2. (2013, August 3, 2010). Retrieved July 3, 2013, from http://www .graphpad.com/support/faqid/591/

Stephenson, G. K., Card, B., Mark, A. F., McLean, R., Thompson, K., & Priest, R. M. (1983). Wetlands: A diminishing resource. *National Water and Soil Conservation Organization, 58.*

Strait, J. (2004). What is "35 mm equivalent focal length?" Retrieved April 4, 2011, from http://www.panoramafactory.com/equiv35/equiv35.html

Sutherland, J., Peet, A. H., & Soulsby, R. L. (2004). Evaluating the performance of morphological models. *Coastal Engineering, 51*(8–9), 917-939. doi: http://dx.doi.org/10.1016/j.coastaleng.2004.07.015

Tal, M., Gran, K., Murray, A. B., Paola, C., & Hicks, D. M. (2004). Riparian vegetation as a primary control on channel characteristics in multi-thread rivers, in riparian vegetation and fluvial geomorphology. *Water Science, 8*, 43–58, AGU, Washington, D. C.

Tal, M., & Paola, C. (2007). Dynamic single-thread channels maintained by the interaction of flow and vegetation, *Geology, 35*, 347–350. doi:10.1130/G23260A.1

Tanino, Y., & Nepf, H. M. (2008). Laboratory investigation of mean drag in a random array of rigid, emergent cylinders. *Journal of Hydraulic Engineering, 134*(1), 34-41.

Thornton, C. I., Abt, S. R., & Clary, W. P. (1997). Vegetation influence on small stream siltation. *Journal of the American Water Resources Association, 33*(6), 1279-1288. doi: 10.1111/j.1752-1688.1997.tb03552.x

Thornton, C. I., Abt, S. R., Morris, C. E., & Fischenich, J. C. (2000). Calculating shear stress at channel-overbank interfaces in straight channels with vegetated floodplains. *Journal of Hydraulic Engineering, 126*(12), 929-936.

Triggs, B., McLauchlan, P., Hartley, R., & Fitzgibbon, A. (2000). Bundle adjustment — A modern synthesis. In B. Triggs, A. Zisserman & R. Szeliski (Eds.), *Vision algorithms: Theory and practice* (Vol. 1883, pp. 298-372): Springer Berlin Heidelberg.

Trimble (2012). Datasheet: Trimble R8 GNSS receiver. Retrieved July 24, 2012 from http://www.trimble.com/trimbler8gnss_ds.asp

van Holland, G., Verheyen, B., Jacobs, S., Vandenbruwaene, W., Temmerman, S., Meire, P., Peeters, P., De Schutter, J. (2010). Simulation of hydrodynamics and transport of fine sediments in vegetated polders with a controlled reduced tide: Pilot project Lippenbroek, in: (2010). 8th International Symposium on ecohydraulics 2010 (ISE 2010): bridging between ecology and hydraulics and leading the society's new need - living with nature, September 12-16, 2010, Coex, Seoul, Korea. Proceedings [CD-ROM]. (pp. 1775-1782).

van Maren, D. S. (2007). Grain size and sediment concentration effects on channel patterns of silt-laden rivers. *Sedimentary Geology*, 202(1–2), 297-316. doi: http://dx.doi.org/ 10.1016/j.sedgeo.2007.04.001

Verhoeven, G. (2011). Taking computer vision aloft – archaeological three-dimensional reconstructions from aerial photographs with photoscan. *Archaeological Prospection, 18*(1), 67-73.

Verhoeven, G., Doneus, M., Briese, C., & Vermeulen, F. (2012). Mapping by matching: A computer vision-based approach to fast and accurate georeferencing of archaeological aerial photographs. *Journal of Archaeological Science, 39*(7), 2060-2070. doi: 10.1016/j.jas.2012.02.022

Viessman, W., Lewis, G. L. (2003). *Introduction to Hydrology*. Upper Saddle River, NY: Prentice Hall.

Voskresensky, K. P. (n.d.*). Computation principles of flood hydrographs.* Paper presented at the Liningrad Hydrometeorological Institute, Liningrad, USSR.

Warburton, J. (1996). A brief review of hydraulic modeling of braided gravel-bed rivers in New Zealand. *Journal of Hydrology, 35(2),* 157-173.

Warburton, J., Davies, T. R. H., & Mandl, M. G. (1993). A meso-scale investigation of channel change and floodplain characteristics in an upland braided gravel-bed river, New Zealand. In Best, J., & Bristow, C. S. (Eds). Braided Rivers, Geological Society, London, (75), 241-255.

Westaway, R. M., Lane, S. N., & Hicks, D. M. (2000). The development of an automated correction -procedure for digital photogrammetry for the study of wide, shallow, gravel-bed rivers. *Earth Surface Processes and Landforms, 25*(2), 209-226.

Westaway, R. M., Lane, S. N., & Hicks, D. M. (2003). Remote survey of large-scale braided, gravel-bed rivers using digital photogrammetry and image analysis. *International Journal of Remote Sensing, 24*(4), 795-815. doi: 10.1080/01431160110113070

Westoby, M. J., Brasington, J., Glasser, N. F., Hambrey, M. J., & Reynolds, J. M. (2012). 'Structure-from-Motion' photogrammetry: A low-cost, effective tool for geoscience applications. *Geomorphology, 179*(0), 300-314. doi: http://dx.doi.org/10.1016 /j.geomorph.2012.08.021

What is 35mm equivalent focal length? (2011). The panorama factory. Retrieved from www.panoramafactory.com

Wheaton, J. M. (2008). Uncertainty in morphological sediment budgeting of rivers. Unpublished PhD Thesis, University of Southampton, Southampton, (pp. 412).

Wheaton, J. M., Brasington J., Darby S. E., & Sear, D. (2010). Accounting for uncertainty in DEMs from repeat topographic surveys: Improved sediment budgets. *Earth Surface Processes and Landforms.* 35(2), 136-156. doi: 10.1002/esp.1886

Wheaton, J. (2012). Geomorphic change detection. Retrieved November, 12, 2012, from http://gcd.joewheaton.org/

Williams, R. D., J. Brasington, D. Vericat, D. M. Hicks, F. Labrosse, and M. Neal (2011). Monitoring braided river change using terrestrial laser scanning and optical bathymetric mapping, in Geomorphological mapping: methods and applications, (Ed) by M. Smith, P. Paron and J. Griffiths, Elsevier, Amsterdam.

Williams, R., Brasington, J., Vericat, D., & Hicks, D. M. (2012a). The fusion of terrestrial laser scanning and optical bathymetric mapping to monitor braided river morphology. (Unpubished article). Aberystwyth University, UK.

Williams, R., Measures, R., Hicks, M., & Brasington, J. (2012b). Braided river simulation: Assessing hydraulic and morphodynamic predictions using high resoution field data. Paper presented at the Delft3D Users' Meeting, Delft, Netherlands.

Williams, R., Brasington, J., Hicks, D. M., Measures, R., Rennie, C. D., & Vericat, D. (2013). Hydraulic validation of two-dimensional simulations of braided river flow with spatially continuous aDcp data. Manuscript submitted for publication. Aberystwyth University, UK.

Williams, P. A., & Wiser, S. (2004). Determinants of regional and local patterns in the floras of braided riverbeds in New Zealand. *Journal of Biogeography*. *31*(8), 1355-1372. doi: 10.2307/j100638

Wilson, G. H. (2001). National distribution of braided rivers and extent of vegetation colonization. Landcare Research.

Winterbottom, S.J., Gilvear, D.J. (1997). Quantification of channel bed morphology in gravel-bed rivers using airborne multispectral imagery and aerial photography. *Regulated Rivers: Research and Management. 13*(6), 489-499.

Wolman, M. G., 1954. A method of sampling coarse river-bed material. Proceedings from the American Geophysical Union, 35(6), 951-956.

Woolmore, C. 2003: Catalogue of specimens collected in the Upper Waitaki Basin braided river vegetation survey 2002/03. Unpublished Project River Recovery Report 03/01, Department of Conservation, Twizel. (pp. 16).

Woolmore, C., Anderson, S., & Kimber, D. (2008). Project River Recovery annual report 1 July 2007 – 30 June 2008. Unpublished Project River Recovery Report 2007/03, DoC.

Woolmore, C.B.; Anderson, S.A.; Garside, R. (2011). Project River Recovery Annual Report, 1 July 2010 – 30 June 2011. Project River Recovery Report 2011/01, Department of Conservation, Twizel. (pp. 17).

Woolmore, C., & Sanders, M. D. (2005). Project River Recovery strategic plan 2006 – 2012. Unpublished Project River Recovery Report 04/05. DoC, Twizel, New Zealand.

Wu, F. C., Shen, H. W., & Chou, Y. J. (1999). Variation of roughness coefficients for unsubmerged and submerged vegetation. *Journal of Hydraulic Engineering, ASCE, 125*, 934-942.

Wynn, T., & Mostaghimi, S. (2006). The effects of vegetation and soil type on streambank erosion, southwestern Virgina, USA. *Journal of the American Water Resources Association, 42*(1), 69-82. doi: 10.1111/j.1752-1688.2006.tb03824.x

Xylem Inc. (2012). Acoustic Doppler systems for water velocity measurements: RiverSurveyor S5 and M9. Retrieved May, 25, 2013, from http://www.sontek.com/riversurveyor-s5-m9.php